

**THE UNIVERSITY OF  
NOTTINGHAM  
FACULTY OF ENGINEERING**



**Cooling of Advanced Aircraft  
Actuation Systems**

by

***Gareth M. Gilson***, BEng (Hons.)

Thesis submitted to the University of Nottingham for the degree of Doctor of  
Philosophy

**May 2012**

# COPYRIGHT NOTICE

---

1. Copyright of the text of this dissertation rests with the Author. No part of this dissertation may be reproduced in any form or by any means, electronic, mechanical, photocopying, recording or otherwise, without either the permission of the Author or in accordance with the regulations held by the Library of the University of Nottingham. This page must form part of any such copies made.

2. Ownership of the right over any original intellectual property which may be contained in or derived from this dissertation is vested in the University of Nottingham and may not be made available for use by third parties without the written permission of the University, which will prescribe the terms and conditions of any such agreement.



# ABSTRACT

---

Electrical machines for aerospace applications often operate close to the allowable thermal limits due to high power density requirements. The power density of electrical machines is generally dependent on the machine and thermal management design. At flight level, a reduced pressure exists which in turn results in more challenging thermal management. Aerospace electric machine manufacturers are often limited with respect to the implemented cooling mechanisms. That is, natural convection systems are the norm, as fan cooled and fluid cooled machines may suffer from reliability issues.

The original contribution of this work, is the design, testing, and implementation of an alternative forced cooling convective system (*FCCS*) based on piezoelectric fans.

This thesis commences by an investigation of the capabilities of *MotorCAD* (a sophisticated analytical lumped thermal package) and how it can be utilised in a fully integrated way to optimise (for a maximum power density and an overall minimum motor mass) both the electromagnetic and thermal aspects of a typical traditional horizontally-mounted permanent magnet synchronous machine (*PMSM*) operating at flight level. The resultant analytical temperature values were then compared to actual experimental temperature data.

Piezoelectric fans are then investigated as a potential, fault tolerant *FCCS* that may enhance the overall cooling of a motor. These fans could be implemented in the aerospace industry as they do not suffer from the same reliability issues as traditional *FFCS*'s. Detailed thermal results indicating the effective piezoelectric fan cooling range together with the overall cooling effectiveness over a traditional vertical straight-finned heat sink (unit – cell) , operating under different operating conditions are also presented. Furthermore, the

## Abstract

fin/fan geometry that minimises the thermal resistance whilst minimising the overall cooling mass is presented. Particle Image Velocimetry (*PIV*) techniques were implemented to further understand the flow fields generated by an oscillating piezoelectric fan. Common parameters governing the fluid flow (vibration amplitude, separation distance, fin spacing and fan orientation) were investigated and the results are herewith presented.

Designs of a supporting structure for the proposed *FCCS* implementation are drawn up and analysed through *FEA*. A prototype structure was built and its durability tested. Furthermore, the reliability (fault tolerance) of the suggested *FCCS* was evaluated. The feasibility of implementing this innovative cooling technique was further investigated by performing a study on the weight saving potential of the *FCCS* over traditional natural convective fins, and the *FCCS* geometry that minimises the thermal resistance whilst minimising the overall mass is selected. Furthermore, a prototype *FCCS* was built and tested.

# PUBLICATIONS

---

## Published Papers:

1. G. M. Gilson, S. J. Pickering, D. Hann, and C. Gerada, University of Nottingham, "Analysis of the End Winding Heat Transfer variation with Altitude in Electric Motors," in *Industrial Electronics, IECON '09 - 35th Annual Conference of IEEE* Porto, Portugal, 2009, pp. 2545 - 2550.
2. G. M. Gilson, T. Raminosa, S. J. Pickering, C. Gerada, and D. Hann, "A Combined Electromagnetic and Thermal Optimisation of an Aerospace Electric Motor," in *XIX International Conference on Electrical Machines* Rome, Italy, 2010, pp. 1 - 7.
3. G. M. Gilson, S. J. Pickering, C. Gerada, and D. Hann, "High Reliability Piezoelectric Fan Cooling for Electric Machine Thermal Management," in *Power Electronics, Machines and Drives PEMD Conference*, Bristol, UK, 2012

## Submitted Papers:

1. G. M. Gilson, S. J. Pickering, C. Gerada, and D. Hann, "Piezoelectric Fan Cooling: A Novel High Reliability Electric Machine Thermal Management Solution," in *IEEE Transactions*, 2012

# ACKNOWLEDGEMENTS

---

I would first of all like to thank my supervisors, Dr. Stephen Pickering, Dr. Chris Gerada and Dr. David Hann, for their invaluable assistance and guidance during the duration of my *Ph.D.* research, all of whom have been more than willing to share their knowledge and guide me through the past three years. I would also like to thank the University of Nottingham for the use of the Department of Mechanical Engineering facilities, and to the technical staff for their professional support.

The financial support available to the project from *EPSRC* is kindly acknowledged.

I would also like to thank my friends and colleagues who made the duration of my studies here in Nottingham enjoyable and helped to make this a more bearable journey.

Last, but not least, I wish to bestow my special thanks to my parents and Ms. Mireille Sacco for their constant support, love and encouragement during my studies.

# TABLE OF CONTENTS

---

<b>COPYRIGHT NOTICE .....</b>	<b>ii</b>
<b>ABSTRACT.....</b>	<b>iii</b>
<b>PUBLICATIONS .....</b>	<b>v</b>
Published Papers: .....	v
Submitted Papers:.....	v
<b>ACKNOWLEDGEMENTS .....</b>	<b>vi</b>
<b>TABLE OF CONTENTS .....</b>	<b>vii</b>
<b>LIST OF FIGURES .....</b>	<b>xvi</b>
<b>LIST OF TABLES .....</b>	<b>xxxii</b>
<b>NOMENCLATURE.....</b>	<b>xxxiv</b>
Greek Symbols .....	xli
Abbreviations .....	xlii
 <b>CHAPTER 1 .....</b>	 <b>1</b>
 <b>1. Introduction .....</b>	 <b>1</b>
1.1 Construction of an Aerospace <i>PMSM</i> .....	1
1.2 Structure of a Piezoelectric Fan.....	7
1.3 Research and Development Techniques .....	8

1.4 Thesis Structure .....	9
<b>CHAPTER 2 .....</b>	<b>11</b>
<b>2. Literature Review .....</b>	<b>11</b>
2.1 Thermal Modelling of Electric Motors .....	11
2.2 Extended Surfaces (Fins) .....	15
2.3 Piezoelectric Fans .....	26
2.4 Discussion on Published Literature .....	36
<b>CHAPTER 3 .....</b>	<b>38</b>
<b>3. Verification and Validation of Thermal Software - <i>MotorCAD</i> .....</b>	<b>38</b>
3.1 Validation of <i>MotorCAD</i> .....	38
3.1.1 Motor Test Facility .....	39
3.1.2 Experimental vs. Simulated – A Comparative Study .....	45
3.1.2.1 Stall Tests .....	46
3.1.2.2 Variable Load and Speed Tests .....	55
3.2 Verification of <i>MotorCAD</i> .....	57
3.2.1 Modification of End Winding Heat Transfer Correlation .....	58
3.3 Concluding Remarks .....	65
<b>CHAPTER 4 .....</b>	<b>67</b>
<b>4. Motor Finned Housing Optimisation .....</b>	<b>67</b>

4.1 <i>PMSM</i> Finned Housing Geometry Optimisation .....	67
4.1.1 Axial Rectangular Fins .....	69
4.1.2 Radial Fins – Zero Corner-Cutout .....	75
4.1.3 Radial Fins – Variable Corner Cutout .....	77
4.1.4 Comparative Study: Axial Longitudinal Rectangular vs. Radial Fins .....	80
4.2 Concluding Remarks .....	82

## **CHAPTER 5 ..... 83**

<b>5. The Experimental Facility .....</b>	<b>83</b>
5.1 Piezoelectric Fan Structure and Fan Drive Circuitry .....	83
5.2 3D Positioning System .....	88
5.3 Thermal Facility .....	90
5.3.1 Carbon Fibre Heating Elements .....	91
5.3.2 <i>IR</i> Transparent Adjustable Viewing Fin .....	96
5.3.3 Assembled Thermal Test Section .....	97
5.4 <i>PIV</i> Facility .....	99
5.4.1 Velocity Measurements .....	104
5.5 Uncertainty Analysis .....	108
5.5.1 Heat Transfer Coefficients.....	108
5.5.2 Time – Averaged Velocities .....	109
5.6 Concluding Remarks .....	110

## **CHAPTER 6 ..... 111**

### **6. Thermal Measurements ..... 111**

6.1 Heat Transfer Coefficient Derivation.....	111
6.1.2 Constant Heat Flux Surface .....	114
6.1.3 Constant Temperature Surface .....	115
6.2 Horizontally-mounted Piezoelectric Fan.....	116
6.2.1 Fin Base Cooling Results .....	116
6.2.2 Fin Side Wall Cooling Results .....	124
6.3 Vertically Mounted Piezoelectric Fan.....	129
6.3.1 Fin Base Cooling Results .....	129
6.3.2 Fin Side Wall Cooling Results .....	136
6.4 Concluding Remarks .....	140

## **CHAPTER 7 ..... 144**

### **7. Flow Measurements on a Vertical Flat Surface ..... 144**

7.1 PIV Flow Correlations.....	145
7.2 Frequency Characteristics .....	146
7.3 Horizontally-mounted Fan .....	147
7.3.1 Flow Measurements Parallel to a Vertical Flat Surface .....	147
7.3.1.1 Effect of Fan Amplitude ( $V_{Pz}$ ) .....	147
7.3.1.2 Effect of Separation Distance ( $G$ ).....	152
7.3.2 Flow Measurements Perpendicular to a Vertical Flat Surface ..	156
7.3.2.1 Effect of Fan Amplitude ( $V_{Pz}$ ) .....	160
7.3.2.2 Effect of Separation Distance ( $G$ ) .....	163



7.4 Vertically-mounted Fan.....	170
7.5 Further Data Analysis – A Comparative Study.....	173
7.6 Concluding Remarks .....	182

## **CHAPTER 8 ..... 184**

### **8. Flow Measurements for a Finned Geometry ..... 184**

8.1 Horizontally-mounted Fan .....	185
8.1.1 Flow Measurements Parallel to Fin Base .....	185
8.1.1.1 Effect of Fan Amplitude ( $V_{Pz}$ ) .....	185
8.1.1.2 Effect of Separation Distance ( $G$ ) .....	191
8.1.1.3 Effect of Fin Spacing ( $S$ ) .....	193
8.1.2 Flow Measurements Parallel to Fin Side Wall .....	197
8.1.2.1 Effect of Fan Amplitude ( $V_{Pz}$ ) .....	197
8.1.2.2 Effect of Separation Distance ( $G$ ) .....	203
8.1.2.3 Effect of Fin Spacing ( $S$ ) .....	205
8.1.3 Summary.....	207
8.2 Vertically-mounted Fan.....	208
8.2.1 Flow Measurements Parallel to Fin Base .....	208
8.2.1.1 Effect of Fan Amplitude ( $V_{Pz}$ ) .....	208
8.2.1.2 Effect of Separation Distance ( $G$ ) .....	215
8.2.1.3 Effect of Fin Spacing ( $S$ ) .....	219
8.2.2 Flow Measurements Parallel to Fin Side Wall .....	223
8.2.2.1 Effect of Fan Amplitude ( $V_{Pz}$ ) .....	223
8.2.2.1 Effect of Separation Distance ( $G$ ) .....	229
8.2.2.1 Effect of Fin Spacing ( $S$ ) .....	231
8.2.3 Section Summary .....	233
8.3 A Comparative Study .....	234

8.4 Concluding Remarks .....	243
<b>CHAPTER 9 .....</b>	<b>245</b>
<b>9. Implementation of Piezoelectric Fan Array.....</b>	<b>245</b>
9.1 Heat Sink Thermal Resistance Evaluation .....	245
9.1.1 Theory and Calculations .....	246
9.1.2 Thermal Resistance Results - Constant Heat Flux .....	250
9.1.2.1 Effect of Fan Amplitude ( $A_{Pz}$ ).....	250
9.1.2.2 Effect of Separation Distance ( $G$ ).....	252
9.1.2.3 Effect of Fin Spacing ( $S$ ) .....	255
9.1.2.4 Effect of Fan Orientation .....	258
9.1.3 Thermal Resistance Results - Constant Surface Temperature...	259
9.1.4 Summary .....	260
9.2 Weight Saving Characteristics .....	261
9.2.1 Design of Piezoelectric Fan Supporting Structure .....	261
9.2.2 Finite Element Model .....	262
9.3 Combined Analysis – Thermal Resistance / FCCS Weight .....	268
9.3.1 Thermal Resistance Constraint .....	270
9.3.2 Cooling Mass Constraint .....	270
9.3.3 Fin Length (Motor Volume) Constraint .....	271
9.4 Concluding Remarks .....	271
<b>CHAPTER 10 .....</b>	<b>273</b>
<b>10. Conclusions and Recommendations.....</b>	<b>273</b>

10.1 Electric Motor Thermal Modelling .....	273
10.2 Electric Motor Housing Optimisation .....	274
10.3 <i>FCCS</i> Cooling Enhancement Characteristics .....	274
10.4 <i>FCCS</i> Flow Characteristics .....	275
10.5 Implementation of <i>FCCS</i> .....	275
10.6 Contribution of the Thesis .....	276
10.7 Future Work .....	277

## **Appendix A ..... 279**

### **Guidelines for Successful Thermal Modelling - *MotorCAD* ..... 279**

Introduction .....	279
Graphical User Interfaces .....	279
1. Radial and Axial Cross Section Definitions .....	280
2. Winding Definition .....	282
3. Loss Definition .....	283
4. Material Selection .....	285
5. Operating Conditions (Steady State / Transient / Duty Cycles) .....	286
Conclusion .....	289

## **Appendix B ..... 290**

### **Guidelines for Successful *PIV* Measurements..... 290**

Introduction .....	290
<i>PIV</i> Elements .....	290
1. Image Calibration .....	292
2. Seeding of Flow .....	293

3. Illumination.....	295
4. Data Capture and Processing .....	296
Conclusion .....	299
 <b>Appendix C .....</b>	 <b>300</b>
 <b>Guidelines for Successful Finite Element Analysis Modelling .....</b>	 <b>300</b>
Introduction .....	300
Theory.....	301
Conclusion .....	302
 <b>Appendix D .....</b>	 <b>303</b>
 <b>Part Drawings: 24 slot – 20 pole PMSM and Rotating Data Logger.....</b>	 <b>303</b>
 <b>Appendix E .....</b>	 <b>312</b>
 <b>Thermal Calibration Curve .....</b>	 <b>312</b>
 <b>Appendix F.....</b>	 <b>314</b>
 <b>Further PIV Data.....</b>	 <b>314</b>
1. Horizontally-mounted Piezoelectric Fan .....	314
Magnitude of Mean Vectors .....	314
Fin Base 2D Contour Plots (S30, S40, S50, Flat Plate).....	315
Fin Side Wall 2D Contour Plots (S30, S40, S50) .....	319

RMS of Fluctuating Component.....	322
Fin Base (S30, S40, S50, Flat Plate).....	323
Fin Side Wall (S30, S40, S50).....	327
2. Vertically-mounted Piezoelectric Fan .....	330
Magnitude of Mean Vectors Fin Base .....	331
Fin Base (S30, S40, S50, Flat Plate).....	331
Fin Side Wall (S30, S40, S50).....	335
RMS of Fluctuating Component.....	338
Fin Base (S30, S40, S50, Flat Plate).....	338
Fin Side Wall (S30, S40, S50).....	342

<b>REFERENCES.....</b>	<b>345</b>
------------------------	------------

# LIST OF FIGURES

---

Figure 1.1:	Snapshot from commercial software depicting the Magnetic Flux Lines .....	3
Figure 1.2:	Thermal Flow Paths in a <i>PMSM</i> .....	4
Figure 1.3:	Sectioned <i>ProE</i> Model of a Horizontally Mounted <i>PMSM</i> – Axial Longitudinal Fins .....	5
Figure 1.4:	Sectioned <i>ProE</i> Model of a Horizontally Mounted <i>PMSM</i> – Radial Fins .....	6
Figure 1.5:	A $V_{p_z} = 115V$ , $60Hz$ Piezoelectric Fan.....	7
Figure 1.6:	Piezoelectric Fan Operation .....	7
Figure 2.1:	Schematic of a <i>PMSM</i> Thermal Resistance Network in <i>MotorCAD</i> .....	12
Figure 2.2:	Detailed <i>CFD</i> Analysis .....	14
Figure 2.3:	Typical Electric Motor Finned Housing Designs .....	17
Figure 2.4:	Vertical Rectangular Straight Finned Array .....	18
Figure 2.5:	Variation of $Q$ with $L_{Fin}$ at $s_{Fin} = 32.4mm$ and $H = 250mm$ .....	19
Figure 2.6:	Variation of $Q$ against $s_{Fin}$ for various $\Delta T$ states .....	19
Figure 2.7:	Horizontal Rectangular Finned array .....	21
Figure 2.8:	Convection Heat Transfer variation with Fin Spacing for various $\Delta T$ - $L_{Fin} = 6mm$ .....	22
Figure 2.9:	Convection Heat Transfer variation with Fin Spacing for various $\Delta T$ - $L_{Fin} = 16mm$ .....	22

Figure 2.10:	Variation of $s_{Opt}$ with $L_{Fin}$ when the Temperature difference is set at $60^{\circ}C$ .....	22
Figure 2.11:	Schematic of Experimental Setup performed by <i>Yildiz et al.</i> ....	24
Figure 2.12:	Variation of Convection Heat Transfer with Fin Spacing for various $\Delta T$ .....	25
Figure 2.13:	Schematic of different Experimental Orientations .....	29
Figure 2.14:	Experimental Results: .....	30
Figure 2.15:	Experimental 2D Local Heat Transfer Coefficient Contour Plots.....	31
Figure 2.16:	Flow Visualisation .....	32
Figure 2.17:	Piezoelectric Fan Mounting Configuration.....	33
Figure 2.18:	Effect of Fan Pitch on the Convective Heat Transfer Coefficient.....	34
Figure 2.19:	Comparative Study between Two Rotational Fans and a Piezoelectric Fan .....	35
Figure 2.20:	Schematics of possible Piezoelectric Fan Array Implementation .....	37
Figure 3.1:	Experimental Setup of Test Rig.....	39
Figure 3.2:	8 - Channel <i>Comark</i> Data Logger, together with its Specifications .....	40
Figure 3.3:	Axial Finned Housing Thermocouple Locations – Front ( <i>F</i> ), Middle ( <i>M</i> ), End ( <i>E</i> ) .....	41
Figure 3.4:	Rotating Data Logger Assembly System.....	42
Figure 3.5:	Graphical Representation of Rotating Data Logger Assembly.....	42
Figure 3.6:	Data Extraction from Rotating Data Logger.....	43

Figure 3.7:	<i>PM's</i> affixed to Rotor showing Thermal Adhesive and identifying Thermocouple Placement Locations .....	44
Figure 3.8:	Radial cross section view of Rotor .....	44
Figure 3.9:	<i>FFT</i> of a <i>10Nm</i> Stalled Motor.....	46
Figure 3.10:	<i>FFT</i> of a <i>20Nm</i> Stalled Motor.....	46
Figure 3.11:	Temperature profiles of a <i>10Nm</i> Stalled Motor .....	48
Figure 3.12:	Temperature profiles of a <i>15Nm</i> Stalled Motor .....	48
Figure 3.13:	Initial Comparison between Experimental Test Data and simulated <i>MotorCAD</i> Results for a <i>15Nm</i> Stalled Motor ..	49
Figure 3.14:	Comparison between Experimental Test Data and Calibrated <i>MotorCAD</i> Model for a <i>10Nm</i> Stalled Motor ..	52
Figure 3.15:	Comparison between Experimental Test Data and Calibrated <i>MotorCAD</i> Model for a <i>15Nm</i> Stalled Motor ..	52
Figure 3.16:	Axial Finned Housing Temperature Variation - Comparison between Experimental Test Data and Calibrated <i>MotorCAD</i> Model for a <i>15Nm</i> Stalled Motor .....	54
Figure 3.17:	Comparison between Experimental Test Data and Calibrated <i>MotorCAD</i> Model for a <i>PMSM</i> running at <i>20Nm</i> - <i>200rpm</i> .....	56
Figure 3.18:	Thermal Images of: (i) Top and (ii) Bottom of Finned Motor Housing during a <i>20Nm</i> Stalled Test Case .....	57
Figure 3.19:	Schematic of a sectioned <i>PMSM</i> .....	59
Figure 3.20:	Published End Space Correlation Results.....	60
Figure 3.21:	$h_{Ewdg}$ variation between pressure independent correlation (Eq. 3.1) and pressure dependent correlation (Eq. 3.13) for a Stalled Motor.....	64



Figure 3.22:	$h_{EWdg}$ variation between pressure independent correlation (Eq. 3.1) and pressure dependent correlation (Eq. 3.13) for a motor running at $z = 11,500m$ .....	65
Figure 4.1:	Detailed Electric Motor Housing Optimisation Strategy ...	68
Figure 4.2:	Axial Rectangular Finned <i>PMSM</i> Housing.....	69
Figure 4.3:	Sample of Data: Determination of Optimum Housing Geometrical Parameters .....	70
Figure 4.4:	Fin Length ( <i>mm</i> ) vs. Fin Array Thermal Resistance ( <i>K/W</i> ) for several Axial Housing Configurations .....	71
Figure 4.5:	Determination of Optimal Fin Spacing – Axial Fins .....	71
Figure 4.6:	Fin Mass ( <i>kg</i> ) vs. Housing Temperature ( $^{\circ}C$ ) for several Axial Housing Configurations .....	72
Figure 4.7:	<i>ProE</i> model of the considered Radial Finned Housing Geometry.....	75
Figure 4.8:	Optimal Fin Spacing Determination – Radial Finned Housing .....	76
Figure 4.9:	Fin Length ( <i>mm</i> ) vs. Fin Array Thermal Resistance ( <i>K/W</i> ) for a Radial Finned Housing Configuration.....	76
Figure 4.10:	Radial Finned Housing with: .....	77
Figure 4.11:	Definition of the <i>Percentage Corner-Cutout</i> ( <i>%cut</i> ) .....	77
Figure 4.12:	Determination of the Optimal <i>%cut</i> for a Radial Finned Housing: $s_{opt} = 20.0mm$ , $t_{Fin} = 2.0mm$ .....	78
Figure 4.13:	Comparative Study between the different Electric Motor Housing Types: <i>R</i> ( <i>K/W</i> ) vs. $L_{Fin}$ ( <i>mm</i> ) .....	81
Figure 4.14:	Comparative Study between the different Electric Motor Housing Types: $T_H$ ( $^{\circ}C$ ) vs. $m_{Housing}$ ( <i>kg</i> ) .....	81

Figure 5.1:	Piezoelectric Fan Characteristic Dimensions – Courtesy of <i>Piezo Systems INC.</i> .....	84
Figure 5.2:	A High Voltage (V115) Piezoelectric Fan.....	84
Figure 5.3:	Piezoelectric Fan Drive Circuitry and Monitoring Equipment .....	85
Figure 5.4:	Piezoelectric Fan Frequency Characteristics when operating at $V_{Pz} = 115.0V$ .....	86
Figure 5.5:	Piezoelectric Fan Amplitude Characteristics - <i>Sine</i> Input Waveform .....	87
Figure 5.6:	2D Positioning System – Courtesy of <i>Machine Building Systems</i> .....	89
Figure 5.7:	3D Positioning System.....	89
Figure 5.8:	Hollow Wooden Structure .....	91
Figure 5.9:	Heating Element Types [53] .....	91
Figure 5.10:	Heating Element Unit .....	93
Figure 5.11:	Insulated Heating Element Assembly – Top View.....	93
Figure 5.12:	Insulated Heating Assemblies.....	95
Figure 5.13:	Adjustable <i>IR</i> Viewing Fin .....	96
Figure 5.14:	Graphical Representation of Thermal Test Rig .....	97
Figure 5.15:	Finalised Thermal Facility .....	98
Figure 5.16:	Temperature Measurement .....	98
Figure 5.17:	Experimental <i>PIV</i> Setup.....	100
Figure 5.18:	Adjustable Glass Heat Sink implemented during <i>PIV</i> Testing.....	101
Figure 5.19:	Piezoelectric Fan Orientation and Critical Dimensions...	102
Figure 5.20:	Piezoelectric Fan Orientation:.....	104

Figure 5.21:	Laser Sheet Parallel to Fin Base - Capturing Fin Base Velocities .....	105
Figure 5.22:	Laser Sheet Perpendicular to Fin Side Wall - Capturing Fin Side Wall Velocities .....	105
Figure 5.23:	Flow Visualisation - Fin Base – Vertically-mounted Fan	107
Figure 5.24:	Flow Visualization - Fin Side – Vertically-mounted Fan	107
Figure 6.1:	Heat Flux Balance of Heating Assembly .....	112
Figure 6.2:	Parameter Definition of a typical Heating Assembly – Top View .....	113
Figure 6.3:	Fin Base 2D Local Heat Transfer Contour Plots – $S = 50.0\text{mm}$ .....	115
Figure 6.4:	Evaluation of the $FB \%h_{inc}$ for a Horizontally-mounted Piezoelectric Fan: $S30$ .....	118
Figure 6.5:	Evaluation of the $FB \%h_{inc}$ for a Horizontally-mounted Piezoelectric Fan: $S40$ .....	119
Figure 6.6:	Evaluation of the $FB \%h_{inc}$ for a Horizontally-mounted Piezoelectric Fan: $S50$ .....	120
Figure 6.7:	Evaluation of the $FB \%h_{inc}$ for a Horizontally-mounted Piezoelectric Fan: Flat Plate ( $S\infty$ ) .....	121
Figure 6.8:	Evaluation of the Cooling Capabilities ( $\bar{h}$ and $\overline{\%h_{inc}}$ ) for a Horizontally-mounted Piezoelectric Fan - Fin Base .....	122
Figure 6.9:	Evaluation of the $FSW \%h_{inc}$ for a Horizontally-mounted Piezoelectric Fan: $S30$ .....	125
Figure 6.10:	Evaluation of the $FSW \%h_{inc}$ for a Horizontally-mounted Piezoelectric Fan: $S40$ .....	126

Figure 6.11:	Evaluation of the $FSW \%h_{inc.}$ for a Horizontally-mounted Piezoelectric Fan: $S50$ .....	127
Figure 6.12:	Evaluation of the $FB \%h_{inc.}$ for a Vertically-mounted Piezoelectric Fan: $S30$ .....	130
Figure 6.13:	Evaluation of the $FB \%h_{inc.}$ for a Vertically-mounted Piezoelectric Fan: $S40$ .....	131
Figure 6.14:	Evaluation of the $FB \%h_{inc.}$ for a Vertically-mounted Piezoelectric Fan: $S50$ .....	132
Figure 6.15:	Evaluation of the $FB \%h_{inc.}$ for a Vertically-mounted Piezoelectric Fan: Flat Plate ( $S\infty$ ).....	133
Figure 6.16:	Evaluation of the Cooling Capabilities of a Vertically-mounted Piezoelectric Fan: Fin Base.....	135
Figure 6.17:	Evaluation of the $FSW \%h_{inc.}$ for a Vertically-mounted Piezoelectric Fan: $S30$ .....	137
Figure 6.18:	Evaluation of the $FSW \%h_{inc.}$ for a Vertically-mounted Piezoelectric Fan: $S40$ .....	138
Figure 6.19:	Evaluation of the $FSW \%h_{inc.}$ for a Vertically-mounted Piezoelectric Fan: $S50$ .....	139
Figure 6.20:	Fin Base Comparative Study: $S = 30.0mm, G = 5.0mm, V_{Pz} = 115.0V$ .....	141
Figure 6.21:	Fin Side Wall Comparative Study: $S = 50.0mm, G = 15.0mm, V_{Pz} = 115.0V$ .....	142
Figure 7.1:	Spectrum Analysis: $V_{Pz} = 115.0V, G10.0mm$ .....	146
Figure 7.2:	Magnitude of the Mean Velocity Vectors for a Horizontally-mounted Fan, $G = 10.0mm$ : i) $V_{Pz} = 30.00V$ , ii) $V_{Pz} = 60.00V$ , iii) $V_{Pz} = 90.00V$ , iv) $V_{Pz} = 115.0V$ .....	148

Figure 7.3:	<i>RMS</i> of Fluctuating Components for a Horizontally-mounted Fan, $G = 10.0mm$ ; ..... 150
Figure 7.4:	Direct comparison of the Turbulence Intensity for $G = 10.0mm$ : ..... 151
Figure 7.5:	Magnitude of the Mean Vectors - $V_{P_z} = 115.0V$ : ..... 152
Figure 7.6:	<i>RMS</i> values of the Fluctuating Component - $V_{P_z} = 115.0V$ : ..... 153
Figure 7.7:	<i>RMS</i> values of the Fluctuating Component - $V_{P_z} = 115.0V$ : ..... 154
Figure 7.8:	Schematic of Modified Experimental Setup - Top View. 156
Figure 7.9:	Experimental Setup showing Laser Light sheet passing through Fan centreline ..... 156
Figure 7.10:	Transient Flow Field generated by a Horizontally-mounted Fan: $G = 10.0mm, V_{P_z} = 115.0V$ ..... 157
Figure 7.11:	Magnitude of the Mean Vectors by a Horizontally-mounted Fan - $G = 10.0mm, V_{P_z} = 115.0V$ ..... 159
Figure 7.12:	Magnitude of the Mean Vectors for $G = 10.0mm$ and;.... 160
Figure 7.13:	<i>RMS</i> of Fluctuating Components for $G = 10.0mm$ and;.. 162
Figure 7.14:	Magnitude of the Mean Vectors for a fan operating at $V_{P_z} = 115.0V$ ; ..... 163
Figure 7.15:	Evaluation of the $\overline{V_Y}$ component by two distinct setups - $V_{P_z} = 115.0V$ ..... 164
Figure 7.16:	Wake Characteristics - Variation in $\overline{V_Y}$ at different $Y_{pos}$ on applying $V_{P_z} = 115.0V$ : ..... 166
Figure 7.17:	Contour Plots of the <i>RMS</i> values of the Fluctuating Component - $V_{P_z} = 115.0V$ : ..... 168

Figure 7.18:	3D contour plots of a Horizontally-mounted Fan - $G = 10.0mm$ , $V_{Pz} = 115.0V$ :.....	169
Figure 7.19:	Magnitude of the Mean Vectors - $V_{Pz} = 115.0V$ :.....	170
Figure 7.20:	RMS values of the Fluctuating Component - $V_{Pz} = 115.0V$ :.....	171
Figure 7.21:	Flow Obstruction - Vertically-mounted Fan.....	172
Figure 7.22:	Dimensional Analysis of a Horizontally-mounted Piezoelectric Fan.....	174
Figure 7.23:	Comparative Study for a Horizontally-mounted Fan: .....	176
Figure 7.24:	Relationship between the Principal Velocity and the governing Empirical Equation for both a Horizontally and a Vertically-mounted Piezoelectric Fan.....	178
Figure 7.25:	Comparative study between the Principal Velocity and the $\%h_{Inc.}$ for both a Horizontally and a Vertically-mounted Piezoelectric Fan.....	179
Figure 7.26:	Comparative Study between Flow and Thermal Results: $FB$ , Horizontally-mounted Fan $G10.0mm$ $V_{Pz} = 115.0V$ : .....	181
Figure 8.1:	Magnitude of the $FB$ Mean Vectors for $S = 40.0mm$ , $G = 10.0mm$ and;.....	187
Figure 8.2:	$FB$ RMS Fluctuating Components for $S = 40.0mm$ , $G = 10.0mm$ and;.....	189
Figure 8.3:	Direct comparison of the $FB$ Turbulent Intensity for - $S = 40.0mm, G = 10.0mm$ :.....	190
Figure 8.4:	Effect of $G$ on the Magnitude of the Mean Vectors - $V_{Pz} = 115.0V, S = 40.0mm$ : .....	191
Figure 8.5:	Contour Plots of the $FB$ STDV Component - $V_{Pz} = 115.0V, S = 40.0mm$ : .....	192

Figure 8.6:	Magnitude of the <i>FB</i> Mean Vectors - $V_{pz} = 115.0V, G = 10.0mm$ : ..... 194
Figure 8.7:	Contour Plots of the <i>FB RMS</i> values of the Fluctuating Component - $V_{pz} = 115.0V, G = 10.0mm$ : ..... 194
Figure 8.8:	Magnitude of the <i>FSW</i> Mean Vectors for $S = 40.0mm, G = 10.0mm$ and: ..... 198
Figure 8.9:	3D Flow Pattern developed in Vertical Finned Channel . 199
Figure 8.10:	Unsteady Flow generated by Piezoelectric Fan, $S40\ G10.0\ V115.0$ – Front View ..... 200
Figure 8.11:	<i>FSW RMS</i> of Fluctuating Components for $S = 40.0mm, G = 10.0mm$ and; ..... 202
Figure 8.12:	Effect of $G$ on the <i>FSW</i> Magnitude of the Mean Vectors - $V_{pz} = 115.0V, S = 40.0mm$ : ..... 203
Figure 8.13:	Contour Plots of the <i>FSW STDV</i> Component - $V_{pz} = 115.0V, S = 40.0mm$ : ..... 204
Figure 8.14:	Effect of $S$ on the Magnitude of the Mean Vectors: $V_{pz} = 115.0V, G = 10.0mm$ : ..... 205
Figure 8.15:	Effect of $S$ on the <i>FSW</i> Turbulence contour plots - $V_{pz} = 115.0V, G = 10.0mm$ : ..... 206
Figure 8.16:	Magnitude of the <i>FB</i> Mean Vectors for $S = 40.0mm, G = 10.0mm$ and; ..... 210
Figure 8.17:	<i>FB RMS</i> of Fluctuating Components for $S = 40.0mm, G = 10.0mm$ and; ..... 212
Figure 8.18:	Direct comparison of the <i>FB</i> Turbulence Intensity for - $S = 40.0mm, G = 10.0mm$ : ..... 213
Figure 8.19:	Effect of $G$ on the <i>FB</i> Magnitude of the Mean Vectors - $V_{pz} = 115.0V, S = 40.0mm$ : ..... 215

Figure 8.20:	Shedding of Vortices - $S = 40.0mm, G = 5.0mm, V_{Pz} = 115.0V$ .....216
Figure 8.21:	Contour Plots of the <i>FB STDV</i> Component - $V_{Pz} = 115.0V, S = 40.0mm$ : .....218
Figure 8.22:	Magnitude of the <i>FB</i> Mean Vectors - $V_{Pz} = 115.0V, G = 10.0mm$ : .....220
Figure 8.23:	Contour Plots of the <i>FB RMS</i> values of the Fluctuating Component - $V_{Pz} = 115.0V, G = 10.0mm$ : .....220
Figure 8.24:	Magnitude of the <i>FSW</i> Mean Vectors for $S = 40.0mm, G =$ $10.0mm$ and: .....224
Figure 8.25:	Unsteady Flow generated by Piezoelectric Fan on <i>FSW</i> - $S40, G10.0 V_{PZ}=115.0V$ : Front View.....226
Figure 8.26:	Direct comparison of the $\overline{V_z}$ for $S = 40.0mm, G = 10.0mm$ and: .....227
Figure 8.27:	Effect of $G$ on the Magnitude of the Mean Vectors <i>FSW</i> - $V_{Pz} = 115.0V, S = 40.0mm$ : .....229
Figure 8.28:	Contour Plots of the <i>FSW STDV</i> Component - $V_{Pz} = 115.0V, S = 40.0mm$ : .....230
Figure 8.29:	Effect of $S$ on the <i>FSW</i> Magnitude of the Mean Vectors: $V_{Pz} = 115.0V, G = 10.0mm$ : .....231
Figure 8.30:	Effect of $S$ on the <i>FSW</i> Turbulence Intensity contour plots - $V_{Pz} = 115.0V, G = 10.0mm$ : .....232
Figure 8.31:	3D Contour Maps depicting the Magnitude of the Mean Vectors for a <i>Horizontally</i> -mounted Fan operating: $V_{Pz} =$ $115.0V, G = 10.0mm$ .....235
Figure 8.32:	3D Contour Maps depicting the <i>STDV</i> vectors for a <i>Horizontally</i> -mounted Fan: $V_{Pz} = 115.0V, G = 10.0mm$ .236



Figure 8.33:	3D Contour Maps depicting the Magnitude of the Mean Vectors for a <i>Vertically</i> -mounted Fan operating: $V_{P_z} = 115.0V$ , $G = 10.0mm$ .....	238
Figure 8.34:	3D Contour Maps depicting the <i>STDV</i> vectors for a <i>Vertically</i> -mounted Fan: $V_{P_z} = 115.0V$ , $G = 10.0mm$ .....	239
Figure 8.35:	Comarative Study between Flow and Thermal Results: <i>FB</i> , Horizontally-mounted Fan $S = 40.0mm$ , $G = 10.0mm$ $V_{P_z} = 115.0V$ :.....	240
Figure 8.36:	Comarative Study between Flow and Thermal Results: <i>FB</i> , <i>Vertically</i> -mounted Fan $S = 40.0mm$ , $G = 10.0mm$ $V_{P_z} = 115.0V$ :.....	241
Figure 9.1:	Schematic of adopted Experimental Thermal Setup – Top View.....	247
Figure 9.2:	Representative Thermal Model of Fin Unit – Cell – Top View.....	247
Figure 9.3:	Effect of Fan Amplitude ( $A_{P_z}$ ) - Horizontally-mounted Fan, $S = 30mm$ , $G = 10.0mm$ .....	250
Figure 9.4:	Effect of Fan Amplitude ( $A_{P_z}$ ) - <i>Vertically</i> -mounted Fan, $S = 30mm$ , $G = 10.0mm$ .....	251
Figure 9.5:	Effect of the Separation Distance ( $G$ ) on a Horizontally-mounted Fan – $V_{P_z} = 115V$ .....	253
Figure 9.6:	Effect of the Separation Distance ( $G$ ) - <i>Vertically</i> -mounted Fan, $V_{P_z} = 115V$ .....	255
Figure 9.7:	Equivalent Thermal Resistance for a Horizontally-mounted Fan – $G = 10.0mm$ , $V_{P_z} = 115V$ .....	256
Figure 9.8:	Equivalent Thermal Resistance for a <i>Vertically</i> -mounted Fan – $G = 10.0mm$ , $V_{P_z} = 115V$ .....	257

Figure 9.9:	Comparative Study between a Horizontally-mounted and a Vertically-mounted Fan – $G = 10.0mm$ , $V_{Pz} = 115V$ .....	258
Figure 9.10:	Direct Comparison between Constant Heat Flux and Constant Temperature Tests - $V_{Pz} = 115$ .....	259
Figure 9.11:	<i>FEA</i> Modelling of a Piezoelectric Fan.....	264
Figure 9.12:	Piezoelectric Fan and Prototype <i>CFRP</i> Supporting Structure .....	265
Figure 9.13:	Numerical <i>FEA</i> Results - <i>Von Mises</i> Stresses ( <i>MPa</i> ) .....	266
Figure 9.14:	Numerical <i>FEA</i> Results - Displacement ( <i>mm</i> ).....	266
Figure 9.15:	Comparative study between the <i>NC</i> and the <i>FCCS</i> mass for different Fin Spacings .....	267
Figure 9.16:	Thermal Resistance vs. Fin Length vs. Cooling Mass for different S - Horiz Fan, $V_{Pz} = 115V$ .....	269
Figure 9.17:	<i>CFRP FCCS</i> Prototype .....	272
Figure A. 1:	Sample of Possible Motor Geometries and Housing Designs.....	280
Figure A. 2:	Radial Cross Section Graphical Editor .....	281
Figure A. 3:	Axial Cross Section Graphical Editor.....	281
Figure A. 4:	Winding Configuration Graphical Editor .....	282
Figure A. 5:	Losses Tab - Typical Losses for a <i>PMSM</i> .....	283
Figure A. 6:	Schematic of a Voltage Source Inverter (Converter).....	284
Figure A. 7:	Material Component Definition .....	285
Figure A. 8:	Schematic of a Mid Spoiler Flight Actuator when applied a Transient Duty Cycle .....	286
Figure A. 9:	<i>MotorCAD</i> Representative Symbols.....	287
Figure A. 10:	Duty Cycle for a Mid Spoiler Flight Actuator .....	288

Figure A. 11:	Temperature Plot for Imposed Duty Cycle.....	289
Figure B. 1:	Elements of a PIV System .....	291
Figure B. 2:	<i>PIV</i> Components .....	291
Figure B. 3:	<i>PIV</i> Calibration Procedure .....	292
Figure B. 4:	Schematic of <i>PIV</i> – Velocity Extraction.....	294
Figure B. 5:	Seeding Density .....	295
Figure B. 6:	Examples of a typical 2 <i>D</i> Laser Light Sheet .....	296
Figure B. 7:	Cross-Correlation Evaluation results in the Flow Velocity Components .....	297
Figure B. 8:	2 <i>D</i> Contour Map depicting the Mean Flow of an Oscillating Piezoelectric Fan.....	298
Figure D. 1:	Constituting Components of the Fabricated <i>PMSM</i> -Exploded View.....	304
Figure D. 2:	Shaft, Rotor and <i>PM</i> Geometry .....	305
Figure D. 3:	<i>PMSM</i> Stator and Simplified End Winding.....	306
Figure D. 4:	<i>PMSM</i> Winding Configuration .....	307
Figure D. 5:	<i>PMSM</i> Axial Finned Housing.....	308
Figure D. 6:	Rotating Data Logger Assembly.....	309
Figure D. 7:	Part Drawing - Rotating Data Logger Casing.....	310
Figure D. 8:	Part Drawing - Data Logger Locating Cover.....	311
Figure E. 1:	Thermal Calibration Curve .....	313

Figure F. 1:	Magnitude of <i>FB</i> Mean Vectors for a Horizontally-mounted Piezoelectric Fan: $S = 30.0mm$ .....315
Figure F. 2:	Magnitude of <i>FB</i> Mean Vectors for a Horizontally-mounted Piezoelectric Fan: $S = 40.0mm$ .....316
Figure F. 3:	Magnitude of <i>FB</i> Mean Vectors for a Horizontally-mounted Piezoelectric Fan: $S = 50.0mm$ .....317
Figure F. 4:	Magnitude of <i>FB</i> Mean Vectors for a Horizontally-mounted Piezoelectric Fan: Flat Plate ( $S = \infty mm$ ).....318
Figure F. 5:	Magnitude of <i>FSW</i> Mean Vectors for a Horizontally-mounted Piezoelectric Fan: $S = 30.0mm$ .....319
Figure F. 6:	Magnitude of <i>FSW</i> Mean Vectors for a Horizontally-mounted Piezoelectric Fan: $S = 40.0mm$ .....320
Figure F. 7:	Magnitude of <i>FSW</i> Mean Vectors for a Horizontally-mounted Piezoelectric Fan: $S = 50.0mm$ .....321
Figure F. 8:	<i>FB RMS</i> of Fluctuating Component for a Horizontally-mounted Piezoelectric Fan: $S = 30.0mm$ .....323
Figure F. 9:	<i>FB RMS</i> of Fluctuating Component for a Horizontally-mounted Piezoelectric Fan: $S = 40.0mm$ .....324
Figure F. 10:	<i>FB RMS</i> of Fluctuating Component for a Horizontally-mounted Piezoelectric Fan: $S = 50.0mm$ .....325
Figure F. 11:	<i>FB RMS</i> of Fluctuating Component for a Horizontally-mounted Piezoelectric Fan: Flat Plate ( $S = \infty mm$ ).....326
Figure F. 12:	<i>FSW RMS</i> of Fluctuating Component for a Horizontally-mounted Piezoelectric Fan: $S = 30.0mm$ .....327
Figure F. 13:	<i>FSW RMS</i> of Fluctuating Component for a Horizontally-mounted Piezoelectric Fan: $S = 40.0mm$ .....328
Figure F. 14:	<i>FSW RMS</i> of Fluctuating Component for a Horizontally-mounted Piezoelectric Fan: $S = 50.0mm$ .....329

Figure F. 15:	<i>FB</i> Magnitude of Mean Vectors for a Vertically-mounted Piezoelectric Fan: $S = 30.0mm$ .....331
Figure F. 16:	<i>FB</i> Magnitude of Mean Vectors for a Vertically -mounted Piezoelectric Fan: $S = 40.0mm$ .....332
Figure F. 17:	<i>FB</i> Magnitude of Mean Vectors for a Vertically -mounted Piezoelectric Fan: $S = 50.0mm$ .....333
Figure F. 18:	<i>FB</i> Magnitude of Mean Vectors for a Vertically -mounted Piezoelectric Fan: Flat Plate ( $S = \infty mm$ ).....334
Figure F. 19:	<i>FSW</i> Magnitude of Mean Vectors for a Vertically -mounted Piezoelectric Fan: $S = 30.0mm$ .....335
Figure F. 20:	<i>FSW</i> Magnitude of Mean Vectors for a Vertically -mounted Piezoelectric Fan: $S = 40.0mm$ .....336
Figure F. 21:	<i>FSW</i> Magnitude of Mean Vectors for a Vertically -mounted Piezoelectric Fan: $S = 50.0mm$ .....337
Figure F. 22:	<i>FB</i> <i>RMS</i> of Fluctuating Component for a Vertically -mounted Piezoelectric Fan: $S = 30.0mm$ .....338
Figure F. 23:	<i>FB</i> <i>RMS</i> of Fluctuating Component for a Vertically -mounted Piezoelectric Fan: $S = 40.0mm$ .....339
Figure F. 24:	<i>FB</i> <i>RMS</i> of Fluctuating Component for a Vertically -mounted Piezoelectric Fan: $S = 50.0mm$ .....340
Figure F. 25:	<i>FB</i> <i>RMS</i> of Fluctuating Component for a Vertically -mounted Piezoelectric Fan: Flat Plate ( $S = \infty mm$ ).....341
Figure F. 26:	<i>FSW</i> <i>RMS</i> of Fluctuating Component for a Vertically -mounted Piezoelectric Fan: $S = 30.0mm$ .....342
Figure F. 27:	<i>FSW</i> <i>RMS</i> of Fluctuating Component for a Vertically -mounted Piezoelectric Fan: $S = 40.0mm$ .....343
Figure F. 28:	<i>FSW</i> <i>RMS</i> of Fluctuating Component for a Vertically -mounted Piezoelectric Fan: $S = 50.0mm$ .....344

# LIST OF TABLES

---

Table 2.1:	Summary of Results - <i>Kimber et al.</i> .....	34
Table 3.1:	Direct Comparison between the Temperature Rise in the Experimental and Simulated Results for a <i>10Nm</i> Stalled Motor.....	53
Table 3.2:	Direct Comparison between the Temperature Rise in the Experimental and Simulated Results for a <i>15Nm</i> Stalled Motor.....	53
Table 3.3:	Percentage Difference Table - Axial Finned Housing .....	54
Table 3.4:	Published End Space Curve Fit Coefficients .....	59
Table 4.1:	Optimal Housing Geometry on applying a Mass Constraint of <i>1.14kg</i> .....	79
Table 5.1:	Voltage – to – Amplitude Conversion Measurements .....	88
Table 5.2:	Uncertainty Analysis - Horizontally-mounted Piezoelectric fan at $G = 10.0mm$ , $V_{Pz} = 115V$ .....	108
Table 6.1:	Effect of Fin Spacing ( $S$ ) on the $FB$ , $V_{Pz} = 115.0V$ , $G = 5.0mm$ : .....	140
Table 6.2:	Effect of Fin Spacing ( $S$ ) on the $FSW$ , $V_{Pz} = 115.0V$ , $G = 15.0mm$ : .....	142

Table 7.1:	Wake Characteristics Evaluation – Effect of $G$ on the location of the maximum $\overline{V}_Y$ , when $V_{PZ} = 115.0V$ .....	167
Table 8.1:	Peak Velocity Measurements $S = 40.00mm, G = 10.0mm$ .....	- 186
Table 8.2:	Effect of Fin Spacing: $G = 10.0mm, V_{Pz} = 115.0V$ .....	195
Table 8.3:	Effect of Fin Spacing on the Disturbance Area Range ....	196
Table 8.4:	$FSW$ Peak Velocity Measurements $S = 40.00mm, G = 10.0mm$ .....	- 199
Table 8.5:	$FB$ Peak Velocity Measurements $S = 40.00mm, G = 10.0mm$ .....	- 209
Table 8.6:	Effect of Fin Spacing ( $S$ ), $G = 10.0mm, V_{Pz} = 115.0V$ on the $FB$ Velocities.....	221
Table 8.7:	Peak Velocity Measurements $S = 40.00mm, G = 10.0mm$ .....	- 225

# NOMENCLATURE

---

$A$	-	Area	$(m^2)$
$Cu$	-	Copper Winding Area	
$FB$	-	Fin Base Area	
$Fin$	-	Exposed Fin Surface Area	
$FS$	-	Fin Side Wall Area	
$s$	-	Carbon Fibre Mat Exposed Surface Area	
$Slot$	-	Motor Slot Surface Area	
$Total$	-	Total Carbon Fibre Mat Area	
$A', B', C, m, q$	-	Constants	$(-)$
$A_{p-p}$	-	Peak-Peak Piezoelectric Fan Amplitude	$(mm)$
$A_{Pz}$	-	Piezoelectric Fan Vibration Amplitude $= \left( \frac{A_{p-p}}{2} \right)$	$(mm)$
$B_s$	-	Saturation Flux Density	$(T)$
$C$	-	Thermal Capacitance	$(J/K)$
$C_d$	-	Skin Friction Coefficient	$(-)$
$C_F$	-	IR Calibration Correction Factor	$(-)$
$c_p$	-	Specific Heat Capacity at Constant Pressure	$(KJ/kg.K)$
$D$	-	Diameter	$(mm)$
$EWdg$	-	Electric Motor End Winding Diameter	
$F$	-	Electric Motor Outer Finned Diameter	



$H$	-	Electric Motor Housing Diameter	
$P_z$	-	Piezoelectric Fan Hydraulic Diameter	
$R$	-	Electric Motor Rotor Diameter	
$S$	-	Electric Motor Stator Diameter	
$E$	-	Young's Modulus	(Pa)
$f$	-	Frequency	(Hz)
$F$	-	Force	(N)
$Bending$	-	Bending Piezoelectric Fan Force = $\frac{3.A_{P_z}.E.I}{L_{P_z}^3}$	
$Oscillation$	-	Oscillating Piezoelectric Fan Force = $m_{Air}\left(\frac{\delta v}{\delta t}\right)$	
$Total$	-	Total Piezoelectric Fan Force = $F_{Bending} + F_{Oscillation}$	
$g$	-	Acceleration due to Gravity = 9.81	(m/s <sup>2</sup> )
$G$	-	Separation Gap	(mm)
$G_F$	-	$G$ - Force	(m/s <sup>2</sup> )
$Gr$	-	<i>Grashof</i> Number	( - )
$h$	-	Heat Transfer Coefficient	(W/m <sup>2</sup> .K)
$Convection$	-	Convective Heat Transfer Coefficient	
$FB$	-	Fin Base Heat Transfer Coefficient	
$FC$	-	Forced Convection	
$FS$	-	Fin Side Wall Heat Transfer Coefficient	
$NC$	-	Natural Convection	
$Radiation$	-	Radiative Heat Transfer Coefficient	
$H$	-	Fin Array Height	(mm)
$H_C$	-	Coercive Force	(A.m)

$I$	-	Moment of Inertia = $\frac{w_{Pz} \cdot (t_{Pz})^3}{12}$	$(m^4)$
$I_s$	-	Supply Current	$(Amps)$
$k$	-	Thermal Conductivity	$(W/m.K)$
<i>Insulation</i>	-	Thermal Insulation Conductivity	
<i>Tufnol</i>	-	<i>Tufnol</i> Sheet Conductivity	
<i>Wood</i>	-	Supporting Wooden Framework Conductivity	
$k_1, k_2, k_3$	-	Curve Fit Coefficients	$(-)$
$L$	-	Length	$(mm)$
<i>Clamp</i>	-	Piezoelectric Fan Mounting Length	
<i>Fin</i>	-	Fin Length	
<i>Pz</i>	-	Piezoelectric Fan Length	
<i>Motor</i>	-	Electric Motor Housing Axial Length	
<i>Rotor</i>	-	Electric Motor Rotor Axial Length	
<i>Stack</i>	-	Electric Motor Stator Axial Length	
$m$	-	Mass	$(kg)$
<i>Air</i>	-	Mass of Air displaced by fan = $\rho \cdot V_{Displaced}$	
<i>Clamp</i>	-	Mass required to Clamp Piezoelectric Fan	
<i>Fan</i>	-	Mass of Piezoelectric Fan	
<i>FCCS</i>	-	Forced Convective Cooling System Mass	
<i>NC</i>	-	Natural Convection (Finned) Mass	
<i>Structure</i>	-	Piezoelectric Fan Supporting Structure Mass	
<i>Motor</i>	-	Total Electric Motor Mass	
<i>Housing</i>	-	Electric Motor Housing Mass	
$M$	-	Frictional Moment	$(N.mm)$

$M_{Con}$	-	Camera Conversion Factor	(pixel/mm)
$N$	-	Fin Number	( - )
$N_I$	-	Number of Images	( - )
$N_T$	-	Number of Copper Turns	( - )
$N_{Motor}$	-	Motor Rotational Speed $= \frac{120.f}{P_{Motor}}$	(rpm)
$Nu$	-	Nusselt Number	( - )
$P$	-	Power	(W)
$P_{Bearing}$	-	Bearing Power Loss	
$P_{Cu}$	-	Copper Power Loss	
$P_{Hysteresis}$	-	Hysteresis Power Loss	
$P_{Motor}$	-	Total Power Output	
$P_{Windage}$	-	Windage Power Loss	
$P_{Clamp}$	-	Piezoelectric Fan Mounting Pressure	(Pa)
$\bar{P}_{Motor}$	-	Number of Motor Poles	( - )
$p_0$	-	Pressure at Sea level	(Pa)
$p_z$	-	Pressure at Altitude	(Pa)
$Q$	-	Current Loading $= \frac{2.N_T.I_s}{\pi.D}$	(A/m)
$Q$	-	Heat Loss	(W)
$Q_{Cond}$	-	Conductive Heat Loss	
$Q_{FB}$	-	Fin Base Heat Loss	
$Q_{Fin}$	-	Extended Surface (Fin) Heat Loss	
$Q_{FS}$	-	Fin Side Wall Heat Loss	

$S$	-	Supplied Heat	
$Total$	-	Total Heat Loss	
$Q''$	-	Heat Flux	$(W/m^2)$
$R$	-	Electrical Resistance	$(\Omega)$
$R$	-	Thermal Resistance	$(W/K)$
$Conduction$	-	Conduction Thermal Resistance	
$Convection$	-	Convection Thermal Resistance	
$Equivalent$	-	Equivalent Thermal Resistance	
$FB$	-	Fin Base Thermal Resistance	
$Fin$	-	Fin Thermal Resistance	
$FS$	-	Fin Side Wall Thermal Resistance	
$Loss$	-	Thermal Resistance	
$Radiation$	-	Radiation Thermal Resistance	
$Total$	-	Total Resistance	
$R$	-	Radius	$(mm)$
$F$	-	Outer Finned Housing Radius = $\frac{D_F}{2}$	
$H$	-	Housing Radius = $\frac{D_H}{2}$	
$R''$	-	Thermal Resistance Flux = $R.A$	$(K.m^2/W)$
$Ra$	-	Rayleigh Number	$(-)$
$Re$	-	Reynolds Number	$(-)$
$s$	-	Distance	$(m)$
$s_{Fin}, S$	-	Fin Spacing	$(mm)$
$s_{Opt}$	-	Optimal Fin Spacing	$(mm)$

$STDV$	-	$RMS$ of Fluctuating Component $= \sqrt{(V_x')^2 + (V_y')^2}$	(m/s)
$t$	-	Time	(s)
$t$	-	Thickness	(mm)
$Fin$	-	Fin Thickness	
$Insulation$	-	Thermal Insulation Thickness	
$Tufnol$	-	$Tufnol$ Sheet Thickness	
$Wood$	-	Supporting Wooden Framework Thickness	
$T$	-	Temperature	(K)
$Actual$	-	Actual Temperature	
$EWdg$	-	End Winding Temperature	
$M$	-	Magnet Temperature	
$Measured$	-	Measured Temperature	
$S$	-	Exposed Surface Temperature	
$B, FB$	-	Fin Base Temperature	
$FS$	-	Fin Side Wall Temperature	
$\infty$	-	Ambient Temperature	
$V$	-	Velocity	(m/s)
$Mean$	-	Mean Velocity Component	
$RMS$	-	Root Mean Square of Fluctuating Component	
$X$	-	x - direction	
$Y$	-	y - direction	
$V_{Displaced}$	-	Volume of Air displaced by Fan $= A_{Pz} \times L_{Pz} \times w_{Fan}$	(m <sup>3</sup> )
$V_{Motor}$	-	Motor Volume $= \left( \frac{\Pi D^2}{4} \right) L_{Motor}$	(m <sup>3</sup> )

$V_s$	-	Supply Voltage	(Volts)
$\overline{V_x}$	-	Resultant Component of Velocity in $x$ -direction = $\frac{\sum_{N_I} V_x}{N_I}$	(m/s)
$\overline{V_y}$	-	Resultant Component of Velocity in $y$ -direction = $\frac{\sum_{N_I} V_y}{N_I}$	(m/s)
$\overline{V_{Mean}}$	-	Magnitude of the Mean Velocity = $\sqrt{(\overline{V_x})^2 + (\overline{V_y})^2}$	(m/s)
$Var_x$	-	Variance in $x$ -direction = $\frac{\sum_{N_I} (V_x^2)}{N_I} - (\overline{V_x})^2$	(m/s)
$Var_y$	-	Variance in $y$ -direction = $\frac{\sum_{N_I} (V_y^2)}{N_I} - (\overline{V_y})^2$	(m/s)
$V_{RMS}$	-	RMS of Fluctuating Component = $\sqrt{(Var_x) + (Var_y)}$	(m/s)
$vel$	-	Local Fluid Velocity	(m/s)
$w$	-	Rotational Rotor Velocity	(rad/s)
$W$	-	Fin Array Width	(mm)
$w_{Fan}$	-	Piezoelectric Fan Width	(mm)
$w_{Fin}$	-	Fin Width	(mm)
$X_{Pos}$	-	$x$ – coordinate with respect to Piezoelectric Fan	(mm)
$Y_{Pos}$	-	$y$ – coordinate with respect to Piezoelectric Fan	(mm)
$z$	-	Flight Level, <i>Altitude</i>	(m)

## Greek Symbols

$\beta$	-	<i>Grashof</i> Constant	( - )
$\delta v$	-	Change in Piezoelectric Fan Velocity	(m/s)
$\delta t$	-	<i>PIV</i> Sampling Rate	(s)
$\varepsilon$	-	Surface Emissivity	( - )
$\eta_{Fin}$	-	Fin Efficiency	(%)
$\sigma$	-	<i>Stefan Boltzmann's</i> Constant = $5.67 \times 10^{-8}$	(W.m <sup>-2</sup> .K <sup>4</sup> )
$\rho$	-	Density	(kg/m <sup>3</sup> )
$\Gamma_{Clamp}$	-	Clamping Torque = $(m_{Clamp} \cdot g) \cdot (\frac{L_{Clamp}}{2})$	(Nm)
$\Delta T$	-	Temperature Change	(K)
$\Delta t$	-	Separation Time	(s)
$\mu$	-	Dynamic Viscosity	(kg/m.s)
$\nu$	-	Kinematic Viscosity	(m <sup>2</sup> /s)
% <i>cut</i>	-	Percentage Corner Cutout	(%)
% $h_{Inc.}$	-	Percentage Increase in the Heat Transfer Coefficient	(%)

## Abbreviations

<i>CCD</i>	-	Charge Coupled Device
<i>CF</i>	-	Carbon Fibre
<i>CRO</i>	-	Cathode Ray Oscilloscope
<i>CFRP</i>	-	Carbon Fibre Reinforced Polymer
<i>DOE</i>	-	Design of Experiments
<i>EWdg</i>	-	End Winding
<i>FB</i>	-	Fin Base
<i>FCCS</i>	-	Forced Cooling Convection System
<i>FEA</i>	-	Finite Element Analysis
<i>FFT</i>	-	Fast Fourier Transform
<i>FSW</i>	-	Fin Side Wall
<i>IA</i>	-	Interrogation Area
<i>IR</i>	-	Infrared
<i>ISA</i>	-	International Standard Atmosphere
<i>MEA</i>	-	More Electric Aircraft
<i>NIOMT</i>	-	Non Intrusive Optical Measurement Technique
<i>PIV</i>	-	Particle Image Velocimetry
<i>PM</i>	-	Permanent Magnet
<i>PMSM</i>	-	Permanent Magnet Synchronous Machine
<i>PSD</i>	-	Power Spectral Density
<i>PTV</i>	-	Particle Tracking Velocimetry
<i>PZT</i>	-	Lead Zirconium Titanate



<i>RMS</i>	-	Root Mean Square
<i>SFF</i>	-	Slot Fill Factor
<i>STD</i>	-	Standard Deviation
<i>VAC</i>	-	Volts - Alternating Current
<i>VDC</i>	-	Volts - Direct Current
<i>VBA</i>	-	Visual Basic for Applications
<i>VF</i>	-	View Factor (Radiation)

# CHAPTER 1

## 1. Introduction

---

Electric machine thermal management is critical for the correct operation of high power density aerospace electrical machines. However, as the dimensions of electric machines are reduced to minimise weight and volume, the amount of heat generated (due to increased motor losses) increases. This heat must be effectively extracted and transferred away from the critical machine components, in particular the magnets and end windings, by means of effective and reliable cooling technologies.

With the advancements in the more electric aircraft (*MEA*), and the introduction of electric motors to actuate flight control surfaces, the passive cooling technologies used are insufficient to maintain the electric motors at safe operating temperatures.

This means that passively cooled (fins) housings are too bulky, and alone cannot cope with this excessive heat build up. On the other hand, axial fans are too unreliable, and are impractical to implement when considering a stalled motor (as fan is mounted on motor shaft) for the *MEA*. Thus, a new lightweight and reliable fault tolerant forced cooling convection system (*FCCS*) must be developed which is capable of enhancing the cooling of such aerospace motors.

### 1.1 Construction of an Aerospace *PMSM*

The typical components making up a permanent magnet synchronous machine (*PMSM*) are shown in Figure 1.3. Such motors utilise the latest permanent magnet (*PM*) technologies and insulation materials. *PM* are usually

neodymium-iron-boron (*NdFeB*) or samarium-cobalt (*SmCo*) magnets, as these can take the largest magnetic and temperature loading, while insulation materials withstanding up to 220 °C are readily available.

The power output from an electric motor is directly proportional to the torque ( $\Gamma$ ) and the rotational speed ( $\omega$ ) developed by the rotor. The full equation is given by Eq. 1.1. This relation indicates that the output power is a function of the motor volume, airgap flux density, current loading and rotational speed.

$$P_{Motor} = \Gamma \cdot \omega = 2 \cdot V_{Motor} \cdot B_s \cdot Q \cdot \omega \quad \dots \text{Eq. 1.1}$$

The internal heat produced by a motor arises from its associated losses. These losses can be categorised into: (a) mechanical and (b) electrical losses. The mechanical losses constitute the windage losses and the friction (bearing) losses. The windage losses can be evaluated according to [1]:

$$P_{Windage} = \pi \cdot C_d \cdot \rho \cdot L_{Rotor} \cdot \left( \frac{D_R}{2} \right)^4 \cdot \omega^3 \quad \dots \text{Eq. 1.2}$$

while the bearing losses may be represented by:

$$P_{Bearing} = 1.05 \times 10^{-4} \cdot n \cdot (M_{Rolling\_Resistance} + M_{Sliding\_Resistance} + M_{Seal} + M_{Drag}) \quad \dots \text{Eq. 1.3}$$

The copper losses and the iron losses make up the electrical losses. For *PMSM*'s, the copper loss is the dominant loss and acts in the windings of the motor. The copper loss may be evaluated according to the relation:

$$P_{Cu} = 3 I_s^2 \cdot R_{Loss} = 3 I_s^2 \left( \frac{\rho \cdot L}{A} \right) \quad \dots \text{Eq. 1.4}$$

The iron losses may further be segregated into hysteresis and eddy current losses. The former describes the loss attributed to the forcing of a magnetic material (the magnets) around a hysteresis loop and is represented by:

$$P_{Hysteresis} = 4.B_S.H_C.f.\left(\frac{1}{\rho}\right) \quad \dots \text{Eq. 1.5}$$

The eddy current losses are attributed to the generation of eddy currents in the soft iron rotor and are proportional to the square of the frequency. As this magnetic material is rotated in a magnetic field, eddy currents form. These currents are a function of the electrical resistance of the rotor and may be described by:

$$R = \frac{\rho.L}{A} \quad \dots \text{Eq. 1.6}$$

However, it is common practice to evaluate eddy current loss through *FEA*.

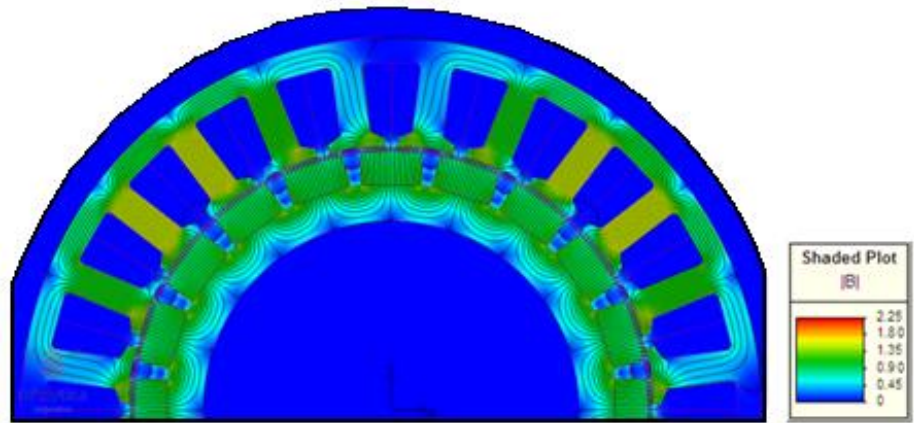


Figure 1.1: Snapshot from commercial software depicting the Magnetic Flux Lines

The heat generated from the numerous motor losses must be transferred to the surroundings as fast and as efficiently as possible. The three mechanisms dictating this heat transfer are; Conduction, Convection and Radiation. *Fourier's* Law of Conduction describes the heat conducted through solids, and for a one-dimensional heat flow scenario in a homogeneous material, the heat loss may be written as:

$$Q = \frac{k.A}{L}.\Delta T \quad \dots \text{Eq. 1.7}$$

Heat transfer from exposed surfaces to the surrounding air is achieved by Convection and Radiation. *Newton's Law of Cooling* describes the heat transfer by convection and is described by *Eq. 1.8* while the heat loss by radiation is described by *Eq. 1.9*.

$$Q = h.A.\Delta T \quad \dots \text{Eq. 1.8}$$

$$Q = \sigma.\varepsilon.A.(T_s^4 - T_\infty^4) \quad \dots \text{Eq. 1.9}$$

Figure 1.2 depicts the primary flow paths present in a *PMSM*. The heat generated by the *EWdg* travels in two distinct flow paths. In the first path, heat is conducted through the copper winding, stator back iron and to the motor housing. This heat is then dissipated by convection and radiation through the finned motor housing to the surrounding air. The second thermal path is that the heat in the *EWdg* is convected and radiated to the surrounding air in the end space. This heat is later dissipated through the motor housing and end cap by convection and radiation as well as to the motor shaft which is dissipated by conduction.

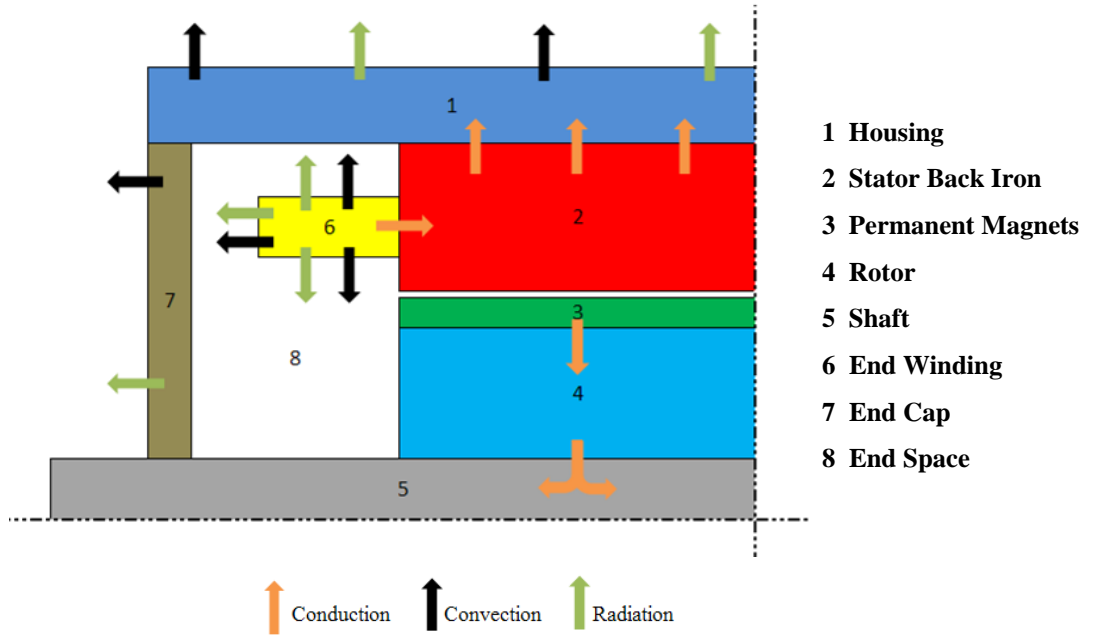


Figure 1.2: Thermal Flow Paths in a *PMSM*

Currently, heat rejection is accomplished passively, by means of fins (extended surfaces) mounted to the motor housing. There exist two main finned housing designs; axial longitudinal fins (Figure 1.3), commonly used in conjunction with blown over machines (contain an axial fan), and radial fins, (Figure 1.4) which are used in a purely natural convection state.

Passive cooling systems are those in which no external energy is required to drive the cooling mechanism. Fins are an example of the latter. On the other hand, active cooling systems require an additional energy input for the cooling to occur, an example being axial fans. A combination of both the passive and active cooling systems is common as it provides an increased overall cooling effect.

However, the aerospace industry is reluctant to utilise axial fans due to their unreliability (bearings) and due to their ineffectiveness during a stalled scenario. Thus, passively cooled motors are normally used. In this work, piezoelectric fans are presented as a viable *FCCS* that may further enhance the overall cooling of a *PMSM* since they do not suffer from the same reliability issues as traditional axial fans.

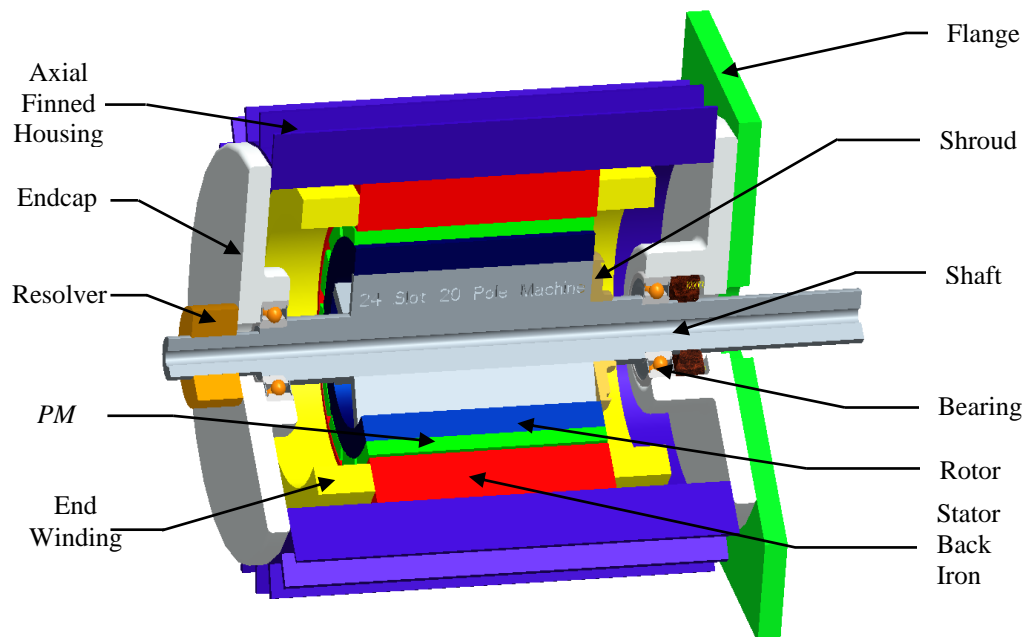


Figure 1.3: Sectioned *ProE* Model of a Horizontally Mounted *PMSM* – Axial Longitudinal Fins

## Introduction

In electric motors the finned housing is responsible for the transfer of heat from the motor to its surroundings by convection and radiation, thus making the fin design of paramount importance.

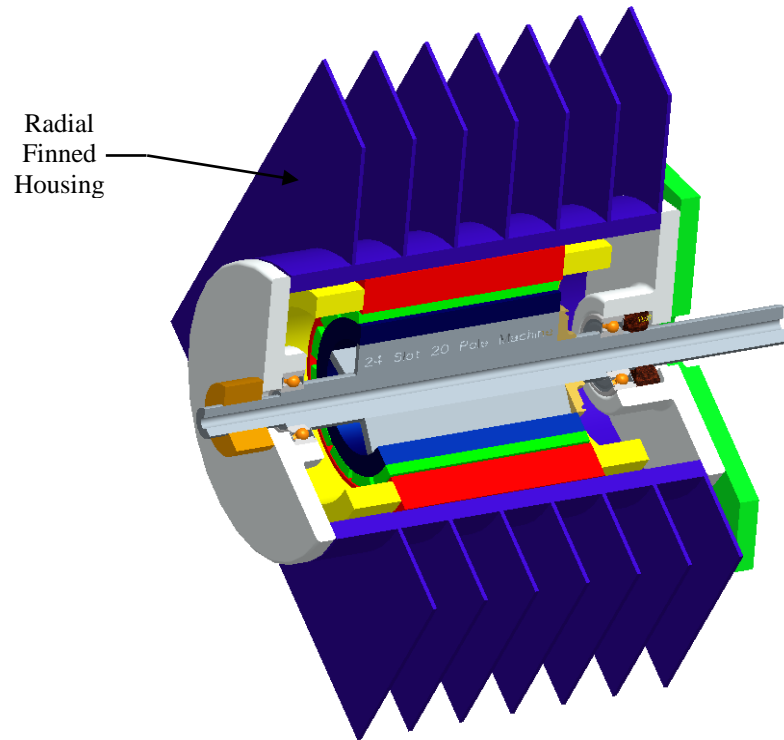


Figure 1.4: Sectioned *ProE* Model of a Horizontally Mounted *PMSM* – Radial Fins

## 1.2 Structure of a Piezoelectric Fan

The simplistic design of a typical piezoelectric fan is illustrated in Figure 1.5. In essence, a piezoelectric fan is fabricated by the bonding of a piezoelectric patch (*PZT*) to a lightweight cantilever beam (made of *Mylar*) – without the presence of any moving parts such as bearings that may be susceptible to wear.

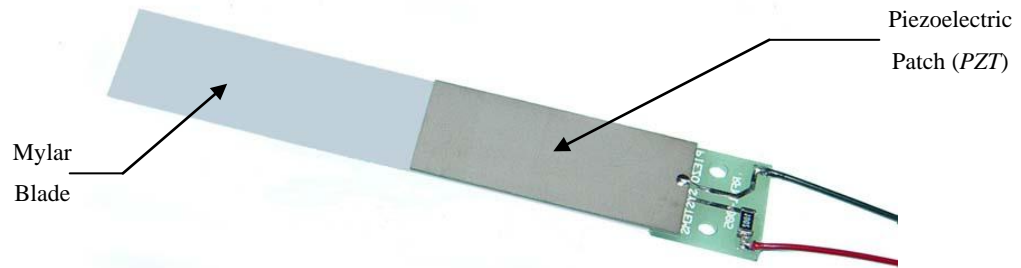


Figure 1.5: A  $V_{Pz} = 115V$ ,  $60Hz$  Piezoelectric Fan

A piezoelectric fan is aptly named as its primary component is a piezoelectric patch which exhibits piezoelectric properties. Piezoelectricity is the coupling between a material's mechanical and electrical behaviours. When a piezoelectric material is subjected to an electric field, the randomly oriented ions go into alignment, which in turn cause a slight deformation of the piezoelectric patch. As the generated displacement is small, piezoelectric patches are commonly compounded with lightweight cantilever beams to further amplify the displacement. Furthermore, on applying an alternating current, the blade vibrates back and forth with the same frequency as the supplied alternating current, thus generating an air flow.

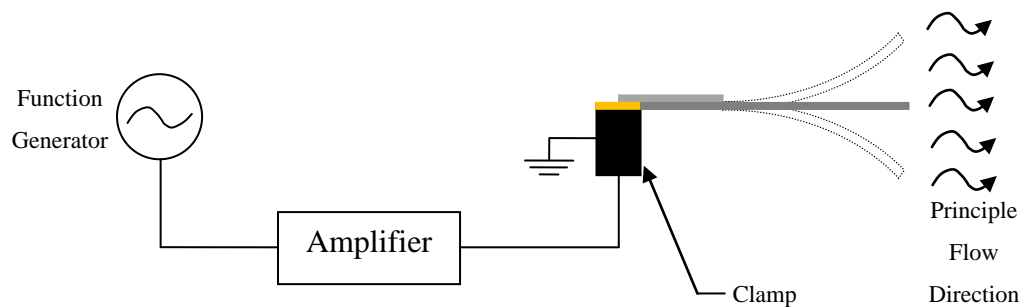


Figure 1.6: Piezoelectric Fan Operation



With any oscillating devices, fatigue may be a limit the device's functionality; however, it has been reported and shall be discussed in further detail (**Chapter 10**), that fatigue is not a limiting factor and is not detrimental to the functionality of piezoelectric fans.

The cooling mechanism involved in this technology is that of acoustic streaming. It has been established that the acoustic streaming velocity is proportional to the displacement amplitude of the vibration wave. Furthermore, it can be shown that the maximum amplitude occurs at a single frequency, better known as the resonant frequency of the piezoelectric fan assembly. Since these fans are driven at resonance, they are designed in such a way that the resonant frequency lies outside the audible human range ( $100\text{Hz}$ ) [2].

In most, if not in all cases, the relationship between amplitude and frequency is highly nonlinear. However, it will be shown that the greater the applied voltage, the larger the vibrational amplitude, the larger the produced fluid mean velocity and thus the larger cooling enhancement.

The small piezoelectric fan mass ( $2.8\text{g}$ ), together with the small fan dimensions, low operational power ( $30\text{mW}$ ) and negligible noise make piezoelectric fans an ideal *FCCS*.

### **1.3 Research and Development Techniques**

The proposed *FCCS* is to implement piezoelectric fans as an innovative cooling mechanism for electric motor finned housings, not to replace the traditional finned housings but to complement them – i.e. to have both fins as well as a piezoelectric fan array to cool the electric motor housing.

The primary objective of this work is to design, fabricate and test an innovative, feasible, reliable, fault tolerant *FCCS* technique, of minimum weight and minimum volume to be implemented on a typical *MEA* commercial aircraft, fully optimised, horizontally - mounted *PMSM*. The said *FCCS* must

be able to withstand all the imposed operating conditions, while maximising performance and lifespan with low maintenance.

The above work can be further reduced into the following sub categories:

1. To verify and validate (by experimentation) an existing thermal modelling software package – *MotorCAD*.
2. To determine an optimised motor geometry based on the combined optimisation of the electromagnetic and thermal designs. The optimised motor housing fin arrangement will be considered as the base case with which the effectiveness of the implemented *FCCS* will be compared.
3. To carry out experimental measurements to determine the thermal enhancement characteristics of the applied *FCCS*.
4. To carry out detailed experimental *NIOMT* to determine the generated flow field characteristics produced by the selected *FCCS*.
5. To implement alternative/innovative *FCCS* and investigate proposed system viability.

## 1.4 Thesis Structure

This thesis is subdivided into ten chapters, followed by an *Appendix*. The review of the relevant literature in this field is presented in *Chapter 2*.

The modelling of a typical aerospace *PMSM* using an analytical lumped thermal package – *MotorCAD* is presented in *Chapter 3*. This chapter also describes the design and manufacture of an experimental rig that was built to validate the *PMSM* representative thermal model and a comparative set of results are presented. Modifications to the software are further presented.

**Chapter 4** incorporates an in-depth fin design methodology with regards to the *PMSM* housing optimisation. A brief explanation of the principle behind the combined optimisation process (i.e. the linking up of the electromagnetic and thermal design aspects) is also presented.

In **Chapter 5**, the thermal facility together with the flow measurement facility are described in detail, while **Chapter 6** goes on to present the findings of the enhancement in heat transfer when implementing piezoelectric fans as alternative *FCCS* when compared to traditional passively cooled vertically oriented fins.

**Chapters 7 and 8** describe the complex *2D* and *3D* flow fields generated by an oscillating piezoelectric fan. The determination of an overall equivalent unit – cell thermal resistance is evaluated and its variation with the critical design parameters are presented in **Chapter 9**. The design of a feasible *FCCS* supporting structure (of minimal weight), together with the manufacture and testing of a complete *FCCS* prototype is also presented. Detailed *FEA* studies were performed to ensure the correct functionality of the supporting piezoelectric fan structure.

General conclusions reached by this work, together with the original contributions in this field, together with some recommendations for possible future advancements in this emerging field are reported in the final chapter, that is **Chapter 10**.

A number of appendices are added at the end of this work for good measure. **Appendix A** and **Appendix B** give a brief insight while offering some practical advice on the good practice afforded when utilising *MotorCAD* and when performing flow measurements using *PIV* respectively. **Appendix C** gives an insight into the *FEA* methodology while, **Appendix D** presents key part drawings implemented in this work. Furthermore, the implemented thermal calibration curve is presented in **Appendix E**, while additional *2D* contour plots complementing **Chapter 7** and **Chapter 8** are presented in **Appendix F**.

# CHAPTER 2

## 2. Literature Review

---

A literature review was conducted which spanned several subject areas, the most relevant of which are documented and presented in this chapter.

This review broadly covers all of the areas of interest, including the thermal modelling and optimisation of electric motors (*Section 2.1*), extended surface (fin) design and optimisation (*Section 2.2*) together with piezoelectric fans as an alternative *FCCS* (*Section 2.3*).

### 2.1 Thermal Modelling of Electric Motors

The design of an electric motor is complex and involves electromagnetic, electrical, stress and thermal analyses to achieve proper motor functionality.

The principal objective of performing a detailed thermal analysis of a motor is that, if successfully performed, the individual motor component temperatures, both under steady state (maximum load applied) and transient conditions (e.g. overloading of motor for a specific period of time) may be evaluated. Ensuring that the critical motor components, such as the permanent magnets (*PM*'s) and the end winding (*EWdg*), do not exceed the allowable operating temperatures is of vital importance. Failure to do so will result in a reduced motor efficiency and machine life.

Over the years, numerous authors have published papers concerning the thermal modelling of electric machines [3-11]. The thermal analysis of an electric motor can be accomplished by a number of methods including: analytical lumped circuit analysis or numerical analysis (*FEA*, *CFD*). The

former analysis encompasses a lumped resistance network method, in which a detailed thermal circuit representing all the heat flow paths in the motor is built and solved, as depicted in Figure 2.1.

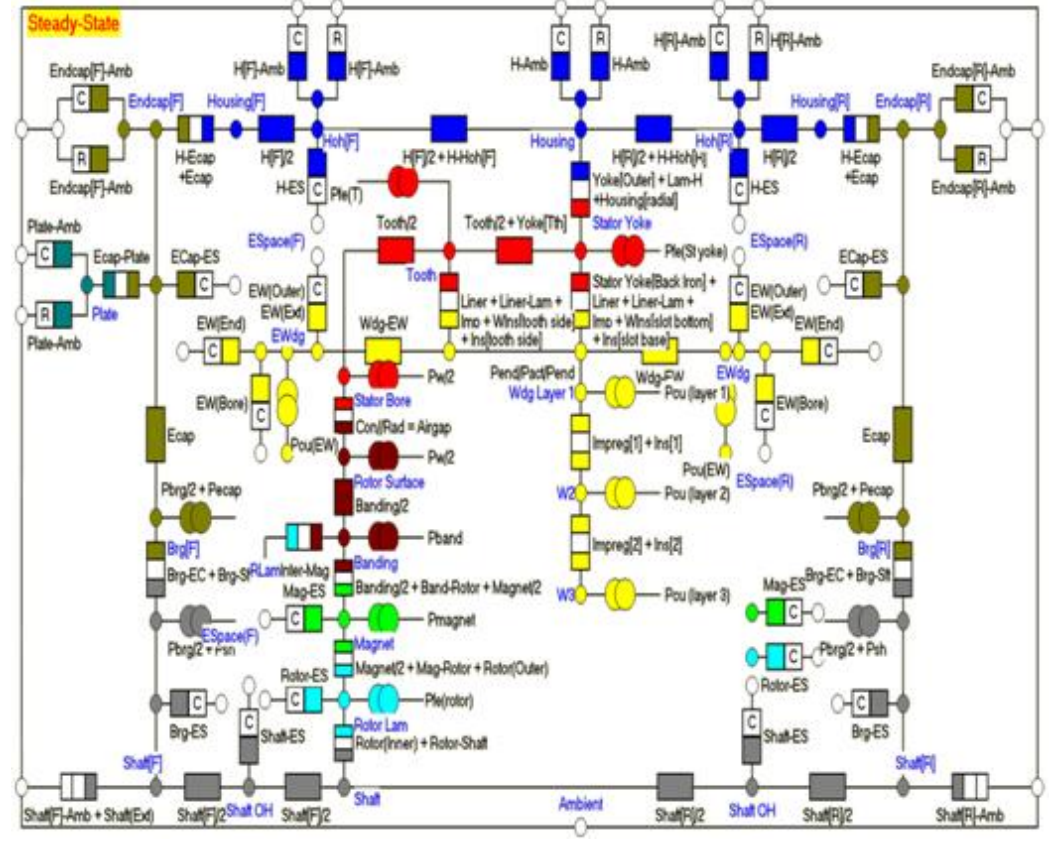


Figure 2.1: Schematic of a PMSM Thermal Resistance Network in *MotorCAD*

This technique employs a network of nodes to represent each of the individual motor components. Each node is connected by both thermal resistances (conduction, convection, radiation) as well as thermal capacitances (for transient operation), the formulations for which are simple to evaluate. The conduction resistance is equal to the path length divided by the product of the path area and the materials' thermal conductivity (Eq. 2.1). On the other hand, the convection (Eq. 2.2) and radiation (Eq. 2.3) resistances are equal to one divided by the product of the surface area and the respective heat transfer coefficient. While the radiation heat transfer coefficient is a function of the individual motor component surface properties ( $\sigma$ ,  $\varepsilon$ ,  $VF$ ), the convection

heat transfer coefficient is based on empirical correlations which are generally readily available in the heat transfer literature such as [12-14].

$$R_{Conduction} = \frac{L}{k.A} \quad \dots \text{Eq. 2.1}$$

$$R_{Convection} = \frac{1}{h.A} \quad \dots \text{Eq. 2.2}$$

$$R_{Radiation} = \frac{T_s - T_\infty}{\sigma.\varepsilon.A.VF.(T_s^4 - T_\infty^4)} \quad \dots \text{Eq. 2.3}$$

Heat sources are further added to the heat generating component nodes (e.g. windings, bearings, windage, etc.) where appropriate. By representing the entire motor as a lumped thermal circuit, it is possible to evaluate the temperatures of each component to a suitable degree of accuracy.

The resistance network is widely used as this method requires minimal computing power whilst giving fast results (for simple analysis with a small number of nodes). The drawback of this method is that motor components are modelled by a single node or just a few nodes. Each node is treated as a homogeneous material, which results in a constant temperature throughout the entirety of the node. To better simulate the reality of the problem, one must increase the number of nodes. However, doing so results in an increase in system complexity, computational time and processing power.

The alternative to the resistance network method described above is the utilisation of numerical techniques. Numerical analysis may be subdivided into two categories: Finite Element Analysis (*FEA*) and Computational Fluid Dynamics (*CFD*).

While *FEA* can generally only be used to model conduction heat transfer in solid components, *CFD* is able to model all heat transfer mechanisms (conduction, convection and radiation). Due to this, *CFD* is primarily implemented in the thermal design of motors as it has the capability of predicting complex flow regimes whilst also being able to evaluate surface heat transfer coefficients [7, 12, 15, 16]. *CFD* techniques solve a set of

coupled, second order, non - linear partial differential equations which satisfy the momentum, energy and continuity equations (*Navier – Stokes* equations). On the contrary to the resistance network, *CFD* techniques demand far greater computational power, and are far more time consuming than the latter. Thus, it is common practice to only model particular regions of electric machines (such as around the *EWdg*'s, or through the air gap) rather than modelling an entire motor in *CFD*. The data obtained from these analyses can then be used as input data for a lumped circuit analysis of the machine as a whole [7].

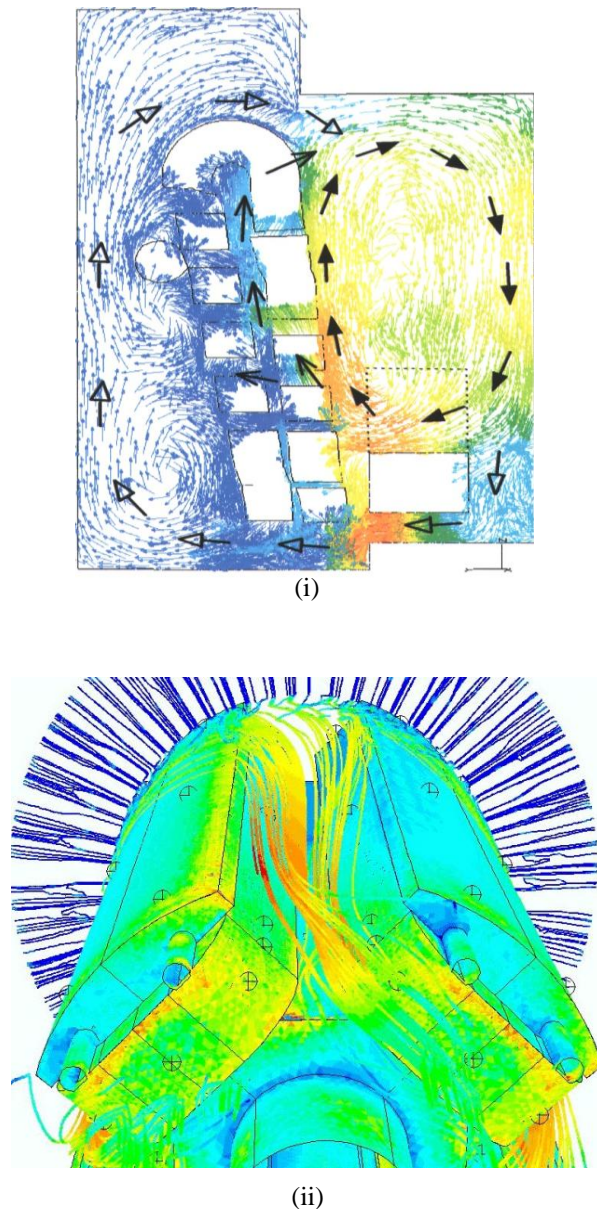


Figure 2.2: Detailed *CFD* Analysis

(i) Flow round the *EWdg* and Wafer of an Induction Motor - *Mugglestone et al.* - 1999

(ii) Velocity Profiles over an entire Electric Motor – *Shanel et al.* - 2003

Detailed resistance network models have great advantages in terms of computational speed, when compared to numerical techniques. The near instantaneous calculation capabilities of the resistance network technique make it possible to run “*what if*” scenarios very quickly. Analytical models also facilitate sensitivity analysis, which help in identifying the critical design components and their affect on the overall thermal performance (i.e. effective interface gaps, impregnation goodness/effectiveness, etc.) of the electric motor [17]. The latter are easily linked up with user *VBA* codes in such a way so as to automate most of the above tedious tasks to easily run several thousands of simulations.

Other strengths of numerical techniques are in the visualisation of flow regimes and in the development of convection formulations. These formulations can then be utilised in the lump-circuit analysis.

## 2.2 Extended Surfaces (Fins)

The operation of many electrical systems (including electric machines) results in the generation of heat. This may cause overheating problems and sometimes, may even lead to system failure. Thus, the heat generated within a system must be dissipated to its surroundings in order to maintain the system operating at its recommended operating temperatures and functioning effectively and reliably [18].

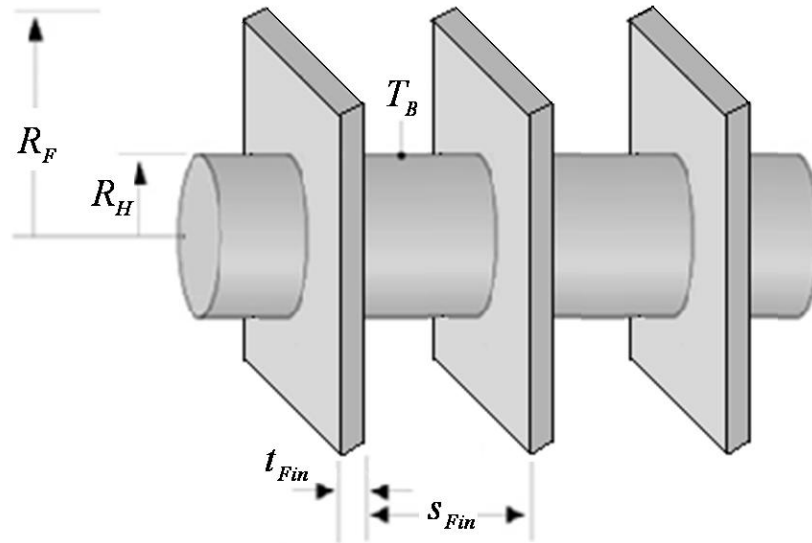
A fin may be described as a highly conductive solid protrusion within which heat transfer by conduction is assumed to be one-dimensional, while heat is transferred by convection and radiation from the exposed fin surface in a direction transverse to that of conduction to the surrounding air. The rate of heat transfer ( $Q_{Fin}$ ) from the fin to its surroundings may be enhanced by either of two methods: (a) An increase in the heat transfer coefficient ( $h$ ) and/or (b) An increase in the fin surface area ( $A_{Fin}$ ). However, it is common practice to alter  $A_{Fin}$ , rather than to increase  $h$ . This is because  $A_{Fin}$  may easily be altered



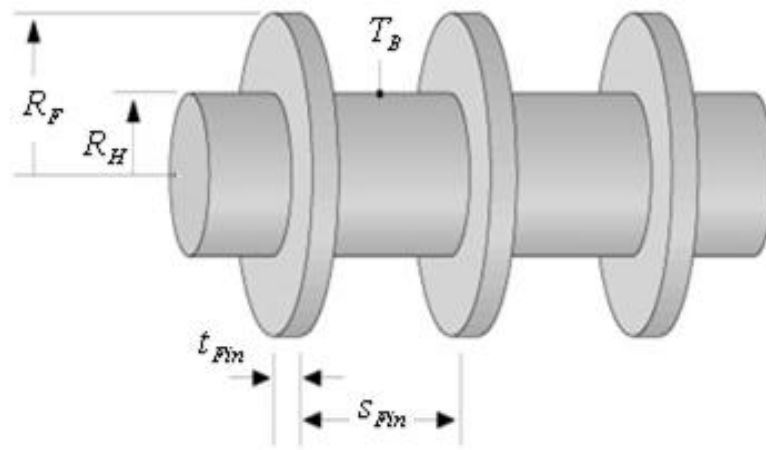
by increasing the fin geometrical parameters ( $L_{Fin}, t_{Fin}, w_{Fin}$ ), whilst an increase in  $h$  implies the use of another fluid (i.e. the use of water or oil rather than air) or a change in the fluid velocity travelling over the exposed surface – i.e. forced convection. Furthermore, when designing a motor finned housing (or any heat sink for that matter), it is of paramount importance to maximise the rate of heat dissipation, while minimising the weight of the cooling arrangement. To accomplish this, it is essential to optimize the fin dimensions ( $L_{Fin}, t_{Fin}, N, s_{Fin}$ ).

Fins are one of the most attractive passive thermal management solutions currently in operation in industry mainly because of their relatively simple design, zero acoustic noise, and generally, simple construction. The utilisation of fins for natural convection enhancement cooling provides a reliable, cheap and widely used method of cooling for dissipating the unwanted heat [19], however, the accurate prediction of heat dissipation requires a solution for complex 3D fluid motion requires *CFD*. In many practical applications there exists a significant temperature drop between the fin and its tip. This variation affects both the natural convection flow as well as the heat transfer. However, scant information is available on the coupling between fin conduction and fluid convection and hence, the fin geometry is traditionally considered to be isothermal [20]. Furthermore, in electrical machines, the finned housing efficiency is taken to be equal to  $\eta_{Fin} = 100\%$  due to the geometry of the manufactured fins (short and thick). However, the fin effectiveness is still accounted for in the calculations.

Two fin geometries commonly implemented in naturally cooled electric machines are; (a) Square finned array's (Figure 2.3i), and (b) Circular/Annular finned arrays (Figure 2.3ii), while axial longitudinal fins are commonly implemented for blown over machines – i.e. forced cooling. In this study, only literature pertaining to the former two finned housing geometries is presented.



(i)



(ii)

Figure 2.3: Typical Electric Motor Finned Housing Designs

(i) Square Finned Housing

(ii) Circular/Annular Finned Housing

There has been much research into natural free-convection from finned surfaces. However, as these finned housings (in particular the square finned housing design) are highly complex to analyse, authors such as [21, 22] have tried to simplify matters by approximating the circular fin base to a vertical flat surface and simply consider longitudinal rectangular fins (Figure 2.4).

While most of the research has been carried out for the latter geometry – i.e. vertical and horizontal finned arrays [18, 19, 23-28], papers based on annular finned housings (Figure 2.3ii) are slowly emerging [29-36].

*Yazicioglu et al.* [18, 19] investigated the steady state natural convection heat transfer from a vertical rectangular aluminium finned array.

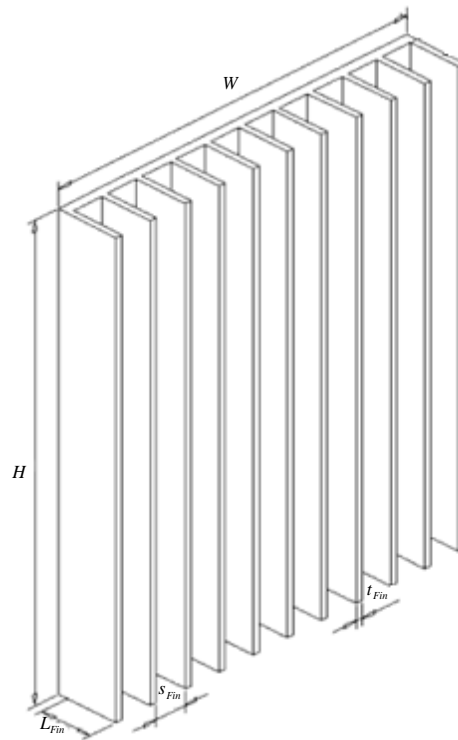


Figure 2.4: Vertical Rectangular Straight Finned Array

The acquired experimental results indicate that higher convective heat transfer rates ( $Q$ ) result with an increase in the fin length ( $L_{Fin}$ ). The authors also report that at low ( $T_B - T_\infty$ ), the increase in convective heat transfer rate with  $L_{Fin}$  is not very significant. However, at higher ( $T_B - T_\infty$ ), the convective heat transfer rate increases significantly with  $L_{Fin}$  (Figure 2.5).

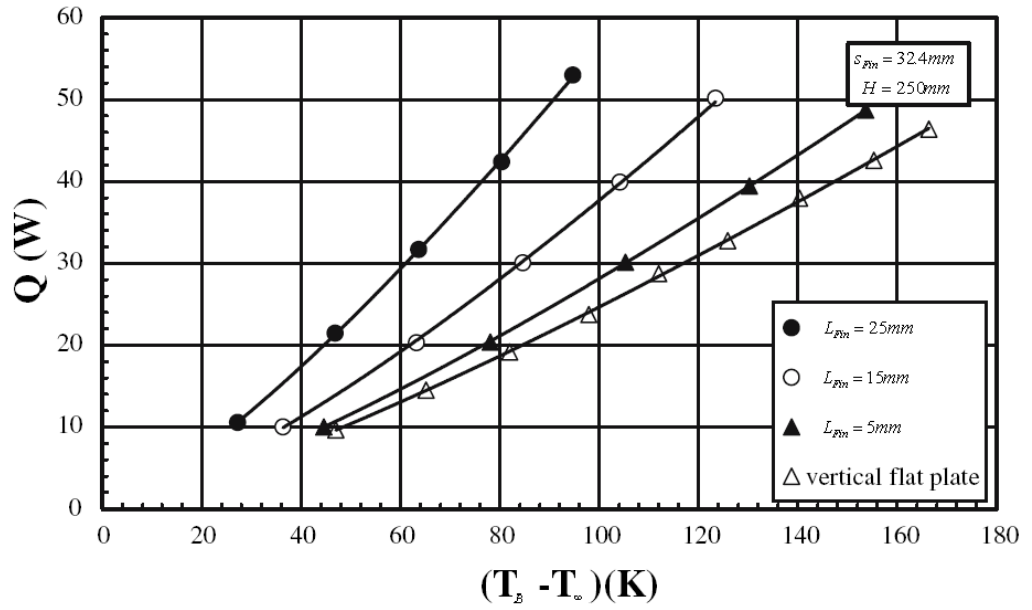


Figure 2.5: Variation of  $Q$  with  $L_{Fin}$  at  $s_{Fin} = 32.4mm$  and  $H = 250mm$

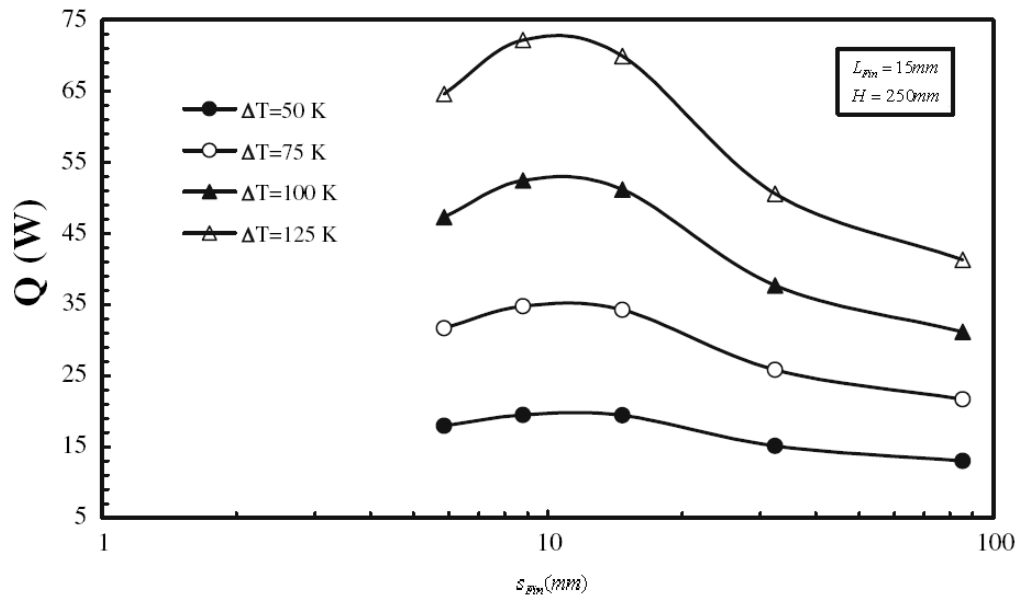


Figure 2.6: Variation of  $Q$  against  $s_{Fin}$  for various  $\Delta T$  states

An optimal fin spacing ( $s_{Opt}$ ) was further established through non-dimensional analysis (Eq. 2.4).

$$s_{Opt} = 3.15H.(Ra_H)^{-1/4} \quad \dots \text{Eq. 2.4}$$

On the other hand, *Jones et al.* [25] performed detailed experimental investigations to evaluate the average heat transfer coefficients from a horizontal finned array. From the collected data, *Jones et al.* derived empirical equations which relate the Nusselt number to the array geometrical parameters. These empirical relations are of the form:

$$Nu_s = 0.00067Gr_s.Pr \left[ 1 - e^{\left( \frac{7460}{Gr_s} . Pr \right)^{0.44}} \right]^{1.7}, \text{ for } s < 50.8mm \quad \dots \text{Eq. 2.5}$$

$$Nu_s = 0.54.(Gr_s.Pr)^{0.25}, \text{ for } s > 50.8mm \quad \dots \text{Eq. 2.6}$$

The above correlations are utilised in *MotorCAD* (an analytical thermal resistance network software package) when evaluating the convective heat lost from the motor finned housing to the surrounding ambient air.

Another paper that investigates the free convection heat transfer from horizontal rectangular finned arrays is that by *Yuncu et al.* [26] published in 1998. In their experiments, 15 different fin configurations ( $L_{Fin}$ ,  $s_{Fin}$ , and  $N$ ) were tested. The fin height  $L_{Fin}$  was varied from 6mm to 26mm while the fin spacing ( $s_{Fin}$ ) was varied from 6.2mm to 83.0mm.

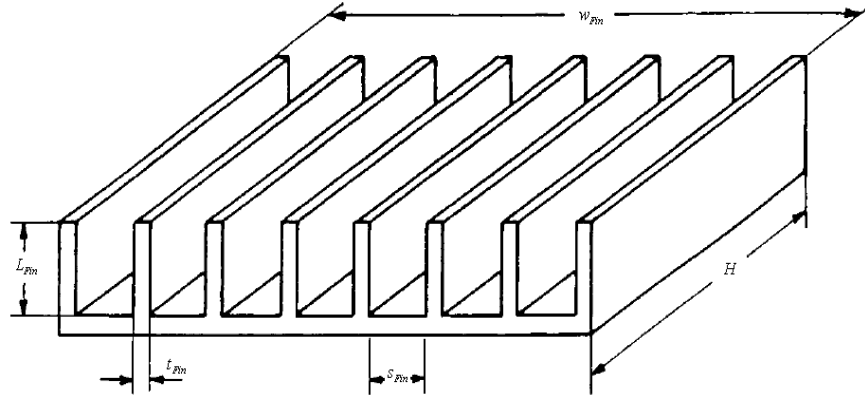


Figure 2.7: Horizontal Rectangular Finned array

It was established that for a given  $(T_B - T_\infty)$ , the enhancement in convection heat transfer rate of the finned array relative to that for a simple horizontal base plate (i.e. no fins) is strongly dependent on the fin spacing to fin length ratio  $(\frac{L_{Fin}}{s_{Fin}})$  as well as the number of fins ( $N$ ).

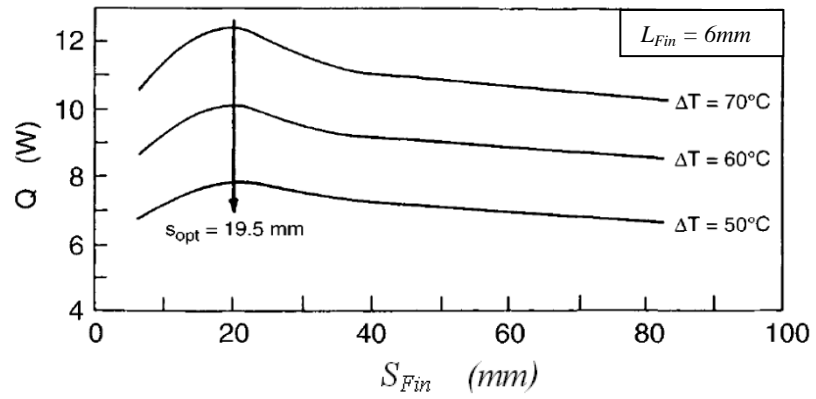


Figure 2.8: Convection Heat Transfer variation with Fin Spacing for various  $\Delta T$  -  $L_{Fin} = 6mm$

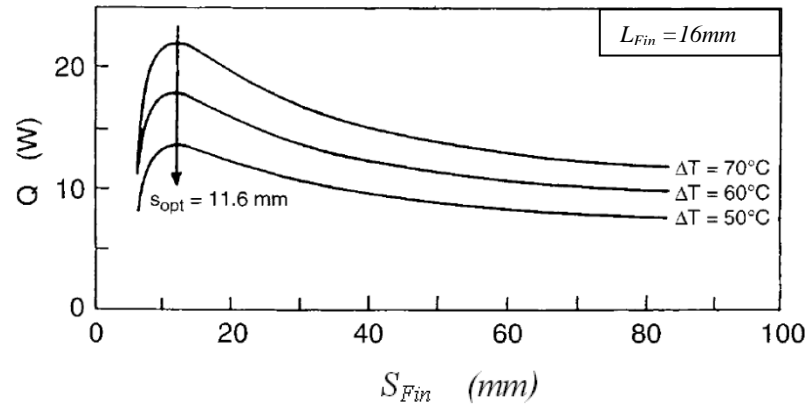


Figure 2.9: Convection Heat Transfer variation with Fin Spacing for various  $\Delta T$  -  $L_{Fin} = 16mm$

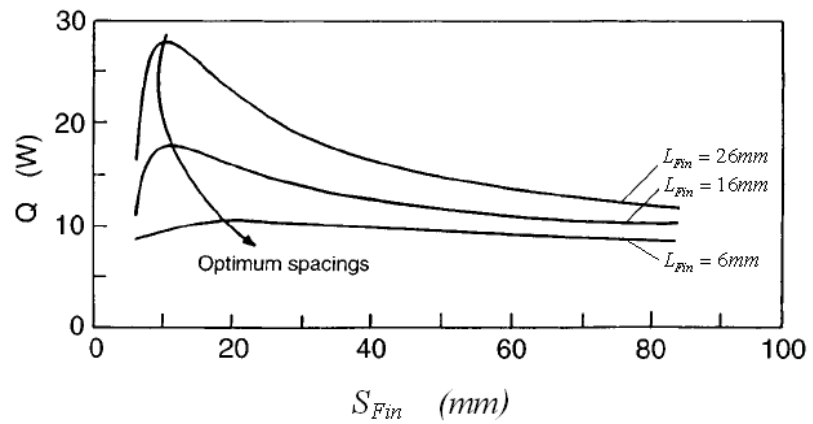


Figure 2.10: Variation of  $s_{Opt}$  with  $L_{Fin}$  when the Temperature difference is set at  $60^\circ C$

The published experimental results indicate that the natural convection heat transfer is governed by  $s_{Fin}$ ,  $L_{Fin}$ ,  $N$ , and  $(T_B - T_\infty)$ . It has also been reported that an increase in the temperature difference  $(T_B - T_\infty)$  results in a monotonous increase in heat transfer (Figure 2.8, Figure 2.9). There also exists an optimum fin spacing ( $s_{Opt}$ ) which is highly dependent on the  $L_{Fin}$ . Selecting the  $s_{Opt}$  results in the highest heat dissipation from the fin array for a given temperature difference. However, selecting any other fin spacing (above or below this optimum fin spacing) results in a reduction in the heat dissipated (Figure 2.10). More importantly, *Yuncu et al.* [26] have shown that, operating the array at a different temperature difference  $(T_B - T_\infty)$  does not shift the location of the  $s_{Opt}$ . Furthermore, the authors concluded that  $s_{Opt}$  decreases with an increase in  $L_{Fin}$  (Figure 2.10).

In 1986, *Yovanovich et al.* [30] investigated the optimisation of annular fins. In this paper, the authors derived two dimensional solutions for circular annular fins of constant cross section having uniform base, and end side conductances. It was observed that the one – dimensional results were accurate when the fin length to thickness ratio ( $\frac{L_{Fin}}{t_{Fin}}$ ) is of the order of 10, or greater. This result agrees with an earlier paper published in 1959, by *Keller et al.* [37]. It was further observed that the two-dimensional results for rectangular fins are useful as approximations to annular fins, when the fin curvature is not significantly large.

*Yildiz et al.* [31], in 2004 published their findings based on heat transfer investigations from annular fins mounted on a horizontal cylinder (Figure 2.11). The utilised experiment consisted of 18 sets of aluminium annular fins mounted to a horizontal cylinder of 24.9mm diameter in ambient atmospheric conditions. While, the fin thickness ( $t_{Fin}$ ) was fixed at 1mm, the fin diameter ( $D_F$ ) was varied from 35mm to 125mm, and the fin spacing ( $s_{Fin}$ ) was varied from 3.6mm to 31.7mm. The base - to - ambient temperature



difference ( $T_B - T_\infty$ ) was also varied by means of a calibrated wattmeter, between 25W to 150W.

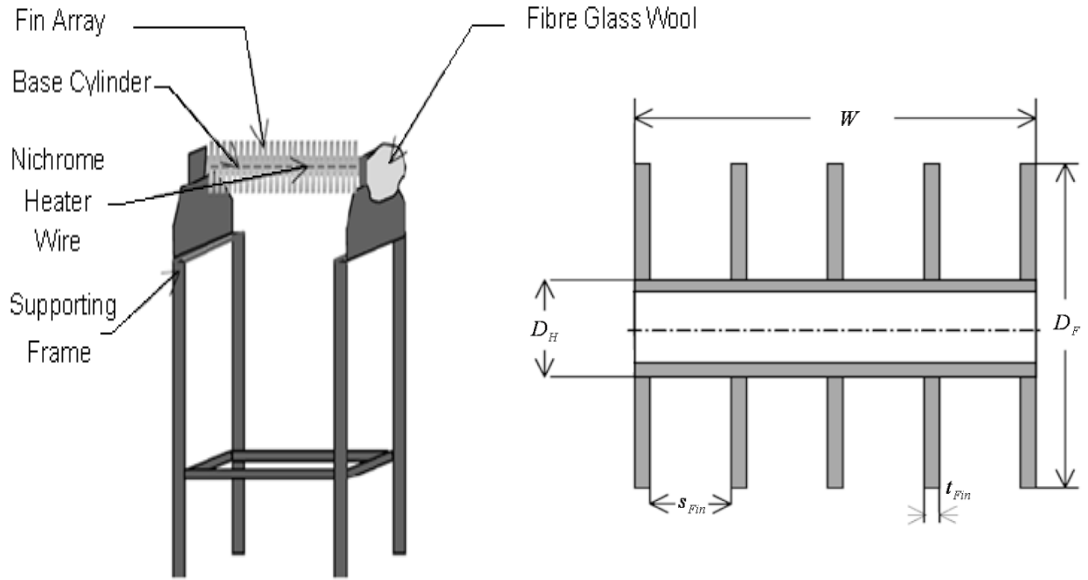


Figure 2.11: Schematic of Experimental Setup performed by Yildiz *et al.*

Throughout their experiments, Yildiz *et al.* considered the radiation effects, and the convective heat dissipated was evaluated by subtracting the radiation loss. The published results (Figure 2.12) indicate that the convection heat transfer rate from annular fin arrays is dependent on: the fin diameter ( $D_F$ ), the fin spacing ( $s_{Fin}$ ) and the base-to-ambient temperature difference ( $T_B - T_\infty$ ). Furthermore, it was established that for every ( $D_F$ ), and a set ( $T_B - T_\infty$ ), there exists an optimum fin spacing ( $s_{Opt}$ ) for which the heat transfer rate from the fin array is maximised.

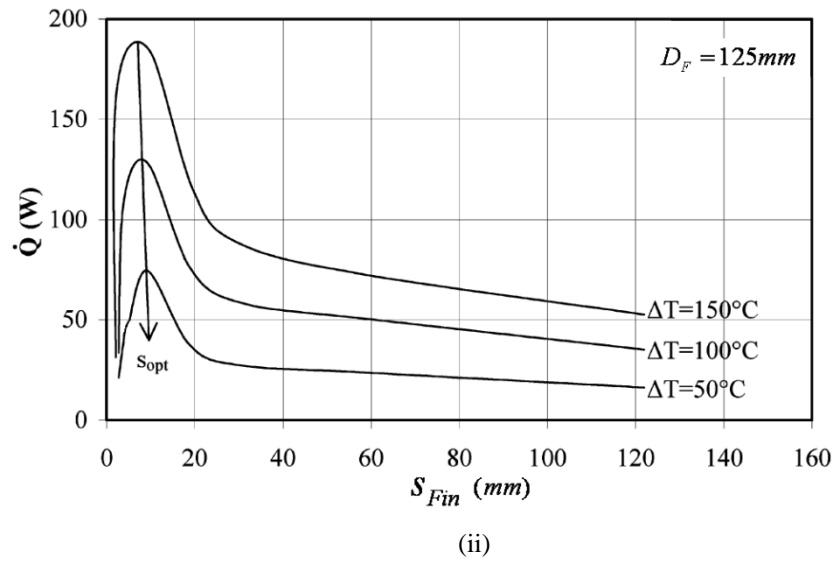
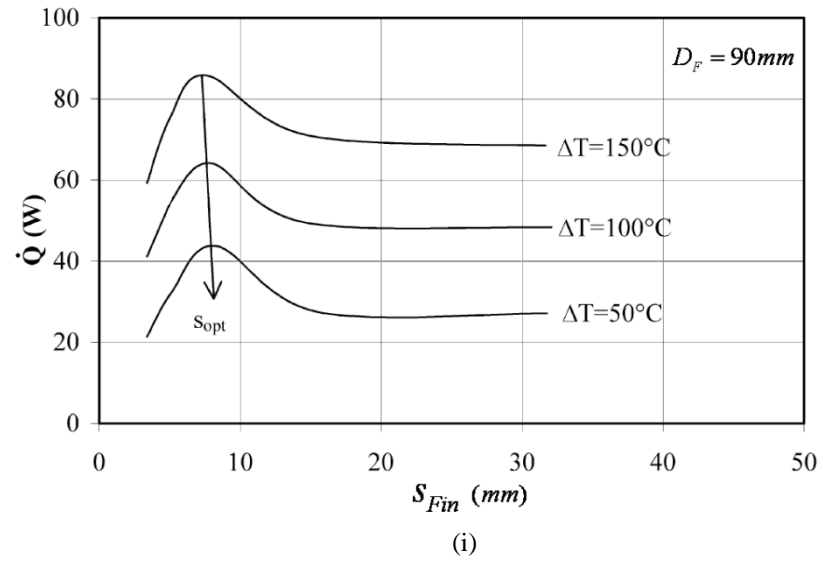


Figure 2.12: Variation of Convection Heat Transfer with Fin Spacing for various  $\Delta T$

(i)  $D_F = 90.0mm$

(ii)  $D_F = 125.0mm$

It was reported that the dissipated heat by convection increases with an increase in fin diameter ( $D_F$ ). Furthermore, at low temperature differences, this increase is not significant whereas the values for convection heat transfer rates are significantly different at higher temperature differences. It is

interesting to note that for all the conducted experiments, initially, the convection heat transfer rate increases with a decreases in  $s_{Fin}$ . However, at a certain value ( $s_{Opt}$ ) the heat dissipated from the array decreases with a decrease in  $s_{Fin}$ . This trend is attributed to the fact that although a reduction in the  $s_{Fin}$  results in an increase in the total finned surface area (and thus theoretically, an increase in the dissipated heat), decreasing the  $s_{Fin}$  below a certain value ( $s_{Opt}$ ) generates a large resistance to the airflow. This airflow resistance results in a reduction in the surface heat transfer coefficients, which in turn results in a reduction in the heat convected away from the array.

The authors concluded that for their geometry and operation conditions, the optimum fin spacing is approximately  $8mm$ . Also, through the use of scale analysis, the authors came up with a relation for the optimal fin spacing which is of the form:

$$s_{Opt} = 3.94D_F.(Ra_D)^{-1/4} \quad \dots \text{Eq. 2.7}$$

Eq. 2.7 is similar to the correlations published by *Yazicioglu et al.* [18, 19] in their correlation for vertical fin arrays (Eq. 2.4). This result further indicates (as reported by [37]), that annular fins may be approximately modelled as straight rectangular fins when the fin curvature is not significantly large.

## 2.3 Piezoelectric Fans

Although the first successful experimental demonstrations of piezoelectric phenomena were first reported in the early 1880's, it was only in the late nineteen seventies [38] that researchers began investigating the prospects of oscillating piezoelectric fans as potential cooling devices. In recent years, the surge in portable electronic devices has generated a renewed interest in the use of piezoelectric fans as a compact, low power, noiseless forced air cooling

technology for applications such as: mobile phones, *PDA*'s, laptop computers, and *DVD* players.

As the electric machine industry develops, higher power density machines are finding their way on the market. Therefore, new, reliable and effective cooling techniques capable of dissipating the generated heat to the surroundings so as to prevent component or even system failure must be developed. Currently, in cooling applications, small rotational fans or small blowers are utilised to increase the bulk fluid motion and cool down the housings of electric motors. However, the weight, space, cost, power and reliability of such axial fans may not be feasible for some of the emerging electric motor applications – such as the *MEA* concept.

It is believed ([39]) that whilst rotary fans may give higher fluid velocities (at a higher power consumption) and thus result in a higher surface heat transfer coefficient, they are inherently unstable. Thus, the scope of this investigation is to evaluate the potential of a piezoelectric fan array, to give an enhancement over natural convection whilst maintaining reliability and overall functionality. The implementation of piezoelectric fans as an alternative forced cooling technique has great potential; however, as yet, not enough is known to fully capitalise on their advantages and to minimise their disadvantages.

Papers highlighting the flow characterisation - the actual flow patterns generated by an oscillating piezoelectric fan, are difficult to come by, whilst papers measuring the *2D* or *3D* flow velocities are virtually non – existent. The first detailed flow visualisation experiments to be performed were those by *Purdue University* in 2003 [40, 41]. Analytical models describing the streaming flow induced by a single vibrating piezoelectric fan were developed. These models exhibit decent qualitative agreement between the predicted flow patterns and experimental visualizations for small fan displacements. *Acikalin* [42] carried out further visualisation experiments on the flow generated by a *50mm* long piezoelectric fan operating at a resonant frequency of *20Hz* and a *40V* voltage yielding a *15.0mm* tip deflection. The fan was placed such that the tip of the fan was placed adjacent to a wall. From the performed transient

analysis, it was concluded that as time passes, vortices of opposite circulation are shed from either side of the fan travelling in opposite directions. Suction was also noted near both the mounting point of the fan and near the blade tip. The authors further indicate that the time averaged flow field generated is symmetric about the fan, and that the maximum fluid rejection velocity is observed slightly before the blade tip and has a value of approximately  $0.3\text{m/s}$ .

*Croucher et al.* [43] produced a paper that uses Particle Image Velocimetry (*PIV*) techniques to physically measure the instantaneous velocities generated by an oscillating piezoelectric fan. In this paper, the authors conduct instantaneous as well as time averaged stereoscopic *PIV* to measure the magnitude and direction of the surrounding flow. Time resolved vector plots are found to indicate a highly complex flow with a downward acting jet for the lower amplitudes ( $Re_a = 356$  and  $1314$ ) while a flow regime variation at the larger amplitude ( $Re_a = 1777$ ) results in an upward acting jet. Instantaneous vector plots indicate the development and periodic nature of the flow throughout a cycle. For all the tested cases, the vortex system was found to be off-axis; this may occur as a result of the initial conditions of the experiment.

*Acikalin et al.* [2] is one of the first authors to report the cooling capabilities of piezoelectric fans. The authors investigate the use of piezoelectric fans in the cooling of electronic components and light emitting diodes (*LED*'s). The effect of varying the fan amplitude ( $A_{P_z}$ ), the distance between the fan and the target heat source ( $G$ ), the fan length, its frequency offset from resonance ( $f$ ), and the fan offset from the centre of the heat source were studied to assess the cooling potential of piezoelectric fans (Figure 2.13).

Through a design - of - experiments (*DOE*) analysis, the authors concluded that the fan frequency offset from resonance ( $f$ ) and the fan amplitude ( $A_{P_z}$ ) are the critical geometrical parameters that have the greatest affect on the cooling capability of piezoelectric fans. The authors reported a convective heat transfer coefficient enhancement ( $\%h_{inc.}$ ) exceeding 375% relative to purely natural convection state (Fan Off). The latter enhancement results in a

temperature drop ( $\Delta T = T_s - T_\infty$ ) at the heat source of more than  $36.4^\circ\text{C}$  from an initial natural convection value of  $70.6^\circ\text{C}$ .

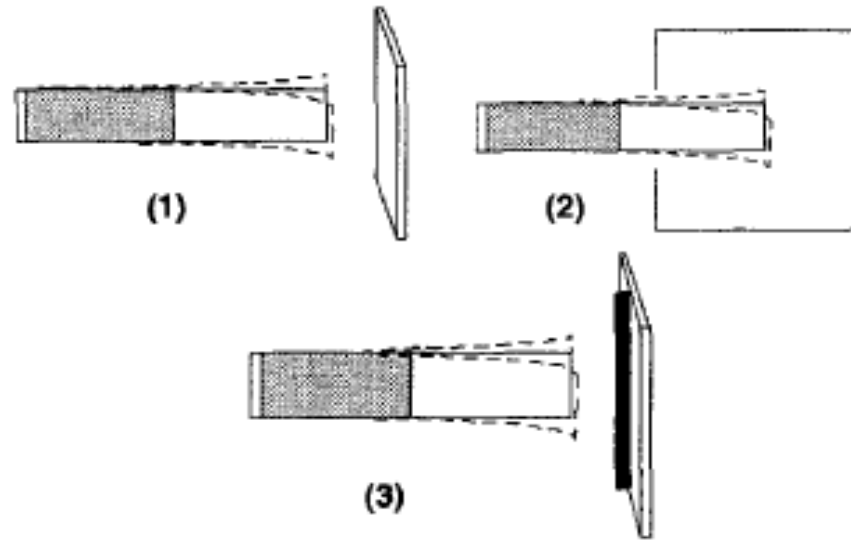
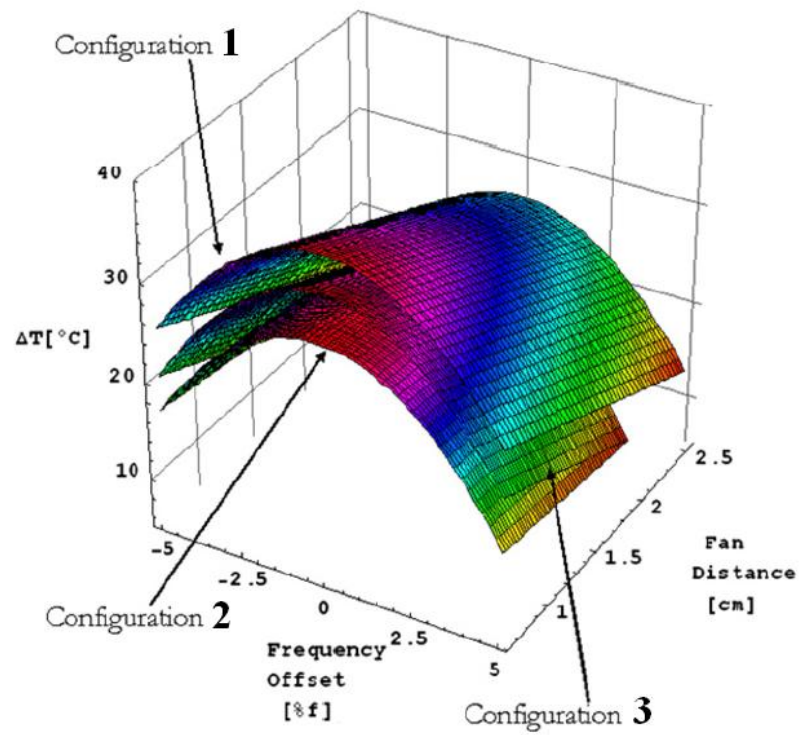


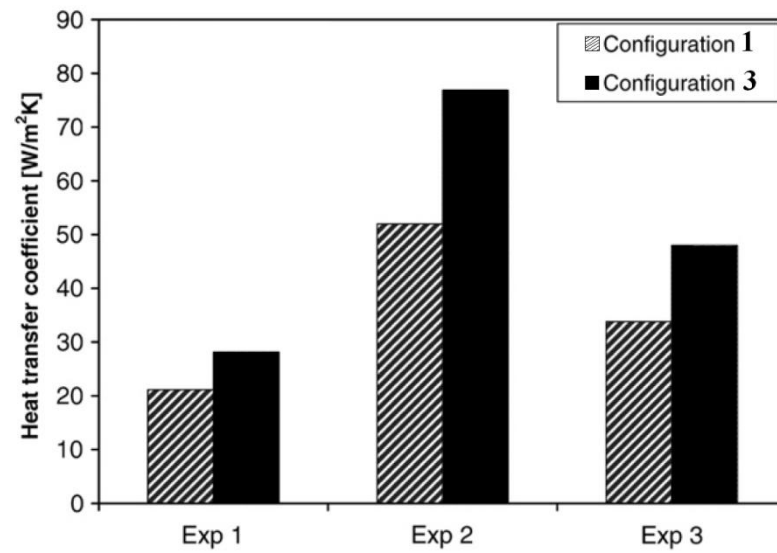
Figure 2.13: Schematic of different Experimental Orientations

(1) Fan in Front      (2) Fan to the Side      (3) Fan in Front with Fin

Figure 2.14i indicates the relationship between the piezoelectric fan orientations and the key parameters tested -  $f$ ,  $G$ , and  $\Delta T$ . The highest temperature differential ( $\Delta T$ ) is generated when implementing fan orientation 1, while the lowest temperature differential ( $\Delta T$ ) results when implementing fan orientation 2. All three fan orientations yield similar frequency dependency characteristics. However, the effect of the fan distance ( $G$ ) on the temperature differential ( $\Delta T$ ) is significantly different for each of the tested orientations - orientations 1 and 3 are more strongly dependent (have a higher slope) on the fan distance than Orientation 2.



(i)



(ii)

Figure 2.14: Experimental Results:

(i) Effect of:  $f$ ,  $G$ , and  $\Delta T$  for the 3 Tested Configurations

(ii) Direct comparison between orientations (1) and (3) for 3 separate runs

Although orientation 3 produces a lower temperature differential than orientation 1, a higher average heat transfer coefficient still results (Figure 2.14ii). This apparent anomaly has been attributed to the fact that in the latter case (orientation 3), a higher input power is required to maintain the heat source temperature at the same constant temperature (due to the increased exposed surface area) as that maintained in orientations 1 and 2. Plotted in this manner (Figure 2.14ii), it is clear that the presence of the oscillating piezoelectric fan and the inclusion of a straight rectangular fin mounted to the vertical surface result in a further enhancement in the heat transfer coefficient.

*Kimber et al.* in their paper [44] perform various heat transfer coefficient measurements on a vertical flat surface. The authors investigated the cooling characteristics of a piezoelectric fan operating at resonance for various different separation distances and various vibration amplitudes.

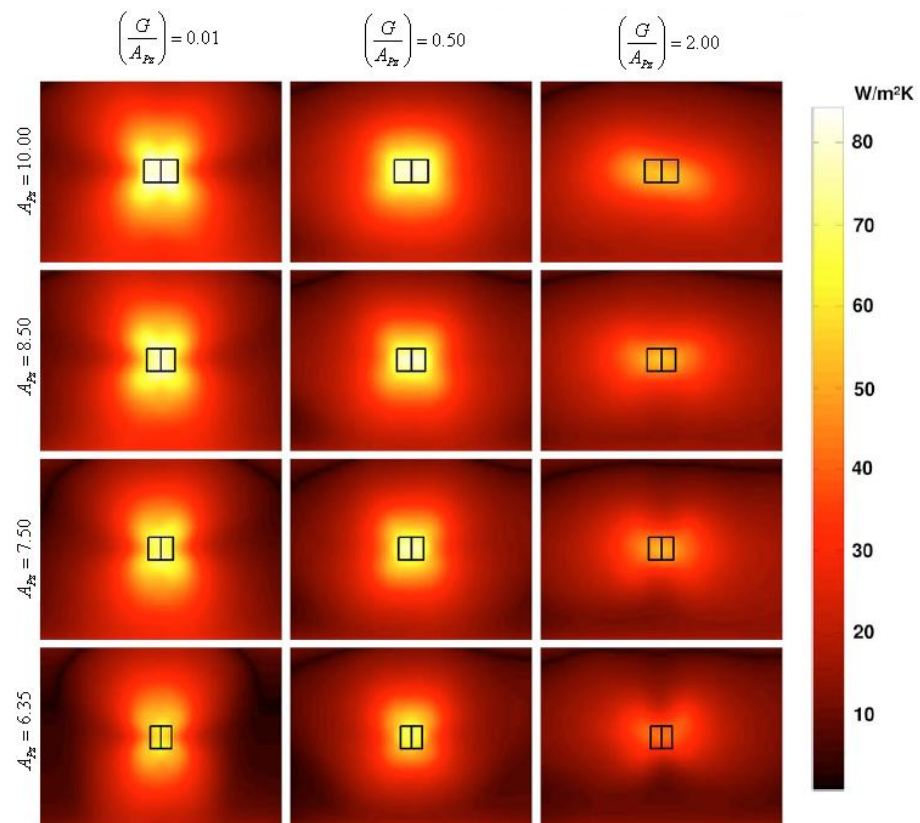


Figure 2.15: Experimental 2D Local Heat Transfer Coefficient Contour Plots



The authors explain how the local heat transfer coefficients 2D plots (Figure 2.15) alter from a lobed shape at small separation gaps ( $G/A_{pz} = 0.01$ ), to an almost circular shape at intermediate gaps ( $G/A_{pz} = 0.50$ ) and to an elliptical shape at even larger separation distances ( $G/A_{pz} = 2.00$ ).

Wait *et al.* [45] considered the performance of piezoelectric fans operating at higher resonance modes (i.e. not operating at resonance frequency). Experiments were performed on a number of commercially available piezoelectric fans of varying length. Both finite element modelling and experimental impedance measurements were used to demonstrate that the electromechanical energy conversion in certain modes is greater than in the first bending mode.

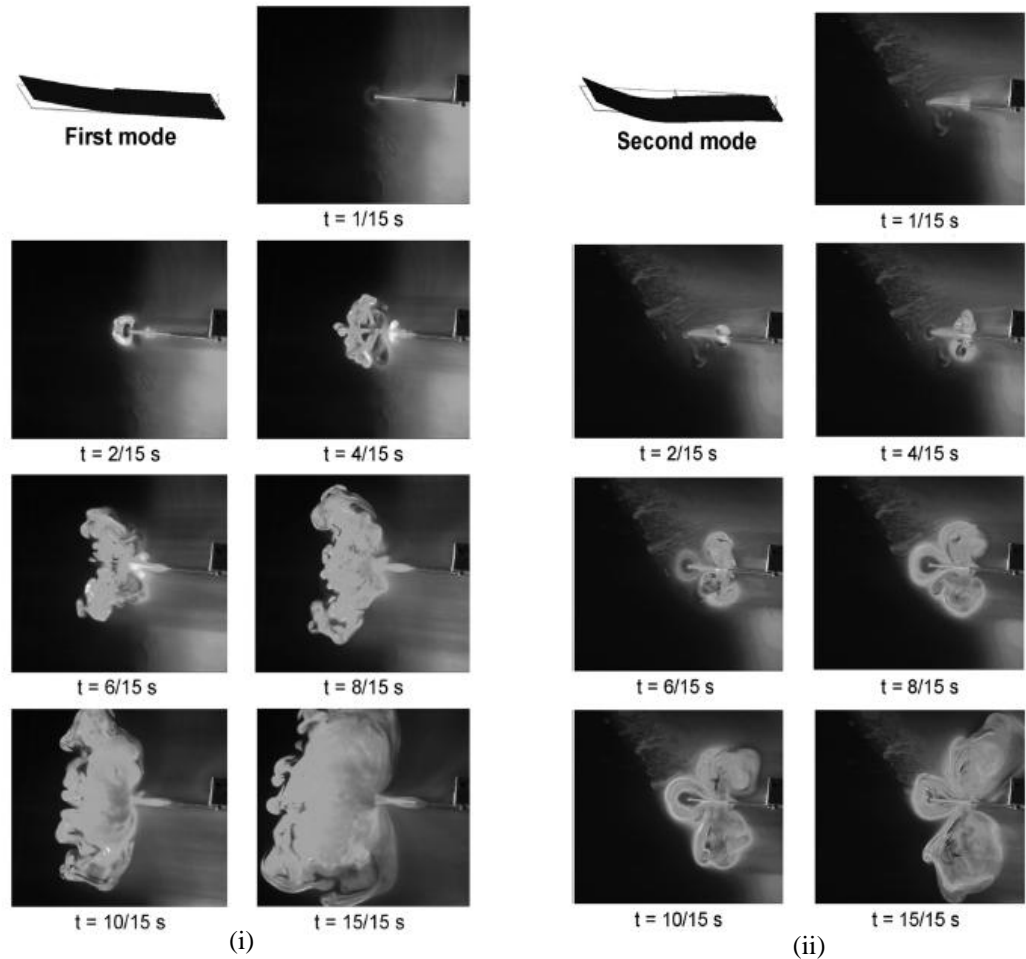


Figure 2.16: Flow Visualisation

(i) First Mode Operation – Fundamental Resonant Frequency =  $90.3\text{Hz}$

(ii) Second Mode Operation – Fundamental Resonant Frequency =  $252.5\text{Hz}$

Detailed flow visualization experiments (Figure 2.16) were also performed to better understand the transient and steady-state fluidic motion generated by piezoelectric fans. Results indicate the flow complexity together with the unsteady *3D* nature of the fluid flow. However, it was concluded that certain advantages of piezoelectric fan operating at higher resonance modes are offset by increased power consumption and decreased fluid flow.

Other authors, namely *Chung et al.* [46] and *Kimber et al.* [47] have experimented with a combination of two or more piezoelectric fans, better known as coupled piezoelectric fans. From the conducted experimental results, it has been established that maximum cooling occurs when the interspacing distance between the piezofans is equal to the distance of the piezoelectric fans from the surface to be cooled [48]. Furthermore, *Kimber et al.* in the series of papers [47, 49] wrote about the results obtained after they conducted numerous experiments to characterize the thermal performance of coupled piezoelectric fans. Two coupled fan orientations; horizontal (Figure 2.17i) and vertical (Figure 2.17ii) were considered and the improvement observed relative to a single fan reported in Table 2.1.

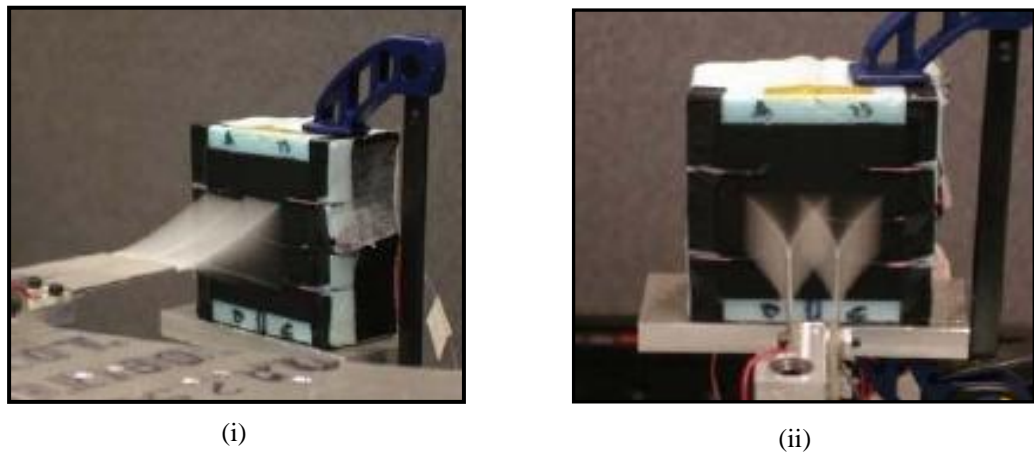


Figure 2.17: Piezoelectric Fan Mounting Configuration

(i) Horizontally-mounted – Vertical Vibration

(ii) Vertically-mounted – Horizontal Vibration

Configuration	Best Case Heat Transfer Convection ( $W/m^2.K$ )
Natural Convection	16.18
Single Fan	88.03
Coupled Vertical Fans	106.51
Coupled Horizontal Fan	104.46

Table 2.1: Summary of Results - Kimber *et al.*

Throughout the duration of the experiment, an input power of  $1.6W$  was supplied to heat up a  $38.1mm \times 38.1mm$  target surface area. The experimental results indicate a significant increase in the heat transfer coefficient on application of a single oscillating piezoelectric fan. A further increase is noted on the utilisation of a coupled piezoelectric fan. Numerically, the utilisation of a coupled fan results in a 650% increase in the heat transfer coefficient over natural convection and a further 19 – 21% increase over the use of a single fan.

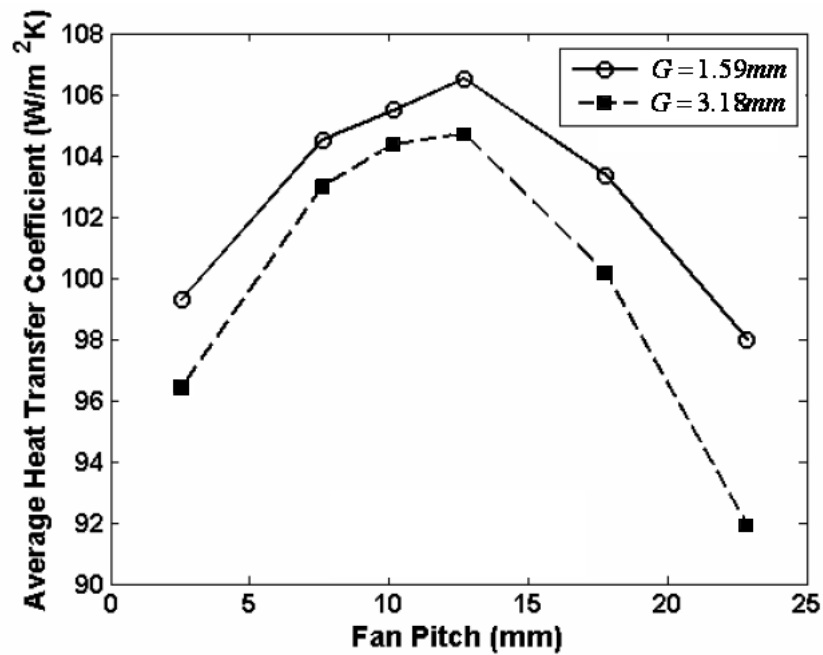


Figure 2.18: Effect of Fan Pitch on the Convective Heat Transfer Coefficient

The authors further investigated the dynamic coupling between the two piezoelectric fans (Figure 2.18). The heat transfer experiments conducted suggest that, two fans vibrating in such close proximity influence the vibration characteristics of the pair and hence the thermal performance. This in turn results in an optimum fin pitch which is in itself independent of the separation distance  $G$  as depicted in Figure 2.18.

In [50], the piezoelectric fan suppliers identify that the fatigue life of the aforementioned structure is difficult to quantify. However, a fan has been running continuously and under observation since 1982.

Another paper of significant interest is that of *Acikalin et al.* [39]. This paper describes how the authors conducted comparative studies between an oscillating piezoelectric fan and two commercially available axial fans.

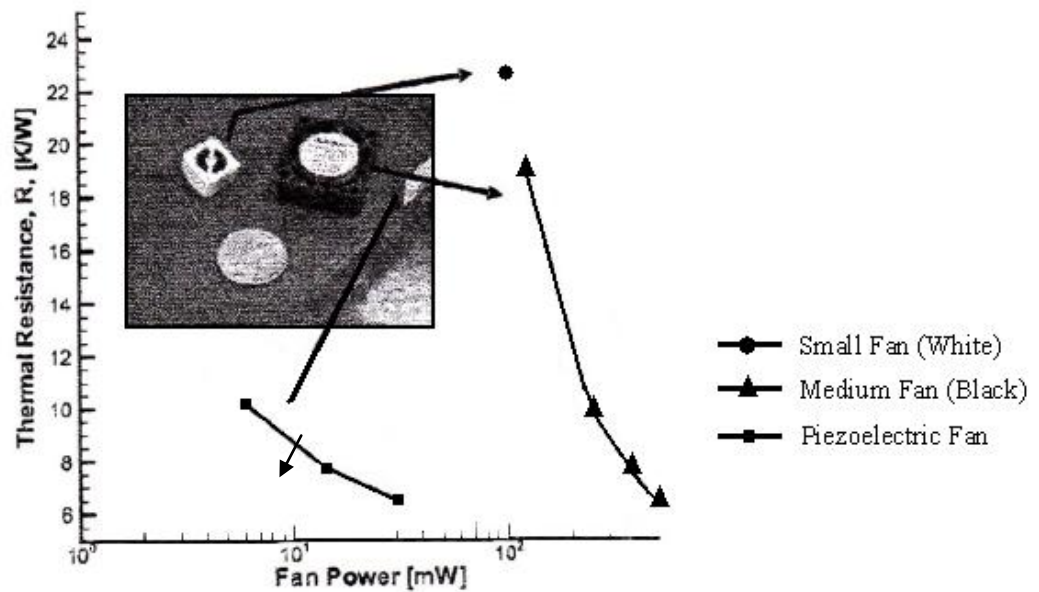


Figure 2.19: Comparative Study between Two Rotational Fans and a Piezoelectric Fan

Figure 2.19 demonstrates that the tested piezoelectric fan performs as well as the larger axial fan, while drawing only a fraction of the power required by the larger axial fan ( $31mW$  vs.  $500mW$ ). This is attributed to the mechanical losses present in the axial fans (bearing loss) being much larger than any losses present in the operation of the piezoelectric fan. Results indicate that piezoelectric fans outperform axial fans both in terms of power consumption as well as cooling volume.

## **2.4 Discussion on Published Literature**

Axial fans may not be implemented in the aerospace industry to cool electric motors due to their cooling ineffectiveness in a stalled scenario. Furthermore, current passive cooling (fins) techniques are solely incapable of limiting the excess heat build up experienced by motor critical components, as the fin area required to cool such motors solely by natural convection is too large, bulky and costly (\$165 per unit) to accommodate the aerospace industry.

Piezoelectric fans have been reported to significantly enhance the surface heat transfer coefficient by as much as 375% over a purely natural convection state. Furthermore, while these fans are ideally suited for the microelectronic industry, this technology has not been applied to larger systems such as electric motor housings and thus its potential in this field is as yet untested. Most, if not all authors, agree that the major advantages of piezoelectric fans are the overall noise, power consumption, weight and volume reduction. While the current cost of piezoelectric fan might still be an issue for some sectors, with the further advancement of this technology throughout the coming years this cost will be significantly reduced.

As shown in the literature survey, results pertaining to the cooling effectiveness of piezoelectric fins on flat surfaces are readily available; however, as yet there has been no publications pertaining to the cooling effectiveness of these miniature fans in conjunction with finned arrays and it is to this effect that this work has been carried out. As previously discussed, the proposed idea is to combine the electric motor finned housings together with a piezoelectric fan array. One such possible horizontal and vertical piezoelectric fan array layout is illustrated by Figure 2.20. This in turn may lead to an overall weight reduction in the electrical machine cooling arrangement. Since no literature was found relating to this (and thus the scope of this work), it was decided to pursue this route.

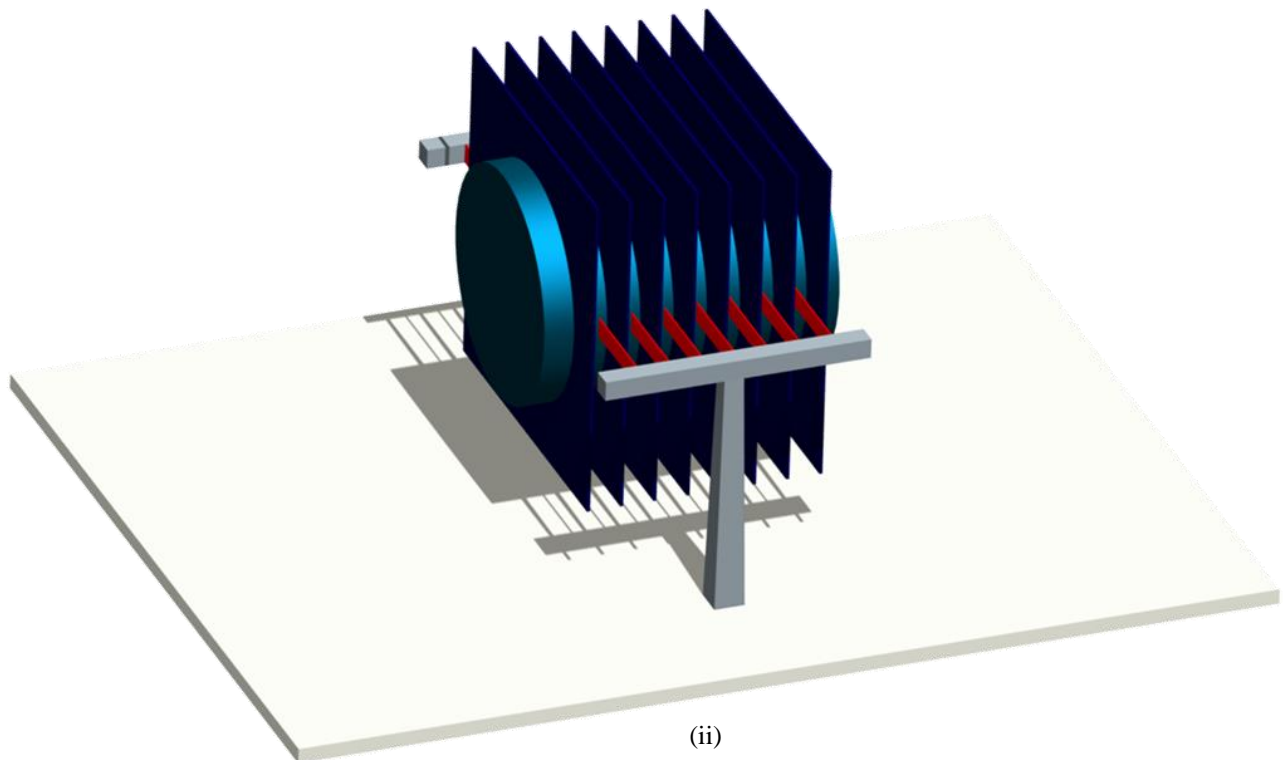
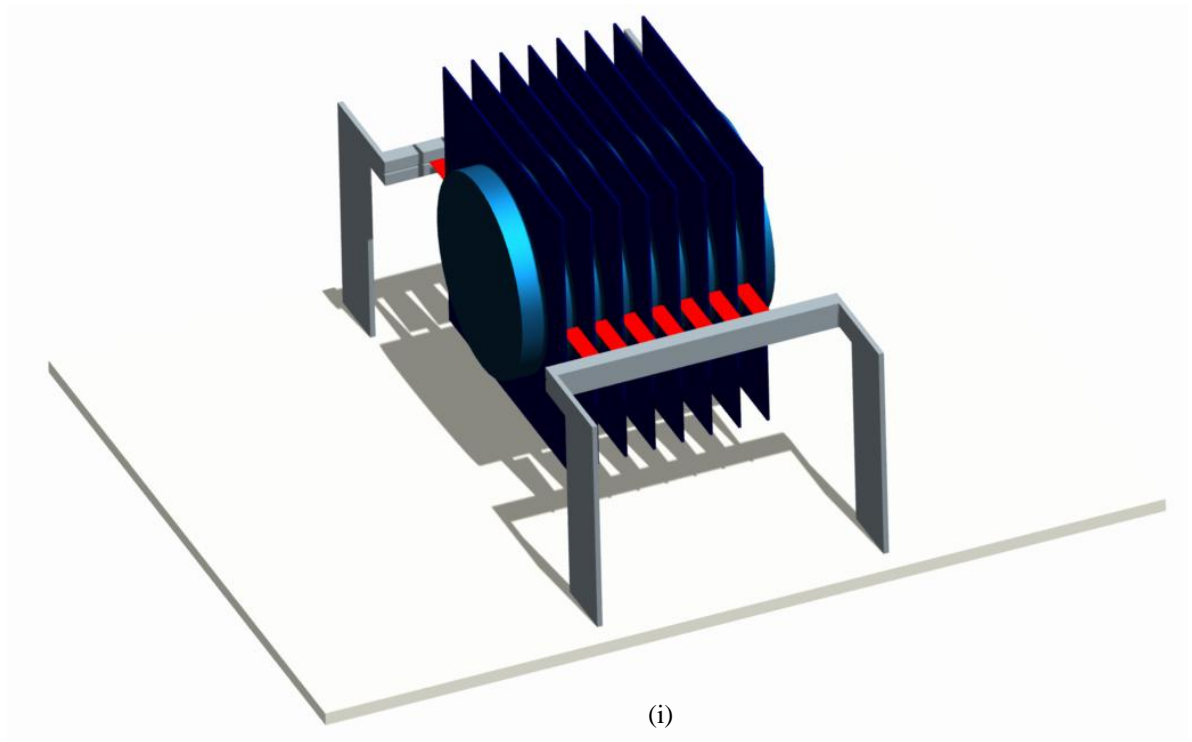


Figure 2.20: Schematics of possible Piezoelectric Fan Array Implementation

(i) Horizontal Piezoelectric Fan Array

(ii) Vertical Piezoelectric Fan Array

# CHAPTER 3

## 3. Verification and Validation of Thermal Software - *MotorCAD*

---

This chapter details the verification and validation of a commercial thermal software based on the lumped circuit resistance network – which is dedicated to the thermal modelling of electric machines - *MotorCAD*. Improvements in the software have also been performed, the key improvements of which are reported in this chapter.

The building of a high density, double layer,  $\Gamma = 40Nm$ , 24 slot – 20 pole aerospace *PMSM* together with the implemented telemetry is described. The motor was run under different loading conditions and for each test, the critical component temperatures were monitored. These temperatures were used in the validation of a representative *MotorCAD* thermal model.

### 3.1 Validation of *MotorCAD*

The validation process involved a direct comparison between experimental test data and analytical results obtained from a user generated *MotorCAD* thermal model. To validate *MotorCAD*, a proposed *MEA* mid-spoiler actuator motor (24 slot – 20 pole, *PMSM*) was fabricated and instrumented with thermocouples. The motor was run in the laboratory, under different loads, speeds and duty cycles (typical of those experienced during flight conditions). The transient and steady-state temperature data obtained was then compared to a representative thermal model in *MotorCAD*.

### 3.1.1 Motor Test Facility

The implemented experimental high speed test rig is depicted in Figure 3.1. In essence, the test facility incorporates: an induction drive (load) motor with its corresponding cooling fan, a torque transducer, an adjustable mounting flange together with adequate shaft guard shields and the fabricated *PMSM* under test. For part drawings of the tested *PMSM*, the reader is referred to **Appendix D**. The *PMSM* was instrumented with thermocouples Figure 3.3, Figure 3.8).



Figure 3.1: Experimental Setup of Test Rig

Furthermore, the supplied motor current, voltage and power characteristics were also monitored.

As previously pointed out, a number of motor temperatures were monitored during the several conducted tests. *K – Type* thermocouples were affixed to both stationary as well as rotating motor components. The instrumentation system comprised: a stationary 8 – channel (*Comark*) data logging system (Figure 3.2) connected to a computer as well as a miniature 5 – channel (*OMEGA*) rotating data logging system (Figure 3.4) which was incorporated in the motor drive shaft. The *Comark* logger monitored the axial finned housing (3 distinct positions), end winding, end space and flange temperatures, while



the *OMEGA* logger monitored the shaft, rotor (2 distinct positions), and magnet temperatures.

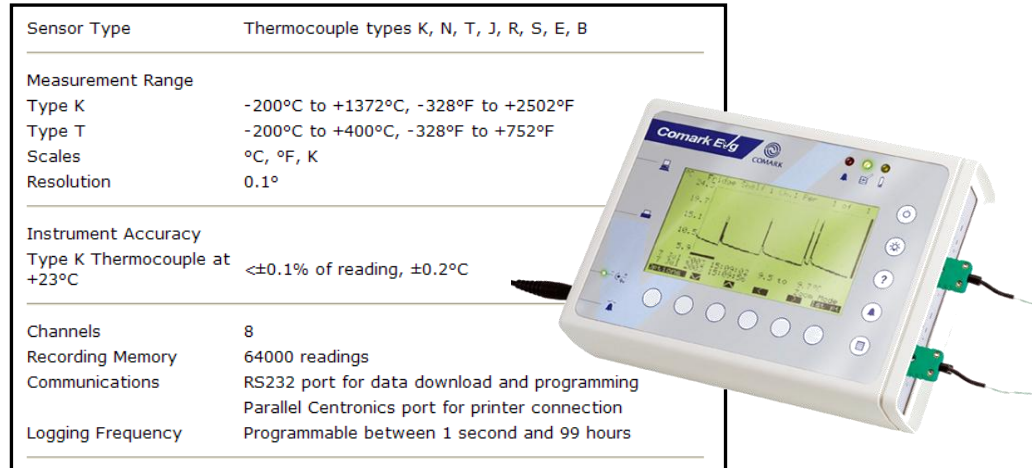


Figure 3.2: 8 - Channel *Comark* Data Logger, together with its Specifications

Figure 3.2 depicts the *Comark* data logger, used to capture temperature data from the stationary motor components. Three distinct axial finned housing temperatures were monitored: *Front* (adjacent to flange), *Middle* and *End* (furthest away from flange), the locations of which are highlighted in Figure 3.3. The adopted thermocouple placement was such to compare directly with the temperature nodes supplied in the user generated thermal model in *MotorCAD*.

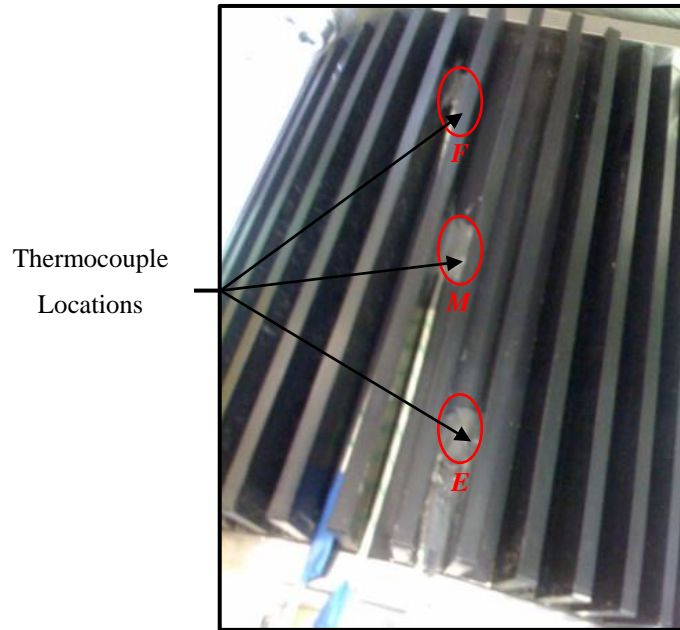


Figure 3.3: Axial Finned Housing Thermocouple Locations – Front (*F*), Middle (*M*), End (*E*)

Additional thermocouples were embedded in the top surface of the motor *EWdg*, end space region and supporting flange.

While the setting up of the stationary data logger was relatively straightforward to implement, the rotating data logger involved the design and manufacture of an additional system (logger casing and an alignment end plate) which was added and attached to the motor shaft. For full part drawings, the reader is referred to **Appendix D**. The rotating miniature data logger was inserted into an aluminium cylindrical casing and mounted as shown in Figure 3.4.

For ease of data acquisition, the data extraction connection port was reproduced and extended to the cylindrical surface of the logger casing as shown in Figure 3.4 and Figure 3.6. Reproducing the data extraction port ensured that the recorded data could quickly be extracted while maintaining the system's accuracy (since no dismantling of the entire system was required after each run).

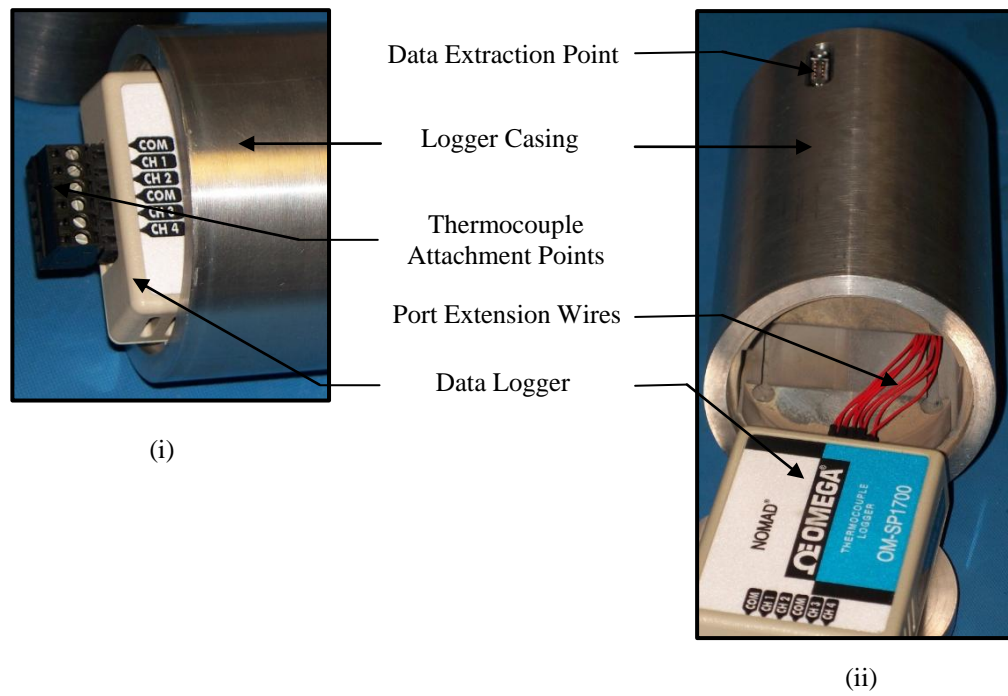


Figure 3.4: Rotating Data Logger Assembly System

(i) OMEGA Data Logger enclosed in Aluminium Casing

(ii) OMEGA Data logger showing port extension

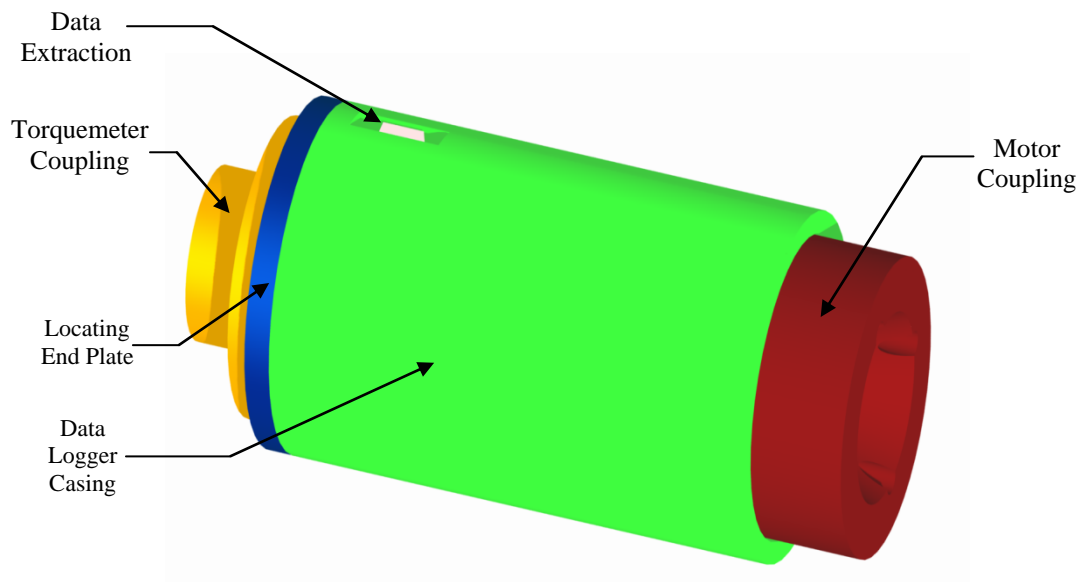


Figure 3.5: Graphical Representation of Rotating Data Logger Assembly

An aluminium locating end-plate was also mounted to the logger casing assembly (Figure 3.5); its sole purpose was to ensure that the entire shaft/data logger assembly ran through concentrically. Furthermore, the entire shaft system was balanced so as to ensure that no erroneous external forces were added due to any shaft imbalance.

Figure 3.7 and Figure 3.8 represent the geometrical location of each of the three *K - Type* thermocouples. The thermocouples were attached to the internal rotating surfaces by means of a thermally conductive, but electrically insulated adhesive (*WLK 5*) and then passed through the hollow motor shaft and attached to the data logger.

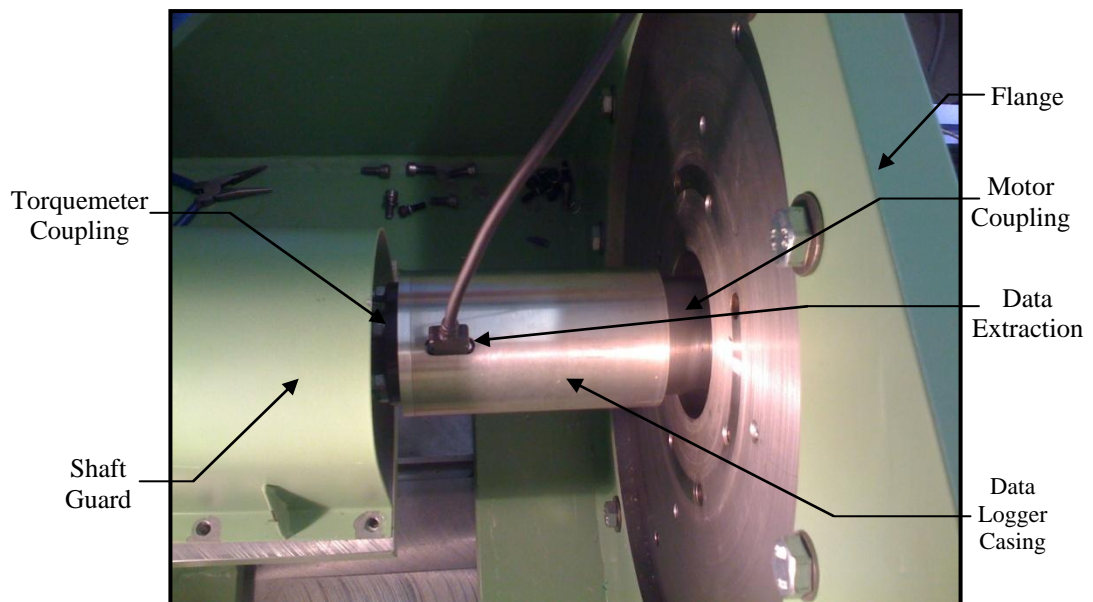


Figure 3.6: Data Extraction from Rotating Data Logger

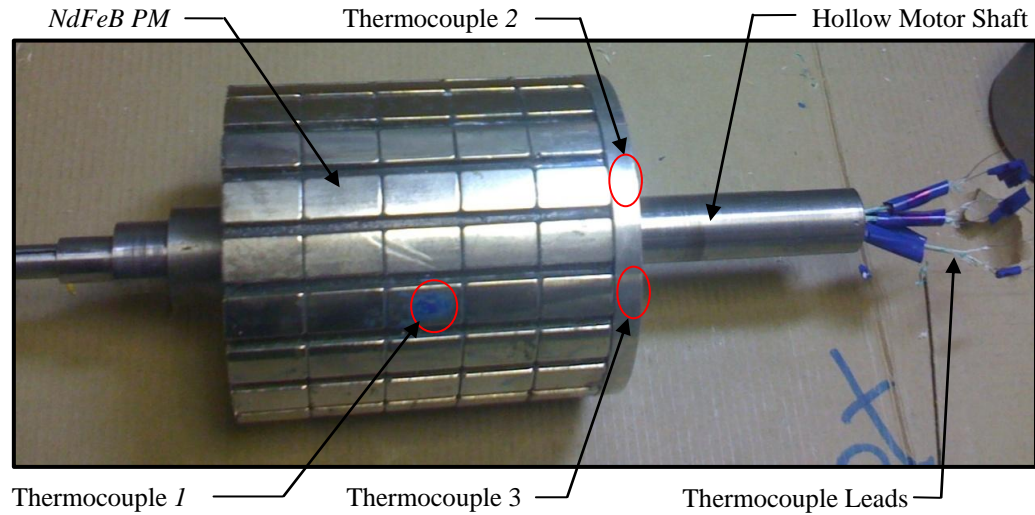


Figure 3.7: *PM's affixed to Rotor showing Thermal Adhesive and identifying Thermocouple Placement Locations*

Thermocouple 1 was directed into the centre of a permanent magnet. On the other hand, Thermocouples 2 and 3 were affixed to the rotor surface and rotor/spoke interface respectively. Thermocouple 2 was passed through a shallow groove on the rotor surface, directly under the *PM's* while thermocouple 3 was passed along a shaft spoke and embedded in the rotor/spoke interface.

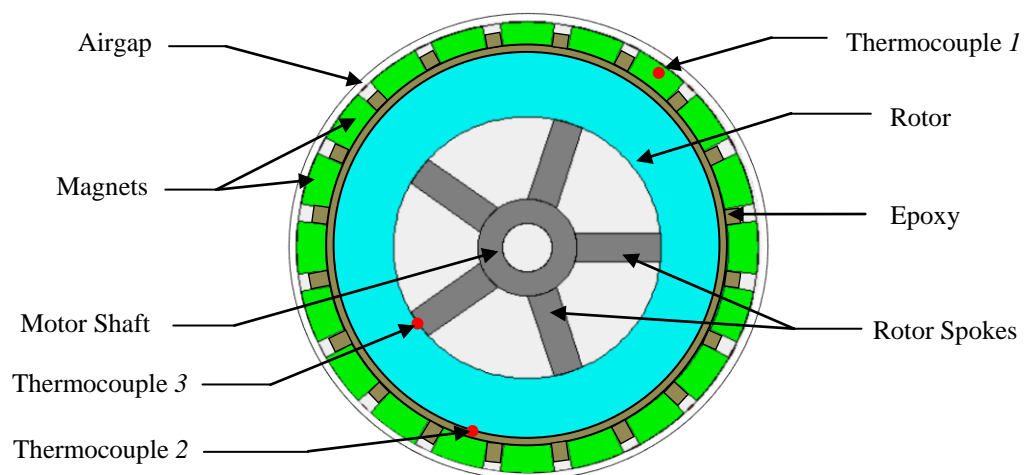


Figure 3.8: Radial cross section view of Rotor

The placement of thermocouples 2 and 3 were purposely selected so as to ascertain whether a temperature gradient exists in the radial direction of the rotor. It was envisaged that there would be a greater heat flow across the spoke rather than in the rotor space. Thus the temperature difference logged between thermocouples 2 and 3 would give a temperature gradient. This temperature gradient would identify the significance or otherwise of temperature variations across the rotor.

As already mentioned in **Chapter 2**, the current version of *MotorCAD* can only model individual motor components by a single node. Thus, the above detailed thermocouple setup, can further shed light on the accuracy of the created representative *PM* thermal model while also indicating how far off the results supplied by *MotorCAD* are from the actual experimental data.

### **3.1.2 Experimental vs. Simulated – A Comparative Study**

The motor was tested under various load conditions; different torques, currents and various duty cycles as early described. All tests were performed using an in-house 6 – phase voltage source inverter (converter) so as to set the rotational speed ( $\omega$ ) of the motor, while the drive control panel was used to supply the load torque ( $\Gamma$ ). The motor current ( $I$ ) was obtained by determining the average current, by means of a user-generated script in the *MatLAB* software.

Figure 3.9 and Figure 3.10 depict the supplied phase current from the 6 – phase converter for a  $10Nm$  and a  $20Nm$  stalled motor case. From the current traces, it is evident that certain minute fluctuations (spikes) exist. The generation of these fluctuations are due to the components making up the implemented converter – in particular the *DC* link. Thus on performing a *FFT* of the supplied motor current, an average current value was obtained. This current value was imported into the *MotorCAD* software package for the comparative study.

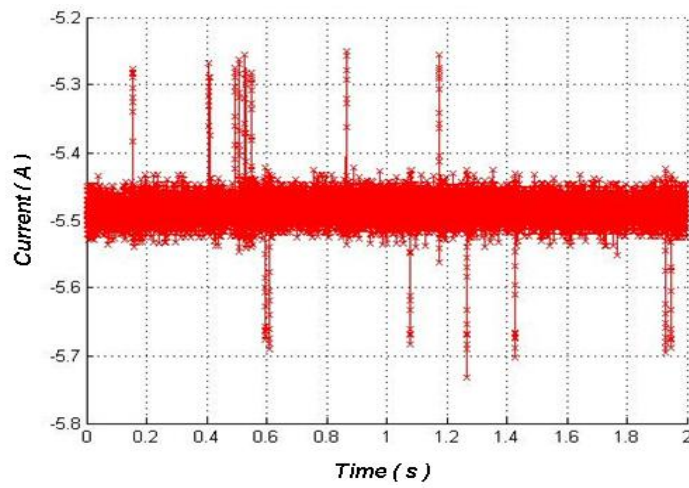


Figure 3.9: *FFT* of a 10Nm Stalled Motor

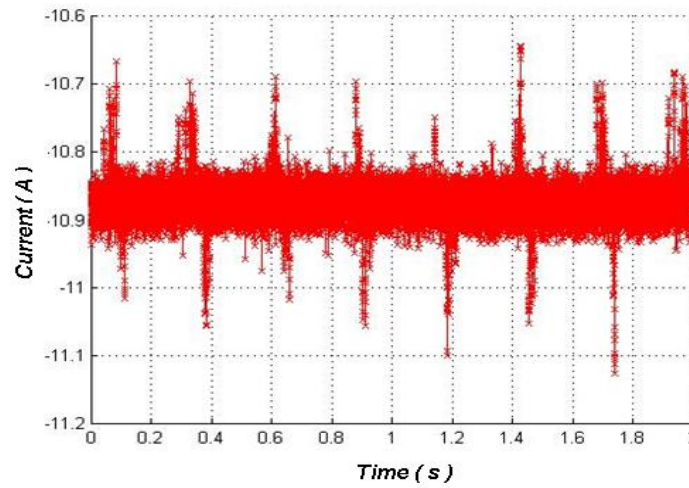


Figure 3.10: *FFT* of a 20Nm Stalled Motor

#### 3.1.2.1 Stall Tests

For the duration of the testing stage, both data loggers (*OMEGA*, *Comark*) were set to sample at 10 second intervals. This ensured a sufficient number of data points to accurately represent the experimental temperature profile which could be further compared to the simulated results from *MotorCAD*.



Stall ( $w = 0rpm$ ) cases were performed, at torques of:  $5Nm$ ,  $10Nm$ ,  $15Nm$  and  $20Nm$  tests, a sample of which is presented and the key trends highlighted.

Figure 3.11 depicts the temperature data obtained during a  $10Nm$  stall test. It is evident that the end winding ( $EWdg$ ) is the critical motor component, as it is the component that heats up the greatest. This is mainly due to the fact that in a stall, only copper losses ( $P_{Cu}$ ) are present, which act on the motor windings. Furthermore, the temperature of the rotor/spoke interface is hotter than the bulk rotor temperature. As mentioned earlier, this is due to the fact, that heat can easily be conducted away from the rotor through the highly conducting steel shaft. However, the same cannot be said for the rotor. Interestingly enough, while a negligible temperature difference arises between the middle and end axial finned motor housing locations, a lower steady state temperature results at the front section of the housing. This has been attributed to the proximity of the mounting flange. As the motor is mounted to a highly conducting flange, the front part of the motor (the part actually being mounted to flange) has a lower conductive thermal resistance, resulting in the efficient conductive heat transfer through the flange.

When performing a test on a  $15Nm$  stalled motor (Figure 3.12), similar trends to the above are seen. In this test, the motor was run for a longer duration of time (5.2 hours) to ensure that steady state temperatures were obtained. At this point, it is worth mentioning that steady state conditions were assumed to be reached when the temperature gradient of the measured components was identical to that of the average ambient temperature gradient.



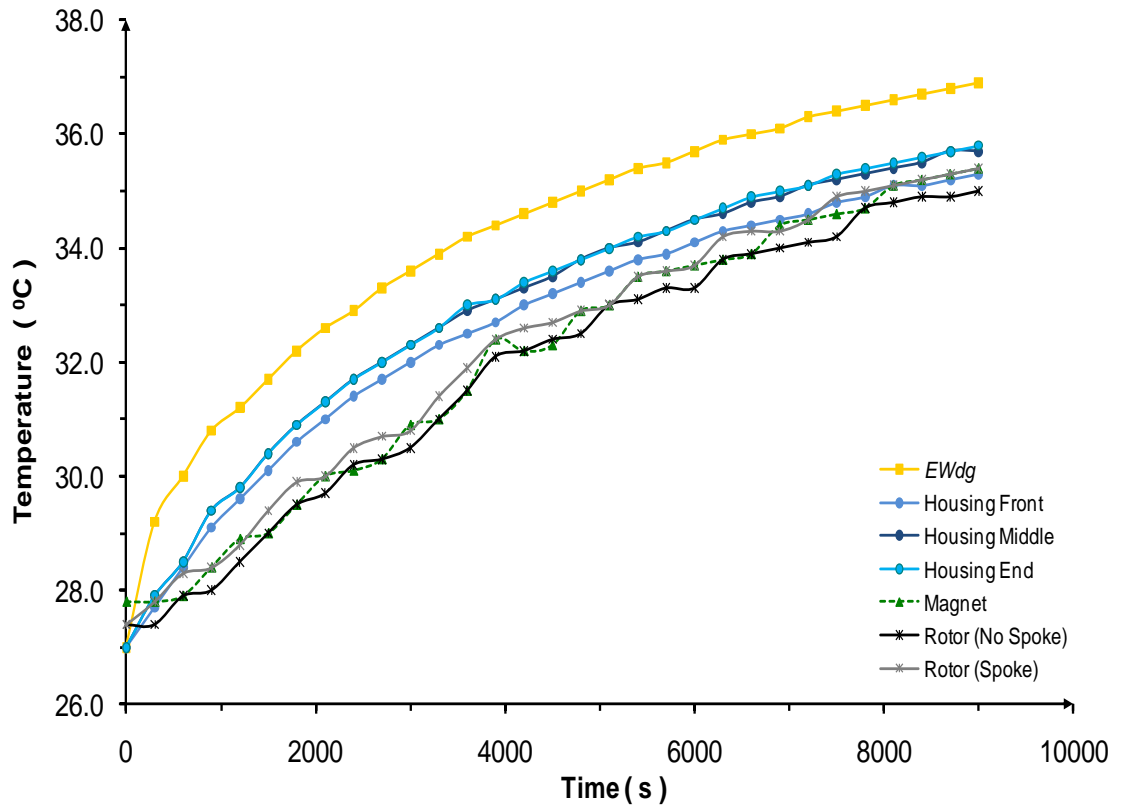


Figure 3.11: Temperature profiles of a 10Nm Stalled Motor

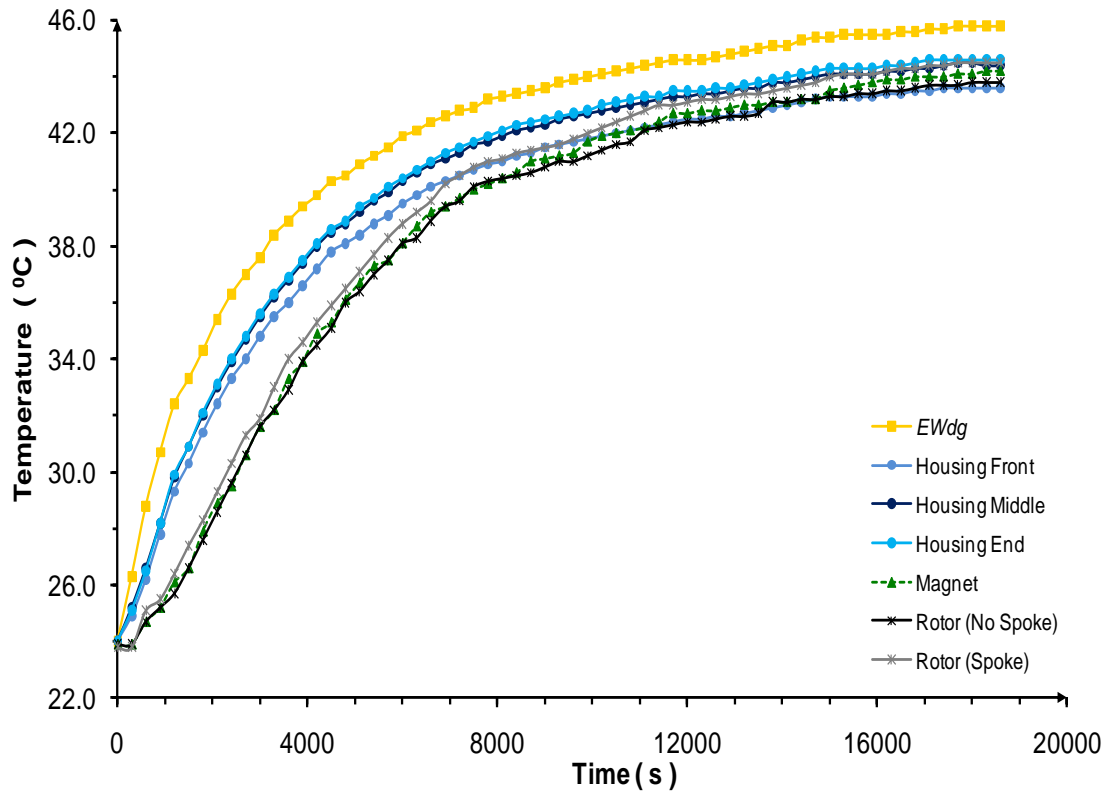


Figure 3.12: Temperature profiles of a 15Nm Stalled Motor

For each of the stalled tests, the temperature data was compared to the simulated results. In the thermal model, all geometrical data, loss data, along with operating conditions ( $\Gamma$ ,  $\omega$ ,  $I$ ,  $T_{Amb}$ ) were input. A direct comparison between the experimental and simulated 15Nm motor test is shown in Figure 3.13.

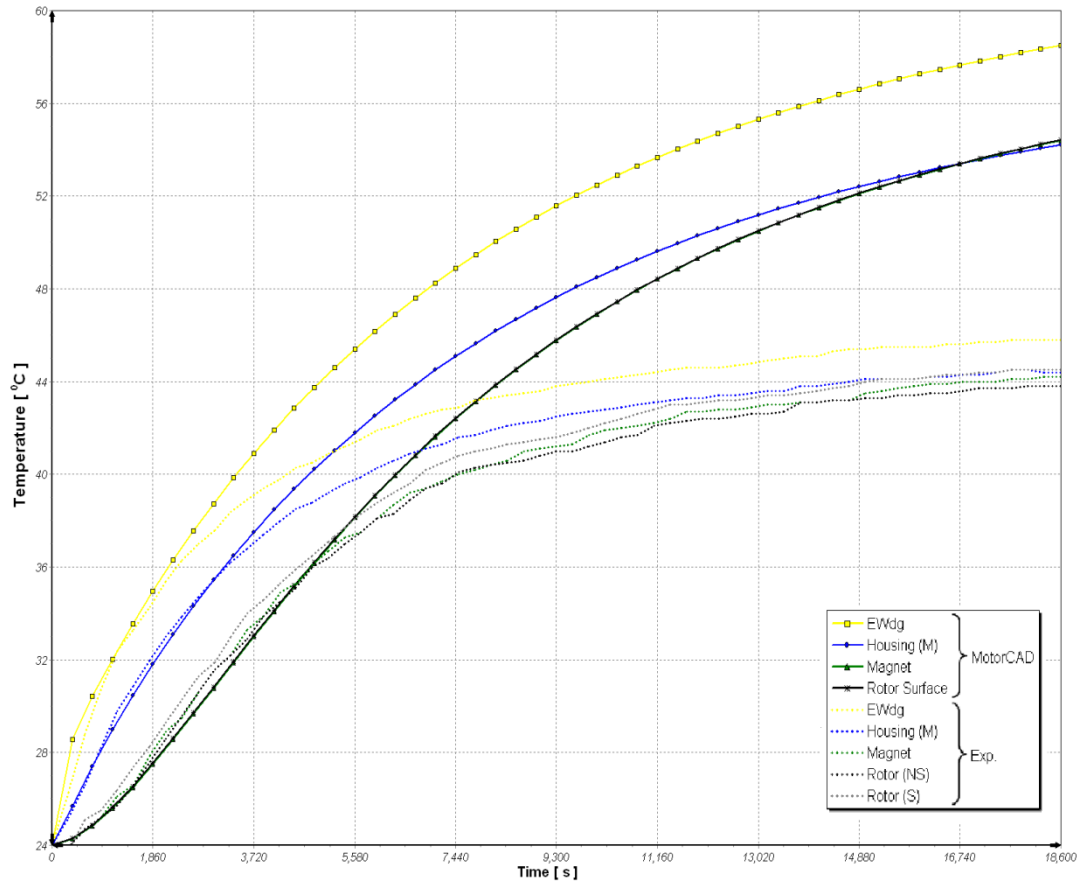
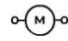
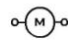
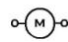

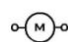




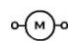
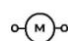
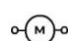
Figure 3.13: Initial Comparison between Experimental Test Data and simulated *MotorCAD* Results for a 15Nm Stalled Motor

From Figure 3.13, it is evident that the curves are not well matched. While the initial thermal gradients, which are governed by the thermal masses, are well matched, indicating that the user input material properties largely agree, the same cannot be said for the final steady state temperatures reached. That is, there exists a significant discrepancy in the final steady state temperatures, indicating that the thermal resistances between the housing and the ambient do not match between the experimental and the thermal model.

In this investigation, the steady state temperature discrepancy resulted due to certain unknown parameters required as inputs in the thermal software. These parameters included, and were not limited to:

-  component clearances (interface resistances)
-  stator stacking factor
-  impregnation goodness
-  impregnation material properties
-  surface emissivity values
-  external axial finned housing heat transfer coefficients

These parameters are difficult to determine, and are a source of error in thermal modelling of electrical machines. However, from the above list, it was established that the external axial finned housing heat transfer coefficients were the critical parameters. Ideally, when performing any thermal test, a natural convection environment should be maintained around the motor. This requires the minimisation, or better, the elimination of all stray air drafts/currents in the test area. Unfortunately, no proper control of the experiment environment could be maintained. This was due to such factors as:

-  high heat input machinery in close proximity to test rig
-  severe air drafts – due to wall ventilations
-  cooling fans – to cool down adjacent machinery
-  presence of other personnel in lab

Due to the above explained anomaly, it was deemed necessary to account for this air unsteadiness by increasing the motor's axial finned housing heat

transfer coefficients by 2.8 times that of the natural convection state. The same exact thermal model was then implemented for the different cases (both stalled and running scenarios), the comparative results of which are presented in Figure 3.14 and Figure 3.15. The temperature rise together with the associated percentage differences between the experimental and simulated data is further presented in Table 3.1 and Table 3.2. The presented results reflect a *10Nm* and a *15Nm* stalled motor operating at ground level respectively.

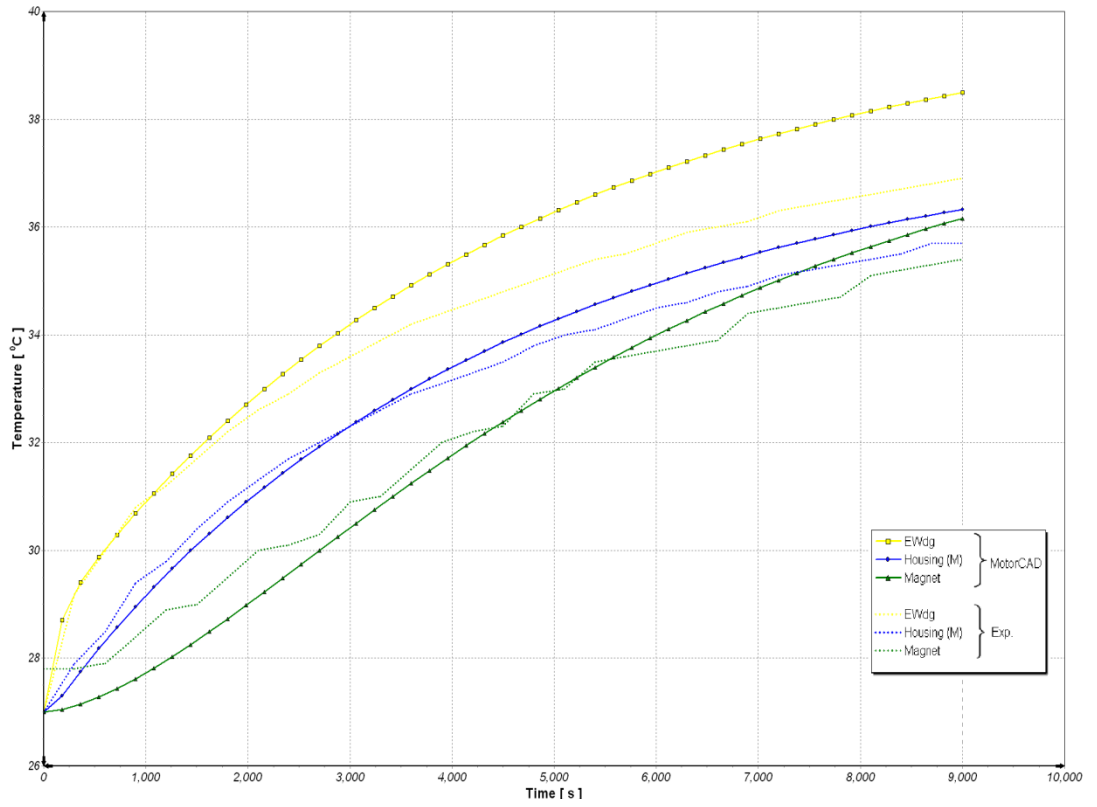


Figure 3.14: Comparison between Experimental Test Data and Calibrated *MotorCAD* Model for a 10Nm Stalled Motor

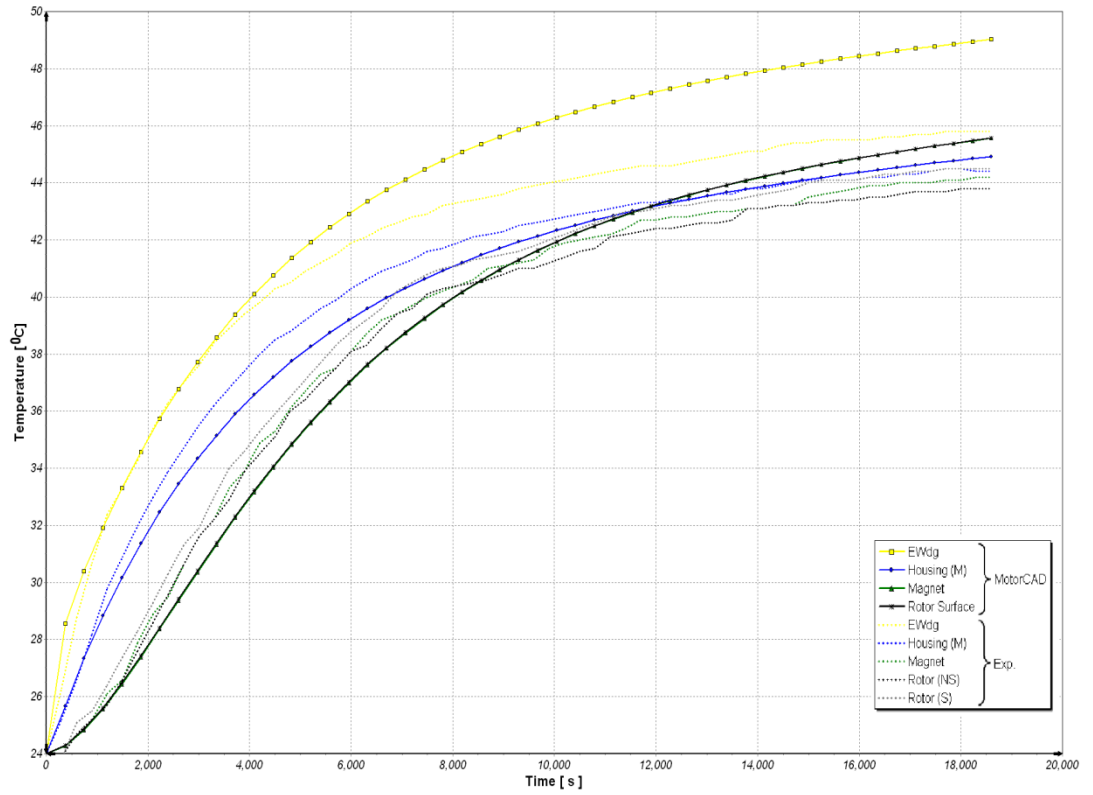


Figure 3.15: Comparison between Experimental Test Data and Calibrated *MotorCAD* Model for a 15Nm Stalled Motor

	Experimental Data				MotorCAD Data							
Location	$t = 1hr$	$t = 1.5hrs$	$t = 2hrs$	$t = 2.5hrs$	$t = 1hr$	$t = 1.5hrs$	$t = 2hrs$	$t = 2.5hrs$	% Diff. ( $t = 1hr$ )	% Diff. ( $t = 1.5hrs$ )	% Diff. ( $t = 2hrs$ )	% Diff. ( $t = 2.5hrs$ )
End Winding	7.20	8.40	9.30	9.90	7.93	9.61	10.74	11.51	10.1	14.4	15.5	16.3
Housing Front	5.50	6.80	7.60	8.30	5.82	7.39	8.45	9.16	5.8	8.7	11.2	10.4
Housing Middle	5.90	7.10	8.10	8.70	5.99	7.57	8.62	9.33	1.5	6.6	6.4	7.2
Housing End	6.00	7.20	8.10	8.80	5.93	7.49	8.54	9.25	-1.2	4.0	5.4	5.1
Magnet	4.50	6.50	7.50	8.40	4.25	6.40	8.02	9.17	-5.6	-1.5	6.9	9.2
Rotor (No Spoke)	4.50	6.10	7.10	8.00	4.27	6.42	8.03	9.18	-5.1	5.2	13.1	14.8
Rotor (Spoke)	4.90	6.50	7.50	8.40	/	/	/	/	/	/	/	/

Table 3.1: Direct Comparison between the Temperature Rise in the Experimental and Simulated Results for a 10Nm Stalled Motor

	Experimental Data				MotorCAD Data							
Location	$t = 1hr$	$t = 2hrs$	$t = 3hrs$	$t = 4hrs$	$t = 1hr$	$t = 2hrs$	$t = 3hrs$	$t = 4hrs$	% Diff. ( $t = 1hr$ )	% Diff. ( $t = 2hrs$ )	% Diff. ( $t = 3hrs$ )	% Diff. ( $t = 4hrs$ )
End Winding	14.90	18.80	20.30	21.30	14.87	19.96	22.19	23.49	-0.2	6.2	9.3	10.3
Housing Front	12.00	16.05	18.10	19.10	11.04	15.79	17.87	19.09	-8.0	-1.6	-1.3	-0.1
Housing Middle	12.80	17.30	19.00	19.90	11.39	16.12	18.20	19.42	-11.0	-6.8	-4.2	-2.4
Housing End	12.90	17.50	19.20	20.10	11.23	15.95	18.02	19.24	-12.9	-8.9	-6.1	-4.3
Magnet	9.30	15.70	18.10	19.20	7.74	14.74	18.06	19.84	-16.8	-6.1	-0.2	3.3
Rotor (No Spoke)	8.90	15.60	17.70	19.20	7.79	14.77	18.07	19.85	-12.5	-5.3	2.1	3.4
Rotor (Spoke)	10.00	16.50	18.60	19.70	/	/	/	/	/	/	/	/

Table 3.2: Direct Comparison between the Temperature Rise in the Experimental and Simulated Results for a 15Nm Stalled Motor

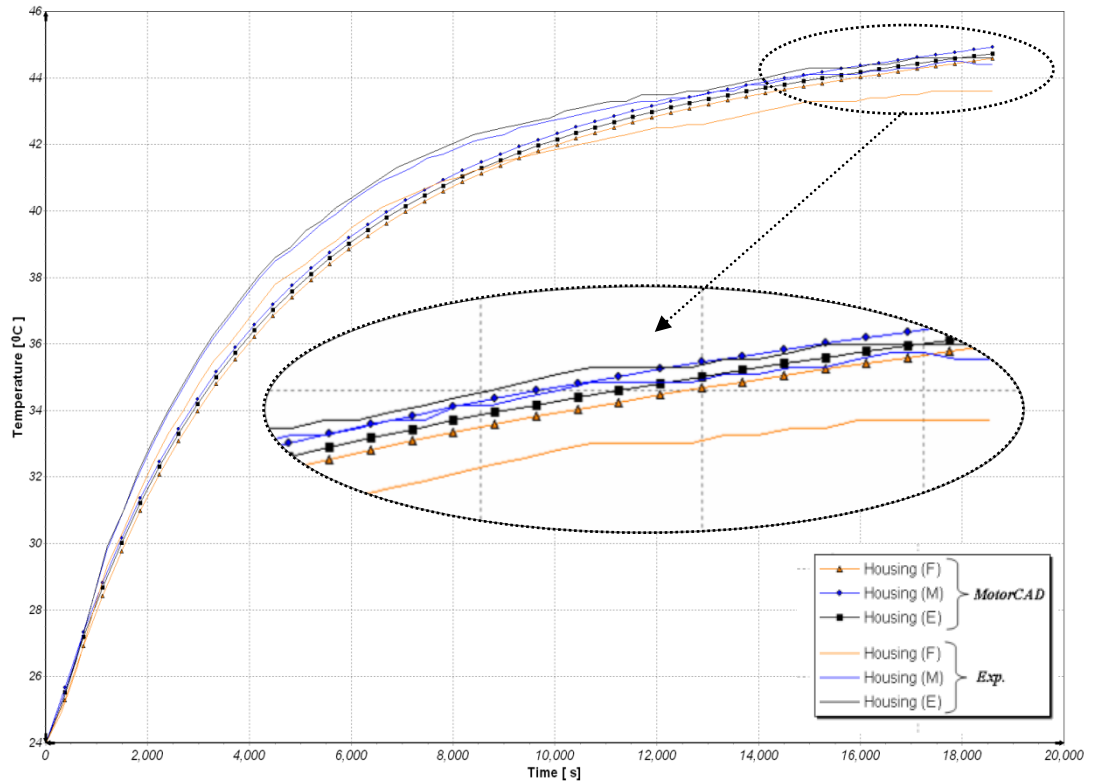


Figure 3.16: Axial Finned Housing Temperature Variation - Comparison between Experimental Test Data and Calibrated *MotorCAD* Model for a 15Nm Stalled Motor

Figure 3.16 depicts the temperature distribution along the motor axial finned housing. At each thermocouple location, both the thermal gradients as well as the steady state temperatures are well matched between the experimental and simulated data. This is further documented in Table 3.3 below.

Location	Temperature Rise ( $^{\circ}\text{C}$ )		% Difference
	Experimental Data	<i>MotorCAD</i> Data	
Housing Front (F)	20.58	19.60	4.8
Housing Middle (M)	20.92	20.40	2.5
Housing End (E)	20.74	20.60	0.7

Table 3.3: Percentage Difference Table - Axial Finned Housing

From Figure 3.14, Figure 3.15, as well as the above tabulated results, it is evident that the thermal model generated in the *MotorCAD* package has been correctly calibrated and is a true representation of the actual 24 slot - 20 pole *PMSM* under test. The model was said to be correctly calibrated due to the fact that both the gradients (thermal capacitance) as well as the steady state temperatures are well matched for several considered scenarios – 5Nm, 10Nm, 15Nm and 20Nm stall cases.

### 3.1.2.2 Variable Load and Speed Tests

In addition to stall tests, further tests at various speeds ( $w \neq 0rpm$ ) and torques (100rpm - 30Nm; 200rpm - 20Nm, 200rpm - 20Nm; 600rpm - 10Nm and 600rpm - 20Nm), were carried out. These additional tests were performed, for a dual purpose (a) to ensure the correct functionality of the user generated thermal model and (b) to monitor and record the steady state temperatures attained by the motor critical components (*EWdg*, Magnet) under the different imposed load conditions. As detailed in **Chapter 1**, while in a stalled motor scenario, only copper losses (in the motor windings) exist, the same cannot be said when running the motor at speed. This means that operating the motor at a particular speed (other than  $w = 0rpm$ ) results in additional motor losses, such as: bearing, windage, hysteresis and eddy current losses.

Agreement between experimental test data and simulated results would imply that the motor losses would have been correctly segregated while further indicating that the user generated thermal model accurately predicts the motor component temperatures under any load conditions.

One such test case is presented in Figure 3.17 and depicts a 200rpm, 20Nm test case.



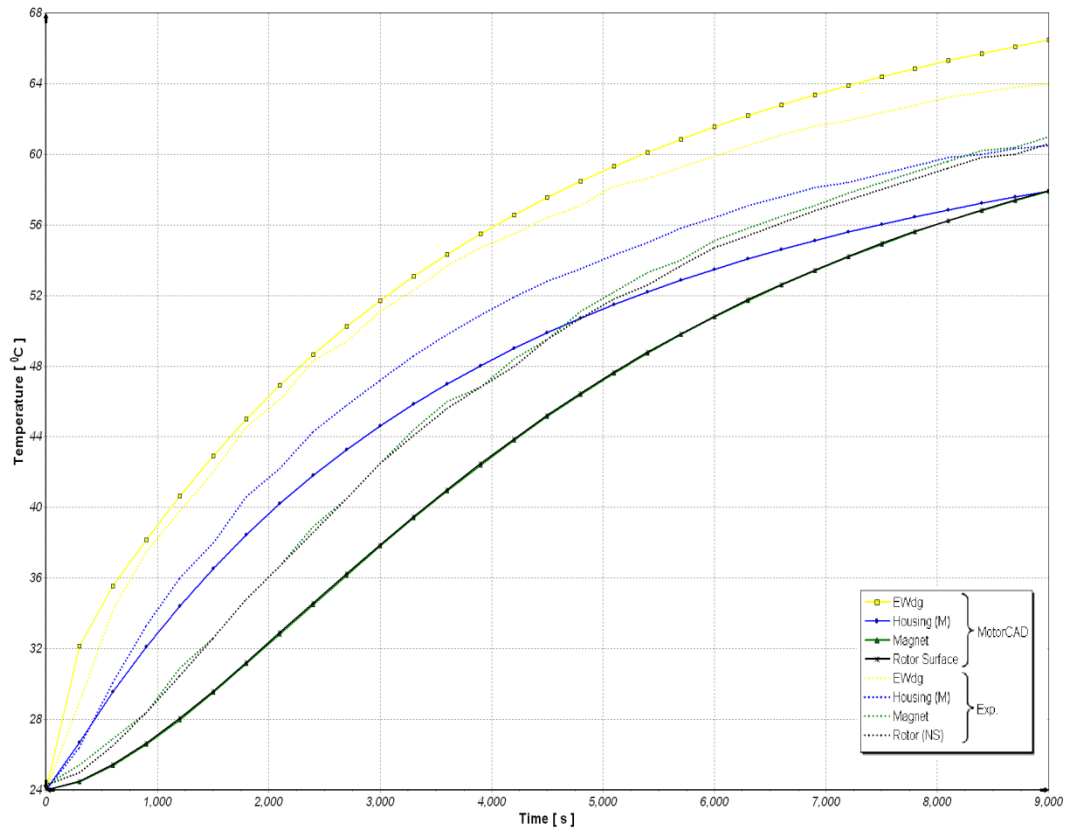


Figure 3.17: Comparison between Experimental Test Data and Calibrated *MotorCAD* Model for a *PMSM* running at *20Nm - 200rpm*

From Figure 3.17, close *EWdg* agreement is attained. However, a slight difference (a maximum of  $4^{\circ}\text{C}$ ) between experimental and simulated magnet and housing temperature results. There are many causes for the above affect; however the principal cause may be attributed to the motor housing temperature distribution. It has been observed that a temperature gradient arises around the circumference of the horizontal motor housing. In some cases this temperature difference is negligible, but in certain cases (Figure 3.18), the temperature difference is highly significant. The said temperature distribution has been attributed to the natural thermal boundary layer that occurs around the cylindrical motor housing.

From boundary layer theory [13, 20], it can be shown that the temperature at the top of a horizontal cylinder is greater than that obtained at the bottom. This was further confirmed when an *IR* thermal imaging camera was used to continuously monitor the motor housing steady state temperatures.

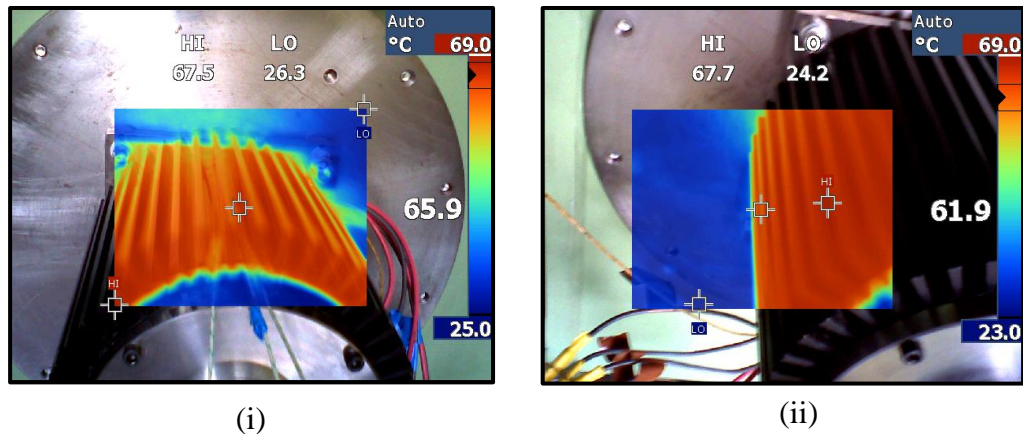


Figure 3.18: Thermal Images of: (i) Top and (ii) Bottom of Finned Motor Housing during a 20Nm Stalled Test Case

It must be pointed out that, in 1980, *Toth* [51] performed an experimental determination of the temperature distribution along the housing circumference of a foot mounted horizontal motor. In the experiment, the author utilised 34 thermocouples to determine the circumferential temperature distribution. He also came up with results that showed that a circumferential temperature distribution exists. The above temperature distribution implies that the natural heat transfer coefficient also varies circumferentially, which in turn implies that the correct prediction of a single heat transfer coefficient for the housing is not easy to achieve. This circumferential distribution is, as yet, not incorporated in the thermal software package, which in turn results in the slight variation in the attained housing temperature values.

### 3.2 Verification of *MotorCAD*

The verification of the *MotorCAD* software consisted of an in depth analysis of the relevant source code and utilised governing correlations so as to ensure that the thermal package was performing to the best of its abilities. Throughout this verification process, several bugs were identified, most, if not all were

successfully eradicated with the help of *Dr. Dave Staton* and the *MotorDesign* team.

In this section, a brief description of one such analysis sequence is documented. It relates to the modification of the external end winding heat transfer convective coefficients.

### 3.2.1 Modification of End Winding Heat Transfer Correlation

This analysis details the correct evaluation of the convective heat transfer coefficients from the end windings of an electric machine. The correct determination of these coefficients is of importance as they are regularly used in the thermal analysis of the same electric machines. The incorrect evaluation of ( $h_{EWdg}$ ) may result in the implementation of the wrong copper winding insulation and/or resin (impregnation) materials. This in turn may result in the overheating of these materials, inducing an *EWdg* short, and motor failure.

The heat transfer equations for the end windings given in the literature [52] are generally in the form of Eq. 3.1 and are not expressed as correlations of non-dimensional parameters and so do not allow for changes in operating conditions such as the variation in pressure with altitude that is found in electric machines operating in aircraft.

$$h_{EWdg} = k_1(1 + k_2(vel)^{k_3}) \quad \dots \text{Eq. 3.1}$$

This implies that the heat transfer coefficient is greatly over-predicted when operating at an altitude other than ground level (Figure 3.21). This is because at higher altitudes ( $z = 11,500m$ ), the air pressure ( $P$ ) and density ( $\rho$ ) are reduced which results in a lower convective heat transfer coefficient ( $h_{EWdg}$ ).

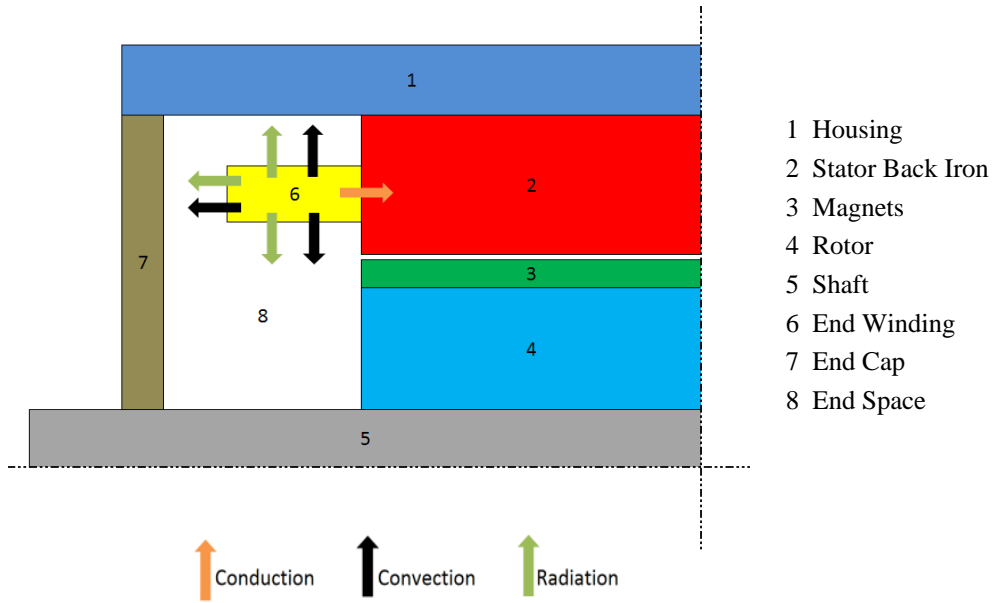


Figure 3.19: Schematic of a sectioned *PMSM*

Figure 3.20 plots Eq. 3.1 with the curve fit coefficients ( $k_1, k_2, k_3$ ) published in the table below [52].

Author	$k_1$	$k_2$	$k_3$
<i>Schubert (EWdg)</i>	15.0	0.400	0.9
<i>Schubert (Bearing Cover)</i>	20.0	0.425	0.7
<i>Mellor</i>	15.5	0.390	1.0
<i>Di Gerlando (EWdg)</i>	10.0	0.540	2.0
<i>Di Gerlando (End Cover)</i>	40.0	0.100	1.0
<i>Stokum</i>	33.2	0.045	1.0
<i>Boglietti</i>	41.4	0.150	1.0
<i>Hamdi (End Cover)</i>	$h_{nc}$	0.300	1.0

Table 3.4: Published End Space Curve Fit Coefficients

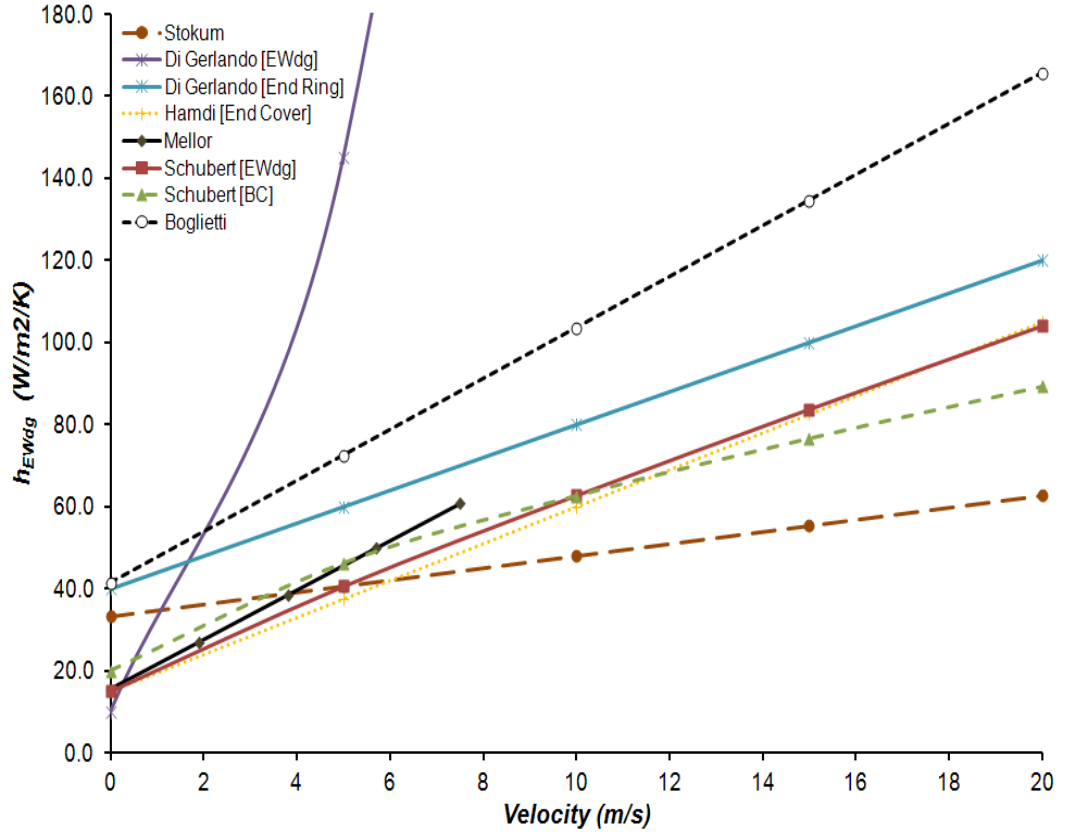


Figure 3.20: Published End Space Correlation Results

It is worth noting the large spread of values obtained in Figure 3.20. This arises due to the fact that each author utilises different electric motors, with different geometries as well as different operating conditions in their analysis. An analysis of the end space region heat transfer was thus undertaken to improve (Eq. 3.1) and make it pressure dependent.

The end winding heat transfer ( $h_{EWdg}$ ) can be expressed as a natural convection component - for a situation where the motor shaft is stationary (stalled), as well as a forced convection component - for a rotating motor. Thus, the general equation at ground level ( $z = 0m$ ) and at flight level ( $z \neq 0m$ ) may be written as:

$$Nu_0 = A'(Ra_0)^m + B'(Re_0)^q \quad \dots \text{Eq. 3.2}$$

$$Nu_z = A'(Ra_z)^m + B'(Re_z)^q \quad \dots \text{Eq. 3.3}$$

For each equation, the first term, the *Rayleigh* number represents natural convection while the second term, the *Reynolds* number describes the forced convection of the system. It is assumed that the constants ( $A'$  and  $B'$ ) remain unchanged (i.e. there is no transition region between the altitudes). Hence, Eq. 3.3 can be written as Eq. 3.4, to yield a relation between the *Nusselt* number at various altitudes to that at ground level.

$$Nu_z = A' \left( \frac{Ra_z}{Ra_0} \cdot Ra_0 \right)^m + B' \left( \frac{Re_z}{Re_0} \cdot Re_0 \right)^q \quad \dots \text{Eq. 3.4}$$

Furthermore, the heat transfer coefficient is related to the *Nusselt* number by the air thermal conductivity ( $k$ ), and the characteristic length ( $D$ ) as depicted in Eq. 3.5. In this analysis, the characteristic length chosen is based on the end winding diameter. This in turn results in Eq. 3.6.

$$h = \frac{Nu \cdot k}{D} \quad \dots \text{Eq. 3.5}$$

$$h_z = \frac{1}{D_{EWdg}} \cdot (Nu_z) \cdot \left[ k_0 \cdot \left( \frac{T_z}{T_0} \right)^n \right] \quad \dots \text{Eq. 3.6}$$

$$h_z = \frac{1}{D_{EWdg}} \cdot \left[ k_0 \cdot \left( \frac{T_z}{T_0} \right)^n \right] \cdot \left[ A' \left( \frac{Ra_z}{Ra_0} \cdot Ra_0 \right)^m + B' \left( \frac{Re_z}{Re_0} \cdot Re_0 \right)^q \right] \quad \dots \text{Eq. 3.7}$$

Expanding Eq. 3.7 results in Eq. 3.8, which reads:

$$h_z = \frac{1}{D} \times \left[ k_0 \left( \frac{T_z}{T_0} \right)^n \right] \cdot \left[ A \left( \frac{\Delta T_z T_{f_0} \rho_z^2 \mu_0^2 \text{Pr}_z}{\Delta T_0 T_{f_z} \rho_0^2 \mu_z^2 \text{Pr}_0} Ra_0 \right)^{\frac{1}{4}} + B \left( \frac{\rho_z \mu_0 Re_0}{\rho_0 \mu_z} \right)^{k_3} \right] \quad \dots 3.8$$

This gives an explicit dependence between the heat transfer coefficient at ground level and at varying altitudes. However, this is too complex to

implement in practice, since too many temperature dependent variables are present. Thus, a simplification is necessary to provide a heat transfer equation which is not only accurate but also easier to implement.

Taking the assumption that most terms in the Rayleigh number are constant over the given altitude range, that is, taking the *Prandtl* number,  $\frac{\Delta T}{T_f}$ , as well as the viscosity to be pressure independent, we can perform the following analysis.

The natural convection is described by the Rayleigh number, which may be defined by the following relation:

$$Ra = Gr \times Pr \quad \dots 3.9$$

In this analysis, the subscript ‘*D*’ refers to the effective end winding diameter which is being taken to be the characteristic length. If the assumption is made that the temperature difference is constant at any altitude and that the viscosity is constant, then the only altitude dependence will be in the density.

$$Gr_D = \frac{\beta g \Delta T D^3}{\mu^2} \times (\rho_z)^2 \quad \dots 3.10$$

Similarly, for the forced convection term the only altitude dependence is in the density.

$$Re = \frac{(\rho_z) D (vel)}{\mu} \quad \dots 3.11$$

Therefore, taking the above mentioned assumptions, Eq. 3.8 can be further simplified to give:

$$h_z = k_1 \left( \frac{\rho_z}{\rho_0} \right)^{0.5} \times \left[ 1 + k_2 \left( \frac{\rho_z}{\rho_0} \right)^{k_3 - 0.5} \times (vel)^{k_3} \right] \quad \dots \text{Eq. 3.12}$$

Upon further analysis, the authors is of the opinion that Eq. 3.12 can be further simplified (by taking into consideration the Ideal Gas Law)

$$h_{EWdg} = k_1 \left( \frac{p_z}{p_0} \right)^{0.5} \times \left[ 1 + k_2 \left( \frac{p_z}{p_0} \right)^{(k_3-0.5)} \times (vel)^{k_3} \right] \quad \dots \text{Eq. 3.13}$$

The above correlation is simple to implement as it is a function of the curve fit coefficients as well as the pressure ratio  $\left( \frac{p_z}{p_0} \right)$ . This ratio can be obtained directly from the International Standard Atmosphere (*ISA*) table. Furthermore, Eq. 3.13 is adaptable – i.e. any of the earlier established authors (Table 3.4) may tailor the suggested correlation according to their own set of curve fit coefficients.

All the above correlations are documented and published in [53].

A comparison between the traditional end winding heat transfer coefficient and the suggested pressure dependent correlation (Eq. 3.13), for a stalled motor is presented in Figure 3.21. Numerically, at ground level,  $h_{EWdg} = 15W/m^2.K$ , while at flight level ( $z = 11,500m$ ),  $h_{EWdg} = 6.83W/m^2.K$  - a 73.6% difference. Thus, the implementation of the traditional correlation results in an *EWdg* heat transfer coefficient over-prediction of 120%.



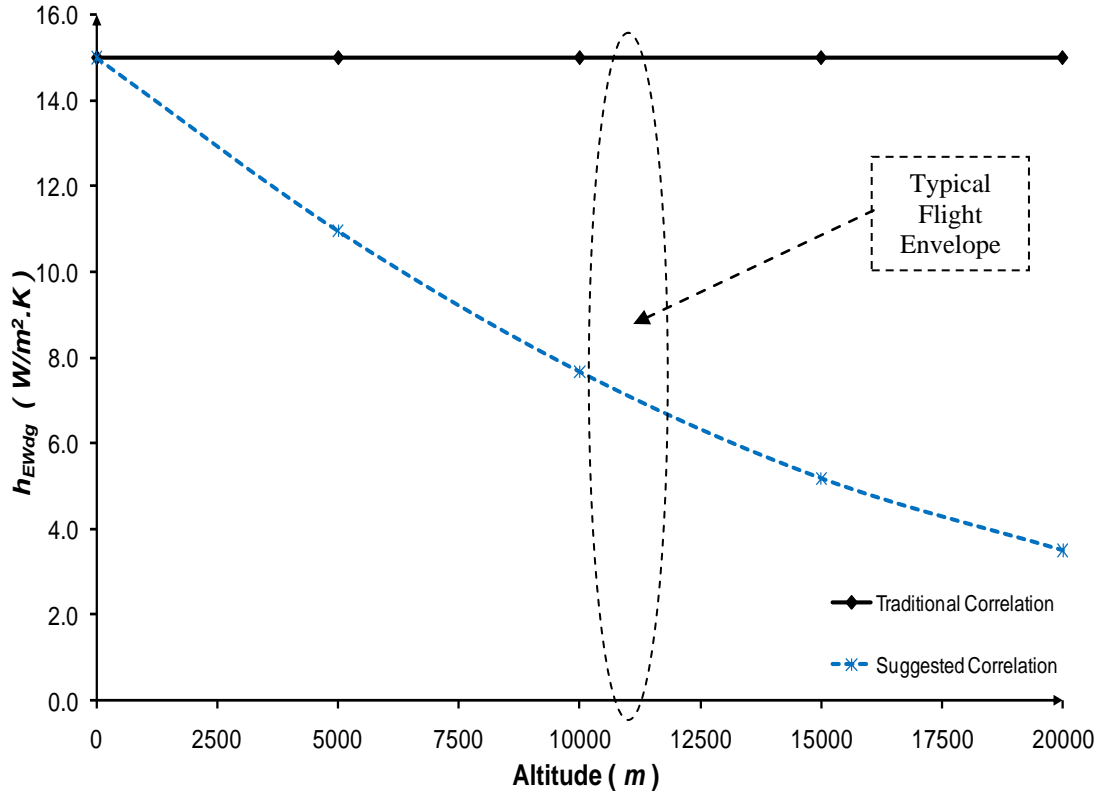


Figure 3.21:  $h_{EWdg}$  variation between pressure independent correlation (Eq. 3.1) and pressure dependent correlation (Eq. 3.13) for a Stalled Motor

The above graph clearly indicates that the traditional, pressure independent  $EWdg$  heat transfer coefficient is maintained constant for different altitudes. On the other hand, the end winding heat transfer coefficient is seen to diminish as altitude increase on applying the suggested correlation. Furthermore, with an increase in altitude, the difference between Eq. 3.1 and Eq. 3.13 is increased.

The variation in heat transfer coefficient for a rotating rotor is shown in (Figure 3.22). This figure highlights the variation between the two correlations as the shaft rotational speed ( $\omega$ ) increases. The results indicate that, while the variation in  $h_{EWdg}$  is small for a stalled motor, the differences are larger at higher rotational motor speeds.

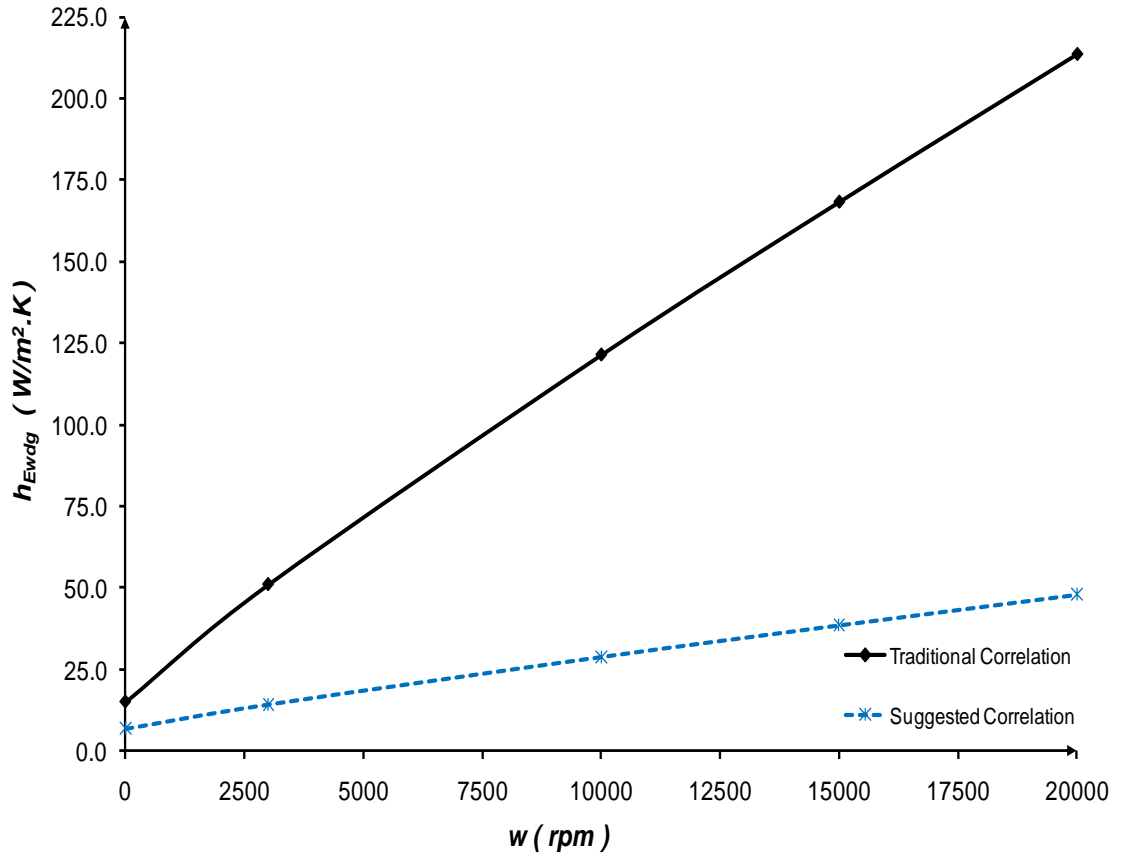


Figure 3.22:  $h_{EWdg}$  variation between pressure independent correlation (Eq. 3.1) and pressure dependent correlation (Eq. 3.13) for a motor running at  $z = 11,500m$

The use of the pressure dependent  $EWdg$  heat transfer correlation (Eq. 3.13) takes the effects of altitude into consideration, and ensures the correct evaluation of the  $EWdg$  heat transfer. Furthermore, the suggested correlation is simple to implement and introduce into commercial software, such as *MotorCAD*.

### 3.3 Concluding Remarks

By direct experimentation at various operating conditions, it has been shown that the user generated lumped circuit thermal model is sufficiently representative of the tested *PMSM*. The creation of the thermal model was

desirable, since a considerable amount of time was saved, as different load scenarios could be simulated rather than tested experimentally. Furthermore, the thermal model was critical in the optimisation of the motor housing geometry. This is presented in the next part, in **Chapter 4**.

Furthermore, the incorporation of  $h_{EWdg}$  as a function of pressure, ensures a more representative simulation study of the *PMSM* when loaded under typical duty cycles commonly encountered during flight level.

# CHAPTER 4

## 4. Motor Finned Housing Optimisation

---

The combined electromagnetic and thermal optimisation of the aforementioned high density, 24 slot – 20 pole aerospace *PMSM* is presented in this chapter. This optimisation was performed as it was established (through *MotorCAD*) that, at flight conditions (i.e.  $z=11,500m$  and  $T_{\infty}=-30^{\circ}C$ ), the critical motor components would exceed their respective allowable operating temperatures.

Due to this, the *MotorCAD* lumped parameter thermal calibrated model described in **Chapter 3**, was used to optimise the motor housing geometry and hence reduce the critical motor component temperatures ( $T_{EWdg}, T_M$ ) while minimising the overall motor weight and volume.

The resulting motor geometry would be deemed the best cooled motor using conventional passive cooling (i.e. fins). This will later be compared to the *FCCS* technique developed.

### 4.1 *PMSM* Finned Housing Geometry Optimisation

The primary objective of the *PMSM* housing optimisation procedure was the maximisation of the overall housing convective heat transfer (i.e. minimum thermal resistance). The conducted analysis spanned several different housing configurations - i.e. axial rectangular fins (Figure 4.2) as well as circular/annular radial fins (Figure 4.7) amongst others. For each housing, or better still, for each fin array configuration, the optimum fin length ( $L_{Fin}$ ), fin thickness ( $t_{Fin}$ ), fin spacing ( $s_{Fin}$ ) as well as percentage corner - cutout ( $\%cut$ ) were established.

In essence, the design strategy that was adopted can be described by the flow chart shown in Figure 4.1.

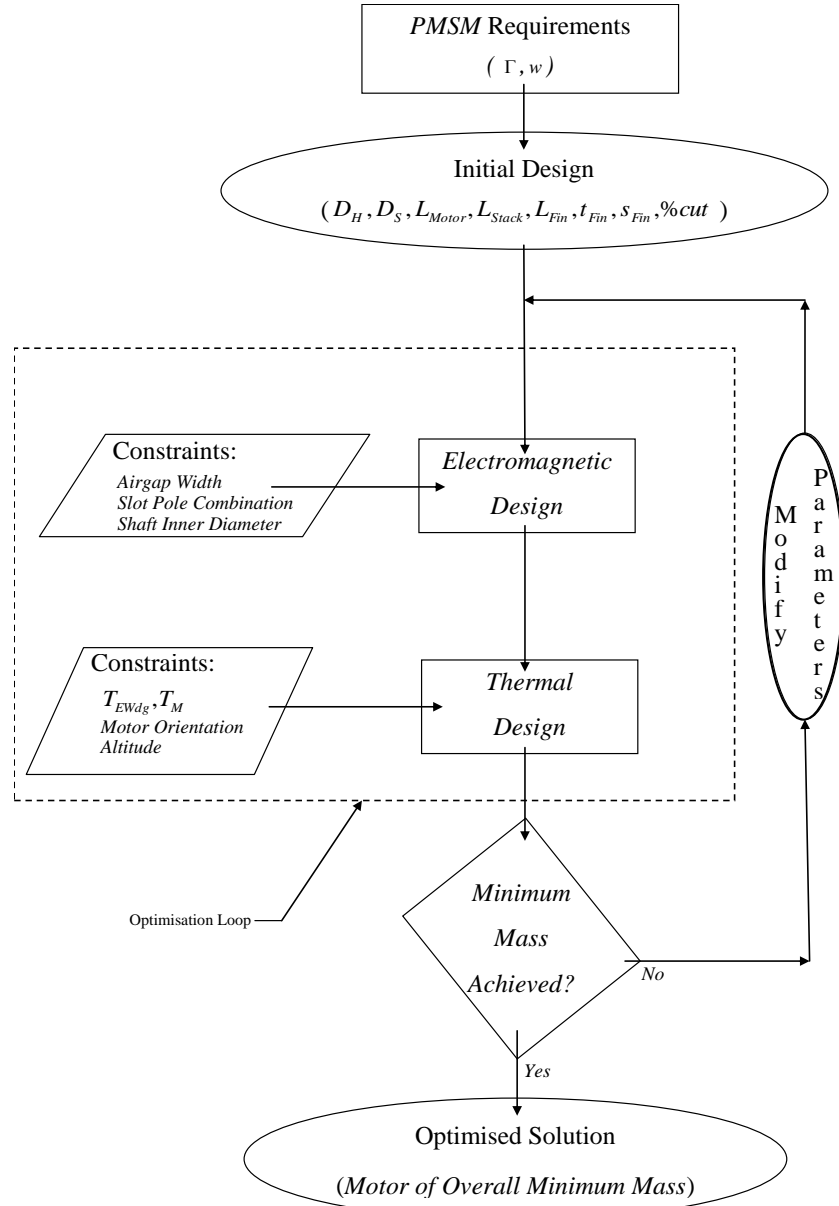


Figure 4.1: Detailed Electric Motor Housing Optimisation Strategy

The optimisation process combines both the electromagnetic as well as the thermal design aspects (conduction, convection and radiation). Given a particular set of requirements, some initial motor dimensions are chosen such as  $D_H$ ,  $D_S$ ,  $L_{Motor}$  and  $L_{Stack}$ . An electromagnetic design study yields the

expected motor losses which are transferred across to *MotorCAD*. On setting up the representative thermal model with the appropriate geometrical parameters and constraints, a sensitivity analysis (with the aid of scripting techniques, *VBA* and a user defined code written in *MathCAD*) was performed for various combinations of geometrical parameters ( $L_{Fin}, t_{Fin}, s_{Fin}, \%cut$ ). The resultant simulated data ( $T_{EWdg}, T_M, m_{Housing}, h_{Convection}, R$ ) from each run were recorded and tabulated. Then the optimisation loop described above is iterated to yield an initial motor mass. The process is then repeated for a range of different motor design parameters (deterministic approach), until the minimum overall motor mass is identified. By adhering to the optimisation technique described, an optimum solution always arises – i.e. a motor with an overall minimum weight for the given constraints. To help simplify the design strategy, automated algorithms were implemented to establish the motor geometry of minimum mass and minimum volume. The adopted methodology, is published in [54].

#### **4.1.1 Axial Rectangular Fins**

The analysis presented hereunder pertains to the optimisation of an axial longitudinal rectangular finned motor housing, the geometry of which is presented in Figure 4.2.

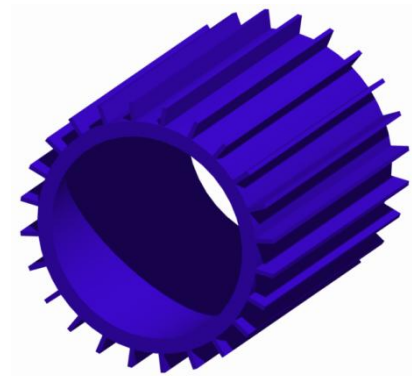
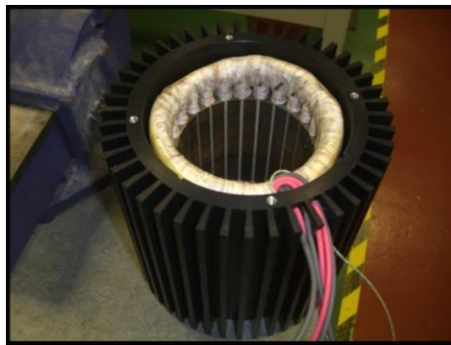


Figure 4.2: Axial Rectangular Finned *PMSM* Housing

Figure 4.3 below depicts a sample set of data when the above mentioned sensitivity analysis was performed. *Microsoft Excel 2007* was further utilised for data manipulation and data presentation.

Fin (mm)				No. Of Fins	Mass of Fins (kg)	T(Housing) (Celsius)	For Single Fin				Fin Array				
Case	Length	Thickness	Fin Spacing				Efficiency	Effectiveness	Constraint	h	Qfin	Efficiency	Qarray	Rarray	
1	0	0	0	0	0.000	362.7	0	0	0	0.000	0	0	0.000		
2	5	1	2.664	136	0.359	365.30	99.99	11.06	1.83E-03	0.670	0.573	99.99	95.88	4.123	
3	10	1	2.664	136	0.718	367.80	99.99	21.10	1.31E-03	0.345	0.567	99.99	86.50	4.599	
4	15	1	2.664												
5	20	1	2.664												
6	25	1	2.664												
7	30	1	2.664												
8	35	1	2.664												
9	40	1	2.664												
10	45	1	2.664												
11	50	1	2.664												
12	5	2	5.33												
13	10	2	5.33												
14	15	2	5.33												
15	20	2	5.33												
16	25	2	5.33												
17	30	2	5.33												
18	35	2	5.33												
19															
20															
21															
22	1	5	2	10	44	0.2318	349.2	99.98756	6.0606	4.53E-03	2.0535	1.846	99.99286	141.51	2.680
23	2	10	2	10	44	0.4648	353.7	99.97418	11.1096	3.56E-03	1.2679	2.114	99.98162	130.7	2.936
24	3	15	2	10	44	0.6966	354.5	99.95923	16.15701	3.08E-03	0.9464	2.300	99.9681	129.38	2.972
25	4	20	2	10	44	0.9296	352.9	99.94133	21.20228	2.81E-03	0.7908	2.511	99.95159	133.94	2.859
26	5	25	2	10	44	1.1616	350.1	99.91987	26.2448	2.65E-03	0.7047	2.750	99.93158	141.74	2.682
27	6	30	2	10	44	1.3944	346.3	99.89459	31.28396	2.55E-03	0.6523	3.004	99.90783	151.17	2.489
28	7	35	2	10	44	1.6264	341.9	99.86528	36.3191	2.49E-03	0.6184	3.268	99.8801	161.58	2.302
29	8	40	2	10	44	1.8582	336.8	99.83172	41.34952	2.44E-03	0.5958	3.535	99.8482	172.46	2.127
30	9	45	2	10	44	2.0916	331.2	99.79379	46.37452	2.41E-03	0.5802	3.802	99.81199	183.52	1.968
31	10	50	2	10	44	2.3226	325.1	99.75138	51.39338	2.39E-03	0.5694	4.065	99.77134	194.52	1.826
32	13	5	3	10	40	0.317	349.9	99.99	4.40	5.62E-03	2.103	2.063	99.99	139.383	2.726
33	14	10	3	10	40	0.634	353.70	99.98	7.78	4.47E-03	1.333	2.335	99.99	129.80	2.956
34	15	15	3	10	40	0.950	354.10	99.97	11.17	3.89E-03	1.007	2.534	99.98	128.90	2.980
35	16	20	3	10	40	1.267	352.5	99.96	14.55	3.56E-03	0.847	2.764	99.96	133.599	2.863
36	17	25	3	10	40	1.584	349.60	99.94	17.93	3.37E-03	0.756	3.020	99.95	141.22	2.688
37	18	30	3	10	40	1.901	345.90	99.92	21.31	3.24E-03	0.701	3.294	99.93	150.51	2.498
38	19	35	3	10	40	2.218	341.50	99.90	24.68	3.16E-03	0.665	3.578	99.91	160.75	2.311
39	20	40	3	10	40	2.535	336.60	99.88	28.06	3.10E-03	0.641	3.870	99.89	171.54	2.137
40	21	45	3	10	40	2.853	331.10	99.85	31.43	3.06E-03	0.625	4.162	99.86	182.52	1.978
41	22	50	3	10	40	3.170	325.00	99.82	34.80	3.03E-03	0.614	4.447	99.83	193.39	1.836
42	23	5	4	10	36	0.380	350.20	99.99	3.57	6.60E-03	2.180	2.316	99.99	138.46	2.746
43	24	10	4	10	36	0.760	353.30	99.98	6.12	5.34E-03	1.424	2.615	99.99	130.43	2.939
44	25	15	4	10	36	1.141	353.30	99.97	8.67	4.67E-03	1.091	2.838	99.98	129.95	2.951
45	26	20	4	10	36	1.521	351.70	99.96	11.72	4.30E-03	0.923	3.092	99.97	134.71	2.833

Figure 4.3: Sample of Data: Determination of Optimum Housing Geometrical Parameters

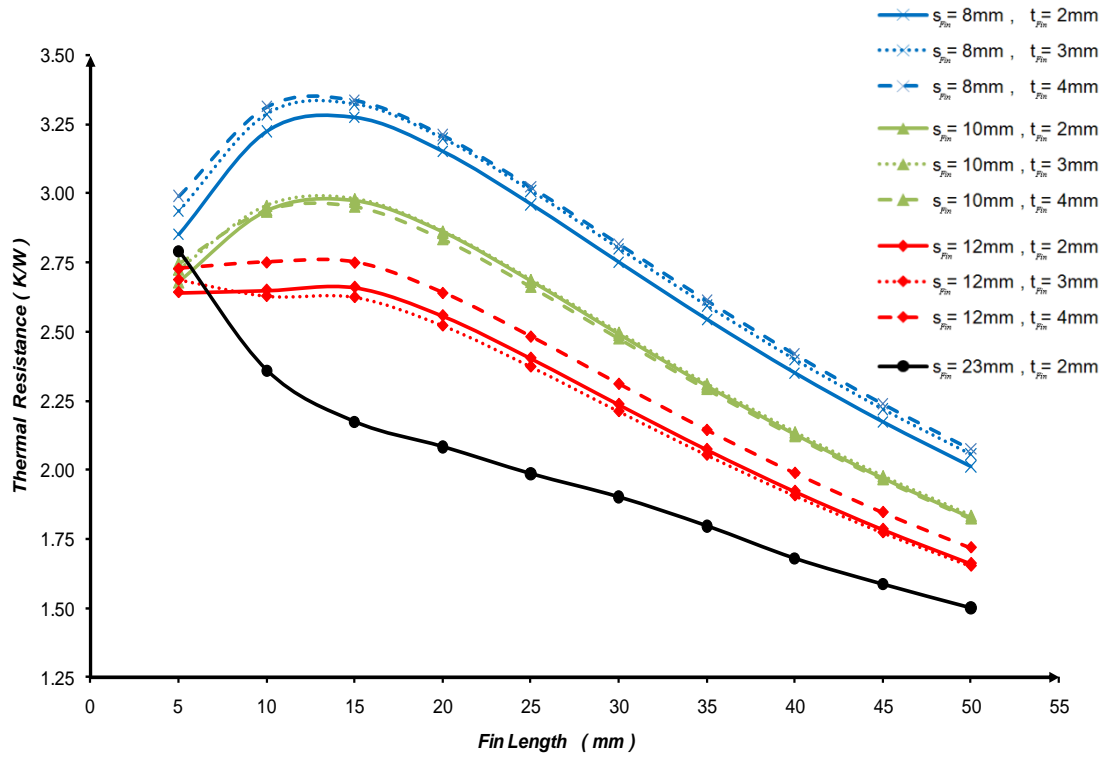


Figure 4.4: Fin Length (mm) vs. Fin Array Thermal Resistance (K/W) for several Axial Housing Configurations

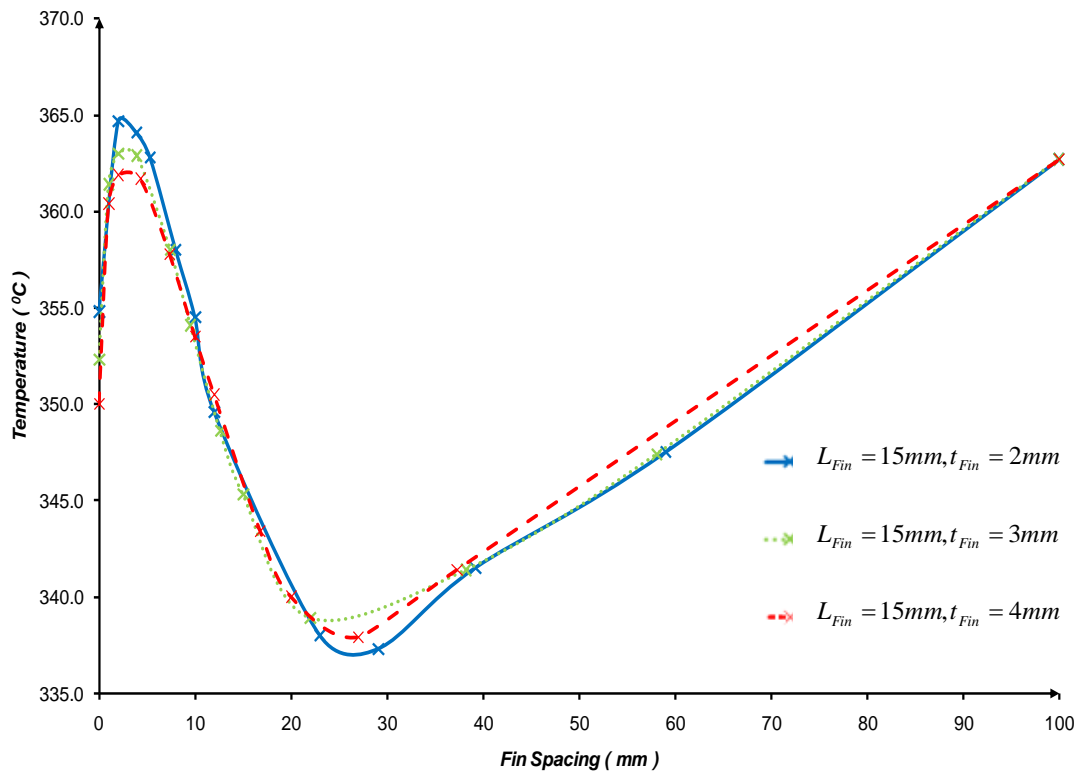


Figure 4.5: Determination of Optimal Fin Spacing – Axial Fins



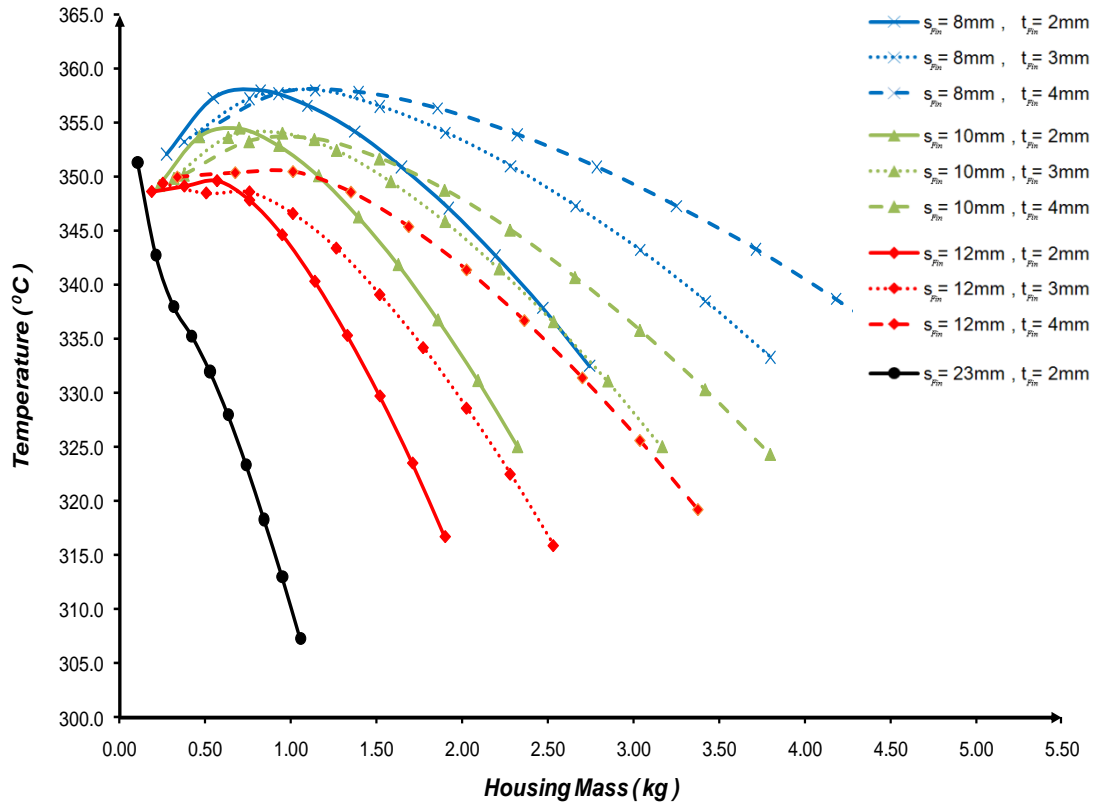


Figure 4.6: Fin Mass (kg) vs. Housing Temperature ( $^{\circ}\text{C}$ ) for several Axial Housing Configurations

While Figure 4.4 highlights the affect of the fin length on the fin array thermal resistance, Figure 4.5 investigates the location of the optimal fin spacing. Furthermore, Figure 4.6 highlights the affect of the housing mass on the housing temperature.

Figure 4.4 indicates that, for all considered geometries, beyond a certain critical  $L_{Fin}$ , an increase in the fin length results in a decrease in the fin array thermal resistance; which correlates directly with what is found in theory [13, 20]. This is attributed to the fact that as  $L_{Fin}$  increases, the fin area available for natural convection also increases, which in turn results in a reduction in the fin array thermal resistance. Furthermore, with an increase in the fin length, the fin heat transfer coefficient is reduced. However, it can be shown that, taking into consideration both factors (the increasing fin surface area, and the

decreasing heat transfer coefficient), an increase in  $L_{Fin}$  results in a decrease in the fin array thermal resistance. This is shown hereunder:

For a vertical flat surface:

$$Nu_L = 0.59(Ra)^{0.25} \quad \dots \text{Eq. 4.1}$$

$$Nu_L = 0.59 \left( \frac{\beta \cdot g \cdot \Delta T \cdot c_p \cdot \mu}{k \cdot \nu^2} \cdot L^3 \right)^{0.25} \quad \dots \text{Eq. 4.2}$$

$$\therefore h = \frac{Nu_L \cdot k}{L} = f \left( \frac{(L^3)^{0.25}}{L} \right) \quad \dots \text{Eq. 4.3}$$

$$h = f(L^{-0.25}) \quad \dots \text{Eq. 4.4}$$

Furthermore:

$$Q = \eta_f \cdot h \cdot A \cdot \Delta T = \eta_{Fin} \cdot h \cdot (W \cdot L) \cdot \Delta T \quad \dots \text{Eq. 4.5}$$

$$R_{Fin} = \frac{\Delta T}{Q_{Convection}} = \frac{\Delta T}{\eta_{Fin} \cdot h \cdot (W \cdot L)} \quad \dots \text{Eq. 4.6}$$

While *Eq. 4.4* indicates that the heat transfer coefficient is a function of ( $L^{-0.25}$ ), *Eq. 4.5* indicates that the convective heat loss, while being a function of ( $h$ ) is also a function of the fin area ( $A$ ) which is a function of ( $L$ ). Thus, on substituting all the data into *Eq. 4.6*, an increase in  $L_{Fin}$  would inherently still result in an increase in heat transfer ( $Q$ ), resulting in a lower fin resistance ( $R_{Fin}$ ).

Another trend noticeable in Figure 4.4, is that, initially, an increase in  $L_{Fin}$  results in an increase in the thermal resistance rather than the converse. This trend has also been identified in Figure 4.5, and furthermore, has been reported by other researchers [18, 19, 26] as highlighted in the literature survey presented in **Chapter 2**. This apparent anomaly can be attributed to the

stagnant air that is trapped between the lengthy closely spaced fins. While the addition of these fins results in an increase in the exposed surface area ( $A_{Fin}$ ), the reduction in  $s_{Fin}$  results in stagnant air being trapped between the fin base and the fin side walls. This stagnant air in turn generates boundary layer interferences which advertently reduce the heat transfer [18]. It is noted, that as the fin spacing increases, this maximum, decreases until, on reaching a significantly large fin spacing ( $s_{Fin} = 23mm$ ) this anomaly completely disappears.

A further study was carried out to determine the optimum fin spacing for the axial housing to minimise weight. Figure 4.5 indicates that, for all considered fin configurations, the optimum fin spacing ( $s_{Opt}$ ) lies between  $20mm$  and  $30mm$ . However, Figure 4.6 clearly indicates that, a reduction in the fin thickness and an increase in the fin spacing results in the housing mass reduction. The latter holds true, as an increase in  $s_{Fin}$  implies a lesser number of fins ( $N$ ) which in turn results in a lower housing mass.

From the presented graphs, it may be concluded that the optimum axial finned housing geometry for the *PMSM* being considered is that of:  $s_{Fin} = 23mm$  and  $t_{Fin} = 2mm$ .

#### 4.1.2 Radial Fins – Zero Corner-Cutout

A similar analysis to that presented in *Section 4.1.1* was conducted for a radial finned housing geometry (Figure 4.7).

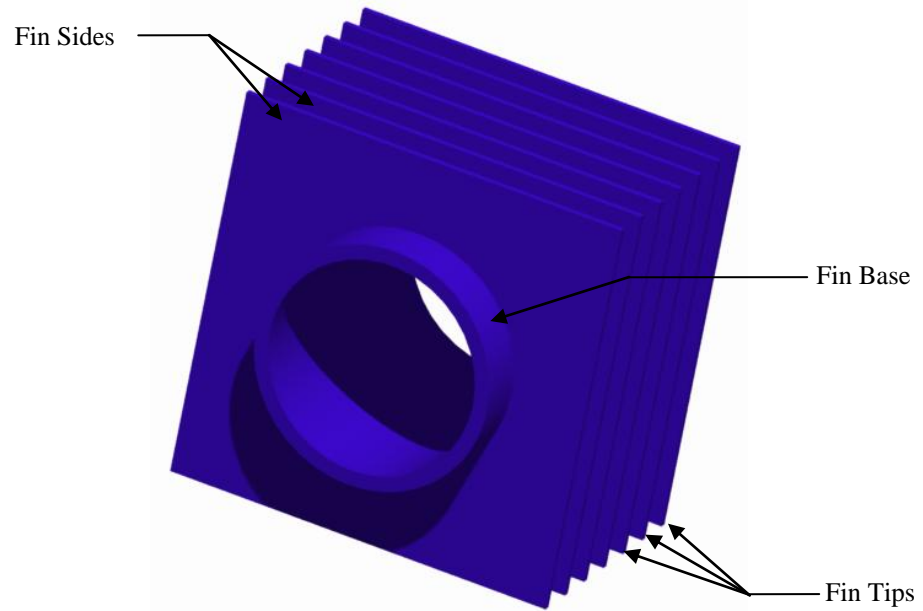


Figure 4.7: *ProE* model of the considered Radial Finned Housing Geometry

For the considered radial finned housing geometry, the optimum fin spacing ( $s_{Opt}$ ) was established to lie between  $16mm$  and  $20mm$ , as depicted in Figure 4.8. Figure 4.9 illustrates the radial finned housing thermal resistance variation with various fin spacings and fin thicknesses.

Examining Figure 4.9, while also considering the mass characteristics of the individual finned geometries, it was established that the optimum radial finned geometry that minimised both the thermal resistance and the housing mass was that of  $s_{Fin} = 20.0mm, t_{Fin} = 2.0mm$ .

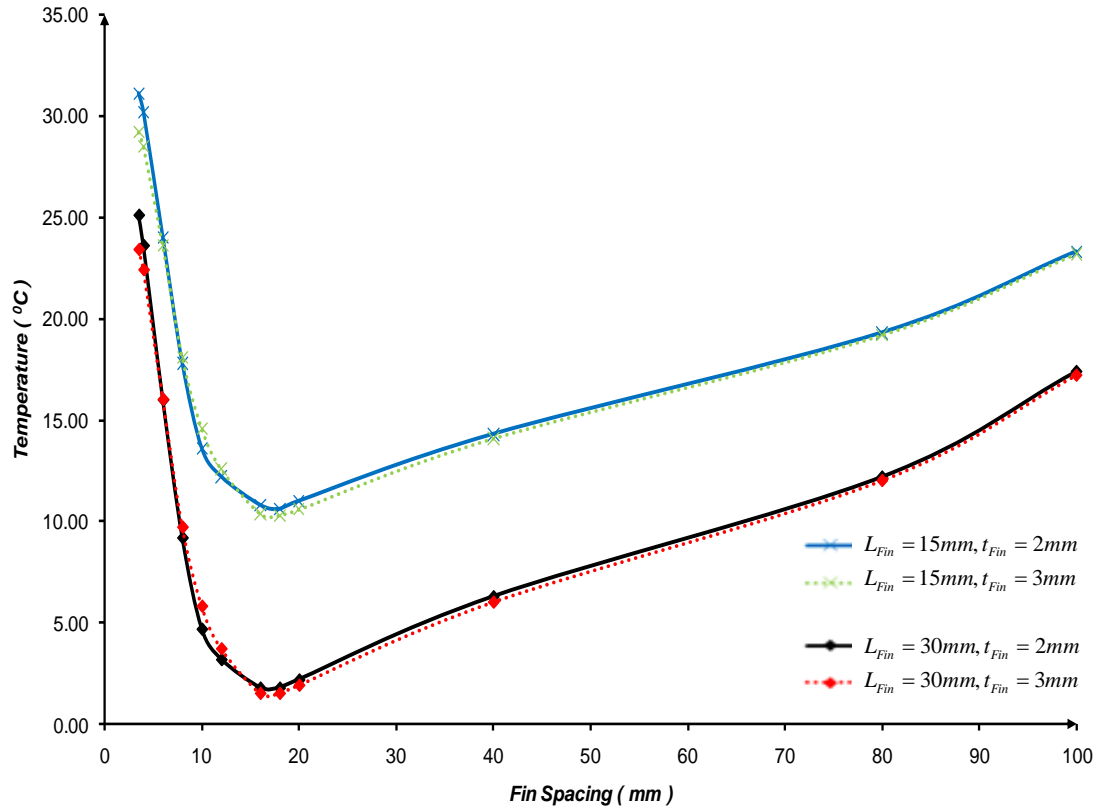


Figure 4.8: Optimal Fin Spacing Determination – Radial Finned Housing

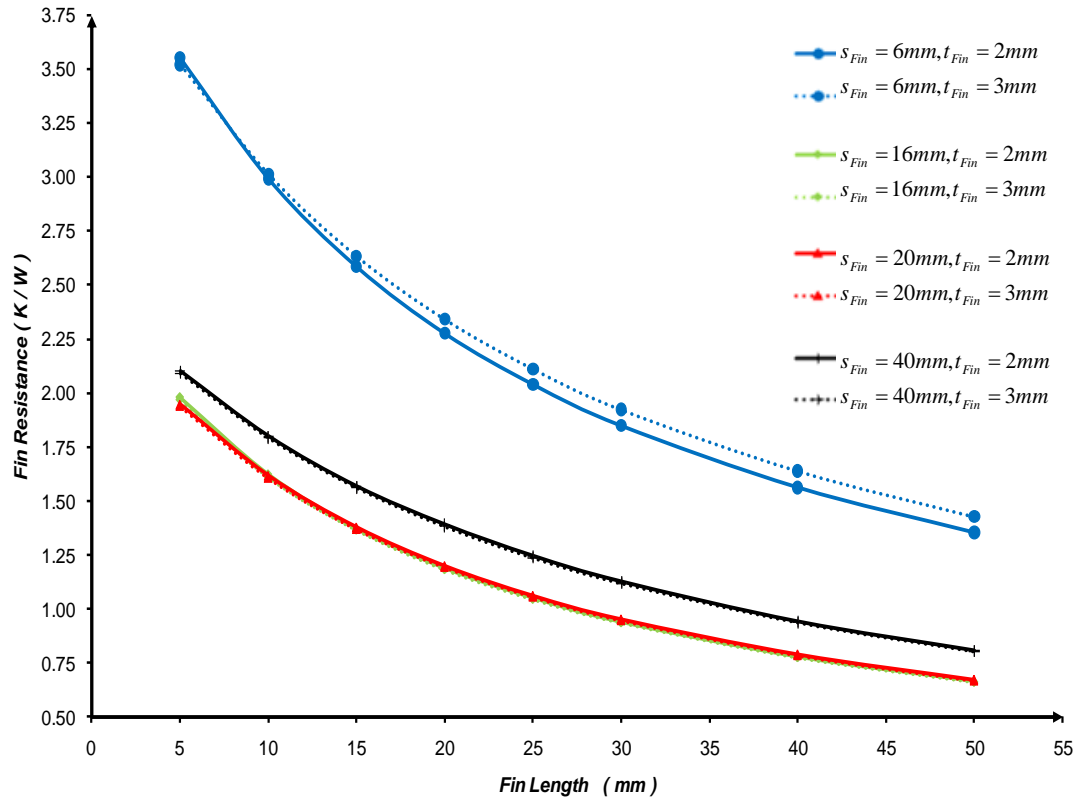


Figure 4.9: Fin Length (mm) vs. Fin Array Thermal Resistance (K/W) for a Radial Finned Housing Configuration

#### 4.1.3 Radial Fins – Variable Corner Cutout

A further analysis was carried out on the radial finned geometry with corner cutouts as described in the previous section. It was envisaged that a reduction in the radial finned surface area (Figure 4.10) while decreasing the convective heat dissipated (i.e. increase in thermal resistance) would result in a lesser housing mass and volume. Thus a trade-off (optimum geometry) should exist. Thus the hereunder analysis was performed to evaluate the affects of this additional parameter -  $\%cut$  .

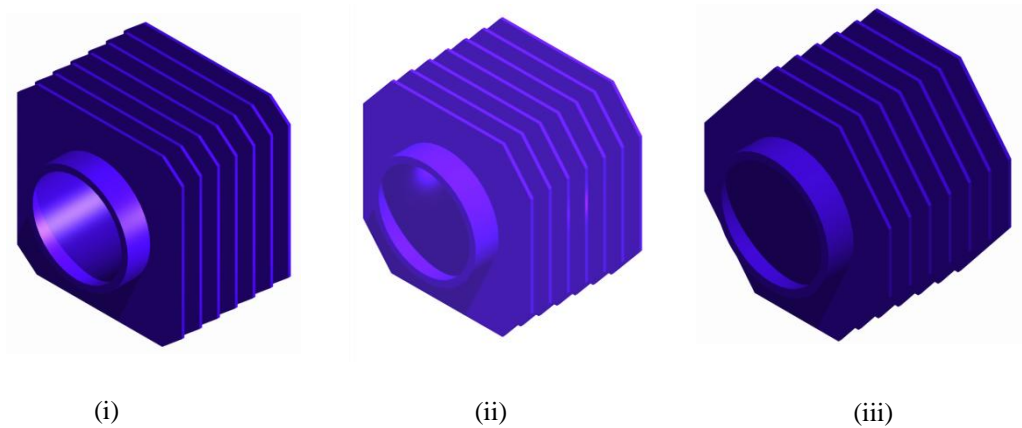


Figure 4.10: Radial Finned Housing with:

(i) 10% Corner-Cutout (ii) 30% Corner-Cutout (iii) 50% Corner-Cutout

The percentage corner-cutout ( $\%cut$ ) may be better explained by considering the below graphical representation:

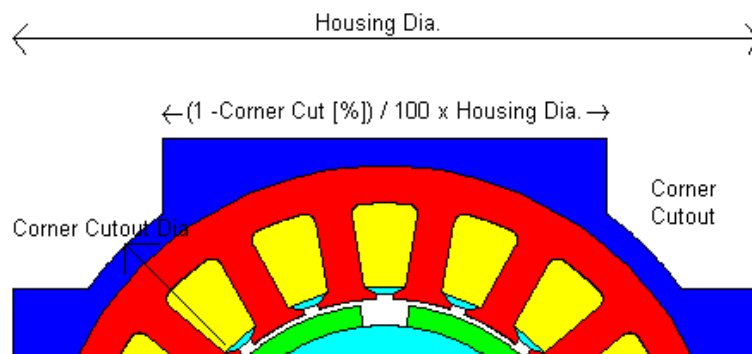


Figure 4.11: Definition of the *Percentage Corner-Cutout* ( $\%cut$ )

In this study, the considered percentage corner-cutouts were; 10%, 30% and 50%. The earlier established optimal geometry ( $s_{opt} = 20.0mm, t_{Fin} = 2.0mm$ ) was used as a base case on which the affect of %cut was investigated. For each distinct housing geometry, the housing fin array thermal resistance and fin housing mass were established - the results of which are presented in Figure 4.12 and tabulated in Table 4.1.

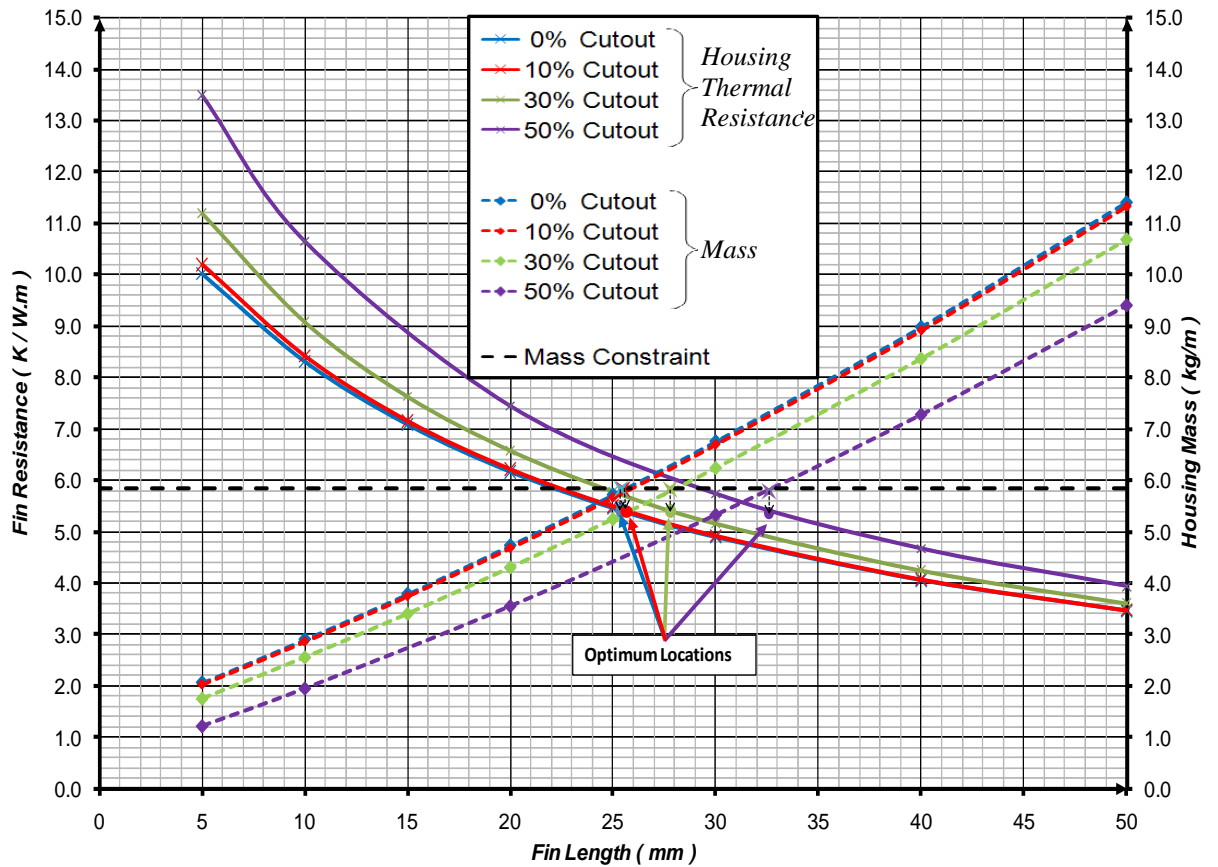


Figure 4.12: Determination of the Optimal %cut for a Radial Finned Housing:  
 $s_{opt} = 20.0mm, t_{Fin} = 2.0mm$

Figure 4.12 graphically depicts the Fin Length (mm) on the x-axis against both the Housing Thermal Resistance (K/W.m) and Fin Mass (kg/m) on the primary and secondary y-axis respectively. To identify the best suited geometrical configuration, a housing mass constraint of 1.14kg (5.83kg/m) was setup. This is typical of high density aerospace PMSM. All housing configurations

exceeding the imposed mass constraint (i.e. above horizontal mass constraint) were neglected.

For each %cut, the optimum location (minimum mass, minimum thermal resistance) occurs at the intersection points between the respective housing mass plot and the housing mass constraint – then noting the accompanying housing thermal resistance.

	Housing Mass ( kg )	Fin Resistance ( K/W )	Optimal Fin Geometry ( mm )
<b>0% Cutout</b>	1.14	1.05	$L_{Fin} = 25, t_{Fin} = 2, s_{Fin} = 20$
<b>10% Cutout</b>	1.14	1.05	$L_{Fin} = 26, t_{Fin} = 2, s_{Fin} = 20$
<b>30% Cutout</b>	1.14	1.05	$L_{Fin} = 28, t_{Fin} = 2, s_{Fin} = 20$
<b>50% Cutout</b>	1.14	1.05	$L_{Fin} = 33, t_{Fin} = 2, s_{Fin} = 20$

Table 4.1: Optimal Housing Geometry on applying a Mass Constraint of 1.14kg

It has been established that the optimum results all lie on the same line, indicating that for the same housing mass constraint, for each of the considered %cut, the same thermal resistance is attained, by means of different fin lengths. However, from Table 4.1, the selection of a 0% cutout results in the minimum occupied volume, and thus is the chosen configuration.



#### **4.1.4 Comparative Study: Axial Longitudinal Rectangular vs. Radial Fins**

In this section, a comparative study between all the considered electric motor finned housing geometries is presented. This was undertaken to establish which finned geometrical housing configuration system is best suited to limit the motor temperatures.

Figure 4.13 and Figure 4.14, are a direct comparison, between the original axial finned housing ( $s_{Fin} = 8mm, t_{Fin} = 3mm$ ), the optimum established axial longitudinal rectangular fin geometry ( $s_{Opt} = 23mm, t_{Fin} = 2mm$ ), and the established optimum radial finned geometry ( $s_{Opt} = 20mm, t_{Fin} = 2mm, \%cut = 0\%$ ).

Figure 4.13 indicates that a radial finned motor housing results in a significantly lower housing thermal resistance when compared to an axial finned housing. Furthermore, considering Figure 4.14, for the same housing mass, a lower housing temperature is attained by means of a radial housing than with an axial longitudinal finned housing. In fact, the above results compare well with literature. This is because the axial longitudinal finned system is suitable for 'blown over machines', i.e. when an axial fan is coupled to the shaft of the electric motor. However, as mentioned earlier, due to reliability issues, in the aerospace industry, natural convection is the preferred and permissible method of cooling.

### Fin Design and Motor Optimisation

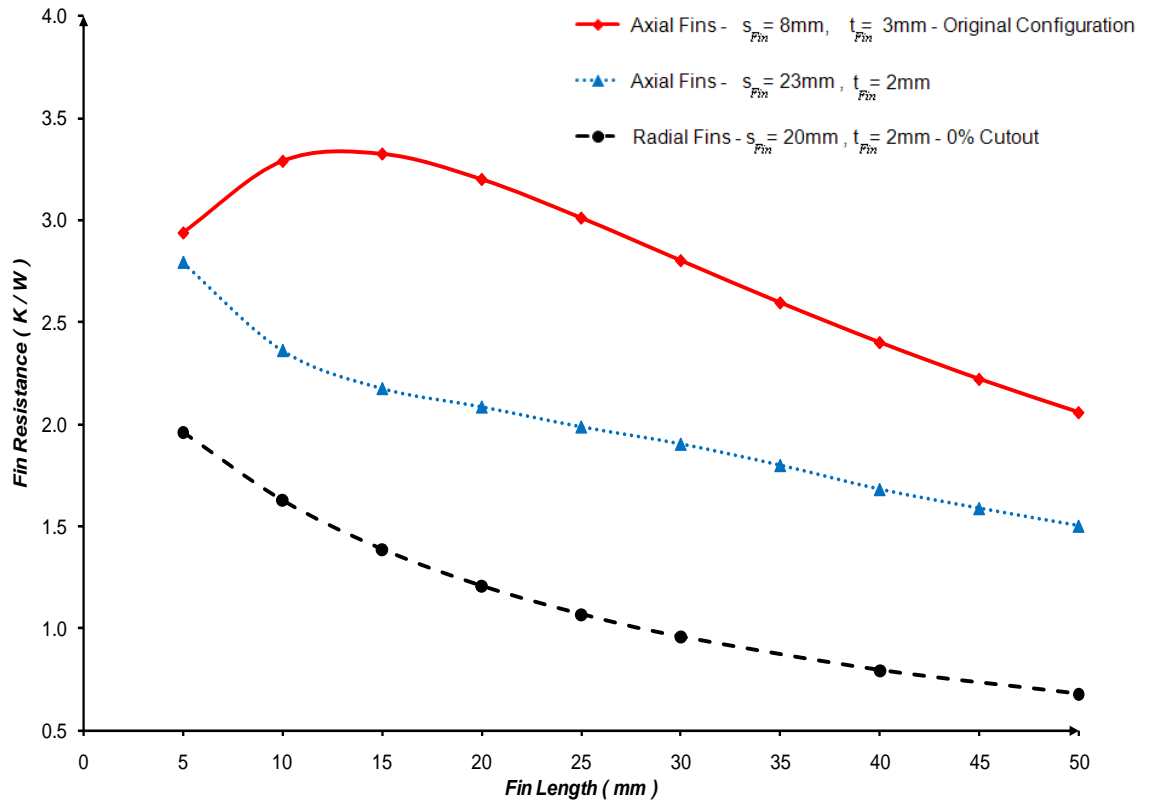


Figure 4.13: Comparative Study between the different Electric Motor Housing Types:  $R$  (K/W) vs.  $L_{Fin}$  (mm)

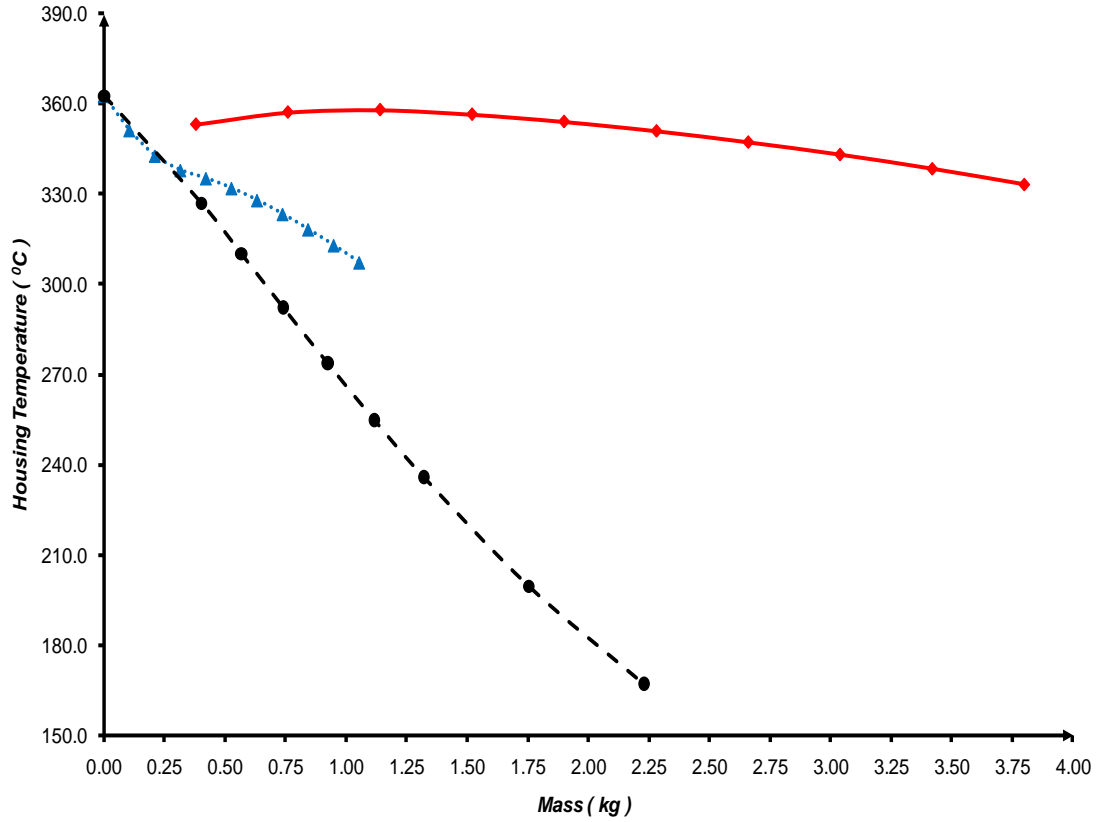


Figure 4.14: Comparative Study between the different Electric Motor Housing Types:  $T_H$  (°C) vs.  $m_{Housing}$  (kg)

## 4.2 Concluding Remarks

In conclusion, it has been established that the best suited natural convection finned housing, for any horizontally-mounted electric motor is a radial one. Furthermore, for the current aerospace *PMSM* with a mass constraint of  $5.83\text{kg/m}$ , the optimal cooling geometry is:

$$\%cut = 0\%$$

$$s_{Fin} = 20.0\text{mm}$$

$$t_{Fin} = 2.0\text{mm}$$

$$L_{Fin} = 25.0\text{mm}$$

The radial finned housing geometry is considered to be the best naturally cooled housing possible using traditional techniques and thus shall be considered as a base case to which the implemented innovative *FCCS* shall be compared.

However, a fully optimised naturally cooled, radial finned housing alone, is still not sufficient to limit the critical motor components (Magnets and *EWdg*) during flight operation.

It was established that the overall housing heat transfer coefficient for the fully optimised naturally cooled, radial finned housing is three times less than what is necessary to limit the temperature build up in the *PMSM*. Thus, it was decided to further improve the thermal management of the considered *PMSM* by additionally introducing an innovative *FCCS* mechanism – an oscillating piezoelectric fan. As discussed in **Chapter 2**, the investigated *FCCS* is subject to the same stringent constraints as traditional cooling techniques: passive system of minimum space (volume) and weight, while being highly fault tolerant.

The following chapters (**Chapter 6, 7, 8 and 9**) evaluate each of the above constraints in turn.

# CHAPTER 5

## 5. The Experimental Facility

---

The following chapter details two distinct experimental facilities (Thermal and *PIV*) that were designed, manufactured, and commissioned to carry out the necessary investigations on the cooling capabilities of an oscillating piezoelectric fan, i.e. *FCCS*.

In *Section 5.1*, the geometry of the implemented piezoelectric fan is described. The design and fabrication of the piezoelectric fan drive circuitry is further presented, along with the *3D* positioning system in *Section 5.2*. The thermal rig used in the measurement of the natural and forced heat transfer coefficients is presented in *Section 5.3*, while *Section 5.4* describes the *PIV* facility used to measure and record the airflow fields generated by an oscillating piezoelectric fan. An error analysis is further presented in *Section 5.5*.

### 5.1 Piezoelectric Fan Structure and Fan Drive Circuitry

The piezoelectric fan used and tested throughout this study was ordered from *Piezo Systems, INC.*, the structure of which is detailed in Figure 5.1.

The piezoelectric fan has a total length of  $76.7\text{mm}$ , a width of  $12.7\text{mm}$ , a thickness of less than a millimetre and weighs just  $2.80\text{g}$ . As detailed in *Chapter 1*, a piezoelectric fan consists of a piezoelectric patch (*PZT*), mounted onto a lightweight cantilever beam.

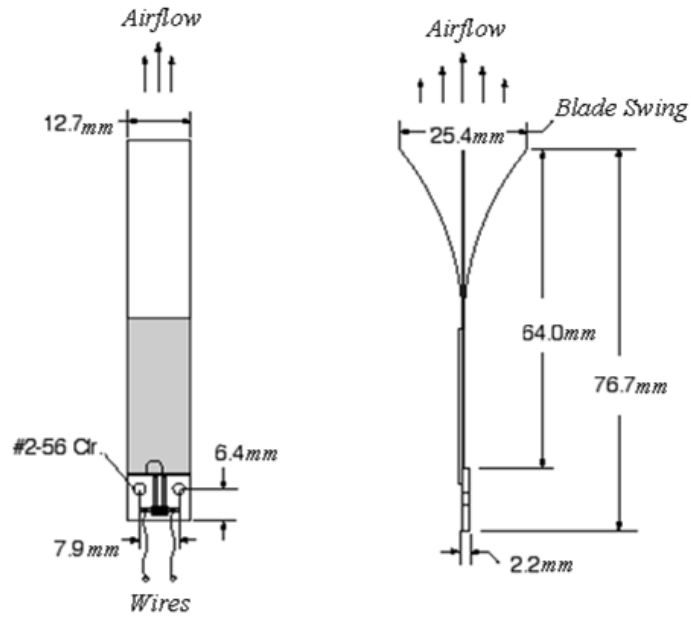


Figure 5.1: Piezoelectric Fan Characteristic Dimensions – Courtesy of *Piezo Systems INC.*

The maximum power consumption of a single piezoelectric fan, operating at the maximum amplitude is of  $30mW$ . Furthermore, the fan has a natural frequency ( $f$ ) of  $60Hz$  and operates at a maximum voltage ( $V_{Pz}$ ) of  $115VAC$ .

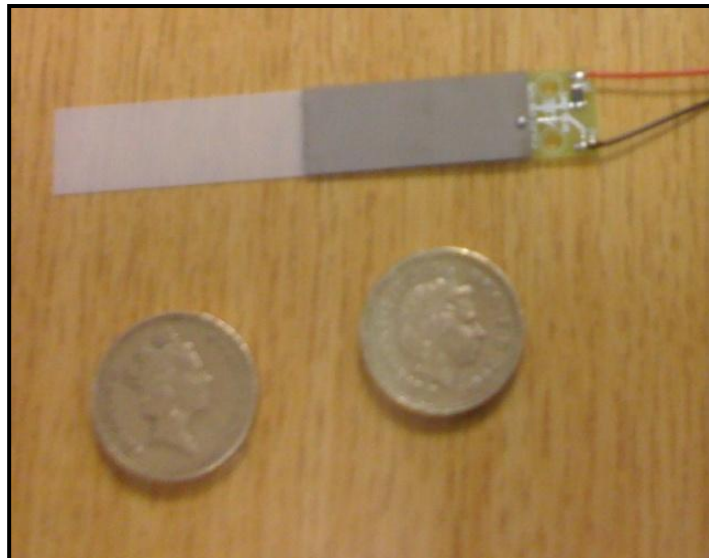


Figure 5.2: A High Voltage (V115) Piezoelectric Fan

A drive circuit, built to operate the piezoelectric fan is depicted in Figure 5.3. The drive circuit comprises an operational amplifier (Op-Amp) coupled to a step-up transformer. The Op-Amp was powered from a 30VDC power supply, while a signal generator connected to the Op-Amp dictated the operational frequency and waveform (sine, square, triangular). The output of the Op-Amp was connected to the primary of a transformer, with the secondary transformer terminals being connected to the piezoelectric fan terminals as shown in Figure 5.3. A high-precision multimeter is further connected across the piezoelectric fan terminals to continuously monitor the input piezoelectric fan voltage, while a CRO monitored and displayed both the supplied current and voltage.

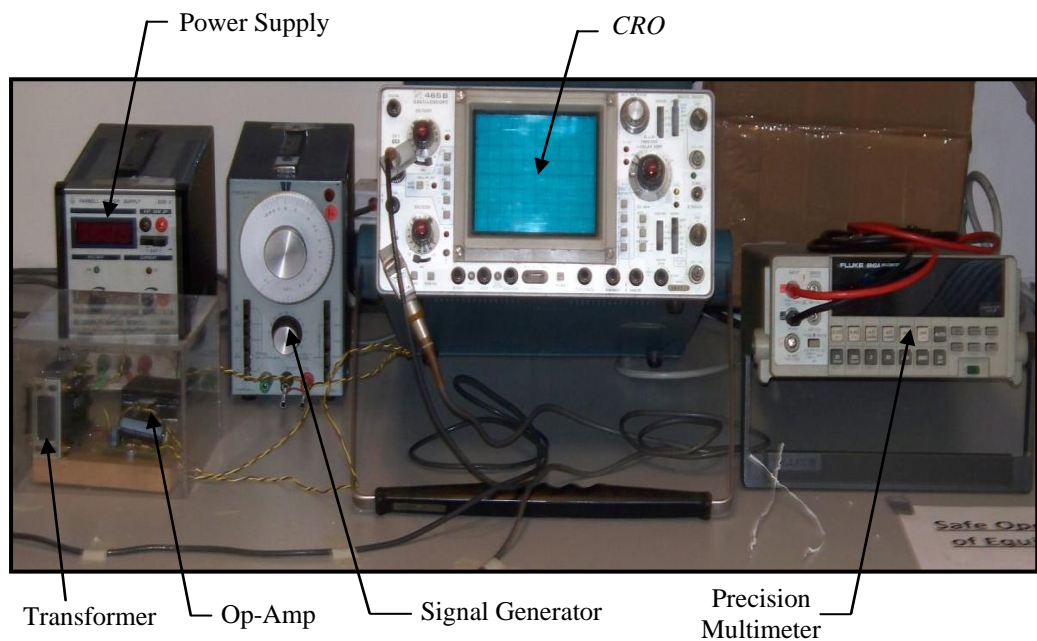


Figure 5.3: Piezoelectric Fan Drive Circuitry and Monitoring Equipment

The drive circuitry, together with the accompanying instrumentation ensured that any voltage ( $0 - 115\text{Volts}$ ), and signal (sinusoidal, triangular and square) and any frequency could be supplied to the piezoelectric fan under test, ensuring the greatest flexibility.

Initial tests (by means of a high speed camera) were undertaken to determine the resonant frequency of the piezoelectric fan. As stated in the literature, operating the piezoelectric fan at the resonant frequency results in the maximum vibrational amplitude, which in turn implies that the highest fan tip velocities are generated, providing the largest amount of cooling.

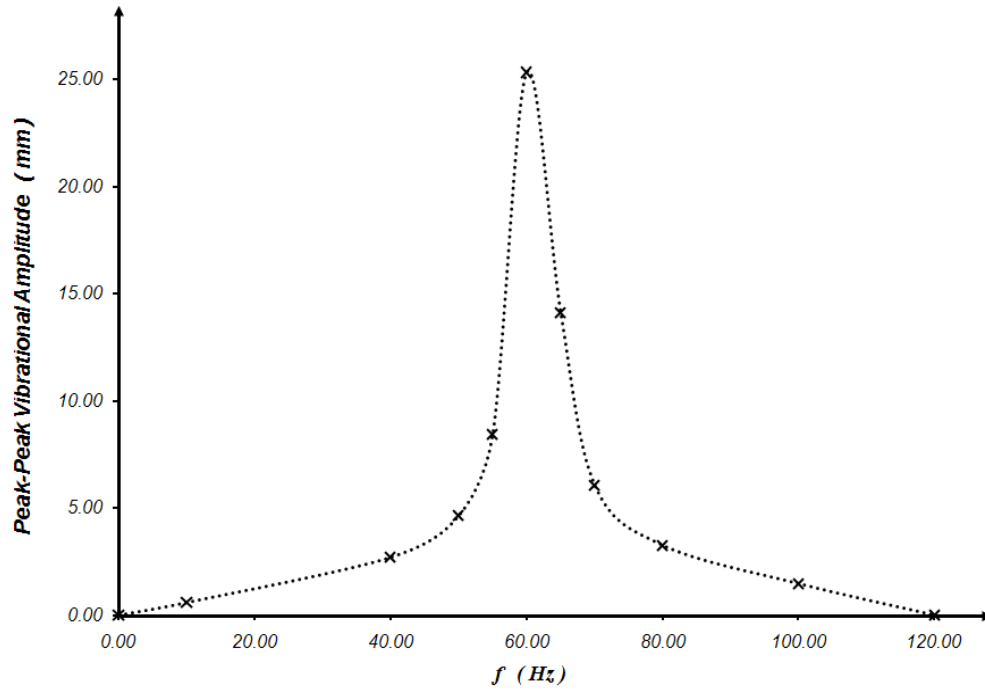


Figure 5.4: Piezoelectric Fan Frequency Characteristics when operating at  $V_{P_z} = 115.0V$

Figure 5.4 indicates that the natural frequency of the piezoelectric fan is located at  $60Hz$ , resulting in a maximum blade tip displacement of  $A_{P-P} = 25.40mm$ . The peak-to-peak amplitude drops steeply as the operating piezoelectric fan frequency is varied from the natural frequency. This is also evident in Figure 5.5.

As the piezoelectric fan amplitude ( $A_{P_z}$ ) is dependent on the applied piezoelectric fan voltage ( $V_{P_z}$ ), during the experimentation stage it was decided to monitor the latter parameter ( $V_{P_z}$ ), as doing so it is far simpler and takes less time. Thus throughout the experimentation stage (both Thermal and *PIV*), the piezoelectric fan voltages are as depicted in Table 5.1. Furthermore,

the selected amplitude range ensured that a broad range of *Reynolds* numbers is considered, which in turn increases the possibility of locating the flow transition point (laminar – turbulent).

The *Reynolds* number ( $Re_{P_z}$ ) calculation is based on the equivalent hydraulic diameter ( $D_{P_z}$ ),  $A_{P_z}$ , and  $w$  as given hereunder.

$$Re_{P_z} = \frac{A_{P_z} \cdot w \cdot D_{P_z}}{\nu} \quad \dots \text{Eq. 5.1}$$

$$D_{P_z} = \frac{4A_{P_z} \cdot w_{Fan}}{2A_{P_z} + w_{Fan}} \quad \dots \text{Eq. 5.2}$$

This transition will have adverse effects on the flow and thus it is essential to be aware of this possibility. This is further characterised in **Chapter 7** and **Chapter 8**.

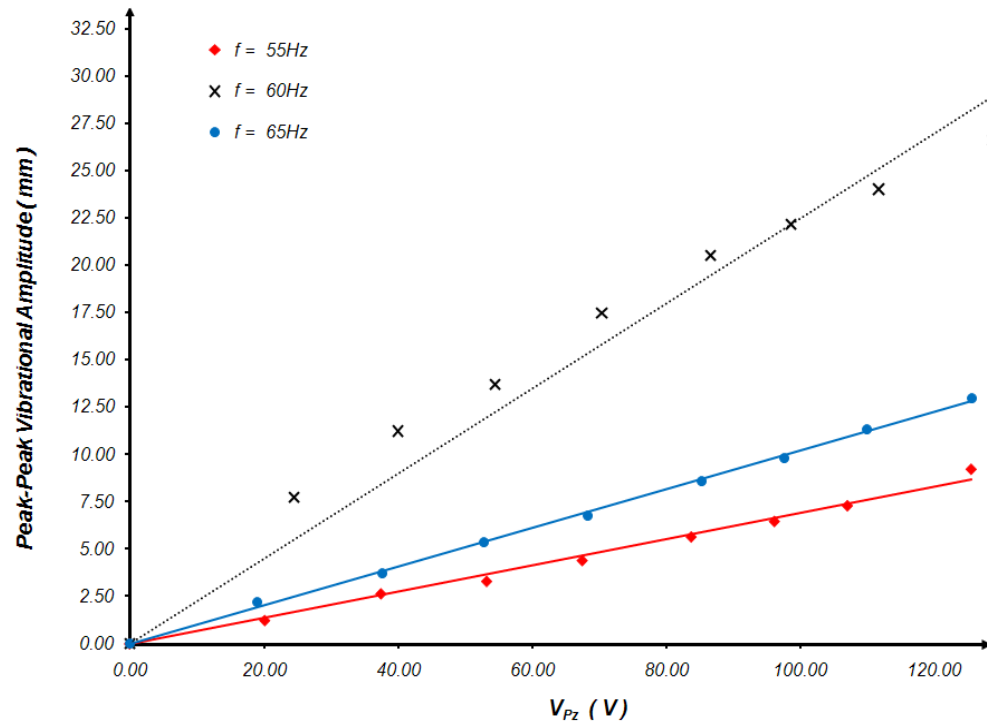


Figure 5.5: Piezoelectric Fan Amplitude Characteristics - Sine Input Waveform

Figure 5.4 and Figure 5.5 both indicate that operating the piezoelectric fan at its natural frequency generates the maximum vibrational amplitude, which in turn will generate the largest fan tip velocities.



Applied Fan Voltage, $V_{P_z}$ (V)	Fan Amplitude, $A_{P_z}$ (mm)	Fan Amplitude, $A_{P-P}$ (mm)	Reynolds No., $Re$
30.00	3.38	6.75	767.7
60.00	6.75	13.50	2279.6
90.00	10.13	20.25	4078.3
115.0	12.70	25.40	5549.1

Table 5.1: Voltage – to – Amplitude Conversion Measurements

## 5.2 3D Positioning System

A methodology for the accurate positioning of the piezoelectric fan in 3D space was required. Thus, a positioning system was designed and ordered from *Machine Building Systems*. The 2D positioning system (Figure 5.6) consisted of two ‘x’ and ‘y’ sliders which traversed on grooves in the aluminium framework. However, the rig was slightly modified to further incorporate the third axis – the z-axis (Figure 5.7), together with the mounting of two micrometer screw gauges. The gauges were mounted on both the ‘x’ and ‘y’ traverses respectively.

A small raised platform was also mounted to the aluminium framework, its sole purpose being to centrally locate and support the test section, both for the velocity measurements as well as the thermal measurements. This platform ensured that the test piece (heat sink unit-cell) is always firmly mounted and level.

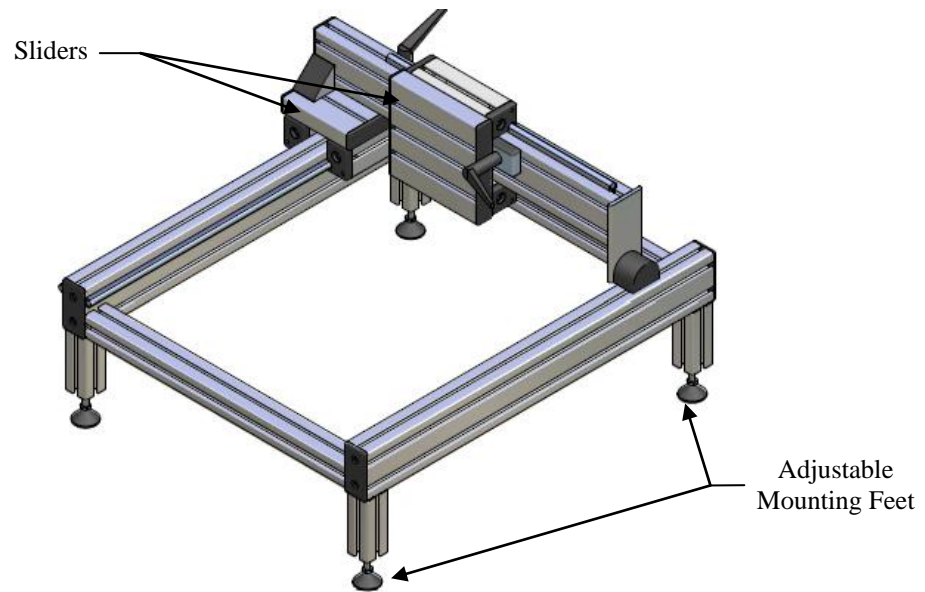


Figure 5.6: 2D Positioning System – Courtesy of *Machine Building Systems*

The 3D positioning system ensured the precise positioning of the piezoelectric fan and was utilised, both during the thermal acquisition stage as well as during the flow field measurements.

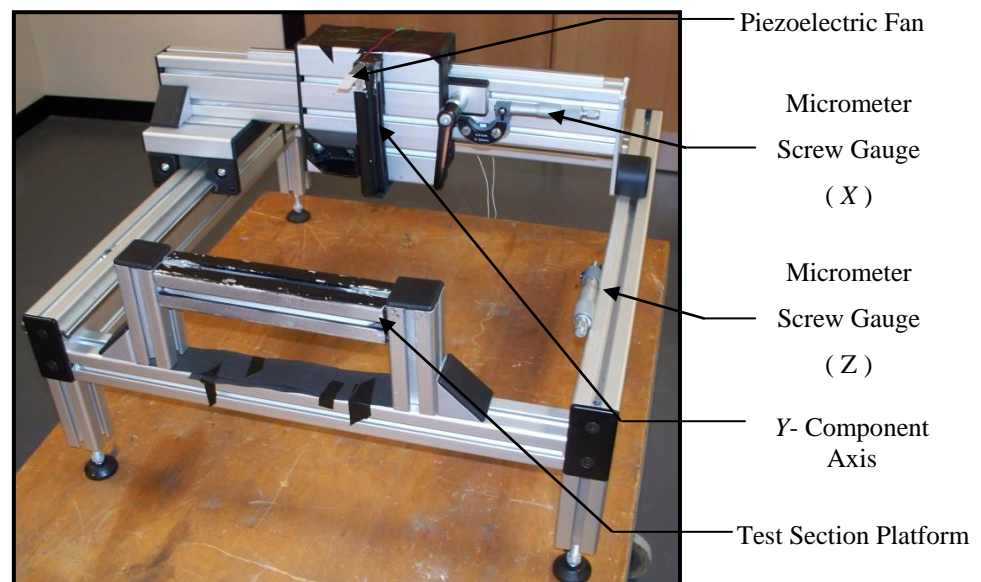


Figure 5.7: 3D Positioning System

A ground connection (i.e. earth) was also added to the 3D positioning framework to eliminate the risk of electric shock. This ground connection was required as atomised water was used in a high voltage environment throughout the *PIV* testing stage. This is further explained in **Section 5.4**

### **5.3 Thermal Facility**

A thermal rig was designed and built with the intention of using a thermal imaging camera to capture the local temperatures on a surface produced by an oscillating piezoelectric fan when tested under different operating conditions ( $G$ ,  $A_{P\pi}$ ,  $S$ , orientation).

In this study, it was decided to implement a flat, vertical finned housing rather than the previously established optimal radial housing. This simplification was chosen for this first point of study as no studies have ever been published to date on the cooling capabilities of piezoelectric fans on finned heat sinks. Thus, it was envisaged that the evaluation of the cooling capabilities of the *FCCS* on a flat vertical heat sink, will be representative of a radial finned housing. Furthermore, it was decided that if the implemented *FCCS* is seen to perform adequately, a future study could be performed on a radial finned housing.

The thermal rig comprised a supporting steel framework onto which were mounted a hollow wooden fin base (measuring  $180mm \times 180mm$ ) and a wooden fin side wall (measuring  $180mm \times 100mm$ ), as depicted in Figure 5.8.

Inside the fin base and fin side wall structures, carbon fibre (*CF*) heating elements together with sufficient insulation material were inserted (Figure 5.10). Five *K-type* thermocouples were also attached to the back of each of the wooden structure (i.e. *FB* and *FSW*) as shown in Figure 5.8 hereunder. These thermocouples were introduced so as to determine the heat loss by conduction from the heating element.

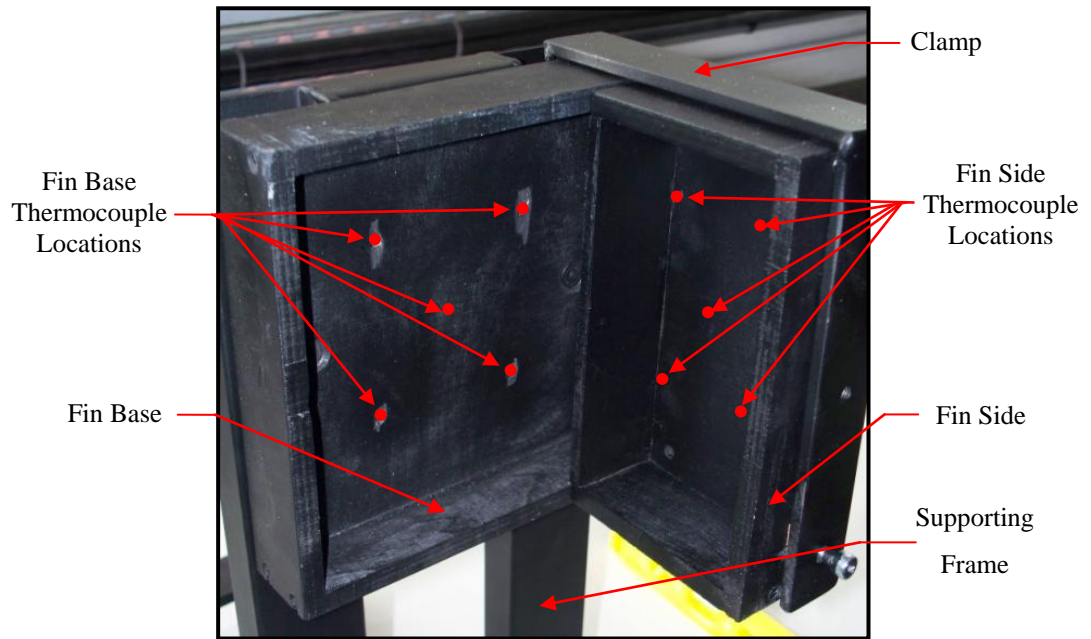


Figure 5.8: Hollow Wooden Structure

### 5.3.1 Carbon Fibre Heating Elements

The heater of choice was a wet-laid nonwoven carbon veil,  $0.21mm$  thick, purchased from *Technical Fibre Products*. Carbon fibre was chosen for the heating element, as it ensured that a uniform heat flux was produced and maintained throughout the duration of the experiment, as shown in Figure 5.9. Another reason for using a minimal heating element thickness was to limit the in-plane  $2D$  conduction effects.

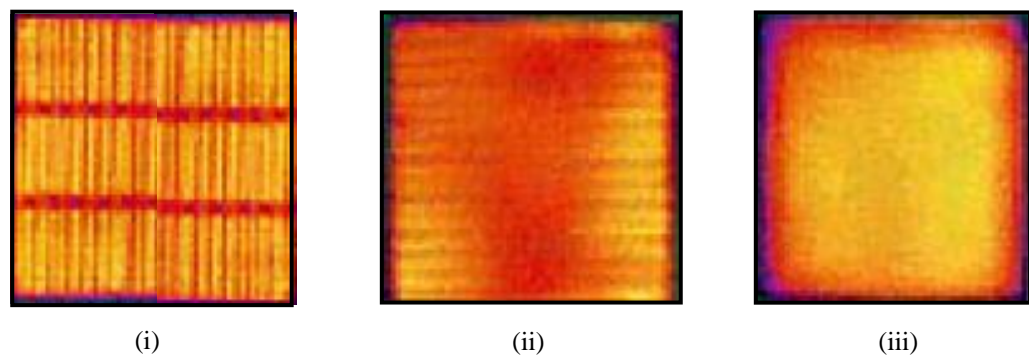


Figure 5.9: Heating Element Types [53]

- (i) Foil Heater
- (ii) Wire Heater
- (iii) CF Veil Heater

Figure 5.9 depicts three commonly used heating element types: Foil, Wire and *CF* Veil. Observing the 2D temperature plots, it is evident that the heat flux generated by the latter heater type (*CF* veil) is more uniform, when compared to a foil or a wire heater. Furthermore, unlike foil or wire heaters, *CF* veil heaters do not become inoperative as a result of single small local failures [55].

Copper strips were attached and clamped by means of several holding screws to the *CF* veil to act as busbars, from which leads were connected to a variable *DC* power supply - Figure 5.10. The *CF* veil and copper assembly was then attached to a 4mm thick, high temperature insulating sheet (*Tufnol*) and then further insulated with high temperature foam, as illustrated in Figure 5.10. The presence of the *Tufnol* sheet is twofold. Firstly as a thermal mass enhancer: since a larger thermal mass would imply that less temperature fluctuations would occur. Secondly, the *Tufnol* sheet would provide a flush and smooth surface to which the *CF* veil can be bonded, thus ensuring precise thermal measurements.

One such heating element unit is depicted in Figure 5.10, while Figure 5.11 represents a top view of a fully insulated heating element assembly when located in the previously mentioned hollow wooden fin base structure.

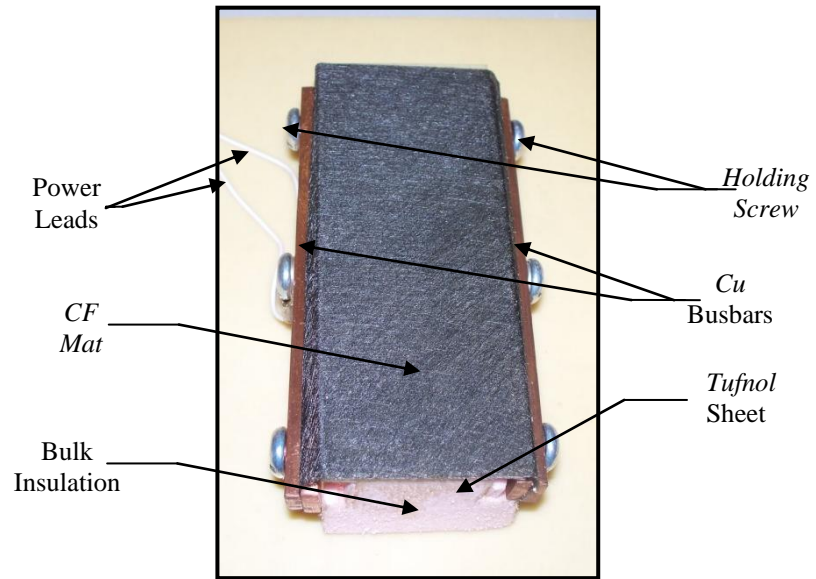


Figure 5.10: Heating Element Unit

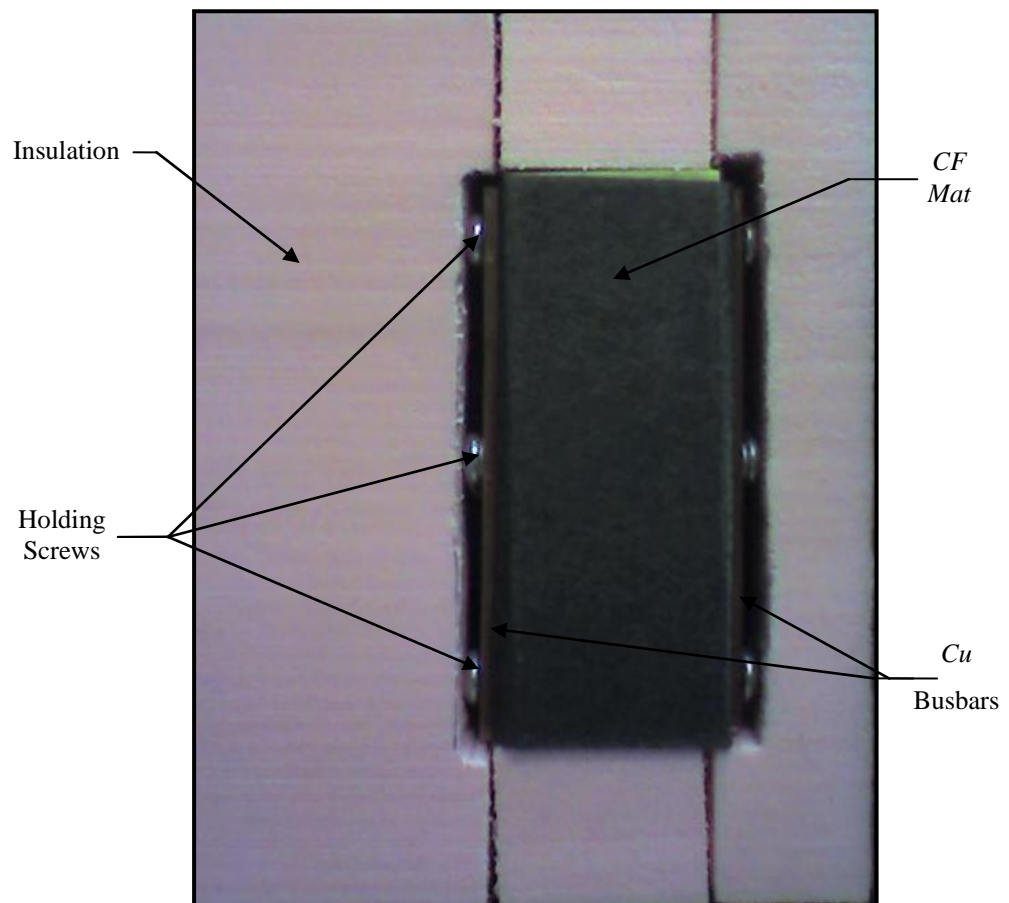


Figure 5.11: Insulated Heating Element Assembly – Top View

The insulated heating assembly unit depicted in Figure 5.11 is located inside the hollow wooden framework shown in Figure 5.8. Thus, five distinct insulated heating element assemblies were manufactured and produced - one for each fin spacing (*Flat Plate*, *S50*, *S40*, *S30*) together with an assembly for the fin side (*S65*). That is, for each test, the relevant insulated heating element assembly was used - Figure 5.12. This method ensured that the dimensions of the *CF* veil always perfectly matched the fin spacing under test, ensuring that the supplied heat input was only produced in the required region (under the fin base), thus ensuring the correct determination of the supplied input power.

During the data acquisition stage, it was important to ensure that a uniform heat flux across the entire heater was generated and maintained. Failure to do so would have resulted in the incorrect determination of the local heat transfer measurements. This principle is further explained in *Chapter 6*.

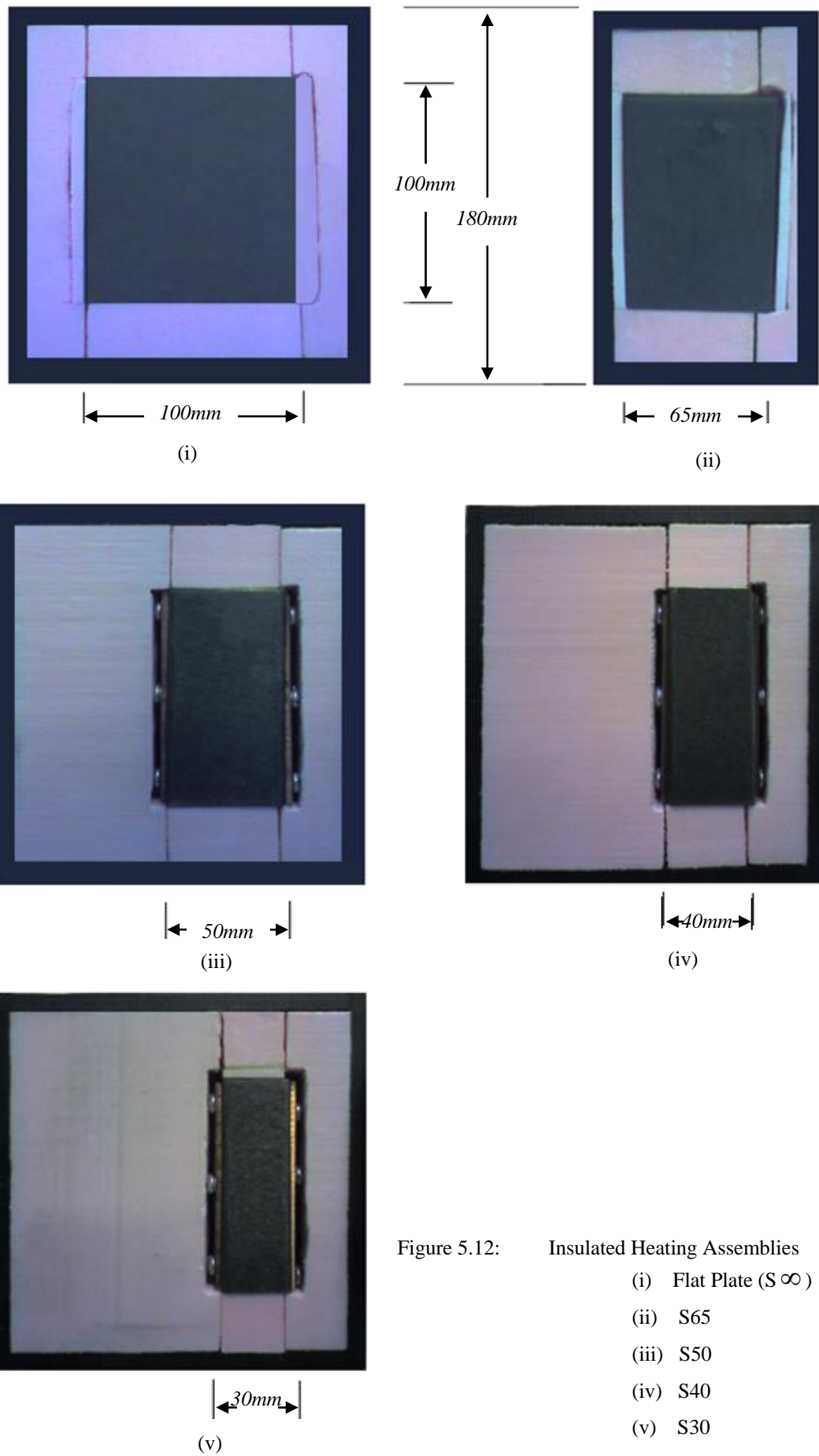


Figure 5.12: Insulated Heating Assemblies

- (i) Flat Plate ( $S \infty$ )
- (ii) S65
- (iii) S50
- (iv) S40
- (v) S30



### 5.3.2 IR Transparent Adjustable Viewing Fin

A custom built movable viewing fin was also fabricated. In essence, the viewing fin consisted of a 5mm thick wooden base onto which two locating aluminium brackets were mounted. These brackets ensured that the adjustable fin always lies flush against the surface, while also allowing the precise location of the moveable fin assembly. A Perspex frame was further constructed around a speciality product bought from *Edmund Optics* and bonded to the wooden frame with a high temperature adhesive. This is one of a handful of materials that is capable of transmitting infrared rays (*IR*). The adjustable viewing fin is depicted by Figure 5.13.

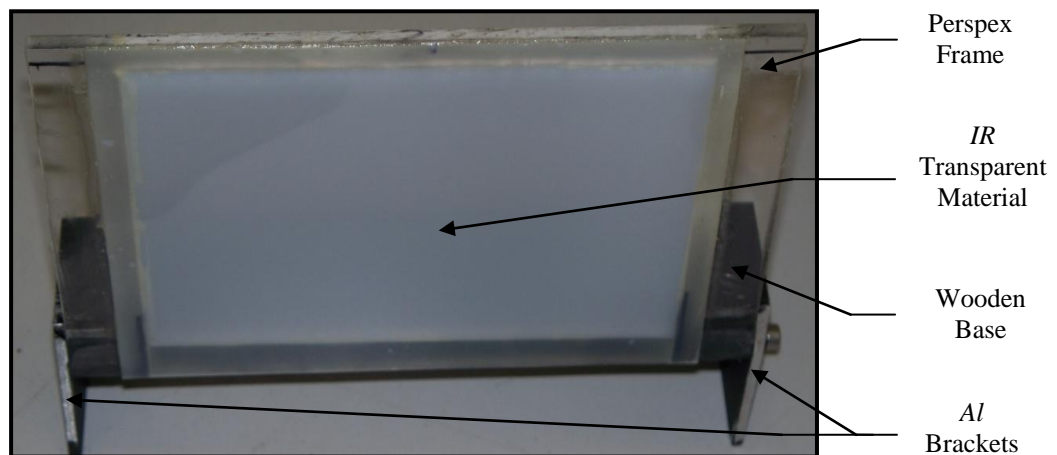


Figure 5.13: Adjustable *IR* Viewing Fin

The purpose of this movable fin was so that it would act as an *IR* transparent fin side wall. The rigid, but smooth-surfaced adjustable fin further ensured that the fin could be shifted according to the particular fin spacing under test. Thus, the fin mimics the second fin of a heat sink and acted as a dummy fin; it was attached to the fin base as illustrated in Figure 5.14. Although it was not heated, its presence was required so as to complete the fin channel and constrain the air flow.

This assembly permitted the measuring of the local fin side wall temperatures (and thus the evaluation of the *FSW* heat transfer coefficients) by the use of a hand held thermal camera.

### 5.3.3 Assembled Thermal Test Section

For each experimental investigation, the required insulated heating element assembly ( $S_{\infty}$  or  $S50$  or  $S40$  or  $S30$ ) was positioned in the wooden fin base structure, while another similar heating assembly unit ( $S65$ ) was placed in the fin side. The thermal rig was further attached to the 3D positioning system as shown in Figure 5.14 and finally placed into a significantly sized enclosure so as to eradicate any atmospheric fluctuations in the test section region, as illustrated in Figure 5.15.

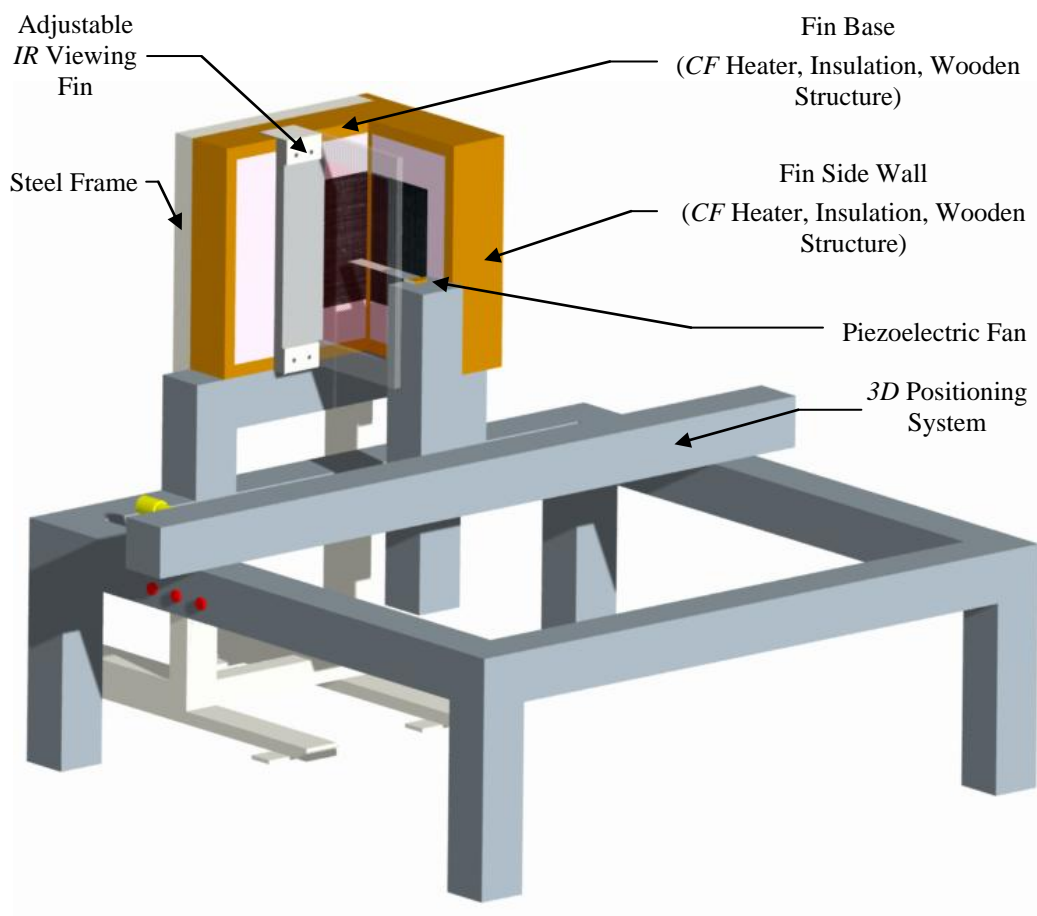


Figure 5.14: Graphical Representation of Thermal Test Rig

The presence of the enclosure ensured that a control volume was maintained, ensuring that stray drafts and other thermal fluctuations were eliminated. Three other *K-type* thermocouples were also placed inside the control volume so as to continuously monitor the ambient air temperature ( $T_{\infty}$ ). These

thermocouples, together with the thermocouples utilised to measure the conduction loss, were all connected to an 8-channel *Pico* data logger.

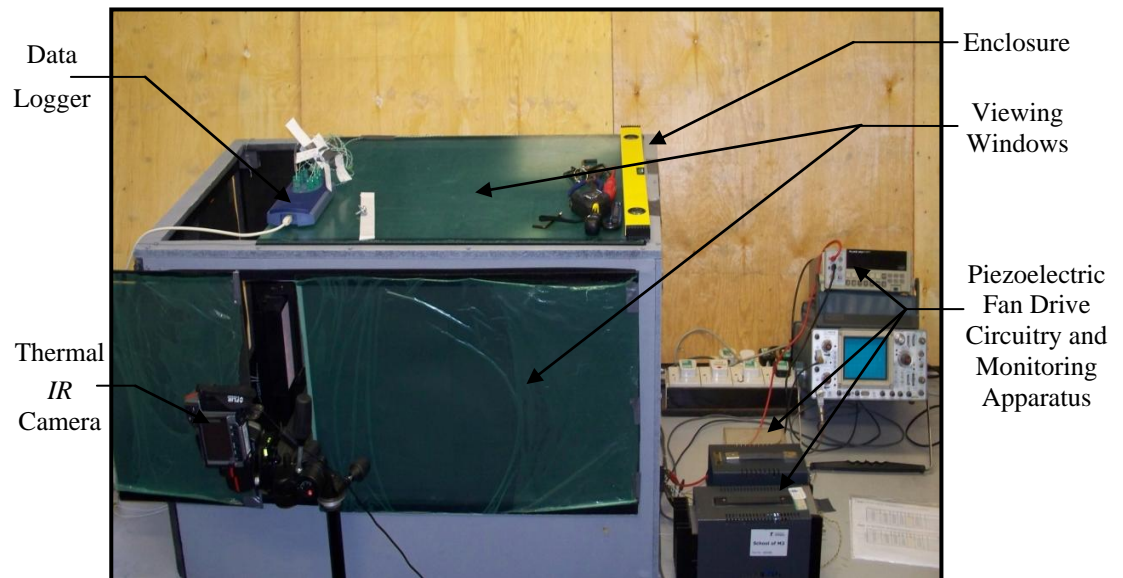


Figure 5.15: Finalised Thermal Facility

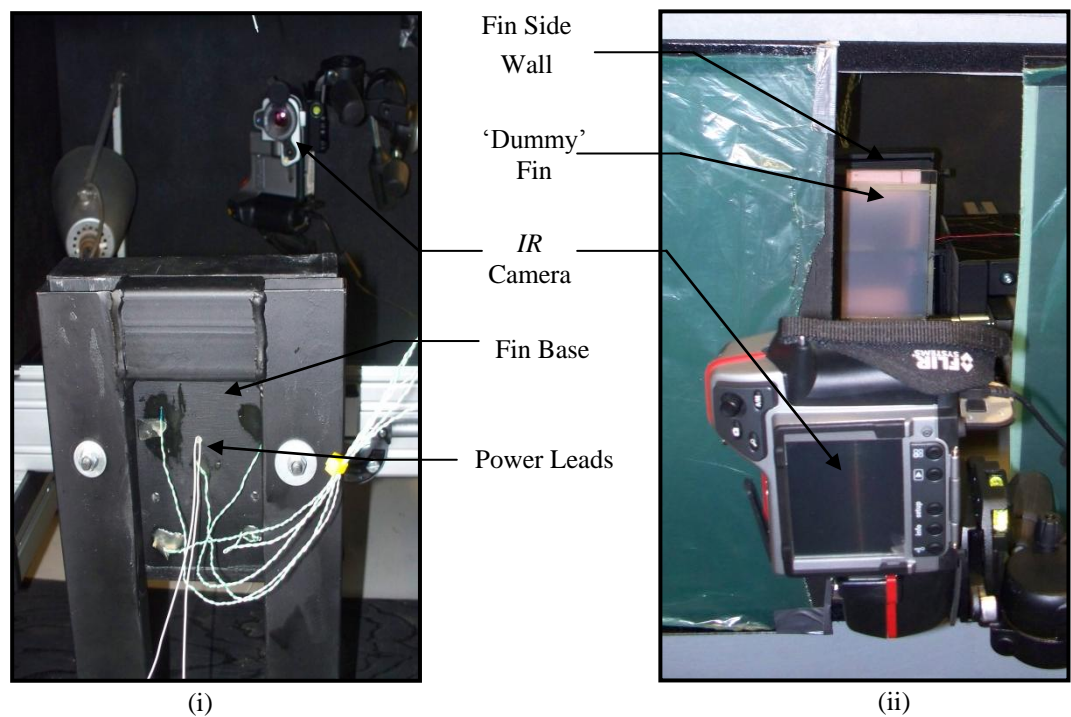


Figure 5.16: Temperature Measurement

(i) Fin Base (*FB*)

(ii) Fin Side Wall (*FSW*)

Finally, an *FLIR T400 Western IR* thermal imaging camera was setup to monitor the temperatures of the fin base and fin side wall in turn during the experiment, Figure 5.16(i) and Figure 5.16(ii) respectively. The acquired 2D temperature plots taken from the thermal camera, together with the thermocouple measurement readings were then exported to the *MatLAB* software package from where the necessary data manipulation was performed. These results are presented in the next chapter, **Chapter 6**.

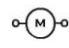
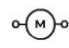
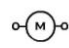
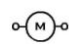
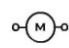
## 5.4 PIV Facility

Flow visualisation and flow measurements were acquired by Particle Image Velocimetry (*PIV*). *PIV* is a contact free, non-intrusive optical measurement technique (*NIOMT*) which is capable of tracking a significant amount of particles which are being affected locally by the fluid flow. By analysing the movement of particles from one frame to another using the equation below,

$$u(t) = \frac{s}{M_{Con} \cdot \Delta t} \quad \dots \text{Eq. 5.3}$$

the velocity in both the ‘x’ and ‘y’ directions can be calculated as the frame rate, or better the separation time ( $\Delta t$ ) is known. Thus by analysing all the particles in the frame, a 2D flow field can be acquired.

The elements that make up a *PIV* facility are:

-  Dual Pulsed Laser
-  Laser Extension Arm (Laser Head)
-  High Speed Camera
-  Seeding Machine
-  Timing Box



## Data Acquisition System (PC with accompanying Software)

Figure 5.17 shows how these elements were linked. Furthermore, the reader is directed to **Appendix B**, where details relating to good *PIV* practices and the governing theory are presented.

The time-resolved *PIV* system comprised a dual pulsed *Nd:YLF Litron* laser with a  $527\text{nm}$  wavelength in conjunction with a *SpeedSense 9060 Dantec 1MP* -  $1280 \times 800$  pixel resolution high speed camera with accompanying *Tamron* *micro*-lenses. All the above components were controlled by a dedicated computer and an 8 channel timing box. Process control and initial data acquisition was provided by *Dantec Dynamics v2.30* commercial *PIV* software. However, further image processing and data manipulation was performed in *MatLAB* by means of user generated scripts.

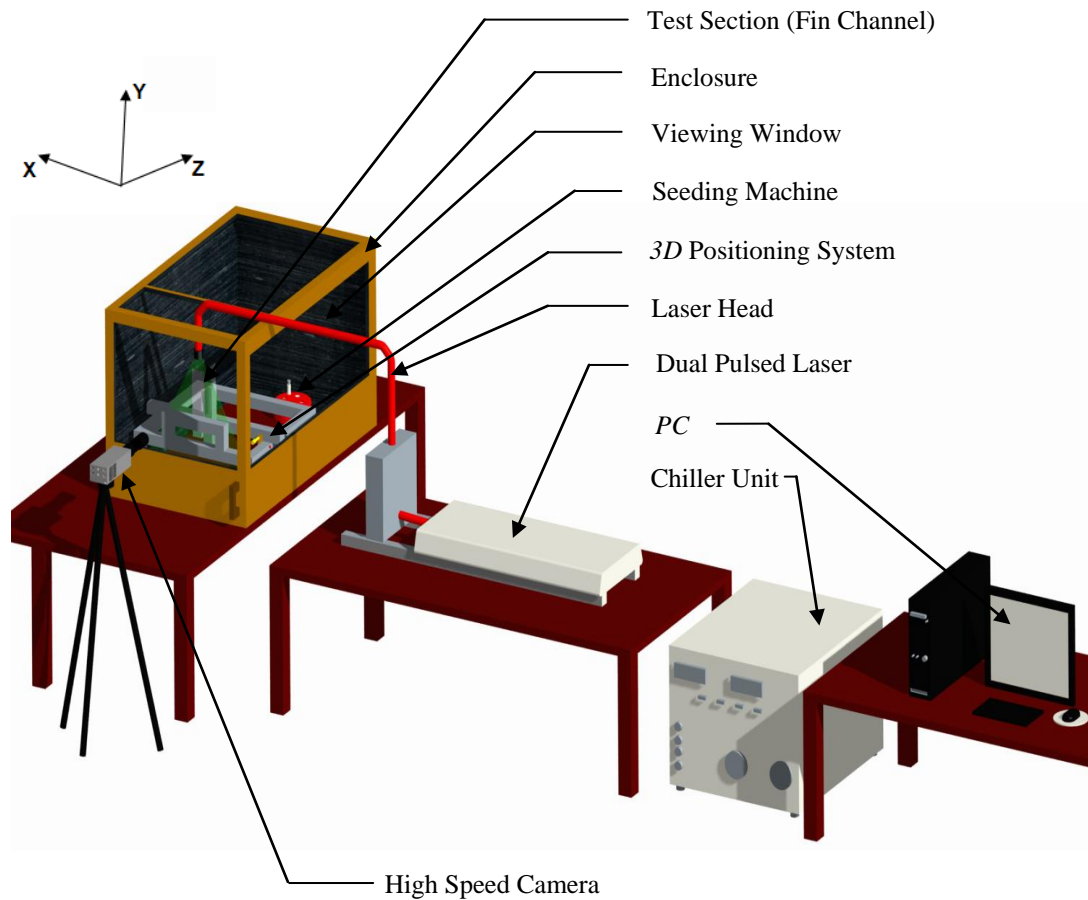


Figure 5.17: Experimental *PIV* Setup

An adaptive correlation technique was implemented using an interrogation area (IA) measuring  $32\text{ pixels}$  by  $32\text{ pixels}$  with a  $50\%$  overlap. No filters were applied, however, a central difference technique with two refinement steps was adopted. A moving average validation was further applied so as to iron out any erroneous vectors caused by uncoupled particle pairs.

A water-based (with a minimal percentage of glycol) seeding was implemented by means of a high output ( $200W$ ) fogger which atomised the water while dispersing the generated microscopic water droplets into the large enclosure. Seeding was pumped into the enclosure and allowed to mix and settle before any measurements were taken. In addition to the above, before recording any flows generated by the oscillating fan, the  $2D$  instantaneous velocity of the seeding was measured (through *PIV*) so as to ensure that the seeding velocity was negligible when compared to the flows produced by the oscillating fan. Further details with regards to seeding, such as, seeding density, quality and size are given in **Appendix B**.

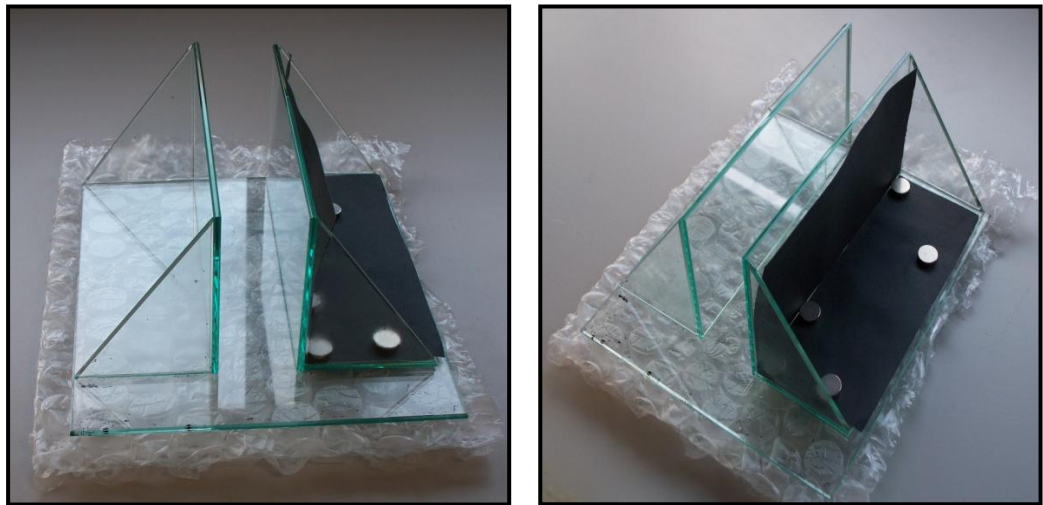


Figure 5.18: Adjustable Glass Heat Sink implemented during *PIV* Testing

In this present work, *PIV* was employed to measure the velocity vector fields generated by the piezoelectric fan on both the fin base (Figure 5.21, Figure 5.23), and the fin side wall (Figure 5.22, Figure 5.24) for both fan orientations (Figure 5.20). Throughout the duration of the *PIV* testing, the following parameters were set and maintained:



$$\text{Separation Time } (\Delta t) = 100 \mu s$$

$$\text{Sampling Frequency } (f) = 610 \text{ Hz}$$

$$\text{Number of Images } (N_I) = 500 \text{ Images}$$

An adjustable glass finned system (representative of a typical heat sink), was designed and manufactured - Figure 5.18. The glass finned geometry ensured that several parameters such as: Fin Spacing ( $S$ ), Separation Gap ( $G$ ), Vibration Amplitude ( $A_{Pz}$ ), Frequency ( $f$ ) as well as the piezoelectric fan Orientation could be investigated (Figure 5.19).

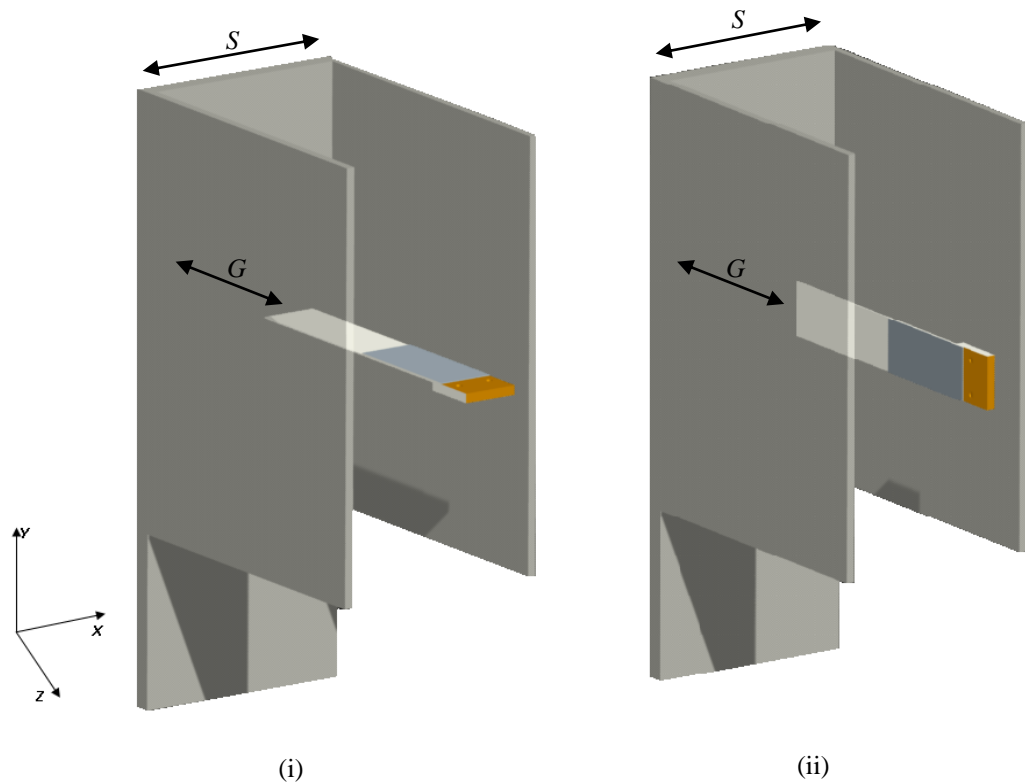


Figure 5.19: Piezoelectric Fan Orientation and Critical Dimensions

(i) Horizontally-mounted

(ii) Vertically-mounted

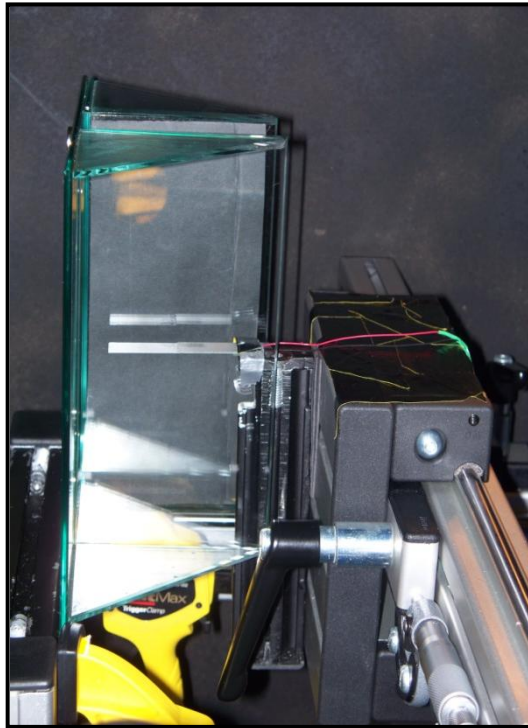
The finned glass assembly (mimicking a heat sink – i.e. fin base and two fin side walls) was assembled in such a manner so that all the mechanical connections were made on the outside. This ensured a smooth fin channel, thus avoiding any possibility of the flow being affected by any machining or joining irregularities, eliminating user induced eddies. The fins protrude by *100mm*, are *200mm* long and have a thickness of *4mm*.

For this work, the parameters investigated are:

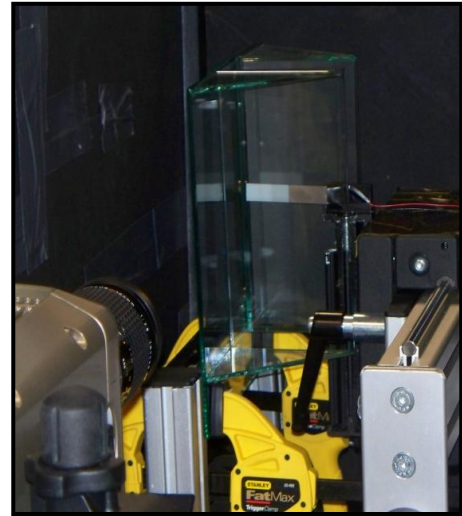
Orientation	-	Horizontal / Vertical
Fin Spacing ( <i>S</i> )	-	Flat Plate, <i>S50mm</i> , <i>S40mm</i> , <i>S30mm</i>
Separation Gap ( <i>G</i> )	-	<i>15.0mm</i> , <i>10.0mm</i> , <i>5.0mm</i> , <i>2.5mm</i>
Fin Amplitude ( $A_{Pz}$ )	-	<i>30.00V</i> , <i>60.00V</i> , <i>90.00V</i> , <i>115.0V</i>

The piezoelectric fan was securely mounted onto the *3D* positioning rig by means of two screws and fastened tightly, to eliminate any damping within the system. Insulating tape covered the end of the *PZT* so as to eliminate any chance of electric shock (since seeding is water based).





(i)



(ii)

Figure 5.20: Piezoelectric Fan Orientation:

- (i) Horizontally-mounted
- (ii) Vertically-mounted

#### **5.4.1 Velocity Measurements**

For each piezoelectric fan orientation labelled above, flow measurements were taken on two distinct planes, namely: the fin base (Figure 5.21) as well as the fin side wall (Figure 5.22). For each setup, the viewing direction was selected in a manner to further shed light on the thermal contour plots presented in *Chapter 6*.

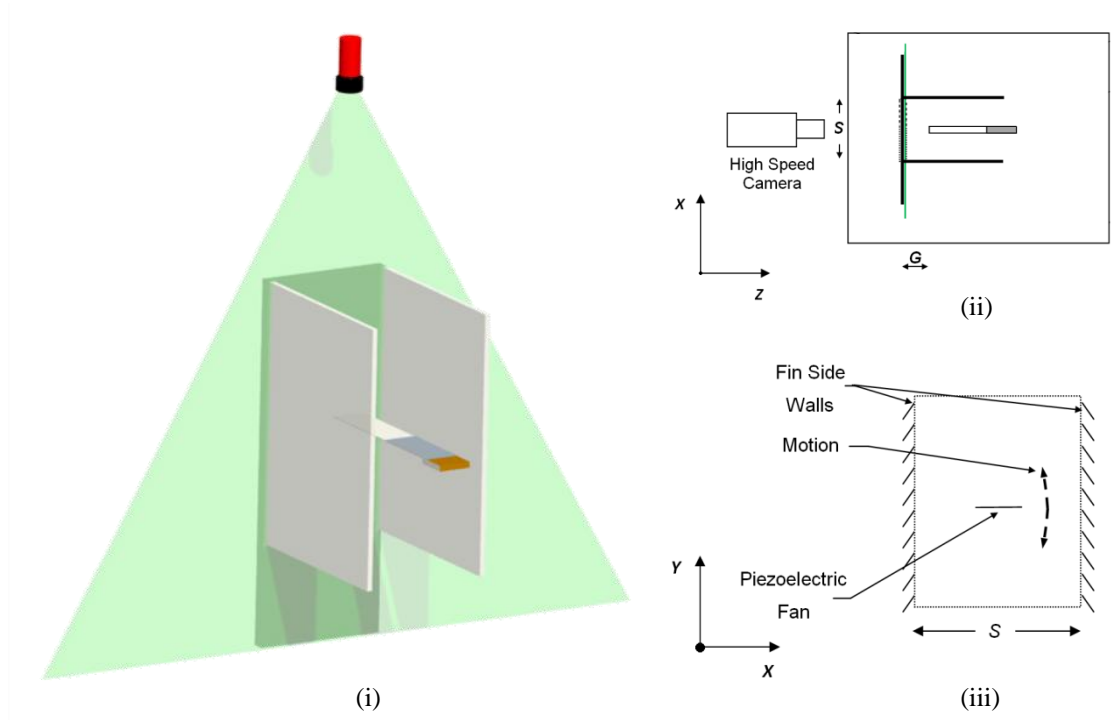


Figure 5.21: Laser Sheet Parallel to Fin Base - Capturing Fin Base Velocities

(i) 3D Representational Model (ii) Top View (iii) Front View

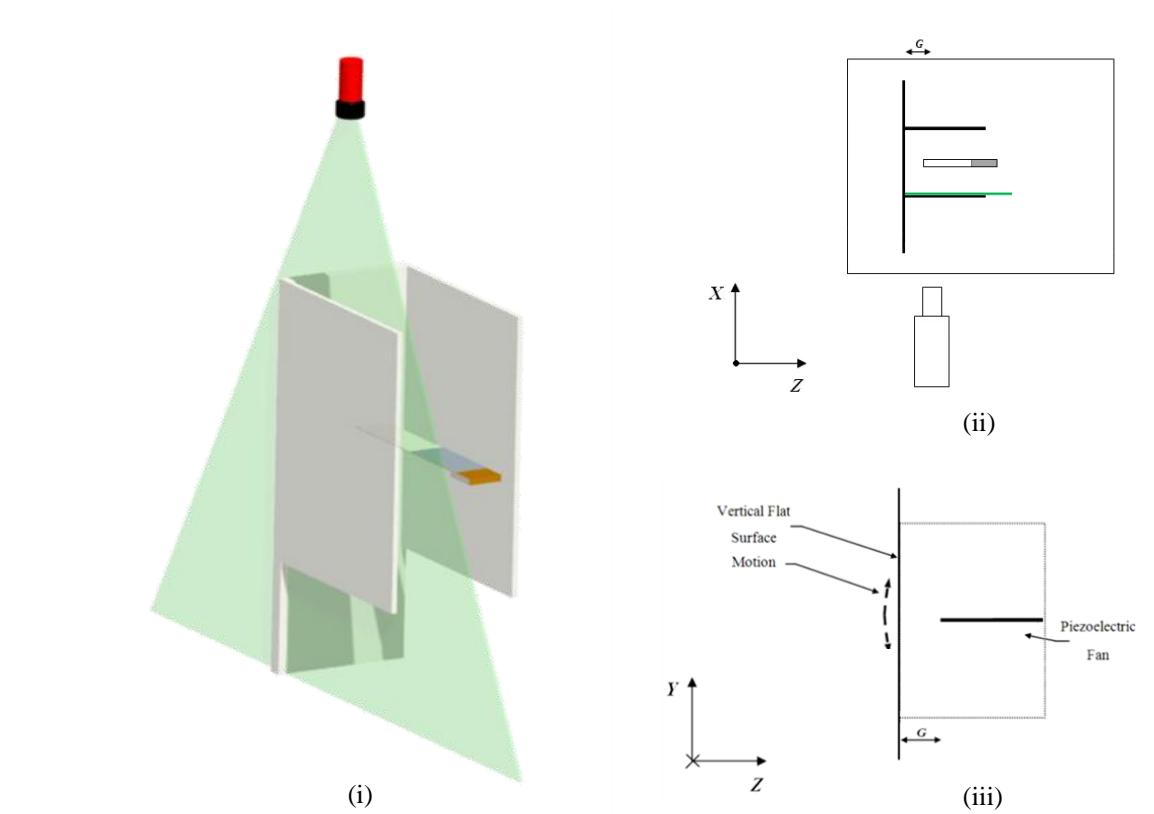


Figure 5.22: Laser Sheet Perpendicular to Fin Side Wall - Capturing Fin Side Wall Velocities

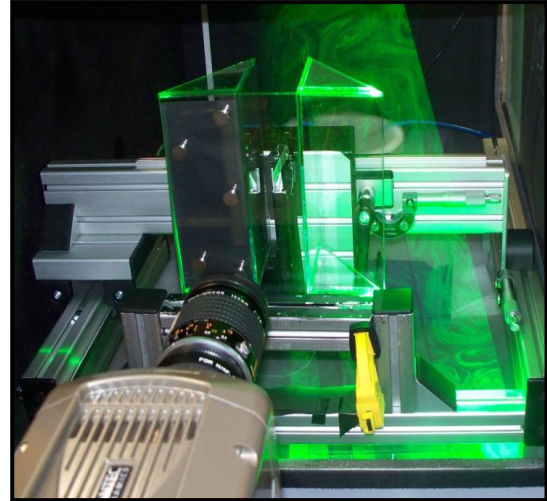
(i) 3D Representational Model (ii) Top View (iii) Front View

In Figure 5.21, the laser light sheet was shone from above and directed parallel to the fin base, while the camera was located behind the fin base, looking through the back of the glass fin base (Figure 5.23). This yielded the 2D flow patterns generated by the piezoelectric fan on the fin base. Similarly to the measurement of the velocities on the *FB*, in Figure 5.22, the laser light sheet was once again directed from above, however, this time, directed parallel to the *FSW* and perpendicular to the fin base. In this setup, the high speed imaging camera was situated adjacent to the fin side wall as illustrated in Figure 5.24.

All the data obtained from the numerous *PIV* tests was exported into *MatLAB*, where several user-defined scripts were created which performed the necessary data manipulation (Mean, Turbulence, *RMS*, Kinetic Energy Density, amongst others) and data presentation. A sample of these results is presented in **Chapter 7** as well as **Chapter 8**, while some additional data may be found in **Appendix F**.



(i)

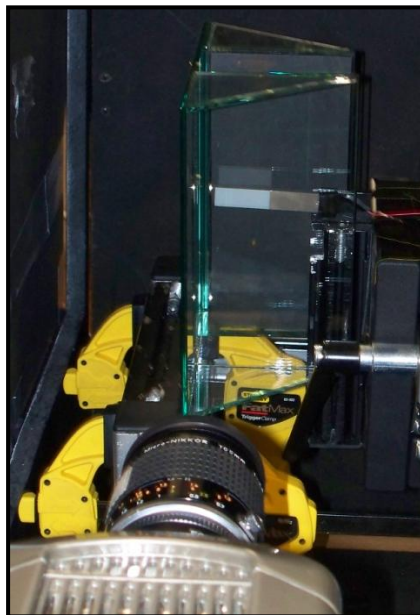


(ii)

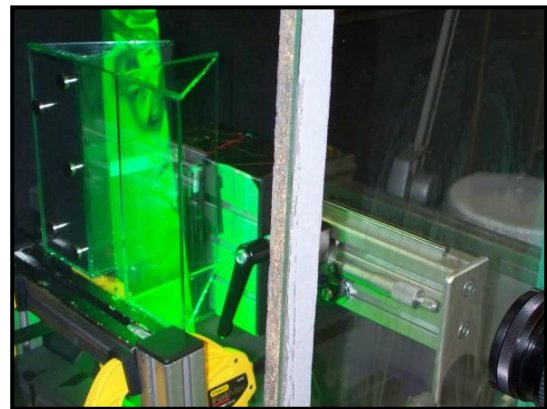
Figure 5.23: Flow Visualisation - Fin Base – Vertically-mounted Fan

(i) Laser Sheet OFF

(ii) Laser Sheet ON



(i)



(ii)

Figure 5.24: Flow Visualization - Fin Side – Vertically-mounted Fan

(i) Laser Sheet OFF

(ii) Laser Sheet ON

## 5.5 Uncertainty Analysis

As with any experimental investigation, the quantification of errors is essential and is almost of the same importance as the measured/calculated quantity itself. In this work, the methodology described by *Kline and McClintock*. [56] was adopted. In their paper, for single sample experiments, the authors proposed the following equation:

$$w_R = \left[ \left( \frac{\partial R}{\partial v_1} \cdot w_1 \right)^2 + \left( \frac{\partial R}{\partial v_2} \cdot w_2 \right)^2 + \dots + \left( \frac{\partial R}{\partial v_m} \cdot w_m \right)^2 \right]^{\frac{1}{2}} \quad \dots \text{Eq. 5.4}$$

In Eq. 5.2 above,  $R$  is a function dependent on the variables  $v_i$ ,  $w_R$  is the uncertainty in  $R$ , and  $w_i$  is the uncertainty in  $v_i$ . The above correlation was used to quantify the uncertainty in the heat transfer measurements.

### 5.5.1 Heat Transfer Coefficients

A detailed investigation into the compounding errors present in the thermal experiment was performed and evaluated according to *Eq. 5.2* above, the results of which are given in Table 5.2.

Variable	Precision	Max/Min Reading	ERROR			Instrument
			Accuracy	%Reading		
$G$ (mm)	+/- 0.01mm	10.0	+/-	0.01	0.1	Micrometer Screw Gauge
$S$ (mm)	+/- 0.1mm	100.0	+/-	0.10	0.1	Vernier Calipers
$T_{amb}$ ( $^{\circ}C$ )	+/- 1.5 ( $^{\circ}C$ )	21.8	+/-	1.5	6.9	K-Type Thermocouple
$T_{heater NC}$ ( $^{\circ}C$ )	+/- 2.0%	80.3	+/-	1.6	2.0	T400 IR Camera
$T_{heater FC}$ ( $^{\circ}C$ )	+/- 2.0%	50.0	+/-	1.0	2.0	T400 IR Camera
$V_S$ (V)	+/- 1.5%	9.5	+/-	0.14	1.5	Precision Multimeter
$I_S$ (A)	+/- 0.5%	0.9	+/-	0.005	0.5	Precision Multimeter
$(T_{heater} - T_{amb})_{NC}$	/	58.5	+/-	2.2	3.8	/
$(T_{heater} - T_{amb})_{FC}$	/	28.2	+/-	1.8	6.4	/
$Q_s$ (Watts)	/	8.55	+/-	0.14	1.6	/
$A_S$ (m)	/	0.01	+/-	1.41E-05	0.14	/
$A_S * (T_{heater} - T_{amb})_{FC}$	/	0.28	+/-	0.02	6.4	/
$h$	/	30.3	+/-	2.00	6.6	/
$R$	/	3.30	+/-	0.22	6.6	/

Table 5.2: Uncertainty Analysis - Horizontally-mounted Piezoelectric fan at  $G = 10.0\text{mm}$ ,  $V_{pz} = 115\text{V}$

Table 5.2 above table lists all the measured and calculated parameters that are required to evaluate the fin base and the fin side wall heat transfer coefficients and the heat sink thermal resistance. The largest inaccuracy results in the measurement of  $T_{\infty}$ , which results in an uncertainty of 6.9%. This in turn results in a maximum uncertainty in the heat transfer coefficient ( $h_{FC}$ ) and the respective thermal resistance ( $R$ ) is equivalent to 6.6%. When the same uncertainty analysis was performed, for all the other tested scenarios, it was established that the maximum uncertainty was equivalent to 7.7% and occurred when operating at the minimum fin spacing ( $S$ ) and the minimum separation distance ( $G$ ).

The above methodology takes into account, only the simultaneous occurrence of the most extreme errors and does not take into account of the possibility of the errors compensating one another. This commonly leads to the over prediction of the experimental errors. Nonetheless, error estimates in engineering analysis are often calculated using the above procedure because they are known to be conservative and hence, allow for an additional margin-of-safety.

### **5.5.2 Time – Averaged Velocities**

The uncertainty in the attained 2D profile velocities ( $PIV$ ) generated by an oscillating piezoelectric fan were also evaluated. *Westerweel*, in his series of papers [57, 58] quotes that  $PIV$  error, per vector, lies between 3% and 5% and is due to certain erroneous vectors that are highly different from the neighbouring vectors whilst also being totally different from the average of the vectors in the  $IA$ . This error is highly dependent on the seeding quality (size, density) as well as the number of captured images ( $N_I$ ). The larger the number of captured images, the lower the  $PIV$  error. However, as imaging technology progresses, it is envisaged that the above quoted error will, in the near future, be further reduced.

For the current setup, the maximum  $PIV$  error attained was calculated at 0.5%.

## **5.6 Concluding Remarks**

This chapter details the commissioned thermal and *PIV* experimental facilities, used to investigate the cooling capabilities of an oscillating piezoelectric fan on a finned setup, the respective results of which are presented in *Chapter 6* and *Chapters 7* and *8* respectively.

Furthermore, the expected experimental uncertainty for both thermal and flow investigations have been evaluated and presented.

# CHAPTER 6

## 6. Thermal Measurements

---

This chapter details the cooling effectiveness of the forced cooling convective system (*FCCS*). The derivation of the heat transfer coefficients, together with the heat balance used for one such insulated heating assembly unit is presented first in *Section 6.1*. The subsequent sections shed light on the cooling capabilities of an oscillating piezoelectric fan. Results pertaining to a horizontally-mounted piezoelectric fan are presented in *Section 6.2*, while results pertaining to a vertically-mounted piezoelectric fan are presented in *Section 6.3*. In each of the latter sections, *2D* temperature contour plots of both the fin base (*FB*) and the fin side wall (*FSW*) are presented and discussed in some detail. Furthermore, the effects of varying amplitude ( $A_{pz}$ ), varying separation distance ( $G$ ), and varying fin spacing ( $S$ ), for each fan orientation, are investigated and presented, while highlighting the key trends.

Lastly, in *Section 6.4*, a direct comparative study between a horizontally-mounted and a vertically-mounted fan is presented and some conclusions are drawn up.

### 6.1 Heat Transfer Coefficient Derivation

The way the heat transfer coefficients were derived from the experimental data is presented here. Figure 6.1 is a graphical representation of one such insulated heating assembly (discussed in *Chapter 5*) and incorporates the heat flux balance.



$$Q_S = Q_{Cond} + Q_{Convection} + Q_{Radiation} \quad \dots \text{Eq. 6.1}$$

$$Q_S'' = Q_{Cond}'' + Q_{Convection}'' + Q_{Radiation}'' \quad \dots \text{Eq. 6.2}$$

For each *CF* mat, the energy balance is given by *Eq. 6.2*, and states that the heat supplied ( $Q_S$ ) is equivalent to the dissipated heat by convection ( $Q_{Convection}$ ), radiation ( $Q_{Radiation}$ ), as well as the heat lost by conduction ( $Q_{Cond}$ ) from the back of the insulated heated assembly unit. In this study, the in-plane conduction in the *CF* mat together with to and from the busbars was neglected.

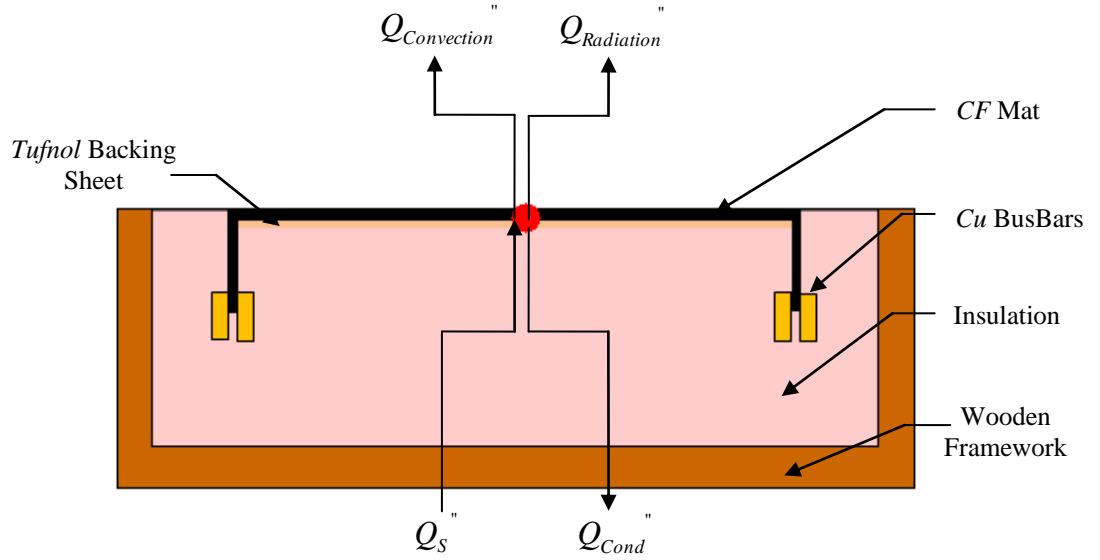


Figure 6.1: Heat Flux Balance of Heating Assembly

Expanding *Eq. 6.2* results in:

$$\left( \frac{V_S I_S}{A_S} \right) = (h\Delta T) + (\varepsilon\sigma [T_S^4 - T_\infty^4]) + \left( \frac{\Delta T}{R_{Loss}} \right) \quad \dots \text{Eq. 6.3}$$

where;

$$\Delta T = T_S - T_\infty \quad \dots \text{Eq. 6.4}$$

$$R_{Loss} = \left[ \frac{t_{Tufnol}}{k_{Tufnol}} + \frac{t_{Insulation}}{k_{Insulation}} + \frac{t_{Wood}}{k_{Wood}} \right] \quad \dots \text{Eq. 6.5}$$

Figure 6.2 gives further details of some of the parameters used in the above heat flux balance equation. The fully expanded local convective surface heat transfer coefficient ( $h$ ), with a maximum error of 7.7% (**Section 5.5.1**) was implemented and is presented in *Eq. 6.6*.

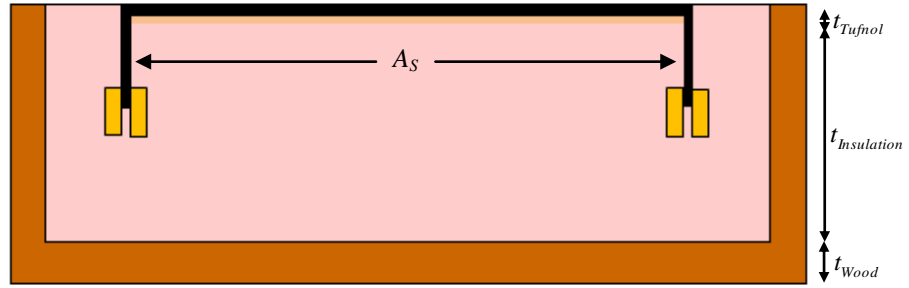


Figure 6.2: Parameter Definition of a typical Heating Assembly – Top View

This equation was used, in conjunction with a user generated *MatLAB* code, to perform the necessary data manipulation and data presentation, the results of which are presented in the subsequent sections.

$$h = \frac{\left( \left( \frac{V_s I_s}{A_s} \right) - \left( \epsilon \sigma [T_s^4 - T_\infty^4] \right) - \left( \frac{\Delta T}{R_{Loss}} \right) \right)}{\Delta T} \quad \dots \text{Eq. 6.6}$$

Average heat transfer coefficients ( $\bar{h}$ ) for both the fin base and fin side walls were further evaluated using *Eq. 6.7*.  $\bar{h}$  is dependent on the respective *CF* heater area under test – i.e. for the *FB*,  $\bar{h}$  is based on an area measuring  $100\text{mm} \times S$ , while for the *FSW*,  $\bar{h}$  is based on an area measuring  $100\text{mm} \times 65\text{mm}$ .

$$\bar{h} = \frac{\sum h_i \cdot A_i}{\sum A_i} \quad \dots \text{Eq. 6.7}$$

Furthermore, an additional equation, *Eq. 6.8*, was used to gauge the cooling effectiveness of the *FCCS*, and represents the percentage increase ( $\%h_{mc.}$ ) in the forced cooling component over natural cooling.

$$\%h_{mc} = \left( \frac{h_{FC} - h_{NC}}{h_{NC}} \right) \times 100\% \quad \dots \text{Eq. 6.8}$$

In *Eq. 6.8*, the subscripts ‘*FC*’ and ‘*NC*’ refer to forced convection and natural convection respectively. The average error in  $\%h_{mc.}$  was evaluated to be equivalent to 12.3%. The resulting  $\%h_{mc.}$  value is critical in evaluating the percentage increase in the heat transfer when the piezoelectric fan is on, when compared to when the piezoelectric fan is off – i.e. a natural convection case.

### 6.1.2 Constant Heat Flux Surface

Two distinct thermal analyses were carried out: constant heat flux tests (discussed hereunder) and constant surface temperature thermal tests (discussed in *Section 6.1.3*). In the former, it was ensured (by means of a high resolution power meter) that for the duration of the experiment the supplied power to the *CF* heater mat was maintained constant. Furthermore, it was ensured that a uniform heat flux was generated over the exposed *CF* mat surface. In this chapter, only results pertaining to constant heat flux tests are presented.

Figure 6.3 depicts an example of typical 2D local heat transfer coefficients obtained for; a natural convection case (Fan Off), a horizontally mounted fan, and a vertically – mounted fan operating at  $G=10.0mm, V_{Pz}=115.0V$  respectively. Distinct differences in both magnitude and cooling pattern arise

for the different piezoelectric fan mounting position. These are explained in further detail in *Section 6.2* and *Section 6.3* respectively.

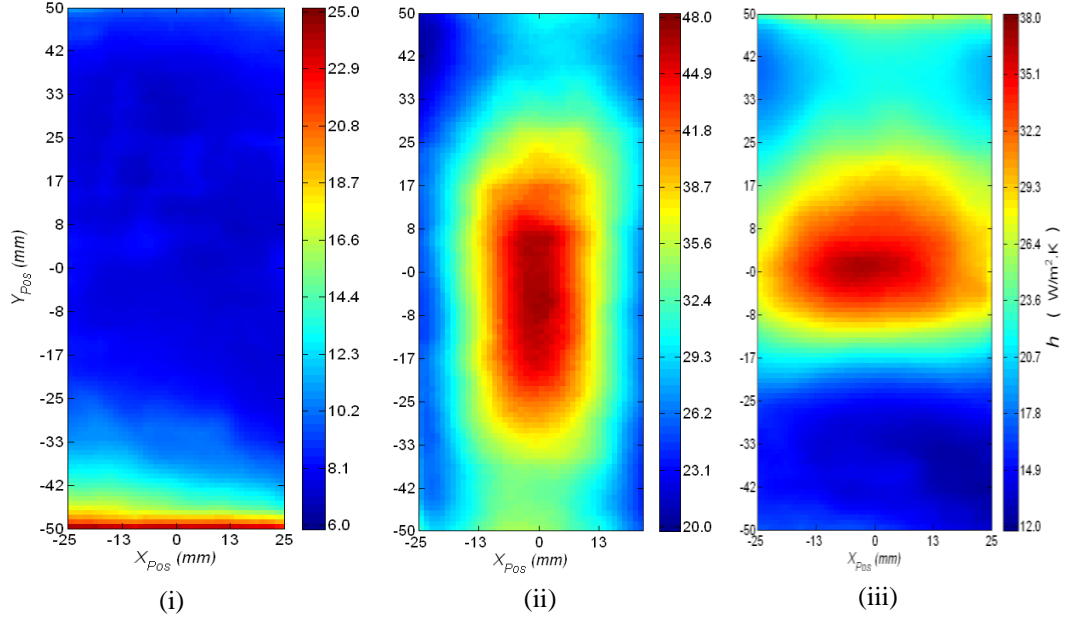


Figure 6.3: Fin Base 2D Local Heat Transfer Contour Plots –  $S = 50.0\text{mm}$

- (i) Natural Convection
- (ii) Horizontally - mounted Fan –  $G = 10.0\text{mm}$ ,  $V_{Pz} = 115.0\text{V}$
- (iii) Vertically - mounted Fan –  $G = 10.0\text{mm}$ ,  $V_{Pz} = 115.0\text{V}$

### 6.1.3 Constant Temperature Surface

While most of the tests performed pertained to a constant heat flux scenario, a few constant surface temperature tests were also carried out. During the constant temperature tests, it was ensured that the average temperature difference  $(\overline{T_s} - \overline{T_\infty})$  between the heated *CF* mat exposed surface and the surrounding ambient air was maintained constant throughout the duration of the experiment. This was accomplished by means of both a high resolution power meter as well as an *IR* camera.

This latter investigation was performed as it was envisaged that the operation of an electric machine is more representative of a constant surface temperature scenario rather than a constant heat flux scenario. While the results of these tests are not reported hereunder, a comparison between the two distinct tests is presented in *Chapter 9*.

## 6.2 Horizontally-mounted Piezoelectric Fan

In this section,  $2D$  contour maps of the  $\%h_{inc.}$  are presented for a horizontally-mounted oscillating piezoelectric fan (the setup of which is depicted in Figure 5.14) for the various geometrical parameters;  $A_{pz}$ ,  $G$ ,  $S$ .

Results pertaining to the  $FB$  are first presented, followed by results pertaining to the  $FSW$ . In each section, the key trends are highlighted and discussed in some detail.

### 6.2.1 Fin Base Cooling Results

In the series of  $2D$  contour plots, Figure 6.4 highlights a fin spacing of  $S = 30.0mm$ , Figure 6.5 a fin spacing of  $S = 40.0mm$ , Figure 6.6 a fin spacing of  $S = 50.0mm$  and Figure 6.7 a simple vertical flat plate, i.e. no fins. In each of these figures, the effect of vibrational amplitude ( $A_{pz}$ ) and separation distance ( $G$ ) is investigated. Furthermore, all presented images have been equally scaled ( $0.0\% - 750.0\%$ ) to better facilitate the understanding of the cooling capabilities of the  $FCCS$ .

From the results presented, it can be concluded that, irrespective of the fin spacing, the best geometrical configuration is that of:  $V_{pz} = 115.0V$  and  $G = 5.0mm$ . Furthermore, it is seen that, both a reduction in the vibrational envelope and an increase in the separation distance, lead to a reduction in the overall cooling capabilities of the  $FCCS$ . This agrees with the earlier literature presented, in particular [44]. For each of the considered finned setups ( $S30, S40, S50$ ), a central vertical elliptical symmetric pattern is generated, indicating that the presence of the fins restricts the flow. This, in turn, results in an elliptical cooling pattern which is highly oriented in the principal oscillation direction. Detailed investigations into the  $2D / 3D$  flow characteristics have been performed (through  $PIV$ ) and are presented in

**Chapter 7** and **Chapter 8**. It was envisaged that, the understanding of the fluid flow regimes would further shed light on the attained cooling plots.

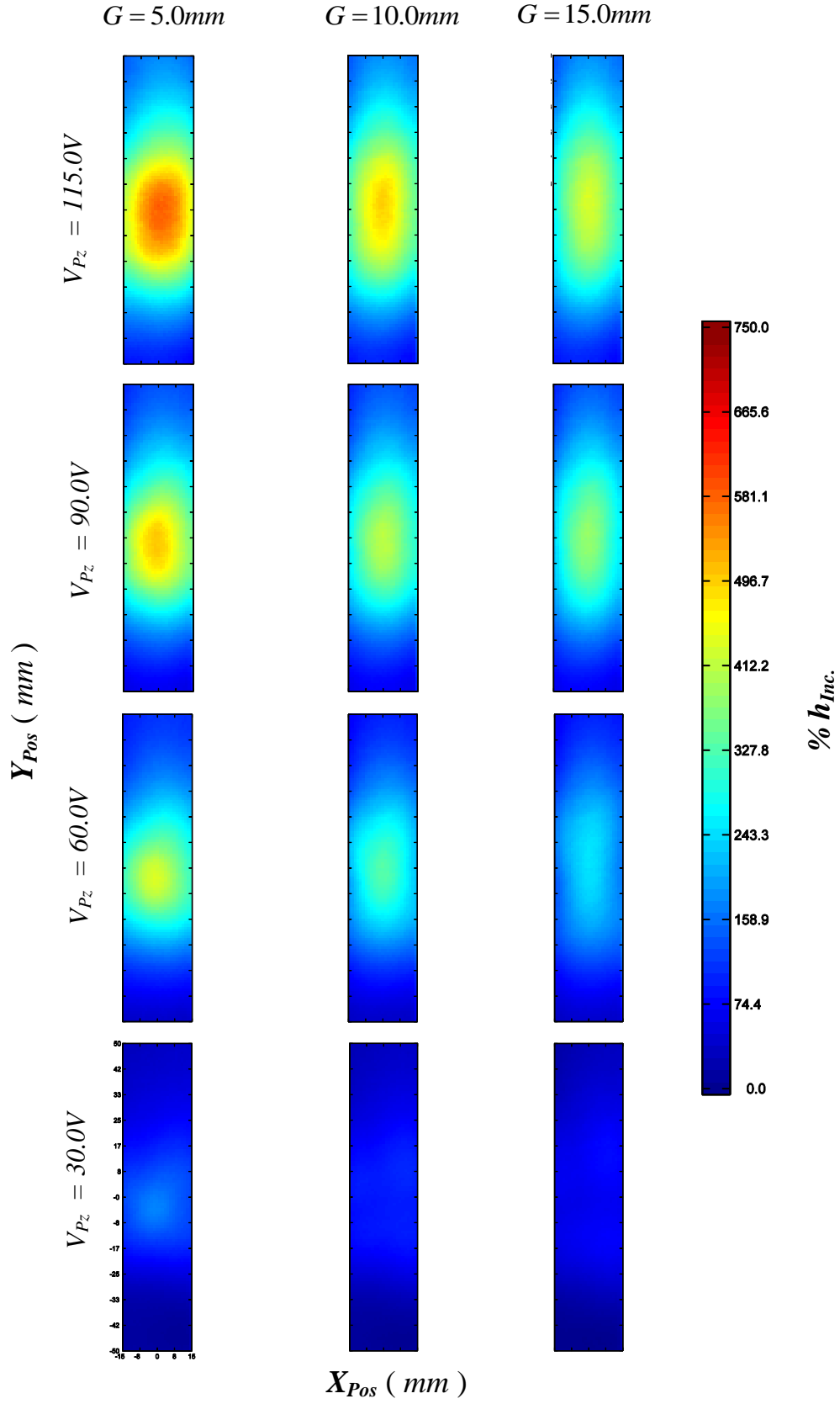


Figure 6.4: Evaluation of the FB  $\%h_{inc.}$  for a Horizontally-mounted Piezoelectric Fan: S30

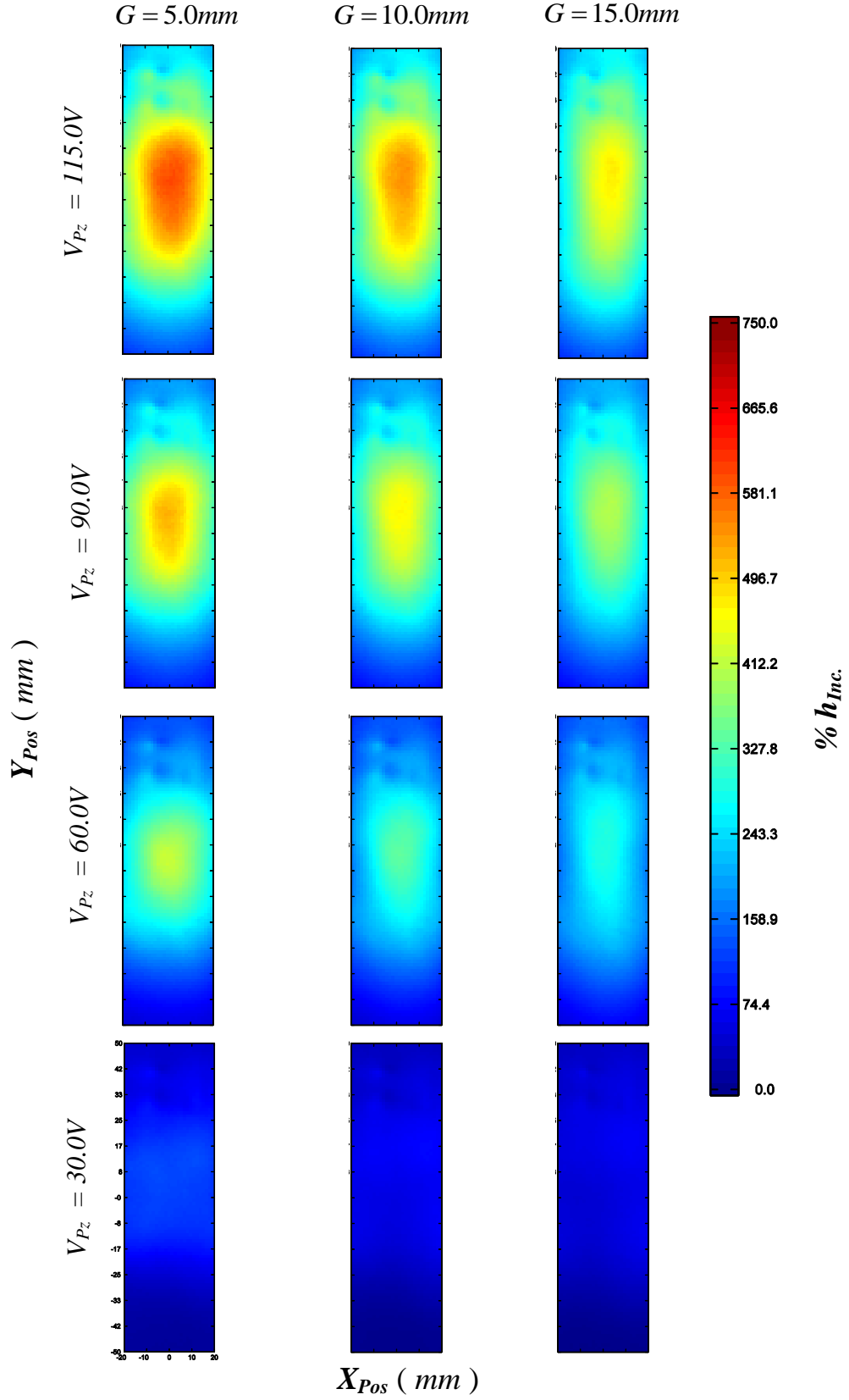


Figure 6.5: Evaluation of the  $FB \ \%h_{inc}$  for a Horizontally-mounted Piezoelectric Fan:  
S40



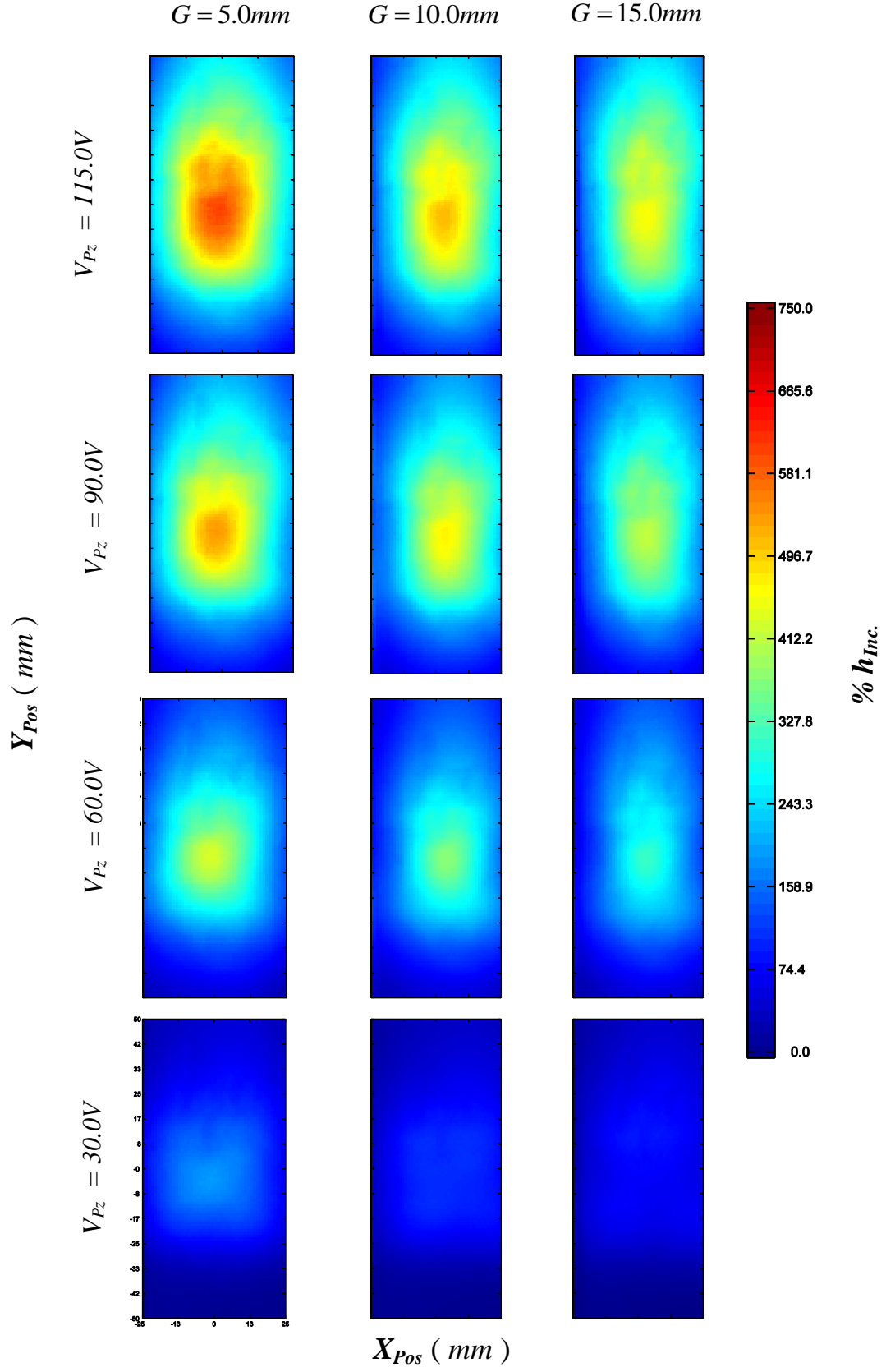


Figure 6.6: Evaluation of the  $FB \ \% h_{inc}$  for a Horizontally-mounted Piezoelectric Fan: S50

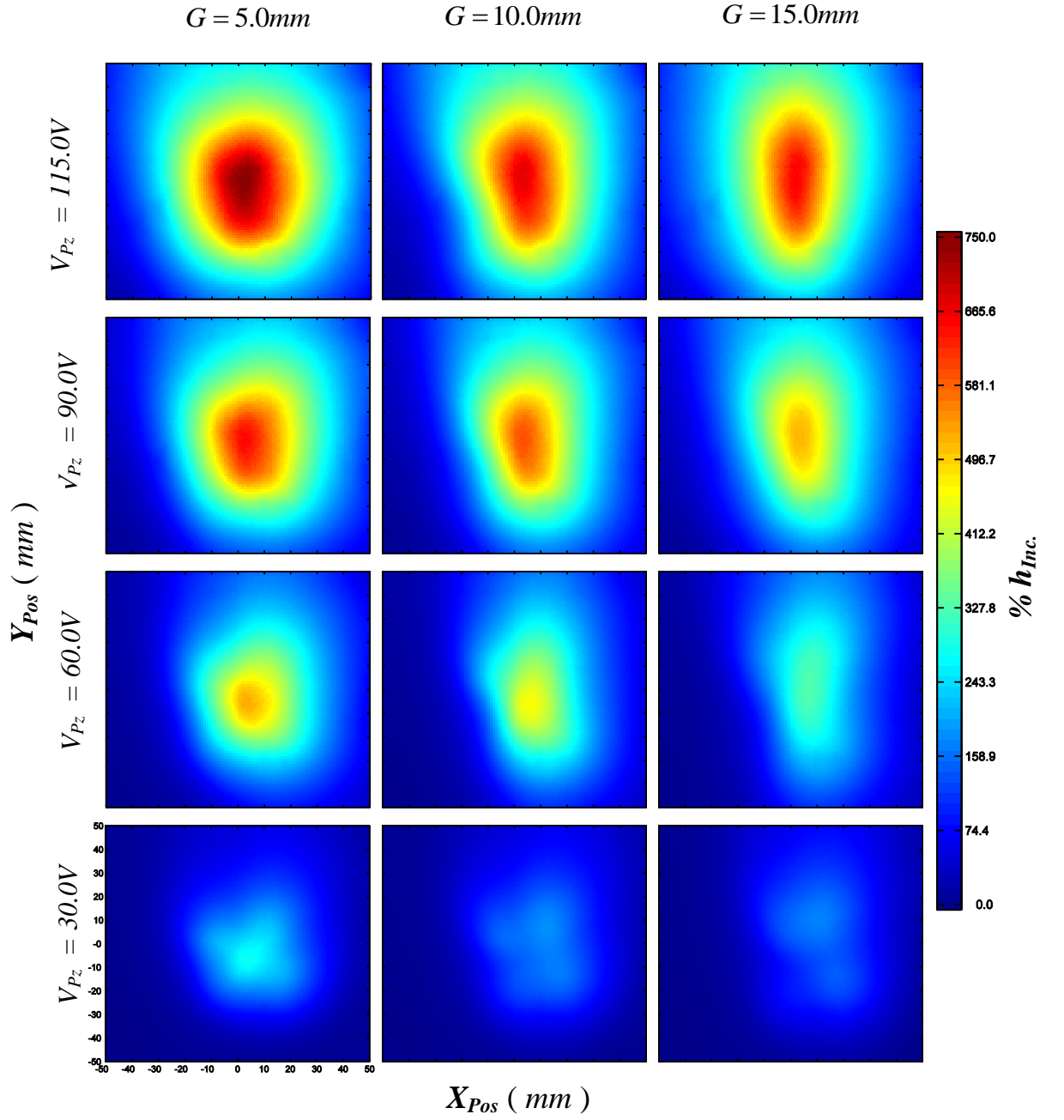


Figure 6.7: Evaluation of the  $FB \%h_{inc}$  for a Horizontally-mounted Piezoelectric Fan: Flat Plate ( $S\infty$ )

On closer inspection of the presented cooling plots, it is noted that operating the FCCS at  $V_{Pz}=115.0V, G=5.0mm$  results in the largest cooling. Furthermore, with an increase in fin spacing, the fin side walls have less effect on the 2D cooling patterns produced. In the extreme case, when the FSW's are completely removed (Figure 6.7), different cooling patterns are generated. A

nearly symmetric circular pattern (or rounded square) is generated when the fan vibrates close to the surface ( $G = 5.0mm$ ), indicating that fluid agitation is roughly similar in the vibrational directional to its orthogonal directional. This behaviour transitions to a vertical elliptical pattern when  $G = 10.0mm$  and the pattern remains elliptical for the largest separation distance. A decrease in  $V_{pz}$  also results in a cooling pattern change. For  $V_{pz} = 115.0V, G = 5.0mm$ , a rounded square pattern results. This also holds true for  $V_{pz} = 90.00V$ . However, this pattern transforms into a central circular pattern at  $V_{pz} = 60.00V$ , indicating that a change in fluid behaviour occurred. However, for larger  $G$  values, a decrease in  $V_{pz}$  has no visible effect on the cooling pattern. The above trends also true for all tested finned cases.

Once again, a decrease in the vibrational amplitude and an increase in separation distance results in an overall reduction in the cooling magnitude ( $\%h_{inc}$ ) of the FCCS.

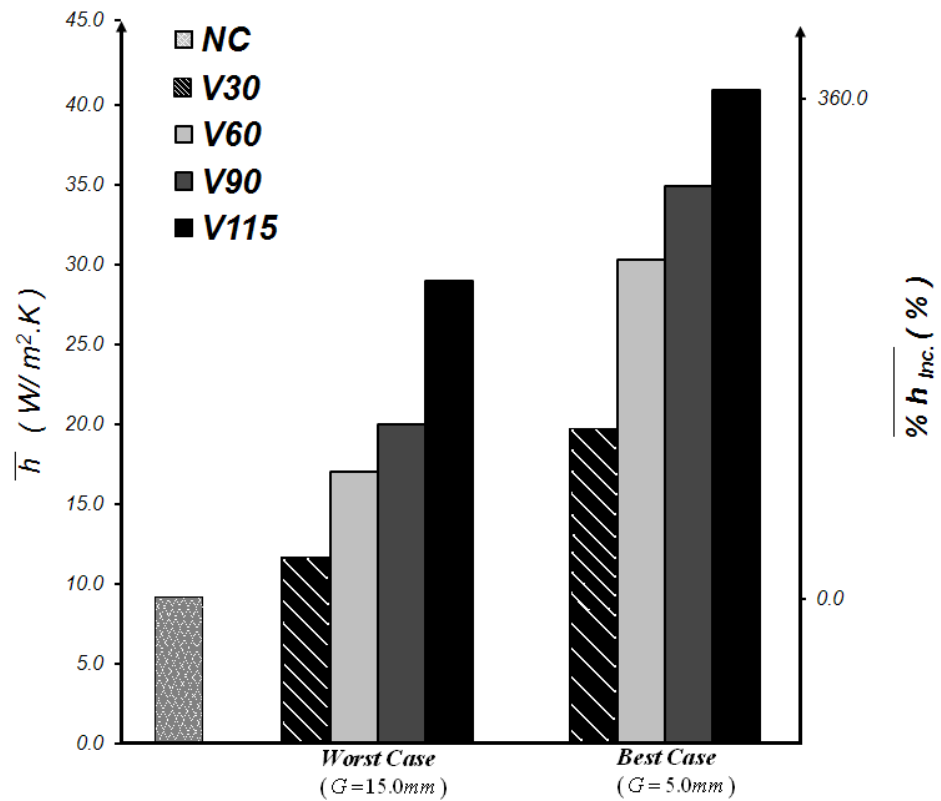


Figure 6.8: Evaluation of the Cooling Capabilities ( $\bar{h}$  and  $\%h_{inc}$ ) for a Horizontally-mounted Piezoelectric Fan - Fin Base

Figure 6.8 above illustrates the expected forced cooling ( $\bar{h}$  and  $\overline{\%h_{inc.}}$ ) produced by a horizontally-mounted piezoelectric fan on the *FB* when compared to the natural convection state. Furthermore, the worst case and the best case scenarios are plotted on the same graph so that the importance of the correct selection of the geometrical positioning of the fan can be seen.

## 6.2.2 Fin Side Wall Cooling Results

The next series of 2D contour plots, Figure 6.9, Figure 6.10 and Figure 6.11 show fin spacings of  $S = 30.0mm$ ,  $S = 40.0mm$ , and  $S = 50.0mm$  respectively. As in the previous section, the effect of vibrational amplitude ( $A_{pz}$ ), separation distance ( $G$ ), and fin spacing ( $S$ ) are investigated.

The first noticeable feature in the contour maps is that the cooling magnitude ( $\%h_{mc}$ ) is significantly lower than that observed on the fin base, indicating that a horizontally-mounted piezoelectric fan is not as effective in cooling the *FSW* as the *FB*. Furthermore, the cooling effect on the *FSW* is constrained in close proximity to the *FB* and runs along the entire length of the fin base (i.e.  $Z_{pos} = 0.0mm$ ) for large vibrational amplitudes. However, on applying the minimal vibrational envelope ( $V_{pz} = 30.00V$ ), enhanced cooling is localised at the centre of the *FB*. These results shall be analysed in further detail in **Chapter 8**, where the resulting complex 3D flow regimes are presented.

On closer inspection of the cooling plots, it can be concluded that for this setup, the best resulting geometrical configuration is that of:  $V_{pz} = 115.0V$  and  $G = 15.0mm$ . That is, a large separation distance is seen to be beneficial when cooling the *FSW*. Furthermore, it is seen that, both a reduction in the vibrational amplitude and a decrease in the separation distance, lead to a reduction in the overall cooling capabilities of the *FCCS*.

A better understanding of the cooling patterns, is given in the ensuing *PIV* chapters, where the flow patterns are presented and discussed in further detail.

Thermal Measurements

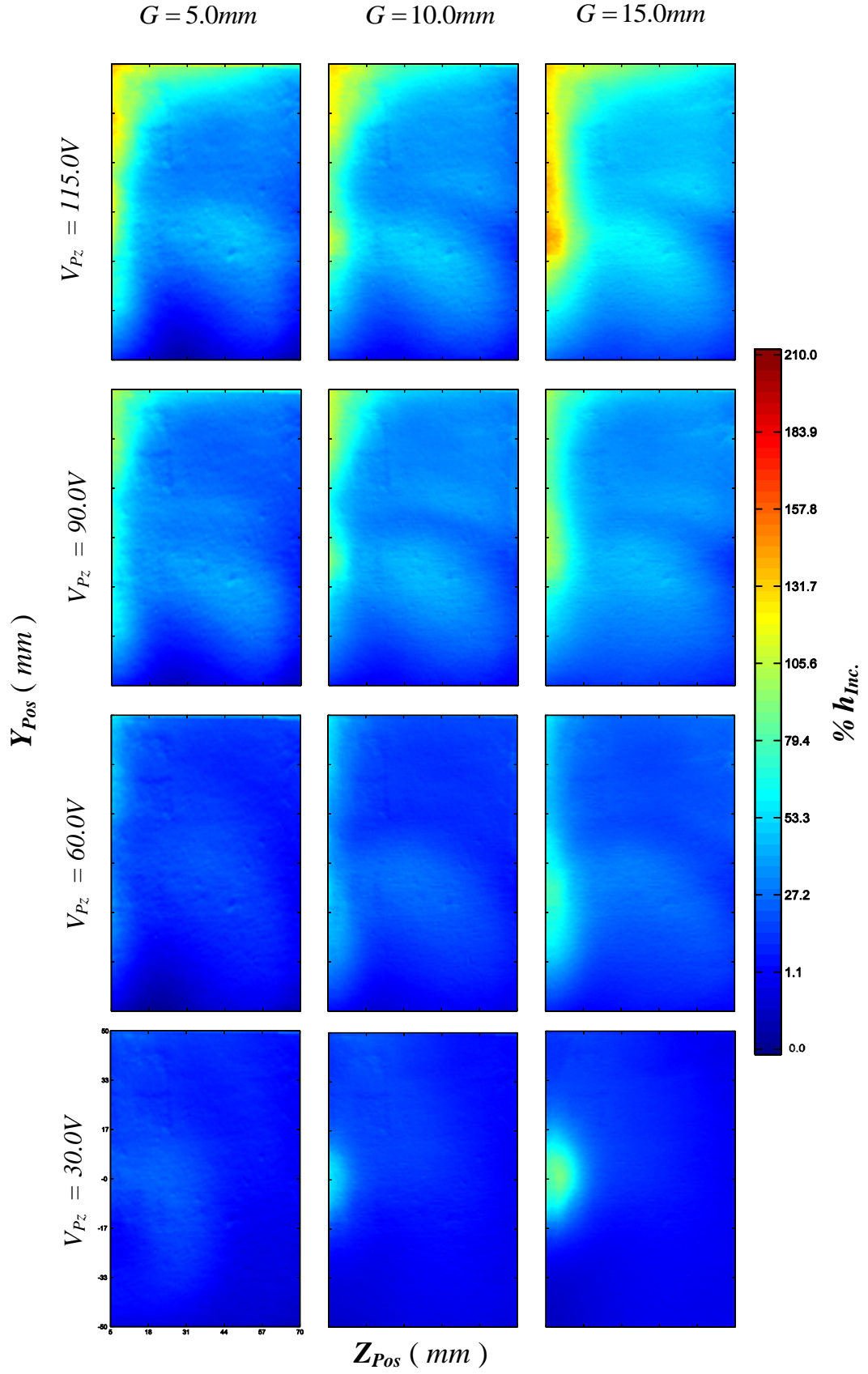


Figure 6.9: Evaluation of the FSW  $\%h_{inc}$  for a Horizontally-mounted Piezoelectric Fan: S30

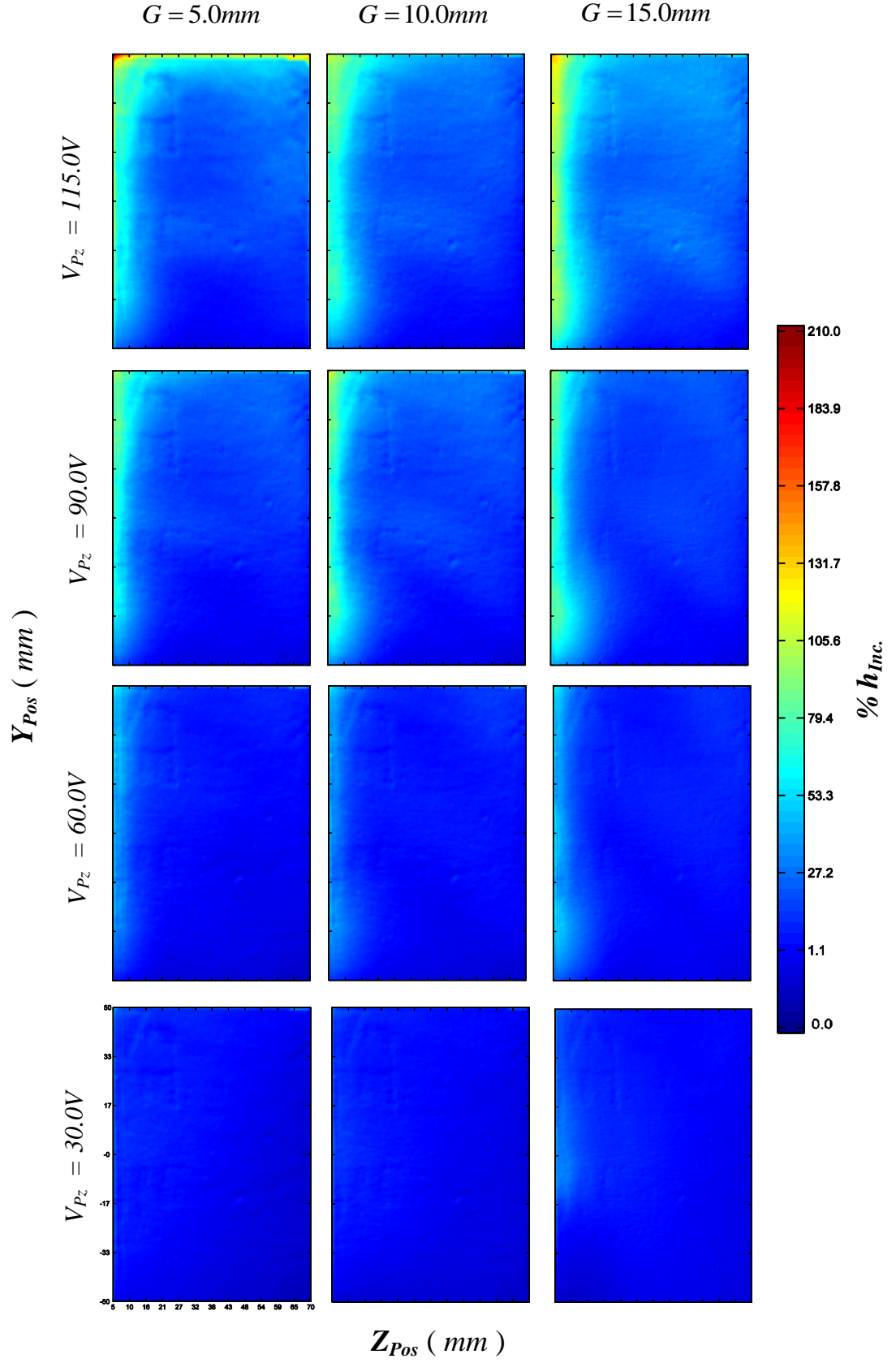


Figure 6.10: Evaluation of the FSW  $\%h_{inc}$  for a Horizontally-mounted Piezoelectric Fan:  
S40

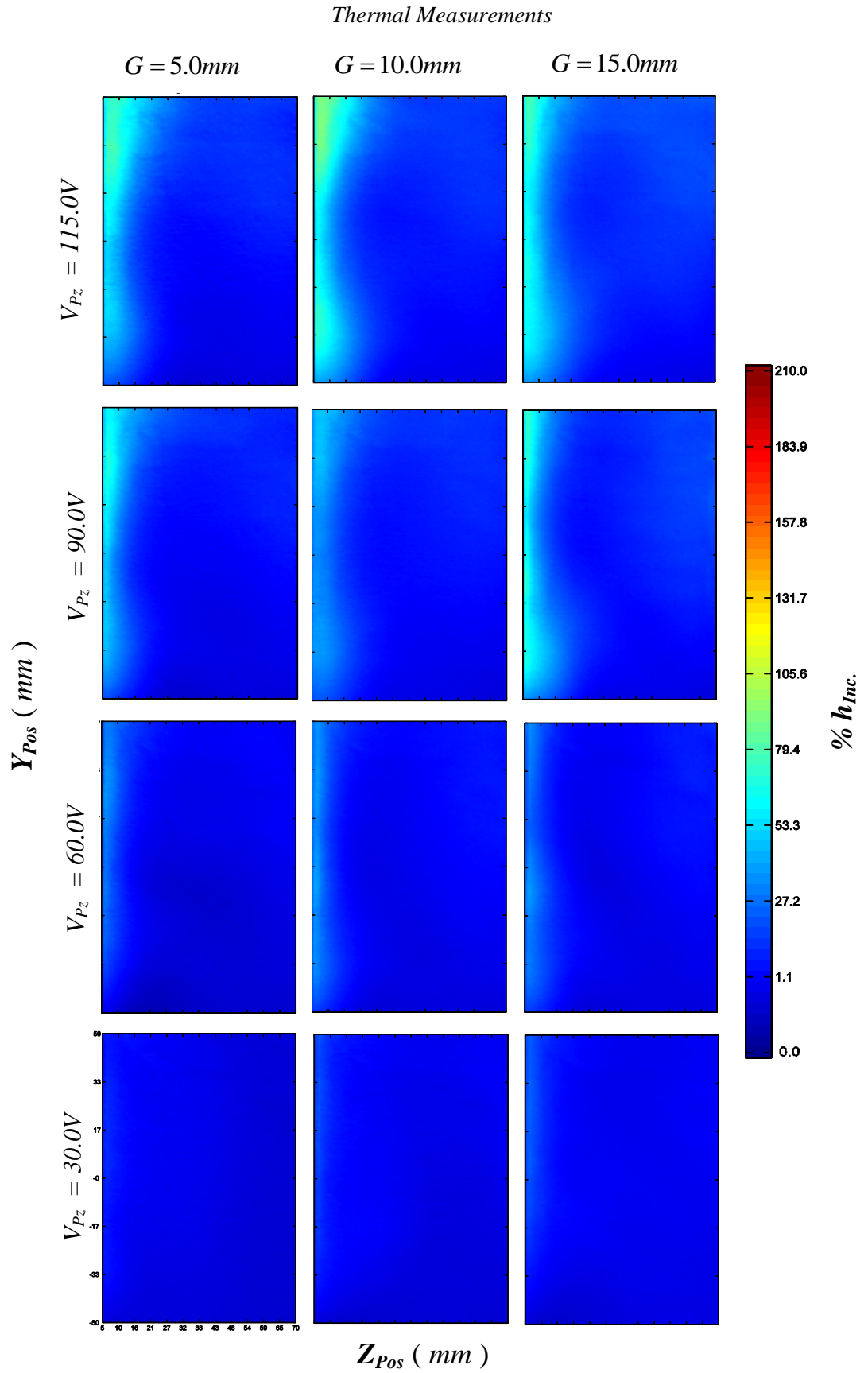


Figure 6.11: Evaluation of the FSW  $\%h_{inc}$  for a Horizontally-mounted Piezoelectric Fan: S50



When considering the cooling capabilities of the *FCCS* on the *FSW*, as the same dimensions of the *FSW* are maintained throughout the different fin spacing tests, it can be concluded that the narrower the fin spacing, the larger the expected cooling. Numerically, when  $S = 30.0mm$ ,  $\overline{\%h_{inc.}} = 55.8\%$ , when  $S = 40.0mm$ ,  $\overline{\%h_{inc.}} = 36.6\%$ , and when  $S = 50.0mm$ ,  $\overline{\%h_{inc.}} = 20.8\%$ .

However, the same cannot be concluded for the fin base. The effect of fin spacing shall be further investigated in **Chapter 8**, and the combined effect of  $S$  on the overall heat sink (*FB* and *FSW*'s) is evaluated and presented in **Chapter 9**.

### 6.3 Vertically Mounted Piezoelectric Fan

In this section, 2D contour maps of the  $\%h_{inc.}$  are presented for a vertically-mounted oscillating piezoelectric fan (the setup of which is depicted in Figure 5.19ii) for the various tested geometrical parameters;  $A_{pz}$ ,  $G$ ,  $S$ .

Results pertaining to the  $FB$  and  $FSW$  are presented and discussed in turn. In each section, the key trends are highlighted and discussed in some detail.

#### 6.3.1 Fin Base Cooling Results

In the series of 2D contour maps shown below, Figure 6.12 is for a fin spacing of  $S = 30.0mm$ , Figure 6.13 is for a fin spacing of  $S = 40.0mm$ , Figure 6.14 a fin spacing of  $S = 50.0mm$  and Figure 6.15 a simple vertical flat plate (i.e. no fins). In each of these figures, the effect of vibrational amplitude ( $A_{pz}$ ) and separation distance ( $G$ ) is investigated. Furthermore, all presented images have been equally scaled (0.0% - 760.0%) so as to facilitate the understanding of the cooling capabilities of the implemented  $FCCS$  in this orientation.

It is clearly noticeable that the attained cooling magnitudes are significantly less than the respective counterparts for a horizontally-mounted piezoelectric fan. Furthermore, results indicate that the best geometrical configuration is that of:  $V_{pz} = 115.0V$  and  $G = 5.0mm$  - a result identical to that attained by a horizontally-mounted fan. Additionally, it is seen that both a reduction in the vibrational amplitude and an increase in the separation distance lead to a reduction in the overall cooling capabilities of the  $FCCS$ .

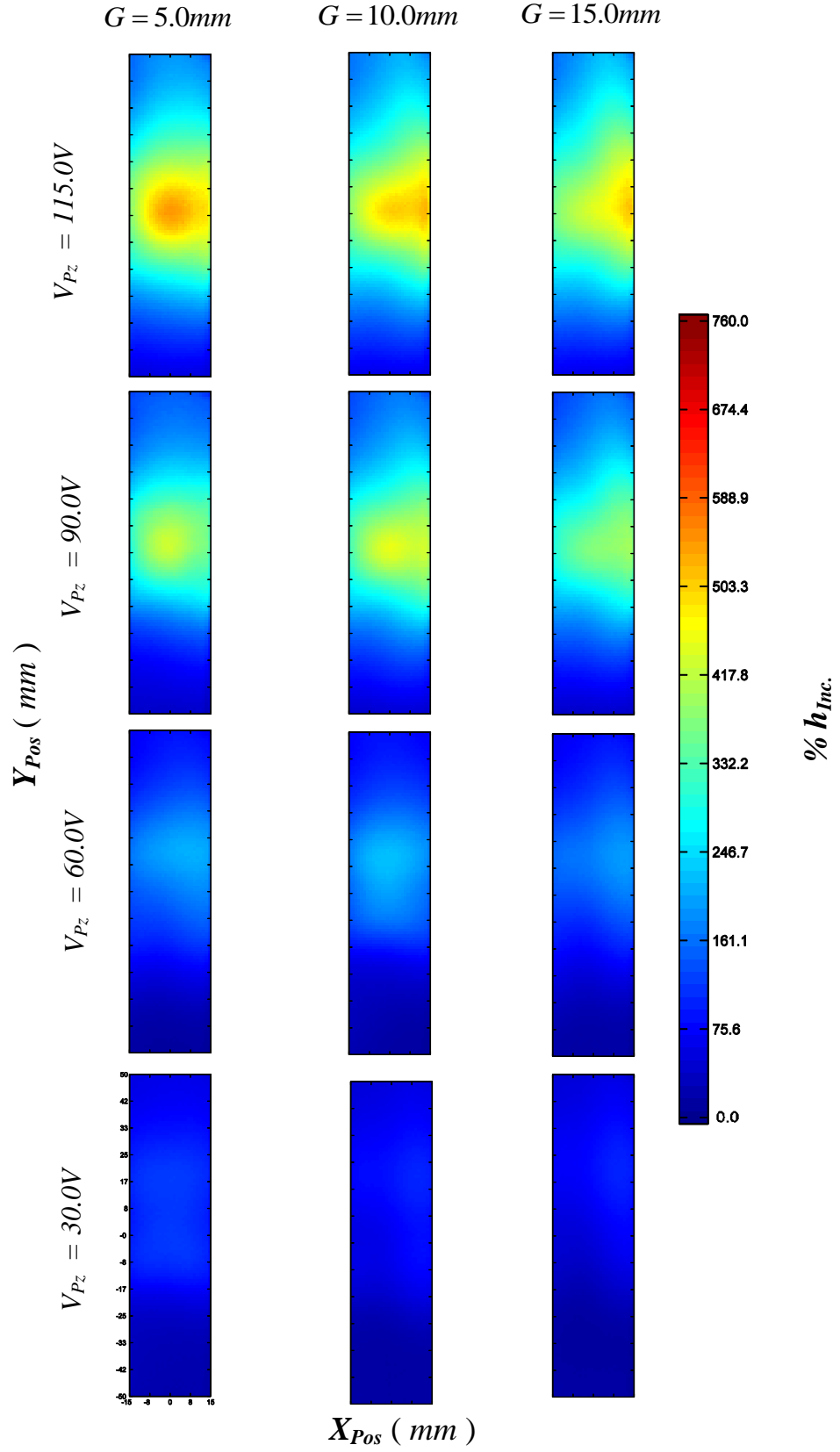


Figure 6.12: Evaluation of the FB  $\%h_{inc}$  for a Vertically-mounted Piezoelectric Fan:  
S30

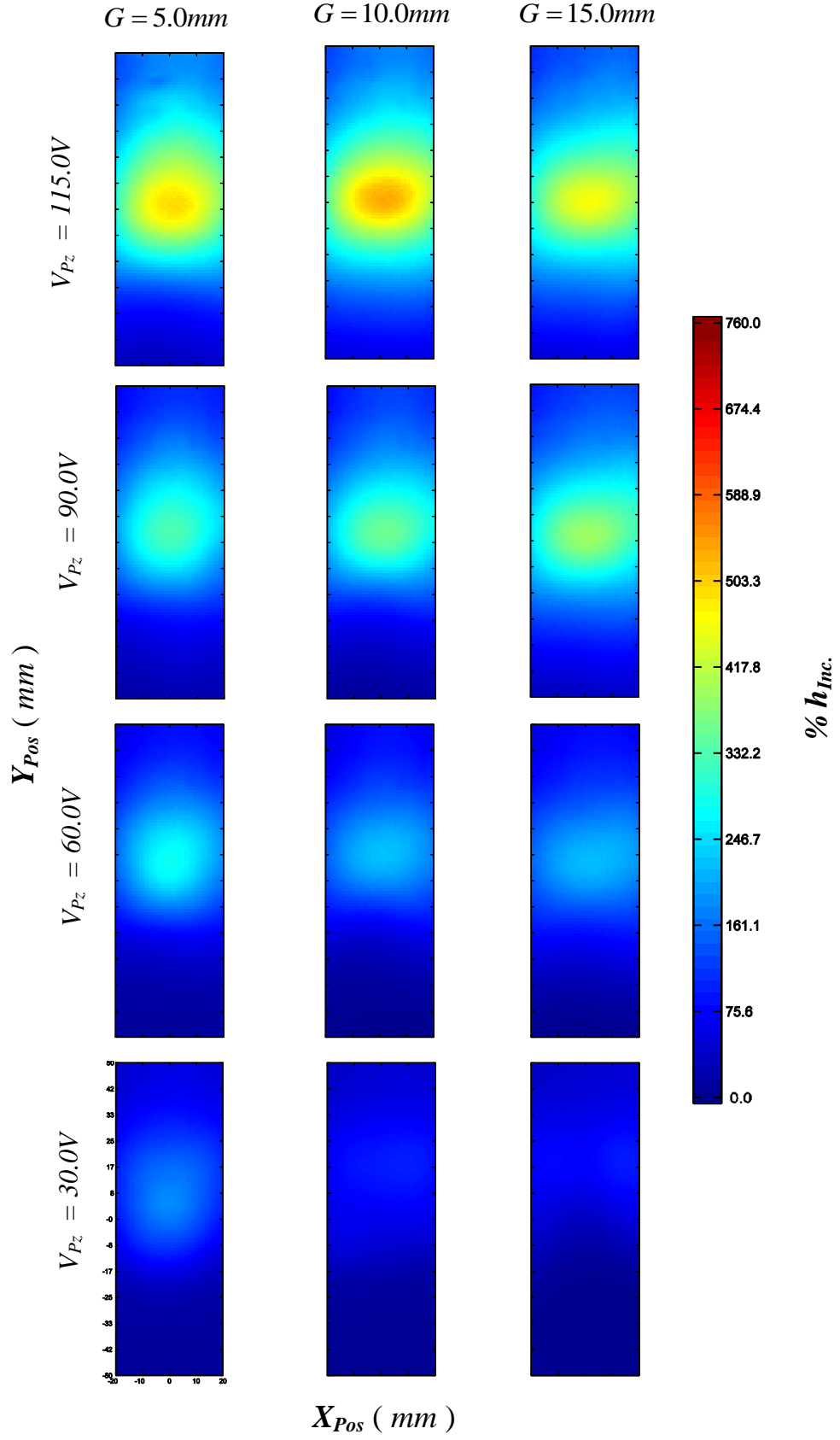


Figure 6.13: Evaluation of the FB  $\%h_{inc}$  for a Vertically-mounted Piezoelectric Fan:  
S40

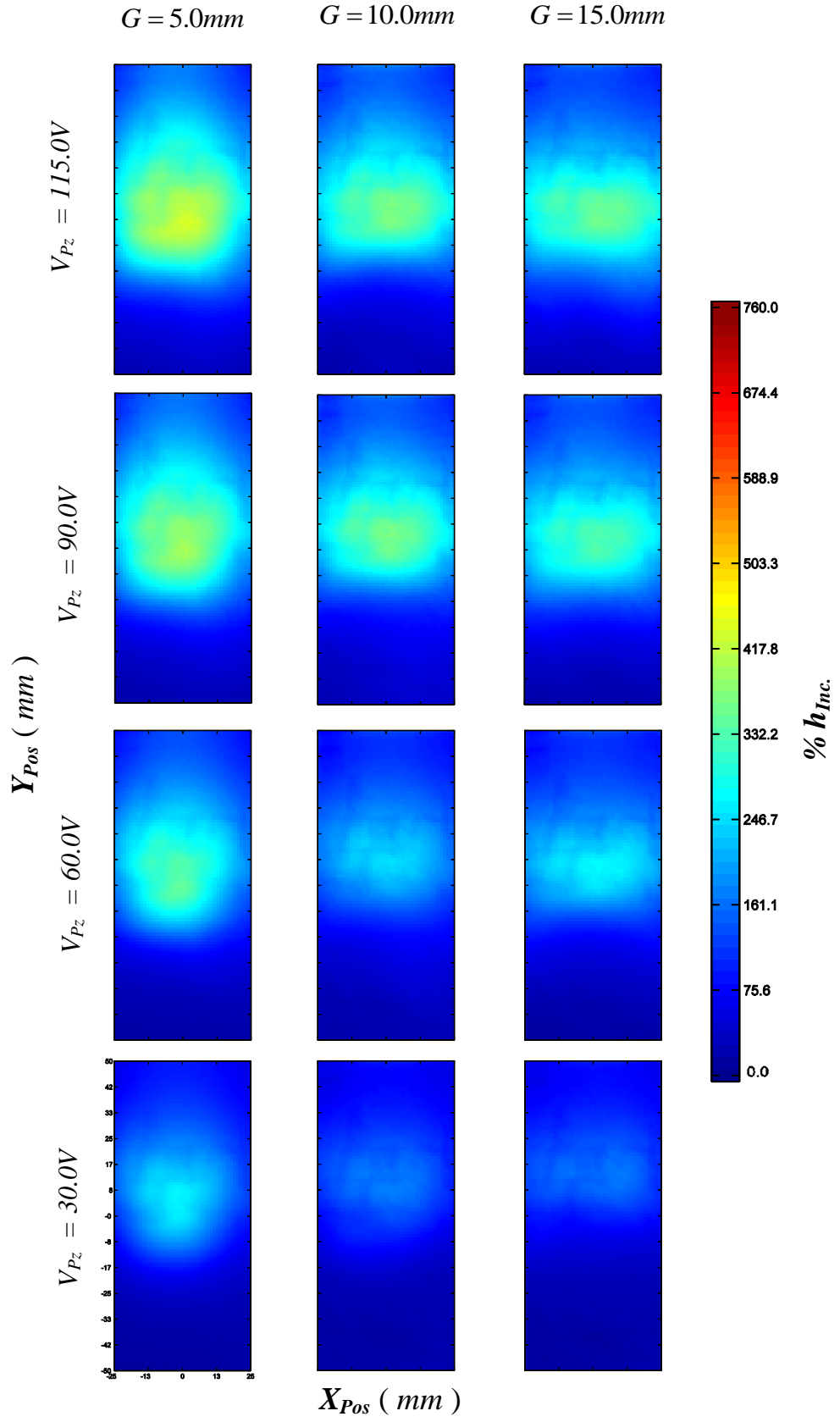


Figure 6.14: Evaluation of the FB  $\%h_{inc}$  for a Vertically-mounted Piezoelectric Fan:  
S50

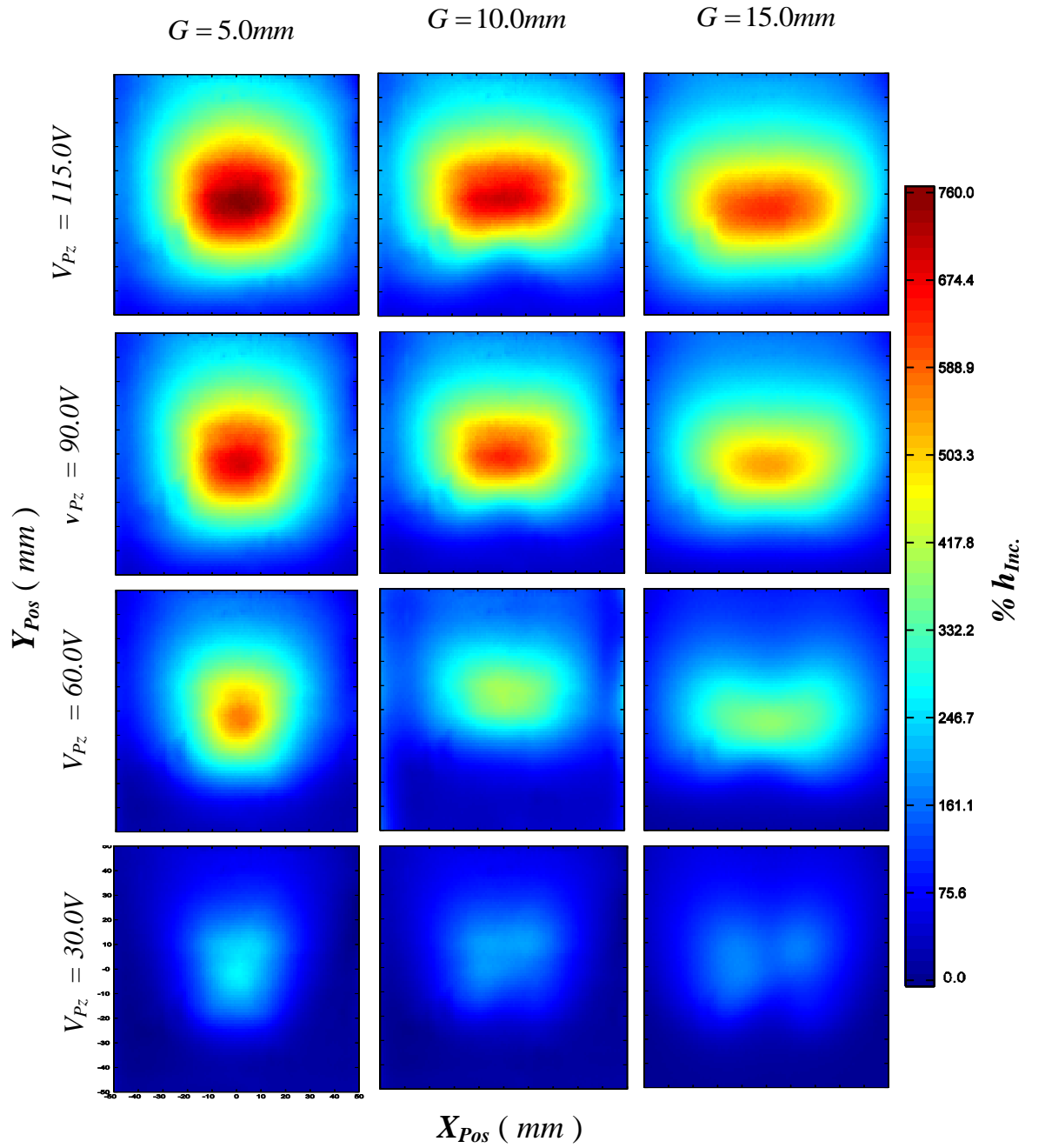


Figure 6.15: Evaluation of the FB  $\%h_{inc}$  for a Vertically-mounted Piezoelectric Fan: Flat Plate ( $S_{\infty}$ )

For each of the considered finned setups ( $S30, S40, S50$ ), a central circular symmetric pattern is generated when the fan vibrates close to the surface ( $G=5.0mm$ ), indicating that fluid agitation is roughly similar, both in the vibrational direction and the orthogonal direction. This behaviour transitions to a horizontal elliptical pattern (in the direction of the fan oscillation) when

$G = 10.0mm$  and the pattern remains elliptical for the largest considered separation distance. Furthermore, with a reduction in  $V_{Pz}$ , the same patterns are maintained.

On considering an unfinned scenario (vertical flat plate), Figure 6.15, noticeable differences are seen in the contour maps. The results presented in Figure 6.7 mimic those presented in Figure 6.15, simply rotated by  $90^\circ$ . A symmetric vertical elliptical pattern is generated when the fan vibrates close to the surface ( $G = 5.0mm$ ). On the other hand, a circular (rounded square) pattern is generated for an intermediate separation distance ( $G = 10.0mm$ ) which finally turns into a horizontal elliptical pattern for the largest separation distance.

Furthermore, a secondary distribution (which once again agrees with published literature [44]) is present in the third row ( $V_{Pz} = 60.00V$ ) of Figure 6.15, in particular when  $G = 15.0mm$ . In this contour plot, a noticeable departure from the horizontal elliptical behaviour arises with a reduction in the vibrational amplitude. This secondary pattern starts to form at the two extreme edges of the elliptical contours, forming two, slightly larger circular patterns. This suggests that, although similar behaviour is observed for different amplitudes, beyond a certain critical vibrational amplitude ( $V_{Pz} = 60.00V$ ) this behaviour alters. There is further evidence of the above mentioned secondary pattern when considering  $V_{Pz} = 30.0V$ . It is seen that the differences observed between the small and large amplitudes could be due to a change in the flow regime (i.e. transition region). However, to better understand the heat transfer results, reference to the PIV chapters (**Chapter 7** and **Chapter 8**) must be made.

The presented cooling plots indicate that, a decrease in the vibrational amplitude and an increase in separation distance results in an overall reduction in the cooling magnitude ( $\%h_{inc}$ ) of the FCCS, matching the results of a horizontally-mounted FCCS.

Figure 6.16 highlights the expected forced cooling ( $\bar{h}$  and  $\overline{\%h_{inc.}}$ ) of a vertically-mounted piezoelectric fan on the fin base when compared to the natural convection state.

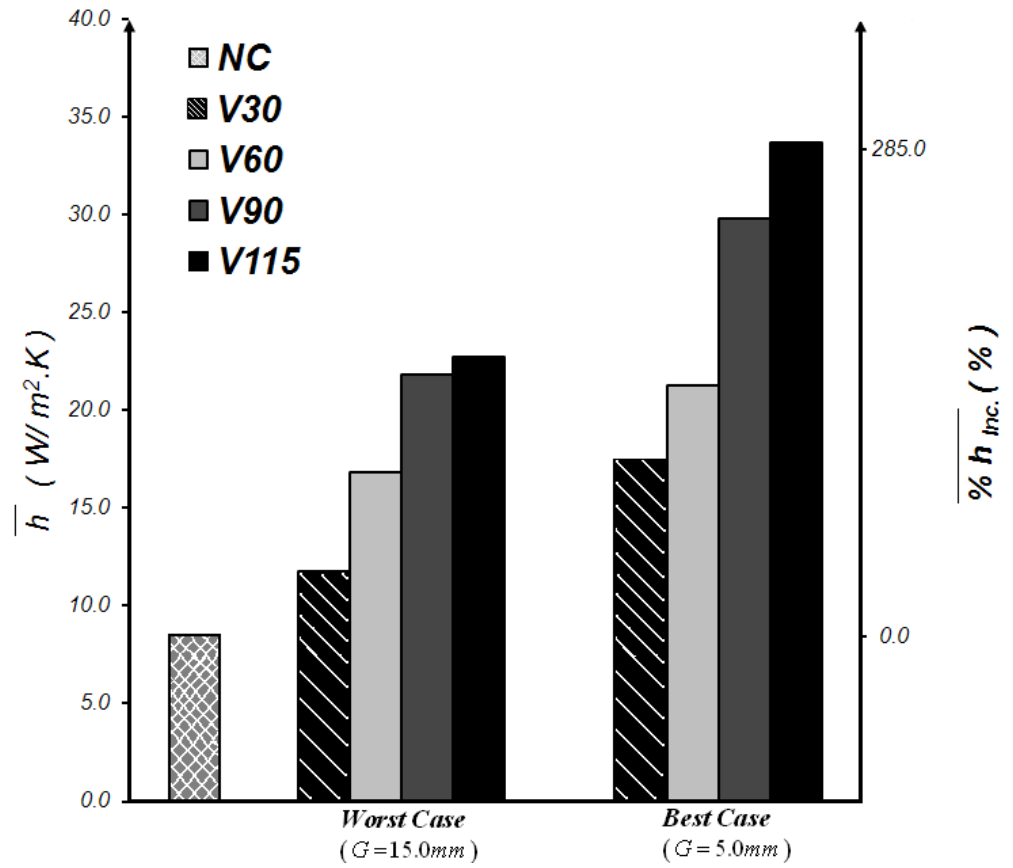


Figure 6.16: Evaluation of the Cooling Capabilities of a Vertically-mounted Piezoelectric Fan: Fin Base

It may thus be concluded that the presence of the *FCCS* significantly cools the fin base, the best scenario resulting in a  $\overline{\%h_{inc.}}$  of just over 300%. Furthermore, by direct comparison to Figure 6.8, it may also be concluded that a horizontally-mounted fan is superior to a vertically-mounted fan.



### 6.3.2 Fin Side Wall Cooling Results

In this last series of 2D contour plots, Figure 6.17, Figure 6.18 and Figure 6.19 illustrate a fin spacing of  $S = 30.0mm$ ,  $S = 40.0mm$ , and  $S = 50.0mm$  respectively. As in the previous section, the effect of vibrational amplitude ( $A_{pz}$ ), separation distance ( $G$ ), and fin spacing ( $S$ ) are investigated.

The first noticeable feature in the presented contour maps is that the cooling magnitude ( $\%h_{inc}$ ) is both, significantly lower and constrained to a smaller area than that observed on the fin base, indicating that a vertically-mounted piezoelectric fan is not as effective in cooling the *FSW* as the *FB*. However, by direct comparison of the 2D contour plots of the *FSW* generated by a horizontally-mounted piezoelectric fan to those generated by a vertically-mounted piezoelectric fan (shown hereunder), it is evident that the latter is far more appropriate.

On closer inspection of the presented results, it can be concluded that for this setup, the best resulting geometrical configuration is that of:  $V_{pz} = 115.0V$  and  $G = 15.0mm$ . This means that, a larger separation distance is seen to be beneficial when cooling the *FSW*. Furthermore, it is seen that, both a reduction in the vibrational amplitude and a decrease in the separation distance, lead to a reduction in the overall cooling capabilities of the *FCCS*. This outcome is once again similar to that obtained for a horizontally-mounted *FCCS*.

In this setup, the enhanced cooling is localised at the stagnant point (rest/datum position) of the vibrating fan at the fin base (i.e.  $Z_{pos} = 0.0mm$ ), while a minimal enhancement is attained in the surrounding regions.

When considering the cooling capabilities of a vertically-mounted piezoelectric fan on the *FSW*, unlike a horizontally-mounted piezoelectric fan, it can be concluded that the larger the fin spacing is ( $S50$ ), the larger will be the expected cooling. This result will be verified in **Chapter 8**, when the detailed flow characteristics are presented.

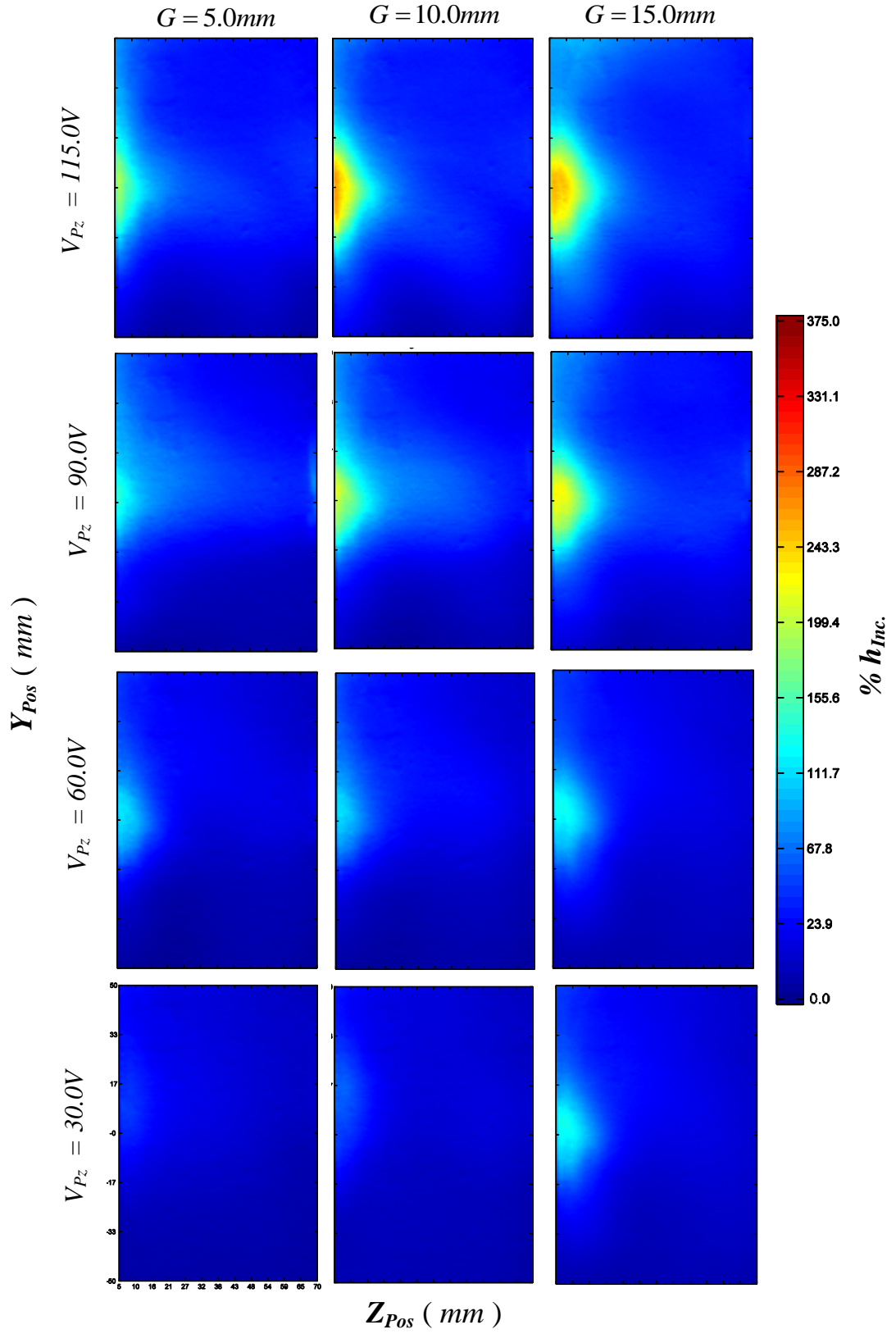


Figure 6.17: Evaluation of the FSW  $\%h_{Inc}$  for a Vertically-mounted Piezoelectric Fan: S30

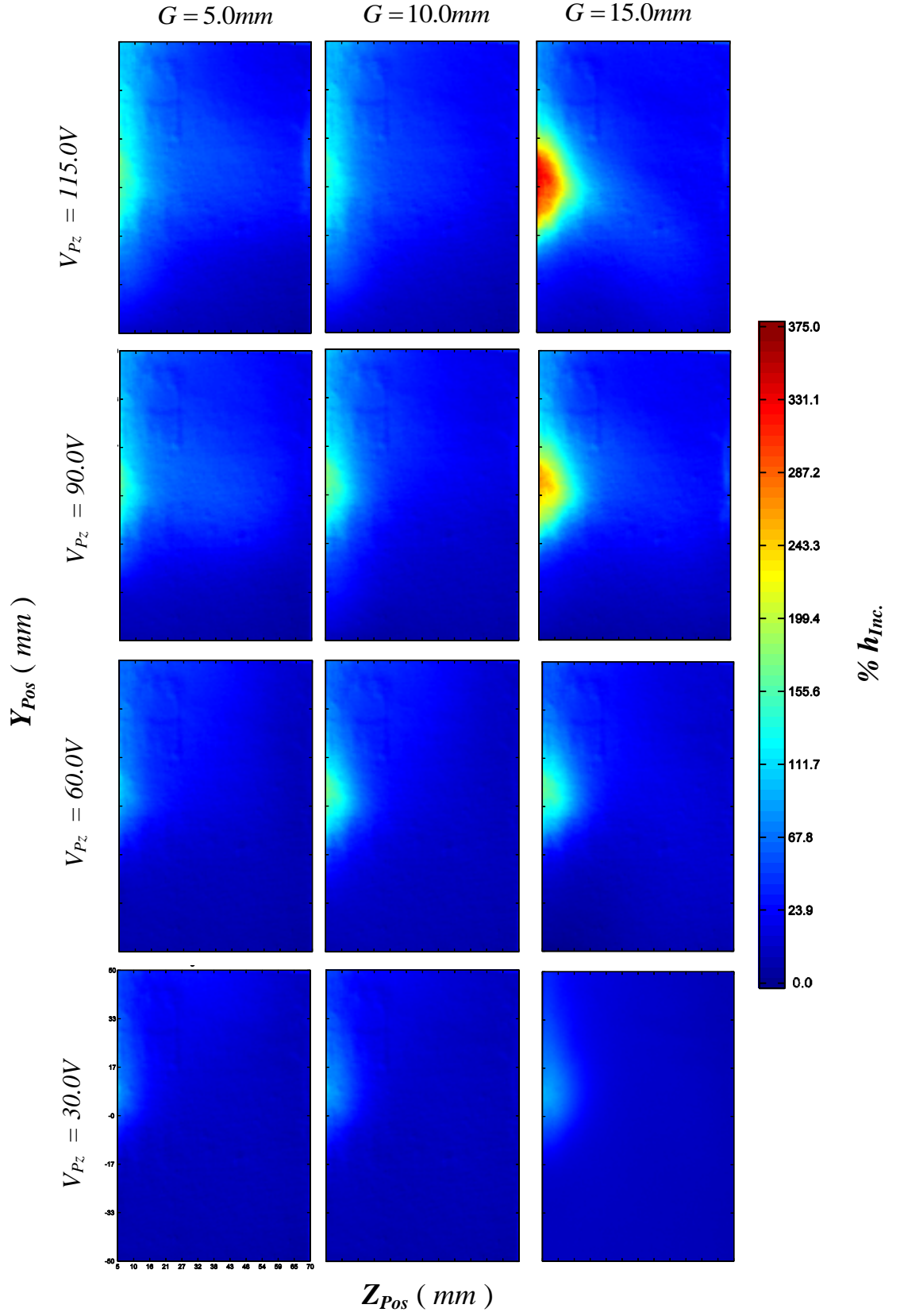


Figure 6.18: Evaluation of the FSW  $\%h_{inc}$  for a Vertically-mounted Piezoelectric Fan:  
S40

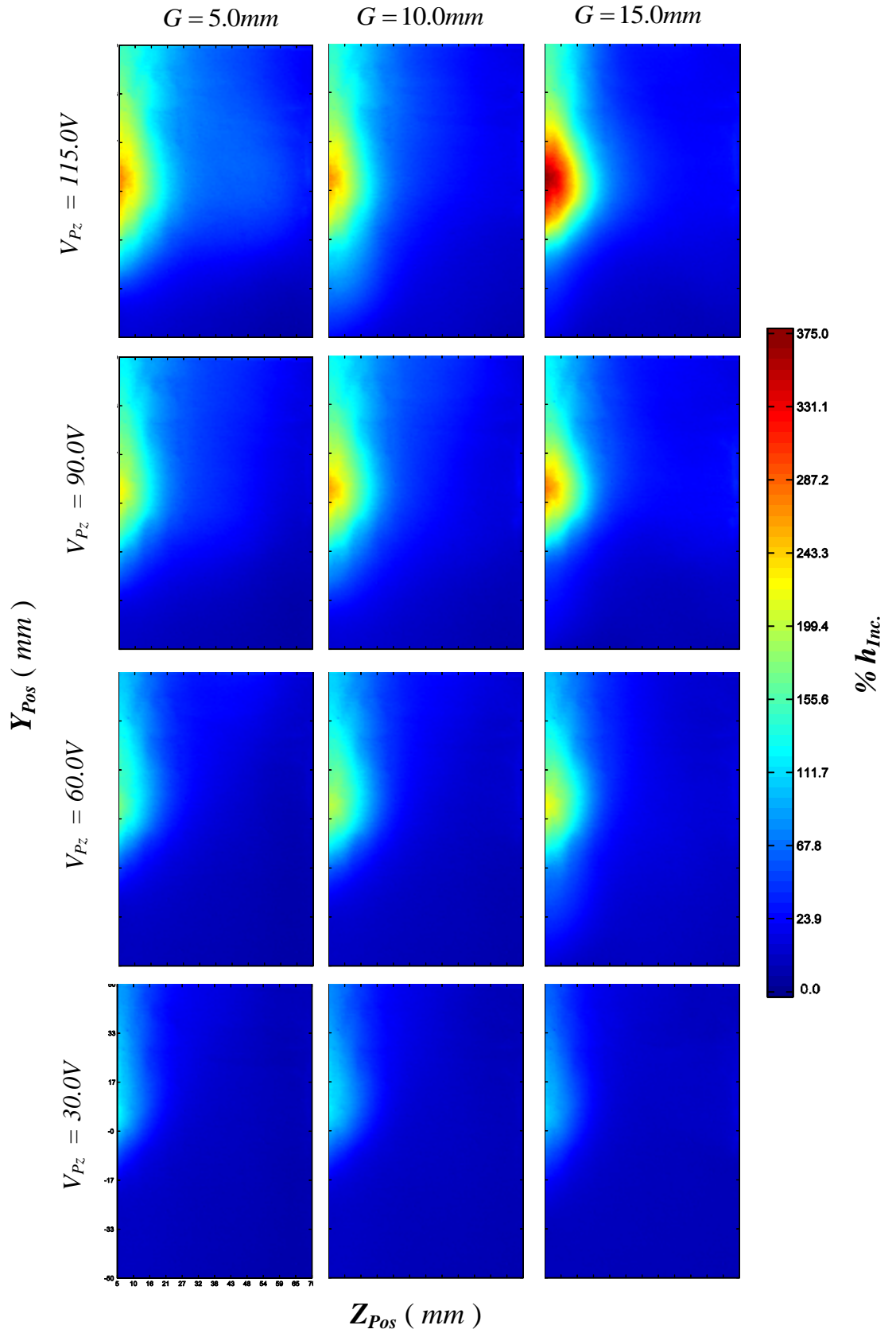


Figure 6.19: Evaluation of the FSW  $\%h_{inc}$  for a Vertically-mounted Piezoelectric Fan: S50

## 6.4 Concluding Remarks

In this chapter, the cooling capabilities of the suggested *FCCS* on the *FB* and the *FSW*, for a number of different configurations (  $A_{pz}$ ,  $G$ ,  $S$ , *Orientation* ) have been investigated, the results of which have been presented and discussed in some detail.

It has been established that when cooling the *FB*, for both a horizontally-mounted piezoelectric fan, and a vertically-mounted fan, the best geometrical configuration is that of:  $V_{pz} = 115.0V$  and  $G = 5.0mm$ . Furthermore, it is seen that, both a reduction in the vibrational amplitude and an increase in the separation distance, lead to a reduction in the overall cooling capabilities of the *FCCS*. However, it has been concluded that a horizontally-mounted fan is superior to a vertically-mounted one, as is highlighted in Table 6.1 and Figure 6.20.

<b>S</b> (mm)	$\overline{h_{NC}}$ (W/m <sup>2</sup> .K)	$\overline{h_{FC}}$ (W/m <sup>2</sup> .K)	$\% \overline{h_{Inc.}}$ (%)
<b>30.0</b>	8.8	40.9	364.8
<b>40.0</b>	8.7	38.4	341.4
<b>50.0</b>	8.6	33.8	293.0
<b>Flat Plate</b>	7.7	31.3	306.5

(i)

<b>S</b> (mm)	$\overline{h_{NC}}$ (W/m <sup>2</sup> .K)	$\overline{h_{FC}}$ (W/m <sup>2</sup> .K)	$\% \overline{h_{Inc.}}$ (%)
<b>30.0</b>	8.7	33.7	287.4
<b>40.0</b>	8.7	29.4	237.9
<b>50.0</b>	8.7	25.6	194.3
<b>Flat Plate</b>	7.6	31.6	315.8

(ii)

Table 6.1: Effect of Fin Spacing ( $S$ ) on the *FB*,  $V_{pz} = 115.0V$ ,  $G = 5.0mm$  :  
(i) Horizontally-mounted (ii) Vertically-mounted

Table 6.1 indicates that the best suited *FCCS* geometrical configuration to cool the *FB* is that of a minimum fin spacing -  $S = 30.00mm$ . Furthermore, with an increase in fin spacing, the cooling capabilities of the *FCCS* ( $\overline{h}_{inc.}$ ) decrease considerably. Thus through the detailed thermal analysis, it has been established that a horizontally-mounted piezoelectric fan positioned at  $S = 30.00mm, G = 5.0mm, V_{pz} = 115.0V$  results in the highest fin base cooling.

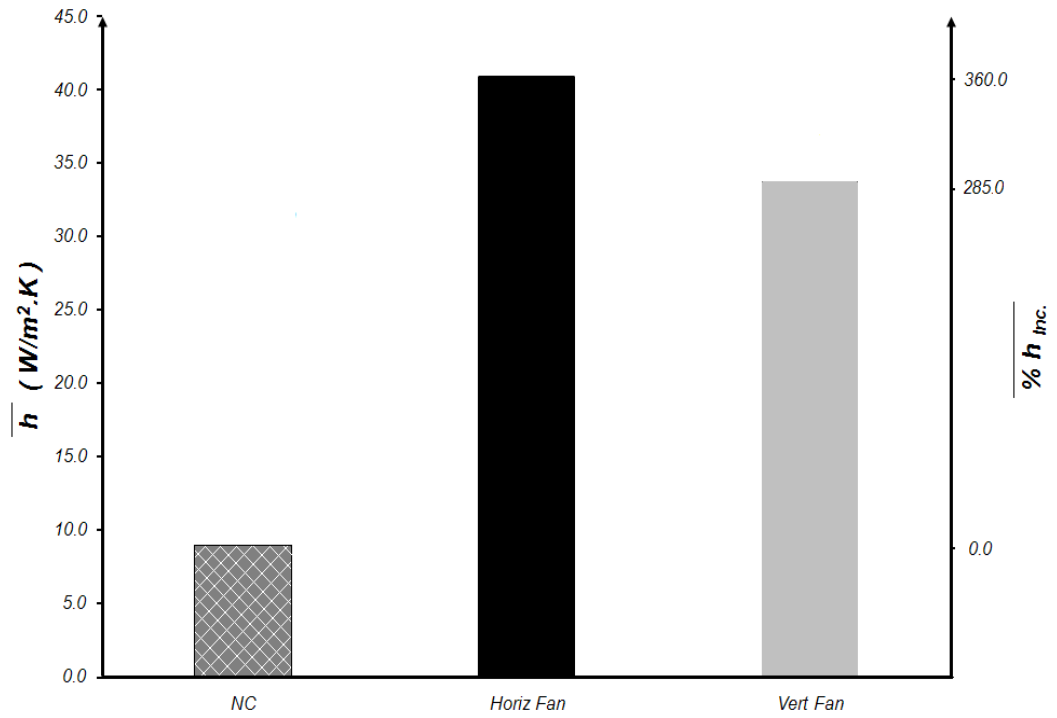


Figure 6.20: Fin Base Comparative Study:  $S = 30.0mm, G = 5.0mm, V_{pz} = 115.0V$

On the other hand, when cooling the *FSW*, for both a horizontally-mounted piezoelectric fan, and a vertically-mounted fan, the best geometrical configuration is that of:  $V_{pz} = 115.0V$  and  $G = 15.0mm$ . Furthermore, it is seen that, both a reduction in the vibrational amplitude and a decrease in the separation distance, lead to a reduction in the overall cooling capabilities of the *FCCS*. Furthermore, a narrow fin spacing ( $S30$ ) leads to the largest cooling with a horizontally-mounted fan, while the converse holds for a vertically-mounted fan, i.e. a larger fin spacing ( $S50$ ) results in an increased cooling - Table 6.2.

<b>S</b> (mm)	$\overline{h}_{NC}$ (W/m <sup>2</sup> .K)	$\overline{h}_{FC}$ (W/m <sup>2</sup> .K)	$\% \overline{h}_{Inc.}$ (%)
<b>30.0</b>	10.3	15.2	47.6
<b>40.0</b>	10.1	13.7	35.6
<b>50.0</b>	10.4	12.5	20.2
<b>Flat Plate</b>	/	/	/

(i)

<b>S</b> (mm)	$\overline{h}_{NC}$ (W/m <sup>2</sup> .K)	$\overline{h}_{FC}$ (W/m <sup>2</sup> .K)	$\% \overline{h}_{Inc.}$ (%)
<b>30.0</b>	9.9	14.7	48.5
<b>40.0</b>	9.7	14.5	49.5
<b>50.0</b>	9.7	14.9	53.6
<b>Flat Plate</b>	/	/	/

(ii)

Table 6.2: Effect of Fin Spacing (S) on the  $FSW$ ,  $V_{Pz} = 115.0V$ ,  $G = 15.0mm$ :

(i) Horizontally-mounted

(ii) Vertically-mounted

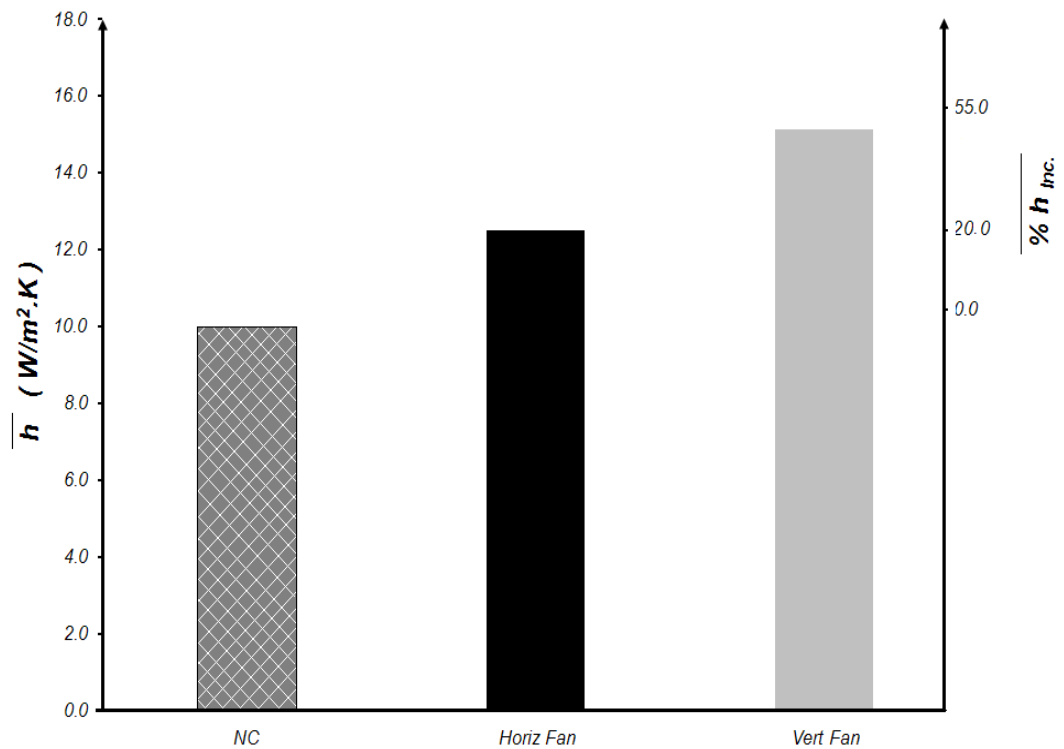


Figure 6.21: Fin Side Wall Comparative Study:  $S = 50.0mm$ ,  $G = 15.0mm$ ,  $V_{Pz} = 115.0V$

However, for this case, it has been established that a vertically-mounted fan is superior to a horizontally-mounted one, as is highlighted in Figure 6.21 and detailed in Table 6.2.

The above results while complex in nature have to be analysed further so that a single optimum *FCCS* configuration, representative of both the *FB* and *FSW*'s (i.e. representative of a finned electric motor housing) may be established. Thus, the effect of fin spacing and the selection of the optimum heat sink design and *FCCS* are discussed and presented in **Chapter 9**.

Furthermore, to better understand the presented 2D contour plots, together with the primary and secondary patterns, time averaged *PIV* was performed, the results of which are presented in **Chapter 7** and **Chapter 8**.



# CHAPTER 7

## 7. Flow Measurements on a Vertical Flat Surface

---

This chapter aims to investigate, characterise and measure the flows generated by the *FCCS* on a plane parallel to a vertical flat surface ( $S^\infty$ ), to complement the heat transfer results presented in *Chapter 6*. The flow relationships are presented in *Section 7.1*, and the piezoelectric fan frequency characteristics are presented in *Section 7.2*.

As previously reported in the review, literature describing the flow patterns generated by an oscillating piezoelectric fan on a vertical flat surface (particularly in conjunction with a heat sink) are few, whilst papers measuring the *2D / 3D* mean and turbulence velocities are virtually nonexistent. This limited research has raised a number of issues which need to be resolved to better understand the cooling characteristics of piezoelectric fans. However, as with all unsteady flow generators, the flow field generated from these fans is complex and dependent on numerous parameters.

Detailed flow visualisation and measurements (*PIV*) generated by a horizontally-mounted oscillating piezoelectric fan are first discussed in *Section 7.3*; this is then followed by those produced by a vertically-mounted oscillating fan in *Section 7.4*. As in the previous chapter, the effects of varying  $A_{P_z}$  and varying  $G$  are investigated, and the most important trends are thereby highlighted and discussed in further detail.

A further in-depth analysis, which includes a dimensional analysis, is presented in *Section 7.5* while the chapter conclusions are drawn up in *Section 7.6*.

## 7.1 PIV Flow Correlations

The correlations utilised in the evaluation of the flow characteristics, in particular,  $\overline{V_X}$ ,  $\overline{V_Y}$ , the magnitude of the mean vectors ( $\overline{V_{Mean}}$ ) and the *RMS* velocity (turbulence) are given here.

$$\overline{V_X} = \frac{\sum_{i=1}^{N_I} V_X}{N_I} \quad \dots \text{Eq. 7.1}$$

$$\overline{V_Y} = \frac{\sum_{i=1}^{N_I} V_Y}{N_I} \quad \dots \text{Eq. 7.2}$$

$$\overline{V_{Mean}} = \sqrt{(\overline{V_X})^2 + (\overline{V_Y})^2} \quad \dots \text{Eq. 7.3}$$

As previously mentioned,  $N_I$  refers to the number of images pairs captured by the *PIV* system. The above formulation (Eq. 7.3) was adopted to calculate the magnitude of the mean vectors ( $\overline{V_{Mean}}$ ). Eq. 7.6 was used to calculate the *RMS* velocity ( $V_{RMS}$ ).

$$Var_X = \frac{\sum_{i=1}^{N_I} (V_X^2)}{N_I} - (\overline{V_X})^2 \quad \dots \text{Eq. 7.4}$$

$$Var_Y = \frac{\sum_{i=1}^{N_I} (V_Y^2)}{N_I} - (\overline{V_Y})^2 \quad \dots \text{Eq. 7.5}$$

$$V_{RMS} = \sqrt{(Var_X) + (Var_Y)} \quad \dots \text{Eq. 7.6}$$

The above formulation is explained further in the literature [59, 60].

## 7.2 Frequency Characteristics

Tests were performed to investigate the surrounding piezoelectric fan air frequency (  $f$  ). These tests were conducted to better understand the effect of the oscillating piezoelectric fan on the surrounding air. On analysing the *PIV* raw data (*FFT* analysis of the velocity field) of the freely vibrating piezoelectric fan, Figure 7.1 was obtained.

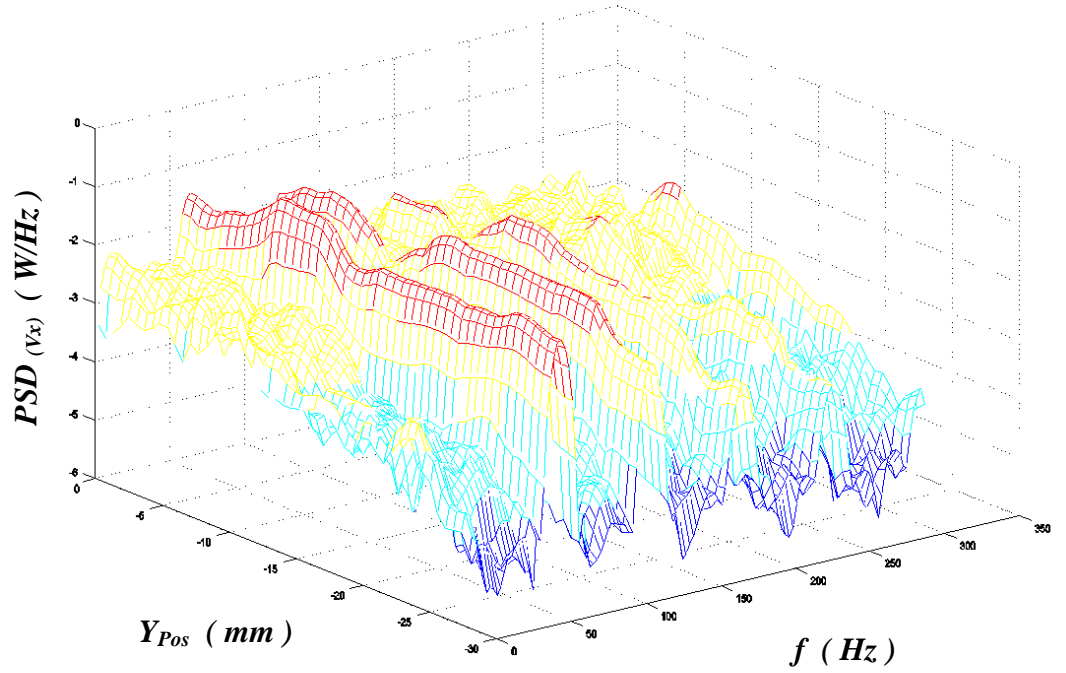


Figure 7.1: Spectrum Analysis:  $V_{Pz} = 115.0V, G10.0mm$

The above spectrum analysis indicates a dominant frequency of  $60Hz$  at all points across the image, together with the accompanying piezoelectric fan harmonic frequencies. The harmonics are generated as a non pure sinusoidal input was supplied to the fan. This result compliments the results presented in *Section 5.1*, while further clarifying the operating fan frequency. As was performed in *Chapter 6*, and for the duration of this work, in particular *Chapter 7* and *Chapter 8*, all results pertain to an operating piezoelectric fan frequency of  $f = 60Hz$ .

## 7.3 Horizontally-mounted Fan

All the results presented here pertain to a horizontally-mounted piezoelectric fan and depict the flows generated on a plane parallel to the surface ( $S_\infty$ ). In the flow setup, the laser sheet was introduced parallel to the vertical surface and displaced  $2mm$  away from it, whilst the high speed imaging camera was placed directly behind, for viewing through the back of the glass (Figure 5.21). The camera field of view measured  $52.0mm$  ( $x$ -axis) by  $83.0mm$  ( $y$ -axis).

### 7.3.1 Flow Measurements Parallel to a Vertical Flat Surface

#### 7.3.1.1 Effect of Fan Amplitude ( $V_{Pz}$ )

The sequence of images depicted in Figure 7.2 indicates that, for all voltages, a symmetric flow is generated, confirming the thermal results in **Chapter 6**. Furthermore, an increase in  $V_{Pz}$ , results in an increase in the magnitude of the mean vectors ( $\overline{V_x}, \overline{V_y}$ ), with the major flow seen to travel preferentially along the oscillation direction ( $y$ -direction) – i.e.  $\overline{V_y}$ . Numerically, for  $G=10.0mm$  the application of  $V_{Pz} = 30.00V$  results in a maximum  $\overline{V_{Mean}} = 0.703m/s$ , while the application of  $V_{Pz} = 115.0V$ , results in  $\overline{V_{Mean}} = 1.900m/s$ .

It should be pointed out that, at either side of the fan blade, a lower air velocity develops. This is due to the fact, that at these locations, the fan is drawing in ‘fresh’ air which is later shed at the blade tip. Furthermore, Figure 7.2iv highlights the expected cooling range of the fan. The latter figure indicates that there is an appreciable flow field spanning around  $45mm$  (along the  $x$ -direction) and at least  $83mm$  (along the  $y$ -direction). This flow field matches the respective cooling plots presented in Figure 6.7.

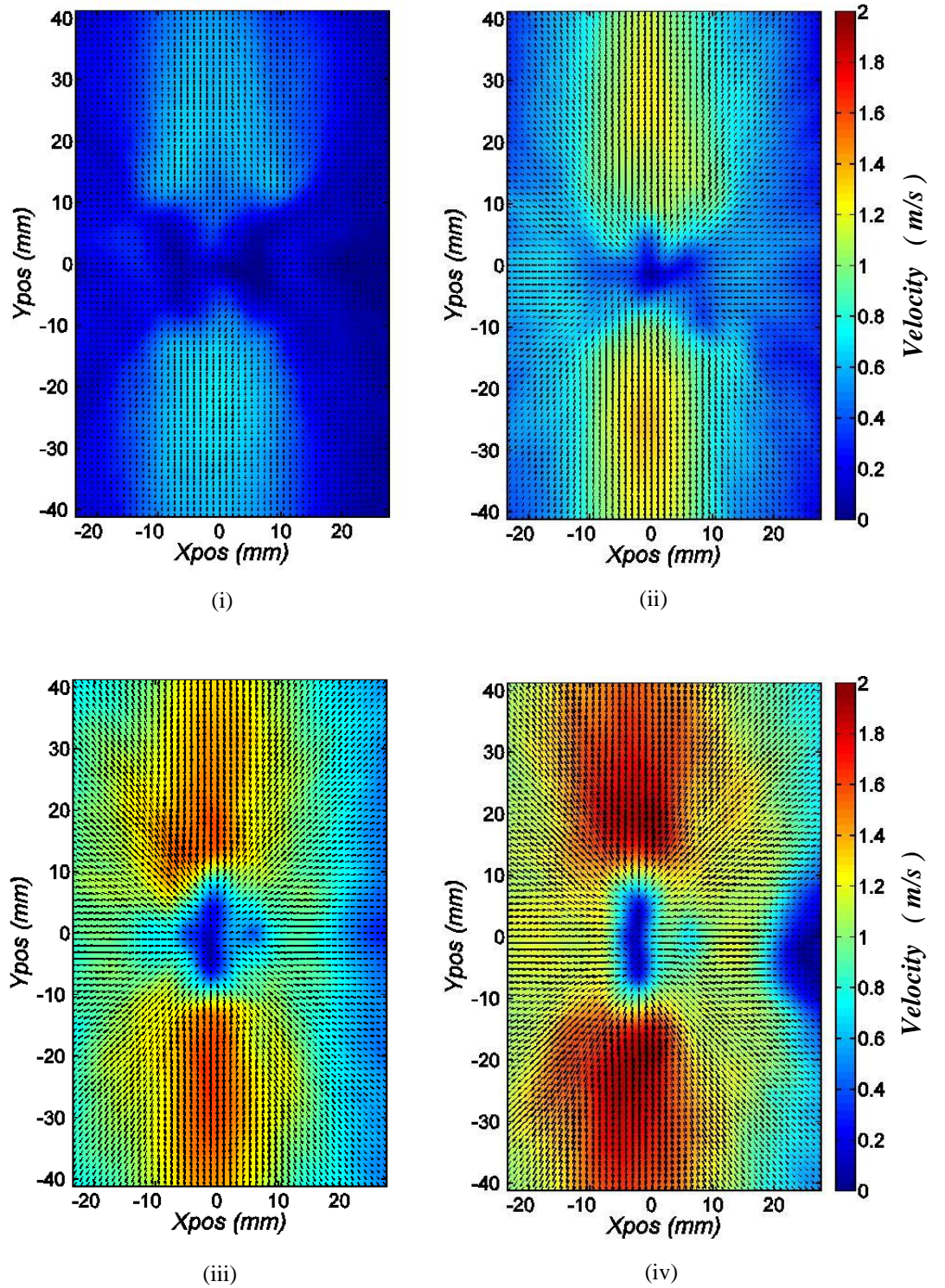


Figure 7.2: Magnitude of the Mean Velocity Vectors for a Horizontally-mounted Fan,  $G = 10.0mm$ :

i)  $V_{P_z} = 30.00V$  , ii)  $V_{P_z} = 60.00V$  , iii)  $V_{P_z} = 90.00V$  , iv)  $V_{P_z} = 115.0V$

For every applied  $V_{pz}$ , the same trends are noted: along  $X_{Pos} = -10mm$ ,  $\overline{V_x}$  is negative, indicating that the flow is moving to the left, and along  $X_{Pos} = 10mm$ ,  $\overline{V_x}$  is positive, indicating that the air flow is moving to the right.

The maximum mean velocity occurs at the peaks of the vibrational amplitude. For  $V_{pz} = 115.0V$ , the peak velocity originates at  $Y_{Pos} = 12.7mm$  and  $Y_{Pos} = -12.7mm$  respectively. However, at the piezoelectric fan datum position, i.e. at  $Y_{Pos} = 0.0mm$ , a near zero velocity is obtained. As the piezoelectric fan has been proved to be symmetrical in its oscillation, the same amount of fluid flow is generated in both directions, which in turn implies the presence of a stagnant region. This result compliments the published literature as well as the experimental results presented, and is further illustrated in Figure 7.3.

The fluctuating velocities generated by the oscillating fan are presented in Figure 7.3. In all the contour plots, the fluctuations radiate from the ‘zero-position’ of the fan outwards, reaching a maximum at the edges of the vibrational amplitude, and decreases as the distance from the fan increases. The *RMS* of the fluctuating component plots indicate that an increase in  $V_{pz}$  also leads to an increase in the magnitude of the disturbance. When  $V_{pz} = 30.00V$ , the disturbance area in the neighbourhood of the fan is minimal, with a magnitude of just under  $0.503m/s$ . However, the application of  $V_{pz} = 115.0V$  results in a maximum *RMS* velocity of  $1.914m/s$ .

The resultant contours (Figure 7.2 and Figure 7.3) are quite symmetrical in nature indicating that, for a horizontally-mounted fan, the flow generated in the upswing motion is equivalent to that produced by the downswing. Furthermore, results compare well with the presented cooling plots in **Chapter 6**. Both the cooling range and the flow/cooling symmetry are well matched for a vertical flat plate ( $S\infty$ ) scenario. Furthermore, a symmetric lobed (rotated hour glass) central stagnation region is generated at low fan vibrational amplitudes (Figure 7.3ii). This pattern transforms into a vertical



ellipse (y-direction) at larger vibrational amplitudes (Figure 7.3iv). This result is similar to the thermal results presented in Figure 6.7.

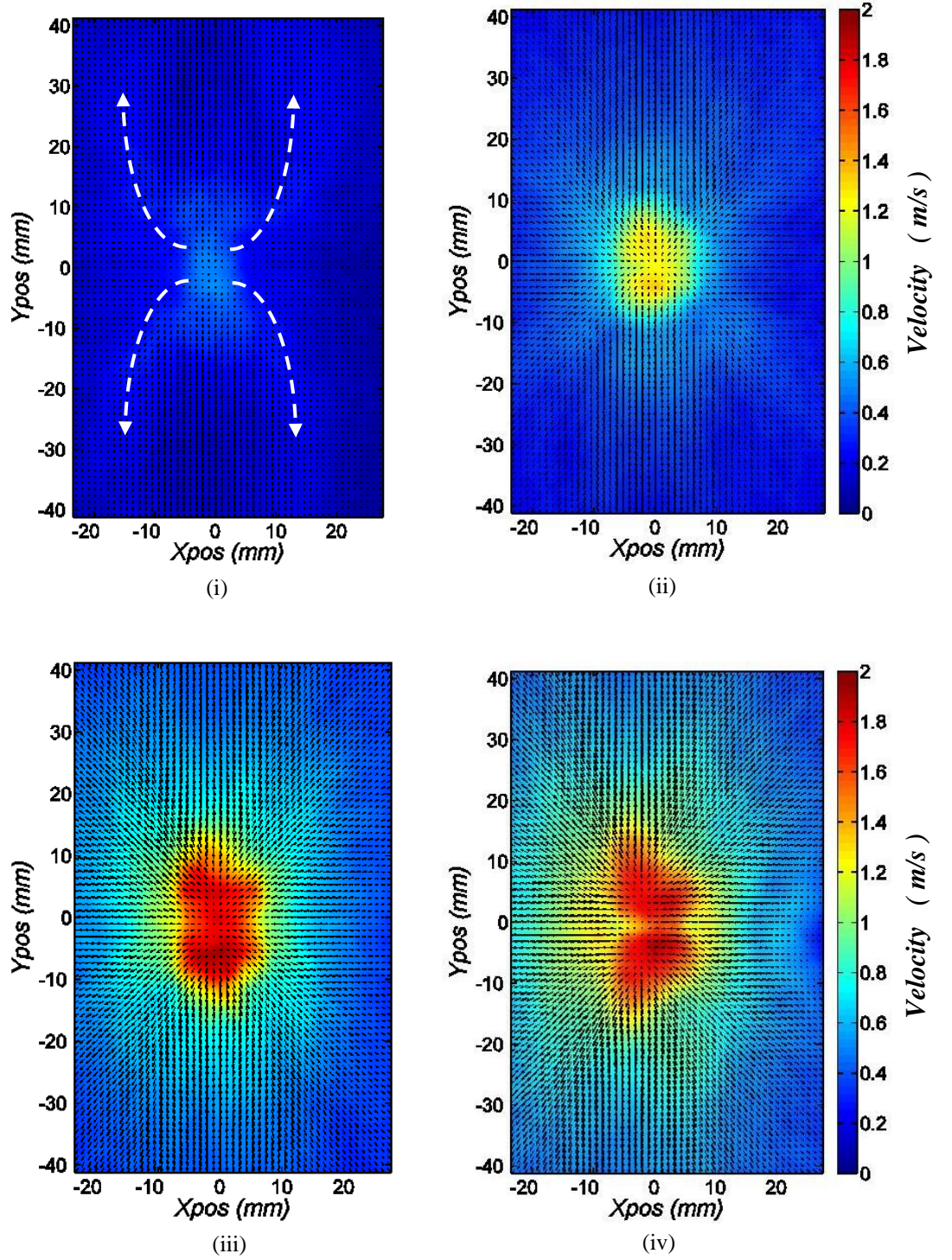


Figure 7.3: RMS of Fluctuating Components for a Horizontally-mounted Fan,  $G = 10.0mm$ ;  
i)  $V_{P_z} = 30.00V$ , ii)  $V_{P_z} = 60.00V$ , iii)  $V_{P_z} = 90.00V$ , iv)  $V_{P_z} = 115.0V$

Figure 7.4 illustrates the turbulence intensity variation along three distinct locations ( $X_{Pos} = -10mm$ ,  $X_{Pos} = 0mm$  and  $X_{Pos} = 10mm$ ), for several of the piezoelectric fan voltages, presented in Figure 7.3.

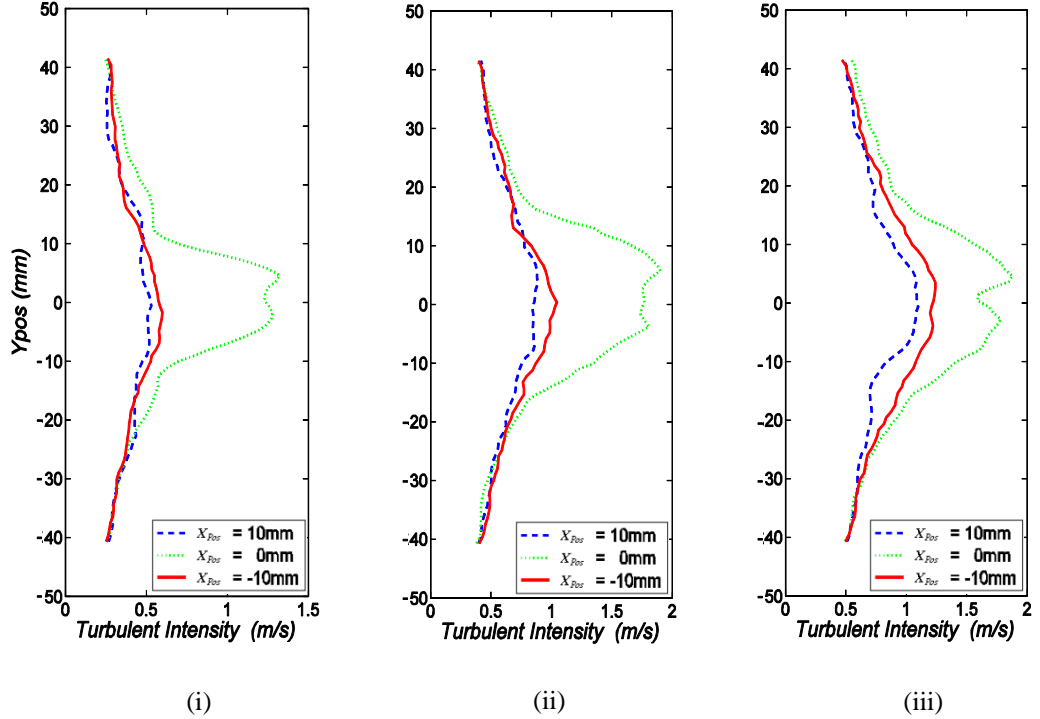


Figure 7.4: Direct comparison of the Turbulence Intensity for  $G = 10.0mm$ :  
 (i)  $V_{Pz} = 60.00V$  (ii)  $V_{Pz} = 90.00V$  (iii)  $V_{Pz} = 115.0V$

In Figure 7.3i a higher turbulence band (denoted by arrows) at the edge of the faster mean flow presented in Figure 7.2i. Once again, this signifies that the flow produced by an oscillating fan is a pulsating, unsteady flow and not a continuous steady flow.

The trends in Figure 7.4 complement earlier results. That is, the turbulence intensity level reaches its maximum at the edges of the vibrational envelope, and decrease as the distance from the fan increases. Furthermore, the turbulence intensity profiles at locations  $X_{Pos} = -10mm$  and  $X_{Pos} = 10mm$  practically have the same shape and magnitude, indicating, once again the flow symmetry.



### 7.3.1.2 Effect of Separation Distance ( $G$ )

In this section, the effect of varying separation distance between the fan and the vertical surface is presented. As explained in **Chapter 6**, varying the separation distance ( $G$ ), greatly affects the fan cooling characteristics, thus it is expected that a change in the flow fields would also arise. This is verified by considering the next sequence of images - Figure 7.5.

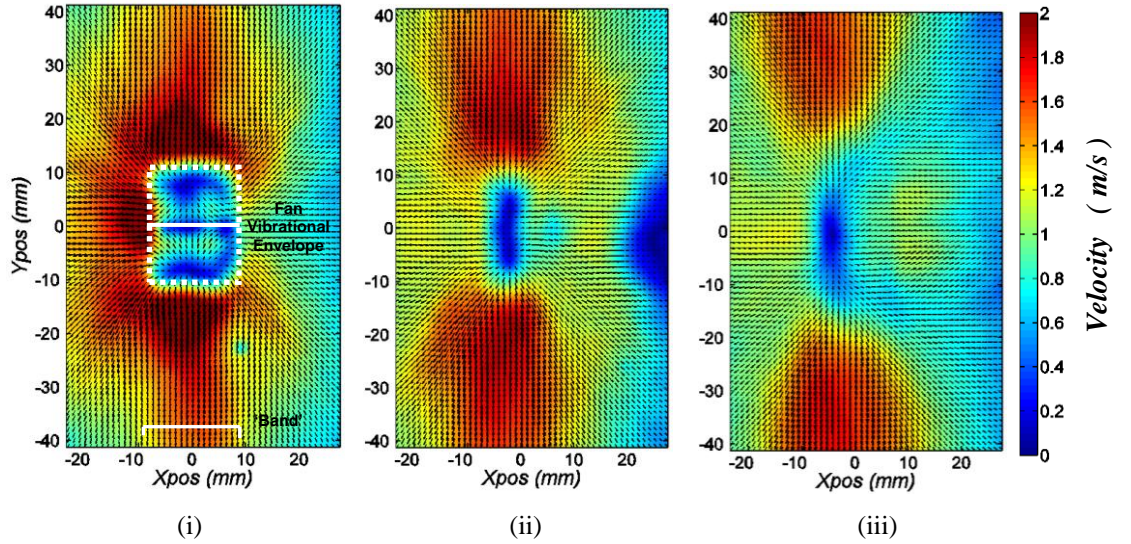


Figure 7.5: Magnitude of the Mean Vectors -  $V_{Pz} = 115.0V$  :

i)  $G = 5.0mm$ ,                      ii)  $G = 10.0mm$ ,                      iii)  $G = 15.0mm$

Some noticeable features and trends can be discerned as the separation distance is reduced. For all values of  $G$ , the primary flow direction is still in the oscillation direction. However, with a reduction in  $G$ , the 'band' of maximum velocity (at  $Y_{Pos} = \pm 40.0mm$ ) is seen to diminish, from  $25.0mm$  when  $G = 15.0mm$  to  $15.0mm$  when  $G = 5.0mm$  (Figure 7.5). Furthermore, with a reduction in the separation distance,  $\overline{V_{Mean}}$  increases in the area closest to the vibration envelope of the fan.

Numerically,  $\overline{V_{Mean}}$  increases from  $1.788m/s$  when  $G = 15.0mm$ , to  $1.900m/s$  when  $G = 10.0mm$  and  $2.409m/s$  when  $G = 5.0mm$ . However, the converse of the above occurs at the extremities of the image (i.e. further away from the piezoelectric fan). As the separation distance decreases,  $\overline{V_{Mean}}$  is seen to

decrease further away from the vibrational envelope of the piezoelectric fan (i.e. at the extremities of the image).

The reduction in  $G$  has a considerable effect on the stagnation pattern. When  $G = 15.0mm$ , a vertical elliptical region forms (Figure 7.5iii), whereas, when  $G = 5.0mm$ , a lobbed pattern arises (Figure 7.5i). The patterns agree well with the cooling plots presented in **Chapter 6** (in particular Figure 6.7) as well as with published literature [44].

While, Figure 7.6 represents the variation in the 2D contour plots of the *RMS* values of the fluctuating component for different  $G$  values, Figure 7.7 depicts the variation in turbulence intensity along different  $x$ -locations:  $X_{Pos} = 10.0mm$ ,  $0.0mm$  and  $-10.0mm$ .

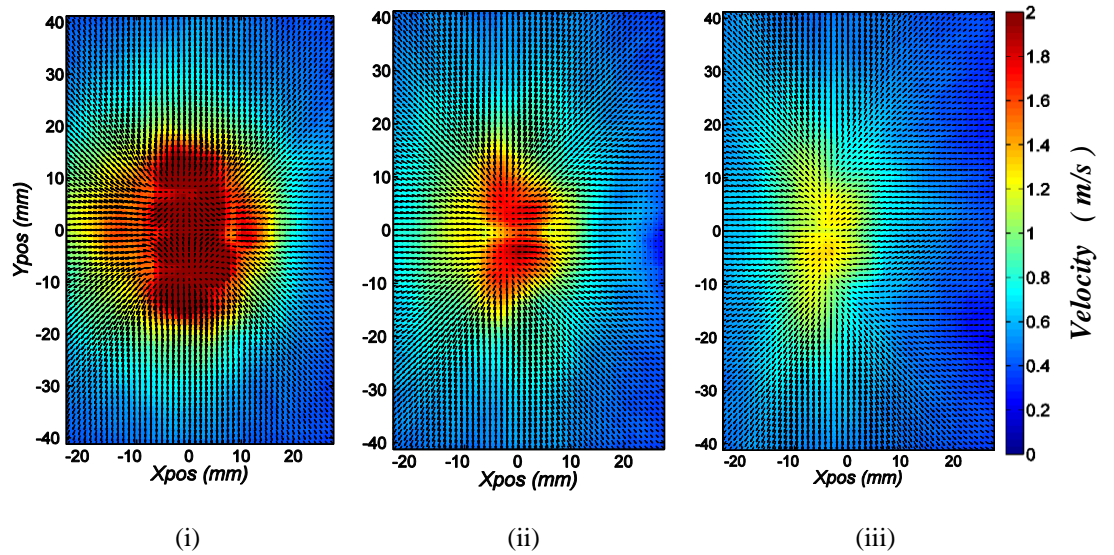
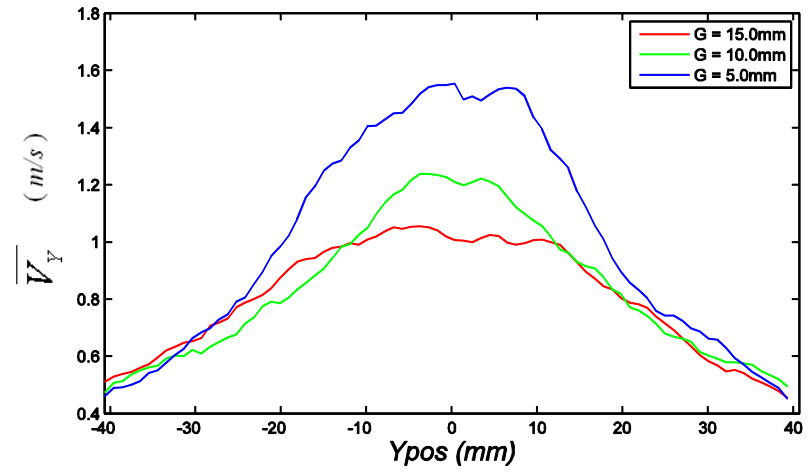
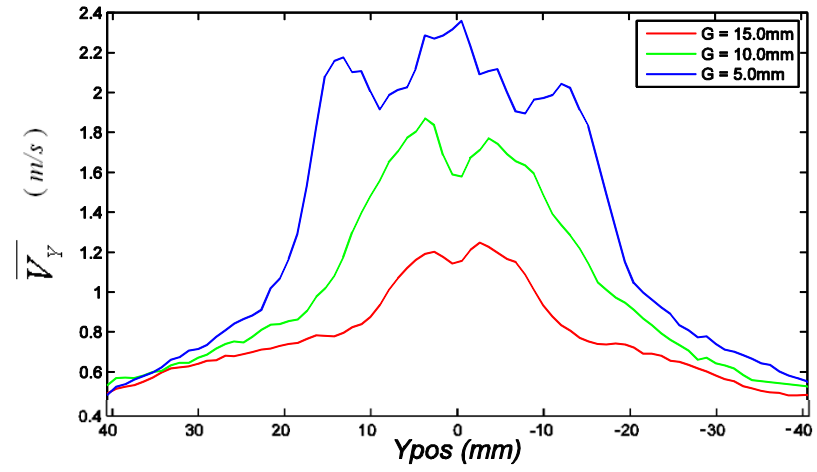


Figure 7.6: *RMS* values of the Fluctuating Component -  $V_{Pz} = 115.0V$  :  
 i)  $G = 5.0mm$ ,                      ii)  $G = 10.0mm$ ,                      iii)  $G = 15.0mm$

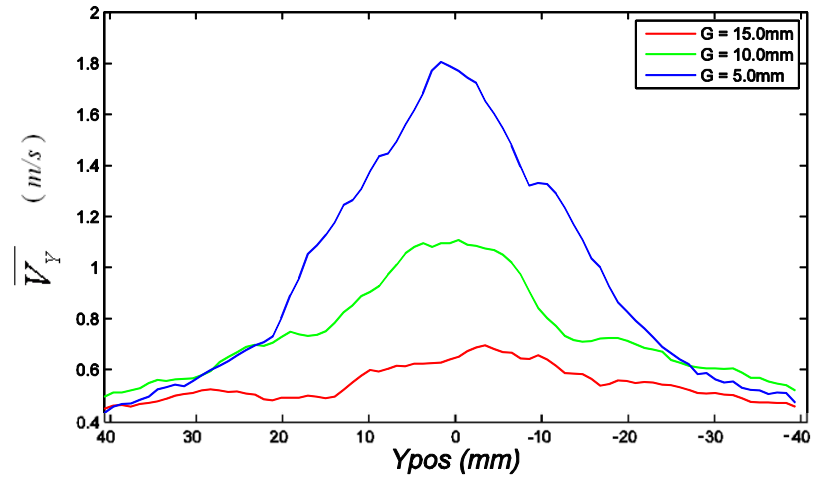
The resulting turbulent flow regimes are highly dependent on  $A_{Pz}$  and  $G$ . In the above sequence of images (Figure 7.6), a lobbed pattern (of high turbulence) is generated for large gaps. However, as the fan is brought closer to the target surface, the behaviour transitions to a vertical elliptical pattern with a significantly higher magnitude.



(i)



(ii)



(iii)

Figure 7.7: RMS values of the Fluctuating Component -  $V_{p_z} = 115.0V$  :  
 (i)  $X_{pos} = -10mm$ , (ii)  $X_{pos} = 0mm$ , (iii)  $X_{pos} = 10mm$

The maximum turbulent velocity occurs at  $X_{Pos} = 0.0mm$ , i.e. the mid-point of the piezoelectric fan, and holds true for all the separation distances. The turbulence level also increases as the fan approaches the vertical surface – i.e. minimal separation distance. However, further away from the fan datum position, the converse applies, i.e. larger separation distances are slightly better suited than small separation distances.

Hence, taking all the above into account, it has been concluded that for a horizontally-mounted fan, a small  $G$  is beneficial. The latter statement further agrees with the cooling plots shown in **Chapter 6**.

### 7.3.2 Flow Measurements Perpendicular to a Vertical Flat Surface

In this section, further flow visualisation and flow measurements are presented, with the imaging done perpendicular to the vertical surface (rather than parallel). The use of this setup gave more insight into the unsteady flows.

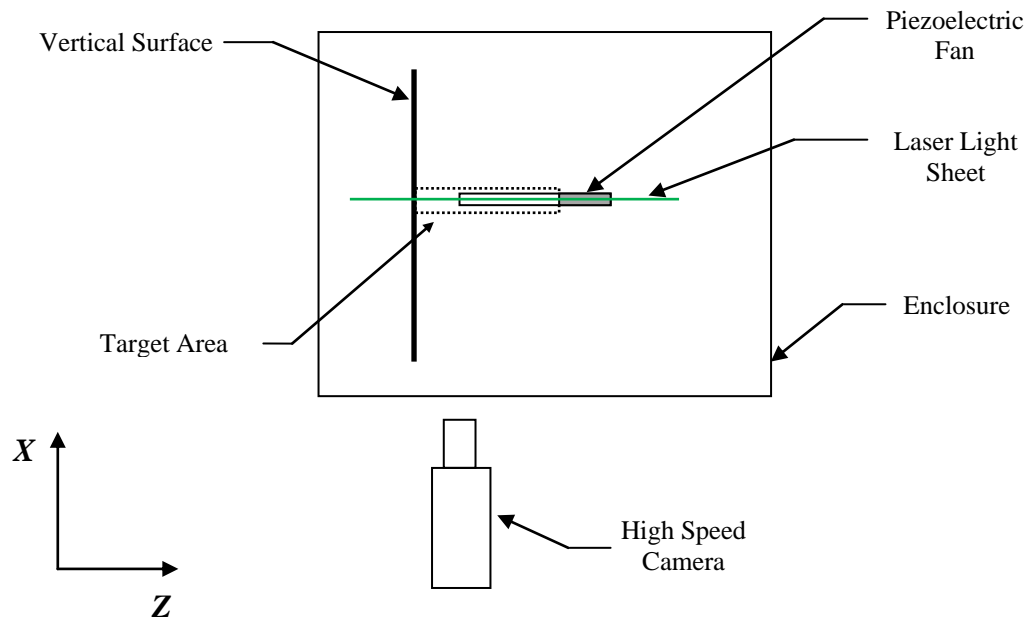


Figure 7.8: Schematic of Modified Experimental Setup - Top View

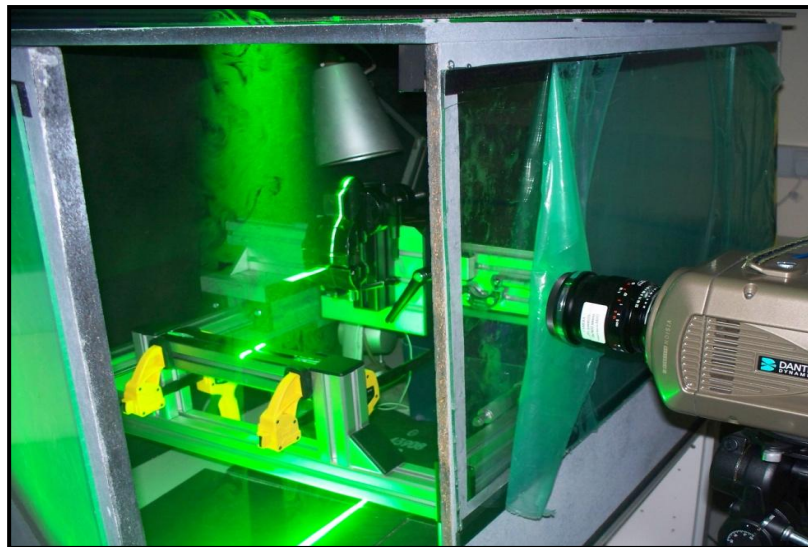


Figure 7.9: Experimental Setup showing Laser Light sheet passing through Fan centreline



In this setup, the camera was aligned so as to capture only half the blade swing. As the generated airflow was shown to be symmetrical, positioning the camera in such a manner, meant that a larger field of view could be captured, which led to a better insight into the cooling range ( $Y_{Pos}$ ) of the FCCS.

For this setup, the same series of tests as those presented in the previous section were conducted, however, only a sample of the results are presented here. Further results, are given in **Appendix F**. The sequence of images below (Figure 7.10), shows a single cycle performed by a horizontally-mounted piezoelectric fan, together with the local instantaneous velocities generated in the region of interest.

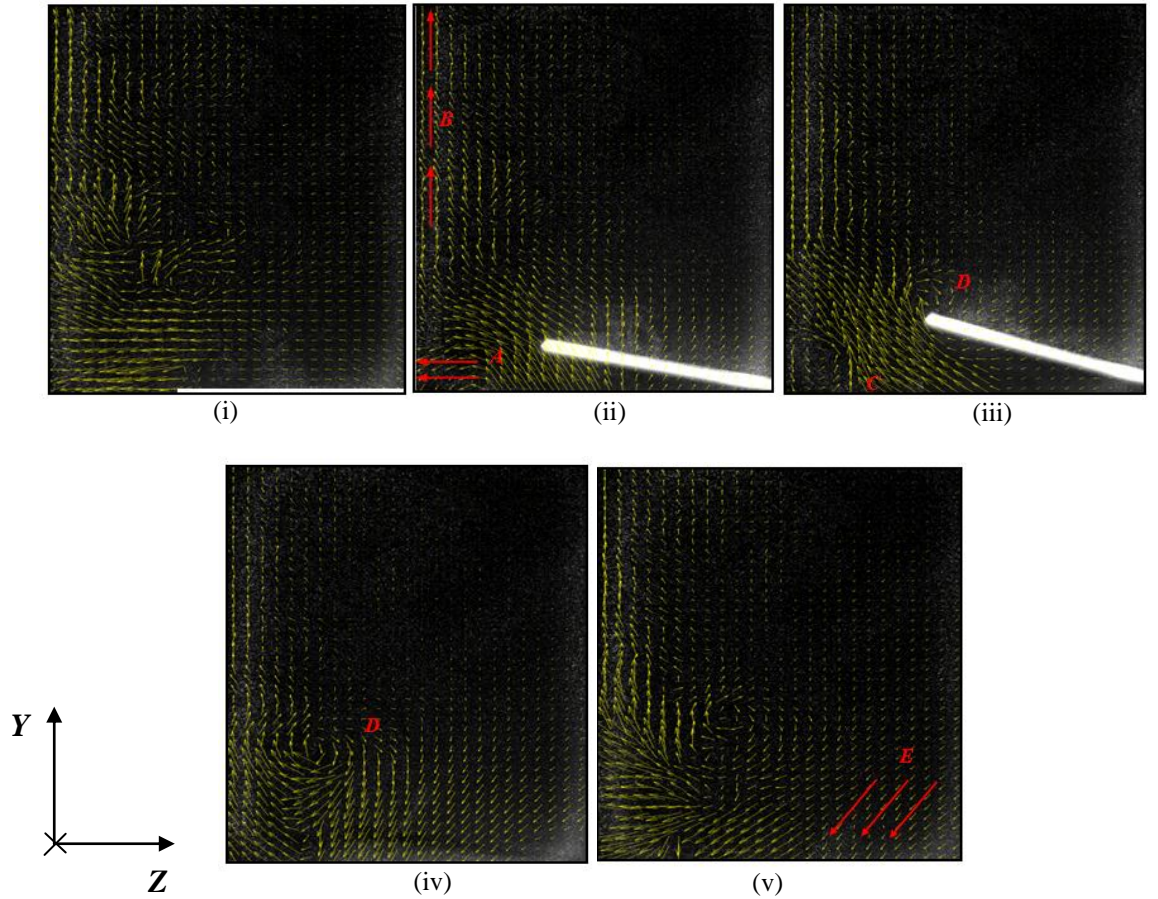


Figure 7.10: Transient Flow Field generated by a Horizontally-mounted Fan:  
 $G = 10.0mm, V_{Pz} = 115.0V$

i)  $t = 0.0s$ , ii)  $t = 0.0033s$ , iii)  $t = 0.0066s$ , iv)  $t = 0.0098s$ , v)  $t = 0.0131s$

The target area under consideration measures  $29.0\text{mm}$  ( $x$ -axis) by  $46.0\text{mm}$  ( $y$ -axis). At  $t = 0.0\text{s}$ , the fan is in its datum position ( $Y_{Pos} = 0.0\text{mm}$ ). At this point air is being drawn in (from right to left) by the fan. In the next image Figure 7.10ii, the fan begins its upward sweep and propels a jet of air forwards along the fan blade tip (**A**). This ejected airflow, on impacting the vertical surface (at  $Z_{Pos} = 0.0\text{mm}$ ) is directed upwards along the vertical surface (**B**). Thus, at this point of contact ( $Z_{Pos} = 0.0\text{mm}$ ), a zero velocity must be attained, which in turn produces a stagnation point/region. This result further agrees with Figure 7.2. In Figure 7.10iii, a counter-clockwise vortex (**C**) emerges at the stagnation point between the blade tip and the vertical surface. This stagnation region results due to the nature of the setup.

At  $t = 0.0066\text{s}$ , while vortex (**C**) is still present, another vortex (**D**) arises. However, vortex **D**, a clockwise rotating one, is seen to travel upward and remains visible till the end of the cycle. At  $t = 0.0098\text{s}$ , the fan again draws in ‘fresh’ air (**E**) which is later expelled by the blade tip. The fan then begins its downswing motion. While only half the motion is presented, it is expected that the same trends occur in the downswing motion due to the flow symmetry.

On analysing several fan cycles, it was noted that when the blade tip swings upward, air spills over from the bottom to the top of the fan and generates a clockwise vortex (**D**). However, on the downswing, air is drawn in from above the fan and travels in the direction of the downswing, producing a counter-clockwise rotating vortex. The latter results, in particular, agree with earlier published flow visualisation experiments [61].

On averaging the local velocities obtained in each of the  $2D$  local velocity maps ( $N_I = 500$ ), the magnitude of the mean vectors is obtained (Figure 7.11).

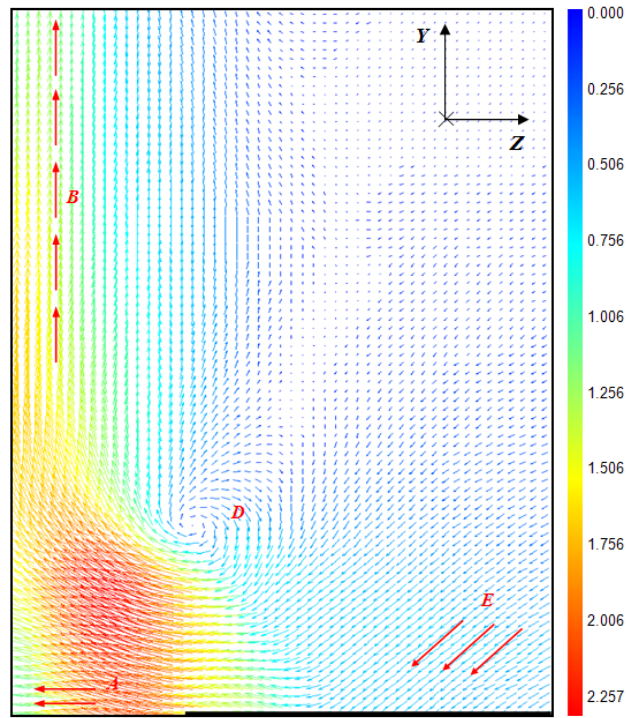


Figure 7.11: Magnitude of the Mean Vectors by a Horizontally-mounted Fan -  $G = 10.0mm$ ,  $V_{pz} = 115.0V$

Figure 7.11 (which is identical to Figure 7.12iv) further emphasises the trends reported in Figure 7.10. The fan draws in ‘fresh air’ at its base (**E**), this is projected forward (**A**) and later travels along the vertical flat surface (**B**). Vortex (**D**) is also seen to originate and is exactly in line with the piezoelectric fan blade tip. The highest flow is seen to originate in the immediate vicinity of the blade tip and has a magnitude of  $\overline{V}_Z = 2.547m/s$ . On the other hand, an average velocity of around  $\overline{V}_Y = 1.500m/s$  is achieved along the vertical flat surface.

Furthermore, the image gives a good indication of the cooling effectiveness of the FCCS – i.e. an appreciable flow field spanning at least  $90mm$  (in the  $y$ -direction).



### 7.3.2.1 Effect of Fan Amplitude ( $V_{P_z}$ )

Figure 7.12 shows the variation in the magnitude of the mean vectors at different  $V_{P_z}$ . With an increase in  $V_{P_z}$ , both the  $\overline{V}_z$  as well as the  $\overline{V}_y$  components increase.

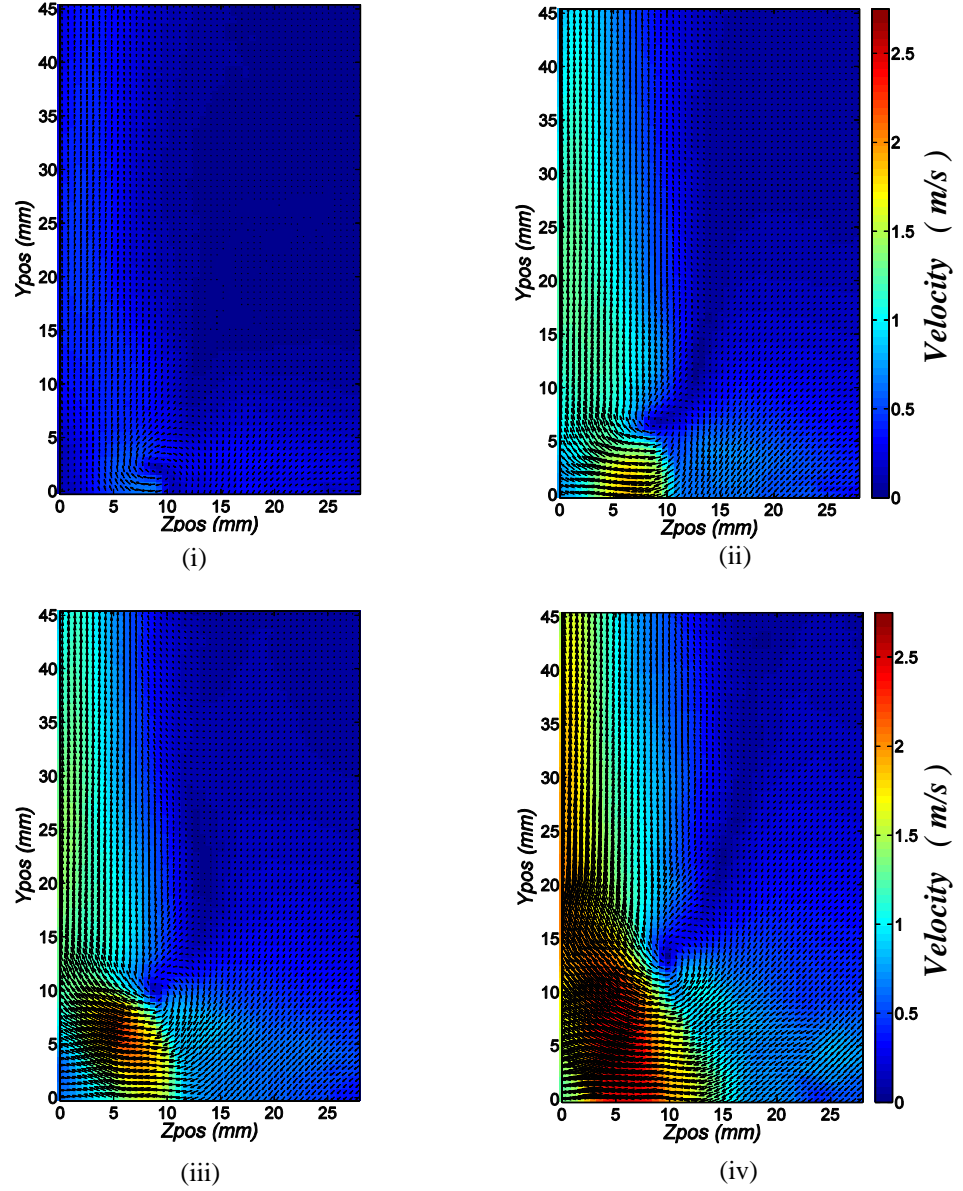


Figure 7.12: Magnitude of the Mean Vectors for  $G = 10.0mm$  and;  
 i)  $V_{P_z} = 30.00V$  , ii)  $V_{P_z} = 60.00V$  , iii)  $V_{P_z} = 90.00V$  , iv)  $V_{P_z} = 115.0V$

A  $V_{P_z}$  of 30.00V , results in a minimal flow disturbance with  $\overline{V_{Mean}}$  reaching 0.665m/s. However, as the vibrational amplitude is increased (Figure 7.12iv), the maximum mean velocity ( $\overline{V_{Mean}}$ ) recorded is 2.547m/s.

The  $\overline{V_Y}$  component of velocity is of primary interest in this study as it sheds more light on the cooling of the vertical flat surface. Initially, on applying  $V_{P_z} = 30.00V$  , the maximum y-velocity component attained is equal to  $\overline{V_Y} = 0.373m/s$ . As  $V_{P_z}$  increases through 60.00V, 90.00V and 115.0V, the  $\overline{V_Y}$  values increase to 1.232m/s, 1.407m/s and 2.029m/s respectively.

The stagnation point/region described in Figure 7.10iii is further highlighted in Figure 7.12ii, Figure 7.12iii and Figure 7.12iv. Furthermore, the clockwise rotating vortex (**D**) is present, yet again.

The turbulence characteristics follow a similar pattern to that of the mean flows, i.e. the turbulence originates at the blade tip. This is noticeable by a clockwise-rotating vortex located at  $Z_{Pos} = 10.0mm$ . As  $V_{P_z}$  increases, so does the disturbance area. The magnitude of the *RMS* of the fluctuating component is equivalent to 1.459m/s when the minimal voltage is applied. However, on application of  $V_{P_z} = 115.0V$  is applied, the maximum value attained is  $V_{RMS} = 3.673m/s$  (Figure 7.13).

Figure 7.13 further indicates that all the fluctuations are concentrated where the jet is formed – i.e. adjacent to the fan tip. This holds true for all tested vibrational amplitudes.

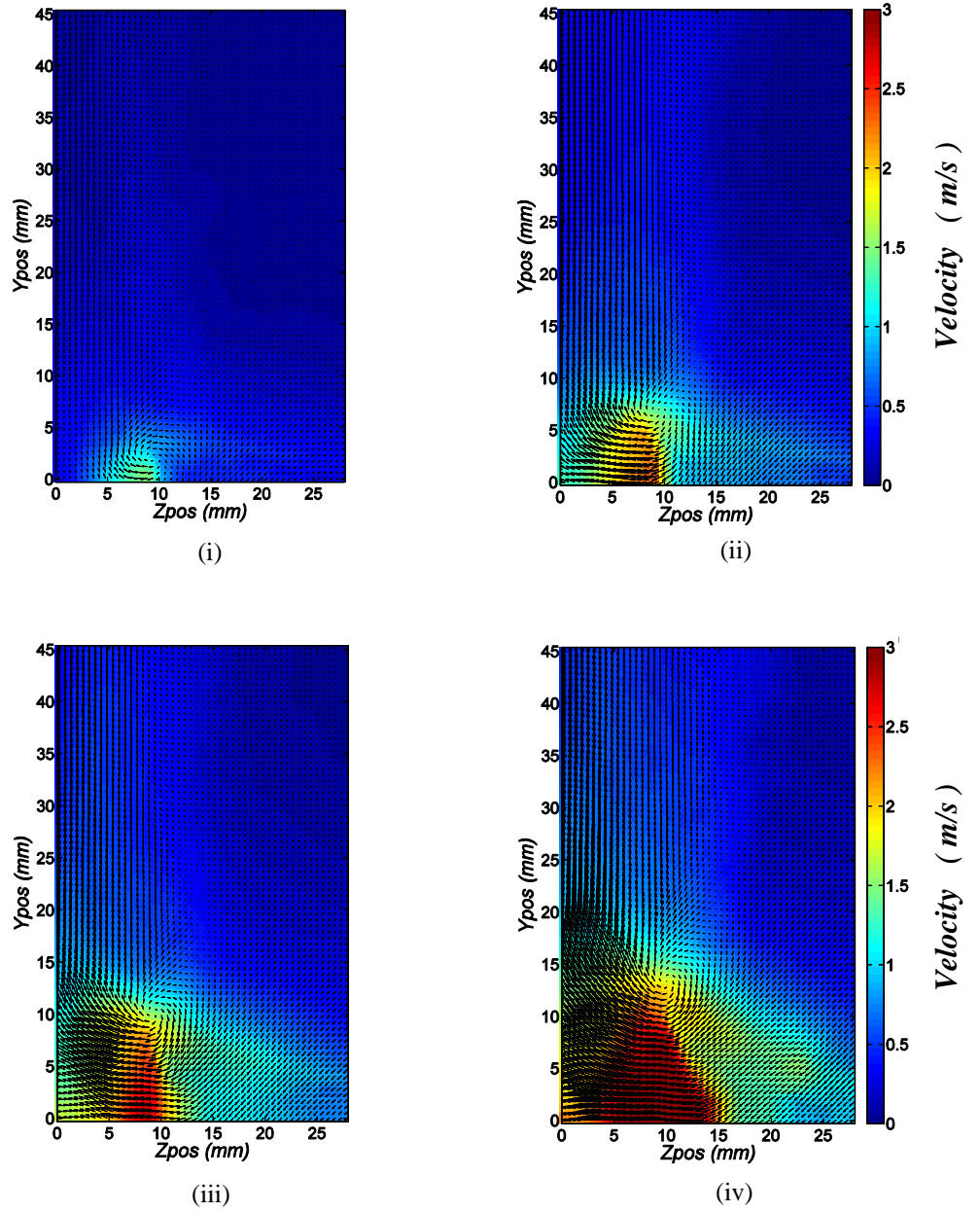


Figure 7.13: *RMS of Fluctuating Components for  $G = 10.0mm$  and;*  
i)  $V_{P_z} = 30.00V$  , ii)  $V_{P_z} = 60.00V$  , iii)  $V_{P_z} = 90.00V$  , iv)  $V_{P_z} = 115.0V$

An increase in  $V_{P_z}$  also shifts the location of the eye of the vortex. This is seen to travel upwards (along the  $y$ -axis) with an increase in  $V_{P_z}$ . When  $V_{P_z} = 30.00V$ , the centre is located at  $Y_{Pos} = 2.37mm$ . When  $V_{P_z} = 60.00V$ ,

$V_{Pz} = 90.00V$  and  $V_{Pz} = 115.0V$ , the location shifts to  $Y_{Pos} = 7.00mm$ ,  $Y_{Pos} = 11.0mm$  and  $Y_{Pos} = 13.9mm$  respectively.

### 7.3.2.2 Effect of Separation Distance ( $G$ )

The first noticeable pattern (Figure 7.14) is that the position of the clockwise rotating vortex feature 'D' is dependent on the separation distance. At  $G = 10.0mm$ , the vortex originates at  $Z_{Pos} = 10.0mm$ , when  $G = 5.0mm$ , the vortex originates at  $Z_{Pos} = 5.0mm$ , and when  $G = 2.5mm$ , the vortex shifts to  $Z_{Pos} = 4.80mm$ . The latter seems to vary from the latter test cases as the small separation distance limits the formation of the vortex.

Figure 7.14 indicates that a reduction in  $G$  results in a reduction in  $\overline{V_z}$  along the fan datum position (i.e.  $Y_{Pos} = 0.0mm$ ). Numerically,  $\overline{V_z}$  decreases from  $2.450m/s$  ( $G = 10.0mm$ ),  $1.777m/s$  ( $G = 5.0mm$ ) to  $0.644m/s$  ( $G = 2.5mm$ ).

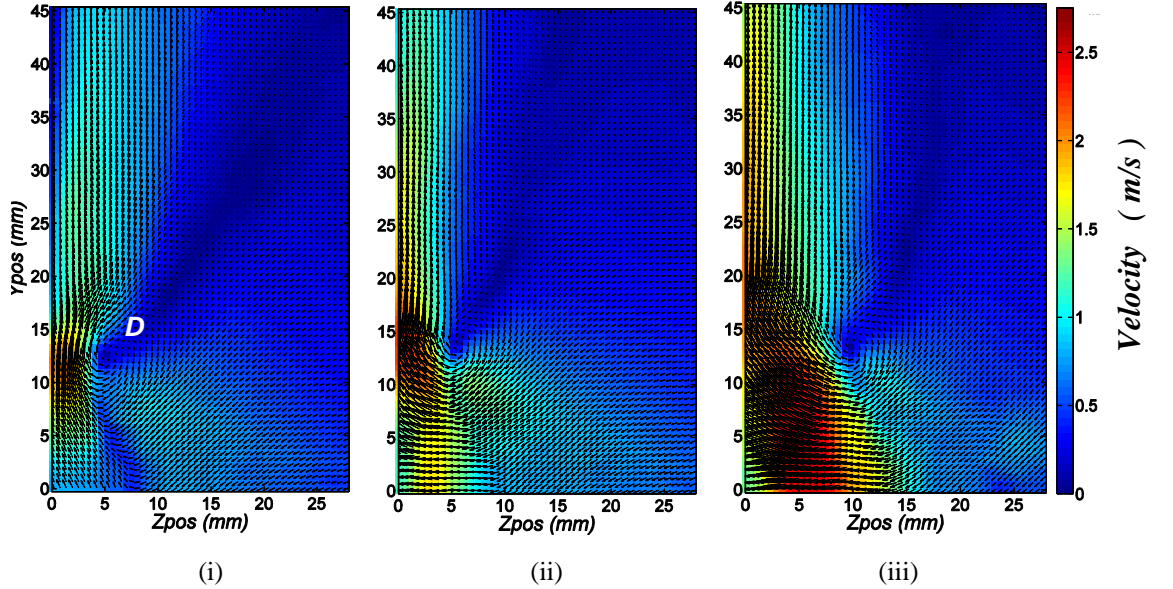


Figure 7.14: Magnitude of the Mean Vectors for a fan operating at  $V_{Pz} = 115.0V$  ;  
 (i)  $G = 2.5mm$ , (ii)  $G = 5.0mm$ , (iii)  $G = 10.0mm$

However, the same does not hold true for the principal velocity ( $\overline{V_y}$ ), as shown in Figure 7.15. This has already been illustrated in **Section 7.3.1**. On comparing these two results (Figure 7.15), good agreement is achieved.

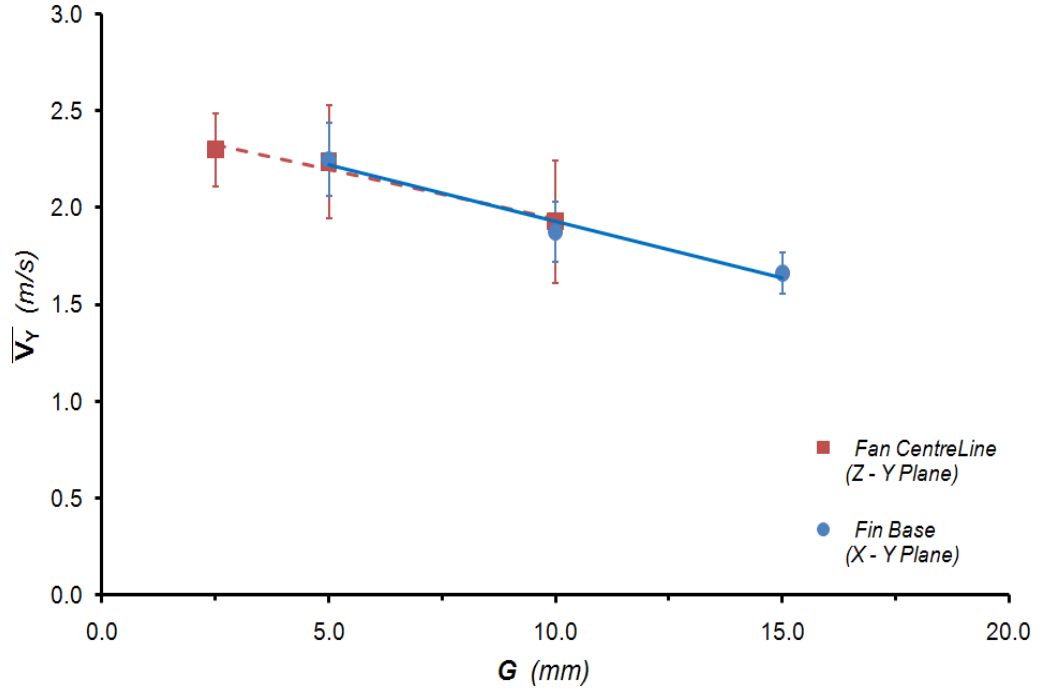


Figure 7.15: Evaluation of the  $\overline{V}_Y$  component by two distinct setups -  $V_{Pz} = 115.0V$

The above plot compares the maximum  $\overline{V}_Y$  obtained when performing *PIV* measurements on the *X-Y* plane (*Section 7.3.1*) to the results obtained when performing *PIV* on the *Z-Y* plane (*Section 7.3.2*). As close agreement is achieved between the two measurement planes, the repeatability and consistency of *PIV* measurements is further highlighted. Furthermore, it can be deduced that the smaller the separation distance the larger the resulting velocities which in turn results in increased *FB* cooling.

The wake characteristics along the vertical surface ( $Z_{Pos} = 0.0mm$ ), were also investigated and evaluated as they shed light on the expected fin base cooling. It has been observed (Figure 7.14) that a decrease in the separation distance alters the wake characteristics. When  $G = 10.0mm$ , the  $\overline{V}_Z$  component of the flow adheres to the wall, and travels upwards along the wall – in excess of  $45.0mm$ . However, at the minimal separation distance ( $G = 2.5mm$ ), the flow is seen to separate from the vertical surface. When the fan is located a significant distance away from the target surface, the ejected stream of air ( $\overline{V}_Z$ ) generated by the fan upswing motion has time to form streamlines before

impacting the surface, and on impact, is directed vertically upwards (and downwards as flow is symmetrical) and travels along the vertical surface. However this does not occur when  $G = 2.5mm$ . When such close proximity between the fan blade tip and the vertical surface exists, the flow has no time to align itself and on impact curls upwards and away from the wall. In this latter scenario, the flow behaviour is significantly different than the latter test cases. Furthermore, this setup ( $G = 2.5mm$ ) may also contribute to a flow transition.

Figure 7.16 depicts three profile plots ( $Y_{Pos} = 20.0mm$ ,  $Y_{Pos} = 30.0mm$  and  $Y_{Pos} = 40.0mm$ ) for each of the considered separation distance presented in Figure 7.14. These profile plots give a further insight to the changing wake characteristics.

For  $G = 10.0mm$ , at  $Y_{Pos} = 20.0mm$  the maximum  $\overline{V_y} = 2.01m/s$ , while at  $Y_{Pos} = 40.0mm$  the maximum  $\overline{V_y} = 1.72m/s$ . It is seen that the maximum  $\overline{V_y}$  component decreases with an increase in  $Y_{Pos}$  (along the vertical surface). This trend is maintained for all of the considered separation distances.

### Flow Measurements for a Vertical Flat Surface

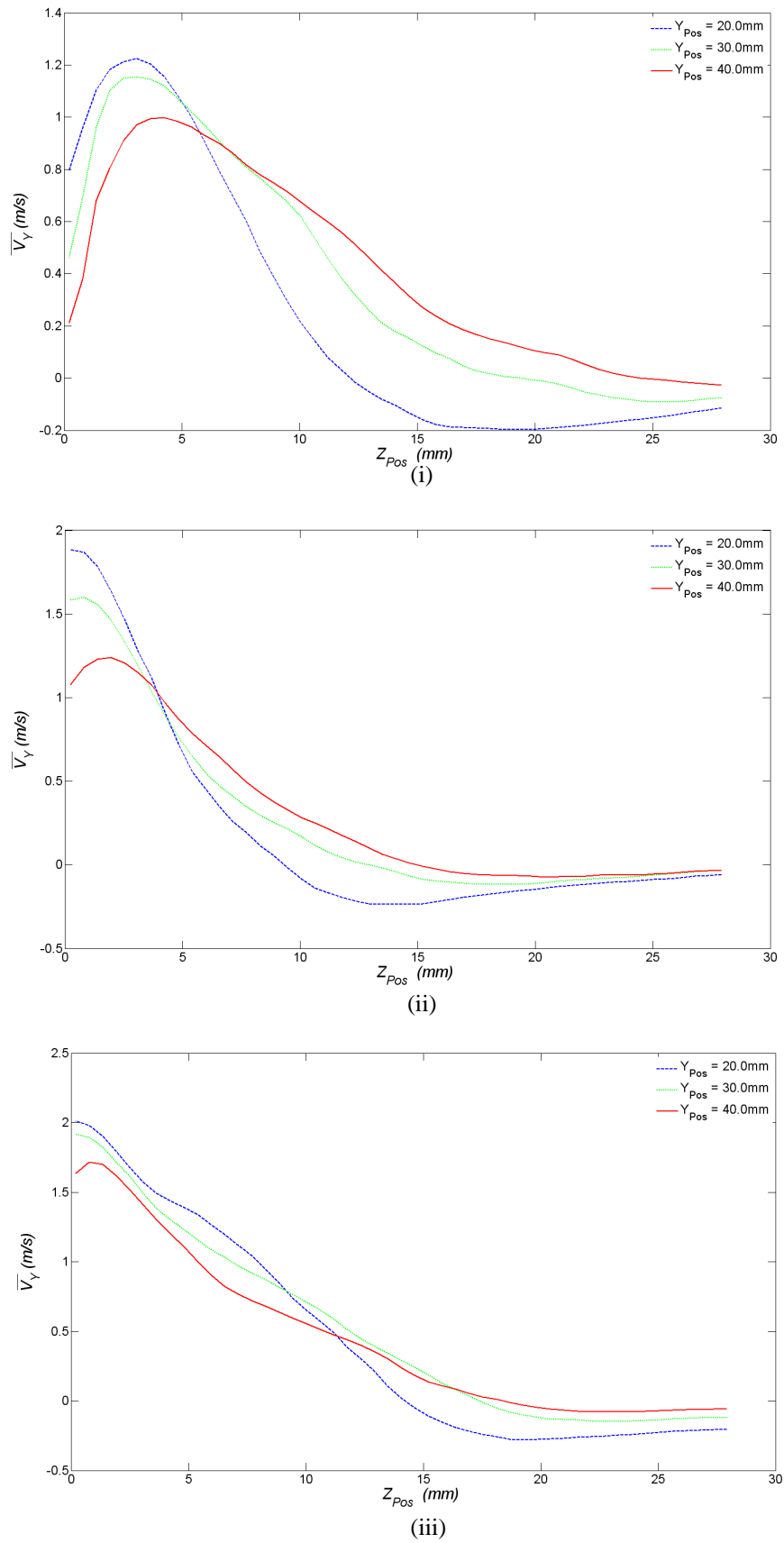


Figure 7.16: Wake Characteristics - Variation in  $\overline{V}_Y$  at different  $Y_{Pos}$  on applying  $V_{Pz} = 115.0V$  :  
 (i)  $G = 2.5\text{mm}$       (ii)  $G = 5.0\text{mm}$       (iii)  $G = 10.0\text{mm}$

A lesser magnitude is also attained at lower  $G$  values. As pointed out earlier, when  $G = 10.0mm$ , at  $Y_{Pos} = 20.0mm$  the maximum  $\overline{V_Y} = 2.01m/s$ , however, at the same  $Y_{Pos}$  at  $G = 2.5mm$ , at the maximum  $\overline{V_Y} = 1.22m/s$  - a significant reduction. Table 7.1 further highlights the produced wake characteristics. The location of the maximum  $\overline{V_Y}$  component (at the three considered  $Y_{Pos}$  profile locations) is presented.

		$Z_{Pos} (mm)$		
		$G10$	$G5.0$	$G2.5$
$Y_{Pos} (mm)$	20.00	0.20	0.24	3.10
	30.00	0.24	0.81	3.30
	40.00	0.77	1.97	4.30

Table 7.1: Wake Characteristics Evaluation – Effect of  $G$  on the location of the maximum  $\overline{V_Y}$ , when  $V_{Pz} = 115.0V$

The above results indicate that for  $G = 10.0mm$ , along  $Y_{Pos} = 20.0mm$ , the maximum  $\overline{V_Y}$  occurs at  $Z_{Pos} = 0.20mm$ . However, this maximum  $\overline{V_Y}$  was seen to shift (away from the wall along the  $z$ -axis) as different  $Y_{Pos}$  were considered. Along  $Y_{Pos} = 30.0mm$ , the maximum  $\overline{V_Y}$  shifted to  $Z_{Pos} = 0.24mm$  and along  $Y_{Pos} = 40.0mm$ , the maximum  $\overline{V_Y}$  shifted to  $Z_{Pos} = 0.77mm$ . This indicated that the flow is no longer adhering to the wall but is beginning to come away from it. This trend is further emphasised in Figure 7.17ii and even more so in Figure 7.17iii. In this latter plot, along  $Y_{Pos} = 20.0mm$ , the maximum  $\overline{V_Y}$  was located at  $Z_{Pos} = 3.10mm$ , along  $Y_{Pos} = 30.0mm$ , the maximum  $\overline{V_Y}$  shifted to  $Z_{Pos} = 3.30mm$  and along  $Y_{Pos} = 40.0mm$ , the maximum  $\overline{V_Y}$  shifted to  $Z_{Pos} = 4.30mm$ .

Similar trends were observed when considering the turbulence contour plots. Figure 7.17 depicts the  $RMS$  of the fluctuating component at  $V_{Pz} = 115.0V$  for the three separation distances.



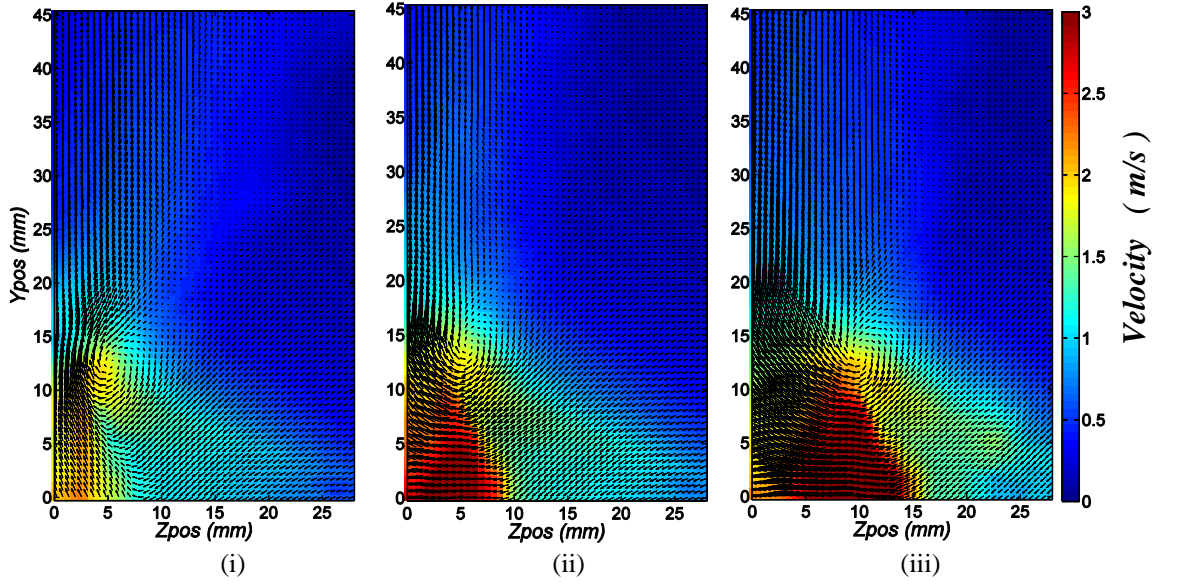


Figure 7.17: Contour Plots of the  $RMS$  values of the Fluctuating Component -  $V_{P_z} = 115.0V$  :

i)  $G = 2.5mm$ ,                      ii)  $G = 5.0mm$ ,                      iii)  $G = 10.0mm$

Once again, the highest turbulence is generated at the fan blade tip. In this current configuration (horizontally-mounted fan), the main component of turbulence is along the  $z$ -axis. A decrease in  $G$  results in the reduction in the  $STDV_z$  along  $Y_{Pos} = 0.0mm$ . It was established that, when  $G = 10.0mm$ , the maximum  $STDV_z$  value was  $1.298m/s$  while when  $G = 2.5mm$ , the maximum  $STDV_z$  value diminished to  $0.850m/s$ .

In conclusion, the results of **Section 7.3.1** ( $X - Y$  plane) and **Section 7.3.2** ( $Z - Y$  plane) have been superimposed to create a single 3D contour plot (Figure 7.18). However, it must be said that the mean vectors are only in the plane of the plot. This explains the discontinuity at  $y = 0.0mm, z = 0.0mm$ . These plots aid in the visualisation and understanding of both the mean and turbulent unsteady flows generated by a horizontally-mounted oscillating piezoelectric fan. Figure 7.18i represents the magnitude of the mean vectors ( $\overline{V_{Mean}}$ ), while Figure 7.18ii represents the turbulence intensity contours ( $V_{RMS}$ ) when the fan is operated at a voltage ( $V_{P_z}$ ) of  $115.0V$  and a separation distance ( $G$ ) of  $10.0mm$ .

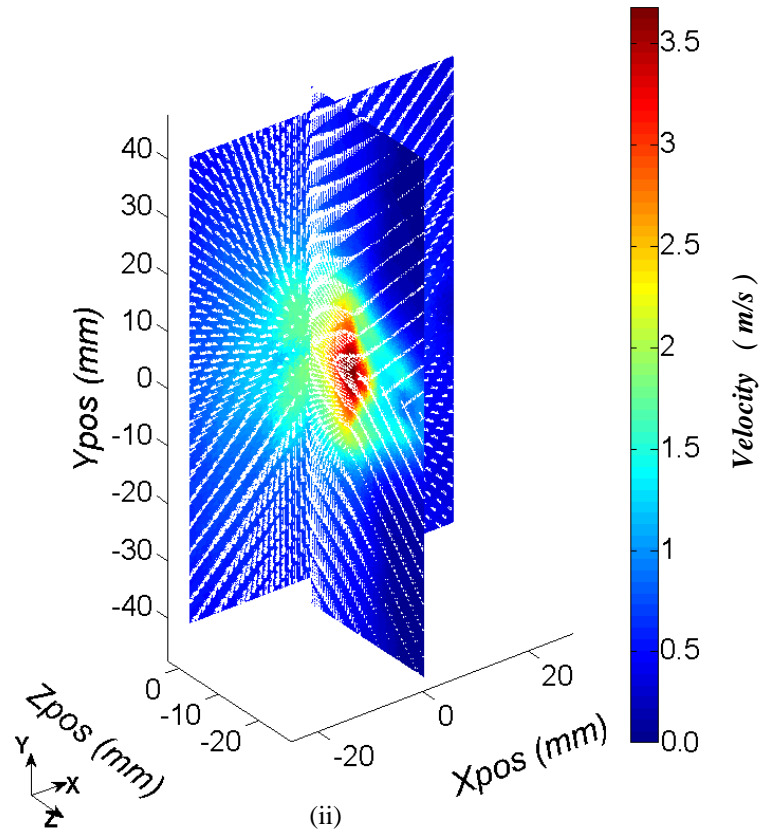
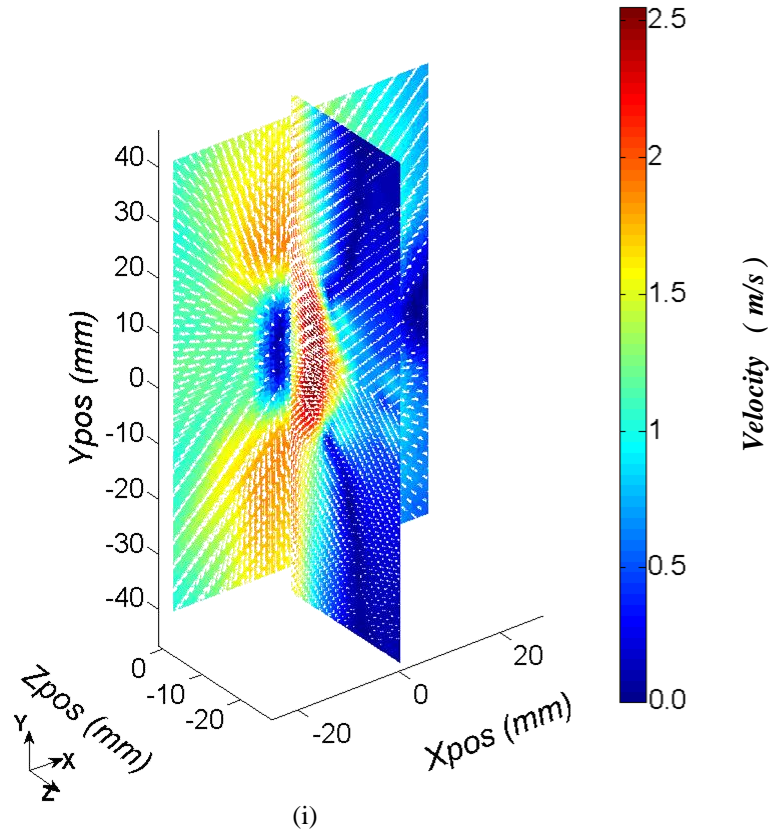


Figure 7.18: 3D contour plots of a Horizontally-mounted Fan -  $G = 10.0\text{mm}$ ,  $V_{Pz} = 115.0\text{V}$  :

i) Magnitude of the Mean Vectors,

ii) Turbulence Characteristics

## 7.4 Vertically-mounted Fan

The same series of experimental tests as those performed on a horizontally-mounted fan were conducted for this orientation. It would be expected that the same results as those presented in *Section 7.3* should have been obtained, with the only difference being that the results should have had to be rotated by  $90^\circ$ . While all results may be found in *Appendix F*, a brief set of results are presented here, and the major differences highlighted.

Figure 7.19 represents the magnitude of the mean vectors when the fan is operated at  $V_{P_z} = 115.0V$  for several separation distances.

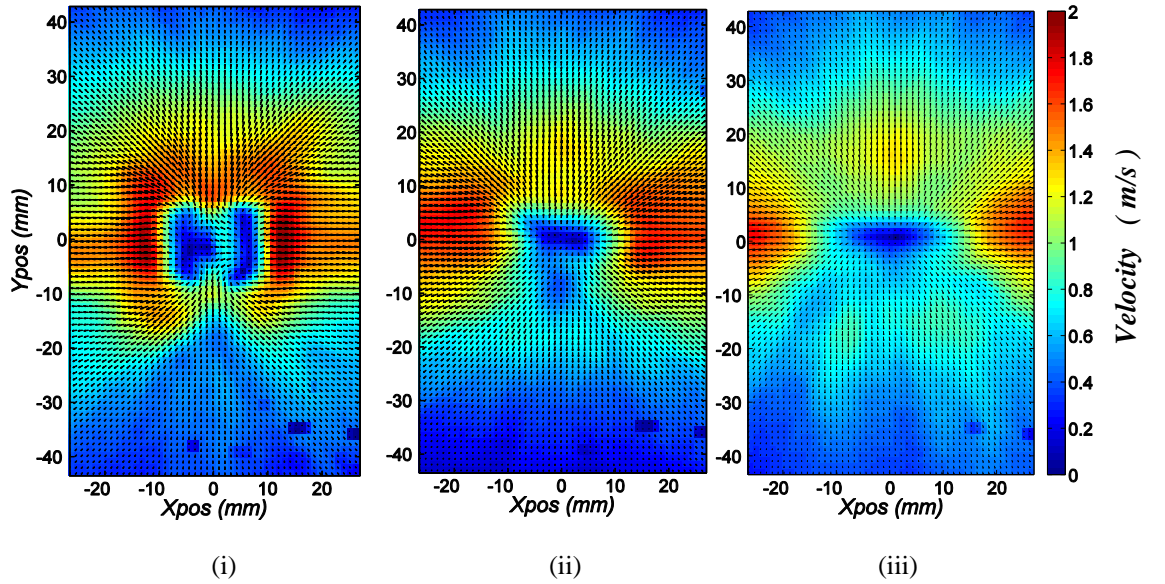


Figure 7.19: Magnitude of the Mean Vectors -  $V_{P_z} = 115.0V$  :

i)  $G = 5.0mm$ ,

ii)  $G = 10.0mm$ ,

iii)  $G = 15.0mm$

The same features as those presented in Figure 7.5 for a horizontally-mounted piezoelectric fan are present. For this fan orientation, the highest flows are produced in the direction of oscillation (along the  $x$ -direction) and are of the same order of magnitude as those produced by a horizontally-mounted fan. Once again, like for a horizontally-mounted fan, at either side of the fan tip, a

lower velocity results, indicating that at these points, ‘fresh’ air is being drawn in by the fan which is later shed at the blade tip.

The resulting stagnation central patterns are similar in nature to those presented for a horizontally-mounted fan. When  $G = 15.0mm$ , a horizontal elliptical region forms (indicating that the fluid agitation is highly influential in the oscillation direction), while when  $G = 5.0mm$ , a lobbed pattern arises. Once again, the presented pattern formation agrees well with the thermal results presented in **Chapter 6** and published literature [44].

Figure 7.20 depicts the turbulence generated by a vertically-mounted piezoelectric fan. Once again, the below sequence of images are in close agreement with the earlier presented horizontally-mounted fan results (Figure 7.6).

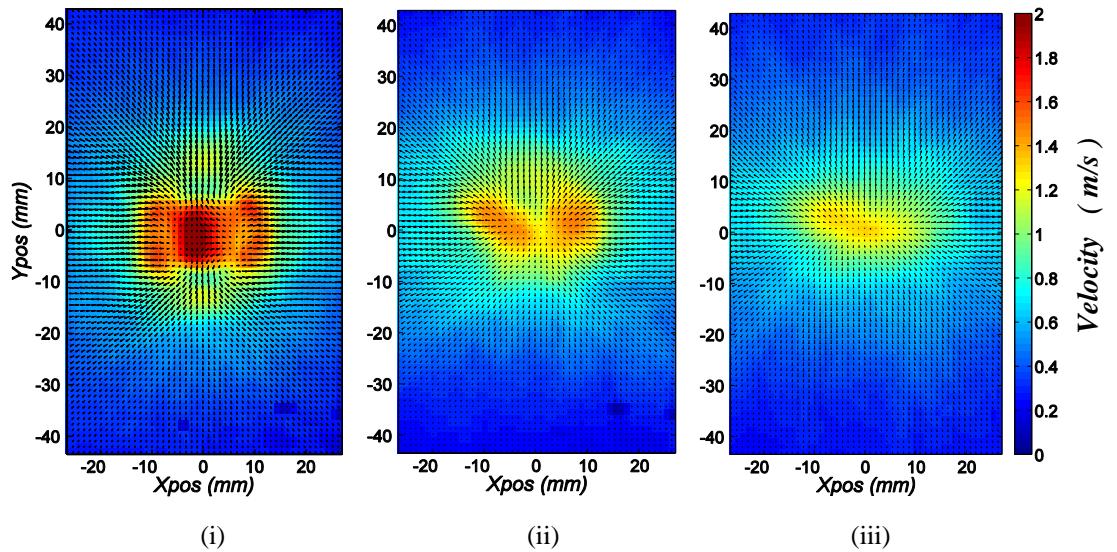


Figure 7.20:  $RMS$  values of the Fluctuating Component -  $V_{pz} = 115.0V$  :

i)  $G = 5.0mm$ ,

ii)  $G = 10.0mm$ ,

iii)  $G = 15.0mm$

The disturbance originates from the fan datum position and spreads outwards preferentially along the oscillation direction ( $x$ -direction). The effective disturbance range is limited to the maximum vibrational envelope of the fan.

However, this disturbance is seen to decrease off significantly further away from the fan.

The central band of maximum turbulence intensity is similar to that attained for a horizontally-mounted fan. A lobed pattern (of maximum turbulence) is generated for large gaps. However, as the fan is brought closer to the target surface, the behaviour transitions to a vertical elliptical pattern.

On closer inspection of the above sequence of images (Figure 7.19 and Figure 7.20), in particular for larger  $G$  values, a slight flow asymmetry develops. It is believed that this asymmetry arose due to the mounting of the piezoelectric fan - Figure 7.21. While the fan is capable of drawing in ‘fresh’ air from above, it is not possible to do so from the underside of the fan due to the obstruction caused by the  $X$  - and  $Y$  - sliders. This in turn generates the flow asymmetry.

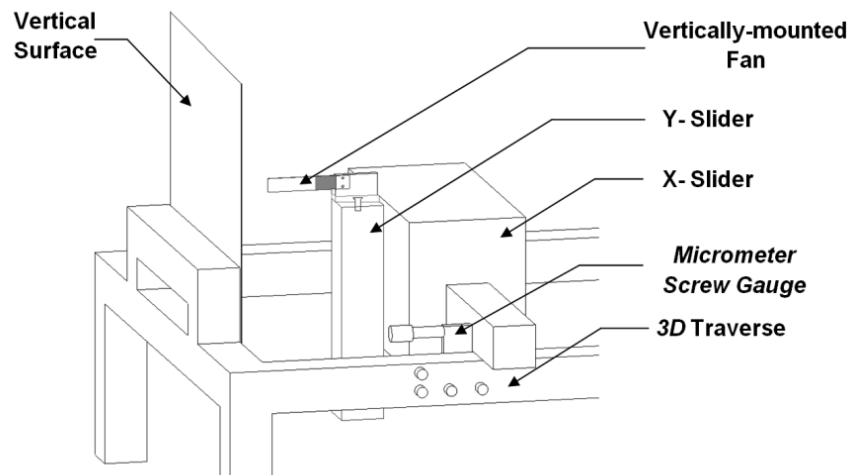


Figure 7.21: Flow Obstruction - Vertically-mounted Fan

However, due to the need to have a  $3D$  positioning system (to perform the numerous tests), this was unavoidable. While there may be ways to improve this, it was beyond the scope of this dissertation.

## 7.5 Further Data Analysis – A Comparative Study

In this section, the key trends and results presented in the previous sections are discussed and evaluated further. Furthermore, a dimensional analysis (*Buckingham* Theorem) was performed to better understand the effect of the varied parameters ( $A_{pz}$ ,  $G$ ,  $w$ ) on the principal velocity.

For both piezoelectric fan orientations, the principal velocity ( $\bar{V}$ ) may be related to the tested parameters according to Eq.7.7 below.

$$\bar{V} = f(A_{pz}, G, w) \quad \dots \text{Eq. 7.7}$$

The dimensions of each variable are:  $\bar{V} = LT^{-1}$ ,  $A_{pz} = L$ ,  $G = L$ ,  $w = T^{-1}$ . This results in  $m=4$  and  $n=2$ , which in turn implies the formation of two  $\pi$  Groups. On adhering to *Buckingham's* Theorem, the resulting  $\pi$  Groups are of the form:

$$\pi_1 = \frac{G}{A_{pz}} \quad \pi_2 = \frac{\bar{V}}{A_{pz} \cdot w} \quad \dots \text{Eq. 7.8}$$

From the above  $\pi$  Groups, the following may be written:

$$\pi_2 = f(\pi_1) \quad \dots \text{Eq. 7.9}$$

$$\frac{\bar{V}}{A_{pz} \cdot w} = K \left( \frac{G}{A_{pz}} \right)^n \quad \dots \text{Eq. 7.10}$$

Eq. 7.10 gives the relation between the principal velocity ( $\bar{V}$ ) and the critical variables, and indicates that the function is not a linear one, but an exponential function. Thus by plotting  $\text{Log} \left( \frac{\bar{V}}{A_{pz} \cdot w} \right)$  on the y-axis, against  $\text{Log} \left( \frac{G}{A_{pz}} \right)$  on

the  $x$ -axis, as depicted by Figure 7.22 below, the exponential power ( $n$ ) may be evaluated.

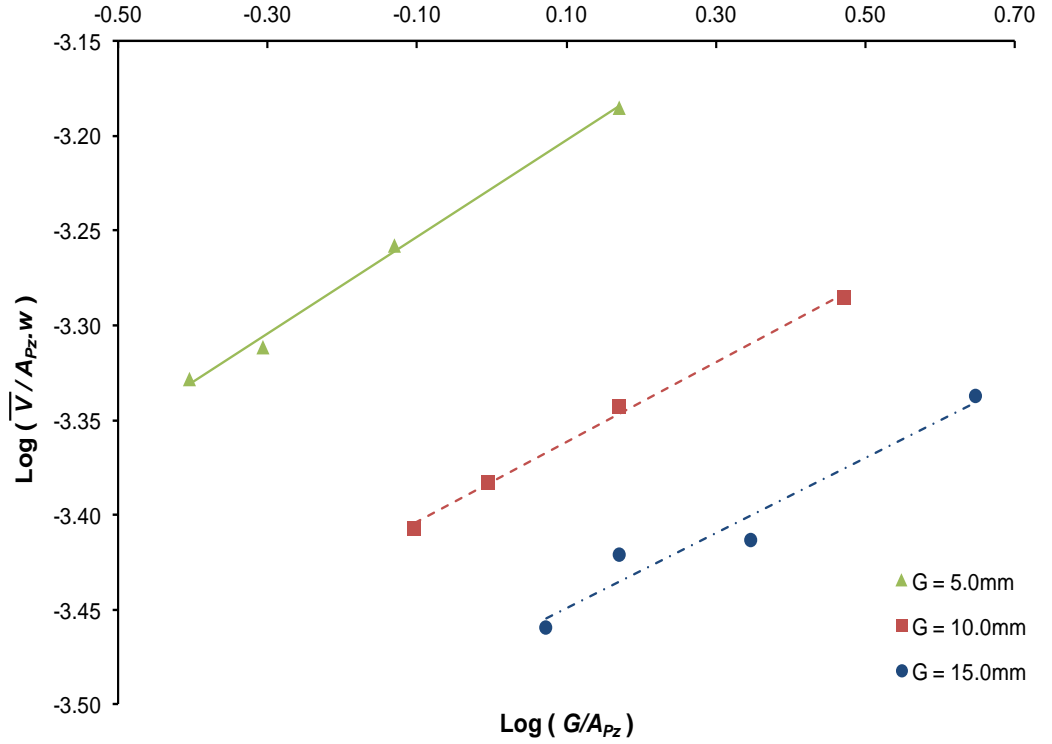


Figure 7.22: Dimensional Analysis of a Horizontally-mounted Piezoelectric Fan

The exponential power was determined to be equivalent to  $n = 0.25$  (average gradient of the three lines) within the error. Thus, the principal velocity may be related to  $A_{Pz}$ ,  $G$ , and  $w$  according to Eq. 7.11 below:

$$\bar{V} = \frac{K \cdot w \cdot (A_{Pz})^{0.75}}{G^{-0.25}} \quad \dots \text{Eq. 7.11}$$

A further analysis was conducted to better understand how the varied parameters, when taken independently, effect the principal velocity (Figure 7.23). For both fan orientations, it was reported that an increase in vibrational amplitude resulted in an increase in the primary oscillation velocity. Figure 7.23 collates all the data recorded for a horizontally-mounted

fan on a plane parallel to the vertical surface whilst highlighting the resulting trends when  $A_{p_z}$  and  $G$  are varied.

Results indicate that an increase in  $V_{p_z}$  leads to an increase in the  $\overline{V_X}$ ,  $\overline{V_Y}$  and  $\overline{V_{Mean}}$  velocity components. These velocity components further increase with a reduction in the separation distance. However as  $\overline{V_Y}$  is the principal velocity component of interest, only these are presented. Figure 7.23i indicates that with an increase in  $A_{p_z}$ , the principal velocity increases with a comparable gradient for all considered gaps. This trend holds for each of the separation distances. On the other hand, Figure 7.23ii highlights the fact that a reduction in  $G$  also results in an increase in the  $\overline{V_Y}$  component.

From **Error! Reference source not found.**, an empirical relationship of the form (Eq. 7.12) arises. This is similar to that presented in Eq. 7.11, the only difference being that,  $w$  is encapsulated in the constant  $C_1$ .

$$\overline{V_Y} = C_1 \frac{(A_{p_z})^{0.75}}{(G)^{-0.25}} \quad \dots \text{Eq. 7.12}$$

Thus, for the considered  $Re_{p_z}$  range, it may be concluded that for a horizontally-mounted fan, the  $\overline{V_Y}$  component of velocity is related to the fan amplitude and separation distance according to the empirical equation detailed by Eq. 7.12 which is equivalent to Eq. 7.11.



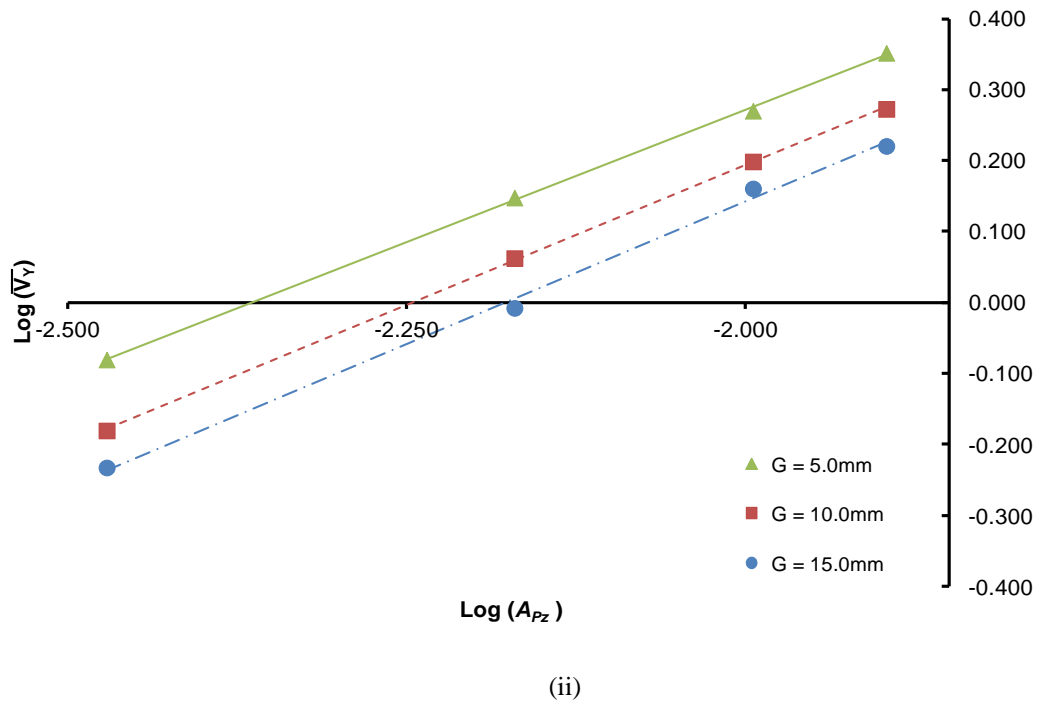
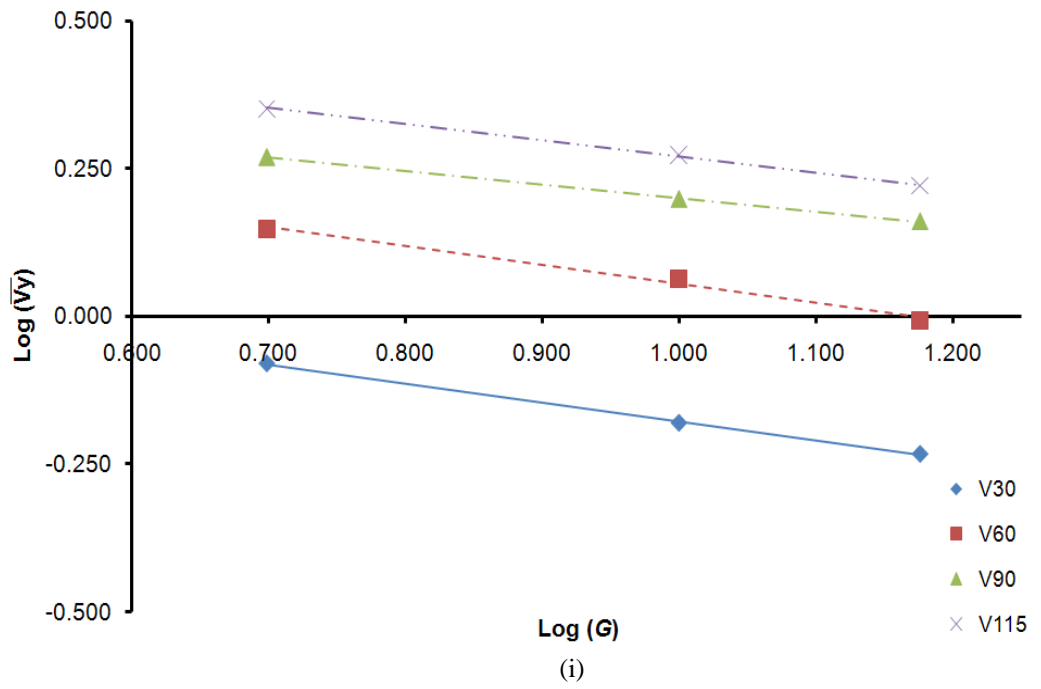


Figure 7.23: Comparative Study for a Horizontally-mounted Fan:

i) Log – Log Graph - Effect of Fan Amplitude on Maximum  $\overline{V}_Y$  Component

ii) Log – Log Graph - Effect of Separation Distance on Maximum  $\overline{V}_Y$  Component

Similar results were obtained for a vertically-mounted fan. It was established that the empirical equation takes the same form as that presented in Eq. 7.12, indicating once again that the principal velocity ( $\overline{V}_x$ ) is related to the oscillatory amplitude, frequency and separation distance according to (Eq. 7.13).

$$\overline{V}_x = C_2 \frac{(A_{Pz})^{0.75}}{(G)^{-0.25}} \quad \dots \text{Eq. 7.13}$$

Figure 7.24 depicts the variation in the principal velocity against the earlier established empirical relations ( $F_n$  – i.e. Eq. 7.12 and Eq. 7.13) for both a horizontally-mounted ( $\overline{V}_y$ ) and a vertically-mounted fan ( $\overline{V}_x$ ). For each fan orientation, the data points are seen to collapse onto a single straight line – a significant result. Figure 7.24 indicates that the flow characteristics (in particular the principal velocity), for a vertical flat plate setup, are independent to the fan orientation. That is, similar peak (and average) principal velocities are obtained in both fan orientations. Error bars of +/- 5.0% (as quoted in **Chapter 5**) are also added to each of the data points.

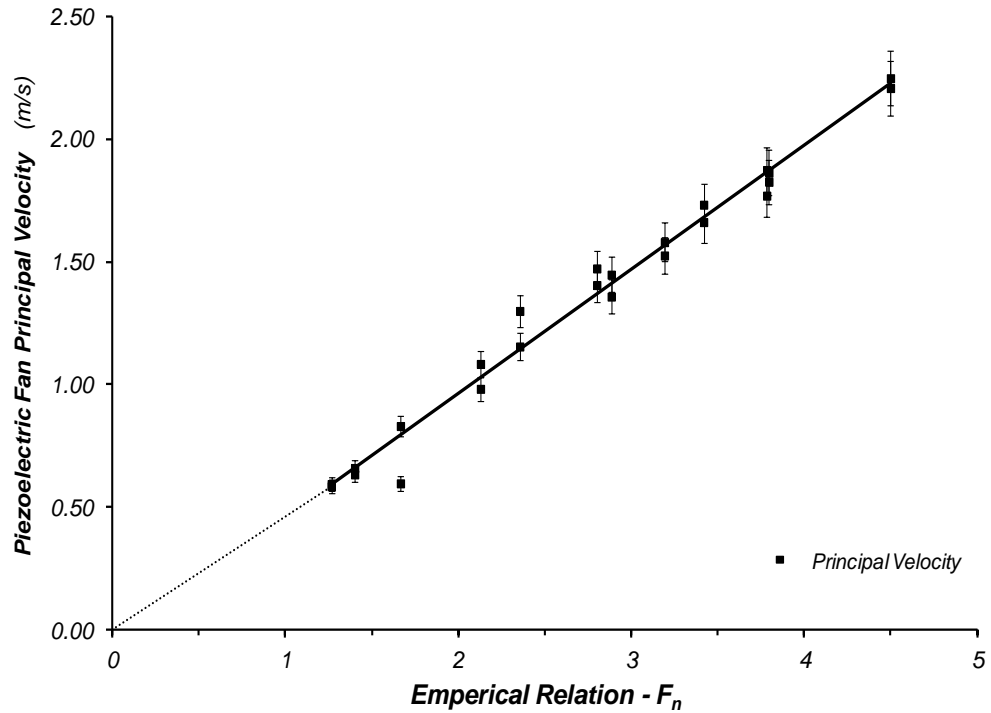


Figure 7.24: Relationship between the Principal Velocity and the governing Empirical Equation for both a Horizontally and a Vertically-mounted Piezoelectric Fan

Furthermore, Figure 7.25 highlights the similarities between the piezoelectric fan principal velocity and the heat transfer characteristics. Firstly, it was deduced that, both a horizontally-mounted and a vertically-mounted piezoelectric fan maintain the same gradient which in turn was found to be similar to the gradient of the above established principal velocity ( $\overline{V_y}, \overline{V_x}$ ).

It was also noted that in this setup, a vertically-mounted fan seemed to slightly outclass a horizontally-mounted fan. However, on considering the error bands ( $\pm 7.7\%$  - as quoted in **Chapter 5**), it was established that the percentage increase in heat transfer for both orientations are similar.

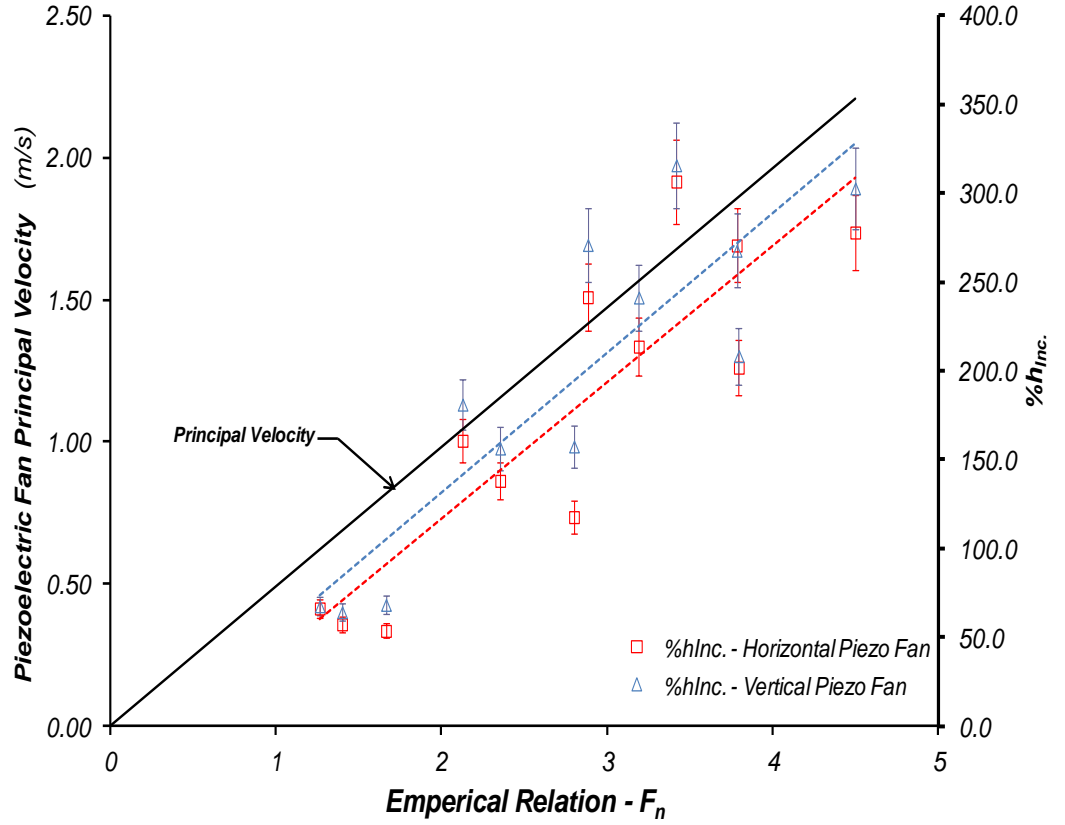


Figure 7.25: Comparative study between the Principal Velocity and the  $\%h_{inc.}$  for both a Horizontally and a Vertically-mounted Piezoelectric Fan

Furthermore, while the principal velocity profile plot is seen to run through the datum, the same cannot be said for the cooling plots ( $\overline{\%h_{inc.}}$ ). The latter is due to the fact that  $\overline{\%h_{inc.}}$  is a non-linear function of the principal velocity. As documented in Eq. 6.7,  $\overline{\%h_{inc.}}$  is a function of the forced convection component (which itself is a function of velocity -  $\overline{h_{FC}} = A'(\text{Re})^B = C(\text{vel})^B$ ) and the natural convection component (which is not a function of velocity -  $\overline{h_{NC}} = m(Ra)^q$ ). Thus, when the piezoelectric fan is off ( $A_{Pz} = 0.0mm$ ),  $\overline{\%h_{inc.}}$  does not run through the datum (as natural convection is still present) but is shifted accordingly.

Furthermore, as previously mentioned, the enhancement in heat transfer is dependent on both the mean flow ( $V_{Mean}$ ) as well as the turbulent fluctuating

velocity component ( $V_{RMS}$ ). This will be further investigated in the subsequent chapter.

Figure 7.25 highlights the similarities in the thermal cooling characteristics (presented in **Chapter 6**) to the flow characteristics (presented in **Chapter 7**) for one such *FCCS* setup. The cooling range ( $X_{Pos}$ ,  $Y_{Pos}$ ), magnitude and symmetry are well matched.

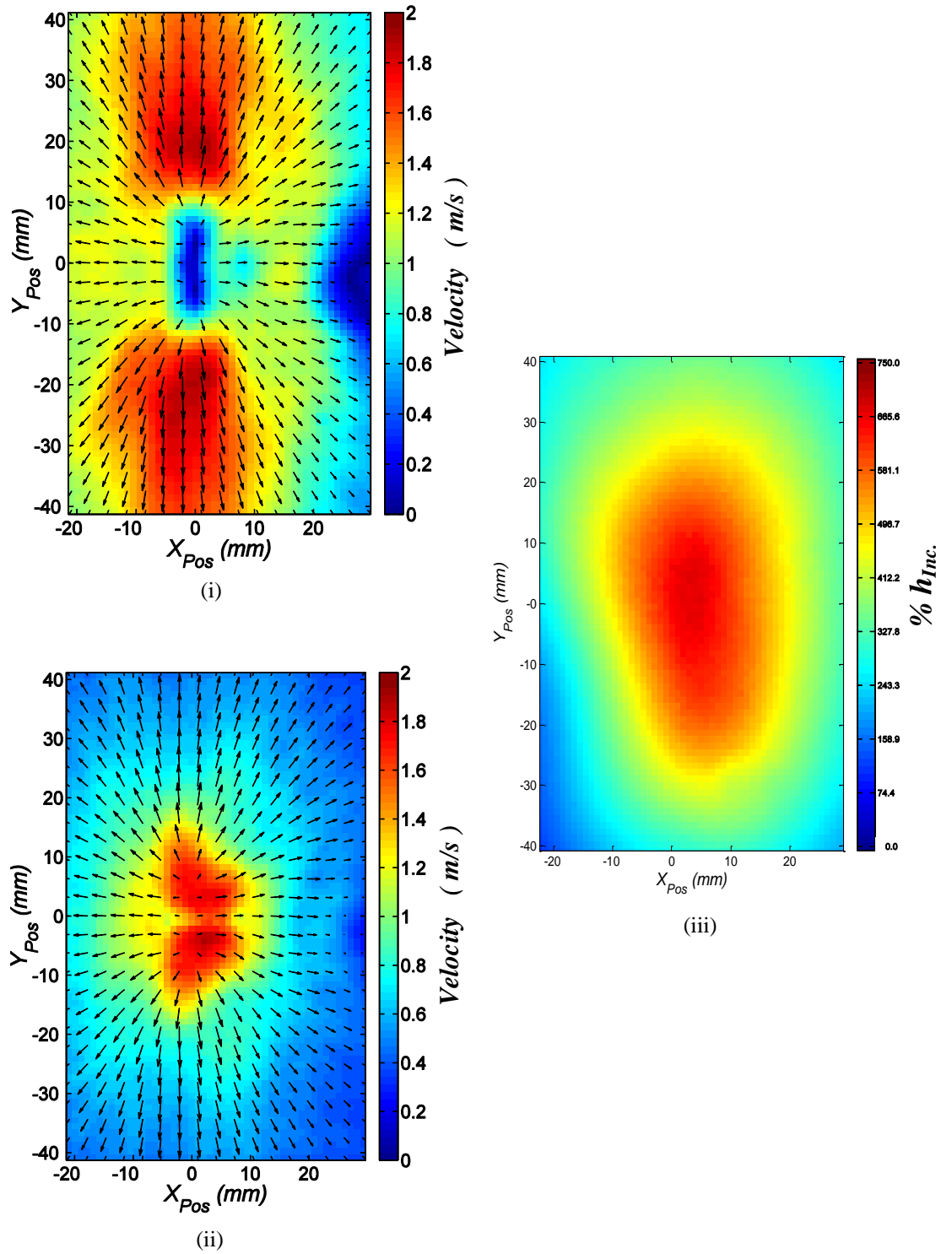


Figure 7.26: Comparative Study between Flow and Thermal Results: *FB*, Horizontally-mounted Fan  $G10.0\text{mm}$   $V_{Pz} = 115.0\text{V}$ :

- (i) Magnitude of the Mean Vectors
- (ii) *RMS* values of the Fluctuating Component
- (iii)  $\% h_{Inc.}$

## 7.6 Concluding Remarks

Flows produced by both a horizontally-mounted and a vertically-mounted oscillating piezoelectric fan have been characterised and the effect of vibrational amplitude ( $A_{p_z}$ ) and separation distance ( $G$ ) on the flows generated have been presented. *PIV* and data analysis have been implemented to determine: instantaneous velocities, bulk mean flows as well the turbulence characteristics.

The fan amplitude was seen to drop off significantly when operated at frequencies other than its natural frequency. For all applied voltages, the same spectrum of harmonic frequencies was produced.

Furthermore, the flows produced by the fan are unsteady and complex with several counter-rotating vortices shed by each swing reflecting a high degree of periodicity. The flows produced seem to be symmetrical with the same characteristics being produced by a horizontally-mounted piezoelectric fan as that of a vertically-mounted one. However, any slight difference in air flow characteristics between the two piezoelectric fan orientations is understood to be due to asymmetries present in the experimental setup.

For a piezoelectric fan, an increase in  $V_{p_z}$  results in an increase in both components of velocity ( $\overline{V_x}, \overline{V_y}$ ), in particular the principal velocity ( $\overline{V_y}$ ). On the other hand, a reduction in the separation distance results in an increase in the  $\overline{V_{Mean}}$  in the area closest to the vibration amplitude of the fan, while the converse occurs at the extremities of the envelope. Similarly, the highest turbulence levels are generated in close proximity of the fan at the minimal considered separation distance. The highest bulk flow velocity to be recorded was  $2.409m/s$  with the highest turbulence value to be measured exceeding  $2.382m/s$  when operating at the maximum amplitude and a separation distance of  $5.0mm$ . It was established that the optimum *FCCS* configuration that results in the largest air flow, for both fan orientations was that of

$V_{pz} = 115.0V, G = 5.00mm$ . This result agrees with the thermal results published in **Chapter 6**.

An empirical equation relating the fan amplitude, frequency and separation distance to the principal velocity was also established. This relation is valid for flows observing *Reynolds* numbers between 767.7 to 5549.2.

From the attained experimental results, it has been established that the local geometry affects the flow characteristics of the fan. Having a high flow resistance (due to mounting plate or other obstructions) will significantly reduce the available air flow, thus significantly reducing the cooling capabilities of such fans. Therefore, it is recommended to take this into account in situ measurements.

Lastly, it was established that the local heat transfer coefficients enhancement,  $\%h_{mc}$ , results on a vertical flat surface are a function of both the mean flow (as described in theory – Eq. 7.14) and the unsteady flow fields generated by the oscillating fan.

$$Nu_L = \frac{h_L \cdot L}{k} \quad \dots \text{Eq. 7.14}$$

$$h_L = \left( \frac{k}{L} \right) \cdot a(Re^b) \cdot Pr^c \quad \dots \text{Eq. 7.15}$$

$$h_L = a \cdot \left( \frac{k}{L} \right) \left( \frac{\rho \cdot \bar{v} \cdot L}{\mu} \right)^b \cdot Pr^c \quad \dots \text{Eq. 7.16}$$

Thus, the cooling plots presented in **Chapter 6** are dependent on both the mean and turbulence plots presented in this chapter. Furthermore, while certain flow characteristics (such as cooling range, magnitude) can be matched to the cooling results (Figure 7.26), one can not directly compare the mean and turbulent patterns to the earlier presented cooling patterns.



# CHAPTER 8

## 8. Flow Measurements for a Finned Geometry

---

The structure of this chapter takes on a similar format to the previous chapter; the aim of which is to investigate, characterise and measure the  $2D / 3D$  bulk and turbulent flows generated by an oscillating piezoelectric fan for a finned geometry.

Detailed flow visualisation and measurements (*PIV*) of a horizontally-mounted oscillating piezoelectric fan are first introduced in **Section 8.1**, followed by those produced by a vertically-mounted oscillating fan in **Section 8.2**. Results are presented for both the fin base (*FB*) and the fins' side walls (*FSW*'s). Furthermore, the effects of varying  $A_{pz}$ ,  $G$  and  $S$  are investigated, and the important trends highlighted and discussed in further detail.

A detailed comparative study between the earlier presented flow results on a vertical flat plate (**Chapter 7**) and several finned cases are presented in **Section 8.3**. An additional comparative study is also performed between the attained finned flow results and the cooling plots presented in **Chapter 6**. Furthermore, key  $3D$  contour plots for several geometrical configurations are presented.

Lastly, in **Section 8.4**, the chapter conclusions are drawn up.

## 8.1 Horizontally-mounted Fan

The results presented here pertain to a horizontally-mounted piezoelectric fan, operating at its natural frequency. 2D flow fields of both the *FB* (*Section 8.1.1*) and the *FSW*'s (*Section 8.1.2*) are presented; the key trends and their contribution to the cooling plots (*Chapter 6*) are also presented and discussed in further detail.

For the scope of data presentation and direct comparison, in the sections below, the results pertain to a test case of:  $S = 40.0mm$ . The latter configuration was utilised as a base case against which the resulting flow characteristics from the other tested geometries were compared.

### 8.1.1 Flow Measurements Parallel to Fin Base

#### 8.1.1.1 Effect of Fan Amplitude ( $V_{P_z}$ )

The results were obtained using the experimental setup depicted in Figure 5.21.

Operating the fan at peak amplitude generates a flow disturbance in excess of  $60mm$  ( $30mm$  in each direction) in the oscillation direction, and a further disturbance of  $40mm$  ( $20mm$  in each direction) in the transverse direction. Furthermore, for the various applied fan voltages, the magnitude of the upward flow is equivalent to that downwards, indicating, once again the flow symmetry.

Figure 8.1 highlights the variation in the magnitude of the mean vectors at different  $V_{P_z}$  when the fin spacing is set to  $S = 40.0mm$  (control experiment). The sequence of images indicates that an increase in  $V_{P_z}$  results in an increase in the magnitude of the mean vectors, in particular, the principal velocity  $\overline{V_Y}$ . Similar to the results presented on a vertical flat plate (Figure 7.2), the flow is seen to originate at the blade tip (according to the set  $V_{P_z}$ ) and travel symmetrically along both the positive and negative  $y$ -axis. On the application

of  $V_{Pz} = 30.00V$ , the disturbance area in the neighbourhood of the fan tip was minimal, with a  $\overline{V_{Mean}} = 0.486m/s$ . However, as the vibrational amplitude increased to  $V_{Pz} = 115.0V$ , the maximum mean velocity  $\overline{V_{Mean}}$  to be recorded increased to  $1.970m/s$ . Table 8.1 lists the peak values attained when the fan was operated under different voltages.

On closer inspection of Figure 8.1 (in particular Figure 8.1iv), the flow is seen to be constrained between the two fin side walls. The latter image indicates that the flow travels vertically along the fin side walls (at  $X_{Pos} = -20.0mm$  and  $X_{Pos} = 20.0mm$ ) resulting in large  $\overline{V_Y}$  values and negligible  $\overline{V_X}$  values.

$V_{Pz}$ (V)	$\overline{V_X}$ (m/s)	$\overline{V_Y}$ (m/s)	$\overline{V_{Mean}}$ (m/s)
30.00	0.175	0.480	0.486
60.00	0.347	1.168	1.264
90.00	0.868	1.535	1.649
115.0	1.013	1.960	1.970

Table 8.1: Peak Velocity Measurements -  $S = 40.00mm, G = 10.0mm$

Figure 8.1 further indicates that as in the previous chapter (**Chapter 7**), a zero velocity (stagnation region) occurs at the fan tip datum region. The reason behind this is simply because the flow is travelling along the negative  $z$ -axis (into the plane of the paper). Therefore, on performing *2D PIV*, an apparent zero velocity region was achieved, as this flow is not in the measurement plane. To clarify the matter, detailed *2D PIV* measurements on the  $Y$ - $Z$  plane are presented in **Section 8.1.2**. Furthermore superimposed results (*FB* and *FSW*) are presented in **Section 8.3**.

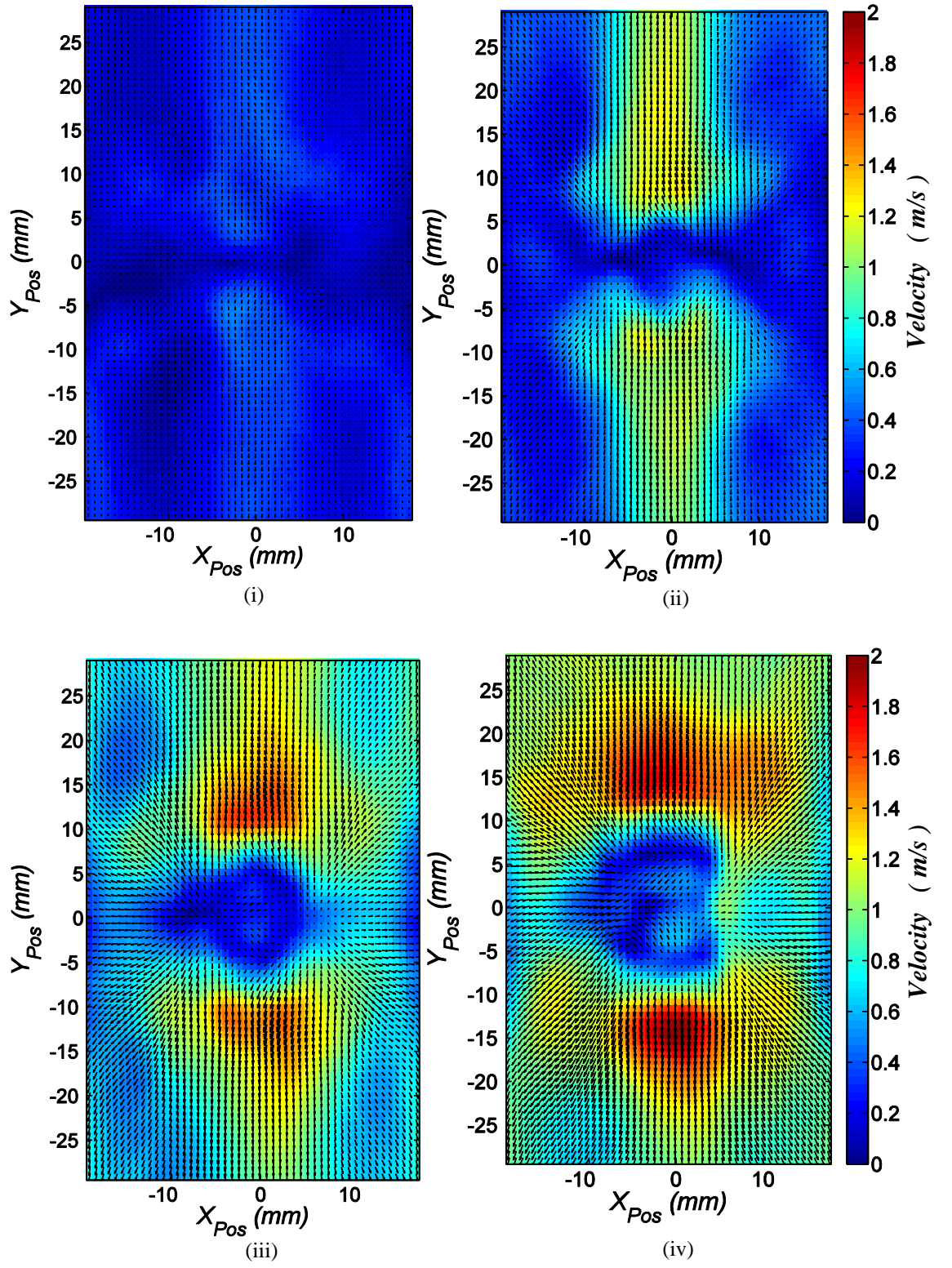


Figure 8.1: Magnitude of the *FB* Mean Vectors for  $S = 40.0mm$ ,  $G = 10.0mm$  and;

(i)  $V_{Pz} = 30.00V$    (ii)  $V_{Pz} = 60.00V$    (iii)  $V_{Pz} = 90.00V$    (iv)  $V_{Pz} = 115.00V$

The above contour plots indicate that the flow regimes differ somewhat from those presented in **Chapter 7** (due to the presence of the *FSW*'s). Initially, a circular central stagnation region occurs at low to medium vibrational amplitudes. However, at  $V_{pz} = 115.0V$ , a lobed (hour glass) region results. The behavioural change has been attributed to the presence of the *FSW*. The *FSW*'s limits the incoming air available to the fan thus hindering the flow, which results in a lesser heat transfer enhancement ( $\%h_{inc.}$ ) values when compared to an unfinned geometry.

The turbulence characteristics for the current setup are depicted in Figure 8.2. While Figure 8.2i indicates a centrally located low magnitude disturbance, at larger vibrational amplitudes (Figure 8.2ii - Figure 8.2iv), a different flow disturbance arises. This takes on the form of a stagnant region (at the fan tip datum position) surrounded by two symmetric circular high magnitude bands. It is believed that the pattern change is due to a change in flow behaviour, i.e. a transition region. This result indicates that, for this setup, flow transition occurs between  $Re = 767.7$  and  $Re = 2279.6$ .

The magnitude of the *RMS* of the fluctuating component is equivalent to  $0.583m/s$  when the minimal voltage is applied. However, with an increase in  $V_{pz}$ , both the affected area as well as the magnitude increase, the maximum value of which peaked at  $2.038m/s$ .

On considering the turbulence patterns, several commonalities to those produced on a flat plate (Figure 7.2 and Figure 7.3) can be made. At low amplitudes a central symmetric disturbance originates. However, with an increase in amplitude, symmetrical circular lobes originate on either side of the stagnation band. These circular bands increase in size and become elliptical in nature when the largest amplitude is applied. The resulting turbulence bands while differing in pattern from those presented in **Section 7.3.1.1**, maintain the same  $X_{Pos}$  and  $Y_{Pos}$  limits. Furthermore, the size of the turbulence correlates directly to the band of maximum cooling ( $\%h_{inc.}$ ) presented in **Chapter 6**.

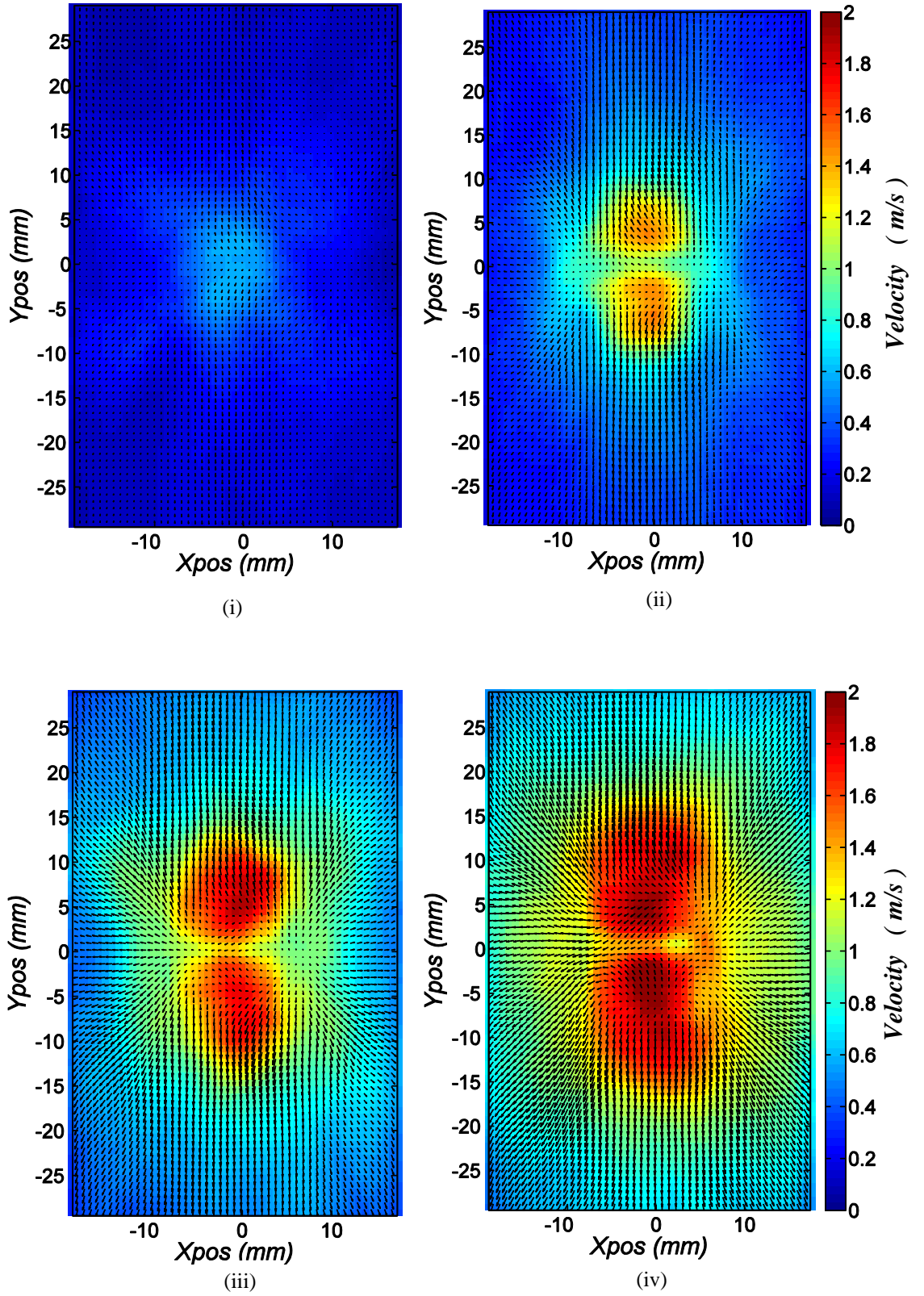


Figure 8.2: *FB RMS* Fluctuating Components for  $S = 40.0\text{mm}$ ,  $G = 10.0\text{mm}$  and;  
 (i)  $V_{P_z} = 30.00V$  (ii)  $V_{P_z} = 60.00V$  (iii)  $V_{P_z} = 90.00V$  (iv)  $V_{P_z} = 115.0V$

Turbulence intensity profile plots, at three locations ( $X_{Pos} = -10mm$ ,  $X_{Pos} = 0mm$  and  $X_{Pos} = 10mm$ ), for the above presented contour plots (Figure 8.2) are illustrated here.

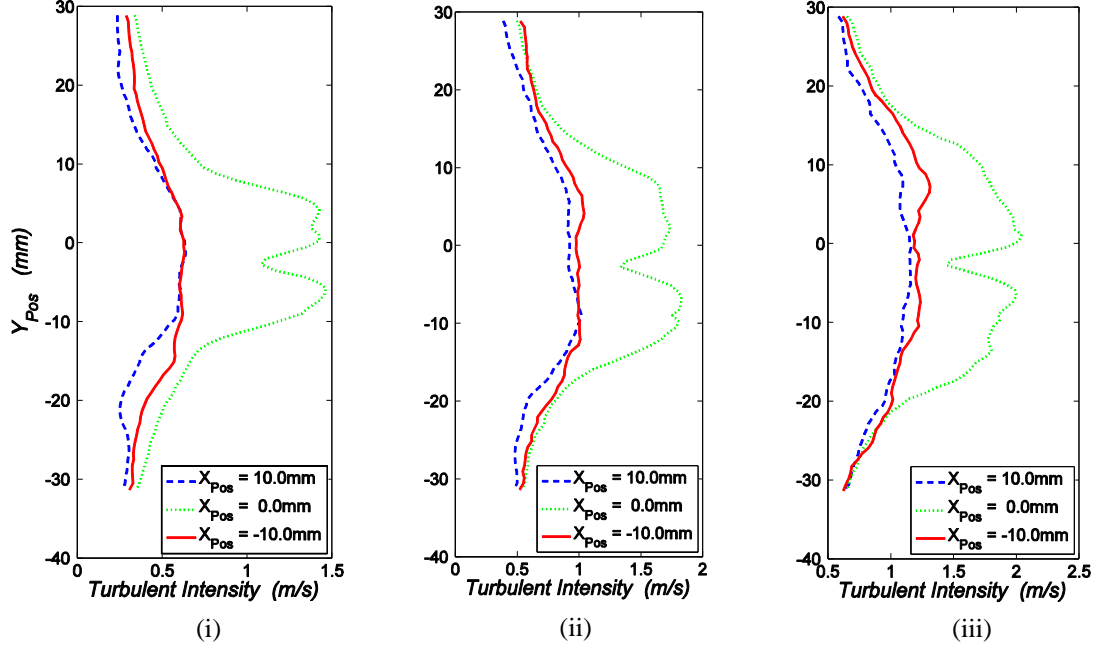


Figure 8.3: Direct comparison of the *FB* Turbulent Intensity for -  $S = 40.0mm, G = 10.0mm$  :

$$(i) V_{Pz} = 60.00V \quad (ii) V_{Pz} = 90.00V \quad (iii) V_{Pz} = 115.0V$$

The trends in Figure 8.3 further complement earlier presented results. That is, the maximum turbulent intensity level occurs in the neighbourhood of the vibrational envelope and increases with an increase in  $V_{Pz}$ . Furthermore, at the fan datum position ( $Y_{Pos} = 0.0mm$ ), a slight dip is achieved, due to the presence of the stagnation region. The turbulent intensity profiles at locations  $X_{Pos} = -10mm$  and  $X_{Pos} = 10mm$  follow the same shape and practically also have the same magnitudes, further indicating the flow symmetry.

Furthermore, these plots bear a close resemblance to those presented for an unfinned surface - Figure 7.4. Both the magnitudes (at the various  $X_{Pos}$  locations) and the profiles at each location are well matched indicating that the same fan characteristics are present.



### 8.1.1.2 Effect of Separation Distance ( $G$ )

The effect of the separation distance ( $G$ ) on the generated flow fields is reported in Figure 8.4. A reduction in  $G$ , yields a significant increase in the principal velocity  $\overline{V}_Y$  together with an increase in coverage area. Numerically, the maximum  $\overline{V}_Y$  increases from  $1.430\text{m/s}$  when  $G = 15.0\text{mm}$ , to  $1.960\text{m/s}$  when  $G = 10.0\text{mm}$  and to  $2.488\text{m/s}$  when  $G = 5.0\text{mm}$ .

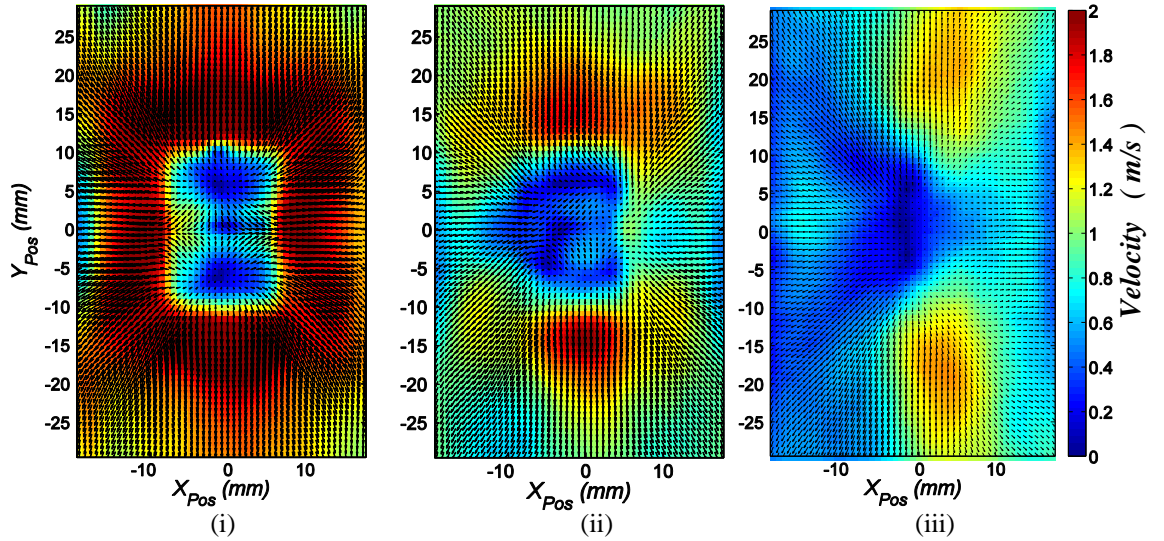


Figure 8.4: Effect of  $G$  on the Magnitude of the Mean Vectors -  $V_{Pz} = 115.0V$ ,  $S = 40.0\text{mm}$ :  
 (i)  $G = 5.0\text{mm}$  (ii)  $G = 10.0\text{mm}$  (iii)  $G = 15.0\text{mm}$

The stagnation patterns generated for the finned case above are in close agreement to those presented for a flat plate. For both geometries, a lobbed (hour glass) pattern results for  $G = 5.0\text{mm}$ . This result indicates that a greater enhancement in heat transfer ( $\%h_{inc.}$ ) should arise at lower separation distances, as can be seen in the cooling plots presented in Figure 6.5.

On closer inspection of Figure 8.4iii, it is evident that a slight asymmetry exists in the  $2D$  mean velocity plot. It is believed that this asymmetry is because the piezoelectric fan was not located centrally between the two fins, but slightly closer to the left fin (at  $X_{Pos} = 20.0\text{mm}$ ).



A similar outcome was obtained on considering the turbulence contour plots (Figure 8.5). Once again, the turbulence originates from the fan datum position and spreads symmetrically outwards.

For  $G = 15.0mm$  and  $G = 10.0mm$ , the main component of turbulence is vertically (oscillation direction), along the  $y$ -axis. However, when  $G = 5.0mm$ , while the turbulence is still seen to be preferentially oriented in the  $y$ -direction, a secondary pattern (due to presence of  $FSW$ 's), oriented horizontally emerges. A decrease in  $G$  results in the increase in the  $STDV_y$  at all points along  $X_{Pos} = 0.0mm$ . It was further established that, at  $G = 15.0mm$ , the maximum  $STDV_y$  value reached was  $1.283m/s$  while when  $G = 5.0mm$ , the maximum  $STDV_y$  value reached was that of  $1.897m/s$ .

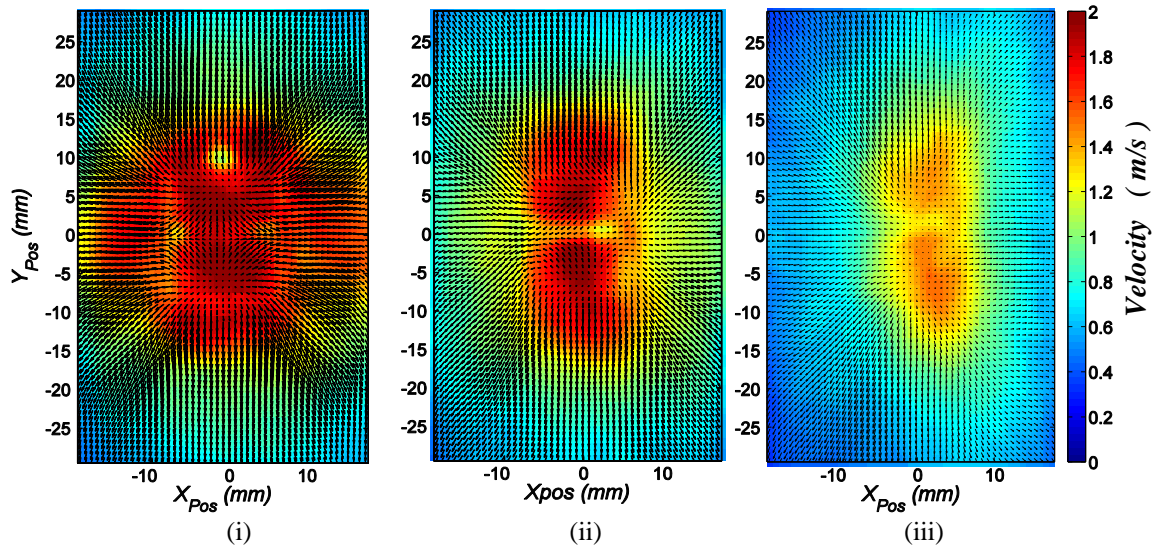


Figure 8.5: Contour Plots of the  $FB$   $STDV$  Component -  $V_{Pz} = 115.0V$ ,  $S = 40.0mm$ :

(i)  $G = 5.0mm$

(ii)  $G = 10.0mm$

(iii)  $G = 15.0mm$

The same trends have been reported in **Chapter 7** (Figure 7.6) when considering the flow patterns produced on a vertical flat plate, where it was shown that, an increase in the fan oscillation amplitude as well as a decrease in the separation distance both result in an increase in the overall magnitude of the mean vectors and turbulence levels.

### 8.1.1.3 Effect of Fin Spacing ( $S$ )

The effects of the interfin spacing on the flow fields are illustrated in Figure 8.6 (magnitude of the mean vectors) and Figure 8.7 (turbulence intensity maps).

The flow vector patterns presented in Figure 8.6, are similar in nature. The flow originates from the piezoelectric fan tip datum and spreads out evenly to the four corners until contact with the  $FSW$ 's occurs. When the air flow meets the two fins (at the various  $X_{pos}$ , depending on the considered fin spacing), the flow is channelled symmetrically along the fins, thus causing a net mass transfer (which in turn generates a significant cooling effect). However, the different considered fin spacings, generate different mean air magnitudes at different locations. At  $S = 30.00mm$ , (Figure 8.6i) the  $FSW$ 's are seen to constrict the flow, resulting in the presence of high velocity vectors in most of the domain, an average  $\overline{V_y}$  of  $1.05m/s$ , and a peak  $\overline{V_y}$  of  $1.608m/s$  result. For a spacing of  $S = 40.0mm$ , the flow is less channelled than in the latter case, with the average flow velocity ( $\overline{V_y}$ ) in the considered region reaching  $0.950m/s$ , and a peak velocity of  $1.960m/s$  (located at the ends of the vibration envelope). On considering  $S = 50.0mm$ , an average mean flow velocity of  $0.991m/s$  and a peak velocity of  $1.934m/s$  (again located at the ends of the vibration envelope) were achieved.

On the other hand, when  $S = 30.0mm$ , the maximum  $STDV_y$  to be recorded was  $1.509m/s$  (Figure 8.7i). For  $S = 40.0mm$ , the peak  $STDV_y$  reached  $1.689m/s$  (Figure 8.7ii), while at  $S = 50.0mm$ , a peak  $STDV_y = 2.218m/s$  was recorded (Figure 8.7iii). When considering the turbulence characteristics, the generated patterns are also of prime importance. For the minimum considered spacing, a symmetrical, nearly circular, pattern of maximum magnitude oriented in the oscillation direction is produced. This also holds true for  $S = 40.0mm$ . However, at  $S = 50.0mm$ , the above described symmetrical turbulent bands merge into a single elliptical band.

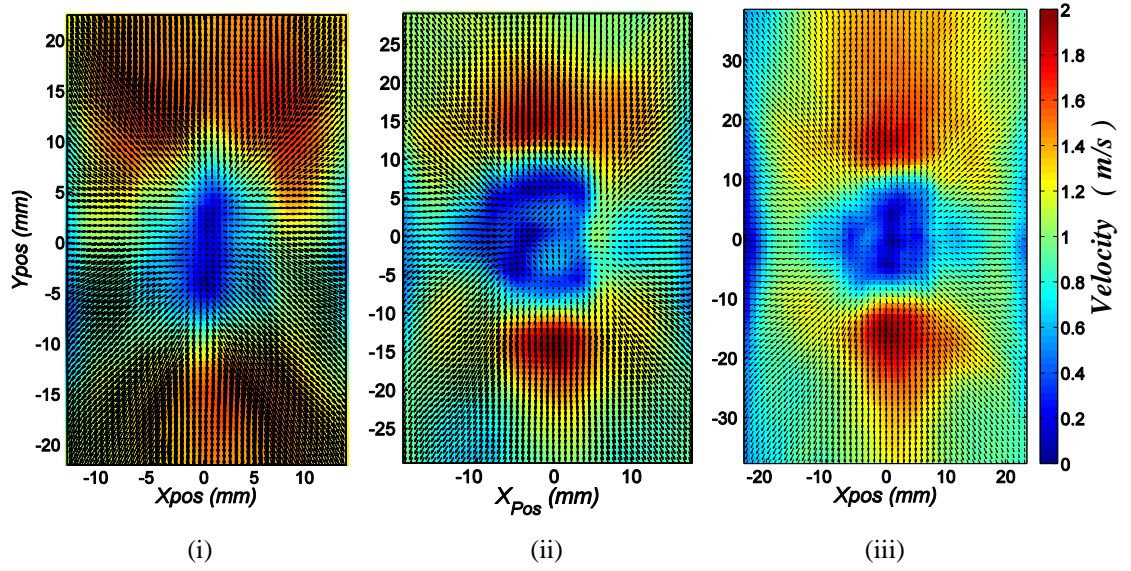


Figure 8.6: Magnitude of the *FB* Mean Vectors -  $V_{Pz} = 115.0V, G = 10.0mm$  :  
 i)  $S = 30.0mm$       ii)  $S = 40.0mm$       iii)  $S = 50.0mm$

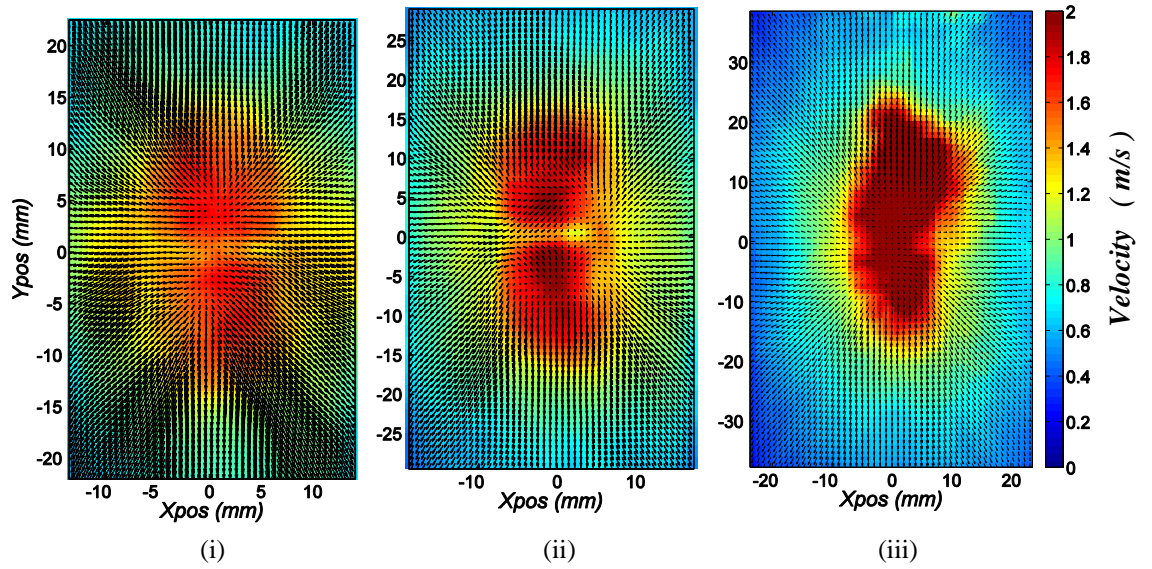


Figure 8.7: Contour Plots of the *FB* RMS values of the Fluctuating Component -  
 $V_{Pz} = 115.0V, G = 10.0mm$  :  
 i)  $S = 30.0mm$       ii)  $S = 40.0mm$       iii)  $S = 50.0mm$

Table 8.2 shows the data (average  $\overline{V_Y}$ , peak  $\overline{V_Y}$ ) together with the turbulence characteristics ( $STDV_Y$ ) and the results attained on a vertical flat plate (**Chapter 7**), while Table 8.3 illustrates the range of the turbulence generated by the oscillating fan.

Fin Spacing ( $S$ ) (mm)	Avg $\overline{V_Y}$ (m/s)	Peak $\overline{V_Y}$ (m/s)	$STDV_Y$ (m/s)
<b>30.0</b>	1.050	1.608	1.509
<b>40.0</b>	0.950	1.960	1.689
<b>50.0</b>	0.991	1.934	2.218
Vertical Flat Surface ( $S = \infty$ )	1.194	1.874	1.727

Table 8.2: Effect of Fin Spacing:  $G = 10.0\text{mm}$ ,  $V_{Pz} = 115.0V$

The average  $\overline{V_Y}$  is based on the channel area.

The  $STDV_Y$  results indicate that a larger fin spacing (in particular  $S = 50.0\text{mm}$ ) is beneficial for enhanced cooling, as both the magnitude of the *RMS* of the fluctuating component of velocity and the affected area (Table 8.3) are greater than at other considered fin spacings. However, for a vertical flat surface (no fins) the magnitude of the turbulence level is seen to drop off. This decline has been attributed to the lack of fins. For the finned cases, the fin side walls constrain the eddies generated by the fan, which lead to both creative and destructive interference. This eddy interaction is the root cause of the resulting high turbulence values. However, for a vertical flat surface, the lack of the *FSW*'s, allows the eddies to be propelled and dissipated away from the fan. This in turn reduces both the size of the eddies, as well as the possibility for eddy interactions. This results in a lower overall  $STDV_Y$  value.

However, the same results are not seen when considering the mean/bulk flow results where, for the minimum considered fin spacing, a larger average  $\overline{V_Y}$  results (Table 8.2).

Fin Spacing ( $S$ ) (mm)	X -Disturbance (mm)	Y -Disturbance (mm)
<b>30.0</b>	12.5	27.5
<b>40.0</b>	15.5	33.0
<b>50.0</b>	20.5	42.5
Vertical Flat Surface ( $S = \infty$ )	19.5	32.0

Table 8.3: Effect of Fin Spacing on the Disturbance Area Range

From these results, the complexity of the unsteady flow fields generated by the oscillating fan can be appreciated. Furthermore, as the heat transfer characteristics are dependent on both the bulk flow and the turbulence characteristics it is not a straightforward task to deduce the optimum geometry. However, on noting the cooling plots presented in *Section 6.2.1*, together with the conclusions presented in *Section 6.4*, the results indicate that a small fin spacing ( $S_{30}$ ) results in a higher overall cooling enhancement ( $\%h_{inc.}$ ) than at larger fin spacings. This indicates that, the bulk flow is more indicative of the cooling characteristics than the turbulence levels.

However, to validate the above statement, and to fully understand the effect of  $S$ , additional detailed flow measurements need to be performed. Furthermore, in *Chapter 9*, the effect of fin spacing is further investigated and the optimum FCCS configuration presented.

## 8.1.2 Flow Measurements Parallel to Fin Side Wall

### 8.1.2.1 Effect of Fan Amplitude ( $V_{Pz}$ )

The results presented here, pertain to a horizontally-mounted fan and were obtained using the experimental setup depicted in Figure 5.22. Figure 8.8 highlights the variation in the magnitude of the mean vectors at different  $V_{Pz}$  for  $S = 40.0mm$  (control experiment). To aid comparison, the mean and turbulence plots presented in this section have been scaled identically to the respective plots presented in **Chapter 7**. In this experimental setup, the flow symmetry is once again noted. For the various fan voltages, the magnitude of the upward flow is equivalent to that travelling downwards. Furthermore, results indicate that the fan is not as efficient in cooling the *FSW* as the *FB*.

The sequence of images depicted in Figure 8.8 indicates that an increase in  $V_{Pz}$  results in an increase in the magnitude of the mean vectors, in particular, the principal velocity  $\overline{V_y}$  along the *FB* (i.e.  $Z_{Pos} = 0.0mm$ ). When a vibrational amplitude equivalent to  $V_{Pz} = 30.00V$  was applied, the disturbance area in the neighbourhood of the fan tip was found to be minimal, with a  $\overline{V_{Mean}} = 0.413m/s$ . However, as the equivalent vibrational amplitude was increased to  $V_{Pz} = 115.0V$ , the maximum mean velocity  $\overline{V_{Mean}}$  recorded increased to  $0.751m/s$ , as shown in Table 8.4. Operating the fan at the peak amplitude (Figure 8.8) generated a flow disturbance in excess of  $60mm$  ( $30mm$  in each direction) in the oscillation direction, and a further disturbance of  $15mm$  in the transverse direction ( $z$ -axis).

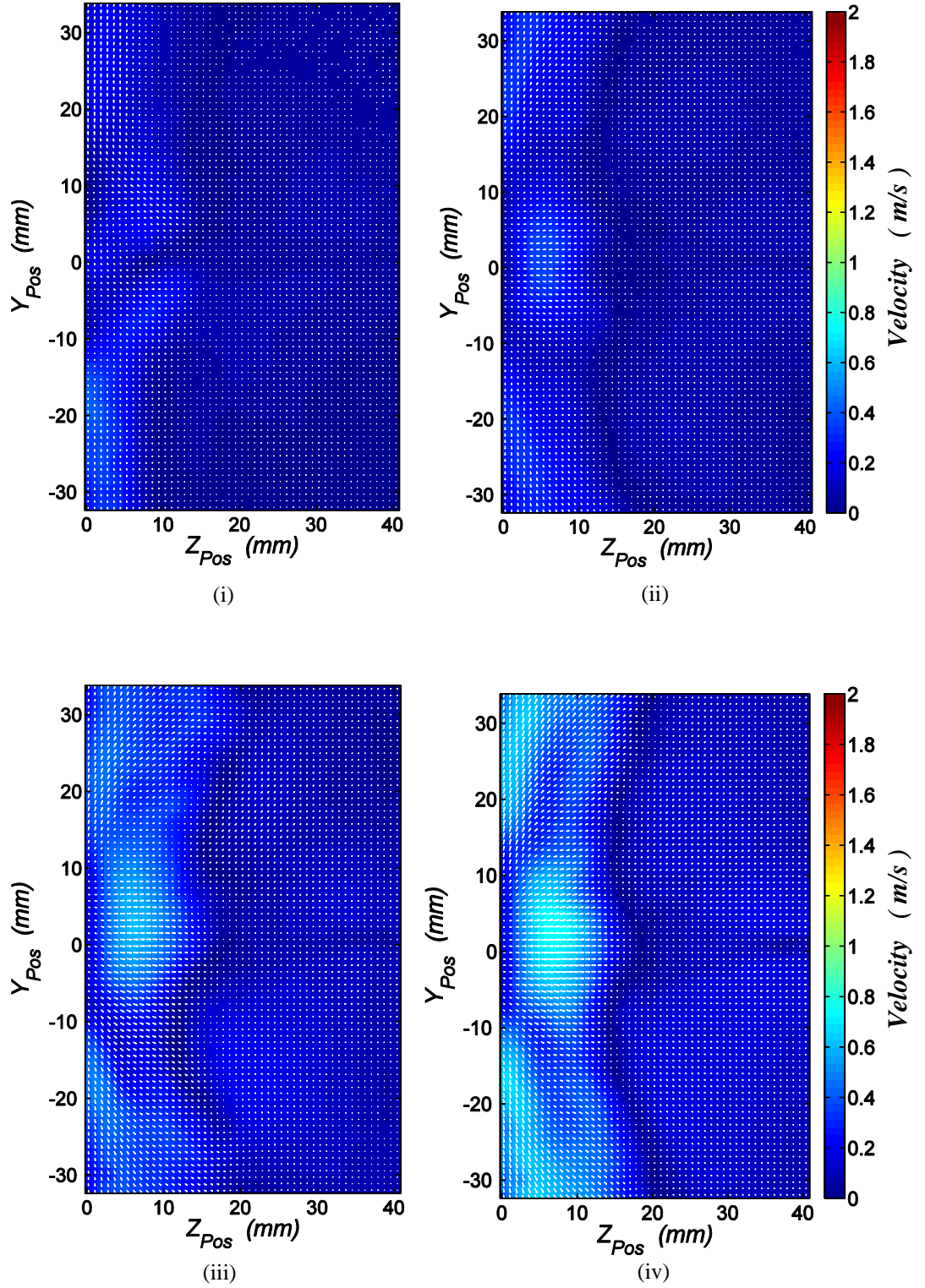


Figure 8.8: Magnitude of the *FSW* Mean Vectors for  $S = 40.0\text{mm}$ ,  $G = 10.0\text{mm}$  and:

(i)  $V_{P_z} = 30.00V$  (ii)  $V_{P_z} = 60.00V$  (iii)  $V_{P_z} = 90.00V$  (iv)  $V_{P_z} = 115.0V$



$V_{Pz}$ (V)	$\overline{V}_Y$ (m/s)	$\overline{V}_Z$ (m/s)	$\overline{V}_{Mean}$ (m/s)
30.00	0.413	0.261	0.413
60.00	0.439	0.371	0.472
90.00	0.473	0.596	0.598
115.0	0.637	0.746	0.751

Table 8.4: FSW Peak Velocity Measurements -  $S = 40.00mm, G = 10.0mm$

A closer inspection of Figure 8.8iv (as well as Figure 8.10) shows a distinct change in the flow behavioural characteristics. While the flow is still being propelled along the *FB* (*Motion A* and *Motion B*), the flow in the immediate vicinity of the piezoelectric fan tip is seen to travel in the opposite direction (+ve  $z$ -direction) to the general direction - (*Motion C*). This can be further explained by considering Figure 8.9 and Figure 8.10.

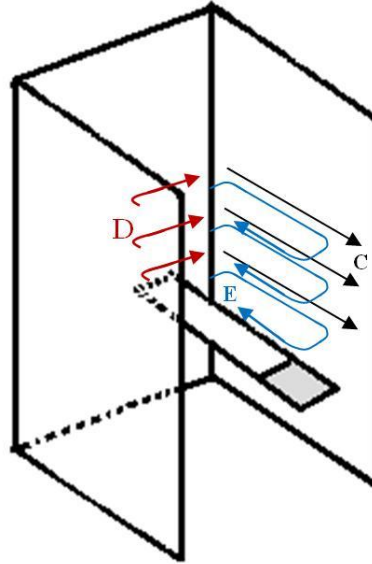


Figure 8.9: 3D Flow Pattern developed in Vertical Finned Channel



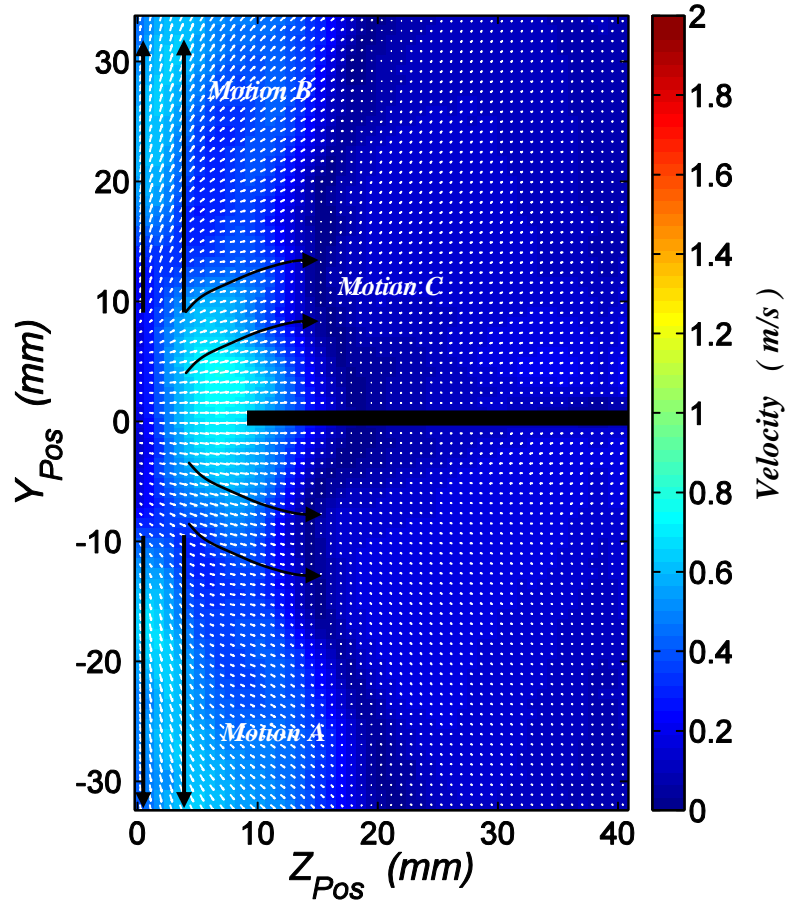


Figure 8.10: Unsteady Flow generated by Piezoelectric Fan, *S40 G10.0 V115.0* – Front View

Figure 8.9 depicts the 3D flow patterns generated by a horizontally-mounted oscillating piezoelectric fan in a straight finned channel. The propelled air is seen to leave the fan tip and impact the *FB*. As discussed in **Section 8.1.1**, the flow travels along both the  $y$  - direction (*Motion A* and *Motion B*), as well in the  $x$  – direction (*Motion D*). The latter flow travels along the *FB* in the  $x$ -direction until contact with the *FSW* is made. On contact with the latter surface, the bulk motion (*Motion C*) travels along the *FSW* in a direction which opposes the flow generated at the fan tip, which explains the previously presented plots (Figure 8.8). The air is then sucked back in by the fan (*Motion E*).

Additional trends are shown when considering the turbulence characteristics on the *FSW* (Figure 8.11). It may be concluded that the effect of the fan on the *FSW* is significantly less than on the *FB*, as seen from the magnitude of the velocities and the affected area. The magnitude of the *RMS* of the fluctuating

component increases from  $0.2394\text{m/s}$  when  $V_{pz} = 30.00V$  to  $0.4636\text{m/s}$  when  $V_{pz} = 115.0V$ .

When the flow characteristics (bulk and turbulence) are compared to the cooling plots (Figure 6.10), adequate agreement is observed. In Figure 6.10, the highest magnitude cooling is located adjacent to the *FB* and this agrees with the mean flow plots (Figure 8.10).

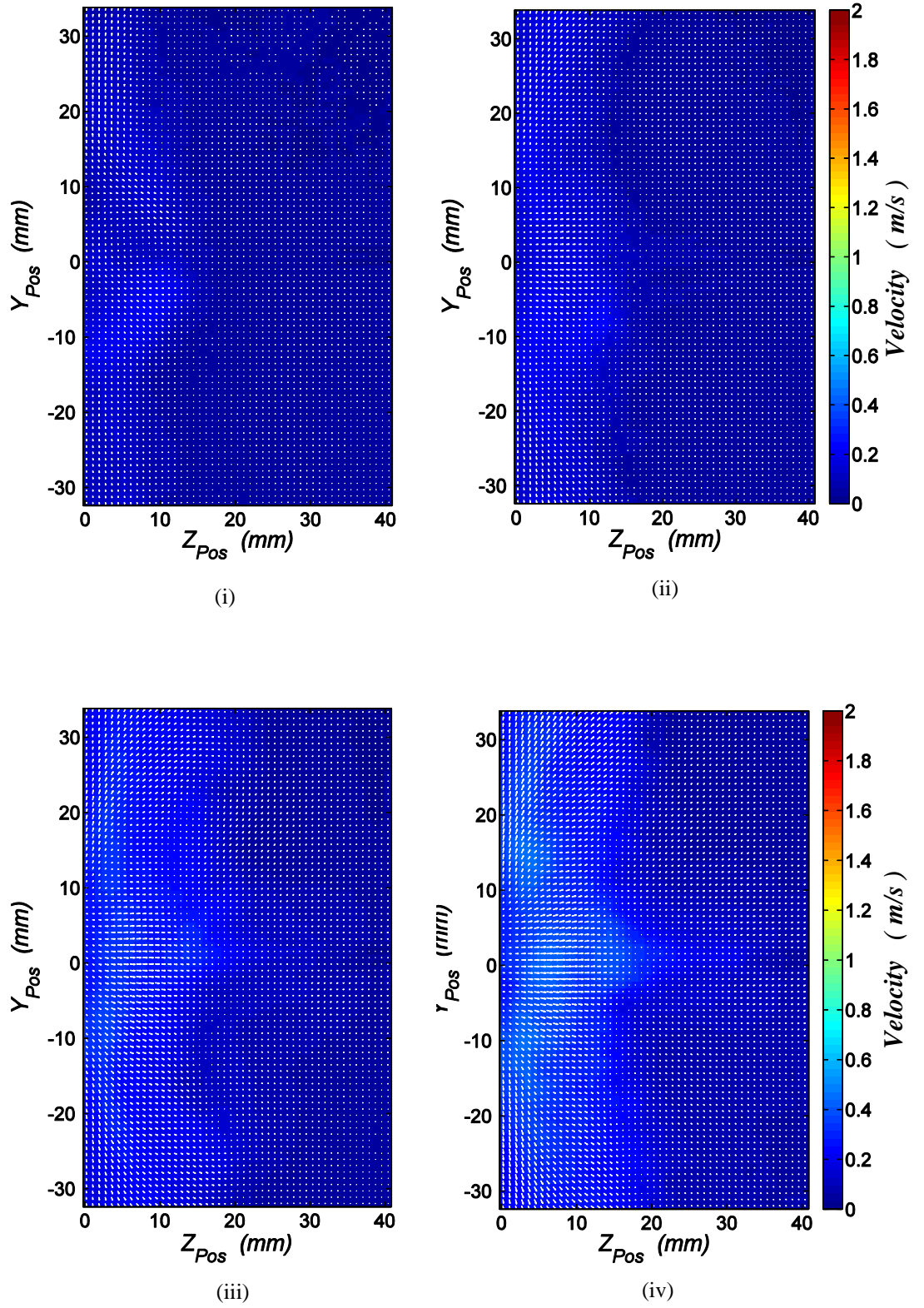


Figure 8.11: FSW RMS of Fluctuating Components for  $S = 40.0mm$ ,  $G = 10.0mm$  and;  
 (i)  $V_{P_z} = 30.00V$  (ii)  $V_{P_z} = 60.00V$  (iii)  $V_{P_z} = 90.00V$  (iv)  $V_{P_z} = 115.0V$

### 8.1.2.2 Effect of Separation Distance ( $G$ )

The effect of separation distance ( $G$ ) on the flow fields generated by a horizontally-mounted fan on the *FSW* are reported here.

A reduction in  $G$ , sees a decrease in the mean velocity together with a decrease in coverage area (Figure 8.12). The maximum  $\overline{V}_{\text{Mean}}$  decreases from  $0.8916\text{m/s}$  when  $G = 15.0\text{mm}$ , to  $0.834\text{m/s}$  when  $G = 5.0\text{mm}$ .

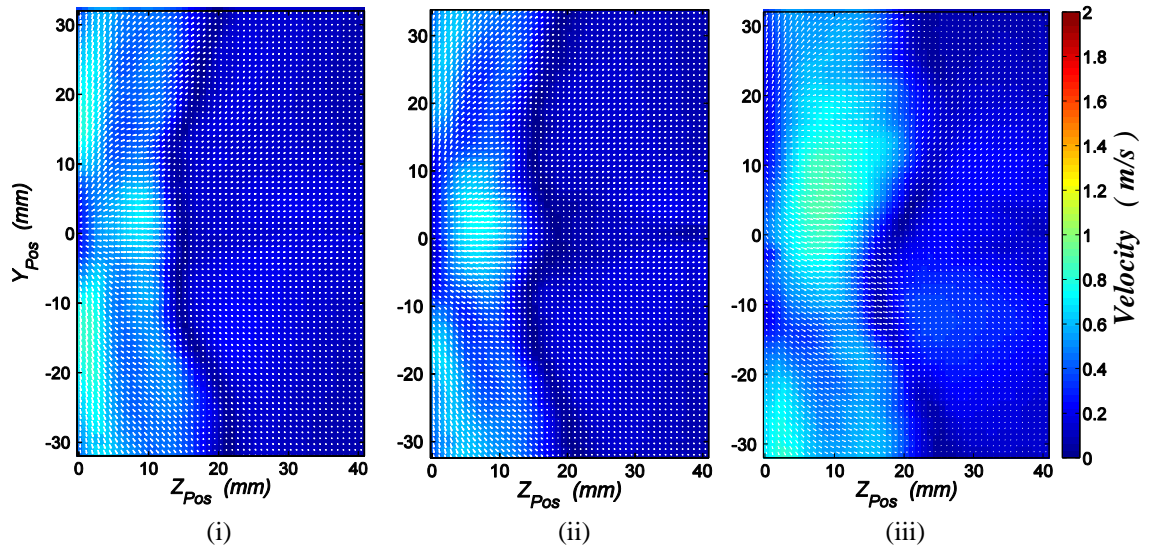


Figure 8.12: Effect of  $G$  on the *FSW* Magnitude of the Mean Vectors -  $V_{p_z} = 115.0\text{V}$ ,  $S = 40.0\text{mm}$ :

(i)  $G = 5.0\text{mm}$

(ii)  $G = 10.0\text{mm}$

(iii)  $G = 15.0\text{mm}$

At the smallest separation distance, little air is available to the fan (due to the presence of the long fin side walls). This in turn results in low fan effectiveness. However, with an increase in  $G$ , more air is readily available to the fan, which in turn results in an increased fan cooling effectiveness and hence in large mean velocities on the *FSW*'s.

On considering the turbulence plots (Figure 8.13), the above scenario is further realised. At small separation distances, as little air finds its way to the fan tip, a minimalistic disturbance originates. However, this disturbance is seen to increase with an increase in  $G$ .

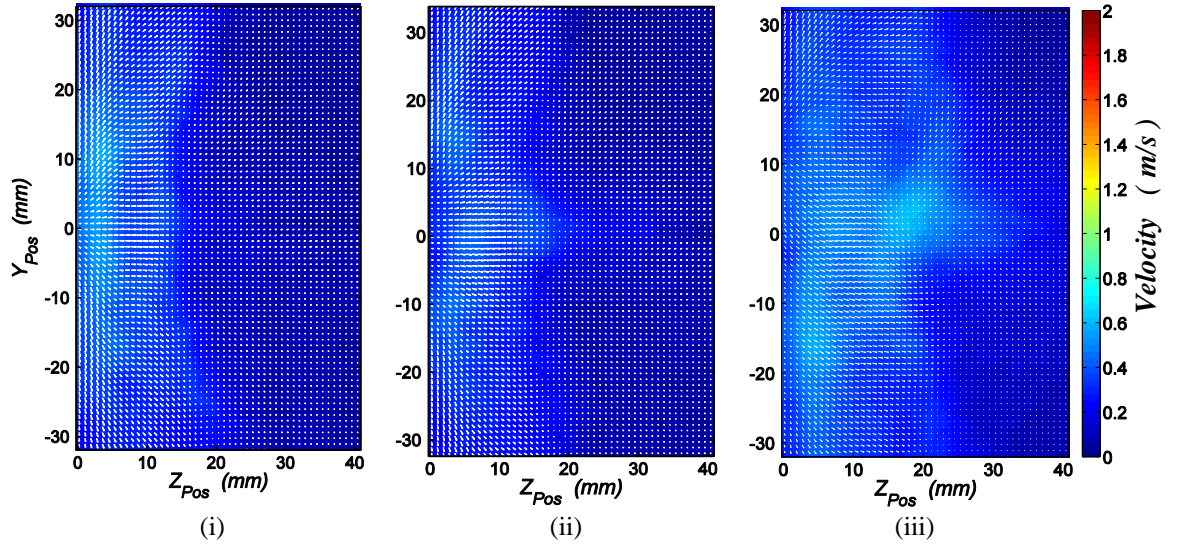


Figure 8.13: Contour Plots of the *FSW STDV* Component -  $V_{Pz} = 115.0\text{V}$ ,  $S = 40.0\text{mm}$ :

(i)  $G = 5.0\text{mm}$

(ii)  $G = 10.0\text{mm}$

(iii)  $G = 15.0\text{mm}$

This ties in well with the cooling plots presented in **Chapter 6**, in particular Figure 6.10, which indicates that larger  $G$  values are beneficial when cooling the *FSW*.

### 8.1.2.3 Effect of Fin Spacing ( $S$ )

Figure 8.14 depicts the effect of  $S$  on the resulting mean vectors. As previously discussed, a small fin spacing constrains the flow (Figure 8.14i), thus channelling the flow along the  $FB$  and the  $FSW$ . However, with an increase in  $S$  (Figure 8.14iii), the airflow is less constrained and thus is able to occupy a larger volume and thus does not adhere to  $FSW$  surface resulting in a lower fan cooling ability (as reported in **Chapter 6**).

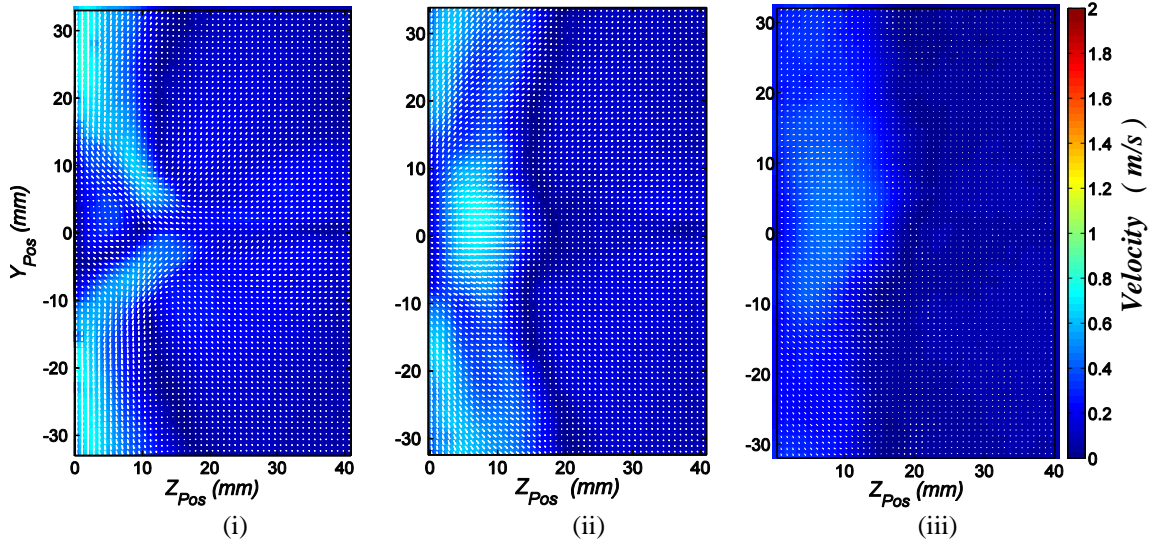


Figure 8.14: Effect of  $S$  on the Magnitude of the Mean Vectors:  $V_{Pz} = 115.0V$ ,  $G = 10.0mm$ :

(i)  $S = 30.0mm$

(ii)  $S = 40.0mm$

(iii)  $S = 50.0mm$

In Figure 8.14i, for a fin spacing of  $30.0mm$ , the flow is seen to originate at the fan tip and is propelled forward along the fin base ( $Z_{Pos} = 0.0mm$ ), the maximum principal velocity of which approaches  $\overline{V}_Y = 0.820m/s$ . On the other hand, for a fin spacing of  $40.0mm$  (the base case configuration) and  $50.0mm$ , the flow spreads out to occupy a larger area, with a maximum principal velocity of  $\overline{V}_Y = 0.637m/s$ , and  $\overline{V}_Y = 0.296m/s$  respectively.

It may be concluded that while the affected cooling area increases with an increase in fin spacing, the magnitude of the flow travelling along the  $FSW$  drops off (from  $0.820m/s$  to  $0.296m/s$ ). The same results are noted on

considering the turbulence contour plots produced in this configuration - Figure 8.15. For the minimal considered fin spacing, a high disturbance originates in close proximity to the oscillating fan ( $Y_{Pos} = 0.0mm$ ). However, this local disturbance disappears when  $S$  increases.

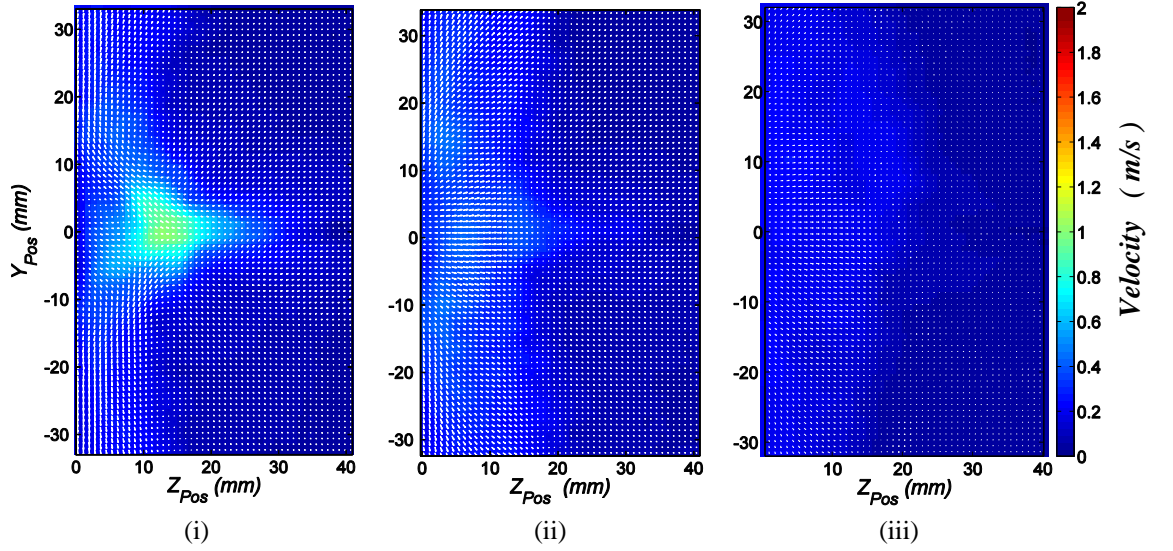


Figure 8.15: Effect of  $S$  on the FSW Turbulence contour plots -  $V_{Pz} = 115.0V$ ,  $G = 10.0mm$  :

(i)  $S = 30.0mm$

(ii)  $S = 40.0mm$

(iii)  $S = 50.0mm$

Once again, the above result has been attributed to the presence of the fin side walls. Maintaining a minimal fin spacing approximates the flow to a 2D flow, resulting in a highly constrained stream of air (of large velocity) flowing over the FSW. However, with an increase in  $S$ , the flow is less channelled and spreads out to occupy a larger volume. Thus, any eddies generated have a larger volume in which to dissipate their energy while increasing the possibility of cancelling each other out.

### 8.1.3 Summary

Experimental results indicate that for a horizontally-mounted fan, operating at the maximum vibrational amplitude, a minimal separation distance ( $G$ ) is beneficial in cooling the  $FB$  (i.e.  $V_{Pz} = 115.0V, G = 5.0mm$ ). However, when cooling the  $FSW$ 's, a larger separation distance is beneficial (i.e.  $V_{Pz} = 115.0V, G = 15.0mm$ ). The determination of the optimum  $G$  shall be evaluated when considering the overall cooling of the entire unit cell (heat sink), the results of which are presented in **Chapter 9**. These results strongly agree with those presented in **Chapter 6** and bear close resemblance to the flow characteristics presented in **Chapter 7**. From this result it may be concluded that the same optimum  $FCCS$  configuration holds for a vertical flat surface and a vertical finned heat sink.

Furthermore, for the present fan orientation, a minimal fin spacing ( $S$ ) is found to be highly more effective on both the  $FB$  and  $FSW$ 's when compared to larger fin spacings. This agrees with the cooling plots presented in **Chapter 6**.



## 8.2 Vertically-mounted Fan

The results presented here pertain to a vertically-mounted piezoelectric fan, operating at its natural frequency of  $f = 60\text{Hz}$ . The 2D flow characteristics on both the fin base (*Section 8.2.1*) and the fin side wall's (*Section 8.2.2*) are presented, and the key trends discussed.

As was performed in the previous section, a base case (control experiment) of  $S = 40.0\text{mm}$  was maintained to which the resulting flow characteristics from the other geometries were compared.

### 8.2.1 Flow Measurements Parallel to Fin Base

#### 8.2.1.1 Effect of Fan Amplitude ( $V_{Pz}$ )

The results here were obtained using the experimental setup depicted in Figure 5.21. As in the previous case (horizontally-mounted fan), operating the fan at peak amplitude generates a flow disturbance of  $40\text{mm}$  ( $20\text{mm}$  in each direction) in the oscillation direction, and a further disturbance of at least  $60\text{mm}$  ( $30\text{mm}$  in each direction) in the transverse direction (Figure 8.16). Furthermore, for the various applied fan voltages, the magnitude of the upward travelling flow is similar to that travelling downwards. However, in this setup, a slight flow asymmetry exists along the y-axis. As mentioned in *Chapter 7*, it is believed that this was caused by the flow obstruction presented to the incoming air by the 3D positioning system.

Figure 8.16 highlights the variation in the magnitude of the mean vectors at different  $V_{Pz}$  when the fin spacing is set to  $S = 40.0\text{mm}$ . The sequence of images indicate that an increase in  $V_{Pz}$  results in an increase in the magnitude of the mean vectors ( $\overline{V_X}$ ,  $\overline{V_Y}$  and  $\overline{V_{\text{Mean}}}$ ).

For this finned geometry, the flow is seen to originate at the blade tip and travel symmetrically along the x-axis until contact with the fin side walls.

After contact, the flow is seen to travel along the *FSW*'s in both the positive and negative *y*-directions. Furthermore, the *FSW*'s limit the incoming air available to the fan thus hindering the flow and resulting in lower  $\%h_{mc}$  values on the *FB* when compared to an unfinned geometry. However, the channelling of the flow along the *FSW*'s (Figure 8.16iv) indicates that an appreciable amount of cooling should arise on these surfaces.

On applying  $V_{Pz} = 30.00V$ , the disturbance area in the neighbourhood of the fan tip is minimal, with a  $\overline{V_{Mean}} = 0.366m/s$ . However, as the vibrational amplitude is increased to  $V_{Pz} = 115.0V$ , the maximum mean velocity  $\overline{V_{Mean}}$  to be recorded increases to  $1.055m/s$  as listed in Table 8.5. A direct comparison between Figure 8.1 and Figure 8.16 (or Table 8.1 and Table 8.5) once again highlights the fact that the magnitude of the mean vectors produced by a vertically-mounted piezoelectric fan on the *FB* is significantly less than that produced by a horizontally mounted piezoelectric fan (from a maximum value of  $1.970m/s$  for a horizontally-mounted piezoelectric fan to  $1.055m/s$  for a vertically-mounted piezoelectric fan).

$V_{Pz}$ (V)	$\overline{V_X}$ (m/s)	$\overline{V_Y}$ (m/s)	$\overline{V_{Mean}}$ (m/s)
30.00	0.315	0.191	0.366
60.00	0.358	0.461	0.461
90.00	0.673	0.852	0.857
115.0	0.908	1.052	1.055

Table 8.5: *FB* Peak Velocity Measurements -  $S = 40.00mm, G = 10.0mm$

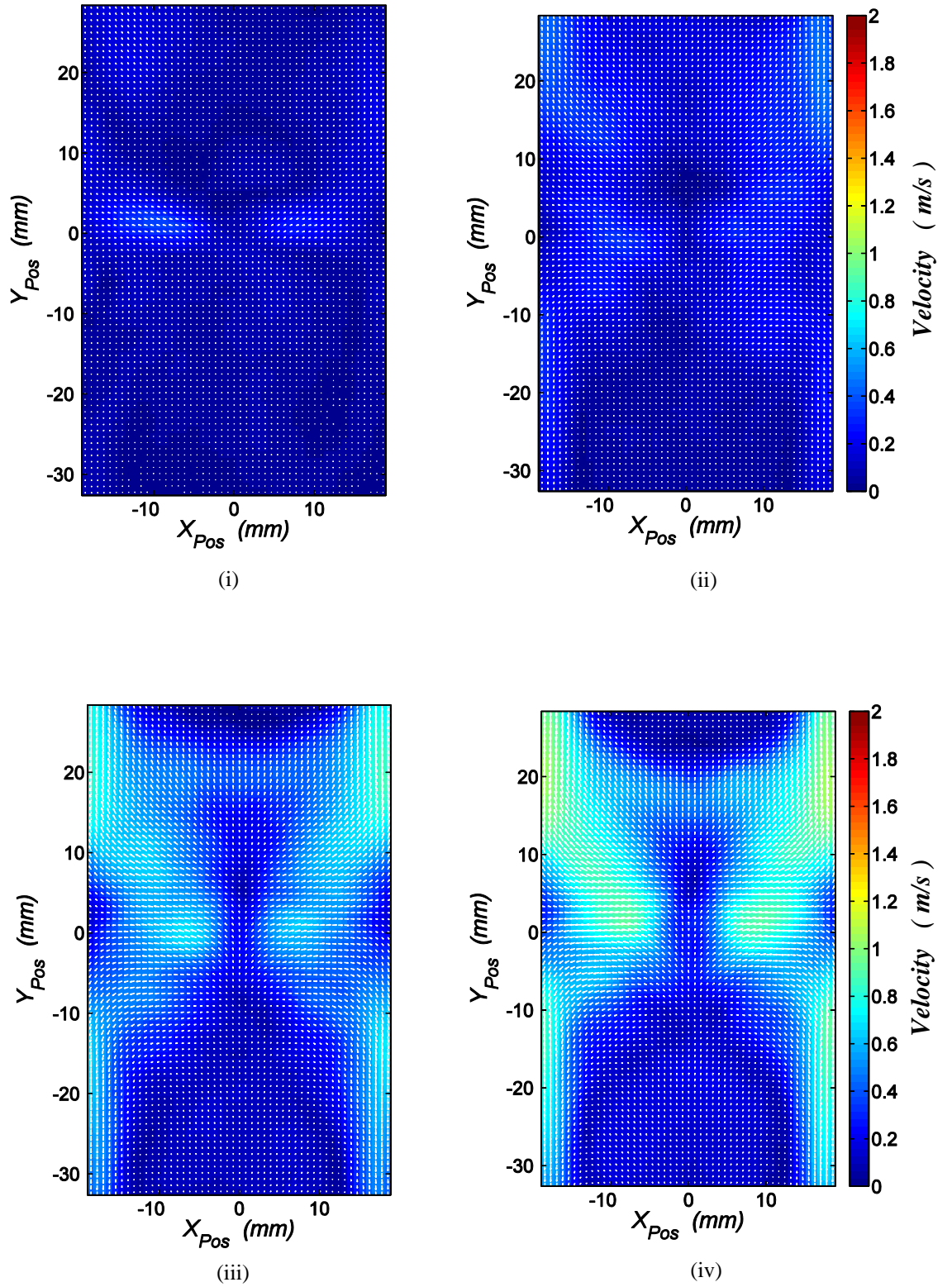


Figure 8.16: Magnitude of the *FB* Mean Vectors for  $S = 40.0mm$ ,  $G = 10.0mm$  and;

(i)  $V_{P_z} = 30.00V$  (ii)  $V_{P_z} = 60.00V$  (iii)  $V_{P_z} = 90.00V$  (iv)  $V_{P_z} = 115.0V$

Figure 8.16 further indicates that like in the previous chapter (**Chapter 7**), a zero velocity (stagnation region) occurs at the fan tip datum region. On closer inspection of the contour plots, it can be seen that the resulting patterns differ significantly from those presented in **Chapter 7**, indicating that the presence of the *FSW*'s greatly affects the resulting flow regimes, and indicating also that different cooling patterns should result. This holds true as the cooling plots presented in **Chapter 6** (in particular Figure 6.13) also indicate that the cooling patterns are preferentially oriented to the principal velocity ( $\overline{V_x}$ ). This result further complements earlier published results that state that, for a horizontally-mounted fan, the recorded cooling patterns were preferentially oriented in the primary oscillation direction ( $\overline{V_y}$ ) – i.e. vertically.

The resulting turbulence characteristics are depicted in Figure 8.17. While negligible turbulence is observed at low  $V_{Pz}$ , at  $V_{Pz} = 90.00V$  a centrally located disturbance of moderate magnitude results, while at  $V_{Pz} = 115.0V$  a different flow regime arises. This takes the form of a stagnant region at the fan tip datum position surrounded by two symmetric circular patterns of high magnitude. It is believed that the pattern change is due to a change in flow behaviour, i.e. a transition region. As the objective of this work was to investigate the cooling potential of piezoelectric fans and gauge if they are a feasible solution to implement to cool aerospace *PMSM*'s, an investigation into the above flow transition was deemed out of scope.

The peak magnitude of the *RMS* of the fluctuating component is equivalent to  $0.207m/s$  when the minimal voltage is applied. However, as the applied voltage increases, both the affected area as well as the magnitude, increases, reaching a maximum peak velocity of  $1.150m/s$ .

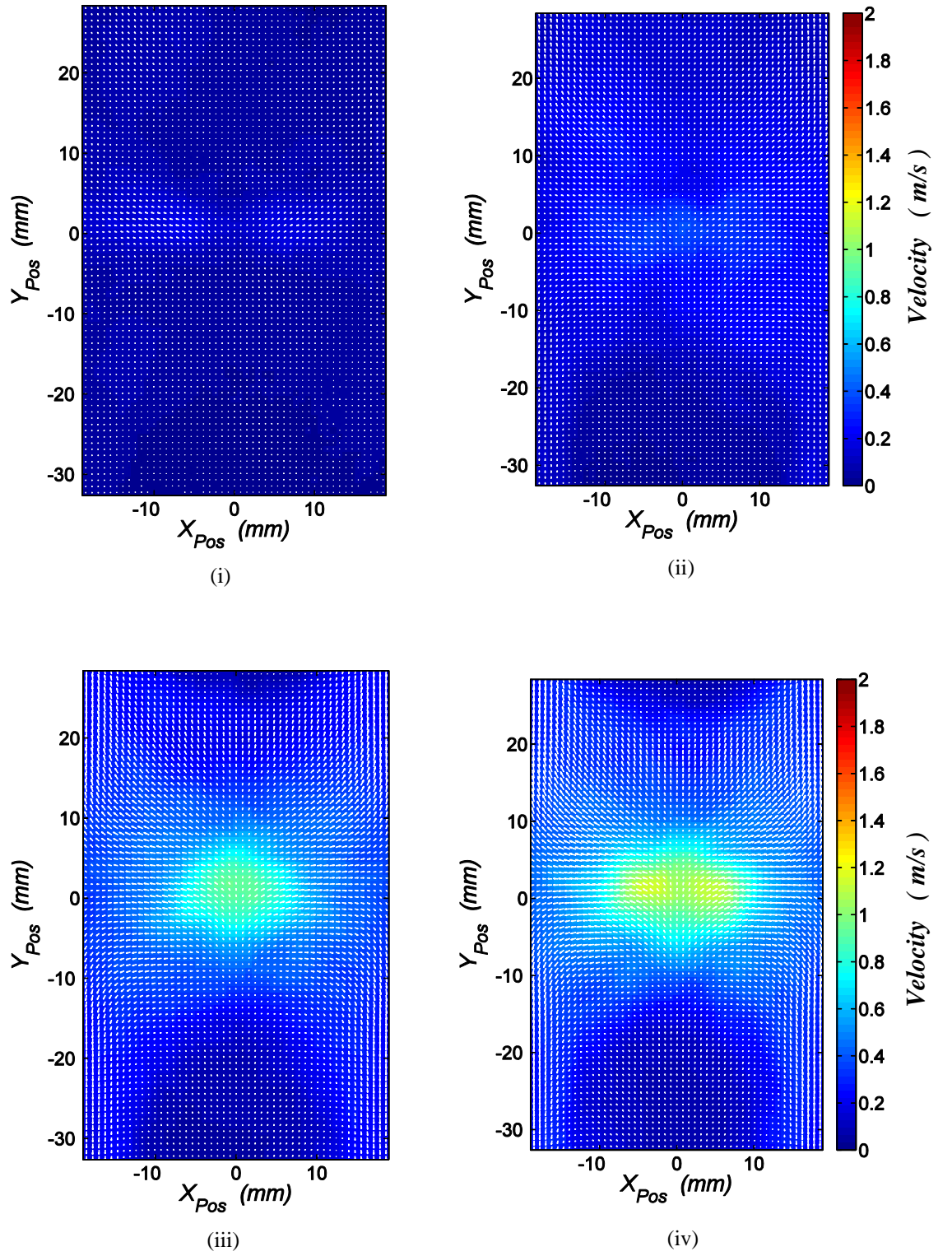


Figure 8.17: *FB RMS* of Fluctuating Components for  $S = 40.0mm$ ,  $G = 10.0mm$  and;  
 (i)  $V_{Pz} = 30.00V$  (ii)  $V_{Pz} = 60.00V$  (iii)  $V_{Pz} = 90.00V$  (iv)  $V_{Pz} = 115.0V$

On considering the turbulence patterns, several commonalities to those produced on a flat plate (Figure 7.20) can be identified. At low amplitudes a central symmetric disturbance originates. However, with an increase in amplitude, symmetrical circular lobes originate on either side of the stagnation band. Furthermore, the size of the turbulence correlates directly to the band of maximum cooling ( $\%h_{inc.}$ ) presented in **Chapter 6** (Figure 6.13). Furthermore, the turbulence generated in this orientation is significantly less than that produced for a horizontally-mounted fan. When the FCCS is operated at  $V_{Pz} = 115.0, G = 10.0mm$ , the maximum disturbance generated by a horizontally-mounted fan is  $V_{RMS} = 2.038m/s$  while for a vertically-mounted fan, the maximum  $V_{RMS} = 1.150m/s$  - a significant reduction.

Turbulence intensity profile plots, at three different locations ( $X_{Pos} = -10mm$ ,  $X_{Pos} = 0mm$  and  $X_{Pos} = 10mm$ ), for the above (Figure 8.17) contour plots are illustrated.

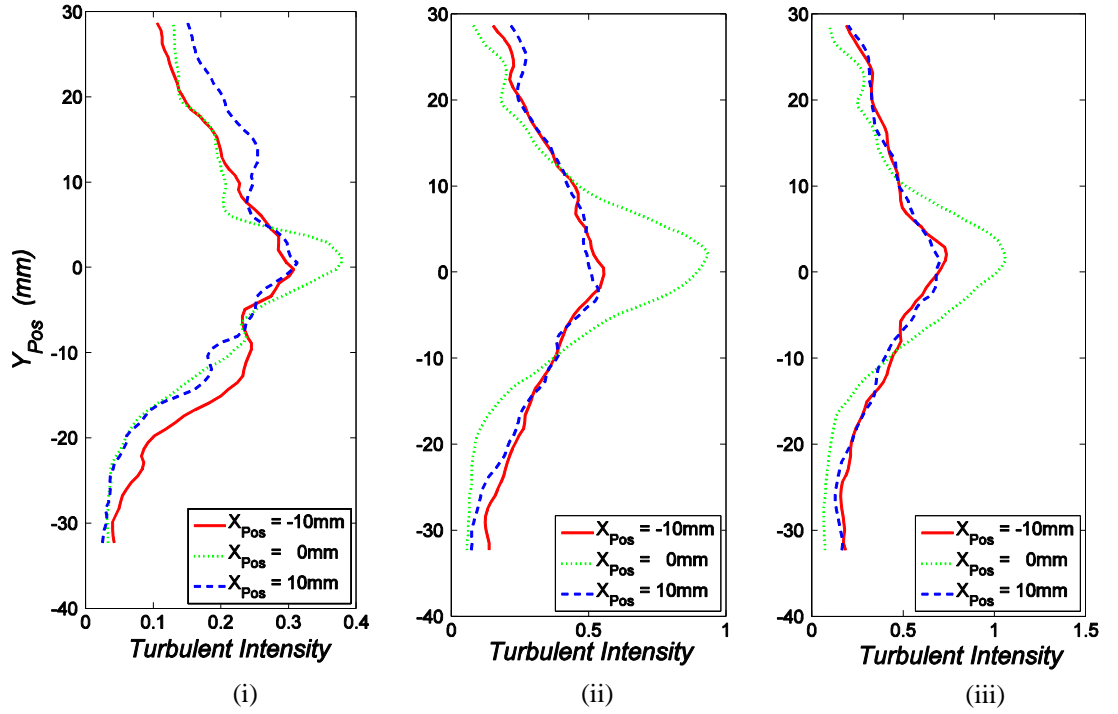


Figure 8.18: Direct comparison of the FB Turbulence Intensity for -  $S = 40.0mm, G = 10.0mm$ :

(i)  $V_{Pz} = 60.00V$       (ii)  $V_{Pz} = 90.00V$       (iii)  $V_{Pz} = 115.0V$

The trends in Figure 8.18 complement earlier presented results. That is, the maximum turbulence intensity level occurs in the neighbourhood of the vibrational envelope, with the peak at the fan tip datum position ( $Y_{Pos} = 0.0mm$ ). Furthermore, the turbulence intensity profiles at locations  $X_{Pos} = -10mm$  and  $X_{Pos} = 10mm$  follow the same shape and practically also have the same magnitudes, once again indicating the flow symmetry. The magnitudes (at all locations) are significantly less than those generated by a horizontally-mounted fan. This result further indicates that a horizontally-mounted fan is more suited to cool the *FB* than a vertically-mounted fan.

### 8.2.1.2 Effect of Separation Distance ( $G$ )

The effect of separation distance ( $G$ ) on the flow fields is illustrated in Figure 8.19. A reduction in  $G$ , sees a decrease in the  $\overline{V}_Y$  component, and an increase in both the principal velocity  $\overline{V}_X$ , and  $\overline{V}_{Mean}$  components. The maximum principal velocity ( $\overline{V}_X$ ) increases from  $0.472\text{m/s}$  when  $G = 15.0\text{mm}$ , to  $0.908\text{m/s}$  when  $G = 10.0\text{mm}$  and to  $1.439\text{m/s}$  when  $G = 5.0\text{mm}$ . Furthermore, at  $G = 15.0\text{mm}$ ,  $\overline{V}_{Mean} = 1.373\text{m/s}$  and when  $G = 5.0\text{mm}$ ,  $\overline{V}_{Mean} = 1.443\text{m/s}$ . It is important to reiterate that the uncertainty in the above velocity measurements is that of  $0.5\%$  as quoted in **Chapter 5**.

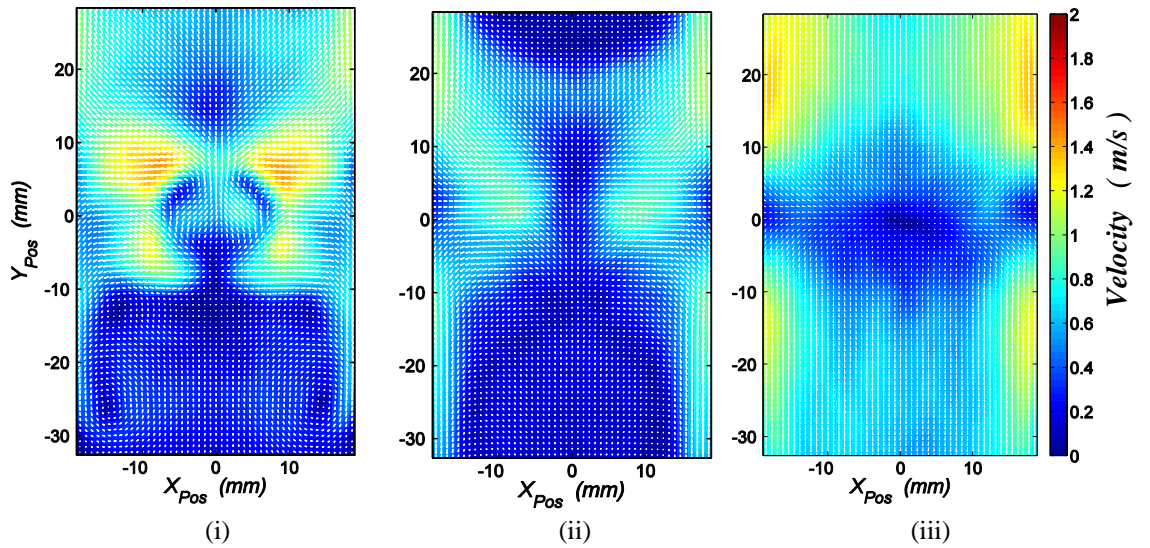


Figure 8.19: Effect of  $G$  on the  $FB$  Magnitude of the Mean Vectors -  $V_{Pz} = 115.0V$ ,  $S = 40.0\text{mm}$ :  
 (i)  $G = 5.0\text{mm}$                       (ii)  $G = 10.0\text{mm}$                       (iii)  $G = 15.0\text{mm}$

A distinct change in the flow behaviour occurs with a reduction in  $G$ . For large separation distances, the bulk of the flow is aligned vertically – i.e. transverse to the oscillation direction and is seen to occupy the full width of the set fin spacing. The intermediate  $G$  results in a decrease in coverage area. In this case, however, the flow is seen to first, travel in the oscillation direction and then, align itself to the  $FSW$  and travel along the length of the fins. On further reducing  $G$ , the flow is seen to be preferentially oriented in the



oscillation direction, with minimal flow along the *FSW*'s. In the latter case, i.e. in Figure 8.20, two distinct circulation regions (vortices) result. These are located adjacent to the *FSW*'s and are labelled (*Vortex A*, *Vortex B*). While a counter clockwise rotating vortex is produced adjacent to the left *FSW* (*Vortex A*), the converse holds on the opposite (right) *FSW*, i.e. a clockwise vortex originates (*Vortex B*). If the flow asymmetry was not a contributing factor, it is believed that an additional two vortices would result at the top of the image flow field.

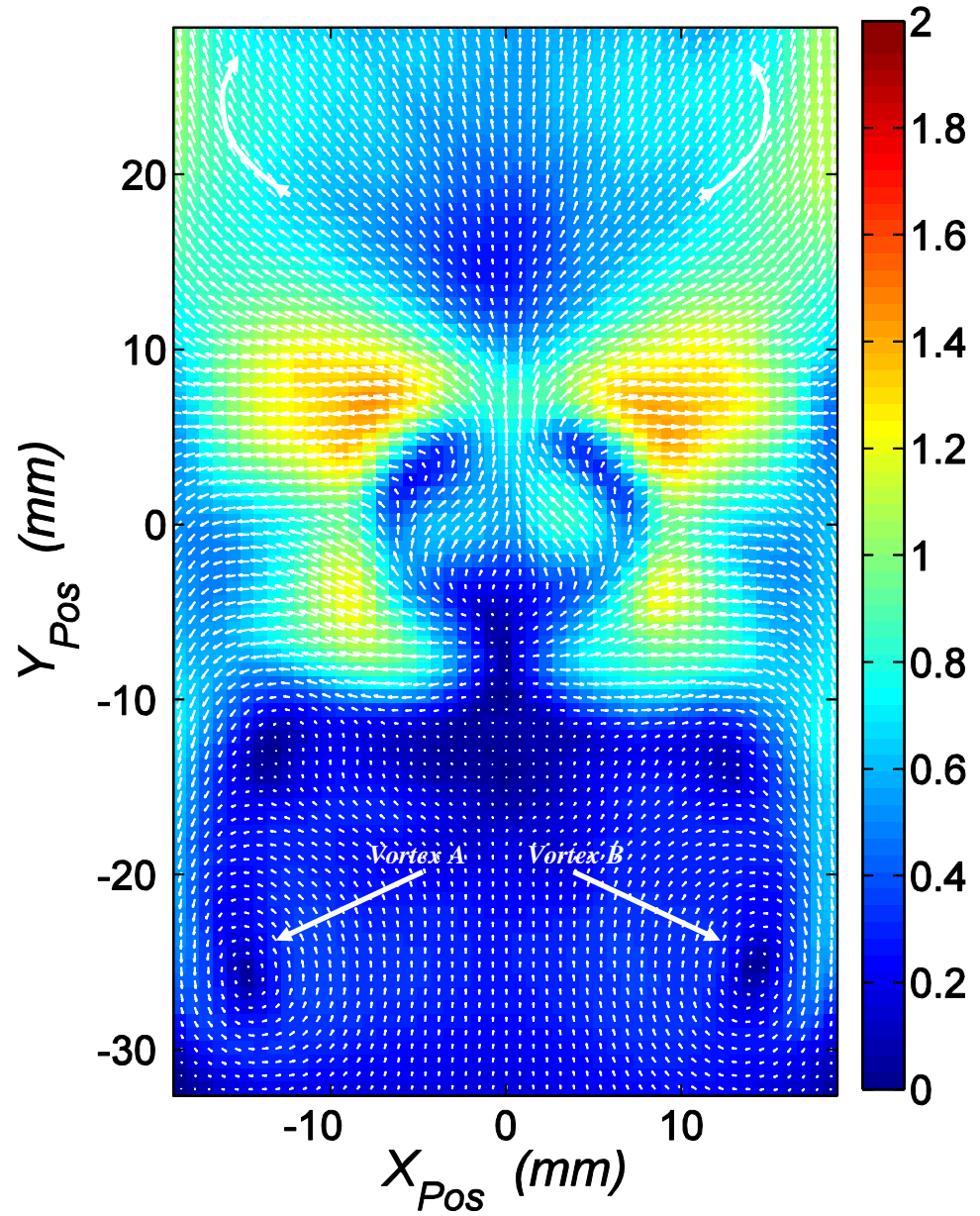


Figure 8.20: Shedding of Vortices -  $S = 40.0\text{mm}$ ,  $G = 5.0\text{mm}$ ,  $V_{Pz} = 115.0V$

The presence of the vortices, together with the flow regime shown indicate that air expelled by the fan, when travelling along the *FSW*, does not adhere permanently to the walls, but at a certain point, comes away from the surface with sufficient energy to produce vortices. These high energy vortices aid in mixing the flow which in turn increases the wall heat transfer coefficients.

The above results indicate that a greater enhancement in heat transfer ( $\%h_{Inc.}$ ) on the *FB* should arise at lower separation distances. This compares well with the cooling plots presented in Figure 6.13.

A similar result is shown when considering the turbulence contour plots (Figure 8.21). Once again, the turbulence originates from the fan datum position and spreads symmetrically outwards. Similar trends to those presented in **Section 8.1.1.2** result for a vertically-mounted fan. For all considered separation distances, the main component of turbulence is horizontally (oscillation direction), along the *x-axis*. A decrease in *G* results in an increase in the maximum  $STDV_x, STDV_y, V_{RMS}$ . It was further established that, at  $G = 15.0mm$ , the maximum  $V_{RMS}$  value reached was  $1.025m/s$  while when  $G = 5.0mm$ , the maximum  $V_{RMS}$  value reached was that of  $1.908m/s$ . Thus, the largest air disturbance occurred for the minimal separation distance,  $G = 5.0mm$ . This trend is also seen in a horizontally-mounted fan. However, in this orientation, both a lesser magnitude and a lesser coverage area result when compared to a horizontally-mounted fan, in particular Figure 8.5.

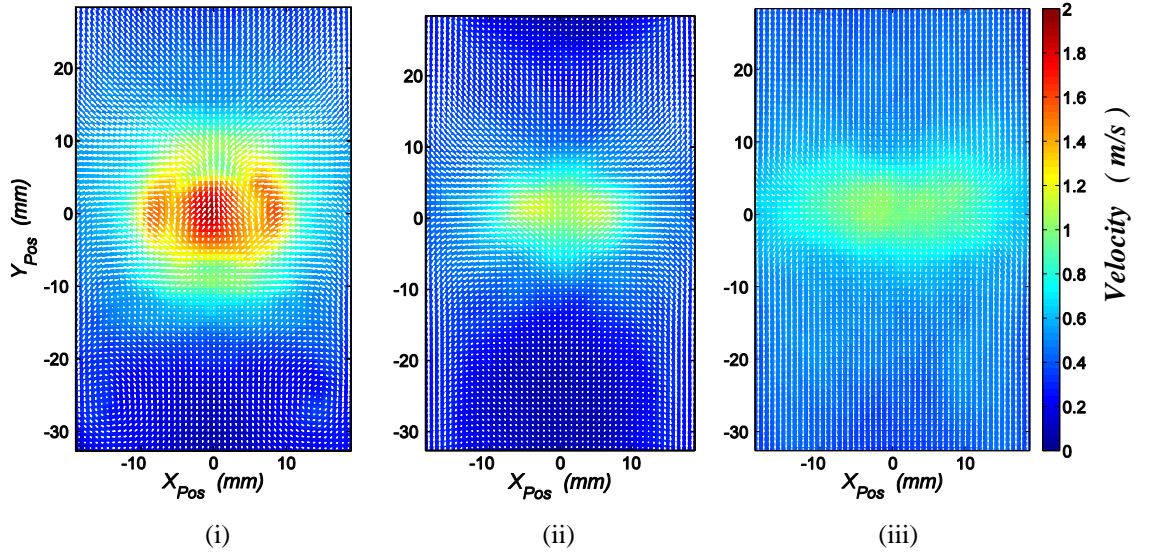


Figure 8.21: Contour Plots of the *FB STDV* Component -  $V_{Pz} = 115.0V$ ,  $S = 40.0mm$ :

i)  $G = 5.0mm$

ii)  $G = 10.0mm$

iii)  $G = 15.0mm$

The above trends once again agree with the results reported and presented in **Chapter 6** and **Chapter 7**. The latter section also indicated that, an increase in the fan oscillation amplitude as well as a decrease in the separation distance both result in an increase in the overall magnitude of the mean vectors and turbulence levels.

### 8.2.1.3 Effect of Fin Spacing ( $S$ )

The effects of the fin spacing on the flow fields produced are illustrated in Figure 8.22 (magnitude of the mean vectors) and Figure 8.23 (turbulence maps). With a decrease in fin spacing, the generated flow regimes differ significantly. For the largest fin spacing ( $S = 50.0mm$ ), the flow originating from the fan tip travels preferentially along the oscillation direction (i.e. along the  $x$ -axis - with a minimal  $\overline{V_y}$  component), until impacting the  $FSW$ 's. When the air comes in contact with the two fin side walls, the flow travels symmetrically along the  $FSW$ 's, as depicted in **Section 8.2.2**. However, the same does not hold for the minimal fin spacing  $S = 30.0mm$ , where a significant change in the flow regime was noted. The flow was not preferentially oriented in the oscillation direction, but along the  $y$ -axis, and negligible air movement was noted along the  $FSW$ 's as depicted in **Section 8.2.2**.

The change in behaviour is due to the proximity of the  $FSW$ 's ( $A_{p-p} = 25.40, S = 30.0mm$ ). In **Chapter 6** it was established that, for the maximum  $FB$  cooling, a narrower fin spacing is beneficial. However, on inspecting the flow characteristics presented in Figure 8.22 and Figure 8.23 respectively, the latter statement is negated. That is, the flow characteristics and the thermal characteristics are not in agreement.

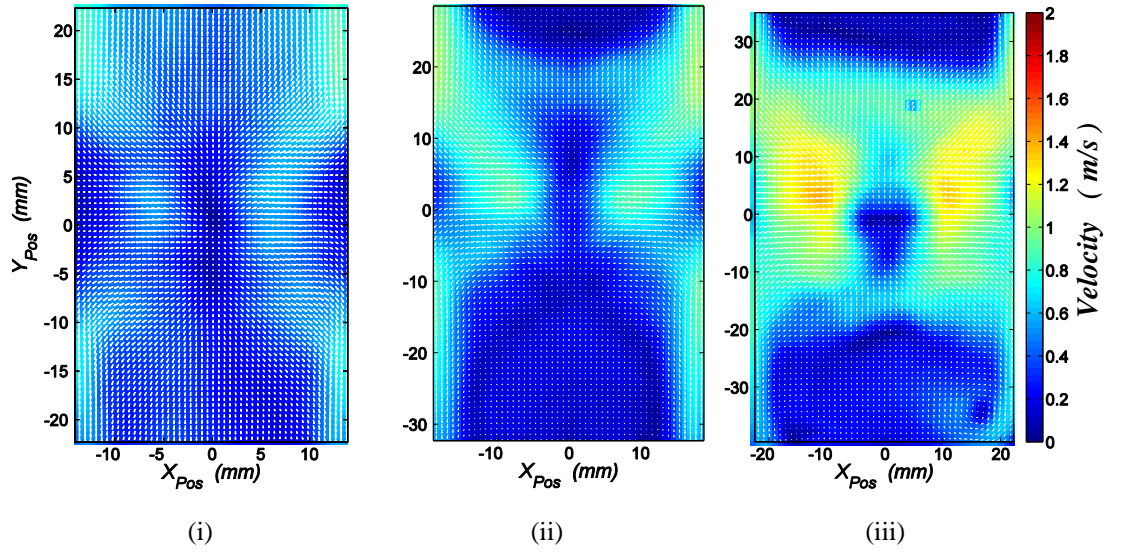


Figure 8.22: Magnitude of the *FB* Mean Vectors -  $V_{P_z} = 115.0V, G = 10.0\text{mm}$  :  
 i)  $S = 30.0\text{mm}$       ii)  $S = 40.0\text{mm}$       iii)  $S = 50.0\text{mm}$

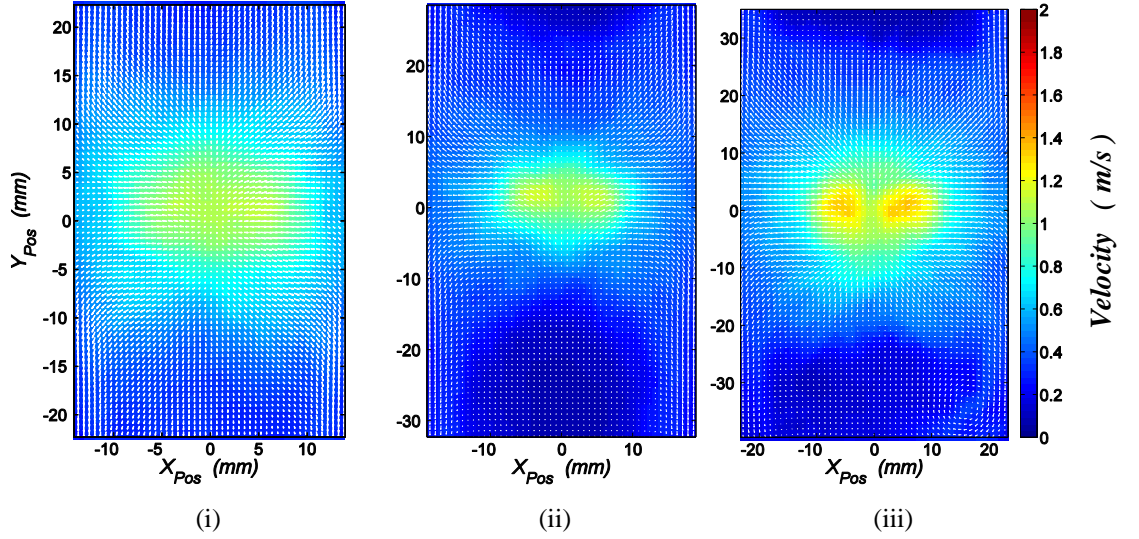


Figure 8.23: Contour Plots of the *FB* RMS values of the Fluctuating Component -  
 $V_{P_z} = 115.0V, G = 10.0\text{mm}$  :  
 i)  $S = 30.0\text{mm}$       ii)  $S = 40.0\text{mm}$       iii)  $S = 50.0\text{mm}$

Table 8.6 lists the numerical data (average  $\overline{V_x}$ , peak  $\overline{V_x}$ ,  $\overline{V_{\text{Mean}}}$ ) together with the turbulence characteristics ( $STDV_x$ ) and the results obtained on a vertical flat plate (**Chapter 7**).

When considering the turbulence characteristics, the patterns are also of prime importance. For the minimum spacing, a symmetrical horizontally-oriented elliptical band of high disturbance results. For a larger fin spacing ( $S = 40.0\text{mm}$ ), two distinct high magnitude symmetrical bands form at either side of the fan tip datum position (stagnation region). At  $S = 50.0\text{mm}$ , the same characteristics are more intensely seen.

Fin Spacing ( $S$ ) (mm)	Avg $\overline{V_x}$ (m/s)	Peak $\overline{V_x}$ (m/s)	$STDV_x$ (m/s)
<b>30.0</b>	0.187	0.558	0.986
<b>40.0</b>	0.253	0.908	0.998
<b>50.0</b>	0.370	1.398	1.146
Vertical Flat Surface ( $S = \infty$ )	0.473	1.770	1.311

Table 8.6: Effect of Fin Spacing ( $S$ ),  $G = 10.0\text{mm}$ ,  $V_{Pz} = 115.0\text{V}$  on the  $FB$  Velocities

From the table of results, further conclusions may be drawn. Firstly, it is noted that the flow characteristics and the thermal characteristics do not match. At first glance, the presented table indicates that a large fin spacing is more beneficial than a narrow fin spacing (which contradicts the cooling plots presented in **Chapter 6**). However, as good agreement between all flow and thermal measurements has been attained (so far), it is believed that the current  $PIV$  measurements presented in this section are also accurate indicating that the mismatch between the thermal and flow characteristics is further indicative of the complex  $3D$  flow regimes generated by the current setup.

A further explanation of the mismatch in results may be attributed to the proximity of the  $FSW$ 's. For a fin spacing of  $S = 50.00$ , the jet of air from the

fan tip is fully developed and attaches itself to the *FB*, and then travels along *FSW*'s. However, for  $S = 30.00$ , due to the close proximity of the *FSW*'s ( $A_{p-p} \cong S$ ) the air from the fan tip on impact, does not attach itself to the *FB* but comes away from the surface generating a significant out of plane motion. It is believed that this out of plane motion is responsible for the cooling plots presented in **Chapter 6**. As the out of plane motion cannot be measured in the current setup, it is recommended, that additional *PIV* measurements are performed on a plane perpendicular to the *FB* (along the fan centre line), with an experimental setup similar to that of Figure 7.8.

From Table 8.6, it can further be deduced that all values (for both bulk and turbulent flow) are less than the corresponding values produced by a horizontally-mounted piezoelectric fan, signifying, once again that a horizontally-mounted piezoelectric fan is more effective than a vertically-mounted one in terms of generating flow over the *FB*. This result further compliments the thermal data presented in **Chapter 6**.

## 8.2.2 Flow Measurements Parallel to Fin Side Wall

### 8.2.2.1 Effect of Fan Amplitude ( $V_{Pz}$ )

The results presented, pertain to a vertically-mounted fan and were obtained using the experimental setup depicted in Figure 5.22. In this experimental setup, flow symmetry is once again noted. For the various applied fan voltages, the magnitude of the upward flow is equivalent to that travelling downwards. Furthermore, initial results indicate that the fan is not as efficient in cooling the *FSW*, as the *FB*. Figure 8.24 highlights the variation in the magnitude of the mean vectors at different  $V_{Pz}$  when the fin spacing is set to  $S = 40.0mm$  (control experiment). It is worth mentioning that for comparative reasons, the mean and turbulence plots presented in this section have been scaled identically to the respective plots presented in **Chapter 7**.

The sequence of images depicted in Figure 8.24 indicate that an increase in  $V_{Pz}$  again results in an increase in the  $\overline{V_Y}$  along the *FB* (i.e.  $Z_{Pos} = 0.0mm$ ) and in an increase in  $\overline{V_Z}$ . On the application of  $V_{Pz} = 30.00V$ , the disturbance area in the neighbourhood of the fan tip is minimal, with a  $\overline{V_{Mean}} = 0.154m/s$ . However, as the vibrational amplitude is increased to  $V_{Pz} = 115.0V$ , the maximum mean velocity  $\overline{V_{Mean}}$  to be recorded increased to  $0.973m/s$ , as listed in Table 8.7. Operating the fan at the latter peak amplitude generates a flow disturbance in excess of  $30mm$  in the  $z$ -direction, and a  $60mm$  ( $30mm$  in each direction) along the  $y$ -axis.



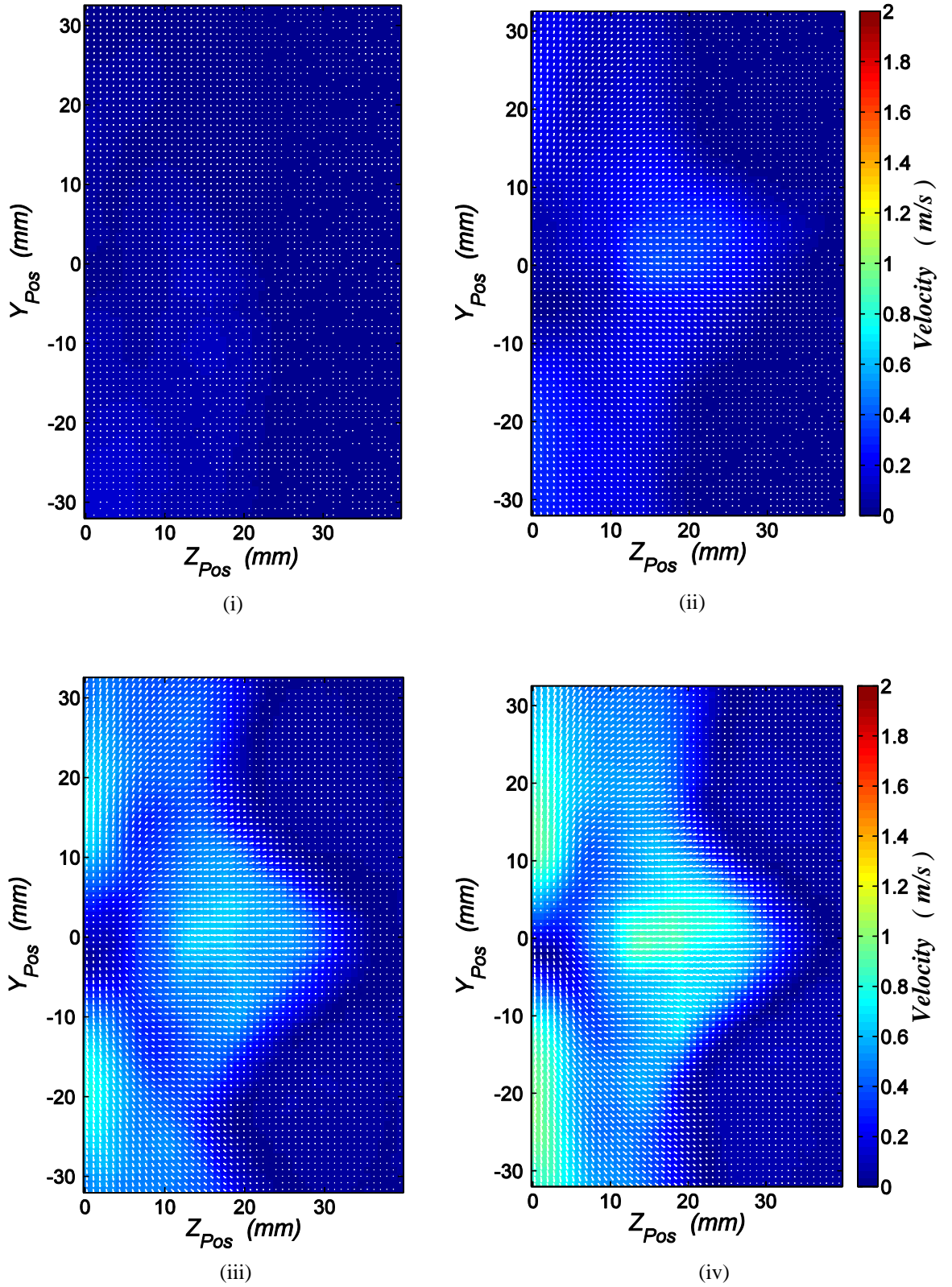


Figure 8.24: Magnitude of the FSW Mean Vectors for  $S = 40.0\text{mm}$ ,  $G = 10.0\text{mm}$  and:  
 (i)  $V_{Pz} = 30.00\text{V}$     (ii)  $V_{Pz} = 60.00\text{V}$     (iii)  $V_{Pz} = 90.00\text{V}$     (iv)  $V_{Pz} = 115.0\text{V}$

Referring to Table 8.7, the magnitude of the mean vectors produced by a vertically-mounted piezoelectric fan is slightly larger than those produced by a horizontally-mounted piezoelectric fan (a maximum value of  $0.751\text{m/s}$  for a horizontally-mounted fan and  $0.973\text{m/s}$  for a vertically-mounted fan).

$V_{Pz}$ (V)	$\overline{V}_Y$ (m/s)	$\overline{V}_Z$ (m/s)	$\overline{V}_{Mean}$ (m/s)
30.00	0.154	0.107	0.154
60.00	0.326	0.375	0.377
90.00	0.753	0.650	0.764
115.0	0.965	0.894	0.973

Table 8.7: Peak Velocity Measurements -  $S = 40.00\text{mm}$ ,  $G = 10.0\text{mm}$

In this setup, similar flow characteristics to those obtained for a horizontally-mounted fan result (Figure 8.10). On closer inspection of Figure 8.25, the flow ejected by the fan tip is propelled forward and travels symmetrically along the *FB* (*Motion A* and *Motion B*). However, the flow is also seen to fold on itself and travel opposite to the general direction ( $\overline{V}_Z$ ) along the *FSW* - *Motion C*, further indicating the unsteady 3D nature of the flow regime. *Motion C* emphasises the fact that there is a significantly large out-of-plane motion. When the piezoelectric fan oscillates (in - and out - of the plane of the ‘paper’), the flow (of higher velocity) is channelled along the *FSW* and results in the reversing of the velocity vectors as depicted in Figure 8.25.

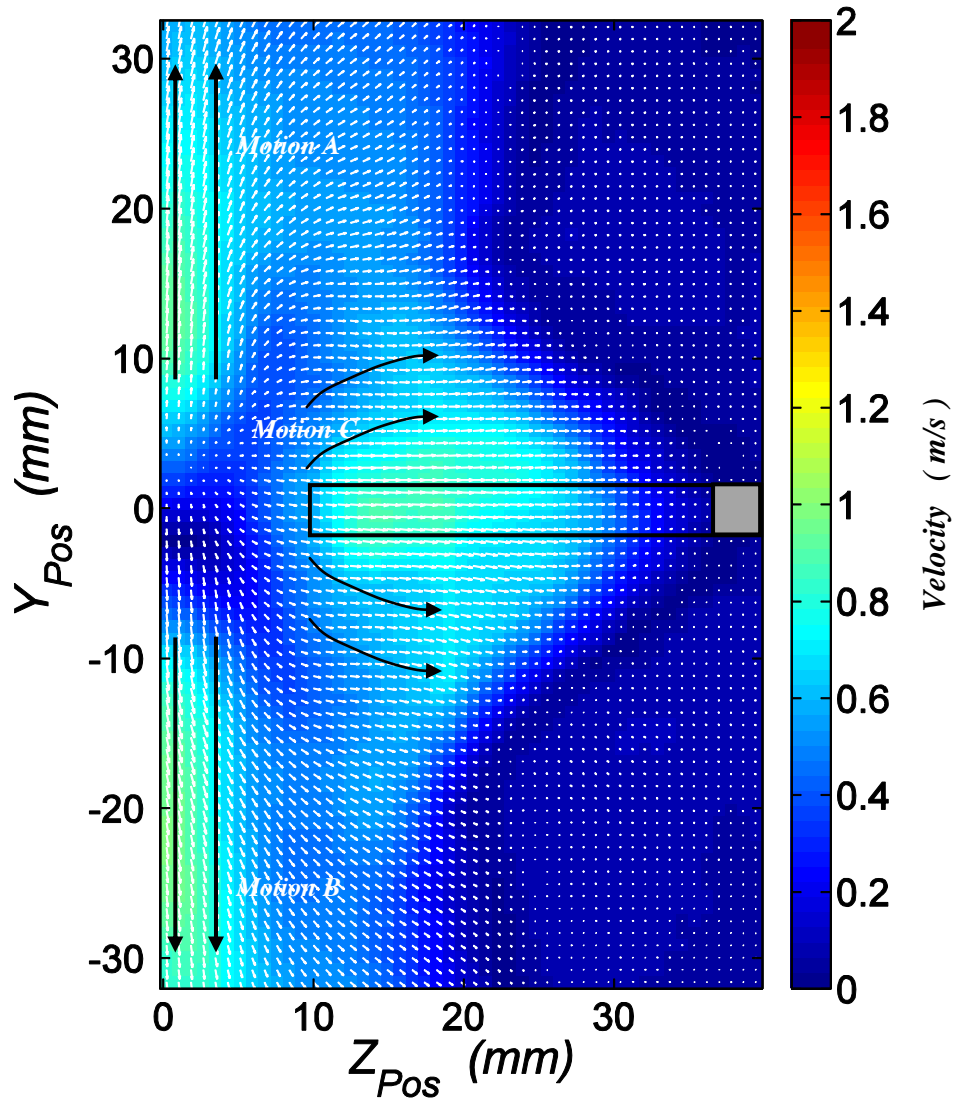


Figure 8.25: Unsteady Flow generated by Piezoelectric Fan on FSW - S40,  $G10.0$   $V_{PZ}=115.0V$ : Front View

A comparison of the individual  $\overline{V_z}$  profiles, at distinct locations ( $Z_{Pos} = 0mm$ ,  $Z_{Pos} = 5.0mm$  and  $Z_{Pos} = 10.0mm$ ) is also presented - Figure 8.26. For all  $V_{Pz}$ , similar trends result. That is, at the fan datum position, a maximum and positive  $\overline{V_z}$  results indicating that the fluid flow is moving to the right. Furthermore, the profile plots complement the presented 2D contour plots (Figure 8.24)

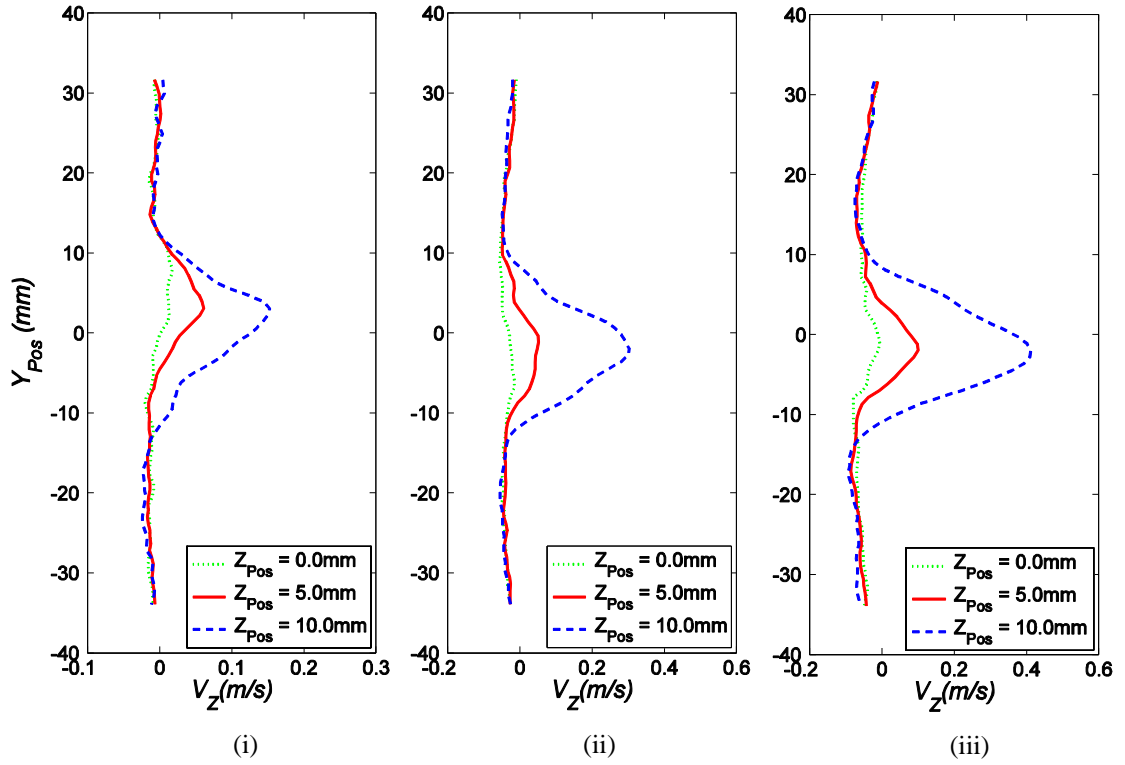


Figure 8.26: Direct comparison of the  $\overline{V_Z}$  for  $S = 40.0mm$ ,  $G = 10.0mm$  and:  
 (i)  $V_{Pz} = 60.00V$       (ii)  $V_{Pz} = 90.00V$       (iii)  $V_{Pz} = 115.0V$

Additional trends are shown when considering the turbulence characteristics on the *FSW*. Results indicate that the effect of the fan is significantly less than on the *FB*. The magnitude of the *RMS* of the fluctuating component increases from  $V_{RMS} = 0.087m/s$  when  $V_{Pz} = 30.00V$  to  $V_{RMS} = 0.4606m/s$  when  $V_{Pz} = 115.0V$ .

Comparing the flow characteristics (bulk and turbulence) to the cooling plots (Figure 6.18), good agreement is observed. In Figure 6.18, the highest cooling is located adjacent to the *FB*. That is high  $\%h_{Inc}$  values are attained on the *FSW* close to the *FB*.

Furthermore, when the flow characteristics were evaluated, it was established that a vertically mounted piezoelectric fan is more efficient in cooling the *FSW* compared to a horizontally-mounted one (Figure 8.13).

### 8.2.2.1 Effect of Separation Distance ( $G$ )

The affect of separation distance ( $G$ ) on the flow fields generated by a vertically-mounted fan on the  $FSW$  are reported here. A reduction in  $G$ , sees a decrease in the mean velocity together with a decrease in coverage area (Figure 8.27). The maximum  $\overline{V}_{Mean}$  decreases from  $1.293m/s$  when  $G = 15.0mm$ , to  $0.804m/s$  when  $G = 5.0mm$ .

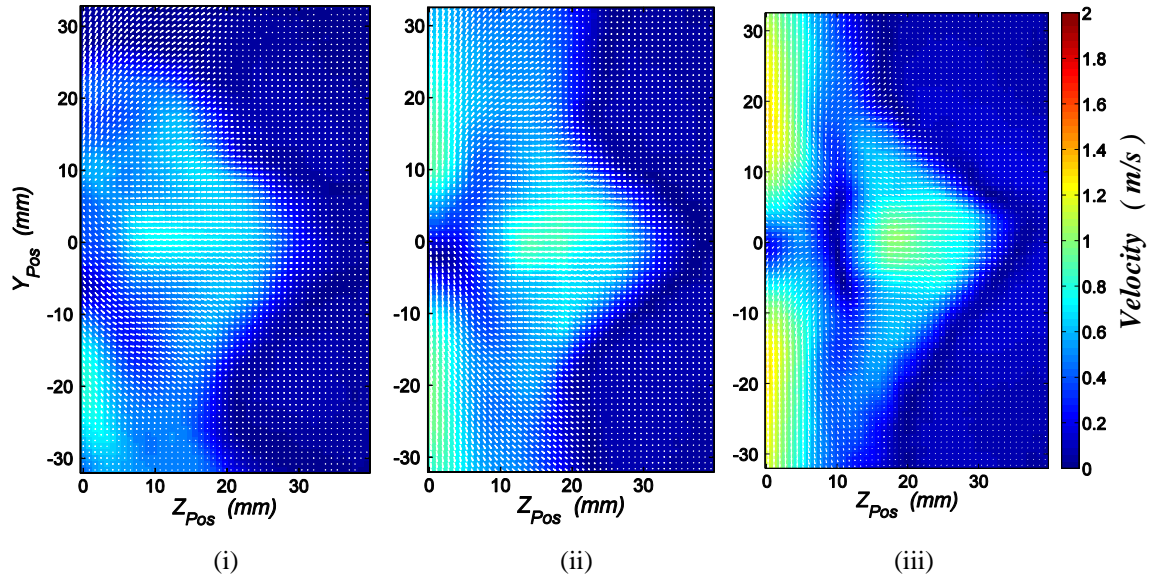


Figure 8.27: Effect of  $G$  on the Magnitude of the Mean Vectors  $FSW$  -  $V_{Pz} = 115.0V$ ,  $S = 40.0mm$ :  
 (i)  $G = 5.0mm$  (ii)  $G = 10.0mm$  (iii)  $G = 15.0mm$

Similar to a horizontally-mounted fan, at minimal separation distances, little air is available to the fan (due to the presence of the long fin side walls). This in turn results in low fan effectiveness. However, with an increase in  $G$ , more air is readily available to the fan, which in turn results in an increased fan cooling effectiveness and results in large mean velocities.

Thus, a reduction in the separation distance results in the decrease of the magnitude of the mean vectors fan (in particular those along the  $FB - \overline{V}_Y$ ). Similar results have been noted on evaluating the turbulence characteristics of the setup (Figure 8.28). At minimal separation distances, as little air finds its

way to the fan tip, a minimalistic disturbance originates. However, this disturbance is seen to increase with an increase in  $G$ .

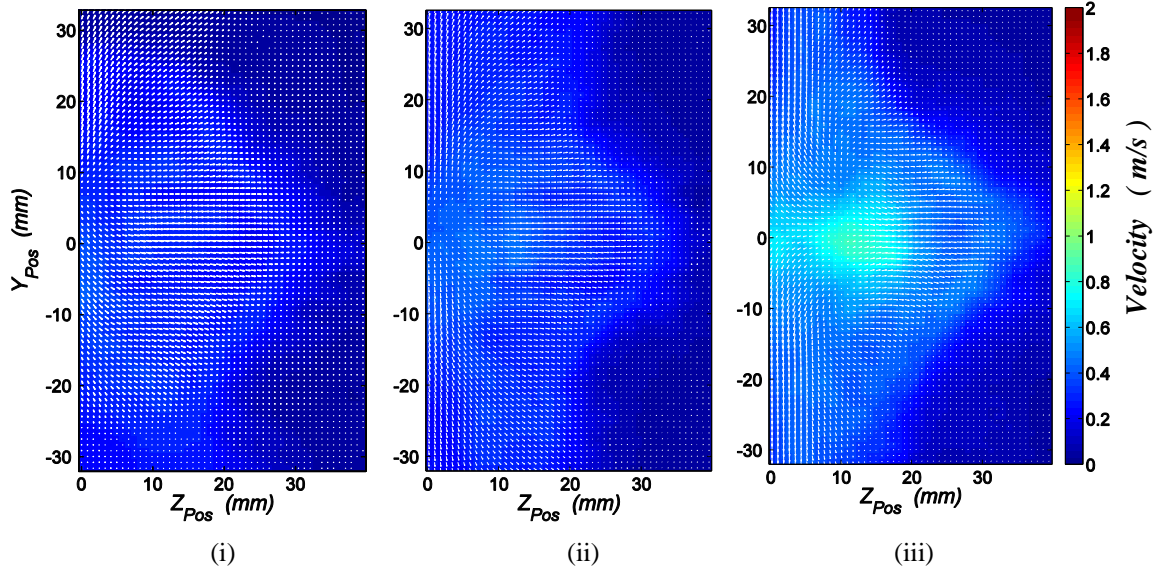


Figure 8.28: Contour Plots of the FSW STDV Component -  $V_{Pz} = 115.0V$ ,  $S = 40.0mm$ :

(i)  $G = 5.0mm$

(ii)  $G = 10.0mm$

(iii)  $G = 15.0mm$

Similar to a horizontally-mounted piezoelectric fan, for a vertically-mounted fan, large separation distances are always preferential to smaller separation distances. This ties in well with the cooling plots presented in **Chapter 6**, in particular Figure 6.18, which further indicates that larger  $G$  values are beneficial when cooling the FSW.

Furthermore, on comparing both the magnitude of the mean vector plots and the turbulence plots, it is evident that a vertically-mounted piezoelectric fan cools the FSW far more efficiently than a horizontally-mounted piezoelectric fan.

### 8.2.2.1 Effect of Fin Spacing ( $S$ )

Figure 8.29 depicts the effect of  $S$  on the mean vectors. As previously mentioned, a small fin spacing constrains the flow (Figure 8.29i), thus channelling the flow along the  $FB$ . However, with an increase in  $S$  (Figure 8.29iii), the airflow is less constrained and is thus able to occupy a larger volume, resulting in a significant  $FSW$  cooling (as reported in **Chapter 6**).

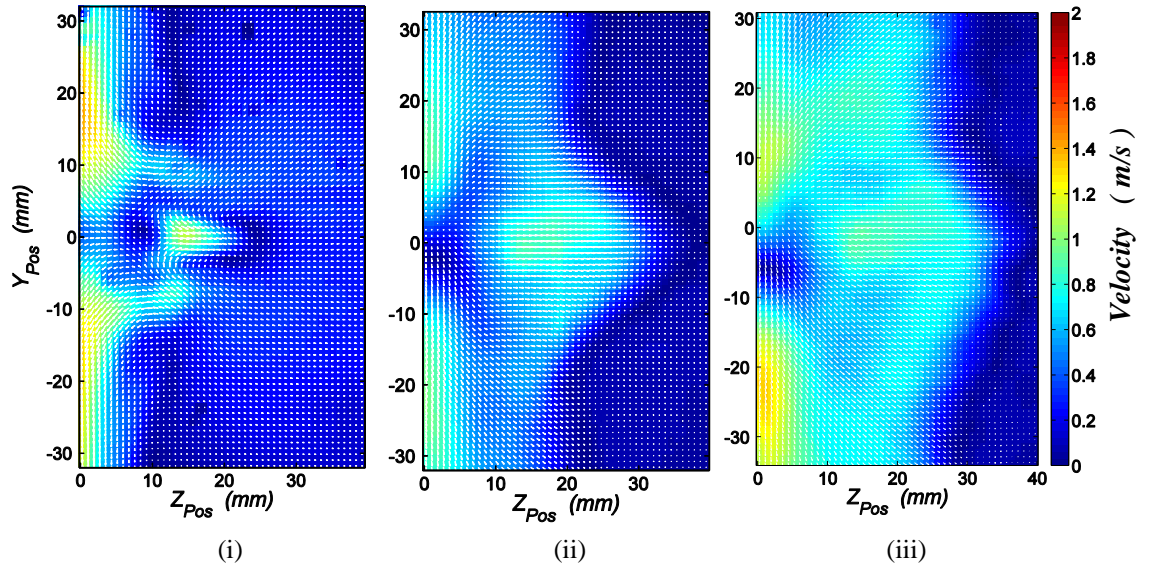


Figure 8.29: Effect of  $S$  on the  $FSW$  Magnitude of the Mean Vectors:  $V_{Pz} = 115.0V$ ,  $G = 10.0mm$ :

(i)  $S = 30.0mm$

(ii)  $S = 40.0mm$

(iii)  $S = 50.0mm$

For a fin spacing of  $30.0mm$ , the maximum resultant velocity approaches  $\overline{V_{Mean}} = 1.410m/s$ . For a fin spacing of  $40.0mm$  (the base case configuration) and  $50.0mm$ , the flow spreads out to occupy a significantly larger area, with a maximum  $\overline{V_{Mean}} = 0.9732m/s$ , and  $\overline{V_{Mean}} = 1.321m/s$  respectively. Therefore, from the above, it may be concluded that while the cooling area increases with an increase in fin spacing, the magnitude of the flow travelling along the  $FSW$  drops off slightly. The same results are noted when considering the turbulence contour plots produced in this configuration - Figure 8.30. For the smallest



fin spacing, a high disturbance originates in close proximity to the oscillating piezoelectric fan. However, this disturbance disappears with an increase in  $S$ .

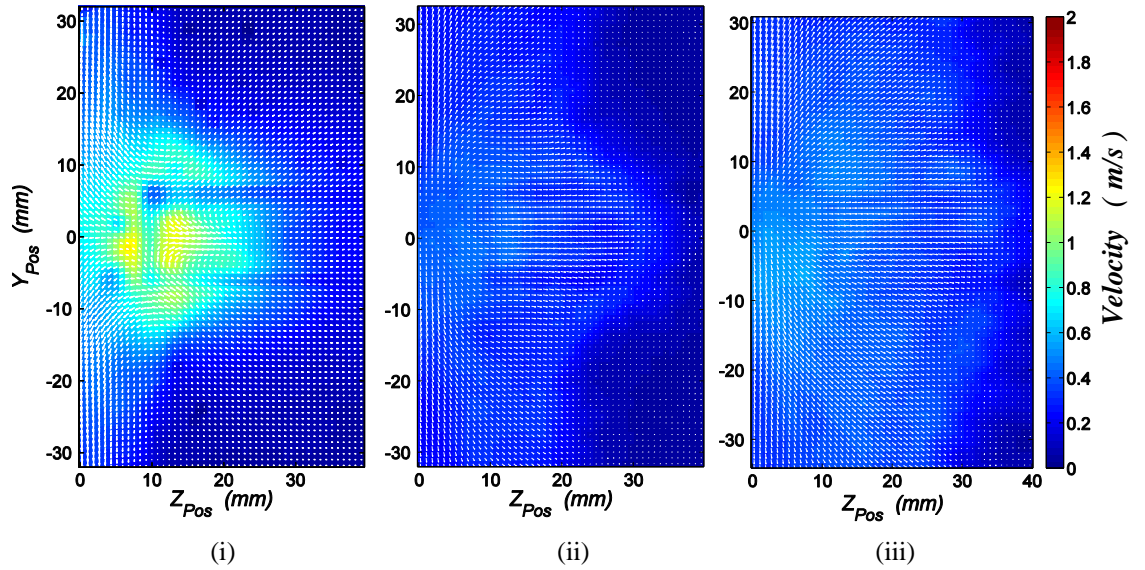


Figure 8.30: Effect of  $S$  on the FSW Turbulence Intensity contour plots -  $V_{Pz} = 115.0V, G = 10.0mm$ :

(i)  $S = 30.0mm$

(ii)  $S = 40.0mm$

(iii)  $S = 50.0mm$

Once again, the result has been attributed to the presence of the fin side walls. Maintaining a small fin spacing approximates the flow to a 2D flow, resulting in a highly constrained stream of air (of large magnitude) flowing over the FSW. However, with an increase in  $S$ , the flow is less channelled and spreads out to occupy a larger volume. Thus, any eddies generated have a larger volume in which to dissipate their energy.

However, as pointed out in a previous section, as the bulk flow is more indicative of the cooling than the turbulent flow, it can be concluded that a large fin spacing ( $S50$ ) is better suited in cooling the FSW's.

### **8.2.3 Section Summary**

Experimental results indicate that for a vertically-mounted fan, operating at the maximum vibrational amplitude, a minimal separation distance ( $G$ ) is beneficial for  $FB$  cooling, the best setup being -  $V_{pz} = 115.0V, G = 5.0mm$ . However, when cooling the  $FSW$ 's, a larger separation distance is beneficial (i.e.  $V_{pz} = 115.0V, G = 15.0mm$ ). Furthermore, for the present fan orientation, a small fin spacing ( $S$ ) is found to be more effective on the  $FB$  while a large fin spacing has been found to be beneficial (when compared to other tested fin spacings) when cooling  $FSW$ . This agrees with the cooling plots presented in **Chapter 6**. The overall unit cell optimum  $FCCS$  geometry selection is presented in **Chapter 9**.

### 8.3 A Comparative Study

This section brings together the results described in the previous sections. Superimposed results (fin base and fin side walls) for both the bulk and the turbulent flows are presented for both a horizontally-mounted and a vertically-mounted fan for  $V_{pz} = 115.0V$  and  $G = 10.0mm$  for several fin spacings (together with a vertical flat plate).

Figure 8.31 depicts the bulk fluid motion (magnitude of mean flow -  $\overline{V_{Mean}}$ ) generated by a horizontally-mounted piezoelectric fan on both the fin base and the fin side wall for the various fin spacings. Figure 8.32 illustrates the 3D turbulence characteristics produced. The flow complexity generated by the oscillating fan (on both the *FB* and *FSW*'s) is clearly seen.

From these images, it is further evident that the primary effect of the oscillating fan is on the *FB*, with a smaller effect on the *FSW*'s. This is true for all considered fin spacings. Furthermore, on considering the turbulence characteristics, the same results are seen.

Once again, on closer inspection of the plots, the results indicate that with an increase in  $S$ , the fan effect on both the fin base and the fin side walls diminished.

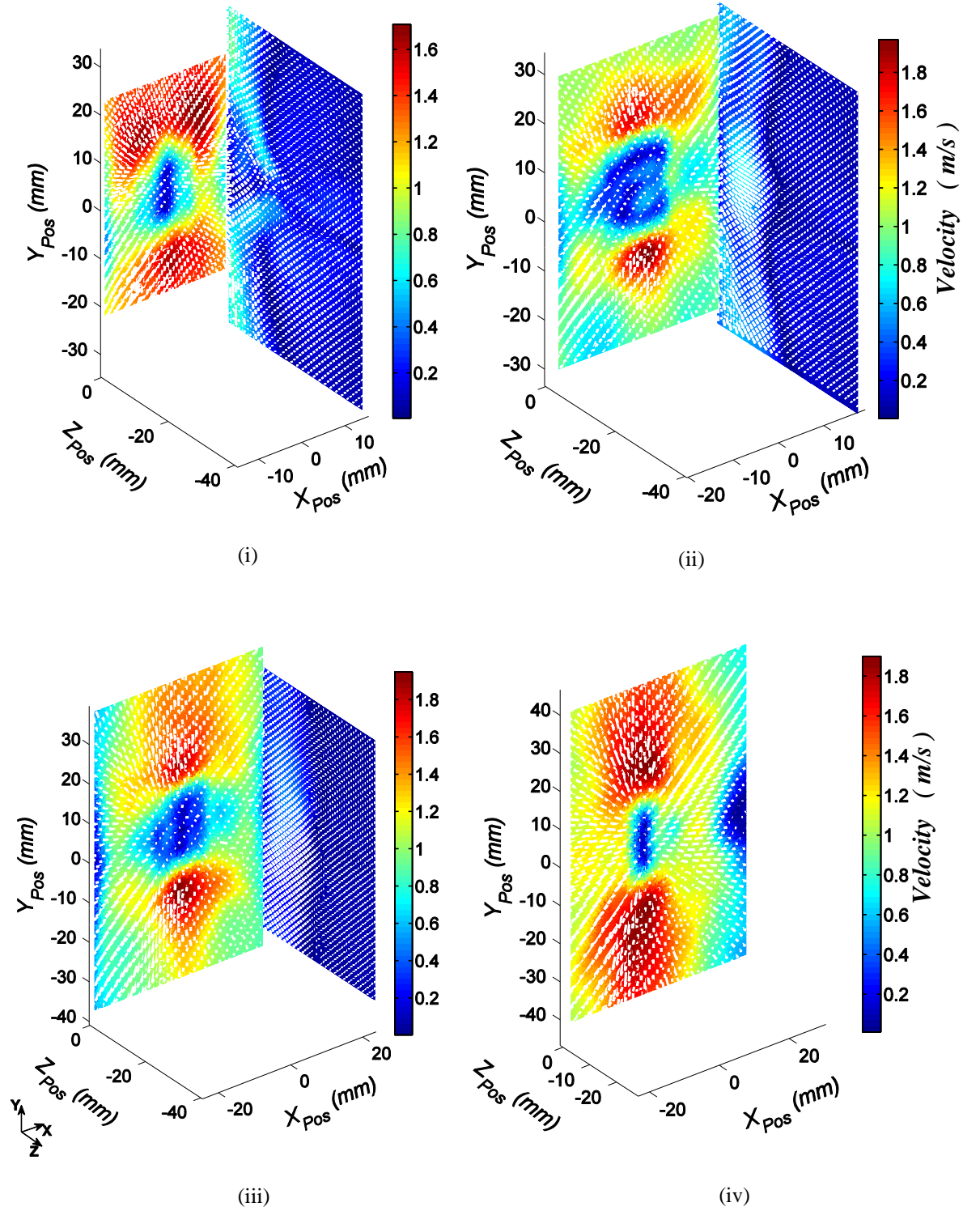


Figure 8.31: 3D Contour Maps depicting the Magnitude of the Mean Vectors for a Horizontally-mounted Fan operating:  $V_{Pz} = 115.0V$ ,  $G = 10.0mm$

(i)  $S = 30.0mm$  (ii)  $S = 40.0mm$  (iii)  $S = 50.0mm$  (iv) Flat Plate ( $S = \infty$ )

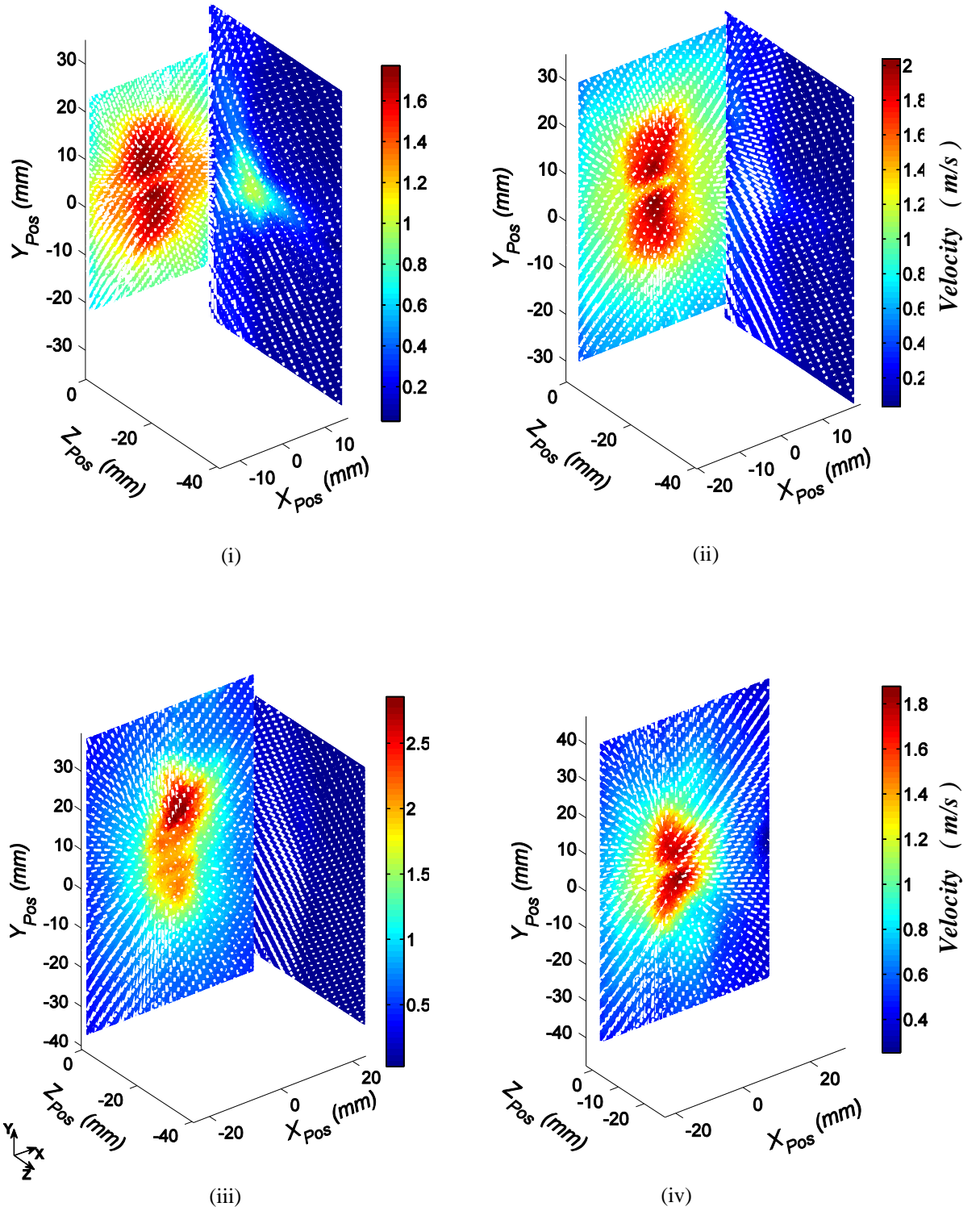


Figure 8.32: 3D Contour Maps depicting the STDV vectors for a Horizontally-mounted Fan:  
 $V_{Pz} = 115.0V$ ,  $G = 10.0mm$

i)  $S = 30.0mm$     ii)  $S = 40.0mm$     iii)  $S = 50.0mm$     iv) Flat Plate ( $S = \infty$ )

Similarly, Figure 8.33 depicts the bulk fluidic motion ( $\overline{V_{Mean}}$ ) generated by a vertically-mounted piezoelectric fan on both the fin base and the fin side wall for various fin spacings. Figure 8.34 illustrates the 3D turbulence characteristics produced. The flow complexity generated by the oscillating fan (on both the *FB* and *FSW*'s) clearly shines through and the difficulties in equating the cooling plots (**Chapter 6**) to the flow characteristics (mean and turbulent flow) may further be appreciated.

In this setup, while the primary effect of the oscillating fan is on the *FB*, a considerable effect on the *FSW*'s also results. Furthermore, on comparing these results to those for a horizontally-mounted fan, it is evident that a horizontally-mounted fan is better suited to cool the *FB* when compared to a vertical-mounted fan. However, the converse holds for the fin side walls where a vertically-mounted fan is better suited in cooling the *FSW* when compared to a horizontally-mounted fan.

For this setup, with an increase in *S*, the fan effect on the *FB* decreases. However, the converse holds for the *FSW* where an increase in *S* results in an increase in the cooling capabilities of the fan.



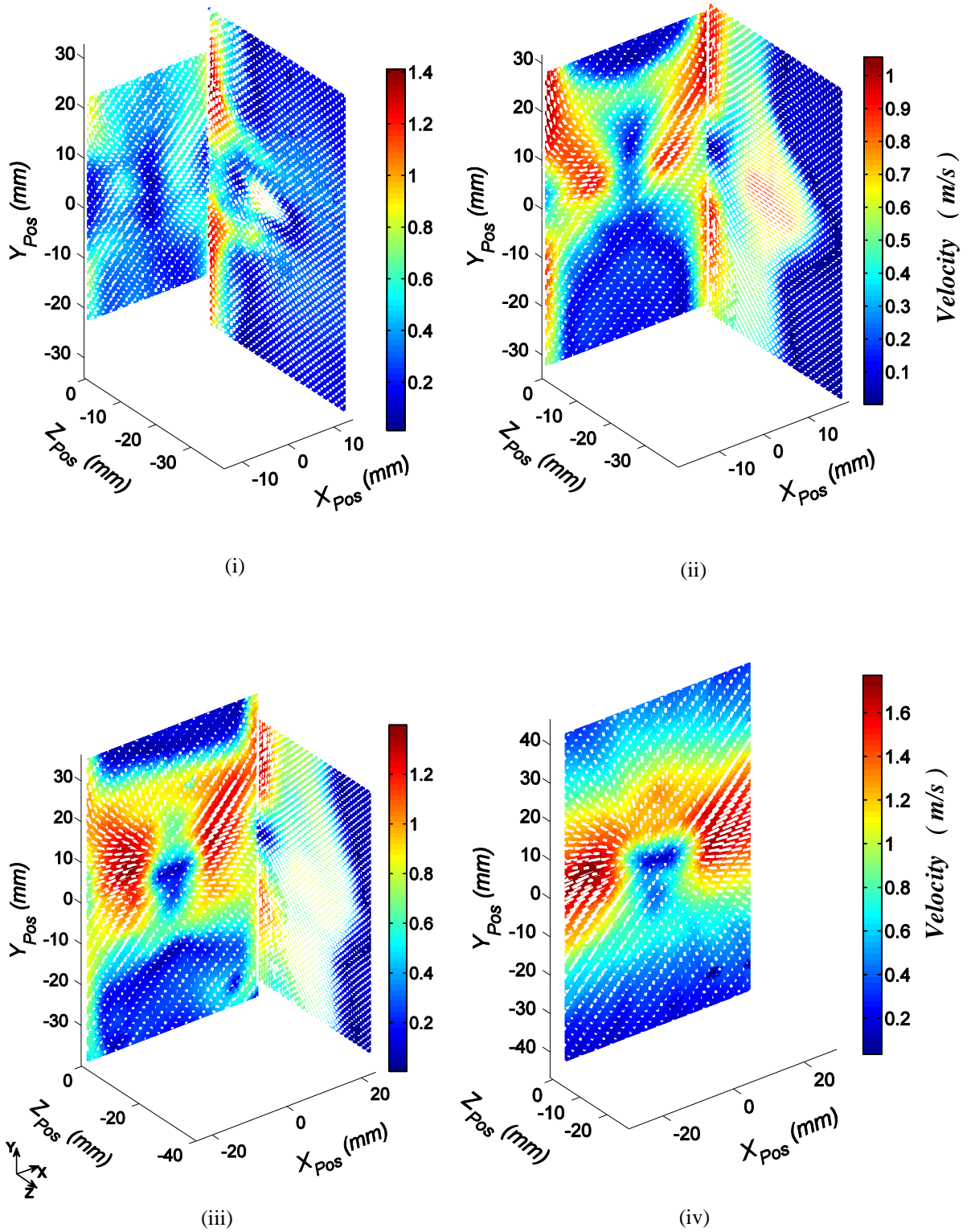


Figure 8.33: 3D Contour Maps depicting the Magnitude of the Mean Vectors for a Vertically-mounted Fan operating:  $V_{Pz} = 115.0V$ ,  $G = 10.0mm$

(i)  $S = 30.0mm$  (ii)  $S = 40.0mm$  (iii)  $S = 50.0mm$  (iv) Flat Plate ( $S = \infty$ )

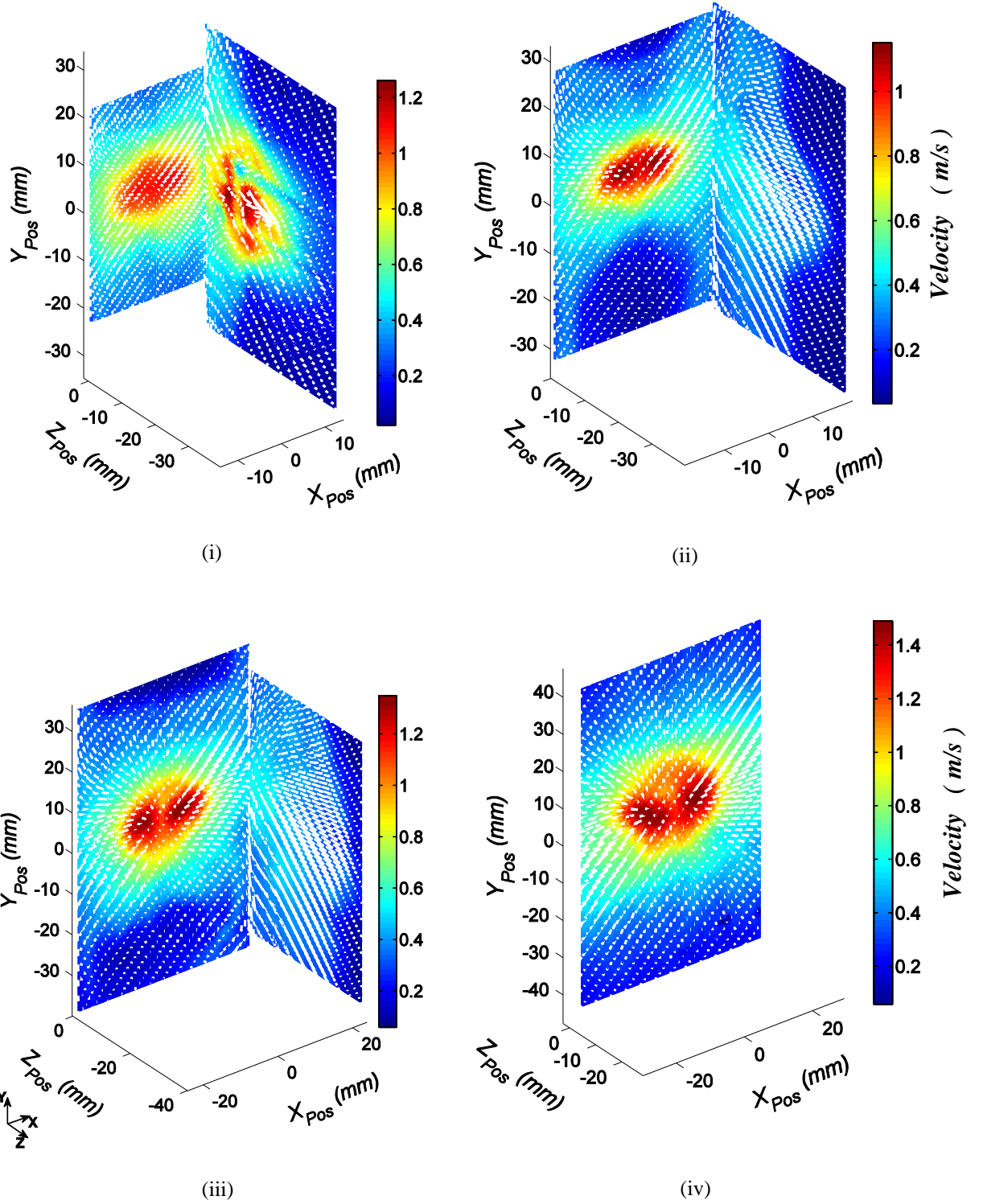


Figure 8.34: 3D Contour Maps depicting the STDV vectors for a Vertically-mounted Fan:  
 $V_{Pz} = 115.0V$ ,  $G = 10.0mm$

i)  $S = 30.0mm$    ii)  $S = 40.0mm$    iii)  $S = 50.0mm$    iv) Flat Plate ( $S = \infty$ )



The flow characteristics ( $V_{Mean}, V_{RMS}$ ) for a both a horizontally-mounted, and a vertically-mounted geometry *FCCS* geometry ( $G=10.0mm, V_{Pz}=115.0V$ ), are compared to the corresponding thermal cooling plots (Figure 8.35, Figure 8.36 repectively).

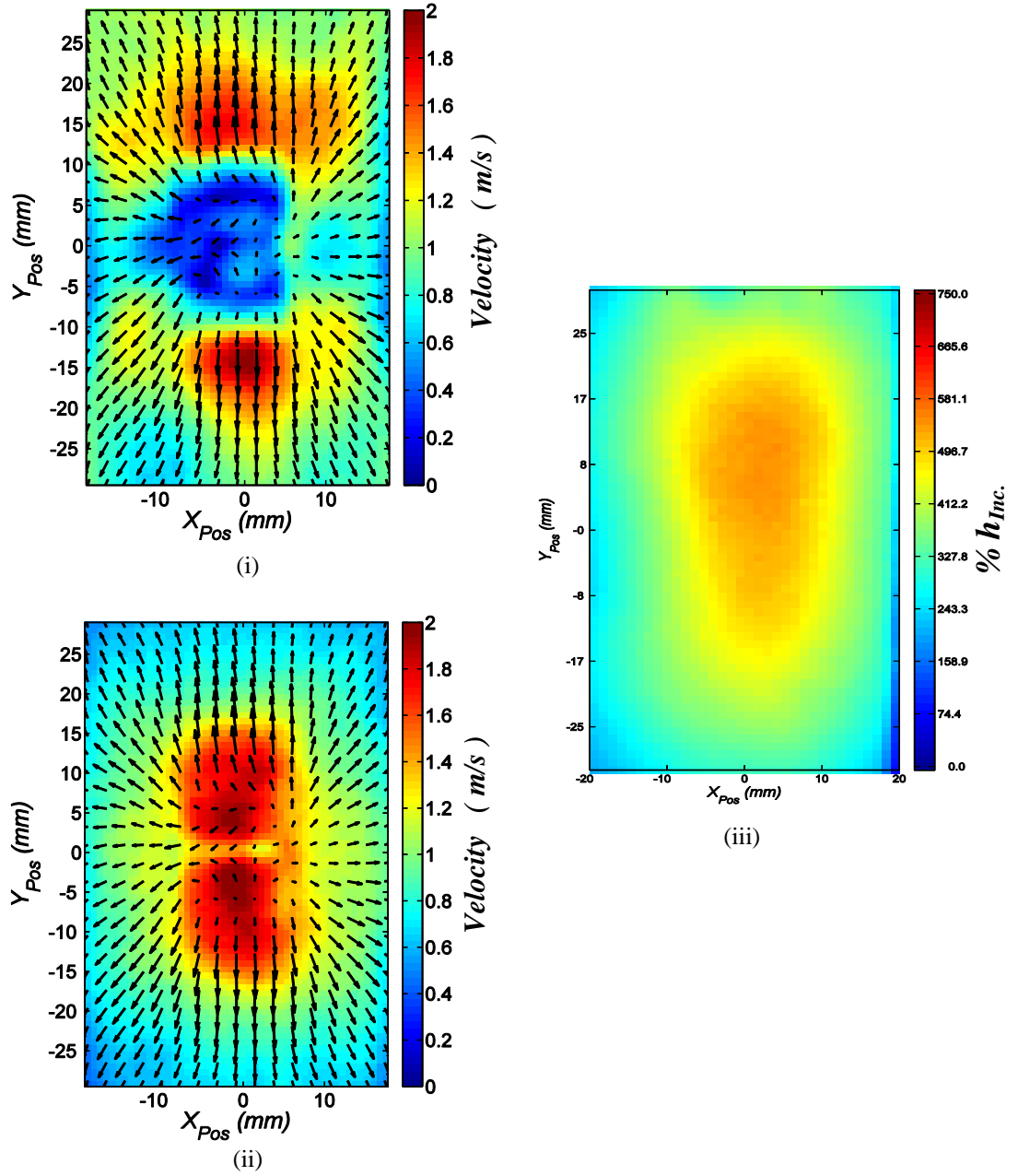


Figure 8.35: Comparative Study between Flow and Thermal Results: *FB*, Horizontally-mounted Fan  $S = 40.0mm, G = 10.0mm, V_{Pz} = 115.0V$ :

- (i) Magnitude of the Mean Vectors
- (ii) *RMS* values of the Fluctuating Component
- (iii)  $\% h_{Inc.}$

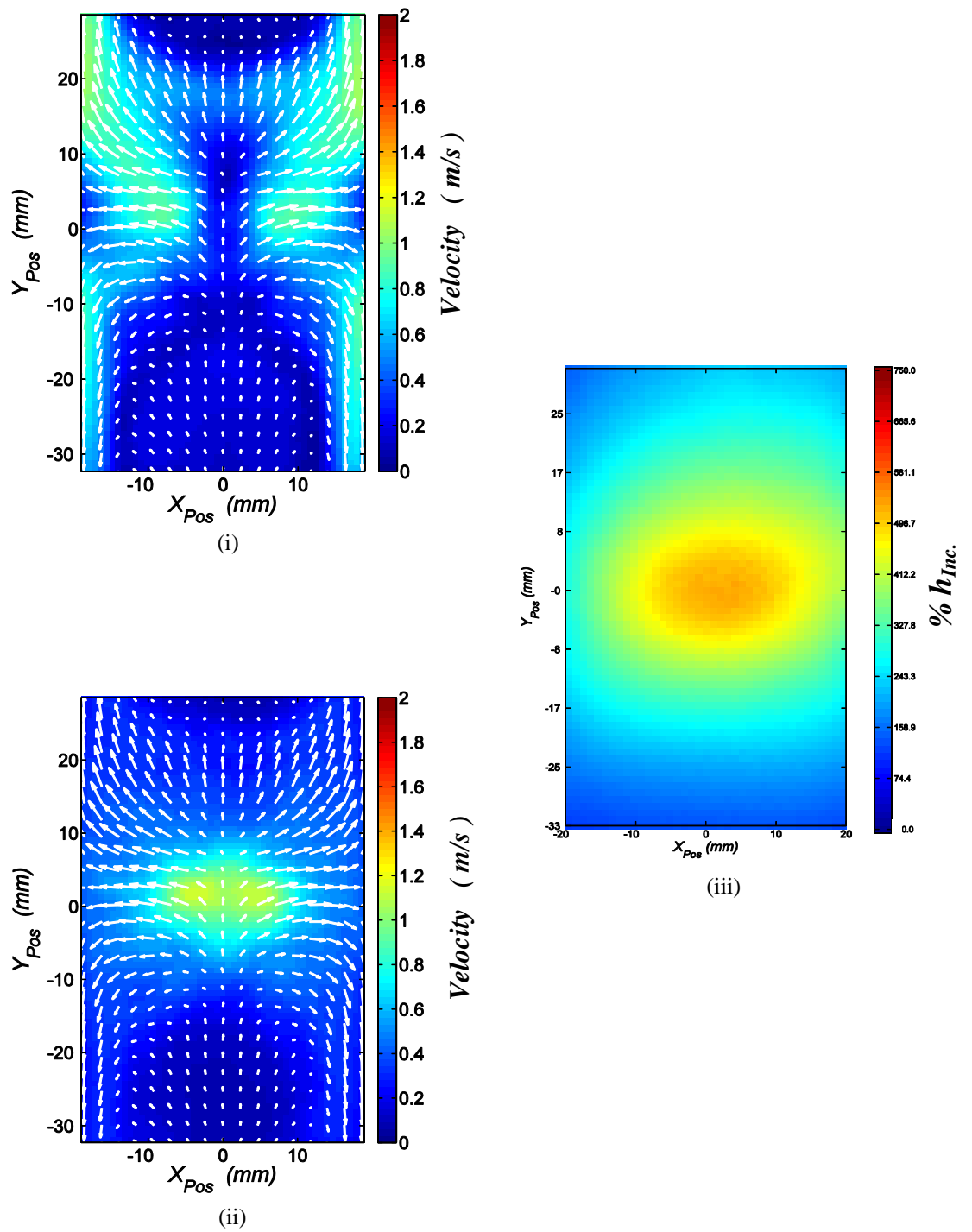


Figure 8.36: Comparative Study between Flow and Thermal Results: *FB*, Vertically-mounted Fan  
 $S = 40.0\text{mm}$ ,  $G = 10.0\text{mm}$   $V_{Pz} = 115.0\text{V}$ :

- (i) Magnitude of the Mean Vectors
- (ii) *RMS* values of the Fluctuating Component
- (iii)  $\%h_{inc.}$

Figure 8.35 highlights the similarities in the thermal cooling characteristics (presented in **Chapter 6**) to the flow characteristics (presented in **Chapter 7**) for one such horizontally-mounted *FCCS* setup. As for a vertical flat plate, the cooling range ( $X_{Pos}$ ,  $Y_{Pos}$ ), magnitude and symmetry are well matched, indicating that there is a close correlation between air flow patterns and heat transfer. These similarities also hold true for all other tested separation distances ( $G$ ), applied fan voltages ( $V_{Pz}$ ) and fin spacing's ( $S$ ). Furthermore, while only the *FB* results are highlighted in this section, similar similarities between the *FSW* flow characteristics and *FSW* cooling plots are also noted.

Similarly, Figure 8.36 highlights the similarities in the thermal cooling characteristics (presented in **Chapter 6**) to the flow characteristics (presented in **Chapter 7**) for one such vertically-mounted *FCCS* setup. The cooling range ( $X_{Pos}$ ,  $Y_{Pos}$ ), magnitude and symmetry are well matched. Once again, the similarities also hold true for all other tested separation distances ( $G$ ), applied fan voltages ( $V_{Pz}$ ) and fin spacing's ( $S$ ). Furthermore, while only the *FB* results are highlighted in this section, similar similarities between the *FSW* flow characteristics and *FSW* cooling plots are also noted.

## 8.4 Concluding Remarks

The aim of this chapter was to investigate, characterise and analyse the flows produced by both a horizontally-mounted and a vertically-mounted oscillating piezoelectric fan on a plane parallel to the fin base as well as on a plane parallel to the fin side wall, so as to further compliment the thermal experimental data presented in **Chapter 6**. For each, the effect of vibrational amplitude ( $A_{pz}$ ), separation distance ( $G$ ) and fin spacing ( $S$ ) was highlighted.

As shown throughout this chapter, the flow fields produced by an oscillating piezoelectric fan for the current finned geometry are unsteady (with numerous vortices being shed in each swing), and comprise a bulk mean flow superimposed onto a highly turbulent fluctuating component. On comparing the fluid flow characteristics to the thermal measurements (cooling plots) presented in **Chapter 6**, it is evident that there is a close correlation between air flow patterns and heat transfer. Furthermore, it was found that the *FB* and *FSW* cooling is dependent on both the bulk and turbulent flow (i.e.  $\%h_{inc.} = f(\overline{V_{Mean}}, V_{RMS})$ ). For a vertically-mounted fan in particular, it was deduced that the mean flow is more indicative (and is the key defining parameter) of the cooling rather than the turbulence characteristics.

For both fan orientations, experimental results indicate that an increase in  $V_{pz}$  and a reduction in the separation distance  $G$ , both result in an increase in the fin base velocities, signalling an increased piezoelectric fan cooling capability. These results and trends are identical to those presented for an unfinned vertical flat plate ( $S\infty$ ) in **Chapter 7** as well as match those published in [44]. However, when investigating the fan cooling effect on the *FSW*'s, for both fan orientations, it was established that a larger separation distance is beneficial. On considering the effect of the fin spacing ( $S$ ), results attained from a horizontally-mounted fan setup indicate that, with an increase in  $S$ , the fan effect on both the fin base and the fin side walls diminished. On the other hand, for a vertically-mounted fan, an increase in  $S$  results in a reduction in the cooling capabilities on the *FB*, but there is an increase in cooling the *FSW* –

i.e. an increase in  $S$  results in an increase in the cooling effectiveness of the fan. The latter complication (i.e. the selection of the optimum *FCCS* geometry) may be evaluated when considering the overall cooling of the entire unit cell, the results of which are presented in the subsequent chapter, **Chapter 9**.

In conclusion, the *PIV* experimentation techniques resulted in a vast amount of data (both visual and numerical), resulting in the full fluid flow characterisation for the various *FCCS* geometrical configurations and are invaluable in the understanding of the complexity of the flow generated by oscillating piezoelectric fans. Furthermore, the *PIV* equipment has proven to be an invaluable tool in this work, as the detailed characterisation of the fluid flow would not have been possible using other traditional fluid flow measurement equipment.

The fluid flow results presented in this chapter bear a close resemblance to the cooling plots depicted in **Chapter 6**. While a full match between the fluid flow characteristics (**Chapter 7** and **Chapter 8**) and the thermal results (**Chapter 6**) is difficult to make, key results such as the: cooling patterns, cooling range, and cooling intensity have been well matched for most of the geometrical configurations.

## CHAPTER 9

# 9. Implementation of Piezoelectric Fan Array

---

This chapter details the evaluation of the overall fin unit - cell heat sink thermal resistance for both *NC* as well as the *FCCS* for varying fan orientation,  $L_{Fin}$ ,  $G$ ,  $S$ , and  $A_{Pz}$ .

The feasibility of implementing piezoelectric fans is further investigated by evaluating the potential weight saving capabilities of the *FCCS* over the traditional passive natural-convecting fins. The design of a supporting structure together with the *FEA* analysis is presented and the key results highlighted.

Lastly, the thermal resistance results and the *FCCS* weight data for the numerous tested parameters (Orientation,  $L_{Fin}$ ,  $G$ ,  $S$ , and  $A_{Pz}$ ) are combined, and the piezoelectric fan/fin geometry of minimum mass and minimum thermal resistance is selected.

### 9.1 Heat Sink Thermal Resistance Evaluation

In *Chapter 6*, the cooling effectiveness of a piezoelectric fan over natural convection is evaluated for the fin base (*FB*) and the fin side walls (*FSW's*), for the several parameters (Orientation,  $G$ ,  $S$ , and  $A_{Pz}$ ). This was achieved by measuring the local heat transfer coefficients. However, to measure the overall cooling effectiveness of piezoelectric fans (combined fin base and fin side) against a traditional vertical straight finned heat sink, thermal resistance plots were generated. These plots are presented and explained in the subsequent sections.

### 9.1.1 Theory and Calculations

A pictorial image of the thermal experimental setup is presented in Figure 9.1. On the other hand, Figure 9.2 is a representative diagram on which the subsequent analysis is performed.

At this point, it should be reiterated that, at no point during the thermal measurements, were both *CF* heater mats simultaneously on. This means that the cooling effectiveness of the *FCCS* was performed on the fin base and the fin side individually. There are numerous reasons behind the set methodology. Firstly, in *Chapter 7* and *Chapter 8*, the flow fields captured by the *PIV* were performed individually for each unheated target surface (fin base and fin side) in turn. That is, the *PIV* setup consisted of unheated flat vertical surfaces. Thus during the *PIV* experiments, as no heat input is present, the flow characteristics captured are solely due to the presence of the oscillating piezoelectric fan. However, in *Chapter 6*, the recorded thermal measurements are due, not only, to the oscillating fan, but also due to (the ever present) natural convection that occurs along the vertical fin (along +ve *Y-axis*). Simultaneously heating the fin base and fin side wall will change the natural convection characteristics of the heat sink, as two intersecting boundary layers form, while radiation heat transfer occurs between the two exposed surfaces. This is further pronounced if both the fin base, as well as the two fin side walls are heated. In this latter scenario (a realistic scenario, which occurs in heat sinks), three natural intersecting boundary layers form, while a complex radiation heat transfer (depending on view factors) occurs between the three individual heated surfaces.

For the above reasons, it was decided, that for this work, the heaters will be operated in turn ensuring that the cooling effectiveness of the oscillating piezoelectric fan can be established for both target surfaces (fin base and fin side) in turn. This simplification assisted in the experimental work and although boundary layer interactions between *FB* and *FSW*'s are neglected, these are considered to be small in affecting the overall convective thermal resistance.

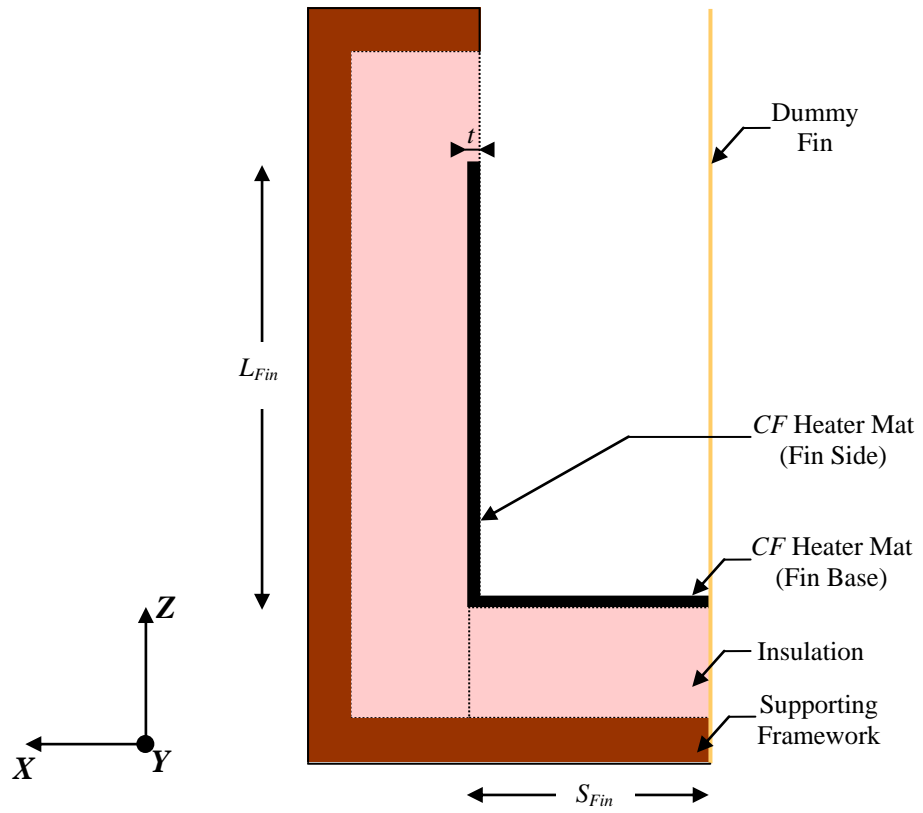


Figure 9.1: Schematic of adopted Experimental Thermal Setup – Top View

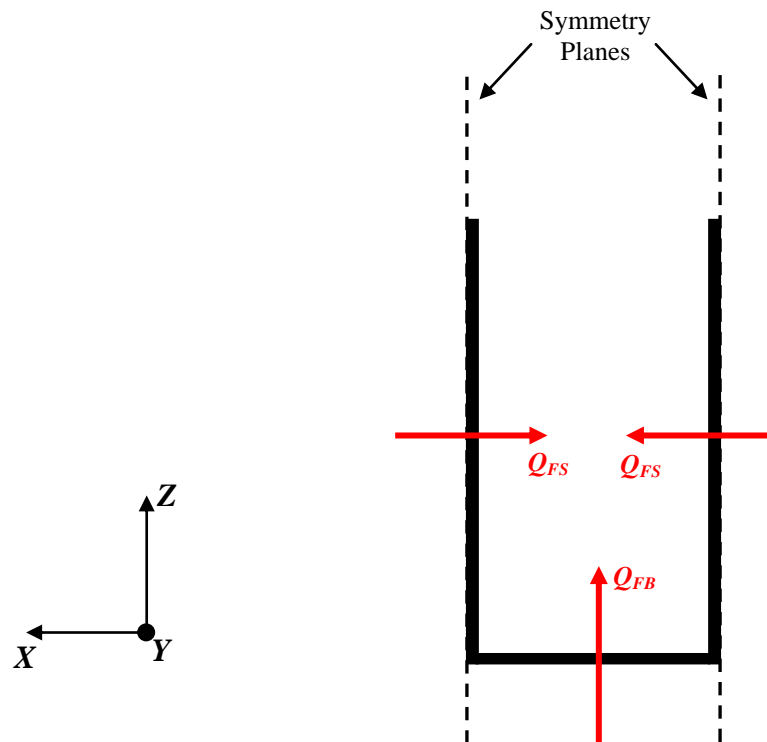


Figure 9.2: Representative Thermal Model of Fin Unit – Cell – Top View



The overextended fin side walls (100mm long) ensure that the fin side walls act as planes of symmetry. This symmetry plane is essential, as the results obtained by analysing a single fin unit-cell (Figure 9.2) can be reproduced linearly according to the number of fins present on the motor casing.

However, for this to be valid,  $t = \left( \frac{t_{Fin}}{2} \right)$ .

In **Chapter 6**, both the natural and forced local heat transfer coefficients for both the fin base ( $h_{FB}$ ) and fin side ( $h_{FS}$ ) were evaluated. These values were independently utilised to work out the average thermal resistances for the fin base ( $R_{FB}$ ) and the fin side ( $R_{FS}$ ) respectively, according to the following equations:

$$Q_{FB} = \overline{h_{FB}} \cdot A_{FB} \cdot (\overline{T_{FB}} - \overline{T_{\infty}}) \quad \dots \text{Eq. 9.1}$$

$$Q_{FS} = \overline{h_{FS}} \cdot A_{FS} \cdot (\overline{T_{FS}} - \overline{T_{\infty}}) \quad \dots \text{Eq. 9.2}$$

$$Q_{Total} = Q_{FB} + 2Q_{FS} \quad (\text{for one fin unit-cell}) \quad \dots \text{Eq. 9.3}$$

$$R_{FB} = \left( \frac{\overline{T_{FB}} - \overline{T_{\infty}}}{Q_{FB}} \right) \quad \dots \text{Eq. 9.4}$$

$$R_{FS} = \left( \frac{\overline{T_{FS}} - \overline{T_{\infty}}}{Q_{FS}} \right) \quad \dots \text{Eq. 9.5}$$

As the fin base and fin side wall thermal resistances can be considered to be in a parallel network, the following total resistance may be evaluated:

$$\left( \frac{1}{R_{Total}} \right) = \left( \frac{1}{R_{FB}} \right) + \left( \frac{2}{R_{FS}} \right) \quad \dots \text{Eq. 9.6}$$

$$\therefore R_{Total} = \frac{R_{FB} \cdot R_{FS}}{R_{FS} + 2R_{FB}} \quad \dots \text{Eq. 9.7}$$

At this point, a total thermal resistance for the entire fin unit – cell is obtained. However, as there are different fin spacings ( $S_{Fin}$ ), an equivalent thermal resistance which takes into account the fin base area ( $A_{FB}$ ) was calculated. This can further be defined by Eq. 9.9.

$$Q_{Total}'' = \frac{Q_{Total}}{A_{FB}} = \left( \frac{\overline{T_{FB}} - \overline{T_{\infty}}}{R_{Total}''} \right) \quad \dots \text{Eq. 9.8}$$

$$R_{Equivalent} = \left( \frac{\overline{T_{FB}} - \overline{T_{\infty}}}{Q_{Total}''} \right) = \left( \frac{\overline{T_{FB}} - \overline{T_{\infty}}}{\left( \frac{\overline{T_{FB}} - \overline{T_{\infty}}}{R_{Total}''} \right)} \right) = A_{FB} \cdot R_{Total} \quad \dots \text{Eq. 9.9}$$

Evaluating the latter parameter,  $R_{Equivalent}$  ( $K.m^2/W$ ) ensures that the equivalent thermal resistance values are expressed per unit area of the exposed motor housing ( $A_{FB}$ ). In Eq. 9.9,  $R_{Equivalent}$  is the reciprocal of the heat transfer coefficient ( $h_{Equivalent}$ ).

In this analysis, it has been assumed that a negligible thermal gradient along the fins exist – i.e. a fin efficiency  $\eta_{Fin} = 100\%$ . This assumption is valid as fin geometries commonly implemented in electric machine are short and thick indicating high fin efficiencies.

Graphs of  $R_{Equivalent}$  against fin length ( $L_{Fin}$ ) were plotted for both natural convection (i.e. when a fan is not present – traditional passive cooling technique) and forced convection (i.e. when a FCCS is introduced). Furthermore, the range of  $L_{Fin}$  was selected on currently available aerospace PMSM.

Graphs showing the affects of the parameters (Orientation,  $G$ ,  $S$ , and  $A_{Pz}$ ) are depicted in **Section 9.1.2**.

As described in *Chapter 6*, two distinct thermal tests were performed, constant heat flux tests and constant surface temperature tests, the results of which are presented in *Section 9.1.2* and *Section 9.1.3* respectively.

### 9.1.2 Thermal Resistance Results - Constant Heat Flux

In the following sections, Eq. 9.9 was utilised to evaluate the thermal resistance ( $R_{Equivalent}$ ) for the various parameters (Orientation,  $G$ ,  $S$ , and  $A_{Pz}$ ), the measurement uncertainties of which were reported in *Chapter 5*.

#### 9.1.2.1 Effect of Fan Amplitude ( $A_{Pz}$ )

Figure 9.3 depicts the effect of fan amplitude ( $A_{Pz}$ ) on the fin unit-cell thermal resistance ( $R_{Equivalent}$ ) with a horizontally-mounted fan set at a fin spacing of  $S = 30.0mm$ , and a separation distance  $G = 10.0mm$  is operated.

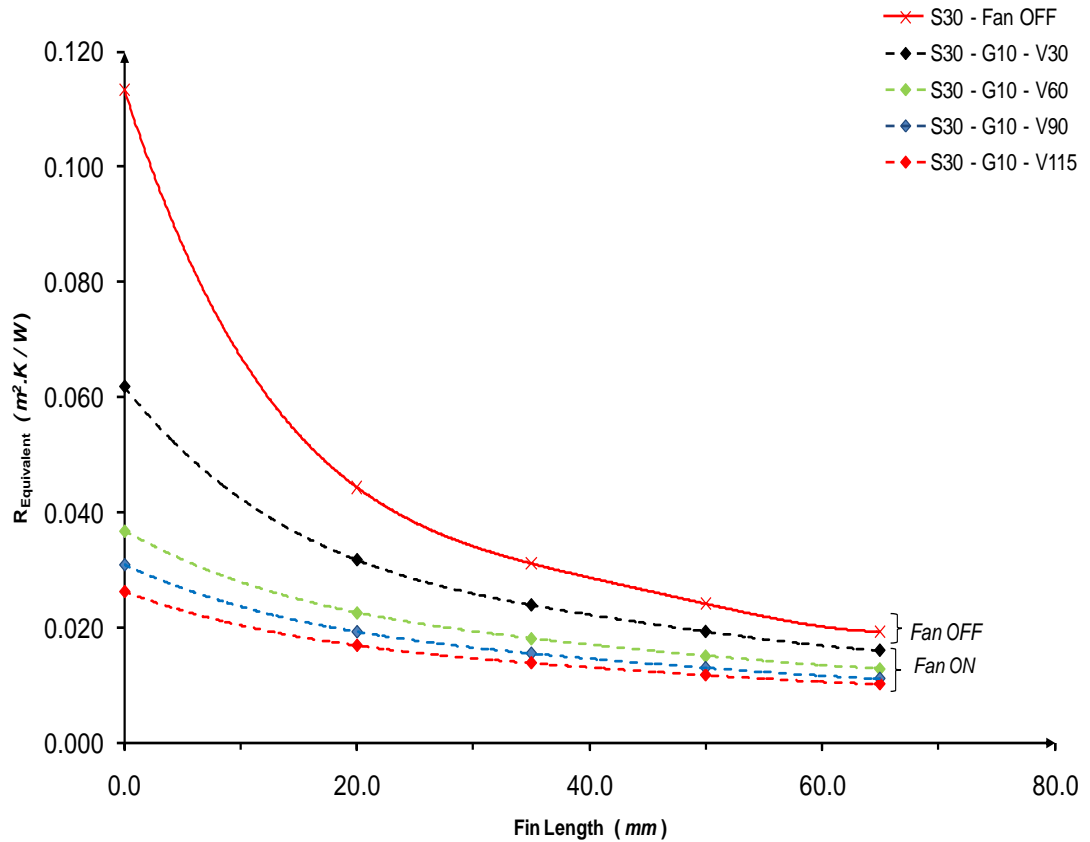


Figure 9.3: Effect of Fan Amplitude ( $A_{Pz}$ ) - Horizontally-mounted Fan,  $S = 30mm$ ,  $G = 10.0mm$

For all applied fan voltages ( $V_{Pz}$ ), the results indicate that an increase in fin length ( $L_{Fin}$ ) results in a decrease in  $R_{Equivalent}$ . Applying a minimal fan voltage of  $V_{Pz} = 30.00V$  shows a significant improvement in the cooling capabilities of the fan. This is further evident when the fan voltage is increased to  $V_{Pz} = 115.0V$ . At the fin base ( $L_{Fin} = 0.0mm$ ),  $R_{Equivalent}$  is reduced from  $0.113m^2.K/W$  ( $V_{Pz} = 0.0V$ ) to  $0.026m^2.K/W$  ( $V_{Pz} = 115.0V$ ) – a 77.0% reduction in the fin unit – cell thermal resistance is observed.

However, as the  $L_{Fin}$  increases the effect of the FCCS decreases. This is due, mainly, because having a larger fin area ( $A_{FS}$ ) results in natural convection becoming more dominant. At  $L_{Fin} = 65.0mm$ ,  $R_{Equivalent}$  is reduced from  $0.019m^2.K/W$  ( $V_{Pz} = 0.0V$ ) to  $0.010m^2.K/W$  ( $V_{Pz} = 115.0V$ ) – a 47.4% reduction. This indicates that the fan effectiveness decreases when  $L_{Fin}$  is increased as the fan affected zone is a smaller proportion of the finned area.

The above trends also hold for the other fin spacings ( $S$ ) and separation distances ( $G$ ).

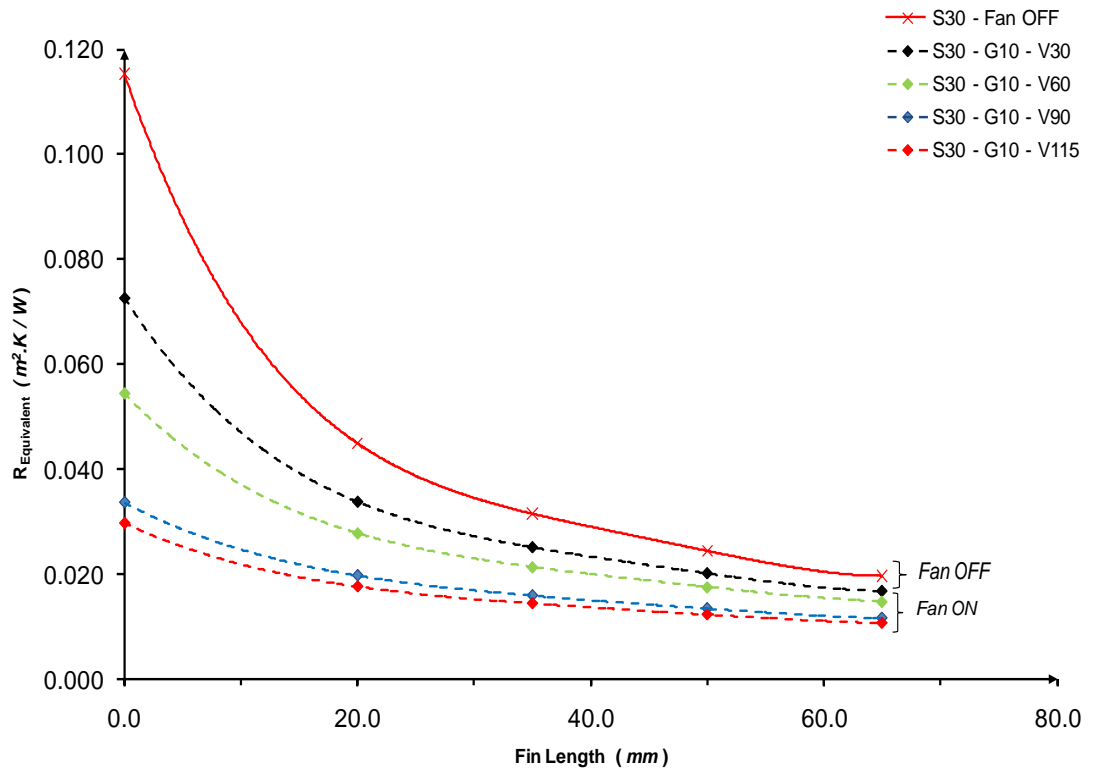


Figure 9.4: Effect of Fan Amplitude ( $A_{Pz}$ ) - Vertically-mounted Fan,  $S = 30mm$ ,  $G = 10.0mm$

A similar plot (Figure 9.4) of the effect of  $L_{Fin}$  on  $R_{Equivalent}$  is generated for a vertically-mounted fan. While the trends are identical to those of a horizontally-mounted fan, the thermal resistances are slightly higher. At the fin base ( $L_{Fin} = 0.0mm$ ),  $R_{Equivalent}$  is reduced from  $0.115m^2.K/W$  ( $V_{Pz} = 0.0V$ ) to  $0.030m^2.K/W$  ( $V_{Pz} = 115.0V$ ) – a 74.0% reduction. On the other hand, at  $L_{Fin} = 65.0mm$ ,  $R_{Equivalent}$  is reduced from  $0.020m^2.K/W$  ( $V_{Pz} = 0.0V$ ) to  $0.011m^2.K/W$  ( $V_{Pz} = 115.0V$ ) – a 45.0% reduction. Like in the previous results, the graph indicates that the fan effectiveness diminishes with an increase in  $L_{Fin}$ , and once again, the above trends hold true for the other tested fin spacings ( $S$ ) and separation distances ( $G$ ).

Therefore, from the above graphs and numerical analysis, it may be concluded that a horizontally-mounted fan operating at the largest displacement ( $V_{Pz} = 115.0V$ ) results in the largest cooling enhancement. This result is in good agreement with both the *PIV* results presented in **Chapter 7** and **Chapter 8**, as well as the thermal results presented in **Chapter 6**.

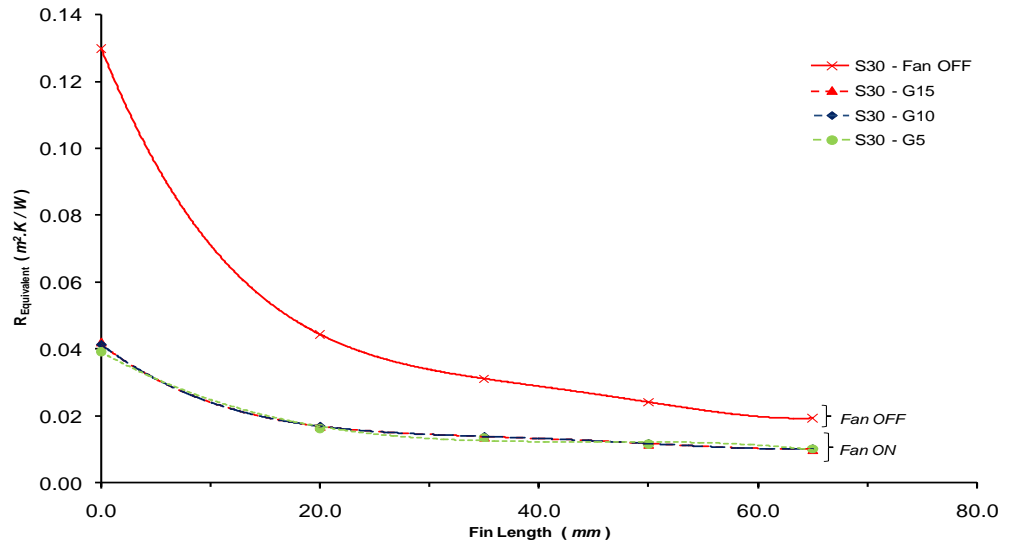
#### 9.1.2.2 Effect of Separation Distance ( $G$ )

The effect of separation distance ( $G$ ) on the resulting fin unit-cell thermal resistance ( $R_{Equivalent}$ ) is presented here. As in the latter section it was established that  $V_{Pz} = 115.0V$  is the optimum operational amplitude and thus only results pertaining to this voltage are presented.

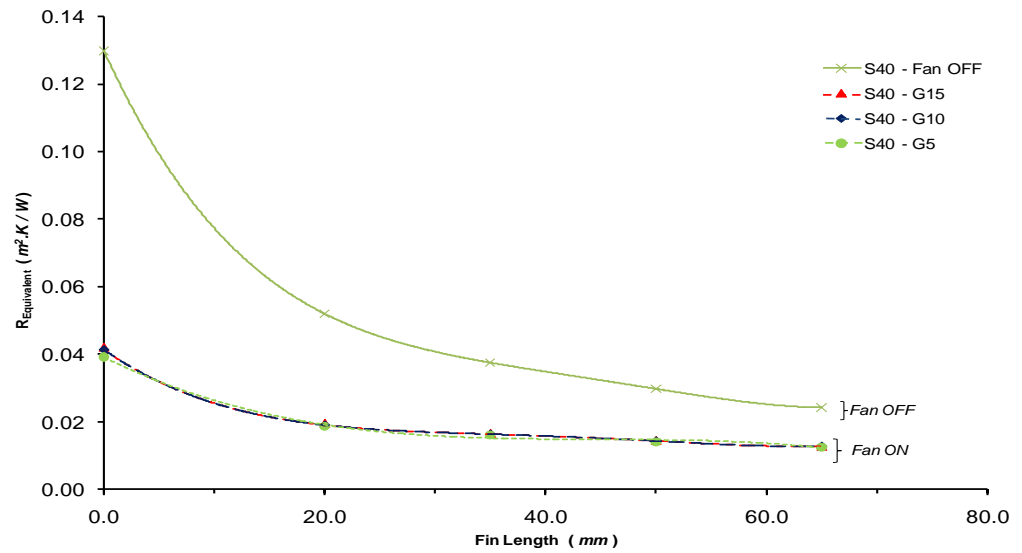
Figure 9.5i, Figure 9.5ii and Figure 9.5iii depict the effect of  $G$  for a horizontally-mounted fan with a fin spacing of  $S = 30.0mm$ ,  $S = 40.0mm$ , and  $S = 50.0mm$  respectively.

For all tested separation distances, it is evident that this parameter is not critical in the design of the *FCCS*. As there is little or no change in the graphs (shown overleaf) for different  $G$  values. The same trends are evident when considering other fin spacings.

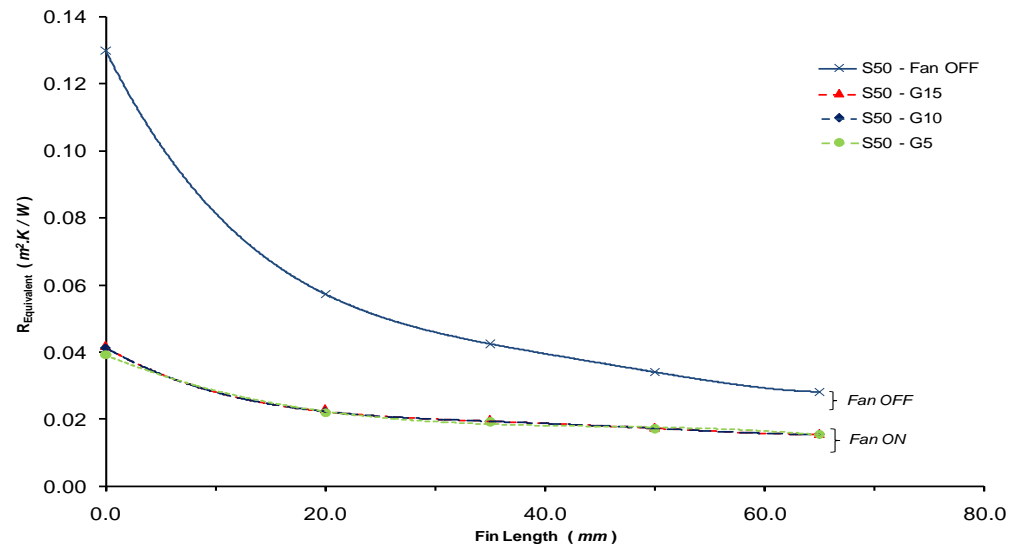
# Implementation of Piezoelectric Fan Array



(i)



(ii)

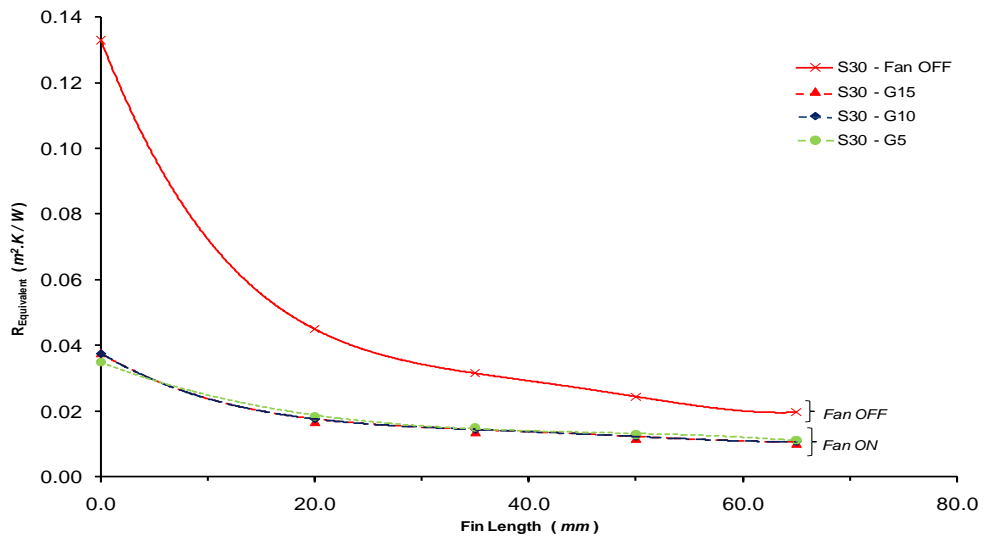


(iii)

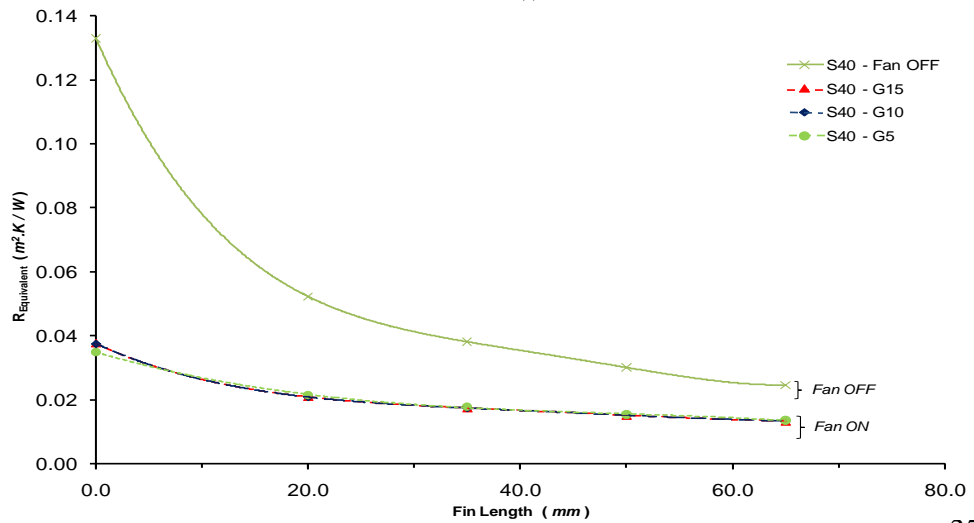
Figure 9.5: Effect of the Separation Distance ( $G$ ) on a Horizontally-mounted Fan –  $V_{pz} = 115V$   
 (i)  $S30$  (ii)  $S40$  (iii)  $S50$

The above may be further explained by consulting the results presented in **Chapter 6**. In this chapter, it was established that a minimal  $G$  is beneficial to cool the fin base. However, the converse holds true when considering the fin side walls. This means, that in order to cool the fin side walls, it is beneficial to maintain a large  $G$ . On superimposing the results (i.e. to maximise the cooling of the entire unit-cell) as is done in Figure 9.5, it has been established that the separation distance no longer remains a critical design component as the  $R_{Equivalent}$  vs.  $L_{Fin}$  plots are practically identical.

A similar conclusion may be drawn when considering a vertically-mounted fan. Figure 9.6i, Figure 9.6ii and Figure 9.6iii depict the effect of  $G$  for a vertically-mounted fan with a fin spacing of  $S = 30.0mm$ ,  $S = 40.0mm$ , and  $S = 50.0mm$  respectively.



(i)



(ii)

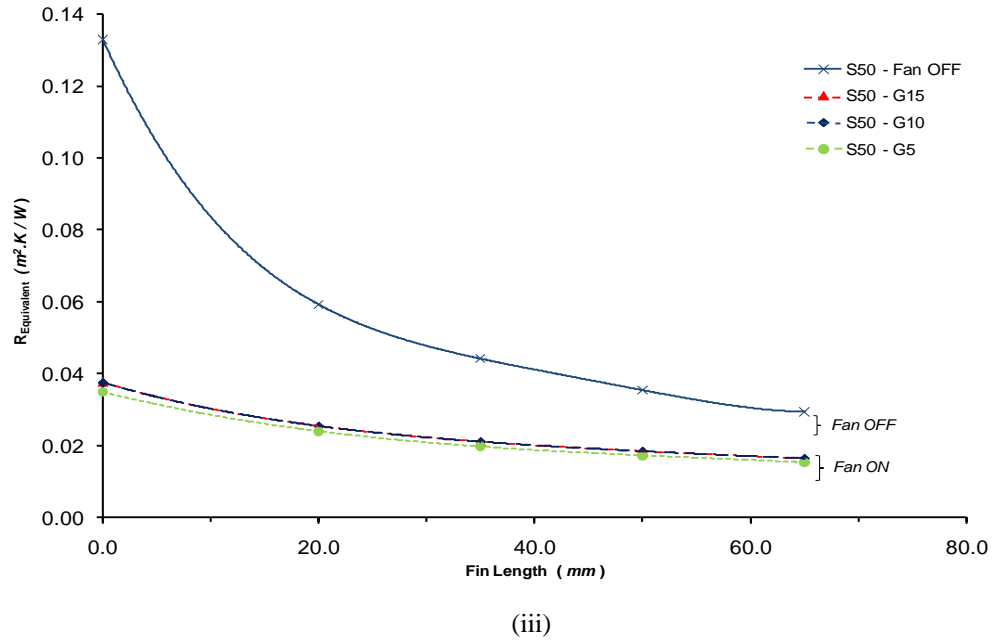


Figure 9.6: Effect of the Separation Distance ( $G$ ) - Vertically-mounted Fan,  $V_{Pz} = 115V$   
 (i)  $S30$  (ii)  $S40$  (iii)  $S50$

In conclusion, the experimental results indicate that, for both fan orientations, the separation distance  $G$  has no effect on the overall cooling enhancement of the fin unit-cell.

#### 9.1.2.3 Effect of Fin Spacing ( $S$ )

A study on the effect of fin spacing ( $S$ ) on the resulting unit-cell thermal resistance ( $R_{Equivalent}$ ) will now be presented. Once again, the results pertain to  $V_{Pz} = 115.0V$  and a separation distance of  $G = 10.0mm$  (Figure 9.7).



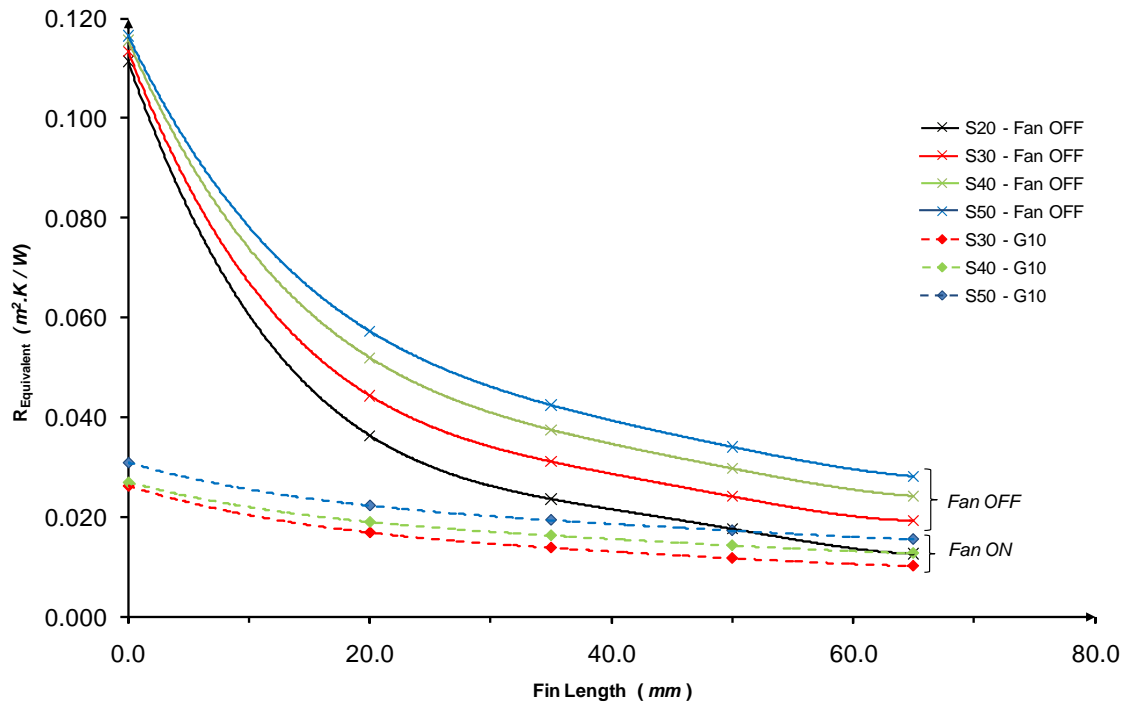


Figure 9.7: Equivalent Thermal Resistance for a Horizontally-mounted Fan –  $G = 10.0mm$ ,  $V_{pz} = 115V$

The plot graphically indicates that the fin spacing is a significant contributing factor in the design of the FCCS. A decrease in the fin spacing results in a reduction in  $R_{Equivalent}$ . This holds true for both the natural convection (Fan Off) plots as well as when the FCCS is in operation (Fan On).

A theoretical natural convection curve (S20) is also superimposed onto the experimental data. From earlier studies (**Chapter 4**), it has been established that the best natural cooling convection state is with a fin spacing of  $S = 20.00mm$ . However, due to the physical dimensions of the fan, and the limitations of the experimental setup under study, no tests could be performed to evaluate the forced cooling characteristics when  $S = 20.00mm$ . It is recommended that for future work, an experimental setup capable of evaluating the forced cooling of the fan with  $S = 20.00mm$  be devised.

Hence, due to the current experimental constraints, to gauge the cooling capabilities of the oscillating piezoelectric fan, a comparison between the best

natural convection state (S20) and the best forced cooling state (S30) must be made.

At the fin base ( $L_{Fin} = 0.0mm$ ),  $R_{Equivalent}$  is reduced from  $0.111m^2.K/W$  ( $V_{Pz} = 0.0V, S = 20.0mm$ ) to  $0.026m^2.K/W$  ( $V_{Pz} = 115.0V, S = 30.0mm$ ) – a 76.6% reduction. On the other hand, at  $L_{Fin} = 65.0mm$ ,  $R_{Equivalent}$  is reduced from  $0.013m^2.K/W$  ( $V_{Pz} = 0.0V$ ) to  $0.010m^2.K/W$  ( $V_{Pz} = 115.0V$ ) – a 23.1% reduction. Once again, results indicate that the fan effectiveness drops off steadily with an increase in  $L_{Fin}$ . This is also the case for a vertically-mounted oscillating piezoelectric fan (Figure 9.8).

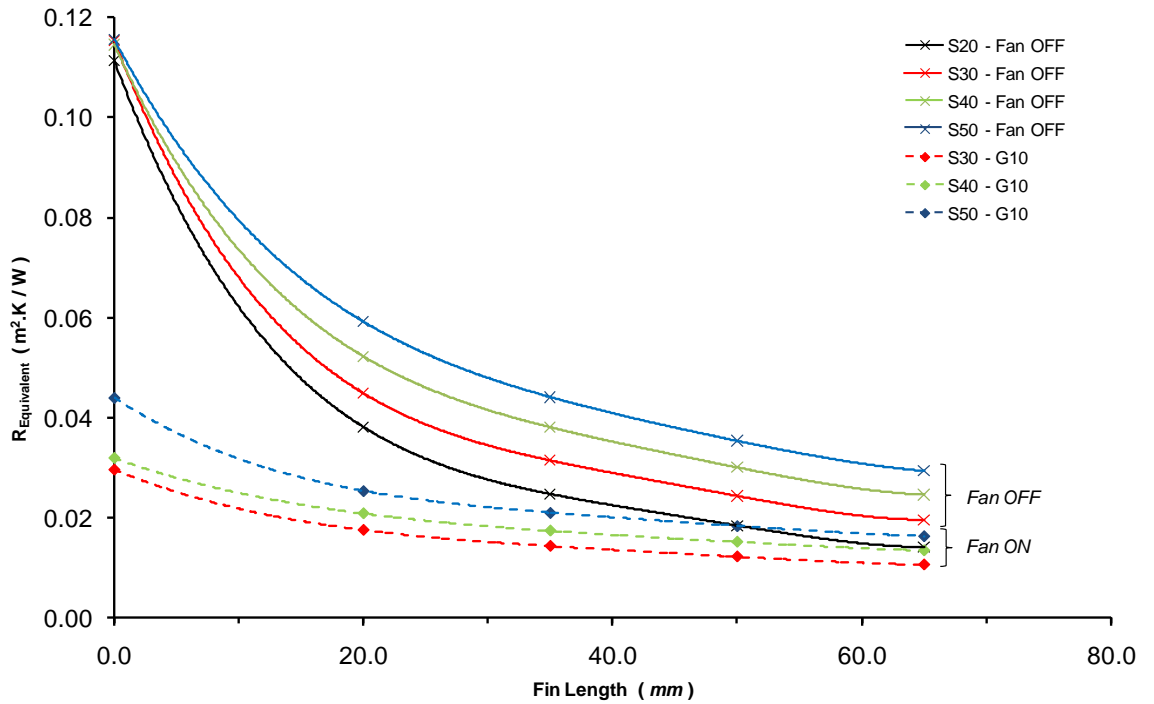


Figure 9.8: Equivalent Thermal Resistance for a Vertically-mounted Fan –  $G = 10.0mm, V_{Pz} = 115V$

In conclusion, it has been established that the fin spacing is a design parameter that should be considered in the design of the FCCS. Moreover, a fin spacing of  $S = 30.00mm$  results in the best cooling geometry.

#### 9.1.2.4 Effect of Fan Orientation

A direct comparison between a horizontally-mounted (Figure 9.7) and a vertically-mounted fan (Figure 9.8) is presented in Figure 9.9.

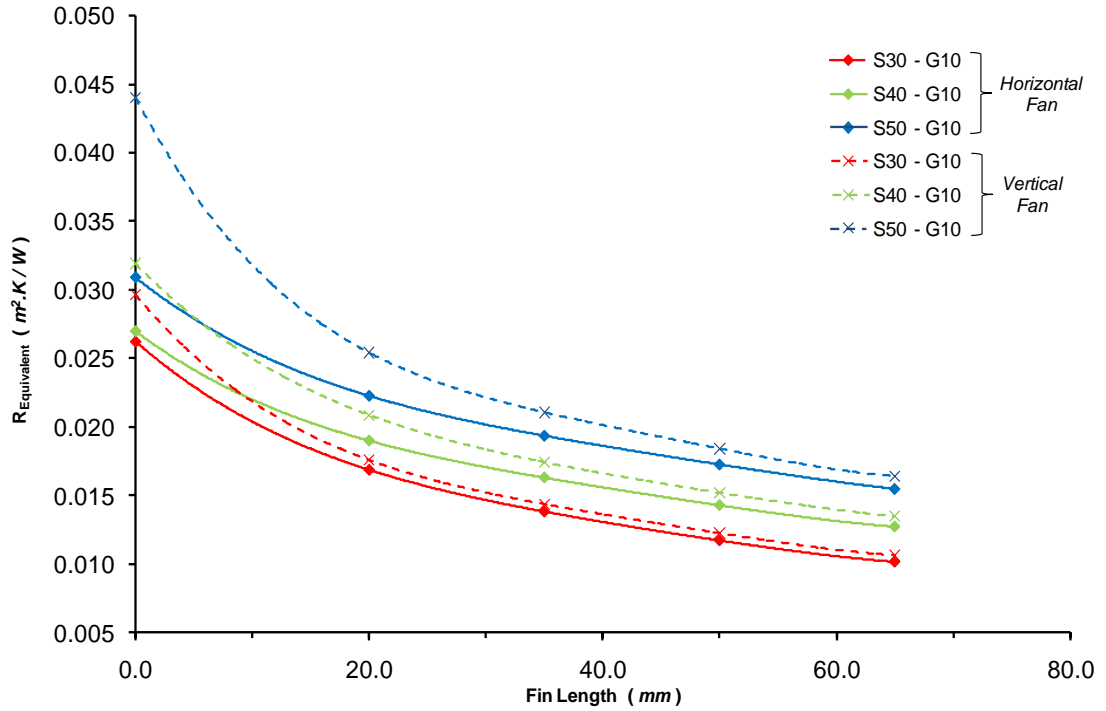


Figure 9.9: Comparative Study between a Horizontally-mounted and a Vertically-mounted Fan –  $G = 10.0\text{mm}$ ,  $V_{Pz} = 115\text{V}$

Figure 9.9 clearly indicates that for all fin spacings, a horizontally-mounted fan gives a lower  $R_{Equivalent}$  than a vertically-mounted fan.

Thus, from the current experimental results, it has been established that the best FCCS geometry to implement is a horizontally-mounted fan, operated at  $V_{Pz} = 115.0\text{V}$ ,  $G = 5.0\text{mm}$  with a fin spacing of  $S = 30.00\text{mm}$ .  $G = 5.0\text{mm}$  was selected, as the smaller the separation distance, the smaller the supporting structure required to attach FCCS to electric motor housing.

### 9.1.3 Thermal Resistance Results - Constant Surface Temperature

While the results in Section 9.1.2 all pertain to a constant heat flux scenario, further experiments were performed to evaluate the change in  $R_{Equivalent}$  when a constant surface temperature ( $\overline{T}_s - \overline{T}_\infty$ ) is maintained. These tests were carried out as it is generally understood that electric machine manufactures prefer to increase the machine power density and have maximum allowable operating temperatures ( $T_M$ ,  $T_{EWdg}$ ) rather than running the machine at the same power density but at lower operating temperatures.

Theoretically, maintaining a constant surface temperature inherently results in an increase in input power. This in turn implies that a lower thermal resistance should arise, as  $h_{NC}$  values are higher at larger  $\Delta T$  values.

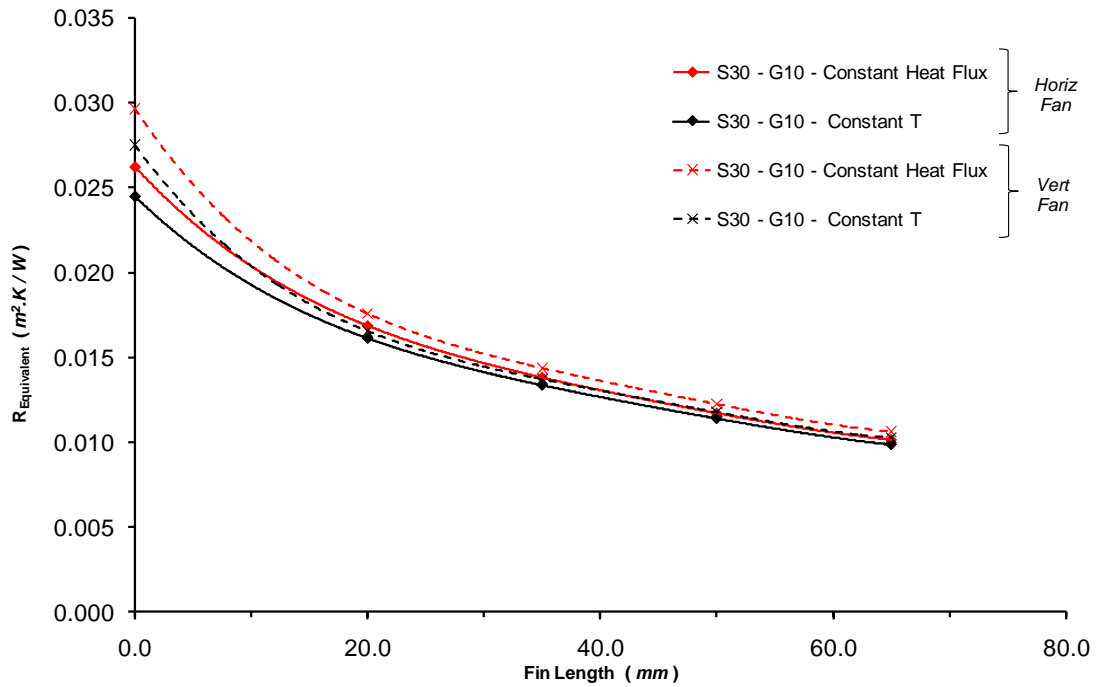


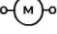





Figure 9.10: Direct Comparison between Constant Heat Flux and Constant Temperature Tests -  $V_{Pz} = 115$

Figure 9.10 compares a constant heat flux test against a constant temperature test for both fan orientations when  $V_{Pz} = 115.0V$ ,  $G = 10.0mm$  and at a fin spacing of  $S = 30.00mm$ . For both a horizontally-mounted and a vertically-

mounted fan, a lower  $R_{Equivalent}$  is obtained in the constant temperature tests when compared to the constant heat flux tests. While this difference is small for large  $L_{Fin}$ , the difference in  $R_{Equivalent}$  is seen to increase with a decrease in  $L_{Fin}$ . Furthermore, similar trends as in the last experiment are evident and results still indicate that a horizontally-mounted fan still outperforms a vertically-mounted one. This result ensured that further constant temperature tests were not required.

#### 9.1.4 Summary

From the experimental data and subsequent analysis, it has been established that:

-  An increase in  $L_{Fin}$  results in an increase in both the natural and forced convection components, represented by a decreasing  $R_{Equivalent}$ .
-  The implementation of the FCCS reduces the fin unit cell thermal resistance. However, the fan effectiveness diminishes with an increase in  $L_{Fin}$ .
-  The separation distance,  $G$ , has little/no effect on the overall reduction in the fin unit cell  $R_{Equivalent}$ .
-  A reduction in the fin spacing  $S$  results in further cooling.
-  Constant Temperature results are similar to constant heat flux results.
-  A horizontally-mounted fan outperforms a vertically-mounted fan.

The established optimum *FCCS* geometry is, that of a horizontally-mounted fan operating at  $V_{Pz} = 115.0V$ ,  $G = 5.0mm$  and  $S = 30.00mm$ . However, this result depends solely on the unit-cell thermal resistance and might change when considering the required *FCCS* mass.

## 9.2 Weight Saving Characteristics

As shown in **Chapter 6** and this chapter, the implementation of a piezoelectric fan significantly enhances the heat sink heat transfer. However, for the *FCCS* to be viable, the *FCCS* weight (piezoelectric fan mass + piezoelectric fan supporting structure mass) must be less than the equivalent *NC* mass, to give the same thermal resistance.

$$m_{NC} = \rho_{Al} \cdot (2 \cdot L_{Fin} \cdot t \cdot H) \quad \dots \text{Eq. 9.10}$$

$$m_{FCCS} = m_{NC} + m_{Fan} + m_{Structure} \quad \dots \text{Eq. 9.11}$$

Hence a study was performed with the objective being; the minimisation of the overall *FCCS* mass.

### 9.2.1 Design of Piezoelectric Fan Supporting Structure

The design criteria for the supporting structure were as follows:

- (M)○ Durability / Rigidity (able to withstand imposed stresses, deflections)
- (M)○ Thermally insulating (not to conduct heat into piezoelectric crystal)
- (M)○ Easy to mount and dismount



Mounted to Fin Base

To meet these engineering constraints, numerous fan supporting structure designs were considered.

### 9.2.2 Finite Element Model

For each structure design, a representative *Pro/E* model was generated, and a detailed *FEA (Pro/Mechanica)* study carried out on the combined oscillating piezoelectric fan and structure. The latter stage was carried out to ensure that the stresses and deflections are not detrimental to the functionality of the supporting structure.

The forces added to the assembly were: the bending force ( $F_{Bending}$ ) experienced by the oscillating piezoelectric fan, the oscillation force ( $F_{Oscillation}$ ) required to displace the air present in the fan's vibrational envelope, and the clamping torque ( $\Gamma_{Clamp}$ ) required to firmly hold down the fan's mounting base, the equations of which are described hereunder:

$$F_{Bending} = \frac{3.A_{Pz}.E.I}{L_{Pz}^3} \quad \dots \text{Eq. 9.12}$$

$$F_{Oscillation} = m_{Air} \left( \frac{\delta v}{\delta t} \right) \quad \dots \text{Eq. 9.13}$$

$$\Gamma_{Clamp} = (m_{Clamp}.g). \left( \frac{L_{Clamp}}{2} \right) \quad \dots \text{Eq. 9.14}$$

Eq. 9.12 is based on the bending of a simple cantilever *ID* beam, rigidly attached at one end and loaded at the free end – i.e. representative of the force experienced by an oscillating piezoelectric fan.

Thus, the total force experienced by the piezoelectric fan equates to the summation of the bending and the oscillation forces and is represented by Eq. 9.15.

$$\therefore F_{Total} = F_{Bending} + F_{Oscillation} = \left( \frac{3.A_{Pz}.E.I}{L_{Pz}^3} + m_{Air} \left( \frac{v_{Max}}{t} \right) \right) \quad \dots \text{Eq. 9.15}$$

On the other hand, the clamping torque ( $\Gamma_{Clamp}$ ) represents the torque required to maintain the piezoelectric fan's mounting plate perfectly still and minimise the possibility of damping. This ensures that the maximum fan tip displacement is reached.  $\Gamma_{Clamp}$  was established by placing small weights on top of the fan's mounting point and establishing at which load, the maximum vibrational envelope was reached. The load at which this occurred is equal to  $8.006N$  which results in a  $\Gamma_{Clamp} = 0.051Nm$ . In the *FEA* simulation, this torque was assumed to act at the centre of the piezoelectric fan's mounting point, as depicted in Figure 9.11.

Figure 9.11 represents the finite element modelling of a piezoelectric fan. The constitutive properties of the implemented Mylar blade are;

$$E = 4.6GPa, \quad \nu = 0.44, \quad \rho = 1240kg/m^3$$

and therefore, a maximum tetrahedral element size of  $0.5mm$  was used. On applying the total load, calculated by Eq. 9.15, the fan tip was seen to deflect by  $12.70mm$  as recorded during the *PIV* measurements when the maximum voltage was applied across the fan.



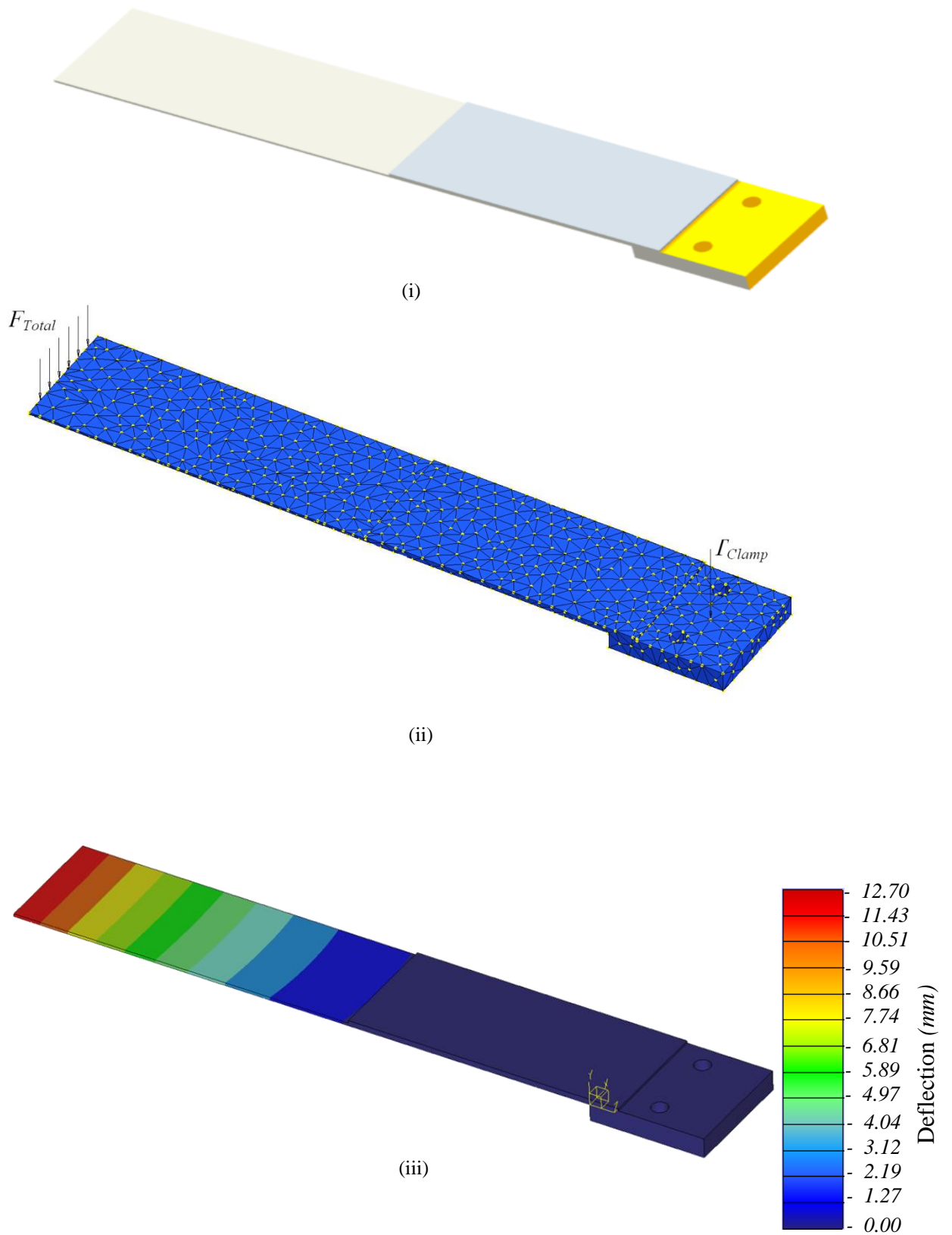


Figure 9.11: FEA Modelling of a Piezoelectric Fan

(i) Geometry

(ii) Discretisation

(iii) Post Processing

After ensuring that the total force defined by Eq. 9.15 was identical (within 11% - acceptable *FEA* error [62]) to the force required to deflect the fan by 12.70mm in *FEA*, a study of the stresses generated in the supporting structure was performed.

The constraints imposed on the structure represent the scenario when the structure is rigidly mounted to the fin base and thus is unable to perform any rigid body motion:

$$\Sigma_x = \Sigma_y = \Sigma_z = Rot_x = Rot_y = Rot_z = 0 \quad \dots \text{Eq. 9.16}$$

It was further decided to design the assembly unit to withstand an additional 2*G* force. The *FCCS* is intended for use in conjunction with an electric motor, but, when airborne, aircraft undergo several *G*-forces. It has been established that the highest *G*-force the assembly will need to resist is  $G_F = 2g$ . *CFRP* was the material of choice because of its high specific strength and stiffness when compared to other engineering materials.

Numerous structure designs were considered however, through a series of optimisation tests, the supporting structure depicted in Figure 9.12 was selected, a prototype of which was manufactured and tested.

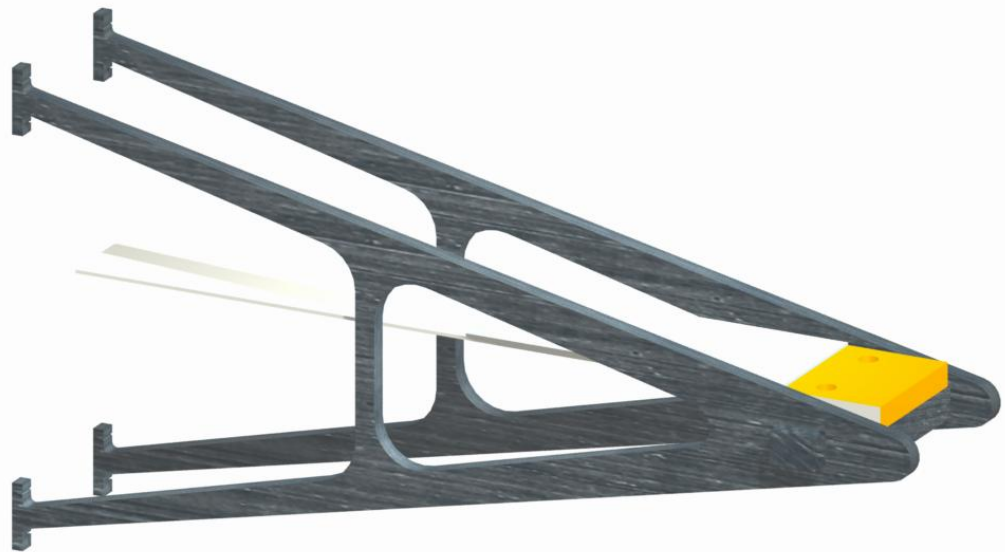


Figure 9.12: Piezoelectric Fan and Prototype *CFRP* Supporting Structure

A *FEA* study on the piezoelectric fan and supporting structure assembly was performed and the results indicate that the maximum *Von Mises* stress experienced by the structure is  $10.5\text{MPa}$  (which is significantly less than the yield stress of *CFRP* –  $55\text{MPa}$ ) and a maximum fan tip deflection of  $13.3\text{mm}$  respectively. Further details on the *FEA* modelling are given in **Appendix C**.

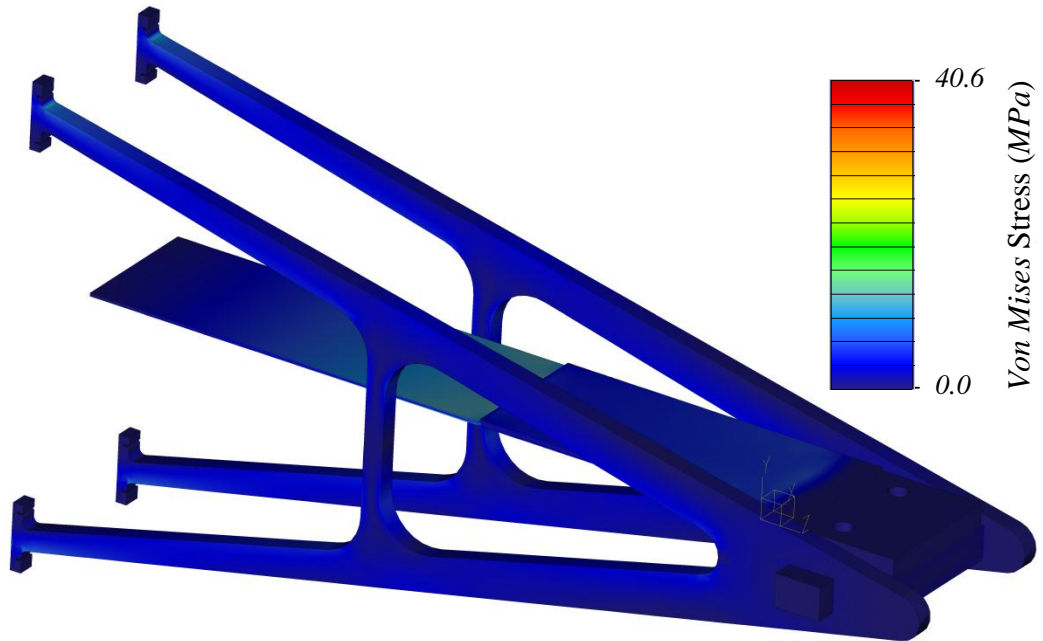


Figure 9.13: Numerical *FEA* Results - *Von Mises* Stresses (*MPa*)

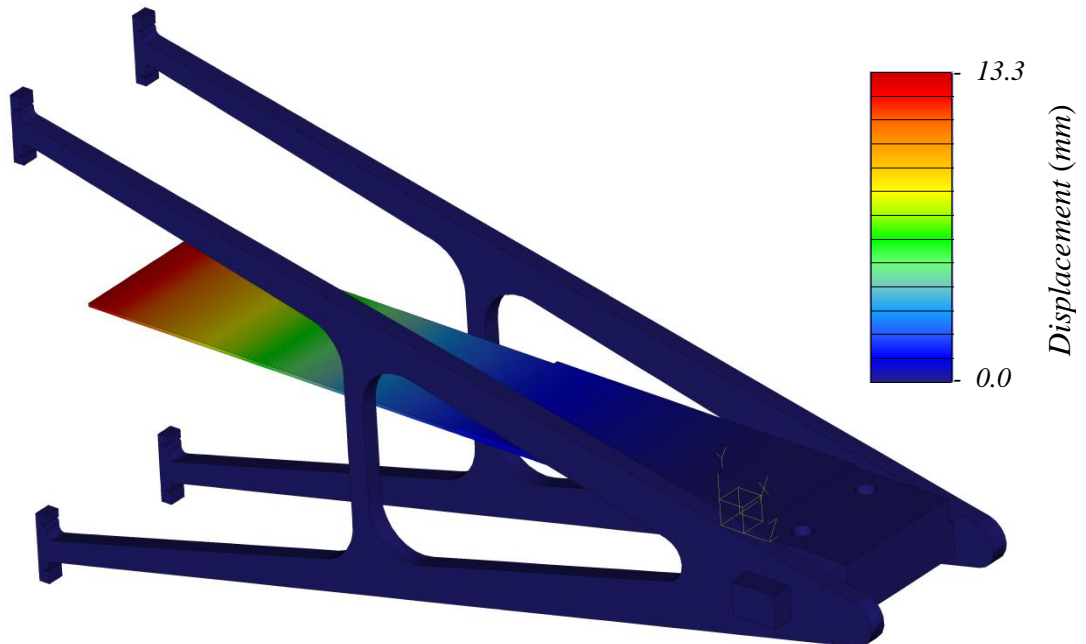


Figure 9.14: Numerical *FEA* Results - Displacement (*mm*)

The piezoelectric fan structure (Figure 9.12) was constructed from *CFRP*, as *CFRP* has a higher strength to weight ratio than steel whilst also being thermally insulating, making it suitable for the job at hand. This resulted in a structure mass of 3.80g, which in turn implied a total *FCCS* mass of 6.60g.

The *NC* and the *FCCS* cooling mass for the different fin spacings are represented in Figure 9.15, and shows that the *FCCS* mass are higher than the corresponding *NC* cooling mass as it incorporates the additional mass of the fan and its supporting structure.

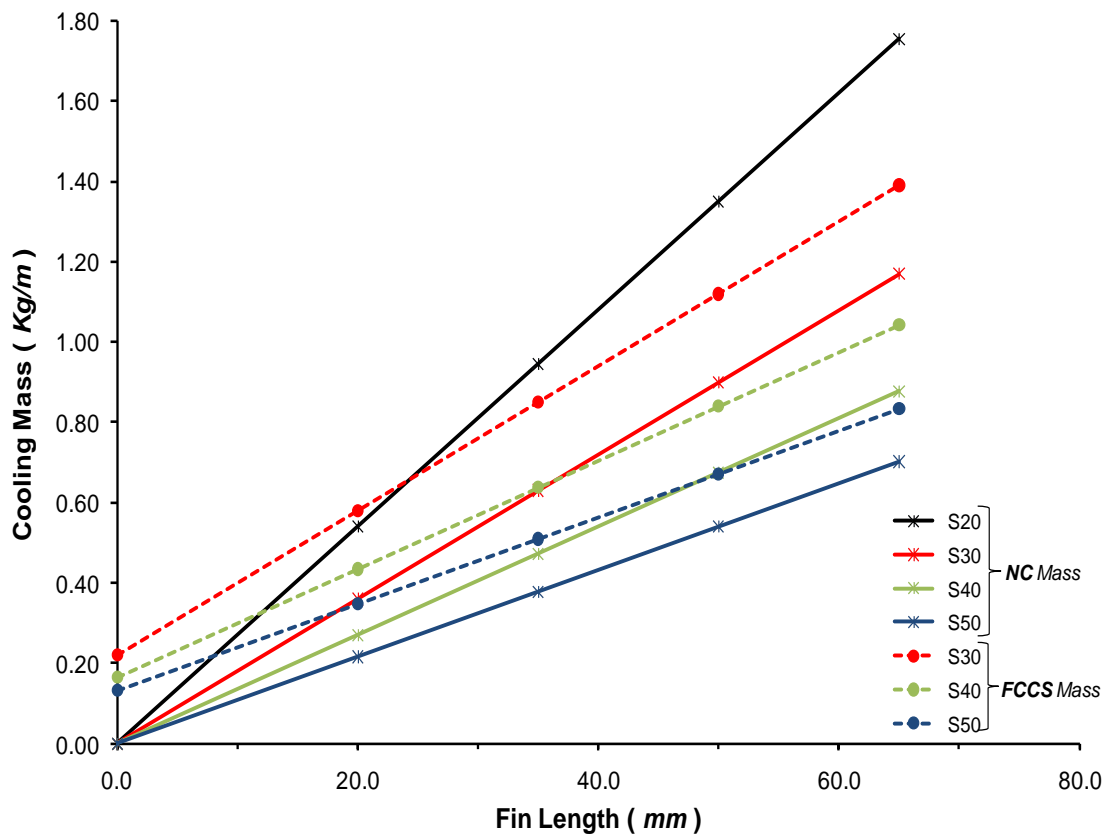


Figure 9.15: Comparative study between the *NC* and the *FCCS* mass for different Fin Spacings

To establish the weight saving capability of the innovative *FCCS*, Figure 9.7 (Thermal Resistance) and Figure 9.15 (Cooling Mass) must be superimposed onto the same plot (Figure 9.16). This is further explained in the next section – **Section 9.3.**

### 9.3 Combined Analysis – Thermal Resistance / FCCS Weight

In *Section 9.1*, it was shown that the optimal *FCCS* geometry solely based on the thermal resistance is that of a horizontally-mounted piezoelectric fan, with a fin spacing of  $30.0mm$ , and a separation distance of  $5.0mm$ , oscillating at the largest magnitude ( $V_{Pz} = 115.0V$ ). However, in Figure 9.16, a clearer idea of both the cooling enhancement and the weight saving capabilities of the *FCCS* may be determined.

As previously discussed, there is no single optimum *FCCS* configuration. That is, the applied optimum *FCCS* configuration is dependent on the imposed constraints: -  $R_{Equivalent}$ ,  $m$  and  $L_{Fin}$  (or cooling volume). To demonstrate this, each constraint shall be taken in turn and the benefits of introducing the *FCCS* will be investigated for each of the three different constraints.

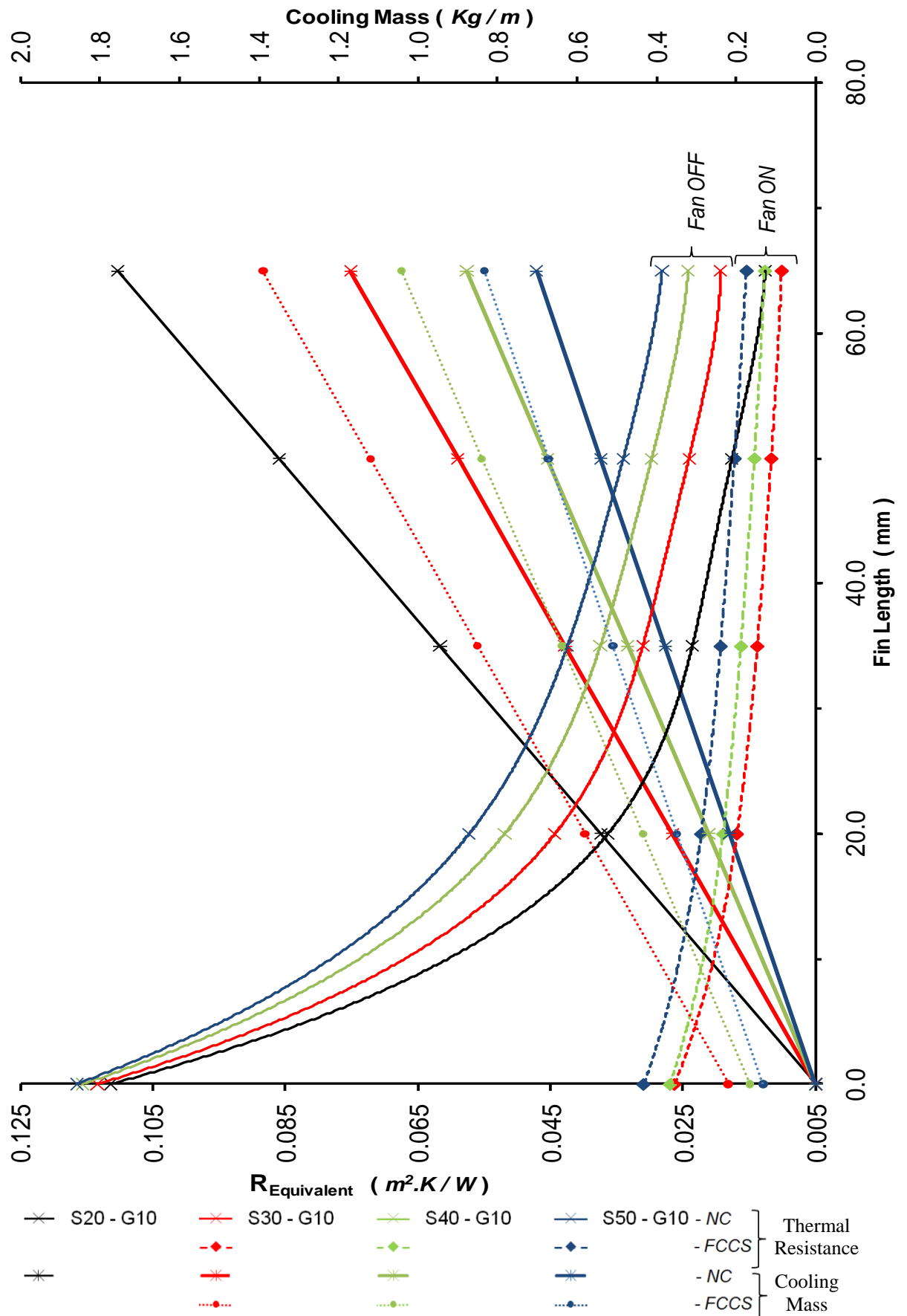


Figure 9.16: Thermal Resistance vs. Fin Length vs. Cooling Mass for different S - Horiz Fan,  $V_{Pz} = 115V$

### 9.3.1 Thermal Resistance Constraint

If a thermal resistance constraint of  $R_{Equivalent} = 0.020m^2.K/W$  is set up; by referring to Figure 9.16 the following results are obtained:

$$NC \quad - \quad S = 20mm, L_{Fin} = 38mm, m = 1.05kg/m$$

$$FCCS \quad - \quad S = 30mm, L_{Fin} = 6mm, m = 0.375kg/m$$

The above results indicate a 84.2% reduction in fin length (which is directly related to the cooling volume) and a 64.3% reduction in cooling mass. On the other hand, on applying a thermal resistance constraint of  $R_{Equivalent} = 0.065m^2.K/W$  yields the following results:

$$NC \quad - \quad S = 20mm, L_{Fin} = 9mm, m = 0.25kg/m$$

$$FCCS \quad - \quad S = 50mm, L_{Fin} = 0mm, m = 0.132kg/m$$

This latter scenario results in the complete elimination of all fin side walls, which in turn results in a 47.2% reduction in cooling mass.

### 9.3.2 Cooling Mass Constraint

The following constraint commonly results when the minimisation of mass is key. On setting up a cooling mass constraint of  $m = 0.80kg/m$  (typical of aerospace *PMSM*) and referring to Figure 9.16 once again, the following results:

$$NC \quad - \quad S = 20mm, R_{Equivalent} = 0.025m^2.K/W, L_{Fin} = 30.0mm$$

$$FCCS \quad - \quad S = 30mm, R_{Equivalent} = 0.015m^2.K/W, L_{Fin} = 32.5mm$$

The above results indicate a 20.0% reduction in the unit-cell thermal resistance. However, the cooling volume increases by 8.33%.

### 9.3.3 Fin Length (Motor Volume) Constraint

The following constraint commonly results when the minimisation of space (volume) is key, as is in the aerospace industry. This inherently means that the geometrical dimensions of the electric motor together with the applied cooling system must be as small as viably possible. On setting up a fin length constraint of  $L_{Fin} = 30mm$  and referring to Figure 9.16 once again, gives the following results:

$$NC \quad - \quad S = 20mm, R_{Equivalent} = 0.025m^2.K/W, m = 0.80kg/m$$

$$FCCS \quad - \quad S = 50mm, R_{Equivalent} = 0.020m^2.K/W, m = 0.435kg/m$$

The above results in a 20.0% reduction in the unit-cell thermal resistance and in a 45.6% reduction in cooling mass.

## 9.4 Concluding Remarks

It has been shown that the optimum FCCS geometry is, that of a horizontally-mounted fan operating at  $V_{Pz} = 115.0V$ ,  $G = 5.0mm$  and  $S = 30.00mm$ .



However, this result may further be optimised depending on the applied constraint (thermal resistance, cooling mass or volume). However, for all scenarios, the implementation of the innovative *FCCS* results in significant benefits, which, implies that that the design is feasible.

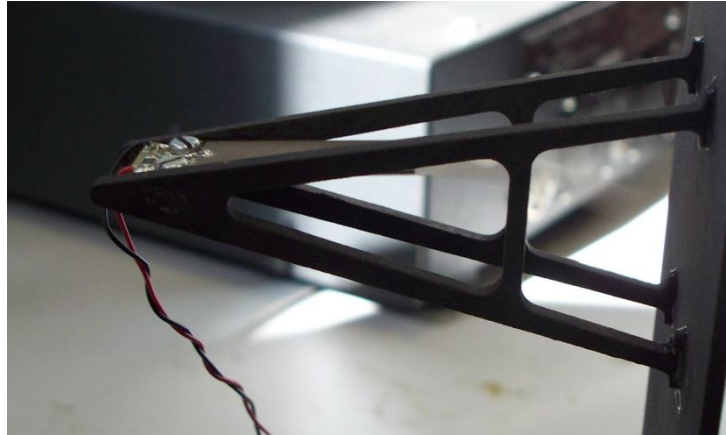


Figure 9.17: *CFRP FCCS* Prototype

A fully-functioning prototype *FCCS* (Figure 9.17) was fabricated and tested, to further ensure that the structure was rigid enough to withstand the loads generated by a horizontally-mounted oscillating piezoelectric fan. The fault tolerant characteristics during continuous piezoelectric fan operation were further evaluated and the effect of fatigue investigated.

# CHAPTER 10

## 10. Conclusions and Recommendations

---

The present research underlines the importance of adequate electric motor housing cooling, and how this can be implemented, through analytical and experimental techniques. The original contribution to knowledge is in the investigation and proposal of one such innovative forced cooling convective system. The suggested *FCCS* is, tested, optimised, characterised and a fully functioning prototype manufactured.

This work is of particular relevance since electric machine manufactures, over the past years, have been striving to reduce the physical dimensions while maintaining (or even yet increasing) the power density. This in turn, generates temperature gradients, which may result in machine failure if no effective cooling mechanism is in place. Furthermore, with the introduction of *MEA* enhanced cooling mechanisms are of even greater importance.

In each of these sections, conclusions, for the numerous design aspects related to the optimisation of an electric motor housing, together with the conducted experimental program for an optimised *FCCS* are drawn up and discussed in some detail. Lastly, in *Section 10.6*, a series of recommendations are presented.

### 10.1 Electric Motor Thermal Modelling

A representative user-generated lumped circuit thermal model of a typical aerospace *PMSM* was created and calibrated using direct experimentation. The thermal modelling software, *MotorCAD* was further modified to include the affects of altitude. The thermal model was further utilised to simulate various

expected loading conditions (duty cycles) on commercial aircraft flight surfaces (mid-spoilers, ailerons, etc.). Furthermore, the thermal model was used to optimise the *PMSM* housing geometry.

## **10.2 Electric Motor Housing Optimisation**

It has been shown that the best suited natural convection finned housing, for any horizontally-mounted electric motor is a radial-finned one. Furthermore, for current aerospace *PMSM*, for minimum weight and minimum volume, the optimal cooling geometry is typically:  $\%cut = 0\%$ ,  $s_{Fin} = 20.0mm$  and  $t_{Fin} = 2.0mm$ . However, the established fully optimised naturally cooled, radial-finned housing alone, is still not sufficient to limit the critical motor component temperatures during flight operation. To this effect, an innovative *FCCS* mechanism (an oscillating piezoelectric fan) was proposed and its cooling capabilities investigated in detail.

## **10.3 FCCS Cooling Enhancement Characteristics**

The cooling capabilities of the suggested innovative *FCCS* were evaluated for numerous different geometrical configurations ( $A_{Pz}, G, S, Orientation$ ). Measurements of local temperatures, local heat transfer coefficients, local and mean percentage increase in heat transfer indicated that a horizontally-mounted piezoelectric fan operating at maximum voltage ( $V_{Pz}$ ) and  $G = 5.0mm$  is better suited in cooling *FB* when compared to a vertically-mounted piezoelectric fan. Furthermore, it has been established that a vertically-mounted fan, operating at maximum voltage ( $V_{Pz}$ ) and  $G = 15.0mm$ , is far superior in cooling the *FSW* of a straight finned heat sink than a horizontally-mounted one.

## 10.4 FCCS Flow Characteristics

*PIV* experimentation techniques indicated that the flow fields produced by an oscillating piezoelectric fan are unsteady (with numerous vortices being shed in each swing), and comprise a bulk mean flow superimposed onto a highly turbulent fluctuating component, which in turn indicated that the convective cooling enhancement is dependent on  $\%h_{inc.} = f(\overline{V_{Mean}}, V_{RMS})$ .

For both fan orientations, experimental results indicate that an increase in  $V_{Pz}$  and a reduction in the separation distance  $G$ , both result in an increase in the *FB* velocities. However, when investigating the fan cooling effect on the *FSW*'s, for both fan orientations, it was established that a larger separation distance is beneficial. Furthermore, it has been established that a horizontally-mounted fan is far better suited in cooling the *FB* when compared to a vertically-mounted fan. However, the converse holds for the *FSW*'s – i.e. a vertically-mounted fan is better suited in cooling the *FSW* when compared to a horizontally-mounted fan.

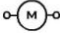
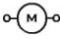
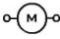
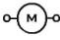
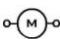
Lastly, the fluid flow results bear a close resemblance to the cooling plots: cooling patterns, cooling range, and cooling intensity have been well matched for most if not all of the tested geometrical configurations.

## 10.5 Implementation of FCCS

It has been shown that the overall optimum *FCCS* geometry is that of a horizontally-mounted fan operating at  $V_{Pz} = 115.0V$ ,  $G = 5.0mm$  and  $S = 30.00mm$ . For all the considered constraints ( $R_{Equivalent}, m, L_{Fln}$ ), the implementation of the *FCCS* results in significant benefits, which in turn, makes the innovative *FCCS* design a viable solution. Furthermore a prototype *FCCS* supporting structure was tested, both to evaluate the structure rigidity (under the generated loads), as well as to evaluate the reliability (fault tolerance) of a horizontally-mounted oscillating piezoelectric fan.

## 10.6 Contribution of the Thesis

The following points list the original contribution to the field of electric machine cooling enhancement this thesis has made.

-  A commercial thermal optimisation software package, *MotorCAD* was modified to include the affects of altitude. This was vital in evaluation the correct motor temperatures reached during flight and is an original contribution of this work.
-  An overall (Electromagnetic and Thermal) optimisation technique was developed to minimise a *PMSM* weight and volume for a given set of operating parameters. The said optimisation technique is new, and adds knowledge in the field of electric machine cooling.
-  An innovative *FFCS* mechanism (oscillating piezoelectric fan) was proposed and its cooling capabilities investigated through a detailed experimental programme. While *FFCS* are not new, the incorporation of oscillating piezoelectric fans to provide forced cooling is original.
-  *2D* local convective heat transfer coefficients, together with local and mean percentage increase in heat transfer generated by an oscillating piezoelectric fan have been evaluated for numerous different geometrical configurations ( $A_{pz}, G, S, Orientaton$ ) for both the fin base and fin side wall surfaces of a vertical heat sink. This adds knowledge in this area.
-  Complimentary airflow (*PIV*) measurements on both a heat sink fin base and fin side wall were taken by means of *NIOMT*, and

the complex flow regimes characterised in detail. While the *PIV* technique has been around for a few years now, the manner in which it was applied (to capture flow fields generated by the proposed *FCCS* in a fin channel) is new and innovative.



Equivalent thermal resistance plots have been developed to characterise the overall benefit of the suggested *FCCS* on a finned motor housing. A prototype *FCCS* was tested to evaluate, both the structure rigidity and reliability.

## **10.7 Future Work**

As discussed earlier, this work was undertaken as a baseline study, as no other studies have so far been published. Thus, a number of recommendations for future work can be underlined:

1. The proposed  $h_{EWdg}$  variation with altitude equation should be validated experimentally by means of an environmental chamber.
2. Acquire *2D IR* temperature data of *FB* and *FSW*, when both surfaces are heated simultaneously. This would yield improved results as radiation effects (*VF*'s), and boundary layer interaction would be taken into account.
3. Conduct airflow investigations (*PIV*) measurements on a heated finned surface. This will take into account the buoyancy effects negated in this work.
4. Perform both thermal and *3D* airflow measurements (stereoscopic *PIV*) with the newly designed *FCCS* supporting structure, rather than the *3D* positioning system.

5. Evaluate the cooling potential of the *FCCS* with a fin spacing of  $S = 20.00mm$ . Alternative fan designs may be further considered.
6. Evaluate the cooling potential of the *FCCS* in conjunction with annular fins on a cylindrical machine. Furthermore, the affect of radial finned housing curvature should be investigated.
7. Evaluate the reduction in the cooling capability when *FCCS* is operated at typical flight levels.
8. The theoretical aspects defining the fluid flow patterns need to be further investigated. Furthermore, the correlation between the fluid flow patterns and the local heat transfer coefficients need to be investigated further.

# Appendix A

## Guidelines for Successful Thermal Modelling - *MotorCAD*

---

### Introduction

*MotorCAD* is a dedicated software package for the thermal analysis of electric machines (motors and generators) and is based on the lumped resistance network method. As the lumped resistance network method is based on analytical algorithms, calculations speeds are almost instantaneous, unlike the time-consuming numerical and costly *CFD* techniques.

*MotorCAD* is governed by several user interfaces, the key to which shall be presented in the following section. Some of the major equations are further detailed.

### Graphical User Interfaces

The *MotorCAD* thermal software is based on several intuitive user interface screens that make for easy data input and interpretation of results [52]. Any successful electric machine thermal analysis should involve:

1. Radial and Axial Cross Section Definitions
2. Winding Definition
3. Loss Definition
4. Material Selection
5. Operating Conditions (Steady State / Transient / Duty Cycles)

The above tabs are further discussed in some detail in the ensuing sections. However, for further in-depth details, the reader is referred to [52].



### 1. Radial and Axial Cross Section Definitions

The machine geometry is firstly defined using the radial and axial cross section tabs. Both the radial (Figure A. 2) and the axial (Figure A. 3) cross section geometrical data is required such that a representative 3D machine model can be built. This in turn implies that the heat transfer paths can be evaluated in three orthogonal directions by the software in question.

The software incorporates a large database of different machine configurations, passively and actively cooled housing geometries as well as several mounting types (flange, foot mounted), a sample of which are depicted in Figure A. 1 hereunder.

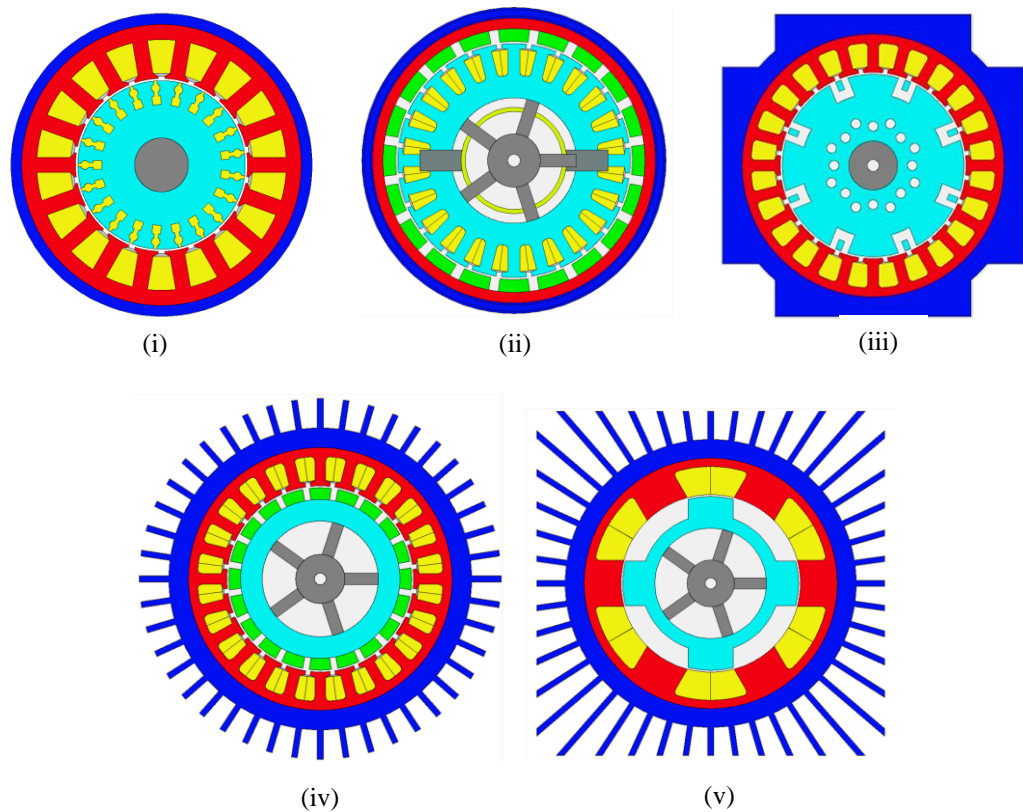


Figure A. 1: Sample of Possible Motor Geometries and Housing Designs

- |   |                                 |
|---|---------------------------------|
| (i) Induction (Asynchronous) Machine                | - Round Housing                 |
| (ii) Permanent Magnet <i>DC</i> Commutator Machine  | - Water Jacket                  |
| (iii) <i>CLAW</i> Pole Machine                      | - Servo Housing + Cooling Ducts |
| (iv) Brushless Permanent Magnet Synchronous Machine | - Axial Rectangular Fins        |
| (v) Switched Reluctance Machine                     | - Axial Square Fins             |

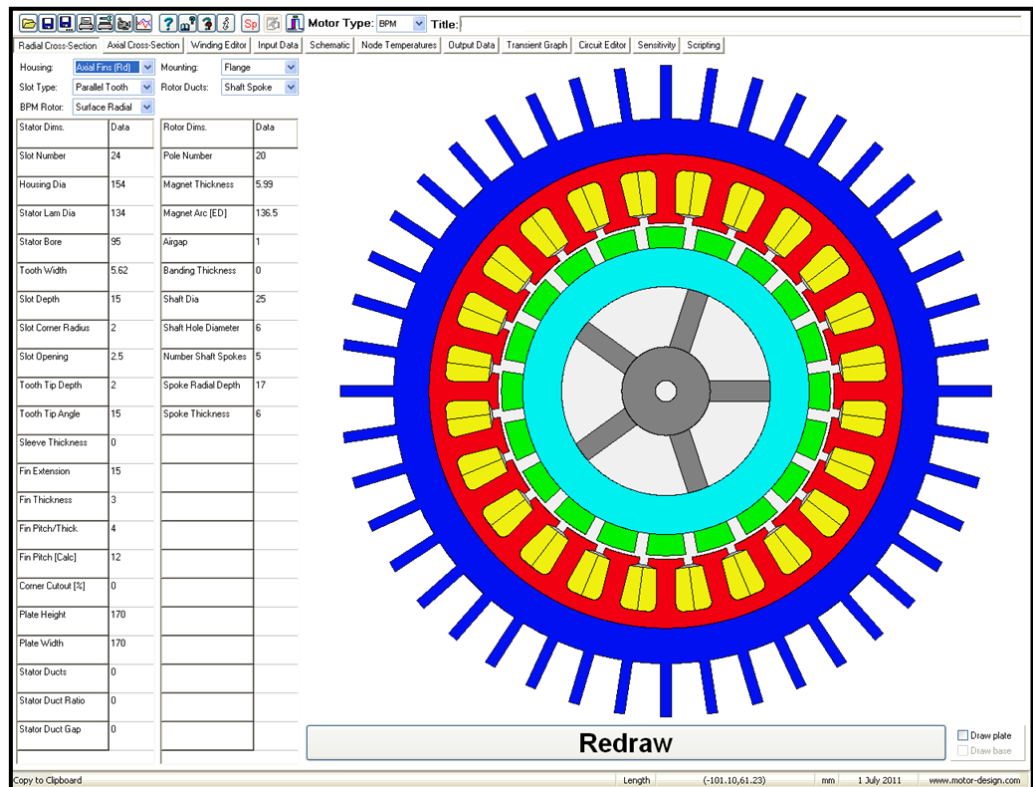


Figure A. 2: Radial Cross Section Graphical Editor

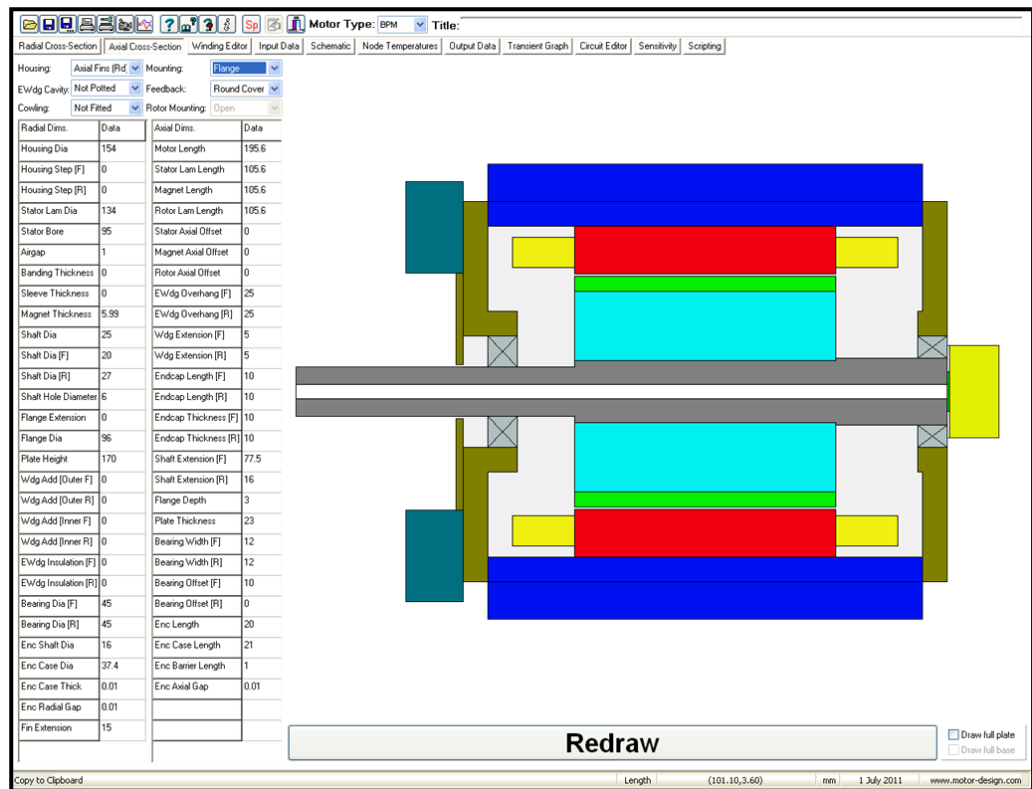


Figure A. 3: Axial Cross Section Graphical Editor

## 2. Winding Definition

The winding definition editor allows the user to input the machine's winding details, such as: copper diameter, slot type (and geometry), impregnation and liner characteristics as well as the slot fill factor amongst others. The indicative diagram (Figure A. 4) present in the winding definition tab is dynamically responsive to any user input.

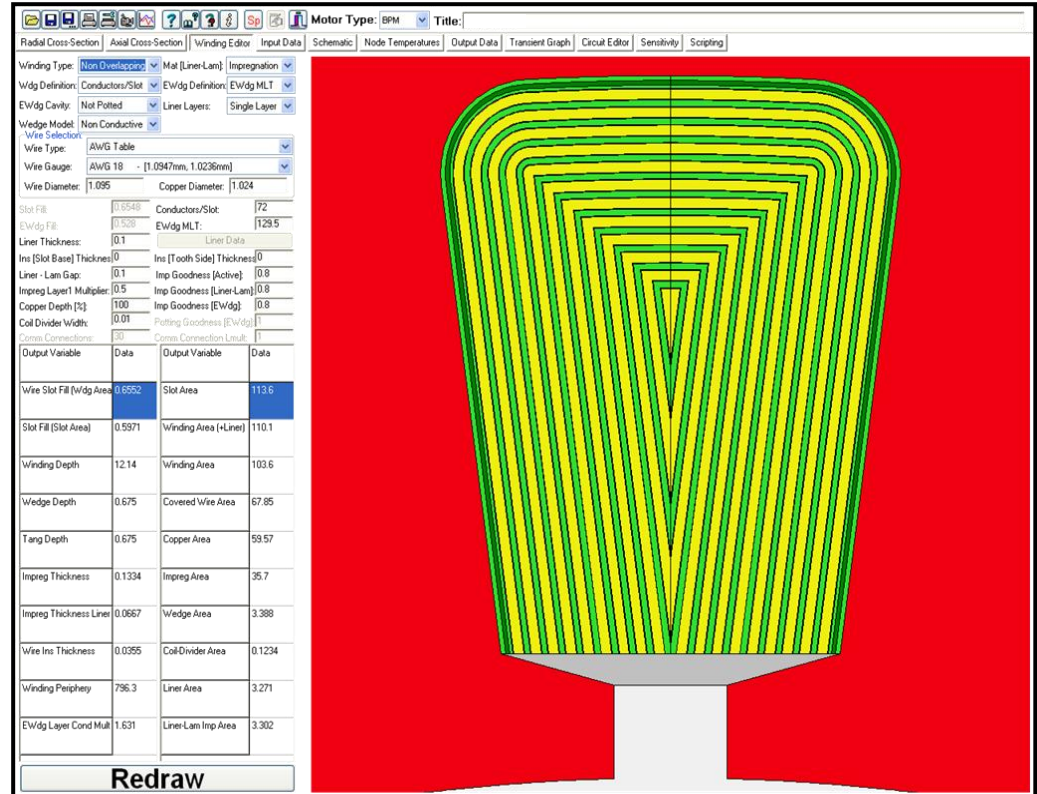


Figure A. 4: Winding Configuration Graphical Editor

The correct modelling of the machine winding is critical. The slot fill factor ( $SFF$ ), identifies how much copper is present in each slot. From this, the total copper volume and weight present in the motor can be established, and as aforementioned (*Chapter 2* and *Chapter 3*), the copper loss ( $P_{Cu}$ ) is generated here and is dependent on the amount of total copper present in the stator slots. Hence,

$$SFF = \frac{A_{Cu}}{A_{Slot}} \quad \dots \text{Eq. A. 1}$$

### 3. Loss Definition

In this tab, the user details all component losses (mechanical and electrical) present during machine operation. The mechanical losses constitute the bearing, and the windage losses, while the electrical losses constitute the copper, hysteresis and eddy current losses.

The friction/bearing losses are represented as a function of the frequency - ( $f$ ), while the windage loss is defined as a function of the cube of the frequency ( $f^3$ ). However, it is common practice to obtain the bearing loss data directly from the bearing suppliers. Supplied data comes as a function of both rotational speed ( $N_{Motor}$ ) and temperature which can be directly imported into *MotorCAD*. Similarly, the eddy current losses are a function of the square of the frequency ( $f^2$ ), while hysteresis losses are a function of the frequency ( $f$ ). On the other hand, the copper losses are speed independent.

**Loss Variation with Speed:**

$P_{\text{speed}} = P_{\text{input}} \times \left[ \frac{\text{Speed}}{\text{Speed(REF)}} \right]^{\text{coef[A]}}$

☒ Speed Dependent Losses  
 Shaft Speed [rpm] 600  
☒ Single value of Speed(REF) [rpm] 600

Component	P[input]	Speed(REF)	coef[A]	W/kg	P[speed]
<b>Units</b>	<b>Watts</b>	<b>rpm</b>		<b>W/kg</b>	<b>Watts</b>
Loss [Stator Copper] @Tm(p)	87.08	600	0	39.96	87.08
Loss [Stator Back Iron] @Tm(p)	9.83	600	1.5	6.897	9.83
Loss [Stator Tooth] @Tm(p)	9.83	600	1	5.403	9.83
Loss [Magnet] @Tm(p)	0.886	600	1.96	0.901	0.886
Loss [Rotor Back Iron] @Tm(p)	3.041	600	1.481	1.524	3.041
Loss [Friction - F Bearing]	0.616	600	0	0	0.616
Loss [Friction - R Bearing]	0.616	600	0	0	0.616
Loss [Windage]	0.005	600	0	0	0.005
Loss [Windage] (Ext Fan)	0	600	0	0	0
Loss [Encoder]	1	600	1	0	1
Power Injected [Endcap Front]	0	600	0	0	0
Power Injected [Endcap Rear]	0	600	0	0	0
Power Injected [Feet]	0	600	0	0	0
Power Injected [Shaft Active]	0	600	0	0	0
Power Injected [Shaft Front]	0	600	0	0	0
Power Injected [Shaft Rear]	0	600	0	0	0
Power Injected [Wdg Front]	0	600	0	0	0
Power Injected [Wdg Rear]	0	600	0	0	0
Power Injected [Plate]	0	600	0	0	0
Power Injected [Wdg Outer]	0	600	0	0	0
Power Injected [ESpace Front]	0	600	0	0	0
Power Injected [ESpace Rear]	0	600	0	0	0

**Check Data**

**Stator Copper Loss Distribution:**  
☒ Equal (Ia = Ib = Ic)  
☐ S-step (Ia = Ib, Ic = 0)  
☐ Sine (Ia/2 = Ib = Ic)

**Winding Temp Variation with Proximity Loss Distribution:**  
 Percentage Winding Temperature Increase (at Proximity RPM): 0  
 Proximity RPM: 1E4

**Copper Loss Variation with Temperature:**  
☐ Copper Losses Vary with Temperature  
 Winding Temperature at which Pcu Input: 20

**Loss Variation with Temperature & Load:**  
☒ Losses Vary with Temperature & Load  
☐ Constant Torque or Constant Current  
☐ Constant Torque  
☐ Constant Current

Winding Temperature - Tw(p): 23.7  
 Magnet Temperature - Tm(p): 23.7  
 Shaft Torque [Nm] (@Pcu defined): 20  
 Motor Current [Amps] (@Pcu defined): 7.619  
 Torque Constant [Nm/A]: 2.625  
 Torque & Current Multiplier: 1  
 Rph @Tm(p): 0.5  
 Magnet Temperature Coefficient Br: -0.12  
 Iron Loss Flux To Power Ratio: 1.5  
 Phases: 3

**Losses Notes:**  
 Type in user notes here

Length: (-4,35,62.49) mm 4 July 2011 www.motor-design.com

Figure A. 5: Losses Tab - Typical Losses for a *PMSM*

Furthermore, all losses are temperature dependent. As the motor temperatures increase (due to operation), the magnetic flux ( $B_s$ ) produced by the magnets decreases. This in turn requires an additional current to be supplied to regain the lost flux. However, an increase in the phase current ( $I$ ), results in a further increase in the copper loss ( $\therefore 3I^2R$ ). This in turn further increases the motor component temperatures – in particular,  $T_{EWdg}$ .

The full equations describing the motor losses are reported in **Chapter 1**.

Figure A. 5 depicts the loss data for the *PMSM* discussed in **Chapter 3**, when operating at  $600rpm$  and a  $20Nm$  torque. Along with the machine losses, the user is responsible for adding information on the: number of motor phases, copper winding thermal resistance ( $R$ ), current ( $I$ ), speed ( $N_{Motor}$ ) and torque loading ( $\Gamma$ ).

Motor losses are difficult to predict accurately. Traditionally, losses were measured from an experimental rig, however, nowadays, with the use of *FEA*, certain losses may be calculated. However, while the latter is more cost effective to implement, certain issues with the software still occur. Primarily, in the determination of the electromagnetic losses (using *FEA*), all material properties are defined at the ambient conditions, rather than the current operating temperatures. This in turn underestimates the losses present during motor operation.

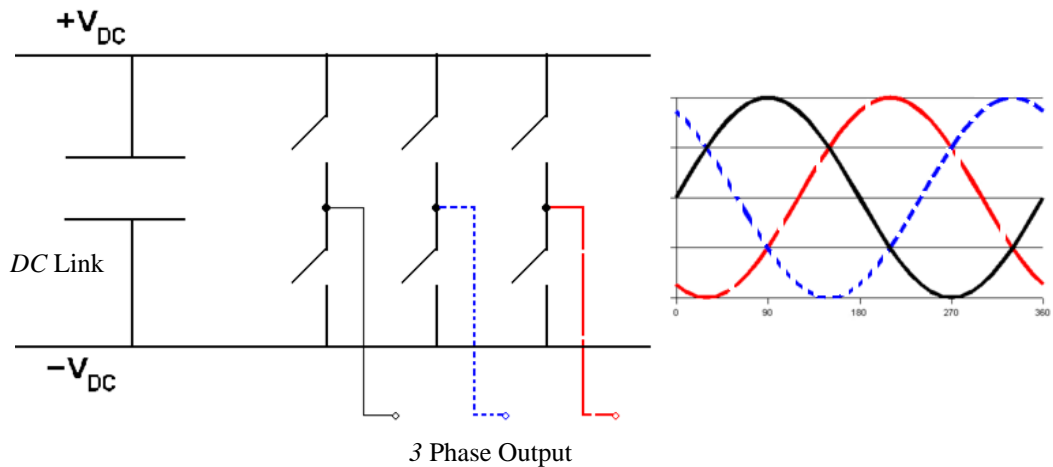


Figure A. 6: Schematic of a Voltage Source Inverter (Converter)

It is important to point out that, current harmonics are not modelled in current electromagnetic *FEA* software packages. Harmonics are a form of distortion produced by a voltage source inverter when switching (at high frequency) from a *DC* current to a 3 phase *AC* current (Figure A. 6). This in turn leads to the production of a non-uniform supplied motor sinusoidal output *ac* waveform, which in turn generates additional losses.

It is a rule of thumb that the predicted *FEA* (using current software) electromagnetic losses are under predicted by a maximum of 20%.

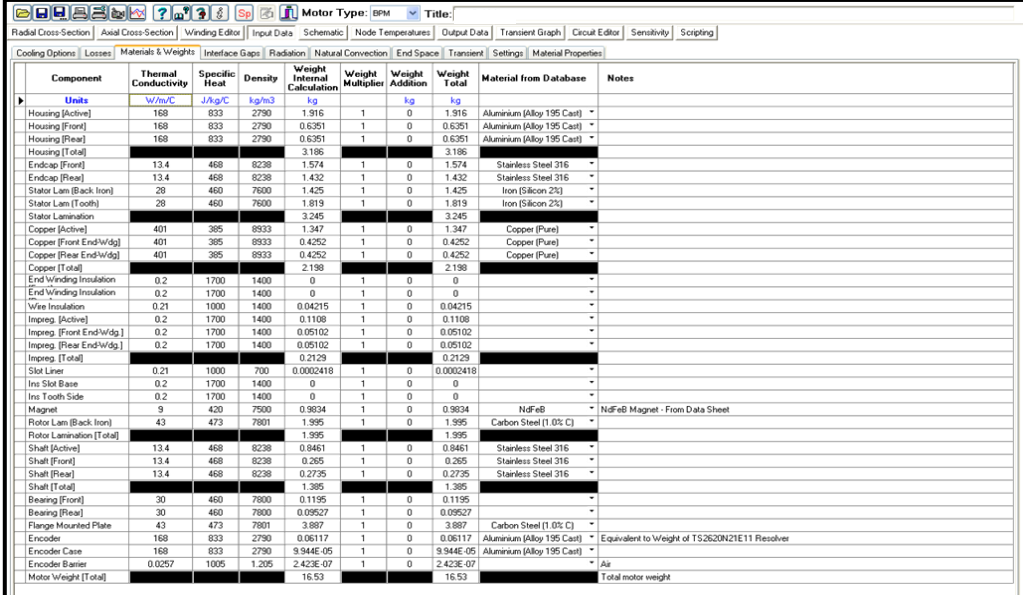
#### 4. Material Selection

The material's data tab (Figure A. 7) allows the user to select the constituting motor components material properties. While an extensive database is provided in *MotorCAD*, the user has the ability to modify and add additional materials if required.

The correct material selection is of importance, as both the thermal gradients (capacitance) as well as the motor weight are affected.

$$C = mC_p$$

... Eq. A. 2



Component	Thermal Conductivity	Specific Heat	Density	Weight Internal Calculation	Weight Multiplier	Weight Addition	Weight Total	Material from Database	Notes
Units	W/m°C	J/kg°C	kg/m³	kg		kg	kg		
Housing [Active]	168	833	2790	1.916	1	0	1.916	Aluminium (Alloy 195 Cast)	
Housing [Front]	168	833	2790	0.6351	1	0	0.6351	Aluminium (Alloy 195 Cast)	
Housing [Rear]	168	833	2790	0.6351	1	0	0.6351	Aluminium (Alloy 195 Cast)	
Housing [Total]				3.186			3.186		
Endcap [Front]	13.4	468	8238	1.574	1	0	1.574	Stainless Steel 316	
Endcap [Rear]	13.4	468	8238	1.432	1	0	1.432	Stainless Steel 316	
Stator Lam (Back Iron)	28	460	7600	1.425	1	0	1.425	Iron (Silicon 2%)	
Stator Lam (Tooth)	28	460	7600	1.819	1	0	1.819	Iron (Silicon 2%)	
Stator Lamination				3.245			3.245		
Copper [Active]	401	385	8933	1.347	1	0	1.347	Copper (Pure)	
Copper [Front End/Wdg]	401	385	8933	0.4252	1	0	0.4252	Copper (Pure)	
Copper [Rear End/Wdg]	401	385	8933	0.4252	1	0	0.4252	Copper (Pure)	
Copper [Total]				2.198			2.198		
End Winding Insulation	0.2	1700	1400	0	1	0	0		
Wire Insulation	0.2	1700	1400	0	1	0	0		
Impreg. [Active]	0.2	1700	1400	0.04215	1	0	0.04215		
Impreg. [Front End/Wdg]	0.2	1700	1400	0.05102	1	0	0.05102		
Impreg. [Rear End/Wdg]	0.2	1700	1400	0.05102	1	0	0.05102		
Impreg. [Total]				0.2129			0.2129		
Slot Liner	0.21	1000	700	0.0002418	1	0	0.0002418		
Ins Slot Base	0.2	1700	1400	0	1	0	0		
Ins Tooth Side	0.2	1700	1400	0	1	0	0		
Magnet	9	420	7500	0.9634	1	0	0.9634	NdFeB	NdFeB Magnet - From Data Sheet
Rotor Lam (Back Iron)	43	473	7801	1.995	1	0	1.995	Carbon Steel (1.0% C)	
Rotor Lamination [Total]				1.995			1.995		
Shaft [Active]	13.4	468	8238	0.8461	1	0	0.8461	Stainless Steel 316	
Shaft [Front]	13.4	468	8238	0.205	1	0	0.205	Stainless Steel 316	
Shaft [Rear]	13.4	468	8238	0.2735	1	0	0.2735	Stainless Steel 316	
Shaft [Total]				1.305			1.305		
Bearing [Front]	30	460	7800	0.09527	1	0	0.09527		
Bearing [Rear]	30	460	7800	0.09527	1	0	0.09527		
Flange Mounted Plate	43	473	7801	3.887	1	0	3.887	Carbon Steel (1.0% C)	
Encoder	168	833	2790	0.05117	1	0	0.05117	Aluminium (Alloy 195 Cast)	Equivalent to Weight of TS2620N21E11 Resolver
Encoder Case	168	833	2790	9.944E-05	1	0	9.944E-05	Aluminium (Alloy 195 Cast)	
Encoder Barrier	0.0257	1005	1.205	2.423E-07	1	0	2.423E-07	Air	
Motor Weight [Total]				16.53			16.53		Total motor weight

Figure A. 7: Material Component Definition



## 5. Operating Conditions (Steady State / Transient / Duty Cycles)

The user needs also to define certain operating conditions, some of which are: altitude/flight level and the surrounding motor ambient temperature ( $T_{\infty}$ ).

As mentioned briefly in **Chapter 2**, *MotorCAD* is based on a lumped circuit resistance network. The network (Figure A. 8) consists of nodes, representative of the individual motor components.

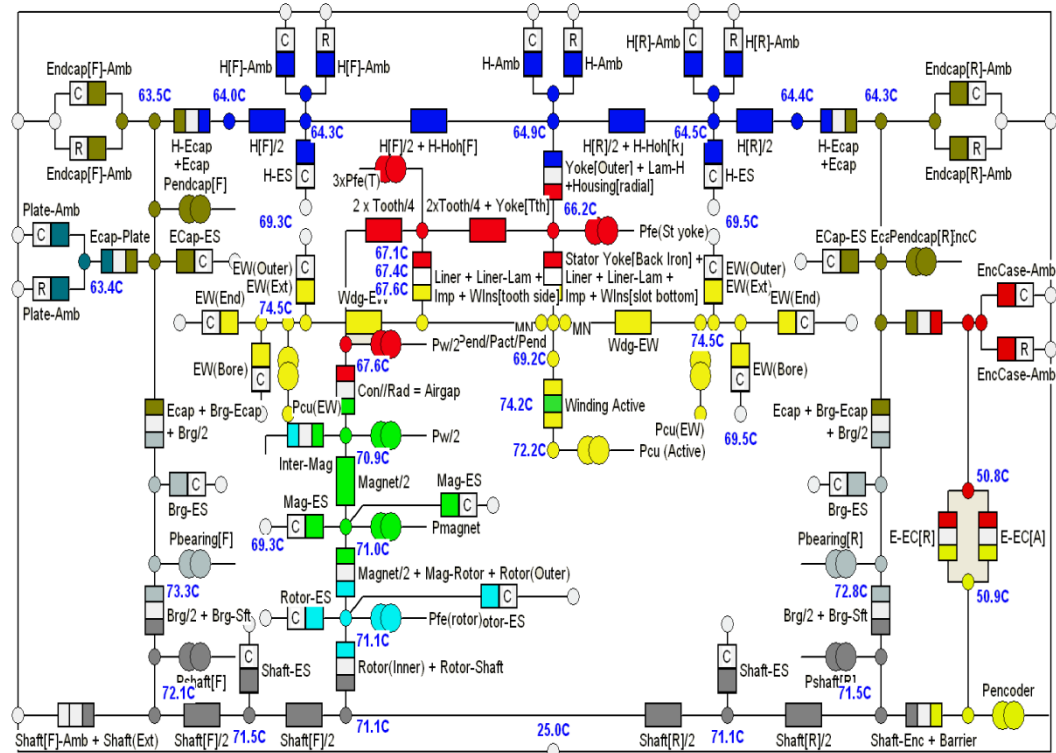


Figure A. 8: Schematic of a Mid Spoiler Flight Actuator when applied a Transient Duty Cycle

Each node is connected by thermal resistances (conduction, convection, radiation), thermal capacitors (for transient operation), as well as power (heat) sources, each of which are colour coded to the components shown in the graphical user interfaces. Furthermore, vertical-oriented thermal resistances represent radial heat transfer, while horizontal-oriented thermal resistances are representative of axial heat transfer. To further aid the user, resistances denoted by a 'C' and an 'R' are representative of convective and radiative resistances respectively. Lastly, resistances marked by two distinct colours represent interface resistances. This is further clarified by Figure A. 9.

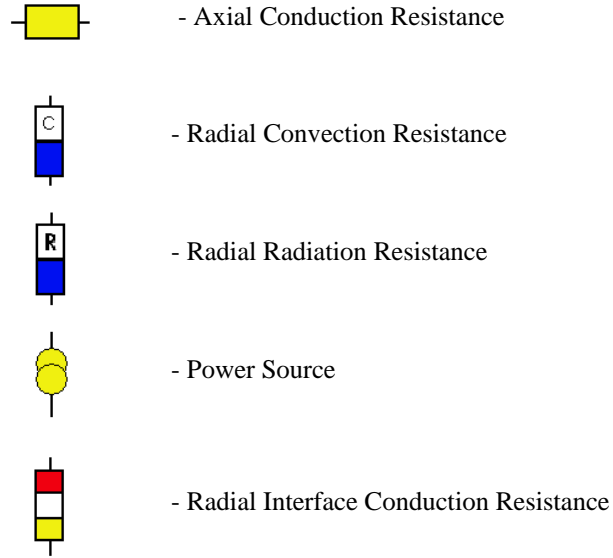


Figure A. 9: *MotorCAD* Representative Symbols

The formulations for the above are simple to evaluate. While the heat sources (losses) are dictated by the user from the Losses tab, the conduction resistances may be evaluated by: dividing the path length ( $L$ ) by the product of the path area ( $A$ ) and the thermal conductivity ( $k$ ).

$$R_{Conduction} = \frac{L}{k \cdot A} \quad \dots \text{Eq. A. 3}$$

It is worth noting that, the convection and radiation resistances are equal to unity divided by the product of the surface area ( $A$ ) and the respective heat transfer coefficient ( $h_{Convection}, h_{Radiation}$ ).

$$R_{Convection} = \frac{1}{h_{Convection} \cdot A} \quad \dots \text{Eq. A. 4}$$

$$R_{Radiation} = \frac{1}{h_{Radiation} \cdot A} \quad \dots \text{Eq. A. 5}$$



The convective heat transfer coefficients (both natural and forced), are defined according to particular geometry: flat, vertical and inclined plates, horizontal and vertical cylinders, open channels, etc. These correlations are well established in *MotorCAD* as they are taken from numerous reliable sources. Similarly, the radiation heat transfer coefficient ( $h_{\text{Radiation}}$ ) may be defined according to Eq. A.6.

$$h_{\text{Radiation}} = \frac{\sigma \cdot \varepsilon \cdot V F \cdot (T_1^4 - T_\infty^4)}{(T_1 - T_\infty)} \quad \dots \text{Eq. A. 6}$$

Along with steady state analysis, the user may wish to perform thermal transients. Transient analyses, along with duty cycles, are indicative of the motor's performance during a practical situation.

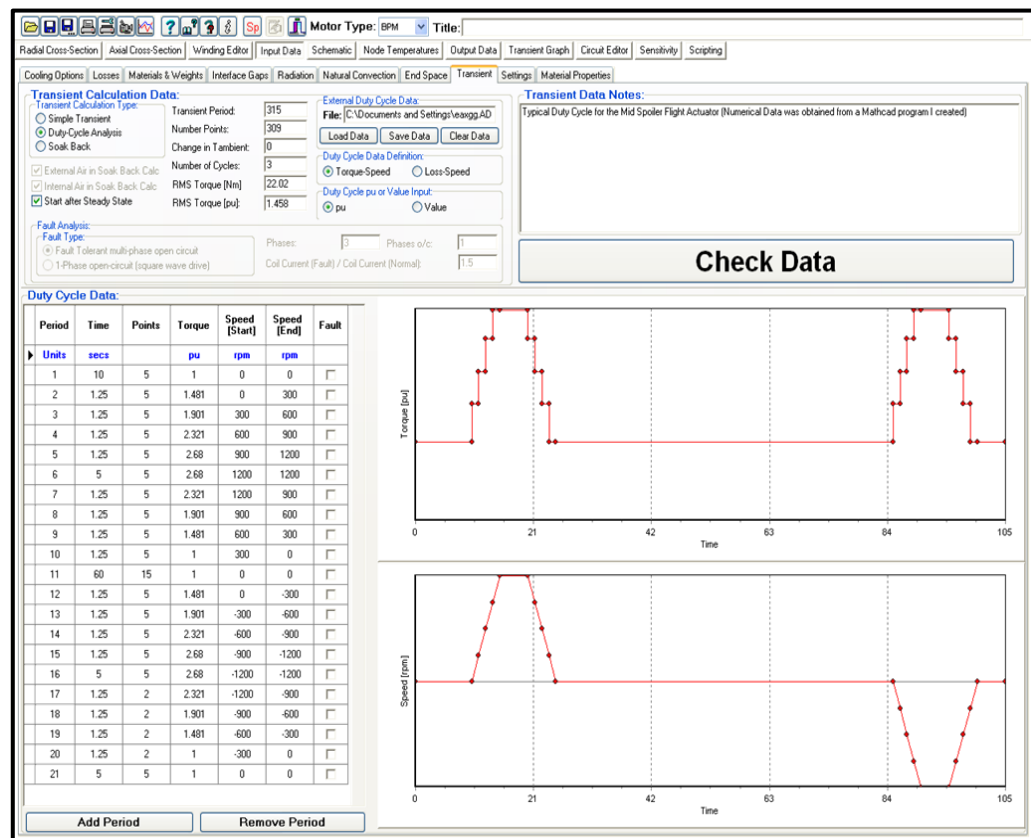


Figure A. 10: Duty Cycle for a Mid Spoiler Flight Actuator

Figure A. 10 depicts the operation of a mid spoiler actuator *PMSM*. The actuator maintains a  $15Nm$  background torque and is run through three continuous extension – retraction cycles. The maximum torque and speed sustained by the *PMSM* is that of  $40.2Nm$  and  $1200rpm$  respectively. Figure A. 11 below, depicts the temperature contour plots when applying the duty cycle depicted in Figure A. 10.

In this scenario, the end winding does not have time to cool down between extension/retraction cycles due to the short transient times. This in turn results in the compounding *EWdg* temperature ( $T_{EWdg}$ ) increase, which may lead to an excess temperature rise, resulting in motor breakdown.

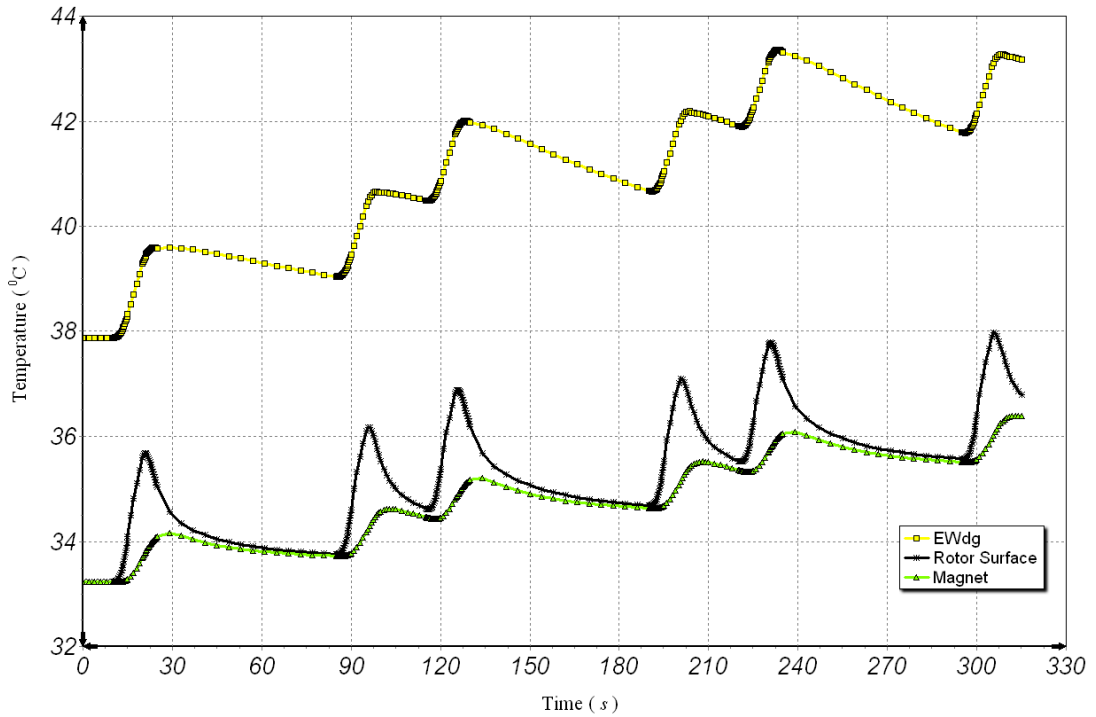


Figure A. 11: Temperature Plot for Imposed Duty Cycle

## Conclusion

In conclusion, by representing the entire motor as a lumped thermal circuit, the *MotorCAD* software is capable of accurately determining the motor component temperatures to a suitable degree of accuracy at minimum cost and time.

# Appendix B

## Guidelines for Successful *PIV* Measurements

---

### Introduction

Particle Image Velocimetry (*PIV*) refers to the accurate, quantitative measurement of fluid velocity vectors at a very large number of points simultaneously [63]. *PIV* is a non intrusive optical measuring technique (*NIOMT*) capable of accurately measuring the motion (liquid, gas) of thousands of tracer particles in an illuminated *2D* plane to give the two dimensional vector field of the fluid under view. The target area under test may be of the order of a few millimetres or a few kilometres.

The principle behind *PIV* is relatively simple. As the fluid under test is commonly air (a transparent medium), adequately sized visible tracer particles are injected into the flow. By monitoring and accurately tracking the motion of numerous particle groups within a user-defined interval by means of a high speed camera, the evaluation of the *2D* velocity components is possible. This process is further described in the below section.

### *PIV* Elements

Figure B. 1 depicts the primary components that make up a typical *PIV* setup. The key components are: a dual pulsed laser, a high resolution high speed imaging camera with appropriate optics, and a dedicated commercial *PIV* software for data acquisition and processing.

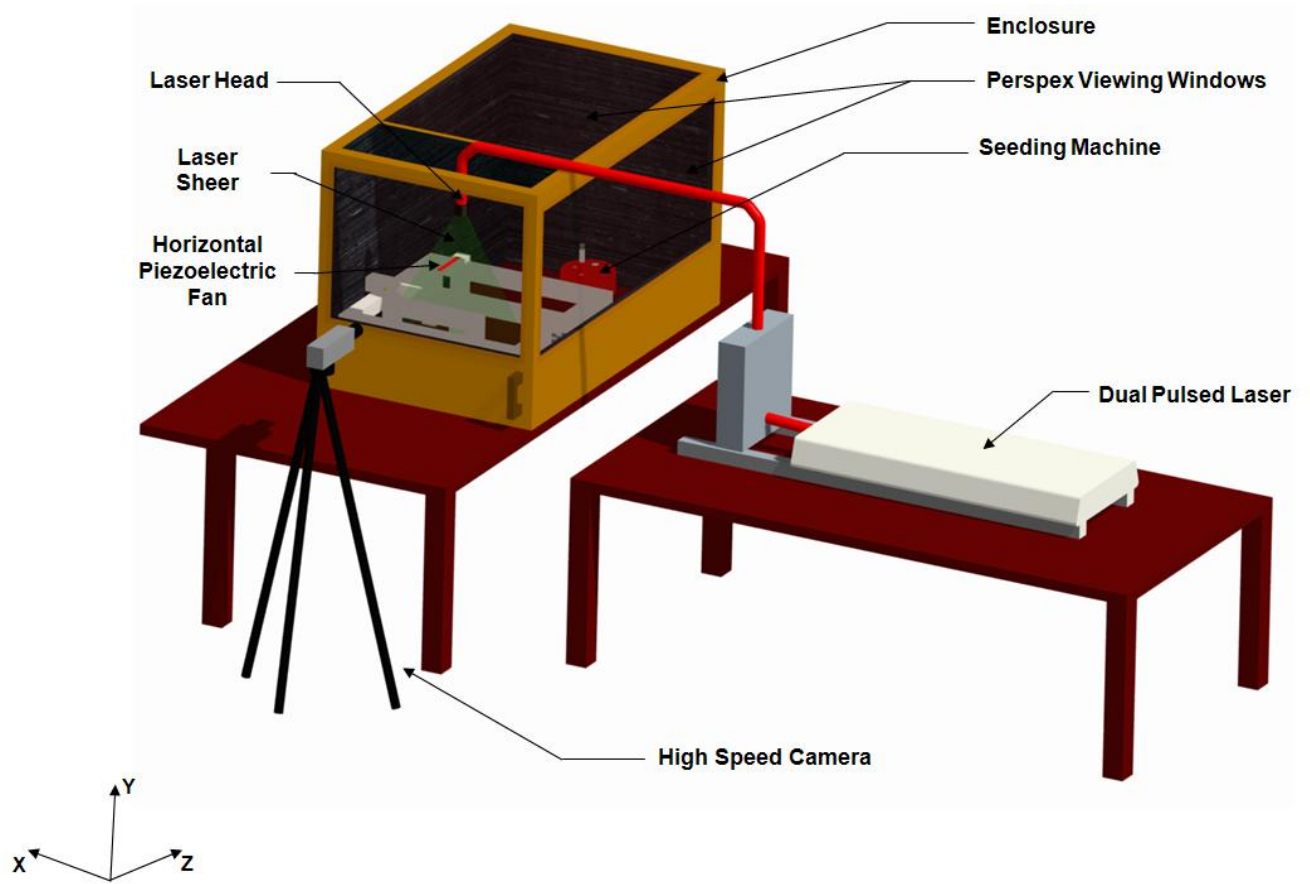


Figure B. 1: Elements of a PIV System



(i)



(ii)



(iii)

Figure B. 2: PIV Components

(i) Dual Pulsed Laser

(ii) Seeder Unit

(iii) High Speed Camera

The *PIV* procedure can be segregated into several distinct steps:

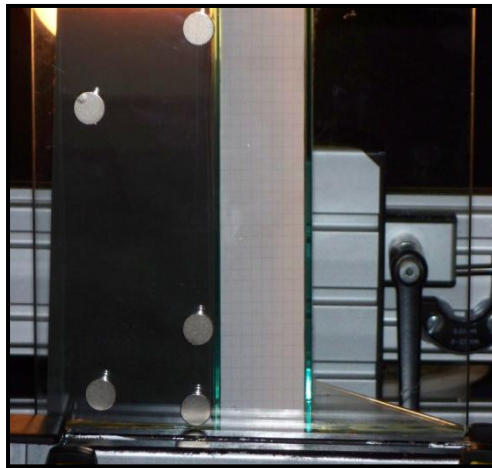
1. Image Calibration
2. Seeding of Flow
3. Illumination
4. Data Capture and Processing

Each of the above will be discussed in some detail in turn.

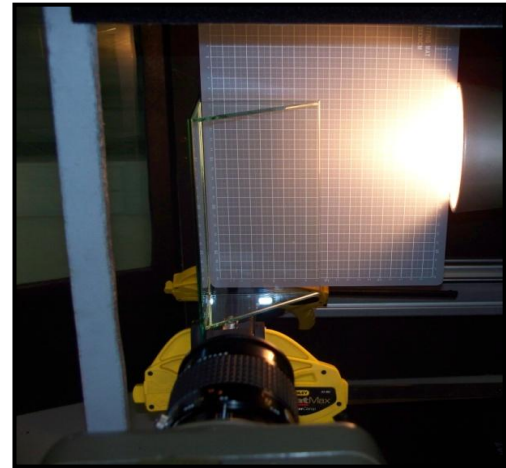
### 1. Image Calibration

The first step in any *PIV* experiment is that of image calibration. As the name implies, image calibration deals with the correct pixel to millimetre conversion. All images captured by the high speed camera are in pixels. However, as the objective of *PIV* is the evaluation of fluid velocity (in  $m/s$ ), it is essential to perform this conversion.

An example of such a calibration is depicted in Figure B. 3. A grid of known dimensions is placed in the position of interest and held perfectly perpendicular to the imaging camera.



(i)



(ii)

Figure B. 3: *PIV* Calibration Procedure

(i) Fin Base

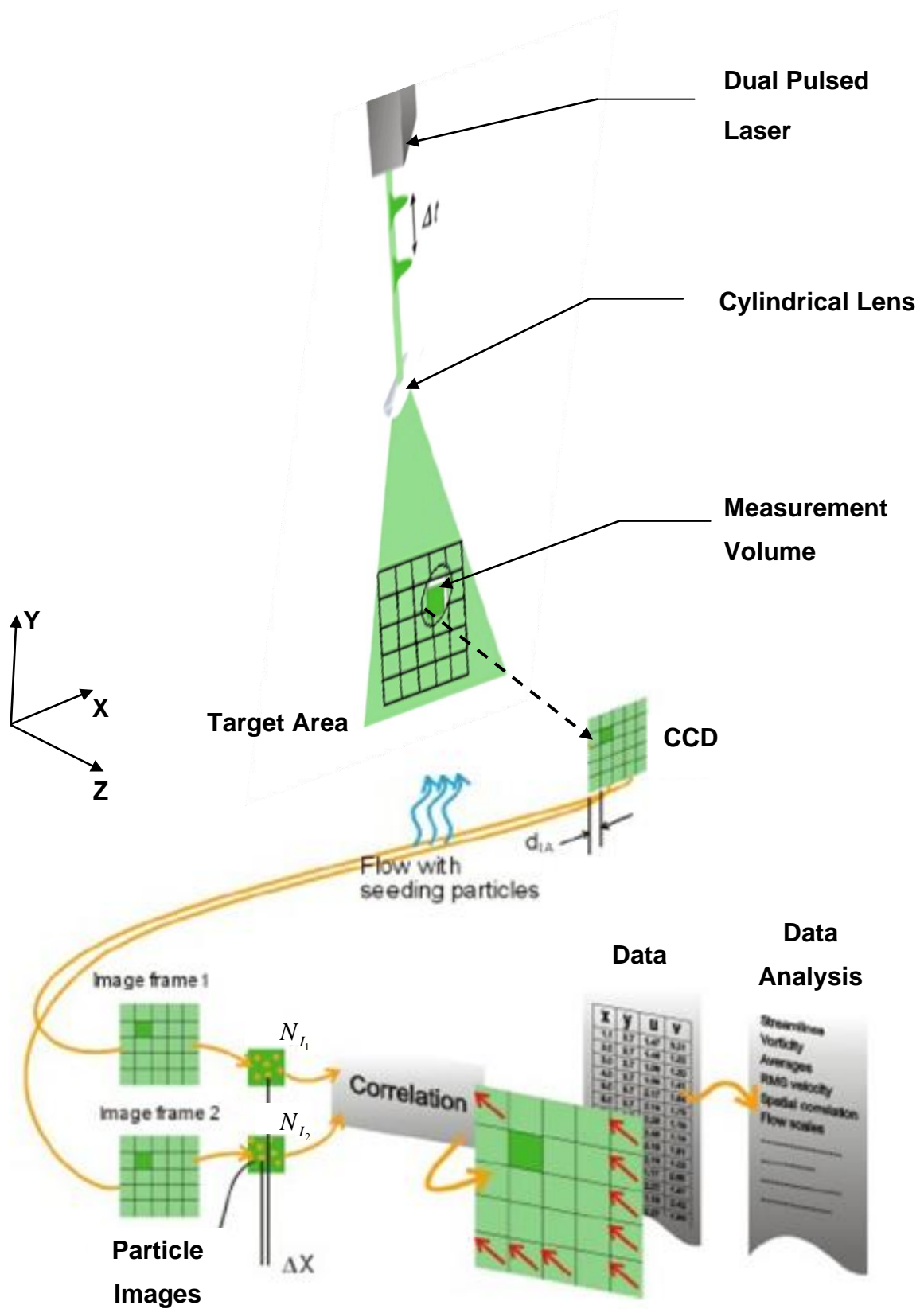
(ii) Fin Side Wall

By capturing a single image of the target area (with the calibration grid present), the pixel conversion may be calculated and stored in the commercial software to be utilised when evaluating fluid velocities.

## 2. Seeding of Flow

On successful calibration, tracer particles are introduced in the fluid medium under study. This step is better known as seeding of the flow (Figure B. 5). Seeding is an important consideration which affects the quality of the final data obtained and is a primary source of error in the data evaluation, as reported in *Chapter 5*.

The tracer particle size and tracer material implemented are highly dependent on the characteristics of the flow (speed, viscosity, minimum flow structure) under investigation. Large tracer particles are easy to monitor, trace and capture with a high speed camera as they reflect a large amount of light. However, these large tracer particles are significantly denser than air and thus have a tendency not to follow the flow under study. On the other hand, small tracer particles adhere well to the flow, but due to their minute size, light reflection off the tracer particles is minimalistic and harder to observe with the high speed camera.

Figure B. 4: Schematic of *PIV* – Velocity Extraction

Furthermore, the size of the implemented tracer particles dictate the smallest flow structure (eddies) measurable. Thus an optimum tracer particle density exists. Typically, oil droplets ( $1\mu m$  to  $5\mu m$ ) are used to seed air flows, while polystyrene, polyamide or hollow glass spheres (in the range of  $5\mu m$  to  $100\mu m$ ) are used in water applications. The quantity of tracer particles in the flow is also of considerable importance. As a rule of thumb, to achieve a good signal peak in the cross-correlation, 10 to 25 particle images should be present in each interrogation area. Furthermore, it is essential to have appropriate venting in place, as seeding (due to its minute size) can be highly carcinogenic.

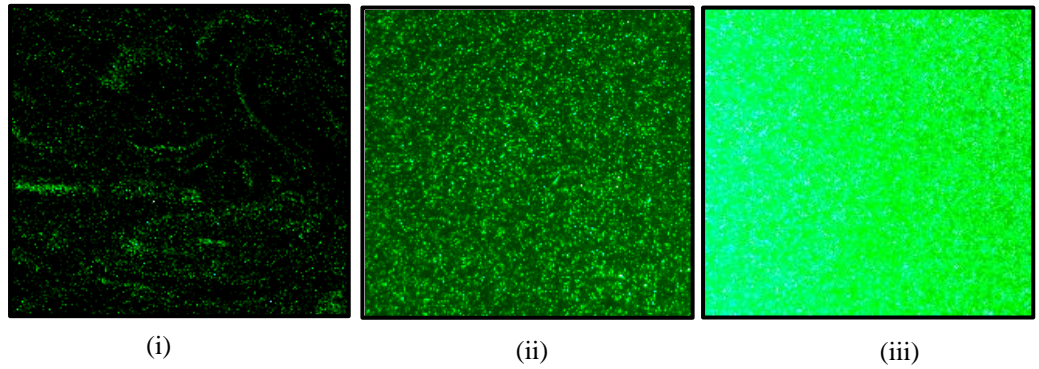


Figure B. 5: Seeding Density

(i) Insufficient Seeding

(ii) Appropriate Seeding

(iii) Densely Seeded

### 3. Illumination

On attaining the correct seeding density and quality, illumination of a laser light sheet in the flow takes place (Figure B. 6). This is produced by a high powered, dual pulse laser. The resultant 2D light sheet acts as the light source (flash) for the high speed camera. Tracer particles are caught in the light sheet scatter light; and it is this scattered light which is captured by the camera. In *PIV*, it is of prime importance to ensure that the laser sheet is at  $90^\circ$  to the high speed camera. Furthermore, for the highest accuracy, it is essential that the laser light sheet produced is as thin as possible. This ensures that the scattered light is only from the particles in a single plane.



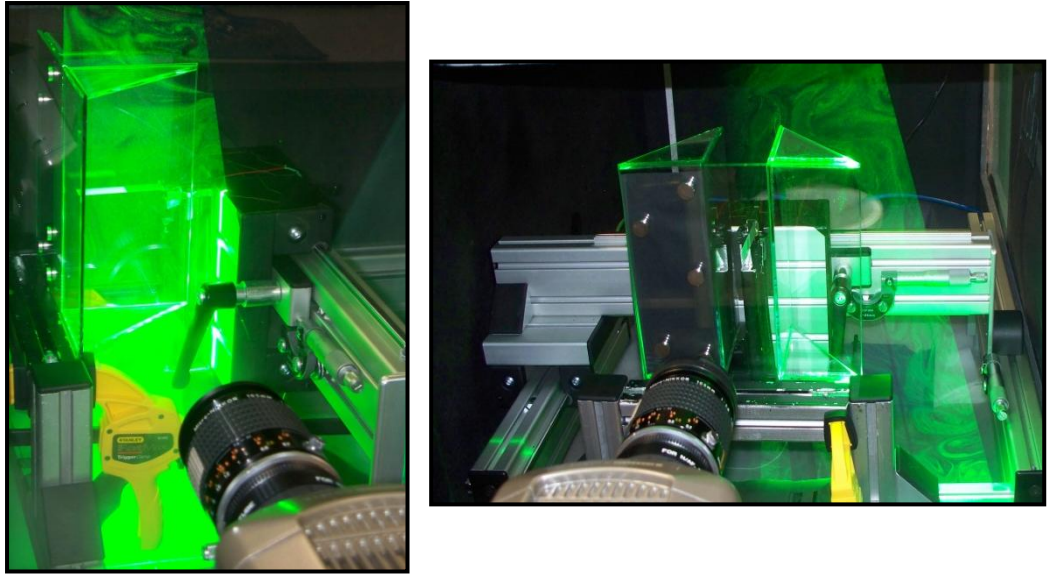


Figure B. 6: Examples of a typical 2D Laser Light Sheet

On shining the laser light sheet, it is essential to minimise any, and if possible eliminate all reflections. These high intensity reflections are hazardous to humans and may also cause irreparable damage to the *CCD* in the high speed camera. Reflections may be minimised by using enclosures, shields and by spraying or covering all reflective surfaces in matt black paint.

#### 4. Data Capture and Processing

Data capture is achieved by means of a high speed camera. The camera lens images the target area illuminated by the laser light sheet onto the sensory array (*CCD*) of the camera. Two consecutive laser light pulses are shone and the camera captures each light pulse in turn and stores each in separate image frames. Each captured image is divided into small subsections (grids) better known as interrogation areas (*IA*).

The interrogation areas (Figure B. 7) from frame 1 ( $I_1$ ) and for frame 2 ( $I_2$ ), are cross-correlated with each other, pixel by pixel. This correlation produces a signal peak (Figure B. 7). The resulting signal peak, in turn, represents the common particle displacement -  $\Delta X$ . The same procedure is repeated to

determine  $\Delta Y$ . Once an accurate measure of the displacement  $(\Delta X, \Delta Y)$  for the group of tracer particles in the  $IA$  is established, then the corresponding velocity components  $(V_x, V_y)$  may be evaluated by applying the below two equations.

$$V_x = \frac{\Delta X}{\Delta t} \quad \dots \text{Eq. B. 1}$$

$$V_y = \frac{\Delta Y}{\Delta t} \quad \dots \text{Eq. B. 2}$$

In the above, the separation time  $(\Delta t)$  between the two laser pulses is precisely known. An instantaneous velocity vector map over the whole target area is obtained by repeating the cross-correlation method for each of the  $IA$ 's over the two image frames captured by the camera [64].

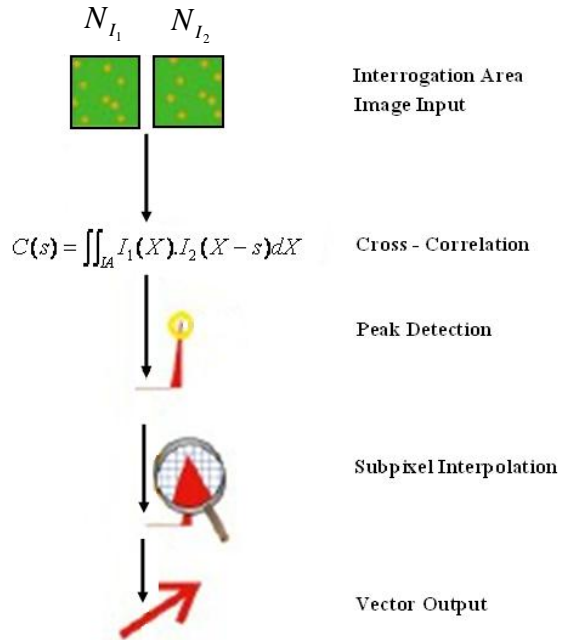


Figure B. 7: Cross-Correlation Evaluation results in the Flow Velocity Components

Using the above technique, a single  $2D$  instantaneous velocity contour map is obtained. However, triggering the laser and camera to capture numerous image pairs results in the complete and accurate flow characterisation over a user – defined set period of time. Further data processing such as the evaluation of the: mean flow (Figure B. 8), turbulence characteristics, vorticity, dynamic mode decomposition, etc. may be performed using user – generated codes, in say, *MatLAB*.

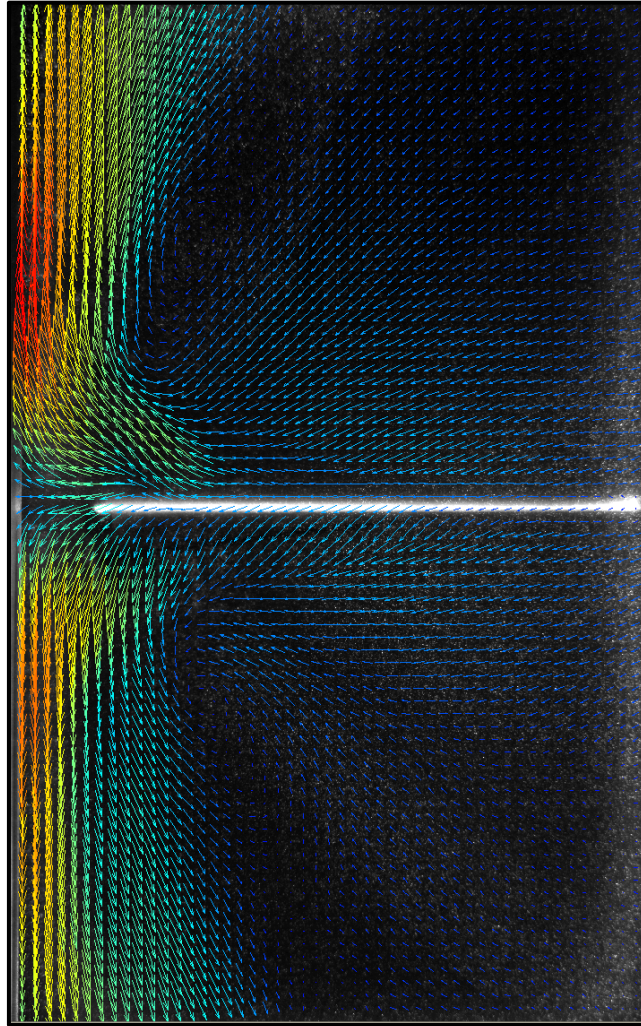


Figure B. 8:  $2D$  Contour Map depicting the Mean Flow of an Oscillating Piezoelectric Fan

While the above described *PIV* procedure relates to a  $2D$  *PIV* system, the technology can further be upgraded to measure all three velocity components in a single plane -  $3D$  *PIV*, better known as stereoscopic *PIV*. This involves

the use of two high speed imaging cameras and is based on the principle of parallax. Each of the two high speed cameras is located in a such a way as to observe the generated light sheet. However, as each camera is oriented at a different angle, the parallax effect results. This means that slightly different *2D* vector maps arise for each camera. This difference is due to the third (out of plane) velocity component and the geometrical positioning of the two high speed cameras. This third component may then be extracted using a similar image calibration as explained above. Experiments involving stereoscopic *PIV* are highly complex and time consuming, and thus many researchers prefer the use of *2D PIV* rather than the latter option.

## Conclusion

In conclusion, *PIV* is a leading contact free optical imaging technique, capable of accurate and repeatable evaluations of local velocities over considerably large areas. *PIV* outclasses traditional velocity measurement techniques such as a: Pitot tube, Hot-wire anemometer or Wind anemometer, as the implemented equipment does not hinder the incoming fluid flow in any manner. Furthermore, unlike traditional equipment or even other *NIOMT* (such as *PTV*, where a single velocity is calculated at a single point), with *PIV*, *2D/3D* flow patterns and turbulence characteristics are evaluated and represented as contour maps. However, the down side to using *PIV*, is that the constituting equipment tends to be relatively expensive and thus not widely available. Furthermore, the system also requires highly skilled users.

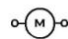
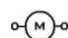
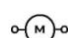
# Appendix C

## Guidelines for Successful Finite Element Analysis Modelling

---

### Introduction

The finite element method, better known as finite element analysis (*FEA*) is a sophisticated but powerful numerical technique devised for solving differential (and integral) equations of initial and boundary-value problems in geometrically complicated regions [65]. *FEA* is commonly implemented in various engineering sectors to solve: structural, thermal, electromagnetic, soil mechanics and dynamics amongst other. These differential equations arise in numerous complex engineering problems, such as:

-  Steady-State problems
-  Eigenvalue problems
-  Transient problems

The *FEA* principle was first introduced successfully in the 1950's, and has been continued to be developed and improved. The *FEA* principle is based on an energy principle such as the virtual work principle or the minimum total potential energy principle (*Rayleigh-Ritz* method).

This methodology is quickly gaining acceptance in the various branches of industry. This is due to the fact that it is not possible to solve complex problems models using the classical mechanics method. Thus, *FEA* software packages, such as *Pro/Mechanica* and *ANSYS*, are ever increasingly being used to model and simulate such applications.

## Theory

Initially a *2D* or *3D* model is created using the *FEA* software package. This can be carried out in two distinct ways, either by building the model from first principles (starting from keypoints, to lines, to areas to volumes, i.e. the bottom-up approach) or else by importing (making use of the \*.iges file format) the model from another application.

The *2D/3D* model, better known as the domain is then divided into an assembly of subdivisions called elements and joined together at certain locations, better known as nodes. The subdivision of a domain into elements is termed finite element discretisation (or meshing). The elements can have various shapes and properties. Common *2D* elements are shaped as triangles or quadrilaterals while tetrahedral and hexahedral shaped elements are used for *3D* models. Meshing is a critical stage in *FEA*. The meshing density and quality have a direct relationship on the computational time, cost as well as quality of results. Thus, it is up to the user to generate a practical mesh that will give reasonable results for the least amount of time and cost.

The model is then loaded according to a particular load function. It is assumed that this load function will act over each element in a predefined manner. That is, the distribution across each element will be either a polynomial or a trigonometric function. Conversely, this latter step is known as redistribution.

Following this redistribution stage, the governing equations for each element are calculated and then assembled to give the system equations which describe the behaviour of the body as a whole. These generally take the form:

$$\{F\} = [k]\{U\} \quad \dots \text{Eq. C. 1}$$

Where:

$\{F\}$  - vector of applied nodal forces

$[k]$  - stiffness matrix

$\{U\}$  - vector of unknown nodal displacements

Once these equations have been obtained, the nodal coordinates, material properties as well as the loading conditions are substituted into the resultant system equations. In order, to find the displacement developed by the applied force, *Eq. C. 1* must be inverted. However, before inverting the matrix, the boundary conditions of the system must be applied. This means that the body must be constrained in order to prevent it from performing unlimited rigid body motion.

Thus in essence, the *FEA* procedure can be broken down into the following steps:

1. Creation of Geometry
2. Defining Element Types
3. Defining Material Properties
4. Defining Real Constants
5. Meshing Model (Discretisation)
6. Applying Loads and Constraints
7. Solving generated Equations
8. Post-Processing (Analysis of Stress-Strain and *Von Mises* criteria).

## Conclusion

The finite element method can produce reliable results when used correctly, but it is important to remember that it only gives an approximate value, and the validity and accuracy of the model and its solution rely on an accurate representation of the problem and correct analysis procedures [62].

# Appendix D

## Part Drawings: 24 slot – 20 pole *PMSM* and Rotating Data Logger

---

This appendix details some of the critical part drawings used in the construction of the 24 slot – 20 pole *PMSM* together with drawings of the implemented rotating data logger as detailed in **Chapter 3**. A graphical representation (exploded view) of the manufactured *PMSM* motor is first presented (Figure D. 1). Part drawings of the rotor assembly (Figure D. 2), stator (Figure D. 3) and motor axial finned housing (Figure D. 5) are presented. Furthermore, the 3 phase winding configuration of the double layer, high speed *PMSM* is also presented in Figure D. 4.

Detailed designs of the in - house fabricated rotating data logger casing (Figure D. 6) are also presented. Figure D. 7 depicts the part drawings of the data logger casing, while Figure D. 8 reflects the part drawings of the data logger locating end cover.



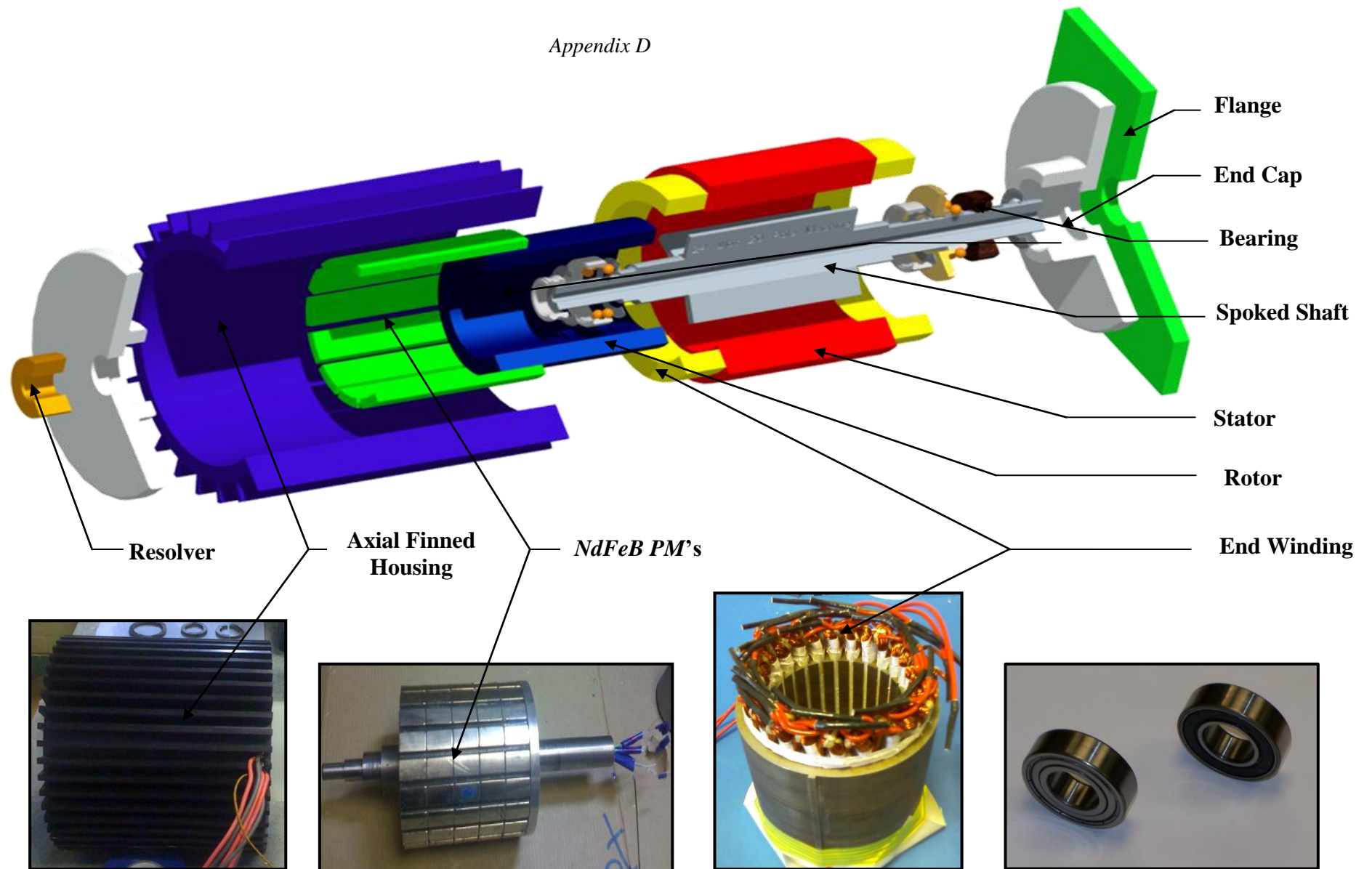


Figure D. 1: Constituting Components of the Fabricated *PMSM*- Exploded View

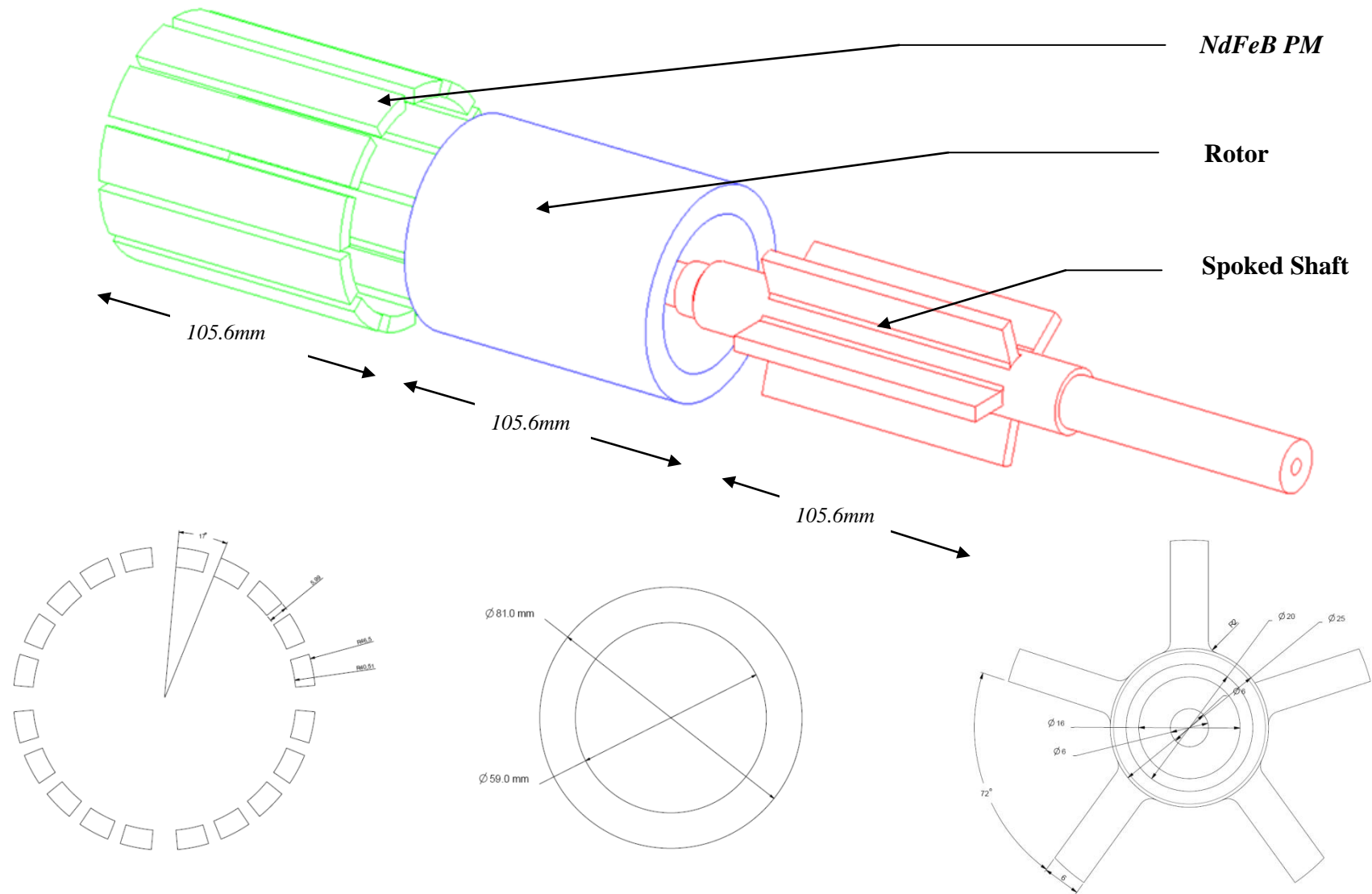


Figure D. 2: Shaft, Rotor and *PM* Geometry

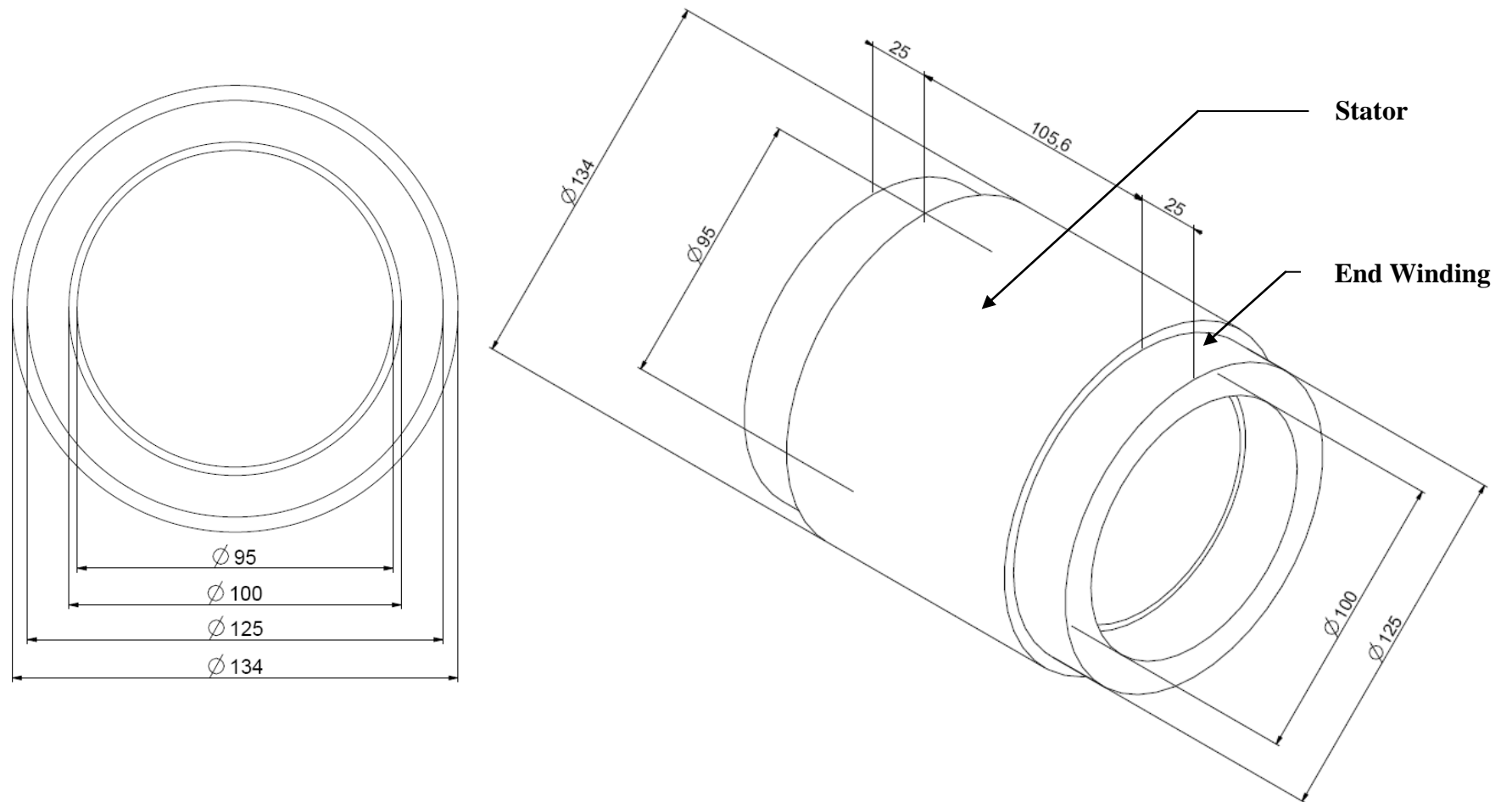


Figure D. 3: *PMSM* Stator and Simplified End Winding

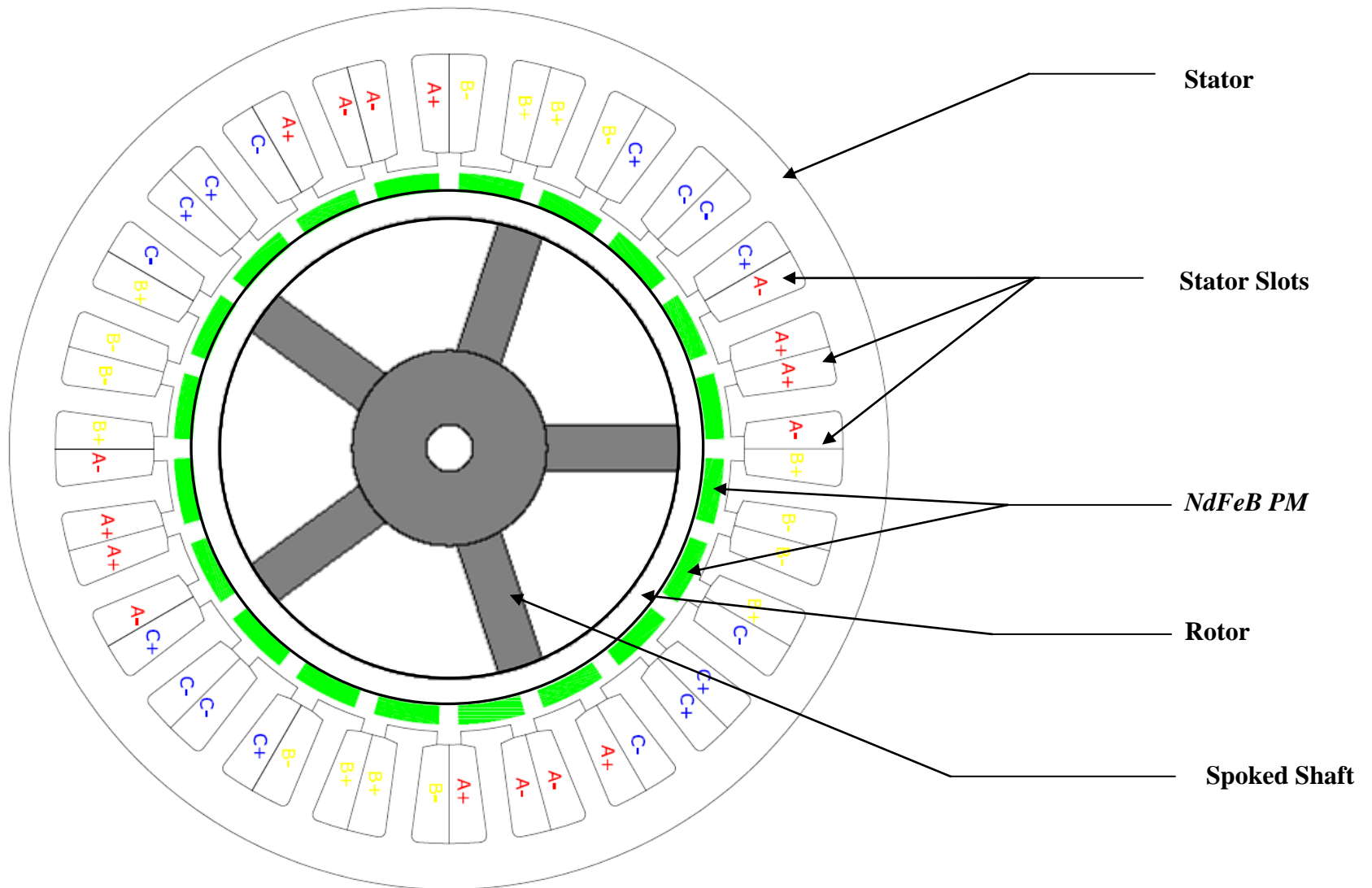


Figure D. 4: *PMSM* Winding Configuration

**No. of Fins = 44**

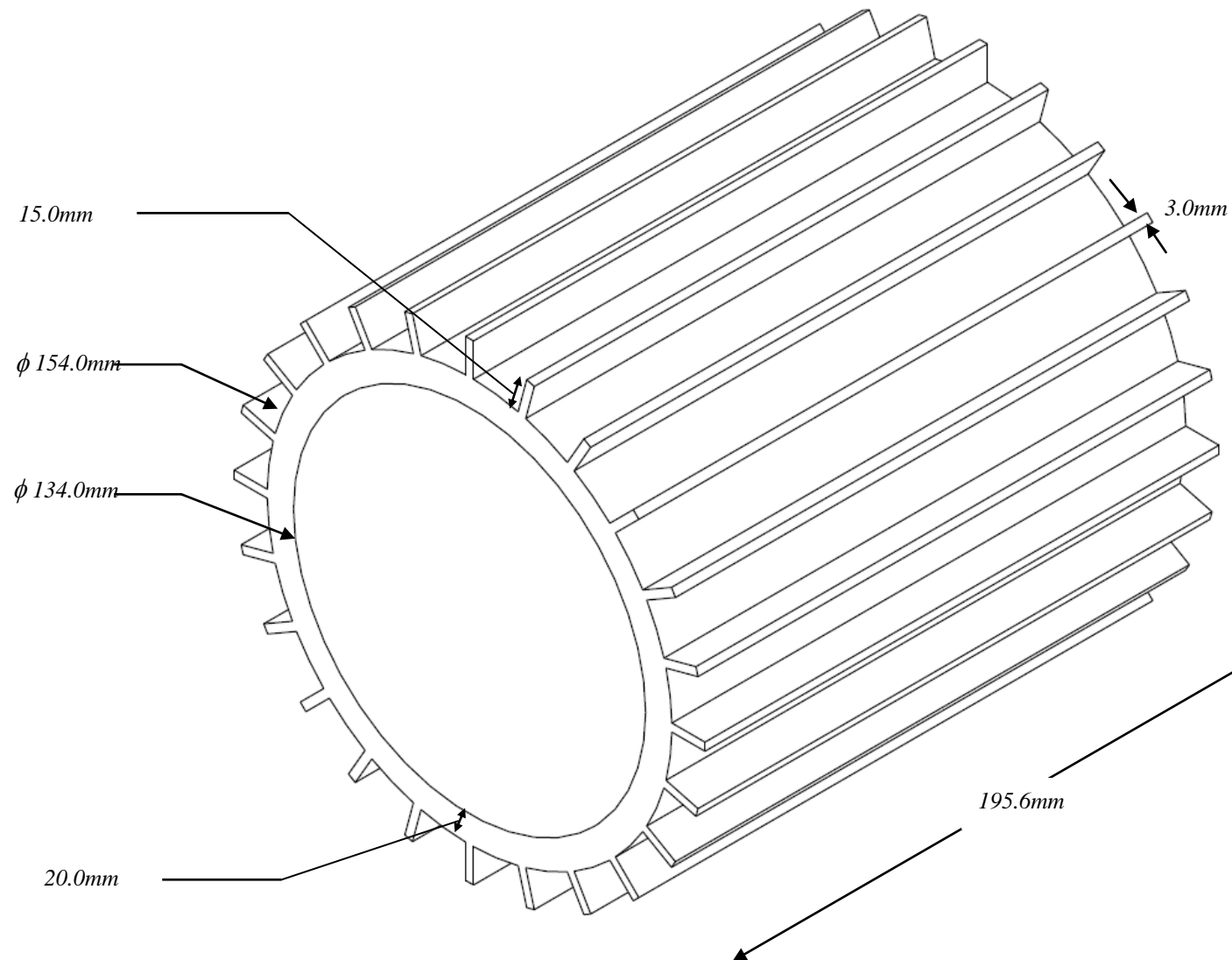


Figure D. 5: *PMSM* Axial Finned Housing

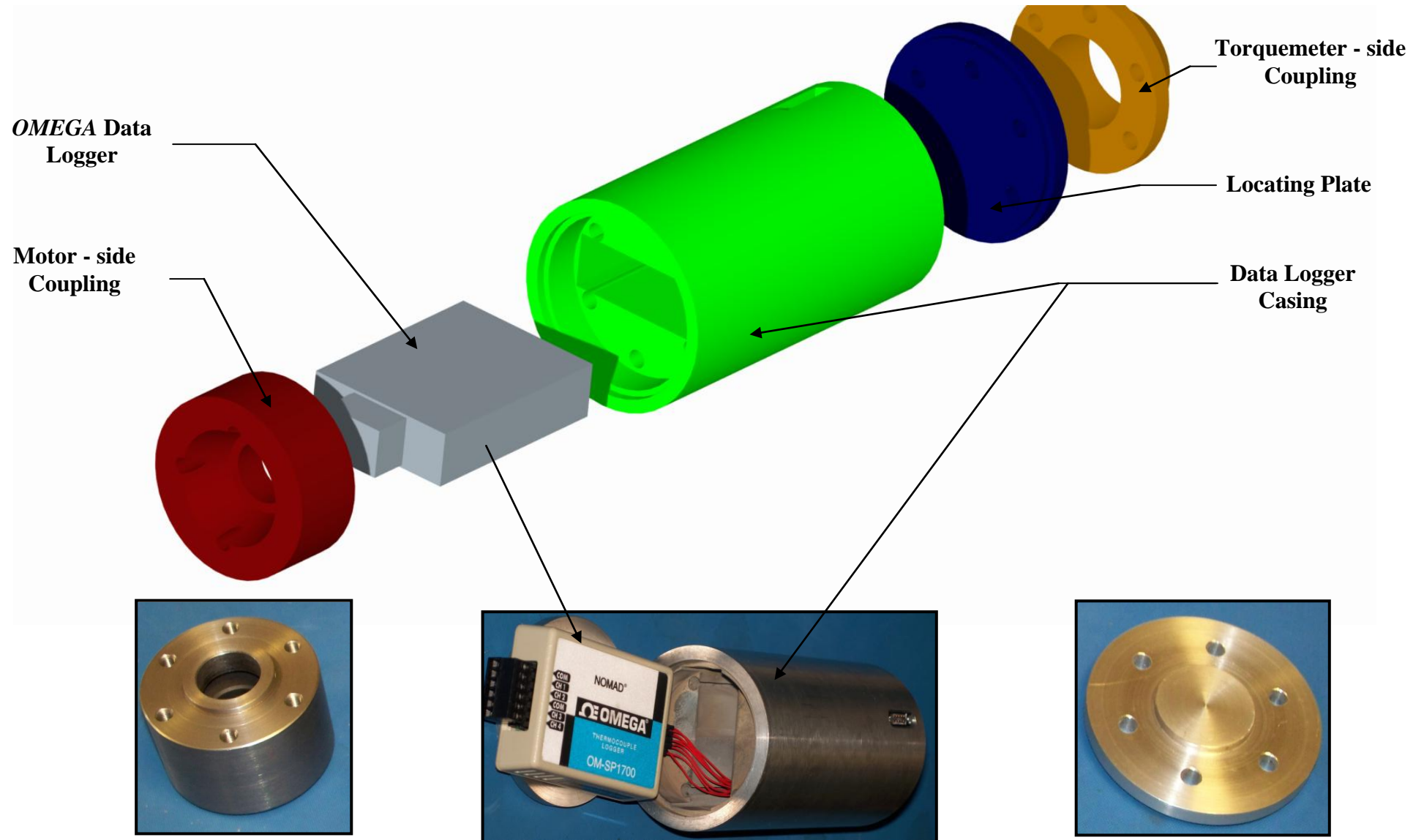


Figure D. 6: Rotating Data Logger Assembly

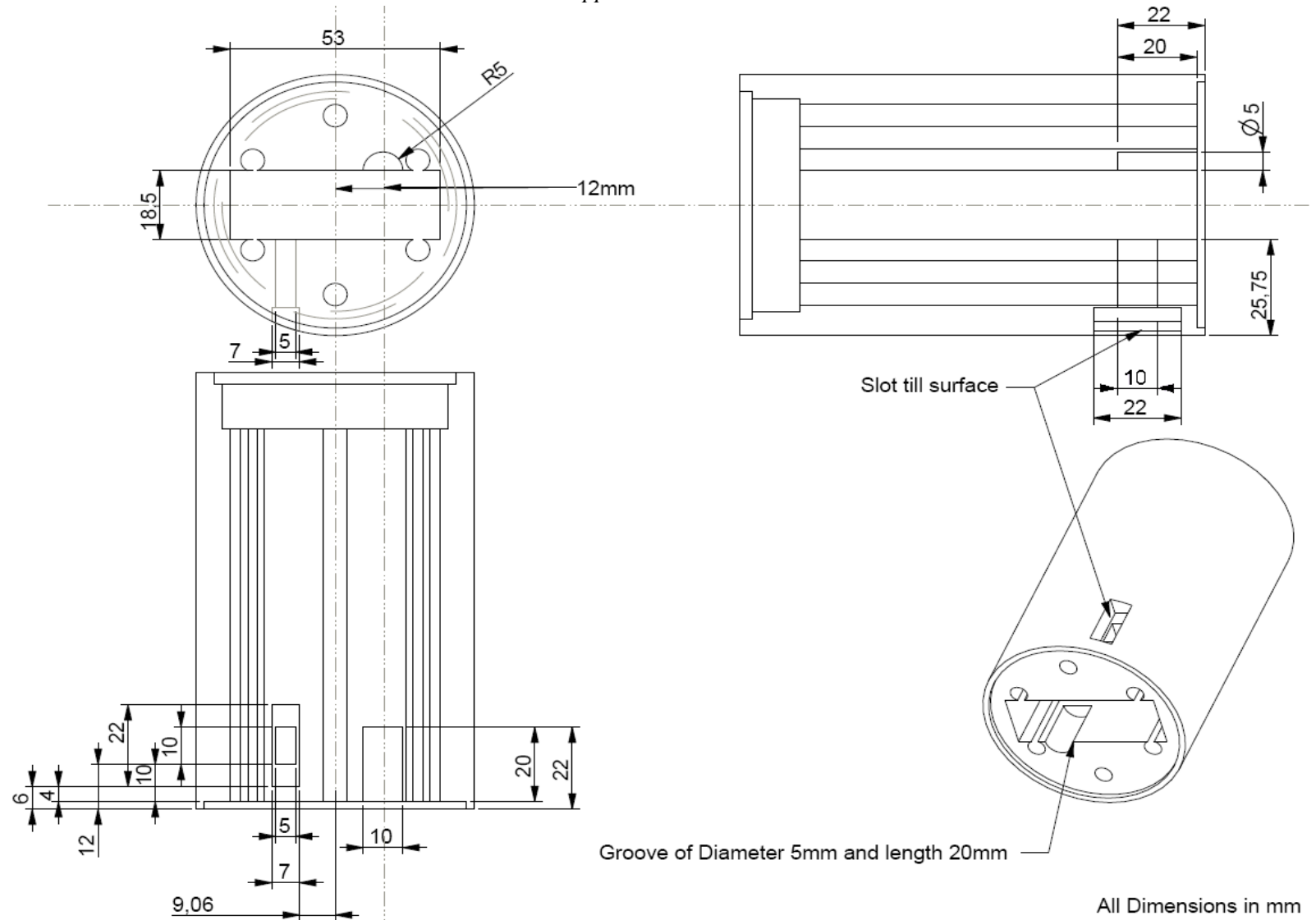
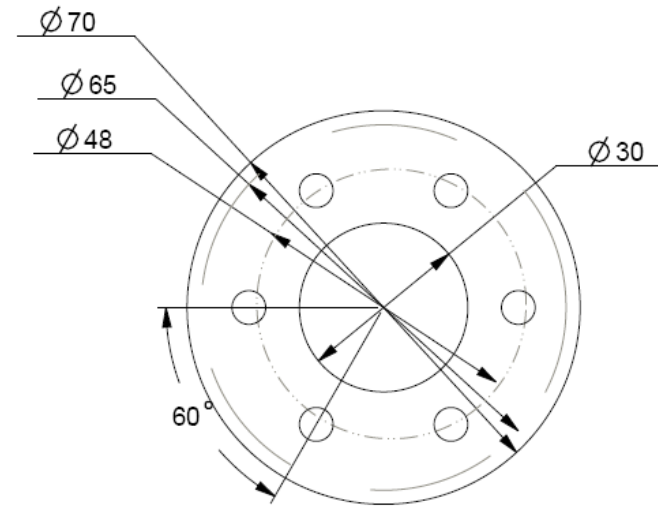
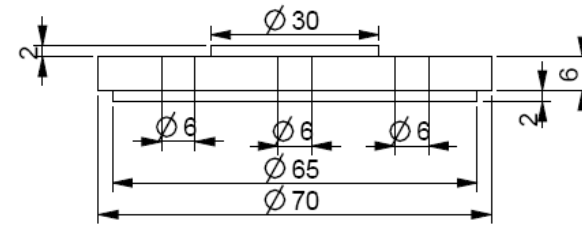
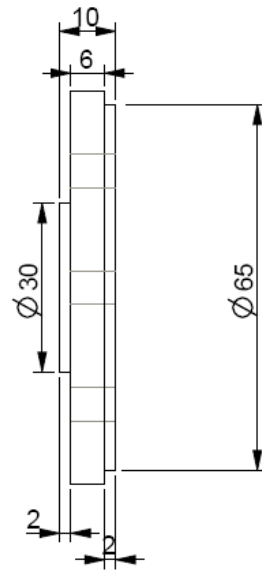
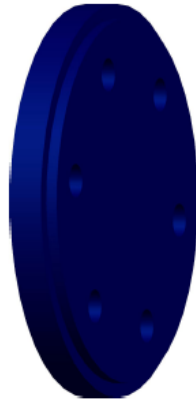


Figure D. 7: Part Drawing - Rotating Data Logger Casing



All Units in mm

Figure D. 8: Part Drawing - Data Logger Locating Cover



# Appendix E

## Thermal Calibration Curve

---

As detailed in *Chapter 6*, when measuring the temperature profiles of the vertical fin side wall, viewing through a semi – transparent *IR* medium (dummy fin) was performed. This procedure resulted in lower apparent local temperatures. Hence, this section details the thermal calibration curve (Figure E. 1) implemented to attain the actual fin side wall local temperature.

The governing calibration curve equation was introduced by a - defined *MatLAB* code, and is depicted in *Eq. E.1*:

$$C_{Factor} = 0.92482(T_{Measured} - 17.937)^{0.07634} \quad \dots \text{Eq. E. 1}$$

The actual fin side wall local temperature was thus evaluated according to *Eq. E.2* hereunder:

$$T_{Actual} = T_{Measured} \cdot C_{Factor} \quad \dots \text{Eq. E. 2}$$

The utilisation of the calibration curve together with the above formulation ensured the correct evaluation of the both the local fin side wall heat transfer coefficients ( $h_{FS}$ ) as well as the corresponding local thermal resistances ( $R_{FS}$ ).

## Appendix E

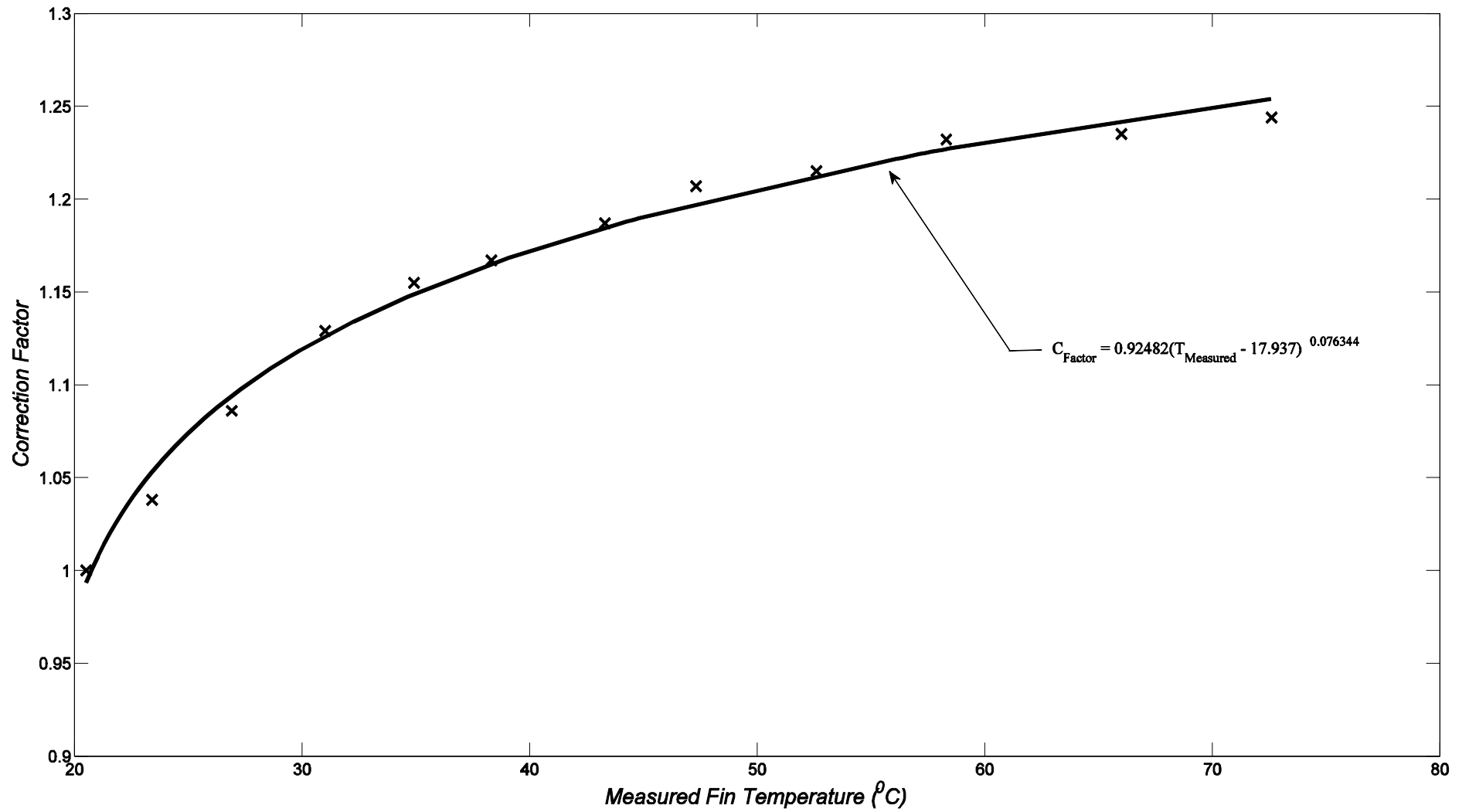


Figure E. 1: Thermal Calibration Curve

# Appendix F

## Further *PIV* Data

---

In this section, additional *PIV* data is presented. The results presented are those obtained using the experimental *PIV* facility described in *Chapter 5*, and further compliments the results presented in *Chapter 7* and *Chapter 8*.

Presented results pertain to *2D* contour plots on both the fin base and fin side wall and depict both the magnitude of the mean vectors as well as the *RMS* of the fluctuating components (i.e. turbulence).

By considering the below *2D* contour plots, the reader may better understand the cooling capabilities of both a horizontal and a vertically-mounted oscillating piezoelectric fan presented in *Chapter 6*.

### 1. Horizontally-mounted Piezoelectric Fan

In this first section, results (magnitude of mean vectors and *RMS* of fluctuating component) pertaining to a horizontally-mounted oscillating piezoelectric fan are presented.

#### Magnitude of Mean Vectors

The formulation adopted to calculate the magnitude of the mean vectors is given in *Chapter 7* and is of the form:

$$\overline{V_{Mean}} = \sqrt{(\overline{V_X})^2 + (\overline{V_Y})^2} \quad \dots \text{Eq. F. 1}$$

## Fin Base 2D Contour Plots (S30, S40, S50, Flat Plate)

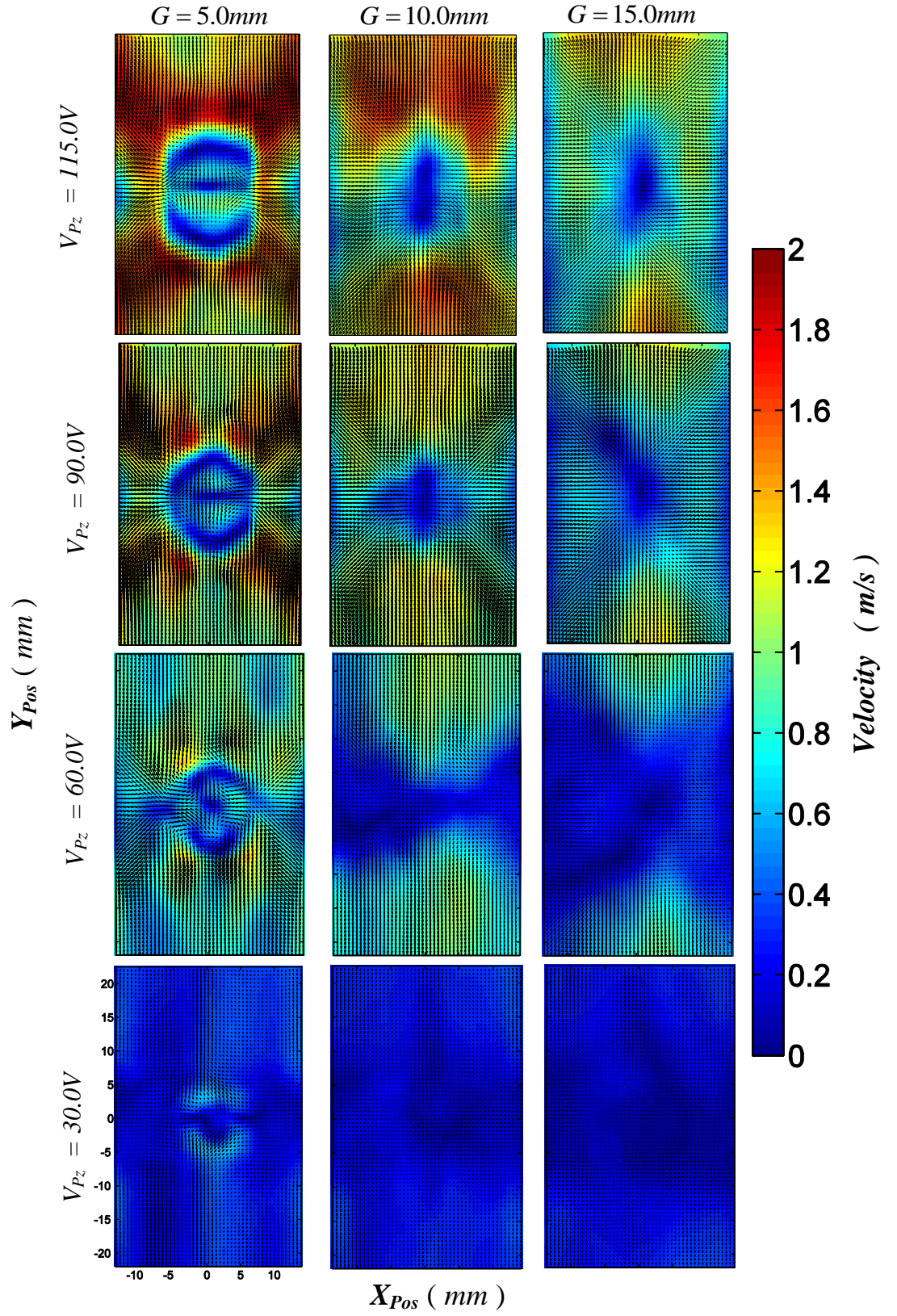


Figure F. 1: Magnitude of *FB* Mean Vectors for a Horizontally-mounted Piezoelectric Fan:  
 $S = 30.0\text{mm}$

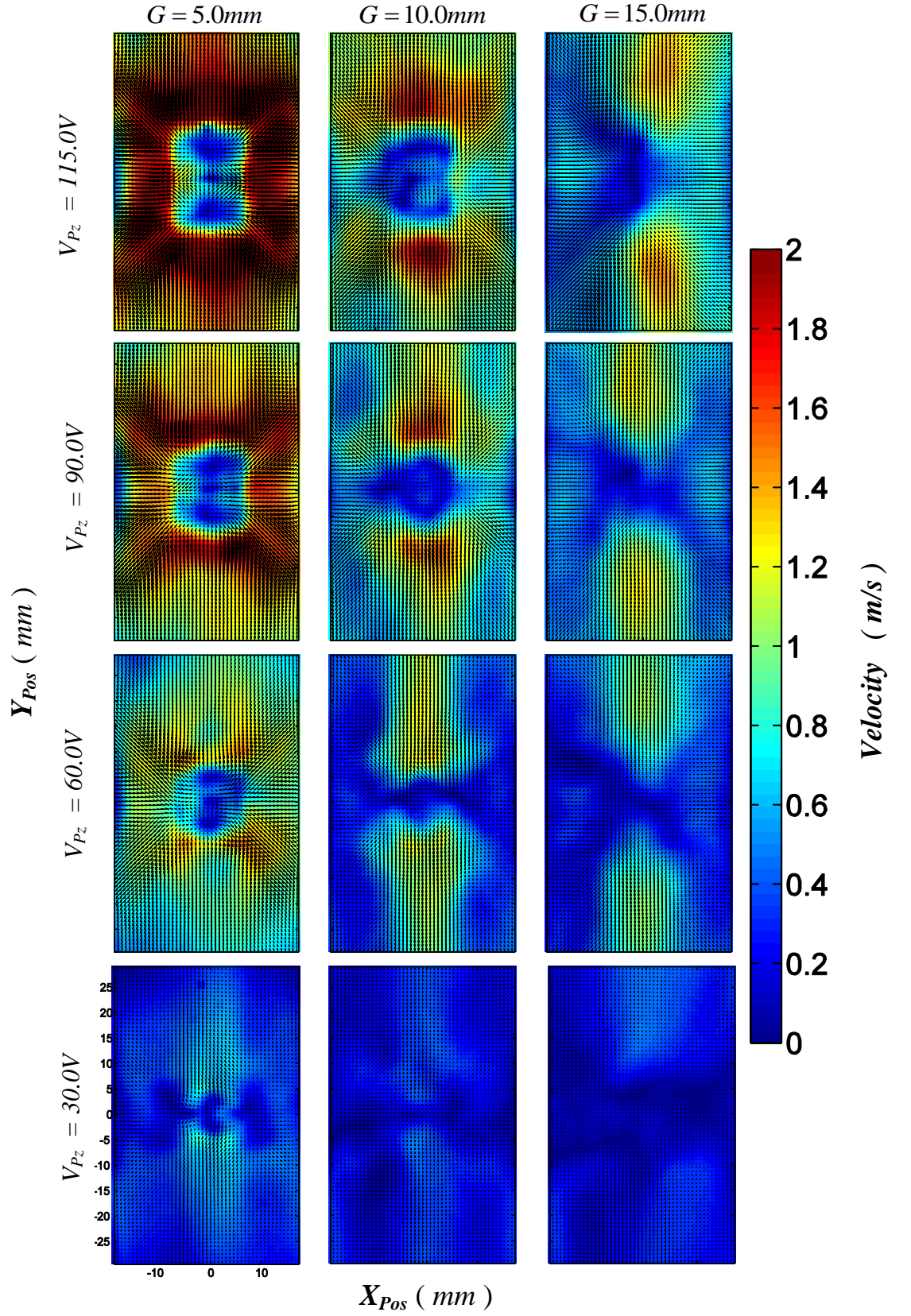


Figure F. 2: Magnitude of *FB* Mean Vectors for a Horizontally-mounted Piezoelectric Fan:  $S = 40.0\text{mm}$



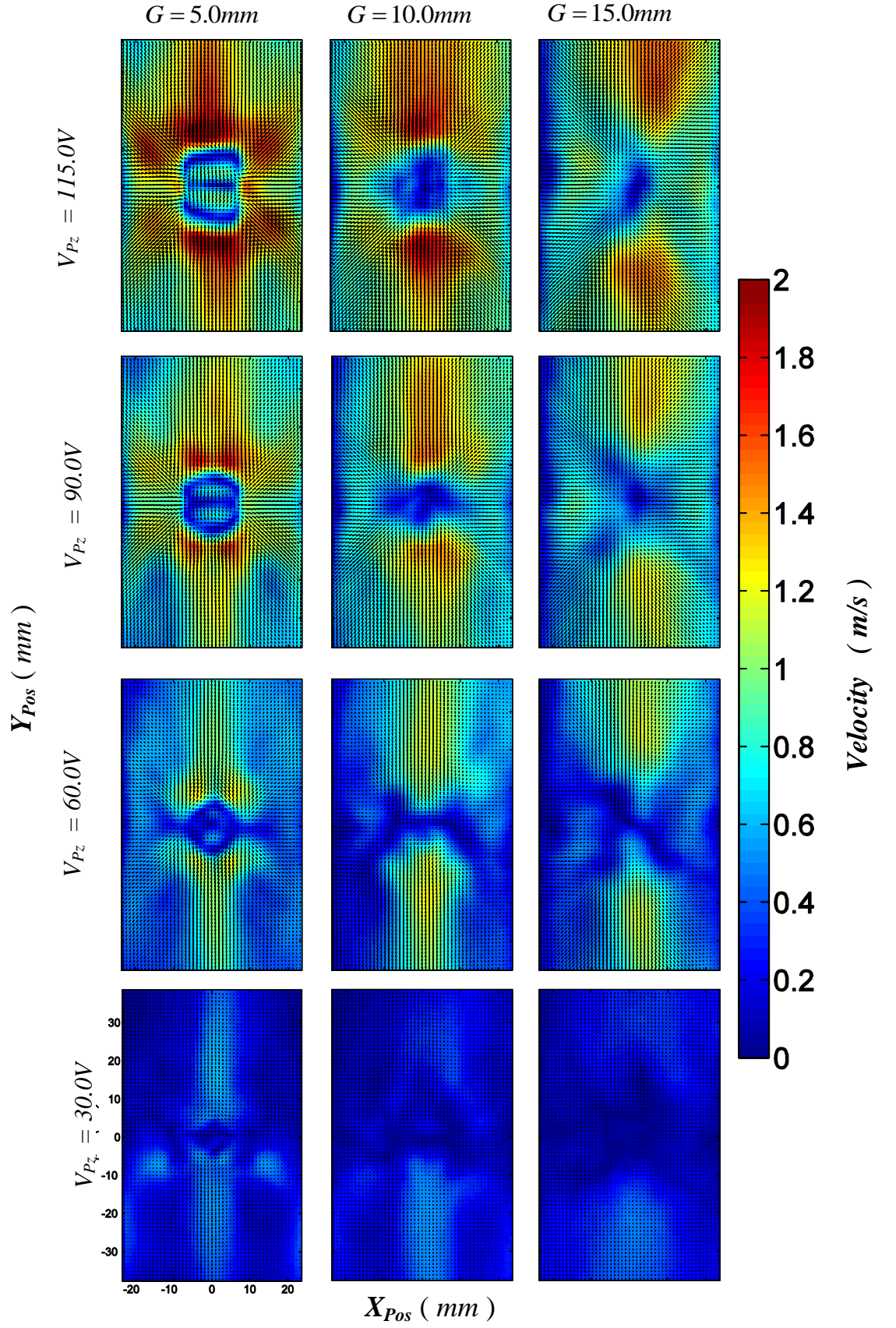


Figure F. 3: Magnitude of *FB* Mean Vectors for a Horizontally-mounted Piezoelectric Fan:  $S = 50.0\text{mm}$

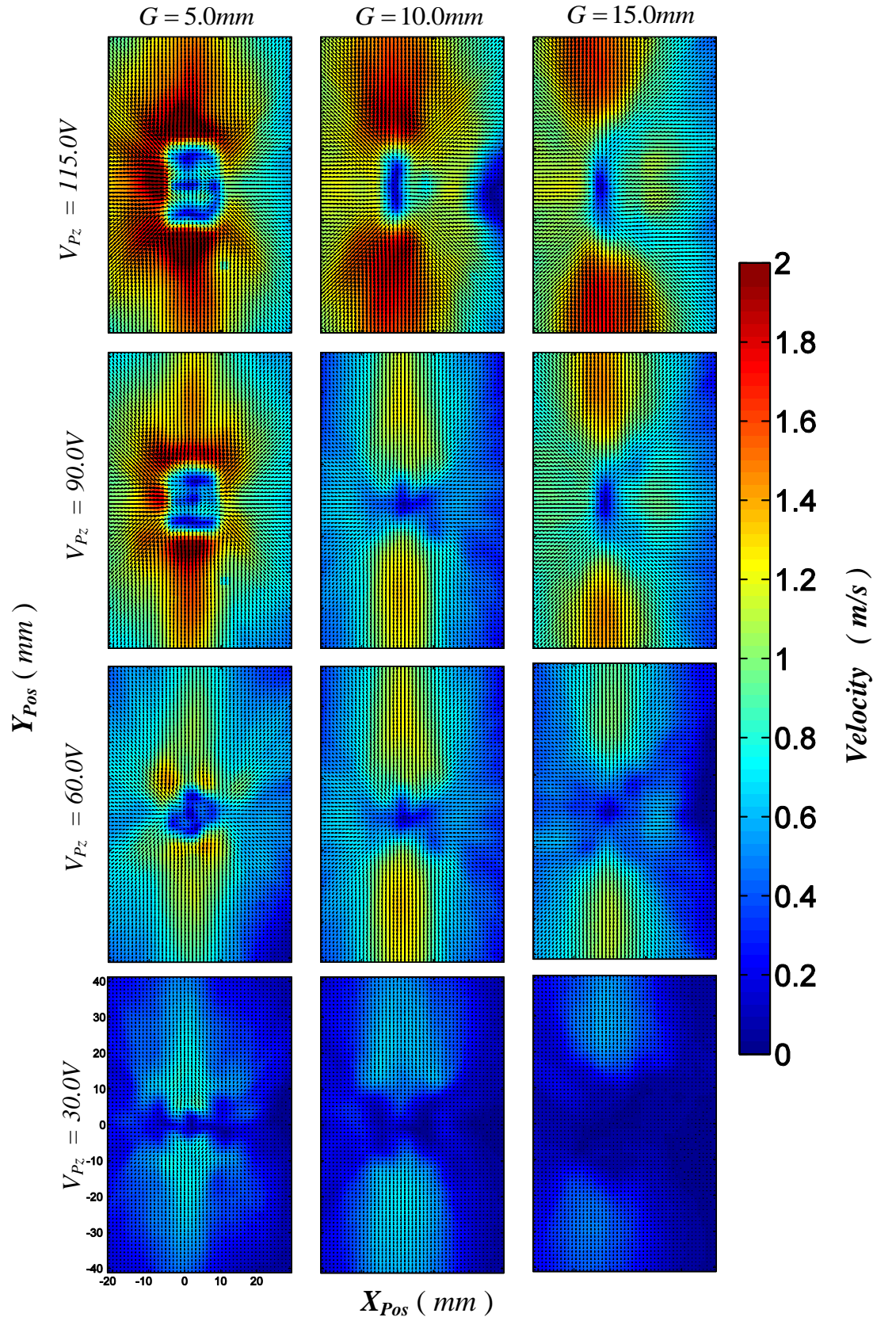


Figure F. 4: Magnitude of *FB* Mean Vectors for a Horizontally-mounted Piezoelectric Fan: Flat Plate ( $S = \infty \text{ mm}$ )



Fin Side Wall 2D Contour Plots (S30, S40, S50)

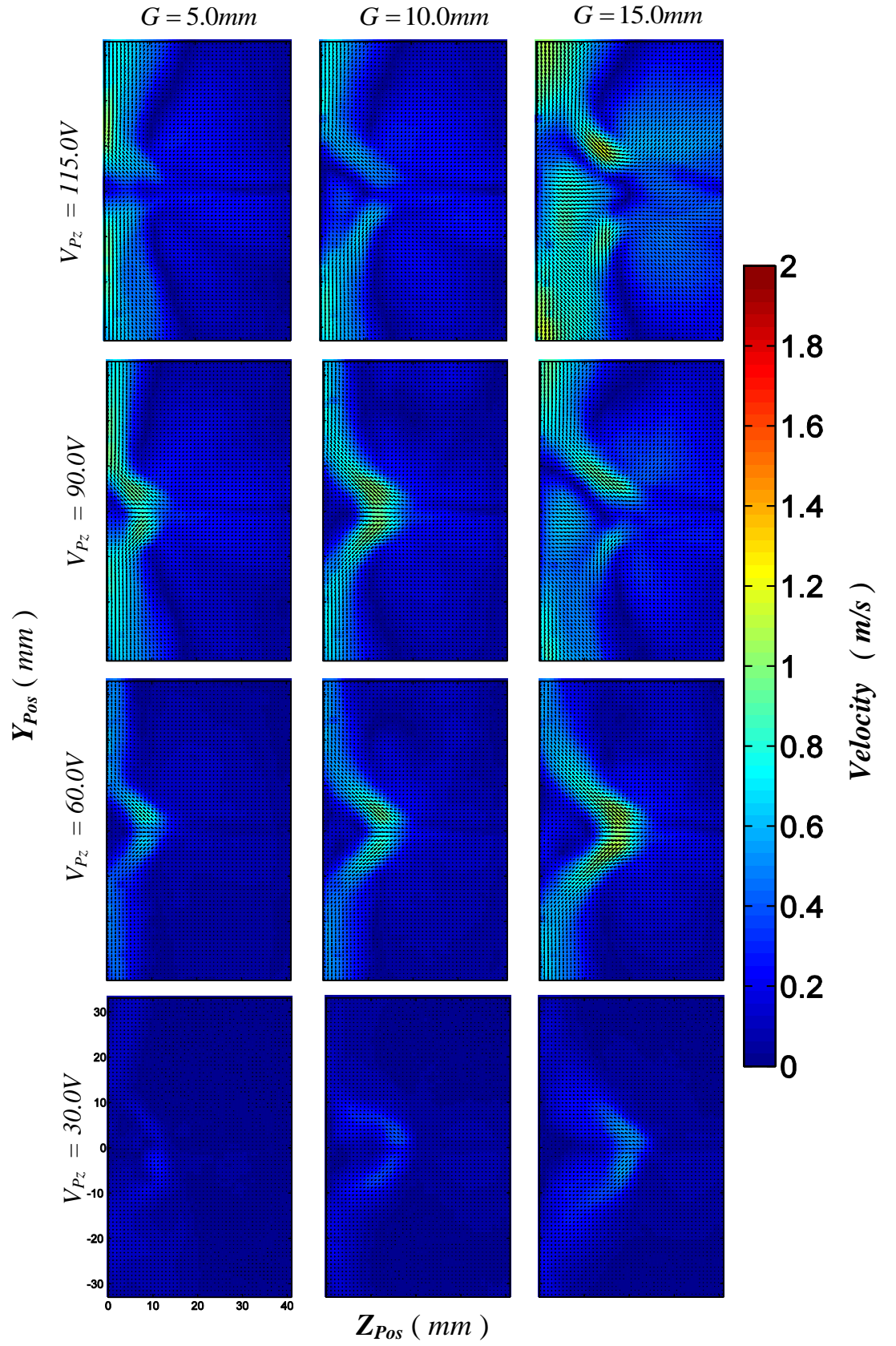


Figure F. 5: Magnitude of FSW Mean Vectors for a Horizontally-mounted Piezoelectric Fan:  
 $S = 30.0\text{mm}$



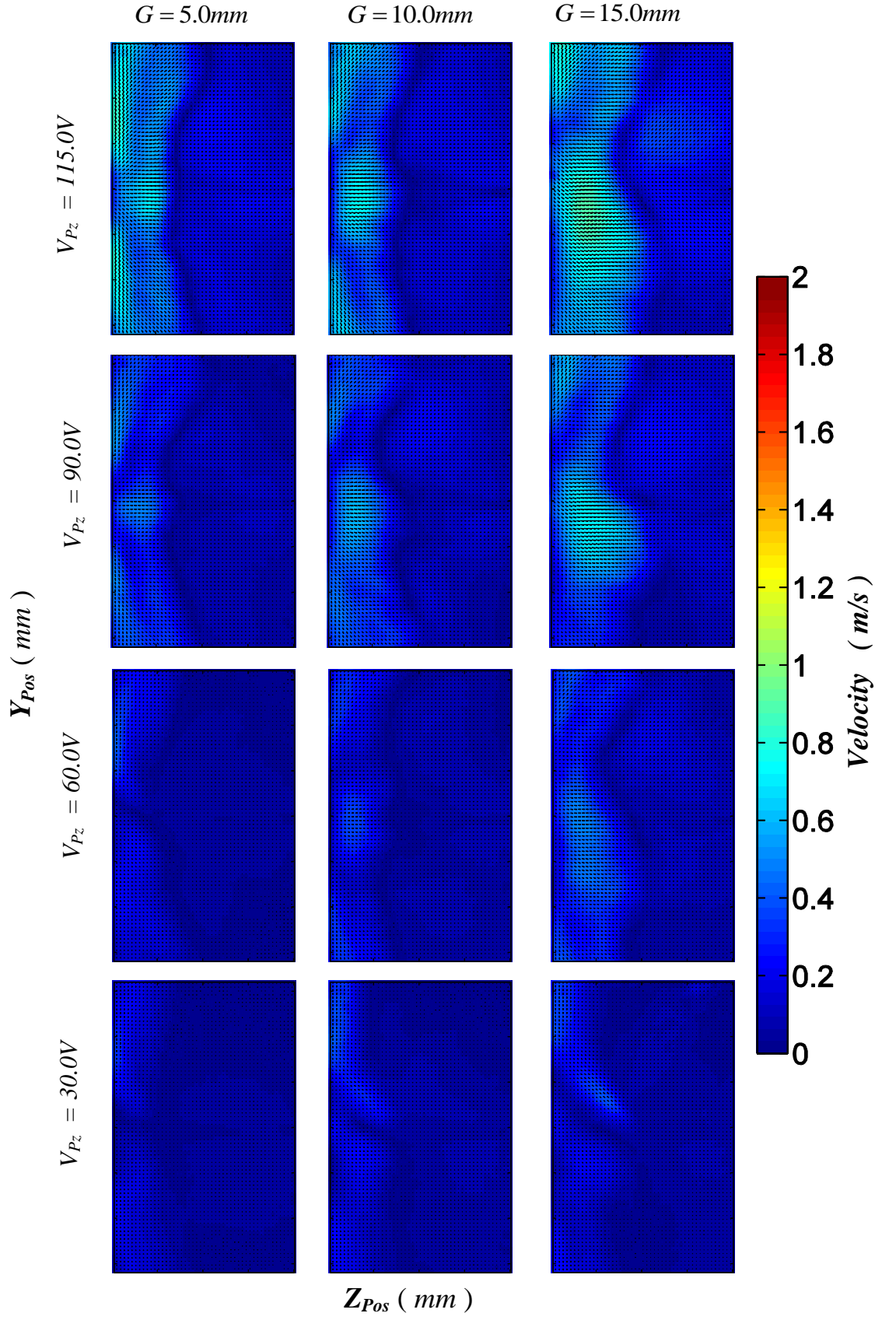


Figure F. 6: Magnitude of *FSW* Mean Vectors for a Horizontally-mounted Piezoelectric Fan:  
 $S = 40.0\text{mm}$

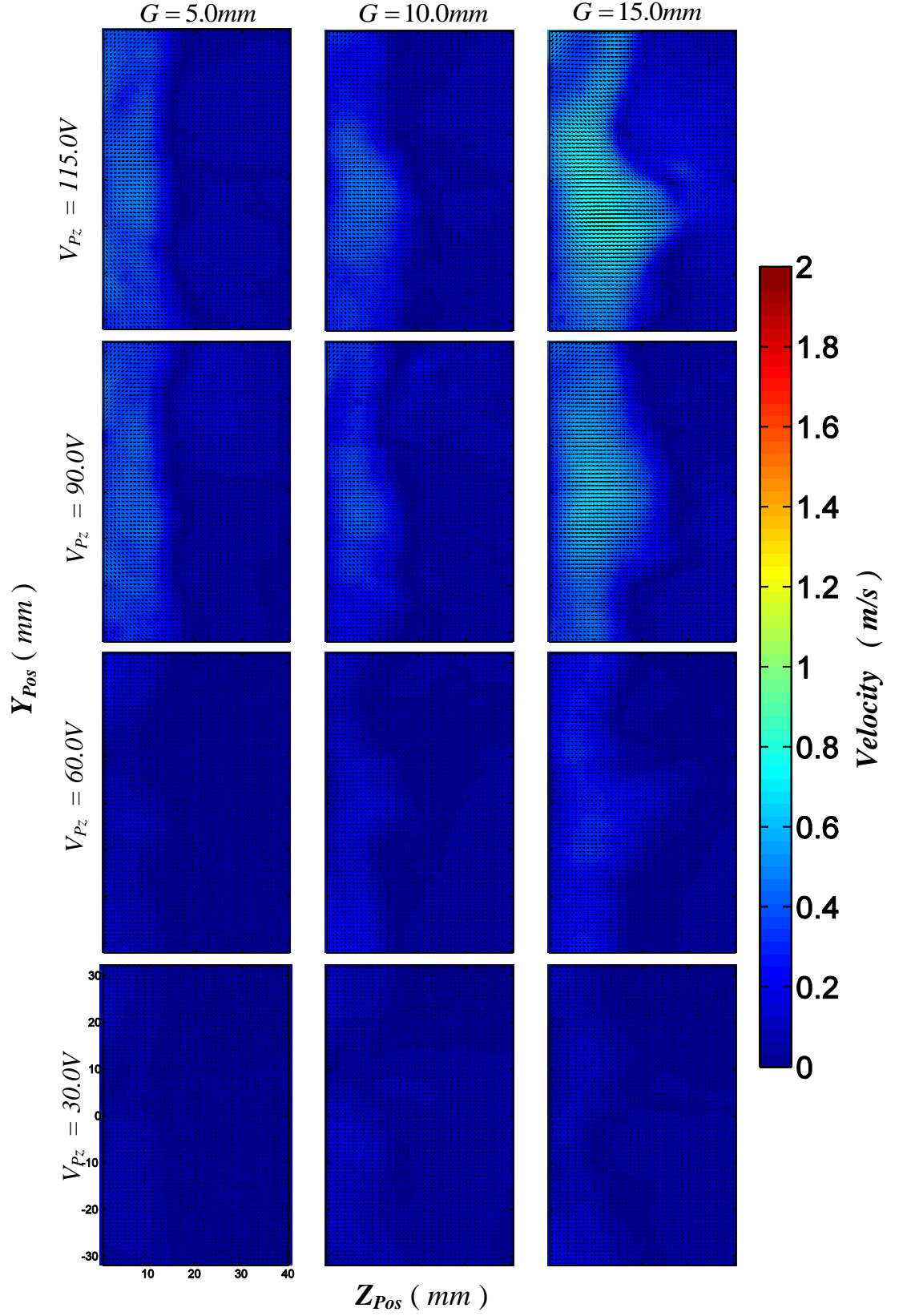


Figure F. 7: Magnitude of *FSW* Mean Vectors for a Horizontally-mounted Piezoelectric Fan:  
 $S = 50.0\text{mm}$

RMS of Fluctuating Component

The formulation adopted to calculate the *RMS* velocity vectors is given in **Chapter 7** and is of the form:

$$Var_x = \frac{\sum_{i=1}^{N_I} (V_x^2)}{N_I} - (\overline{V_x})^2 \quad \dots \text{Eq. F. 2}$$

$$Var_y = \frac{\sum_{i=1}^{N_I} (V_y^2)}{N_I} - (\overline{V_y})^2 \quad \dots \text{Eq. F. 3}$$

$$V_{RMS} = \sqrt{(Var_x) + (Var_y)} \quad \dots \text{Eq. F. 4}$$

Fin Base (S30, S40, S50, Flat Plate)

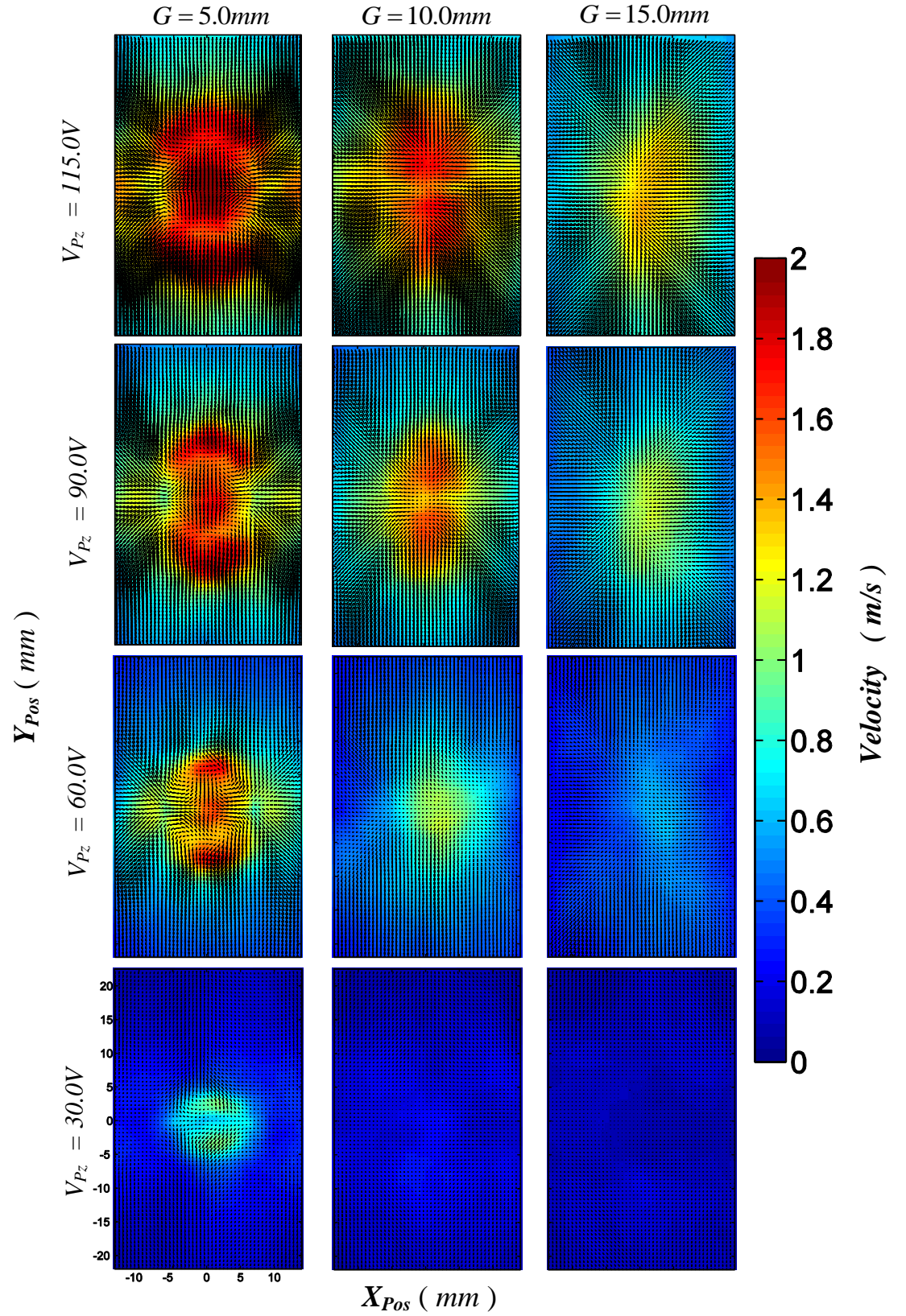


Figure F. 8: *FB RMS* of Fluctuating Component for a Horizontally-mounted Piezoelectric Fan:  
 $S = 30.0\text{mm}$



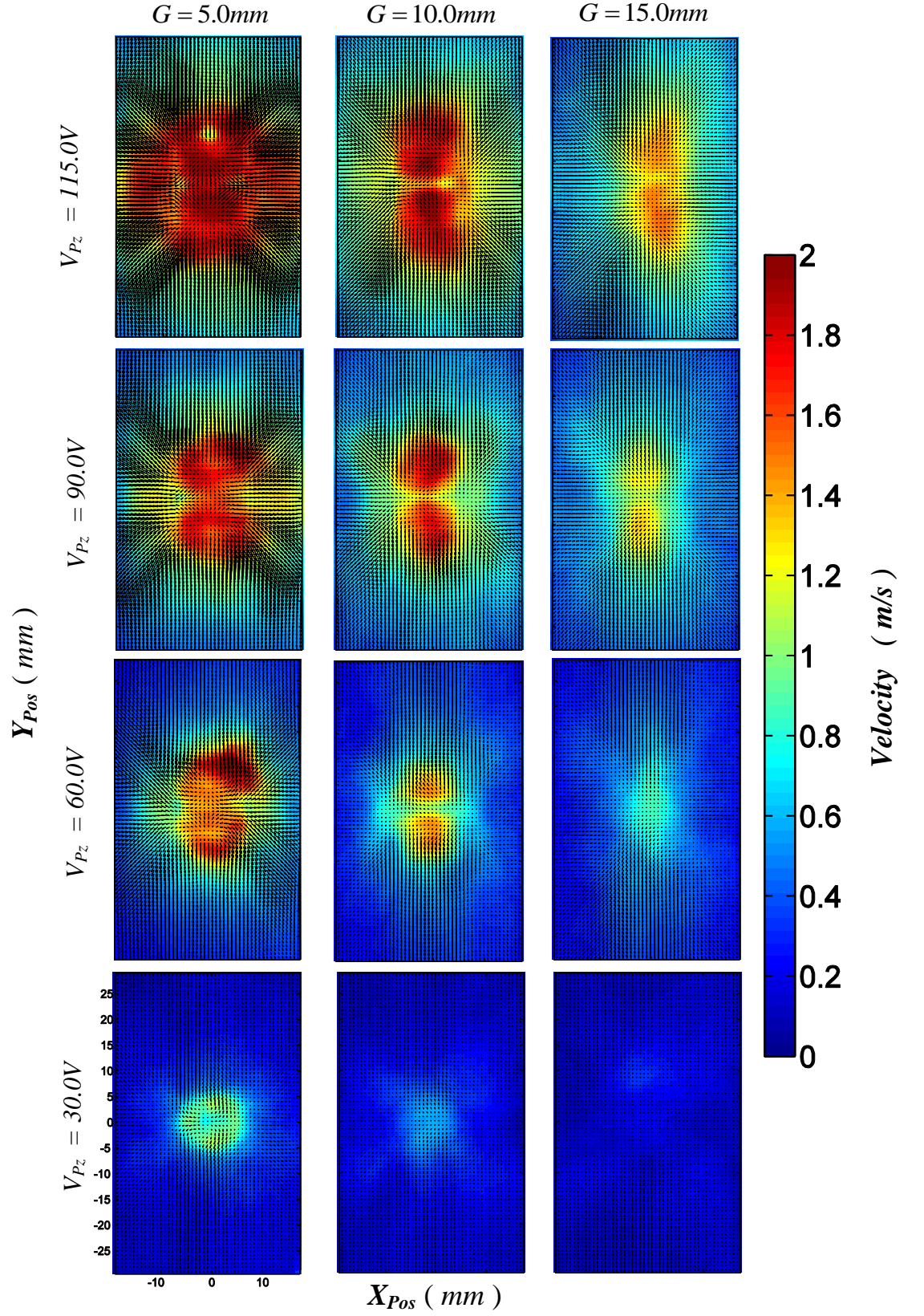


Figure F. 9: *FB RMS of Fluctuating Component for a Horizontally-mounted Piezoelectric Fan:  $S = 40.0mm$*

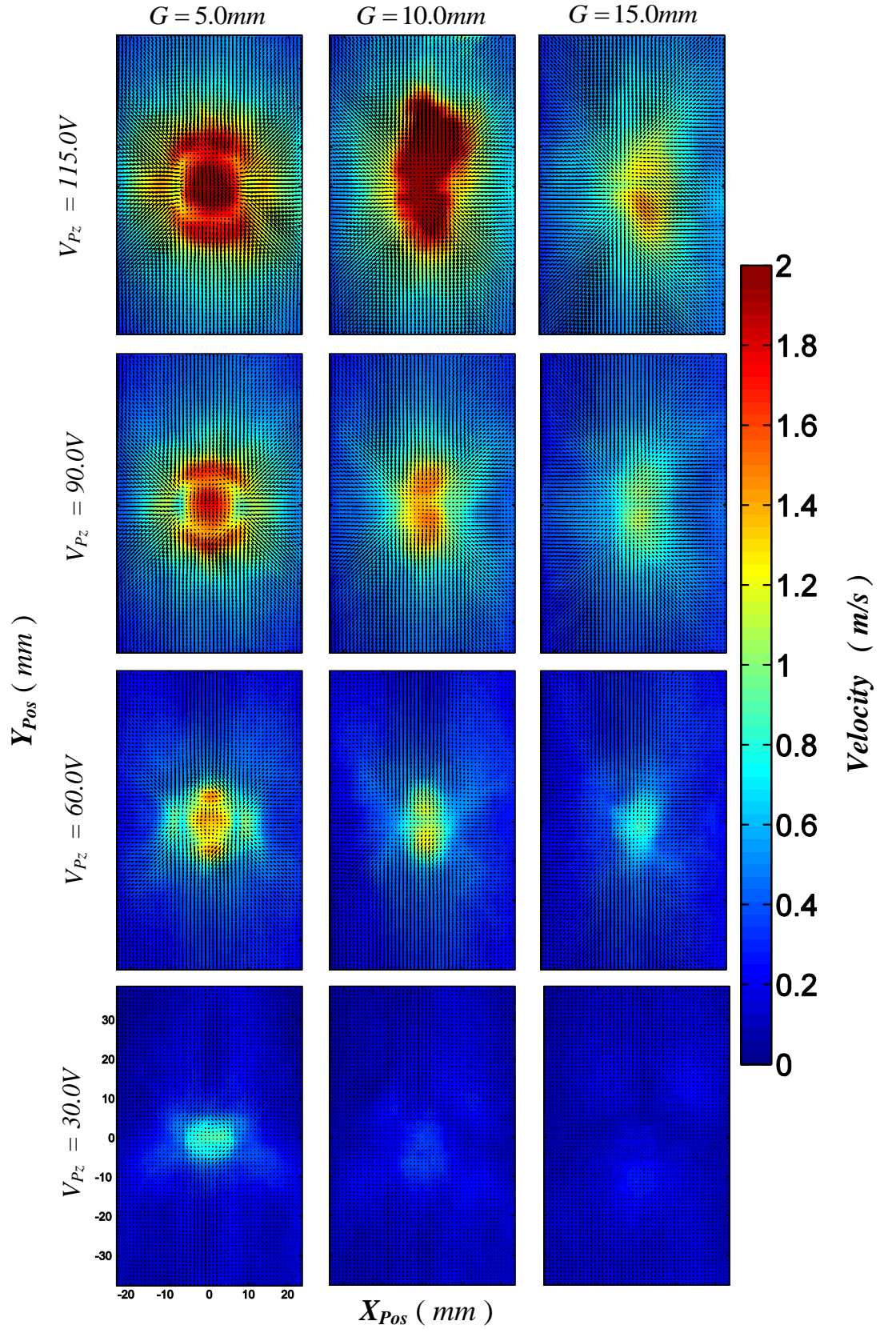


Figure F. 10: *FB RMS of Fluctuating Component for a Horizontally-mounted Piezoelectric Fan:  $S = 50.0\text{mm}$*



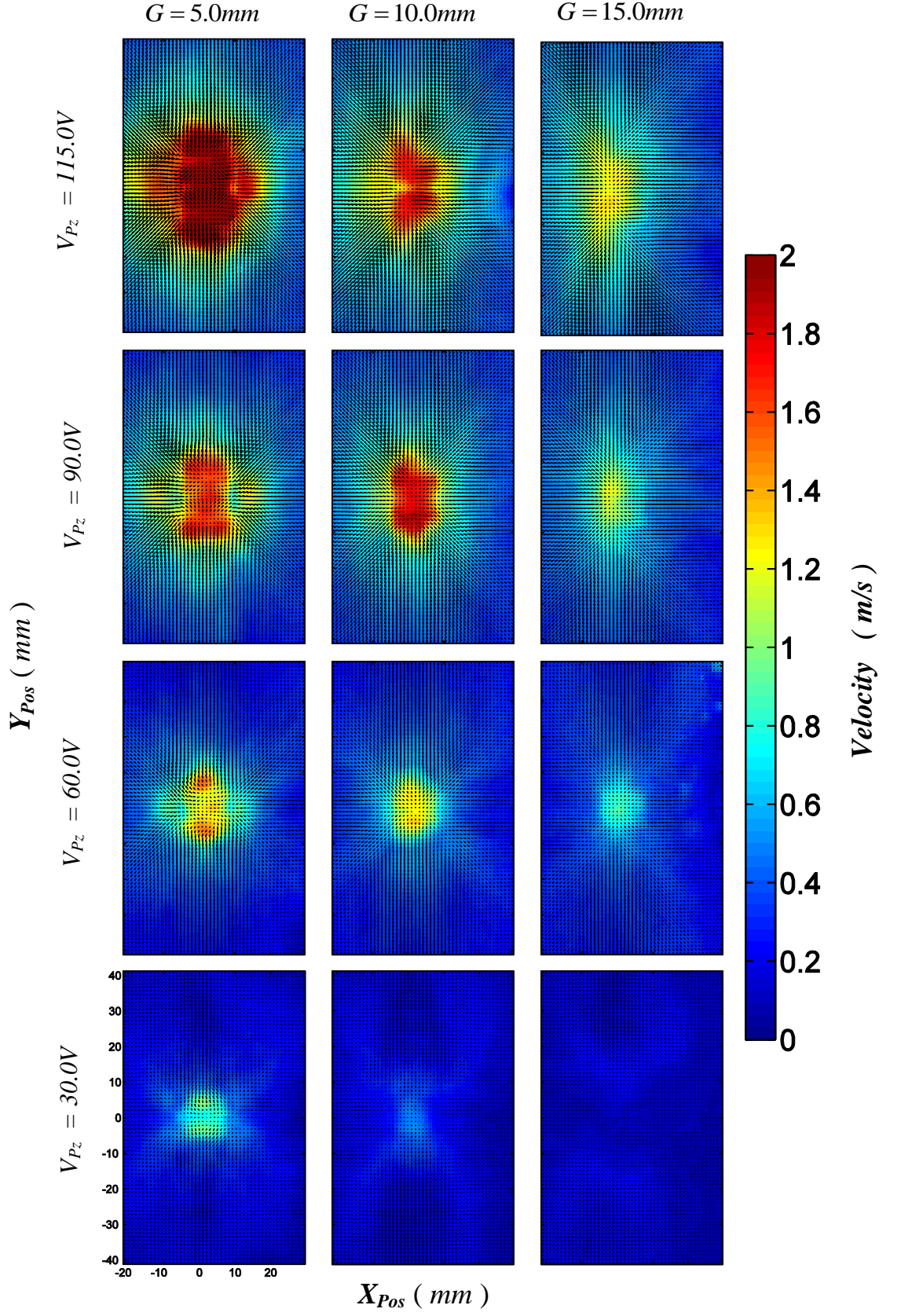


Figure F. 11: *FB RMS of Fluctuating Component for a Horizontally-mounted Piezoelectric Fan: Flat Plate ( $S = \infty \text{ mm}$ )*

Fin Side Wall (S30, S40, S50)

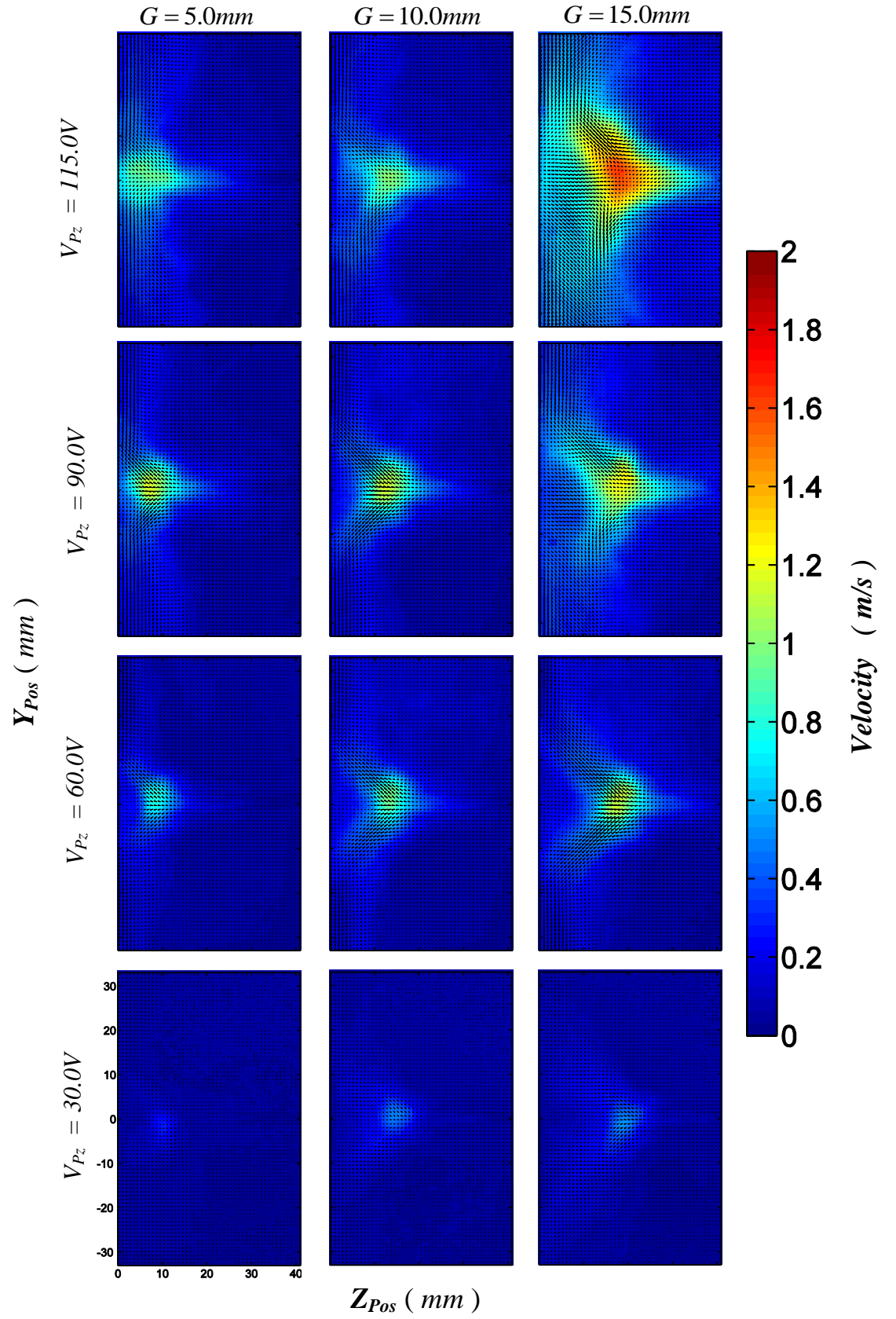


Figure F. 12: FSW RMS of Fluctuating Component for a Horizontally-mounted Piezoelectric Fan:  
 $S = 30.0\text{mm}$



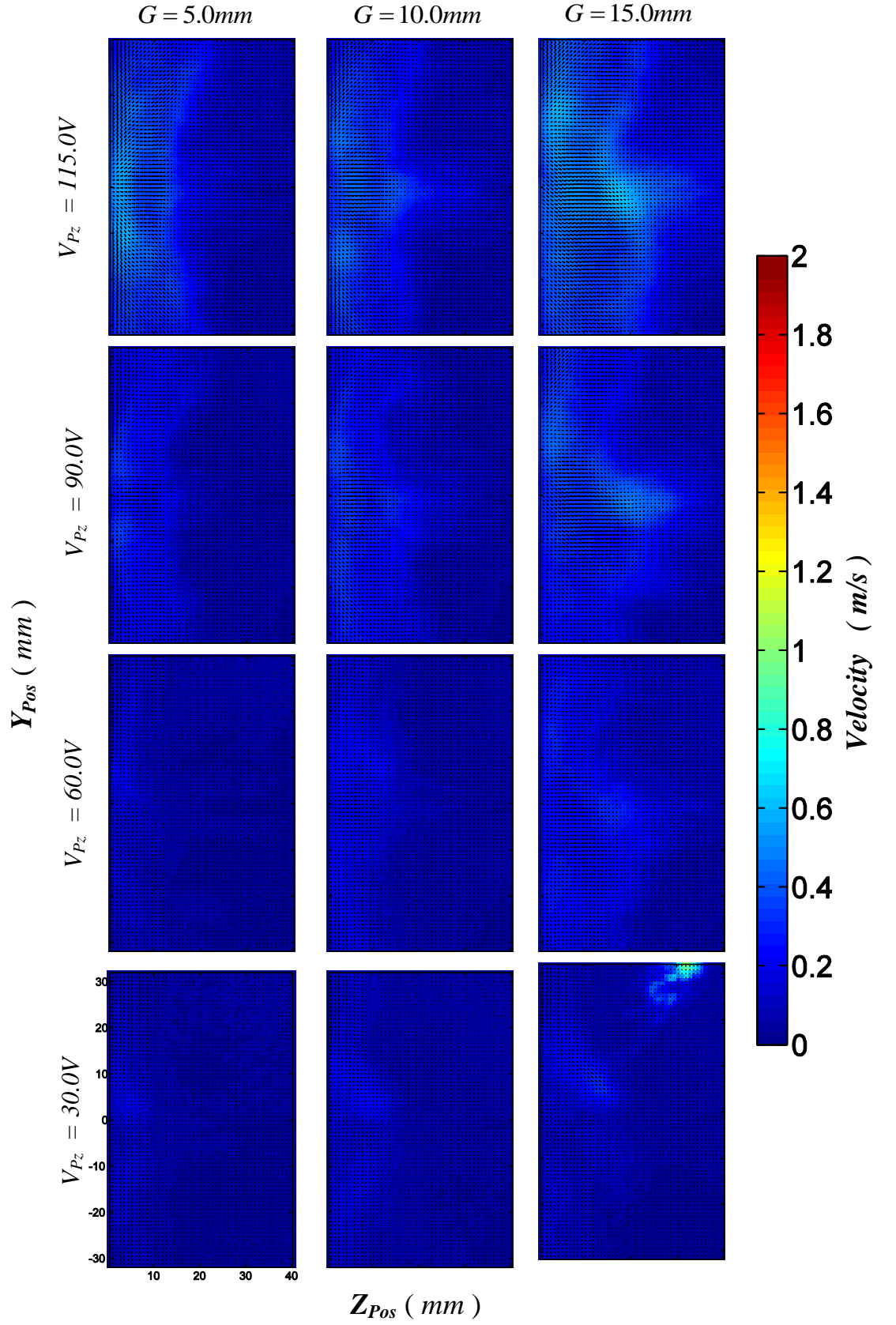


Figure F. 13: *FSW RMS* of Fluctuating Component for a Horizontally-mounted Piezoelectric Fan:  
 $S = 40.0\text{mm}$

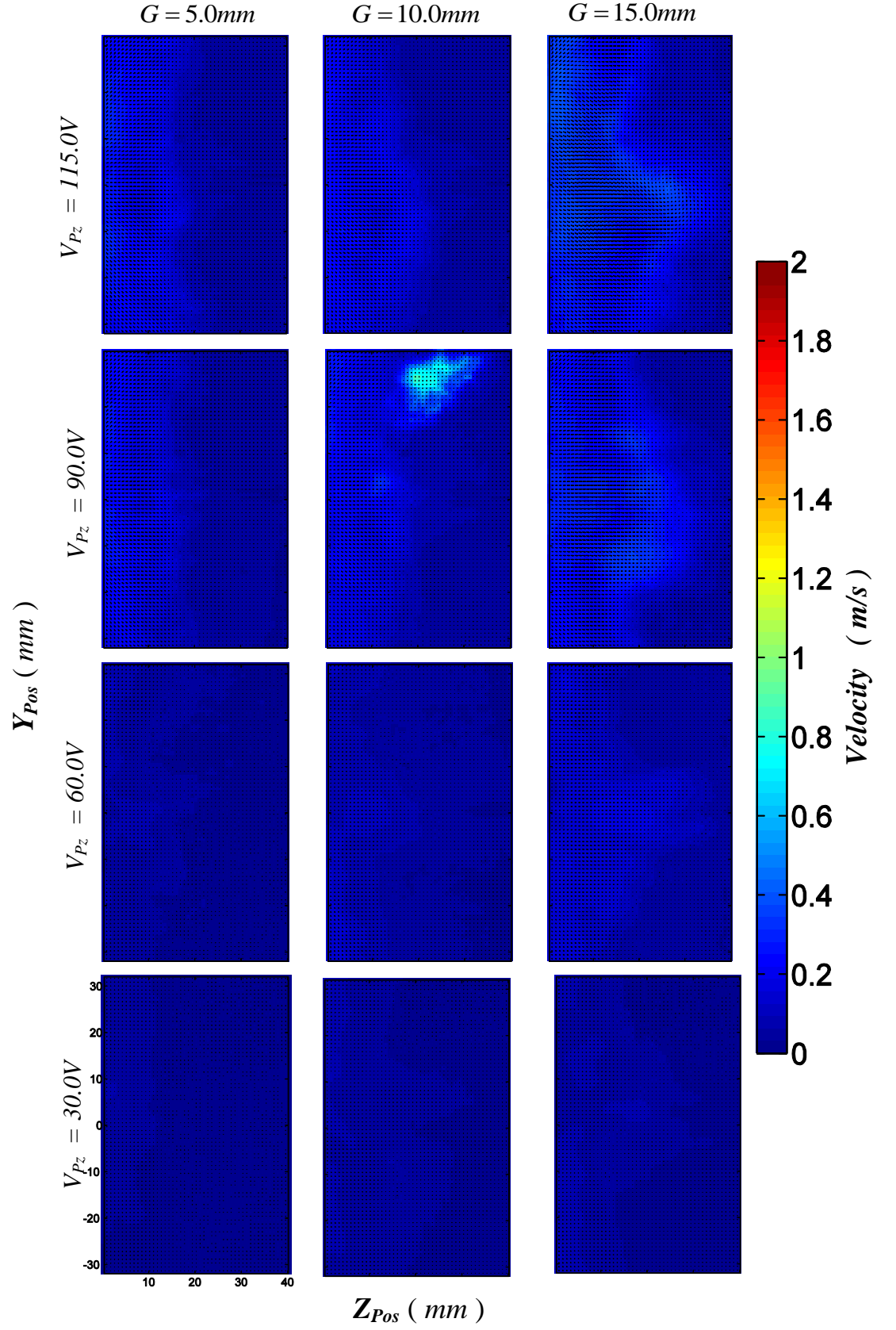


Figure F. 14: FSW RMS of Fluctuating Component for a Horizontally-mounted Piezoelectric Fan:  $S = 50.0\text{mm}$

## **2. Vertically-mounted Piezoelectric Fan**

In this section, like in the previous section, results (magnitude of mean vectors and *RMS* of fluctuating component) pertaining to a vertically-mounted oscillating piezoelectric fan are presented.

## Magnitude of Mean Vectors Fin Base

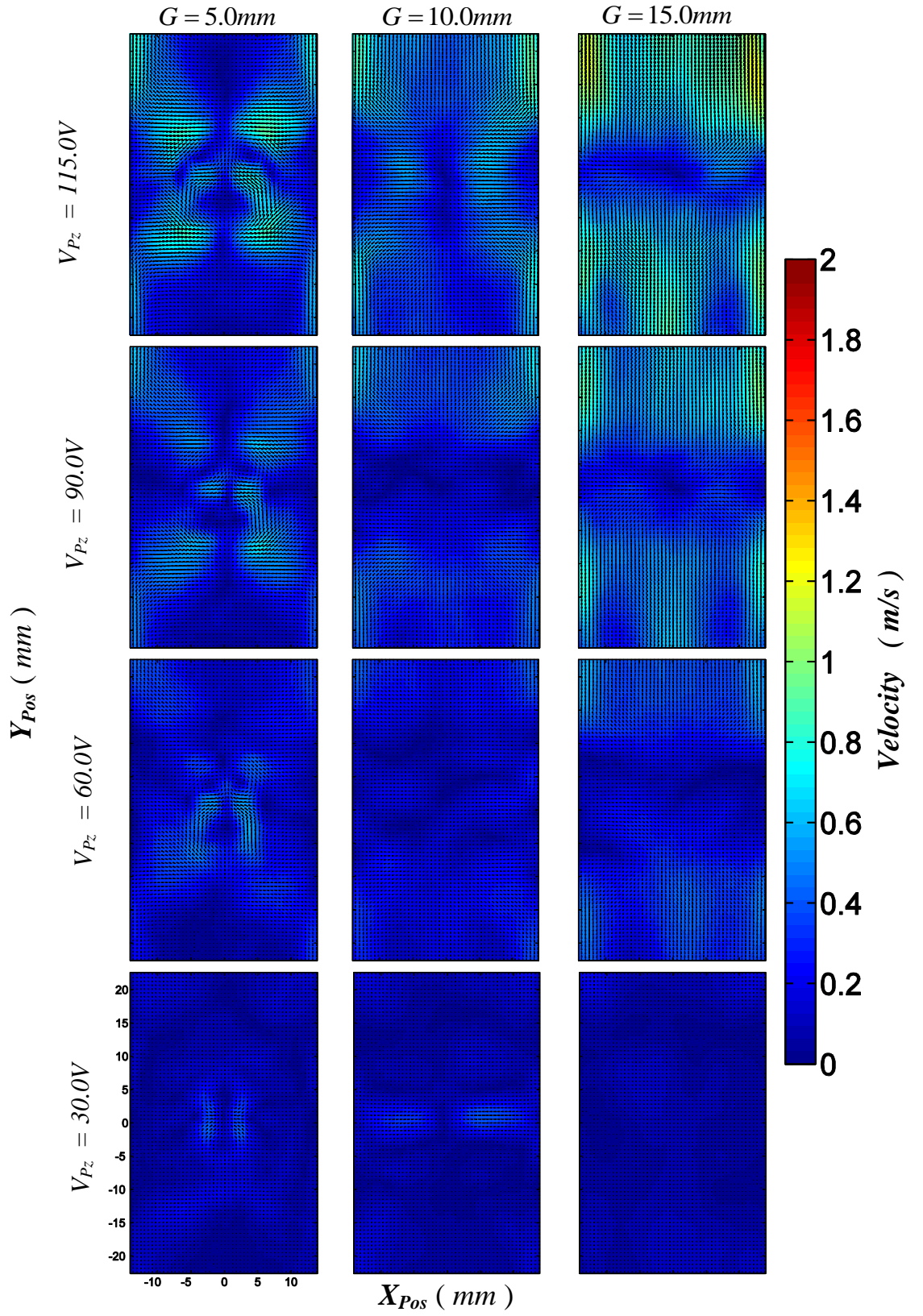
*Fin Base (S30, S40, S50, Flat Plate)*

Figure F. 15: *FB* Magnitude of Mean Vectors for a Vertically-mounted Piezoelectric Fan:  
 $S = 30.0mm$

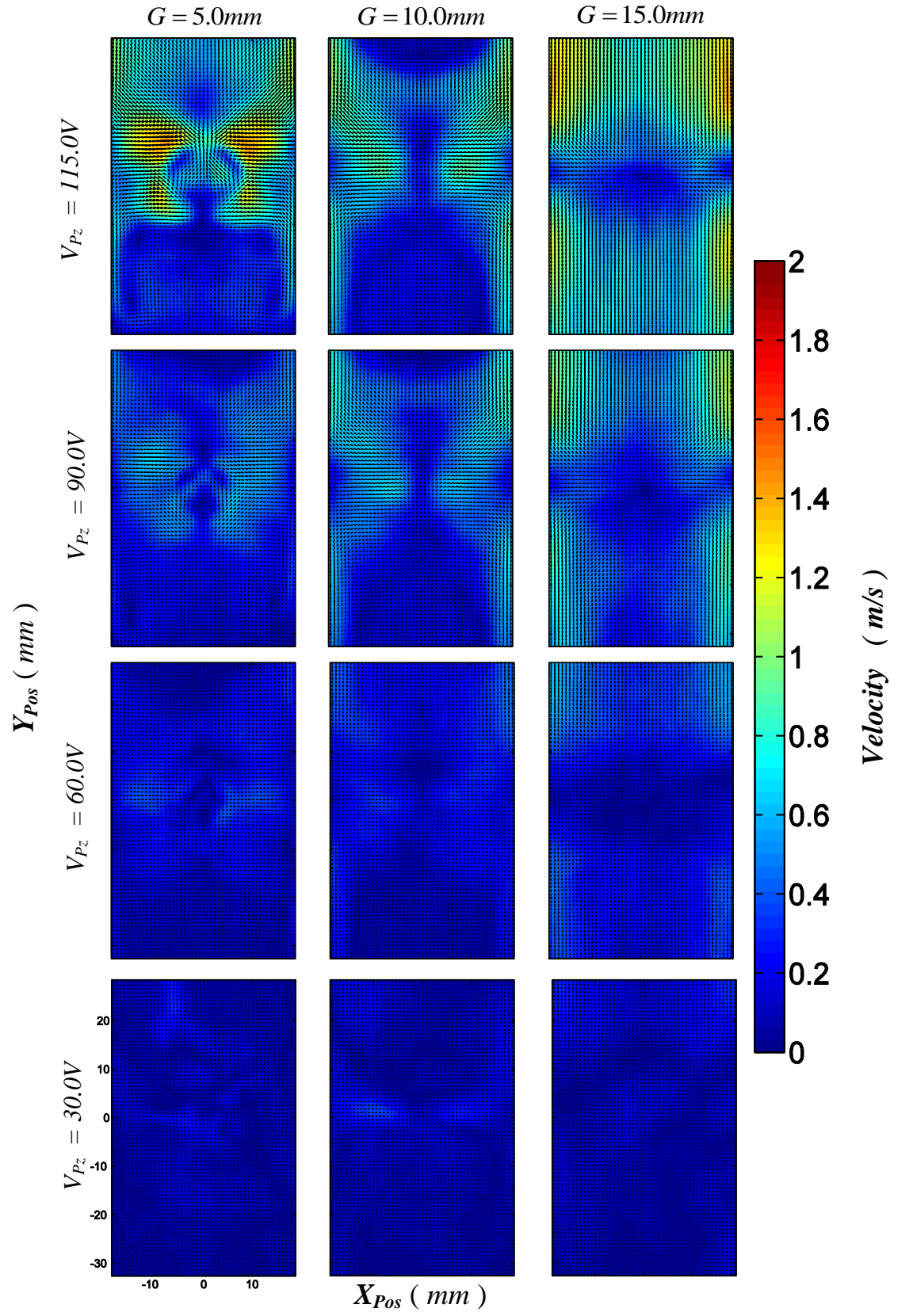


Figure F. 16: *FB* Magnitude of Mean Vectors for a Vertically -mounted Piezoelectric Fan:  
 $S = 40.0mm$



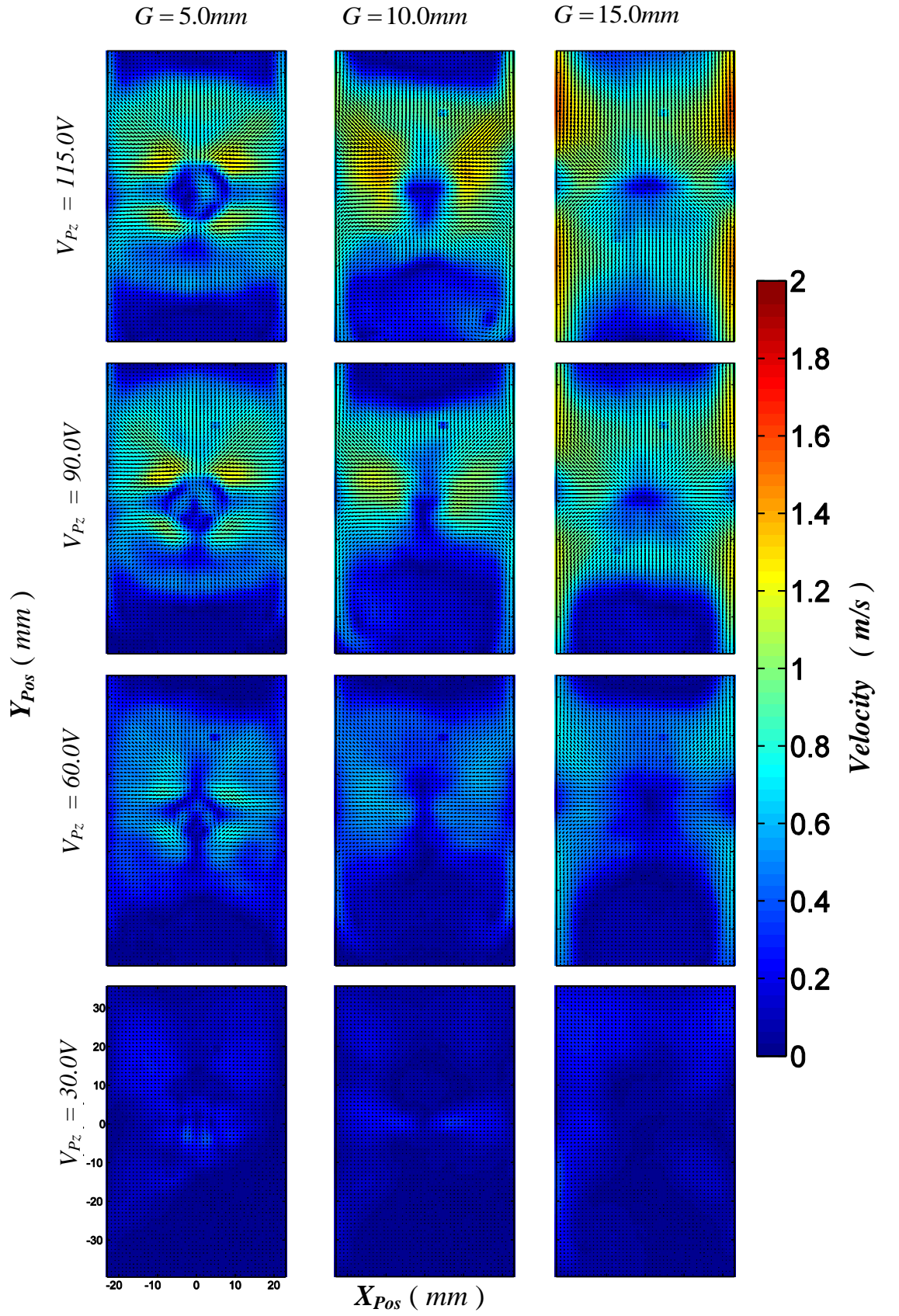


Figure F. 17: *FB* Magnitude of Mean Vectors for a Vertically -mounted Piezoelectric Fan:  
 $S = 50.0mm$

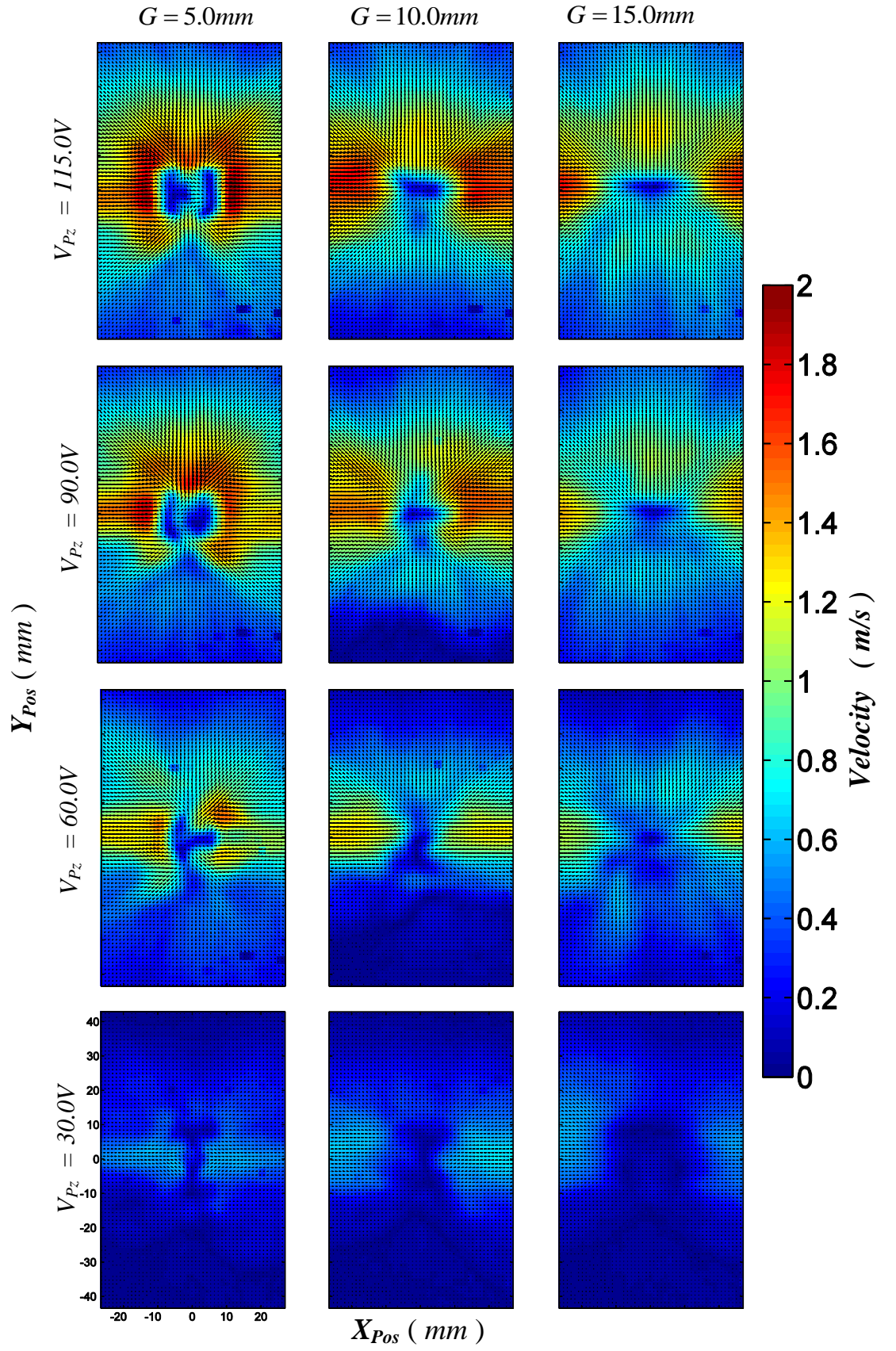


Figure F. 18: *FB* Magnitude of Mean Vectors for a Vertically -mounted Piezoelectric Fan:  
Flat Plate ( $S = \infty$  mm)

Fin Side Wall (S30, S40, S50)

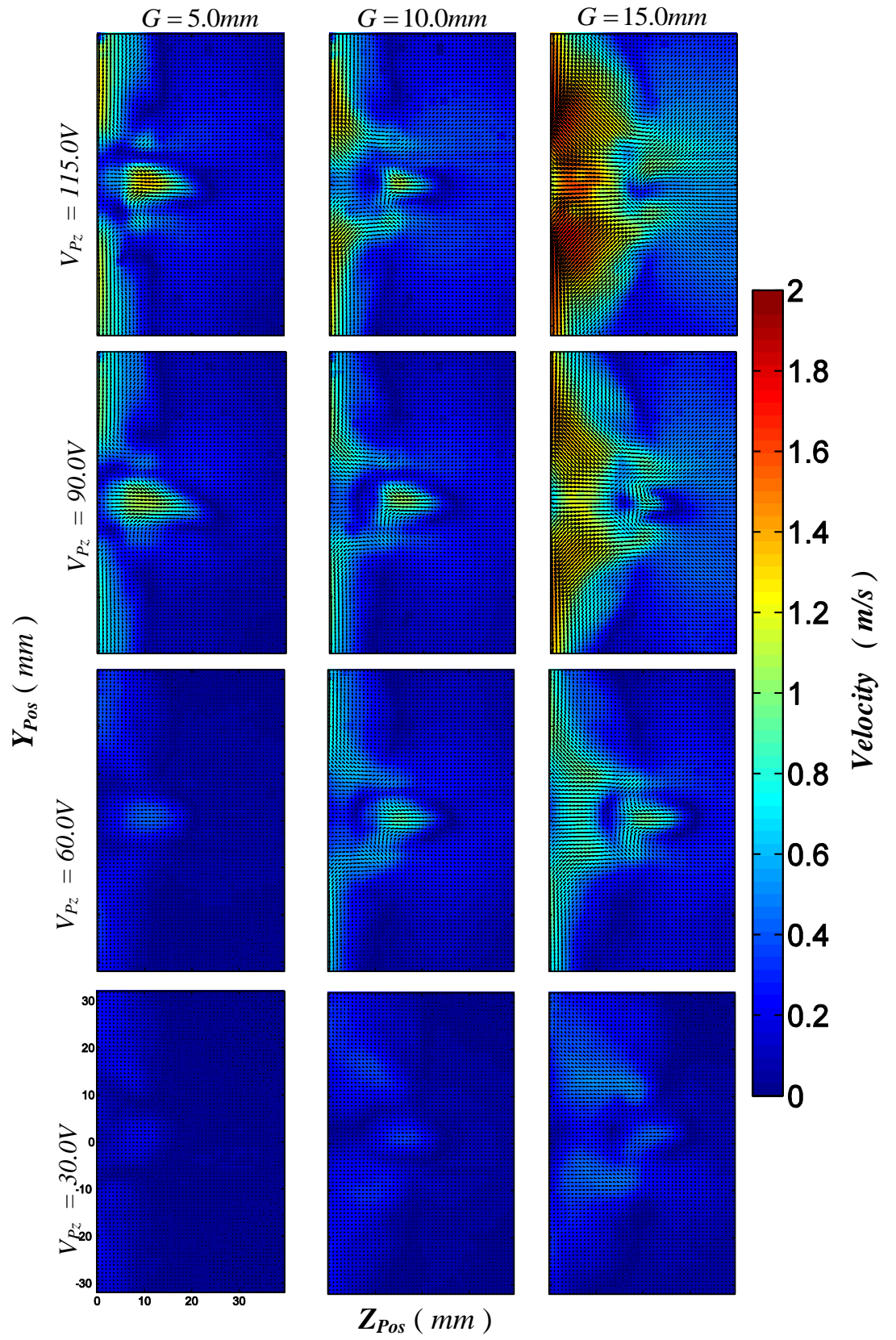


Figure F. 19: FSW Magnitude of Mean Vectors for a Vertically -mounted Piezoelectric Fan:  
 $S = 30.0mm$



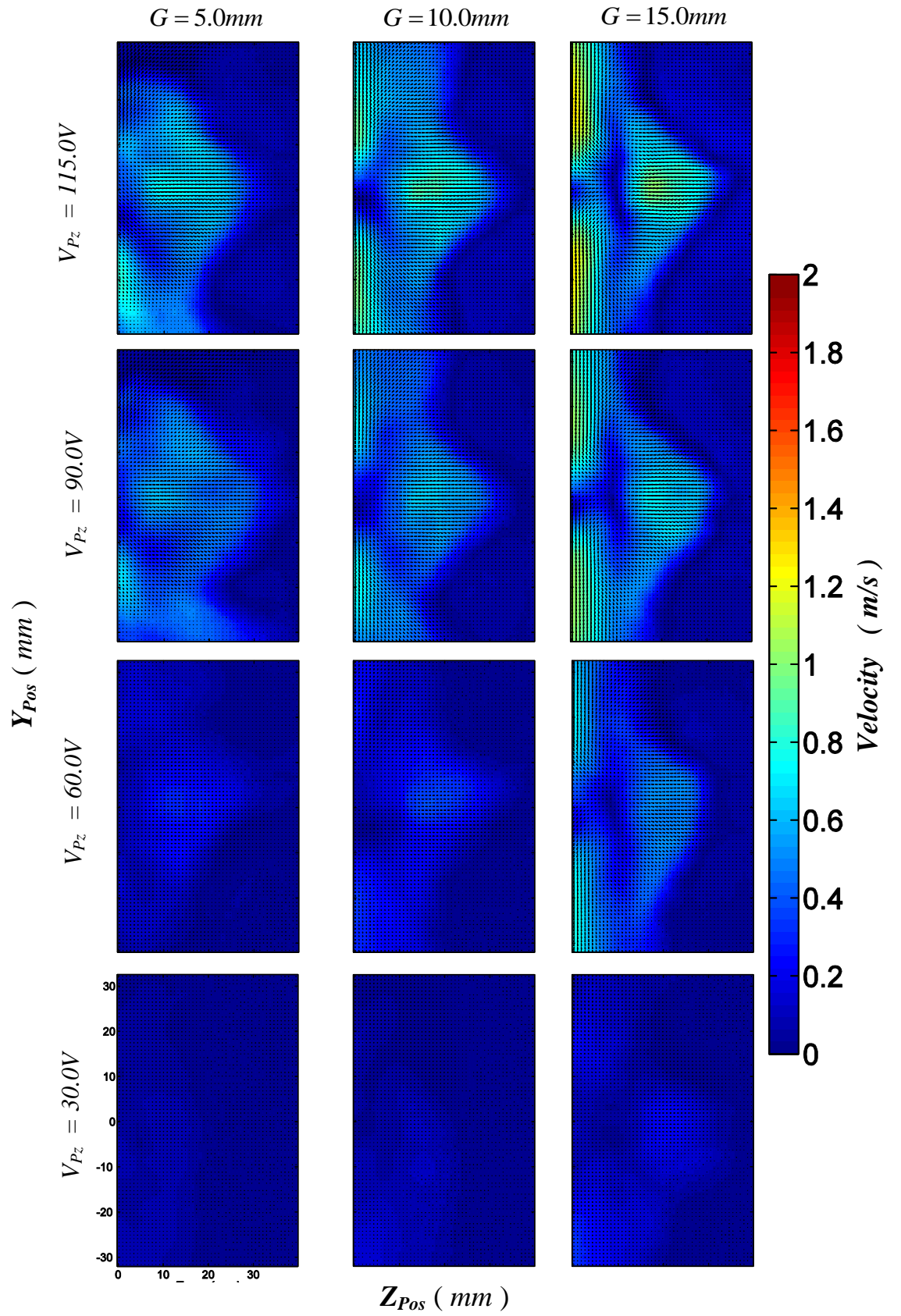


Figure F. 20: FSW Magnitude of Mean Vectors for a Vertically -mounted Piezoelectric Fan:  
 $S = 40.0\text{mm}$

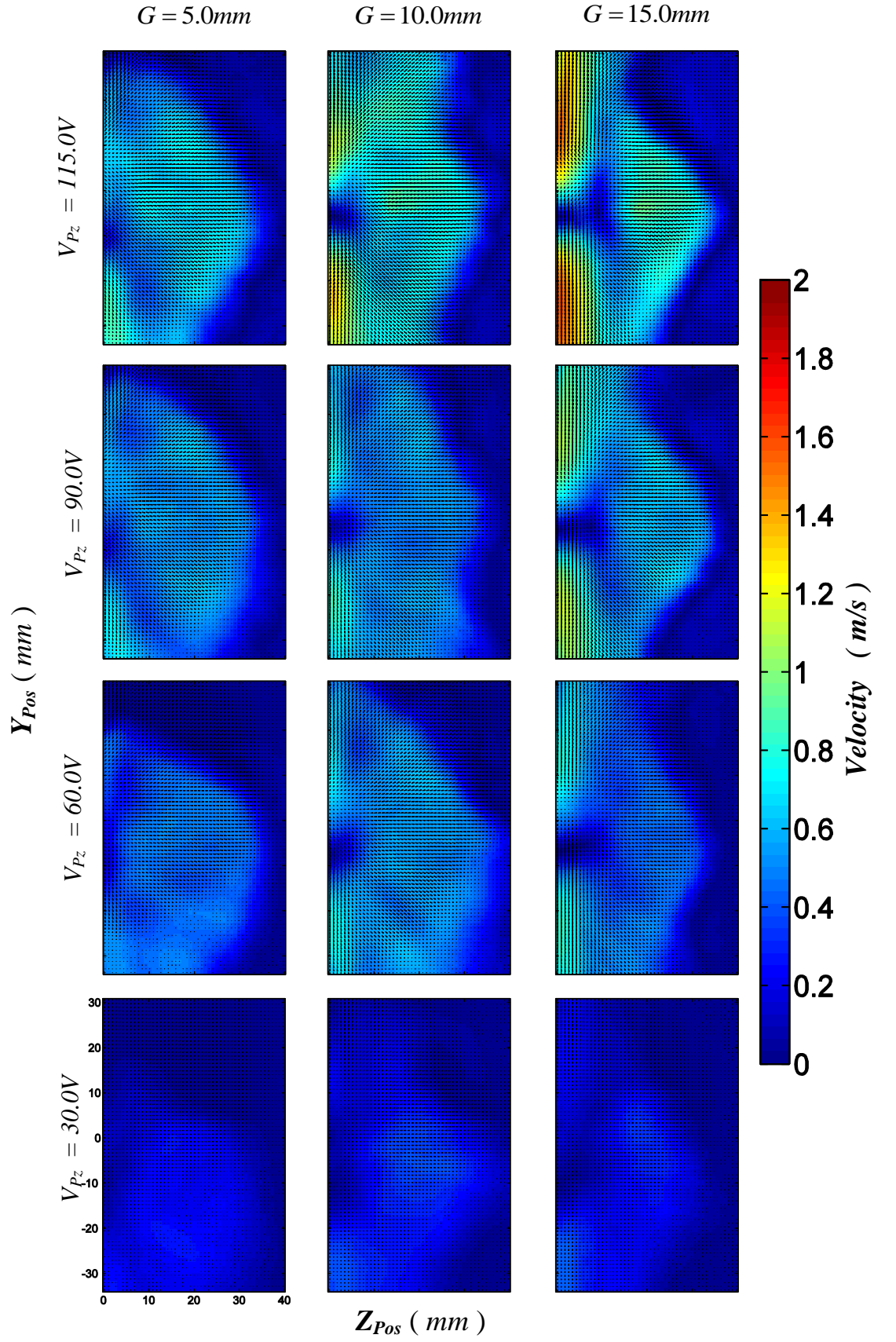


Figure F. 21: FSW Magnitude of Mean Vectors for a Vertically -mounted Piezoelectric Fan:  
 $S = 50.0mm$

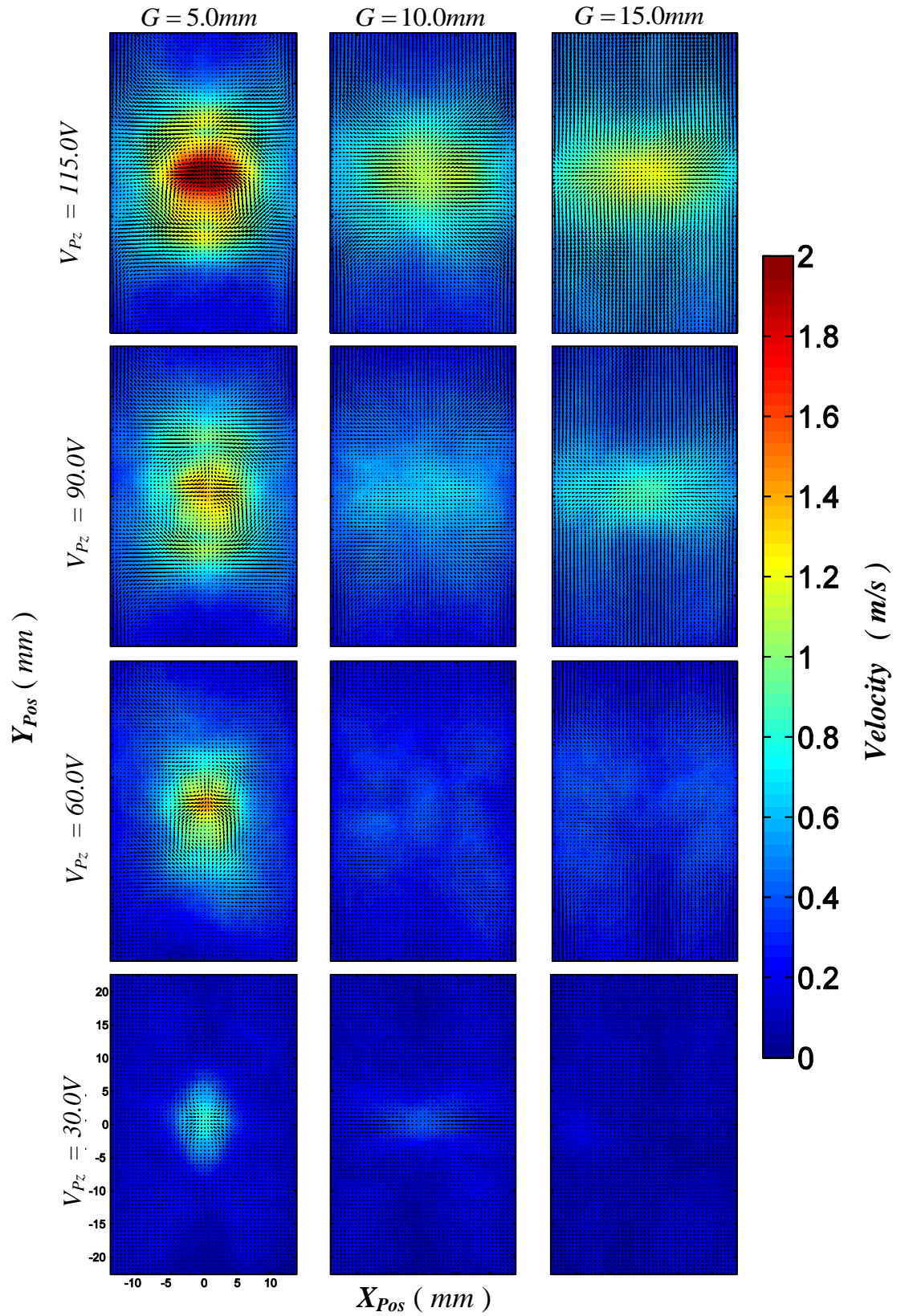
RMS of Fluctuating Component*Fin Base (S30, S40, S50, Flat Plate)*

Figure F. 22: *FB RMS of Fluctuating Component for a Vertically -mounted Piezoelectric Fan:*  
 $S = 30.0\text{mm}$



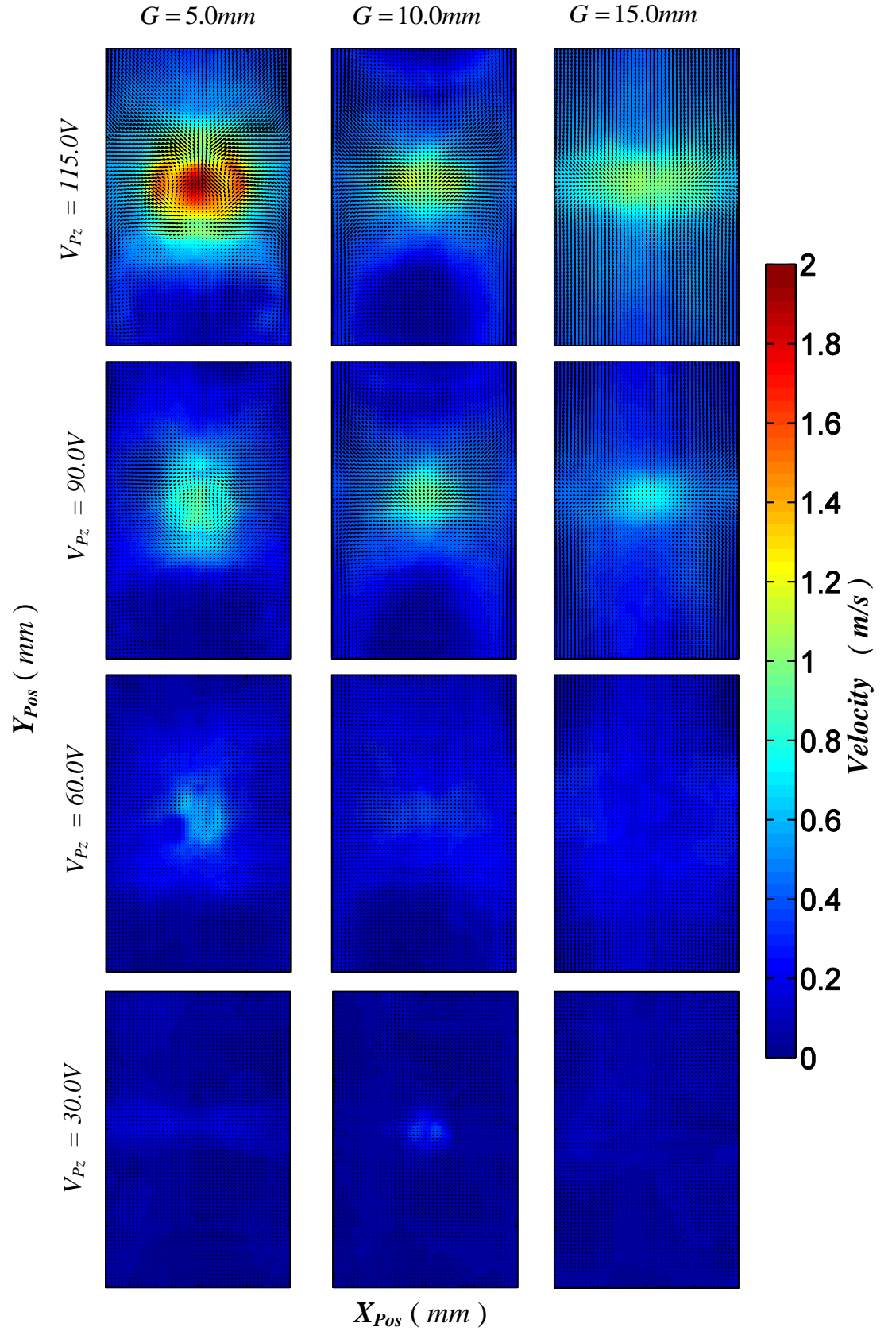


Figure F. 23: *FB RMS of Fluctuating Component for a Vertically -mounted Piezoelectric Fan:  $S = 40.0mm$*

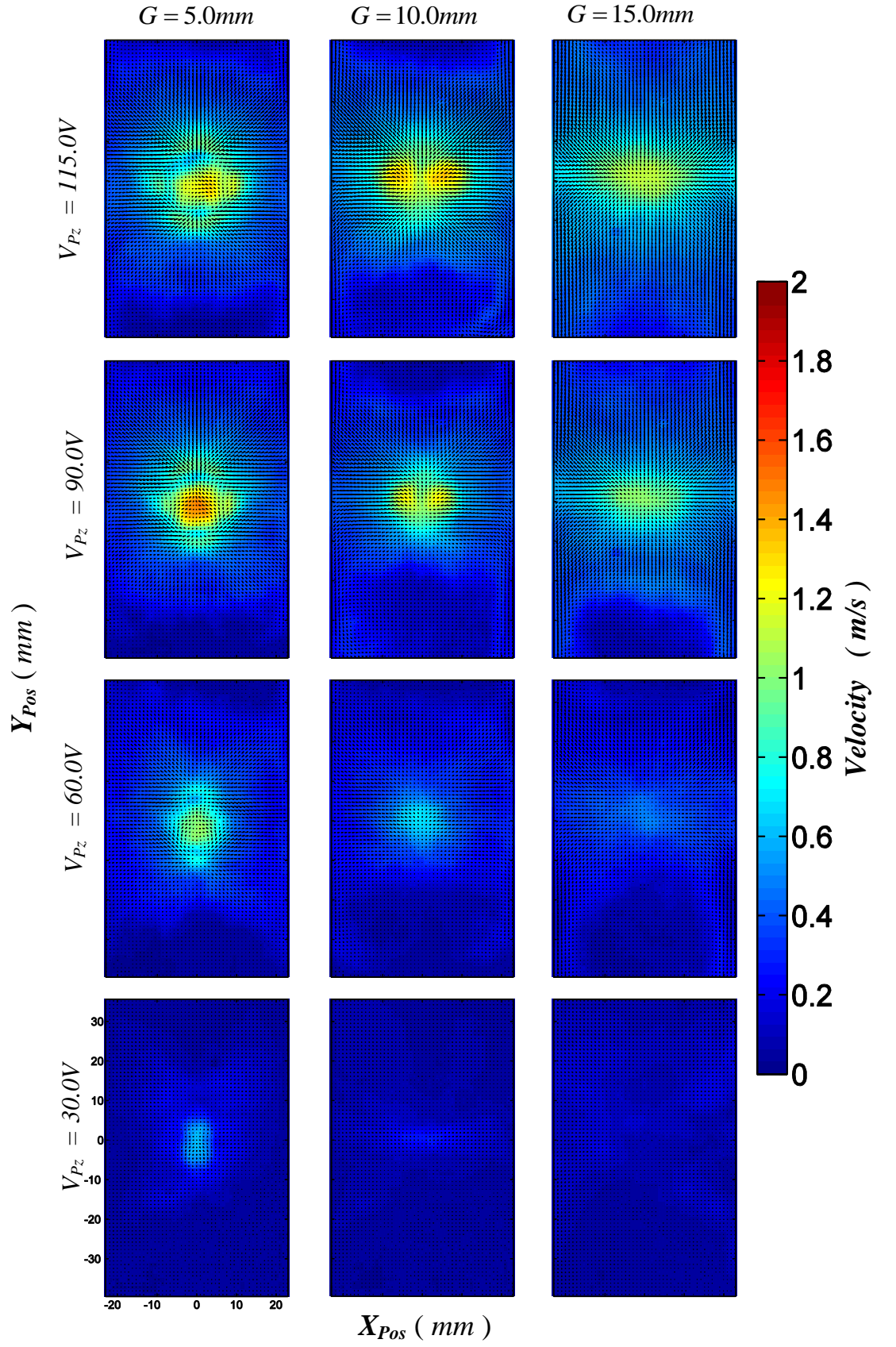


Figure F. 24: *FB RMS* of Fluctuating Component for a Vertically -mounted Piezoelectric Fan:  
 $S = 50.0mm$

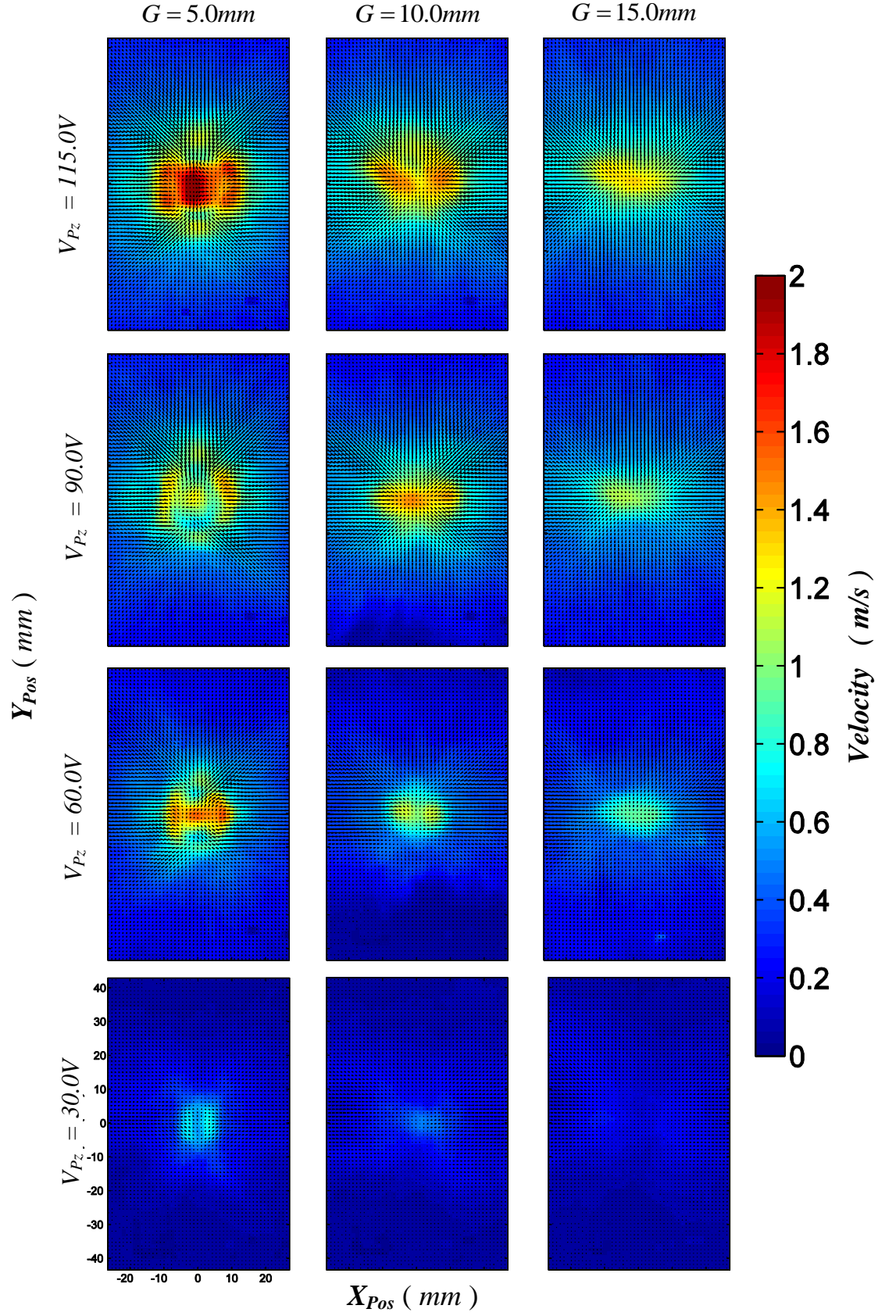


Figure F. 25: *FB RMS of Fluctuating Component for a Vertically -mounted Piezoelectric Fan: Flat Plate ( $S = \infty \text{ mm}$ )*



Fin Side Wall (S30, S40, S50)

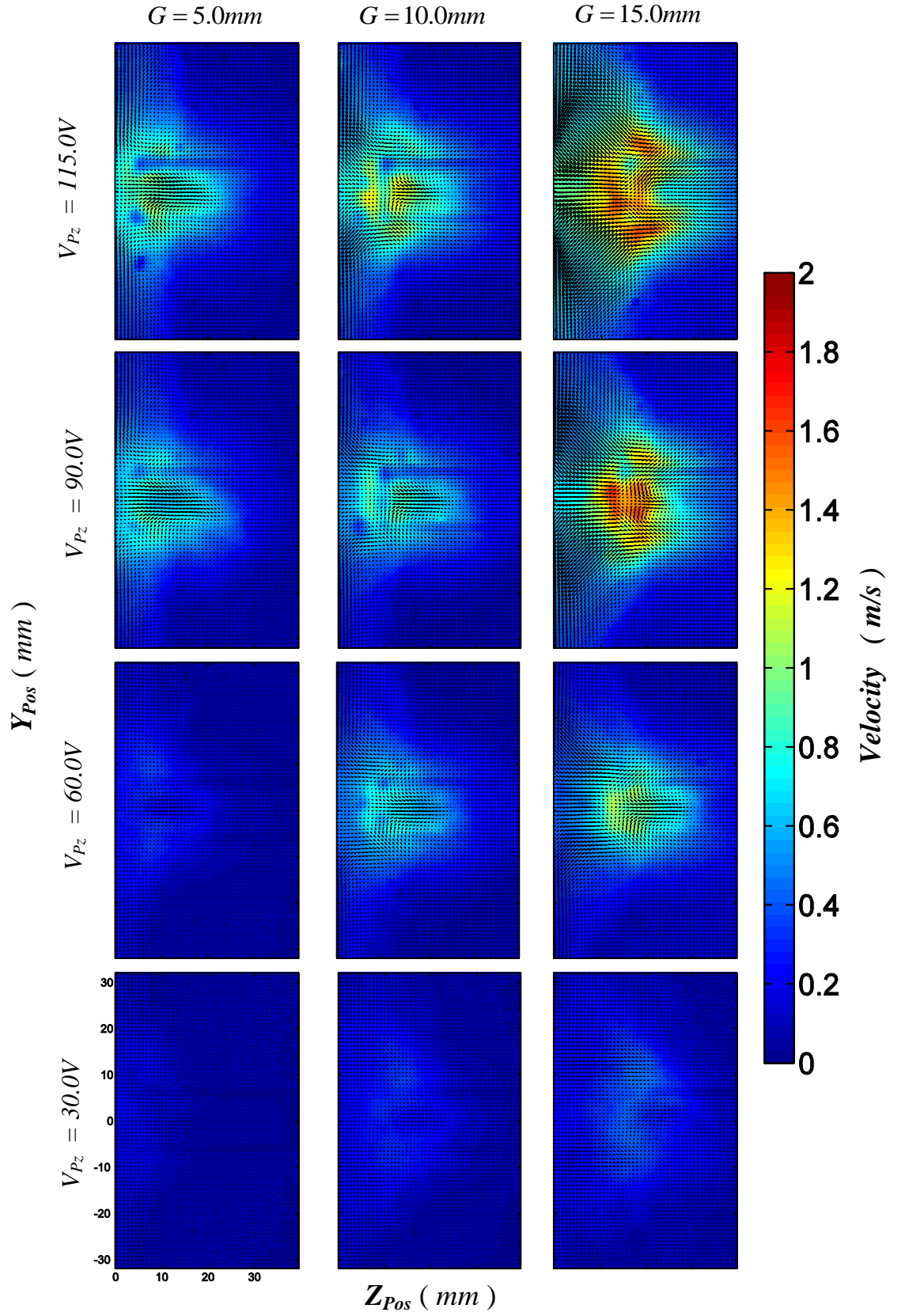


Figure F. 26:  $FSW_{RMS}$  of Fluctuating Component for a Vertically -mounted Piezoelectric Fan:  
 $S = 30.0mm$

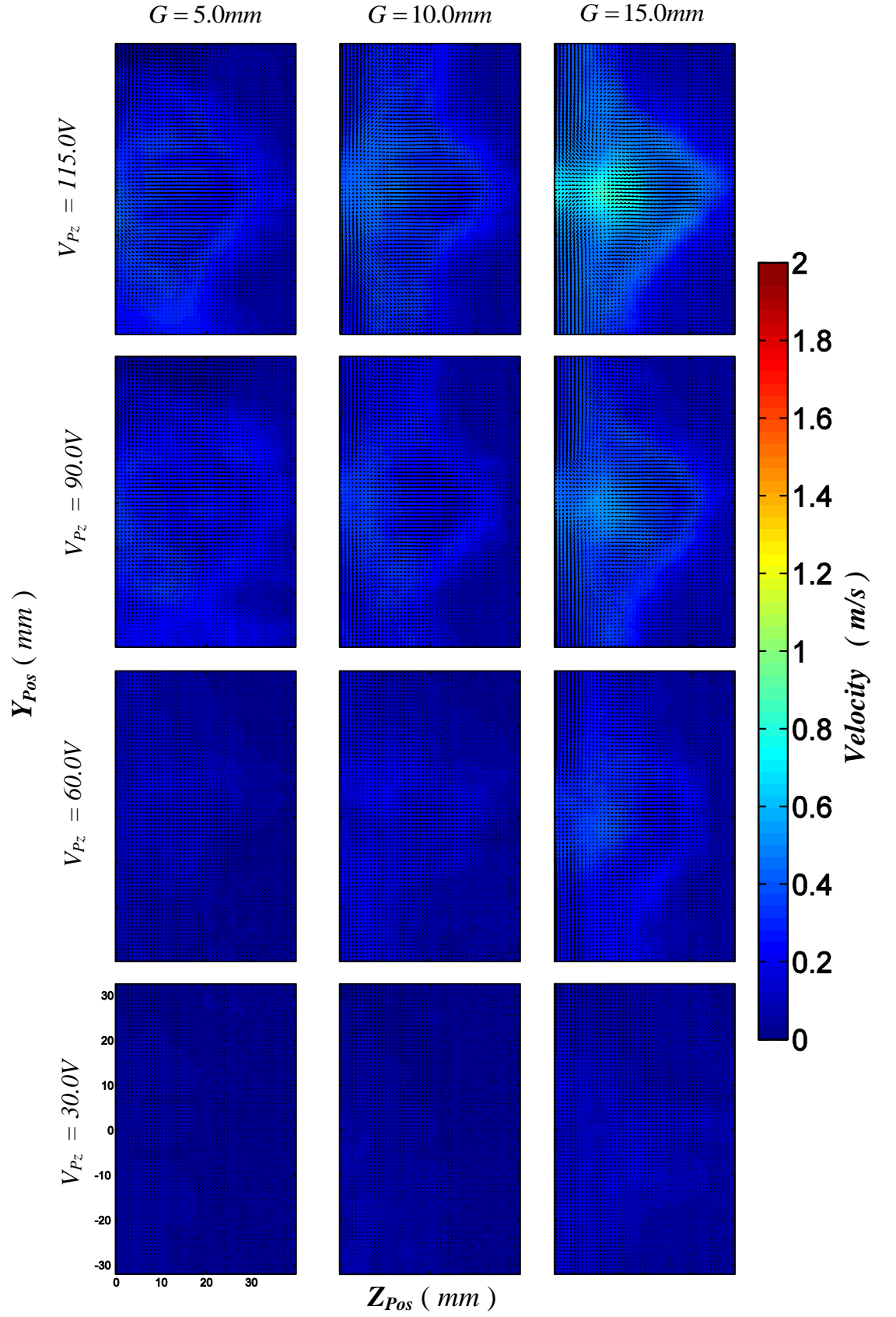


Figure F. 27: FSW RMS of Fluctuating Component for a Vertically -mounted Piezoelectric Fan:  
 $S = 40.0mm$



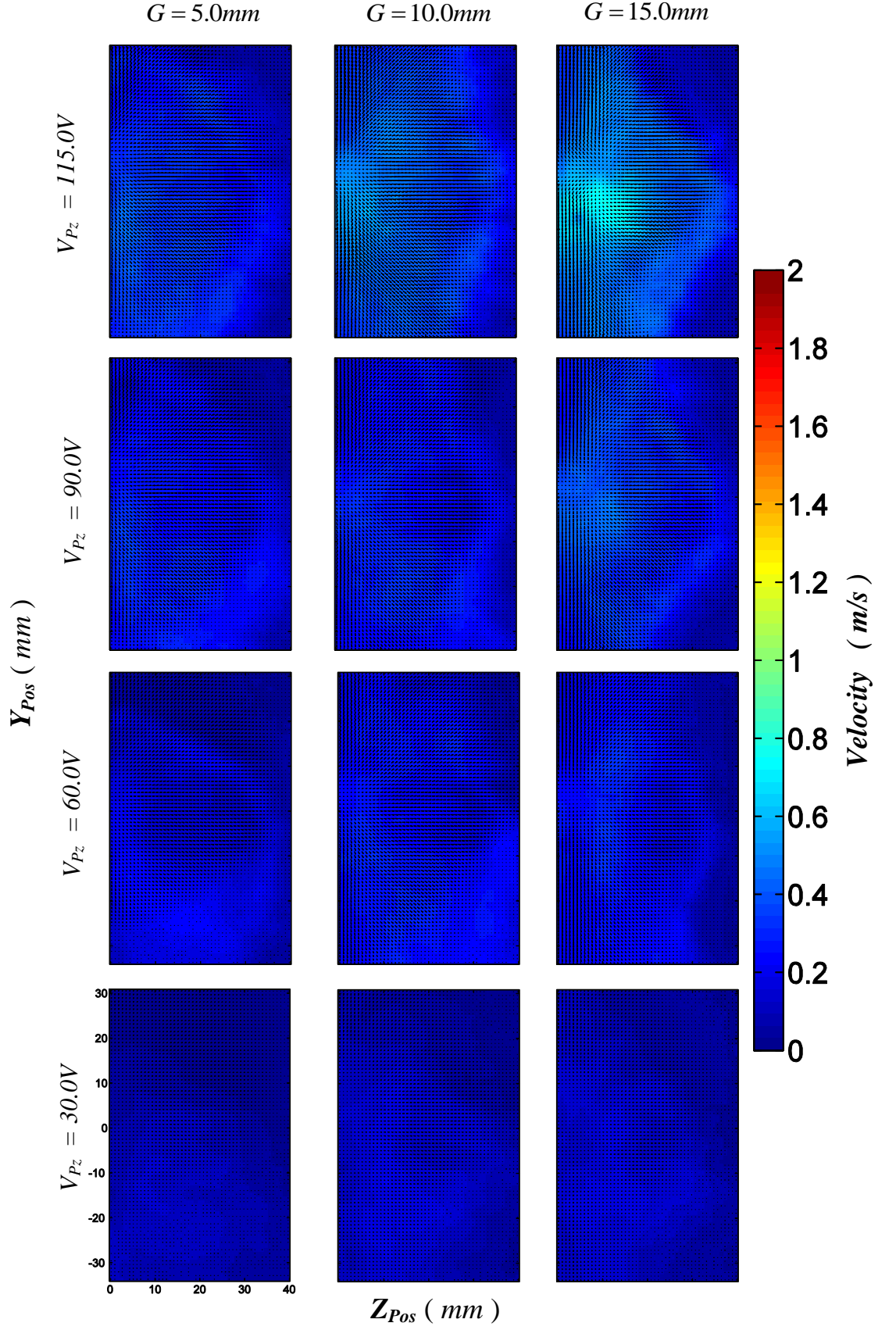


Figure F. 28: *FSW RMS of Fluctuating Component for a Vertically -mounted Piezoelectric Fan:  $S = 50.0mm$*

# REFERENCES

---

- [1] C. Gazley and S. M. Calif, "Heat - Transfer Characteristics of the Rotational and Axial Flow between Concentric Cylinders," *Journal of Heat Transfer* vol. 80, pp. 79-90, 1958.
- [2] T. Acikalin, S. V. Garimella, J. Petroski, and Arvind Raman, Purdue University, USA, "Optimal Design of Miniature Piezoelectric Fans for Cooling Light Emitting Diodes," *Intersociety Conference on Thermal Phenomena*, 2004.
- [3] C. Mejuto, A. Mebarki, D. Staton, N. Al-Khayat, and M. Mueller, "Thermal modelling of TEFC alternators," in *IEEE Industrial Electronics, IECON 2006 - 32nd Annual Conference*.
- [4] D. G. Dorrell, D. A. Staton, J. Kahout, D. Hawkins, and M. I. McGilp, "Linked Electromagnetic and Thermal Modelling of a Permanent Magnet Motor," *University of Glasgow, Glasgow, UK*.
- [5] A. Tassi, G. Zanocchi, and D. Staton, "FEM and Lumped Circuit Thermal Analysis of External Rotor Motor," in *IEEE Industrial Electronics, IECON 2006 - 32nd Annual Conference*.
- [6] D. A. Staton and A. Cavagnino, "Convection Heat Transfer and Flow Calculations Suitable for Analytical Modelling of Electric Machines," *IEEE*, 2006.
- [7] D. Staton, S. Pickering, and Desmond Lampard, University of Nottingham, "Recent Advancement in the Thermal Design of Electric Motors," *SMMA 2001 Fall Technical Conference "Emerging Technologies for Electric Motion Industry"*, Durham, North Carolina, USA, pp. 3-5 Oct 2001.
- [8] P. H. Mellor, D. Roberts, and D. R. Turner, "Lumped parameter thermal model for electrical machines of TEFC design," *IEEE Proceedings - B*, vol. 138, September 1991.

- [9] A. Boglietti, A. Cavagnino, and D. A. Staton, "TEFC Induction Motors Thermal Models: A Parameter Sensitivity Analysis," *IEEE Transactions on Industry Applications*, vol. 41, May/June 2005.
- [10] A. Boglietti, A. Cavagnino, and D. Staton, "Determination of Critical Parameters in Electrical Machine Thermal Models," in *42nd Annual Meeting of the IEEE-Industry-Applications-Society*, New Orleans, LA, 2007, pp. 1150-1159.
- [11] H. P. Liu, V. Lelos, and C.S. Hearn, Center for Electromechanics, The University of Texas at Austin, "Transient 3-D Thermal Analysis for an Air-Cooled Induction Motor," *IEEE*, 2005.
- [12] A. Boglietti, A. Cavagnino, D. Staton, M. Shanel, M. Mueller, and C. Mejuto, "Evolution and Modern Approaches for Thermal Analysis of Electrical Machines," *IEEE Transactions on Industrial Electronics*, vol. 56, March 2009.
- [13] A. Bejan and A. D. Kraus, *Heat Transfer Handbook*. New Jersey: John Wiley & Sons, Inc., 2003.
- [14] Incropera, DeWitt, Bergman, and Lavine, *Fundamentals of Heat and Mass Transfer*, Sixth ed.
- [15] C. Micallef, S. J. Pickering, K. A. Simmons, and K. J. Bradley, "An Alternative Cooling Arrangement for the End Region of a Totally Enclosed Fan Cooled (TEFC) Induction Motor," in *Power Electronics, Machines and Drives, PEMD 2008 - 4th IET Conference*.
- [16] J. Mugglestone, D. Lampard, and S. J. Pickering, "Effects of end winding porosity upon the flow field and ventilation losses in the end region of TEFC induction machines," *IEEE Proc.-Electr. Power Appl.*, vol. 145, September 1998.
- [17] D. Staton, M. Popescu, C. Cossar, M. McGilp, S. Omari, and T. Kurimoto, "Analytical Thermal Models for Small Induction Motors & Thermal Analysis," in *ICEM Vilamoura*, Portugal, 2008.
- [18] B. Yazicioglu and H. Yuncu, "Optimum fin spacing of rectangular fins on a vertical base in free convection heat transfer," *Heat Mass Transfer*, pp. 11 - 21, 2007.

- [19] B. Yazicioglu and H. Yuncu, "A Correlation for Optimum Fin Spacing of Vertically - based Rectangular Fin Arrays subjected to Natural Convection Heat Transfer," *Journal of Thermal Science and Technology*, pp. 99-105, 2009.
- [20] W. M. Rohsenow, J. P. Hartnett, and E. N. Ganic, *Handbook of Heat Transfer Fundamentals*, Second ed. USA: McGraw - Hill Book Company, 1973.
- [21] D. A. Staton and E. So, "Determination of Optimal Thermal Parameters for Brushless Permanent Magnet Motor Design," *IEEE*, 1998.
- [22] D. A. Staton, "Thermal Analysis of Naturally Ventilated Servo Motor Housings," *Control Techniques R&D*.
- [23] D. W. V. D. Pol and J. K. Tierney, "Free Convection Nusselt Number for Vertical U-Shaped Channels," in *Transactions of the ASME*, 1973.
- [24] A. Bar-Cohen, M. Iyengar, and A. D. Kraus, "Design of Optimum Plate-Fin Natural Convective Heat Sinks," *Journal of Electronic Packaging*, vol. 125, June 2003.
- [25] C. D. Jones and L. F. Smith, "Optimum Arrangement of Rectangular Fins on Horizontal Surfaces for Free-Convection Heat Transfer," *Journal of Heat Transfer*, Feb 1970.
- [26] H. Yuncu and G. Anbar, "An experimental investigation on performance of rectangular fins on a horizontal base in free convection heat transfer," *Heat and Mass Transfer*, vol. 33, pp. 507 - 514, 1998.
- [27] J. R. Simonson, *Engineering Heat Transfer*, Second ed. London: The Macmillian Press Ltd., 1988.
- [28] M. Sasikumar and C. Balaji, "Optimization of convective fin systems: a holistic approach," *Heat and Mass Transfer*, vol. 39, pp. 57 - 68, 2002.
- [29] A. Brown, "Optimum Dimensions of Uniform Annular Fins," *Journal of Heat and Mass Transfer*, vol. 8, pp. 665 - 662, 1965.
- [30] M. M. Yovanovich, J. R. Culham, and T. F. Lemczyk, "Simplified Solutions to Circular Annular Fins with Contact Resistance and End Cooling," *Journal of Thermophysics*, vol. 2, Jan 1986.

- [31] S. Yildiz and H. Yuncu, "An experimental investigation on performance of annular fins on a horizontal cylinder in free convection heat transfer," *Heat and Mass Transfer*, vol. 40, pp. 239-251, 2004.
- [32] G. Y. Kahwaji and Z. M. Al-Makhyoul, "Validation of the Total Resistance Heat Dissipation Model for Heat Transmission through Annular Fins," *Al-Rafidain Engineering*, vol. 14, 2006.
- [33] C.-Y. Lai, H.-S. Kou, and J.-J. Lee, "Optimum thermal analysis of annular fin heat sink by adjusting outer radius and fin number," *Applied Thermal Engineering*, vol. 26, pp. 927-936, 2006.
- [34] H. T. Chen and W. L. Hsu, "Estimation of heat transfer coefficient on the fin of annular-finned tube heat exchangers in natural convection for various fin spacings," *International Journal of Heat and Mass Transfer*, vol. 50, pp. 1750-1761, 2007.
- [35] M. H. Sharqawy and S. M. Zubair, "Efficiency and optimization of an annular fin with combined heat and mass transfer - An analytical solution," *International Journal of Refrigeration*, vol. 30, pp. 751 - 757, 2007.
- [36] B. Kundu and P. K. Das, "Performance and optimum design analysis of convective fin arrays attached to flat and curved primary surfaces," *International Journal of Refrigeration*, vol. 32, pp. 430 - 443, 2009.
- [37] H. H. Keller and E. V. Somers, "Heat Transfer from an Annular Fin of Constant Thickness," *Journal of Heat Transfer ASME*, vol. 81, pp. 151 - 156, May 1959.
- [38] M. Toda, "Voltage-induced large amplitude bending device - PVF2 bimorph - its properties and applications," *Ferroelectrics*, vol. 32, 1981.
- [39] T. Acikalin, I. Sauciuc, and S. V. Garimella, "Piezoelectric Actuators for Low-Form-Factor Electronics Cooling," *ASME Summer Heat Transfer Conference*, vol. 2, 2005.
- [40] T. Acikalin, A. Raman, and S. V. Garimella, "Two-dimensional streaming flows induced by resonating, thin beams," *J. Acoust. Soc. Am.* 114 (4), Pt. 1, 2003.

- [41] P. Bürmann, A. Raman, and S. V. Garimella, "Dynamics and Topology Optimization of Piezoelectric Fans," *IEEE Transactions on Components and Packaging Technologies*, vol. 25, 2003.
- [42] T. Acikalin, S. M. Wait, S. V. Garimella, and A. Raman, "Experimental Investigation of the Thermal Performance of Piezoelectric Fans," *Heat Transfer Engineering*, vol. 25, pp. 4 - 14, 2004.
- [43] S. J. Croucher, N. J. Lawson, K. K. L. Kummari, H.-C. Chung, Z. Huang, and R. Whatmore, "Stereoscopic PIV Analysis of an Oscillating Piezoelectric Unimorph," in *13th Int Symp on Applications of Laser techniques to Fluid Mechanics* Lisbon, Portugal, 2006.
- [44] M. Kimber, S. V. Garimella, and A. Raman, "Local Heat Transfer Coefficients Induced by Piezoelectrically Actuated Vibrating Cantilevers," *Transactions of the ASME*, vol. 129, 2007.
- [45] S. M. Wait, S. Basak, S. V. Garimella, and A. Raman, "Piezoelectric Fans Using Higher Flexural Modes for Electronics Cooling Applications," *IEEE Transactions on Components and Packaging Technologies*, vol. 30, March 2007.
- [46] H.-C. Chung, K. L. Kummari, S. J. Croucher, N. J. Lawson, S. Guo, and Z. Huang, Cranfield University, "Coupled piezoelectric fans with two degree of freedom motion for the application of flapping wing micro aerial vehicles," *Sensors and Actuators* vol. A 147, pp. 607-612, 2008.
- [47] M. Kimber, S. V. Garimella, and Arvind Raman, Cooling Technologies Research Center, Purdue University, "An Experimental Study of Fluidic Coupling Between Multiple Piezoelectric Fans," *IEEE*, 2006.
- [48] R. R. Schmidt, "Local and Average Transfer Coefficients on a Vertical Surface due to Convection from a Piezoelectric Fan," *Intersociety Conference on Thermal Phenomena*, 1994.
- [49] M. Kimber, K. Suzuki, N. Kitsunai, K. Seki, and Suresh V. Garimella, Cooling Technologies Research Center Purdue University, USA, "Quantification of Piezoelectric Fan Flow Rate Performance and Experimental Identification of Installation Effects," *IEEE*, 2008.
- [50] [www.piezo.com](http://www.piezo.com), Woburn, MA, USA: *Piezo Systems INC*.

- [51] K. Toth, "Examination of Heat Transfer Conditions of Finned Motor Case for Shell-Heated Motors," *Department of Electric Machines, Technical University, Budapest*, vol. 24, pp. 169 - 178, 1980.
- [52] *MotorCAD*, available from: [www.motor-design.com](http://www.motor-design.com).
- [53] G. M. Gilson, S. J. Pickering, D. Hann, and C. Gerada, University of Nottingham, "Analysis of the End Winding Heat Transfer variation with Altitude in Electric Motors," in *Industrial Electronics, IECON '09 - 35th Annual Conference of IEEE Porto, Portugal*, 2009, pp. 2545 - 2550.
- [54] G. M. Gilson, T. Raminosa, S. J. Pickering, C. Gerada, and D. Hann, "A Combined Electromagnetic and Thermal Optimisation of an Aerospace Electric Motor," in *XIX International Conference on Electrical Machines Rome, Italy*, 2010, pp. 1 - 7.
- [55] F. Smith, "Carbon Fibre Based Heating Elements," in *Materials Works*. vol. 9, December 2001, pp. 17-18.
- [56] S. J. Kline and F. A. McClintock, "Describing uncertainties in single-sample experiments. ," *Mechanical Engineering*, p. 6, Jan 1953.
- [57] J. Westerweel, "Fundamentals of digital particle image velocimetry," *Meas. Sci. Technol.*, vol. 8, pp. 1379 - 1392, 1997.
- [58] J. Westerweel, "Theoretical analysis of the measurement precision in particle image velocimetry," *Experiments in Fluids*, vol. S3 - S12, 2000.
- [59] M. Raffel, C. Willert, and J. Kompenhans, *Particle Image Velocimetry*: Springer, 1998.
- [60] R. J. Adrian and J. Westerweel, *Particle Image Velocimetry*: Cambridge University Press, 2011.
- [61] S. M. Wait, S. Basak, S. V. Garimella, and A. Raman, "Piezoelectric Fans Using Higher Flexural Modes for Electronics Cooling Applications," *IEEE Transactions on Components and Packaging Technologies*, vol. 30, 2007.
- [62] M. J. Fagan, *Finite Element Analysis Theory and Practice*: Prentice Hall (UK), 1992.

## References

- [63] R. J. Adrian, "Twenty years of particle image velocimetry," *Experiments in Fluids*, vol. 39, pp. 159-169, 2005.
- [64] "Dantec Dynamics," *Reference Manual*.
- [65] B. D. Reddy, "Convergence of Mixed Finite Element Approximations for the Shallow Arch Problem," *Numerische Mathematik*, pp. 687-700, 1988.